University of Nevada, Reno

Timescales and mechanisms of crustal thickening and post-orogenic extension in the North American Cordillera

A dissertation submitted in partial fulfillment of the requirements for the degree of

Doctor of Philosophy in Geology

by

Drew Alexander Levy

Dr. Andrew V. Zuza/Dissertation Advisor

May 2022

THE GRADUATE SCHOOL

We recommend that the dissertation
prepared under our supervision by

DREW ALEXANDER LEVY

entitled

Timescales and mechanisms of crustal thickening and post-orogenic extension in the North American Cordillera

be accepted in partial fulfillment of the
requirements for the degree of

DOCTOR OF PHILOSOPHY

Andrew V. Zuza, Ph.D.
Advisor

Stacia M. Gordon, Ph.D.
Committee Member

Wenrong Cao, Ph.D.
Committee Member

Philipp Ruprecht, Ph.D.
Committee Member

Adam Z. Csank
Graduate School Representative

David W. Zeh, Ph.D., Dean
Graduate School

May 2022

ABSTRACT

Plate boundary forces are transmitted far into the interior of continents creating wide orogenic belts that modify large continental regions and extends geological hazards far from plate margins. Understanding the mechanisms that accommodate intracontinental deformation requires knowledge of the timescales over which fault systems develop in relation to other components of the orogenic system. The Basin and Range province is wide zone of distributed crustal extension that developed within the hinterland of the North American Cordillera. Extensional exhumation of the hinterland crust exposes the contractional structures that accommodated crustal shortening and thickening within the Cordillera. Evaluating the timing, magnitude and kinematics of hinterland thrust belts improves our understanding of the mechanisms of crustal thickening during Mesozoic orogenesis, and the effect on the Cenozoic tectonics of western North America. Furthermore, factors controlling the initiation of extension and the significance of metamorphic core complexes in the evolution of the Basin and Range province remain debated. To understand the factors controlling the timing and localization of initial Basin and Range extension, and the influence of Mesozoic orogenesis, this dissertation presents an integrated study of initial subduction initiation and crustal shortening along the incipient convergent North American plate boundary and the Jurassic to Miocene structure, metamorphism and magmatism within the Sevier hinterland of northeast Nevada and northwest Utah, USA.

We investigated the driving mechanism of the Permian Last Chance thrust system in southwest Laurentia to understand the transition from transform margin to subduction zone prior to the development of the Mesozoic Cordilleran arc. Here we present the results of new geological mapping, detrital zircon U-Pb geochronology, and a synthesis of regional tectonics to inform a kinematic model of the Last Chance thrust system and outline the Permian-Triassic tectonic evolution of the plate boundary during induced subduction initiation. The evolution of this transpressional system and subduction zone is recorded by development of the Last Chance thrust system of the Death Valley region. Geological

mapping in the Last Chance Range, northern Death Valley National Park, and the Inyo Mountains reveals the east-directed Last Chance thrust system was constructed by repetitive out-of-sequence deformation consistent with transpressional strain. The Last Chance thrust system accommodated a minimum of >75 km (60%) shortening across these thrust faults, based on cross-section restorations guided by regional stratigraphic relationships and restoration of subsequent Mesozoic deformation. Large-magnitude shortening along the CCt accommodated a significant component of the convergent plate motion as the Panthalassan crust was thrust below the continental margin before initial slab sinking.

Development of the Last Chance thrusts system accommodated initial thickening of the Cordilleran hinterland. Early to Late(?) Jurassic crustal shortening progressed eastward in the retroarc region, which likely played a key role in the cumulative thickening of the hinterland region. Understanding the timing and magnitude of Jurassic shortening in modern northeast Nevada is key to resolve the crustal structure of the Cordillera and the influence on subsequent extensional tectonics.

The Elko extensional domain of northeast Nevada encompasses the set of highly extended ranges from the Ruby Mountains in the west to the Grouse Creek Mountains in the east. The kinematic development of the Pilot-Toano ranges, within the eastern Elko extensional domain, was reconstructed and $^{40}Ar/^{39}Ar$ thermochronology and zircon U-Pb geochronology were applied to constrain the timing of faulting. Retrodeformation of ~30 km of extension along the Pilot Peak detachment fault and later high-angle normal faults yields the structure of the Middle-Late Jurassic thrust belt of the Elko Orogeny. Northeast striking thrust faults accommodated ~12 km of shortening and <5 km of burial of the Neoproterozoic-lower Cambrian section in the lower plate. Initial extensional faulting 20-15 Ma was accommodated by the Pilot Peak detachment fault, which initiated at high angle and rooted into and reactivated the regional Late Jurassic thrust décollement. Imbrication of the upper plate resulted in east-tilted fault blocks and a west-migrating extensional front that propagated westward to the Ruby Mountains-East Humboldt Range (REH) metamorphic core complex. Despite exposing the same Neoproterozoic-Cambrian

protolith as the REH metamorphic core complex, the Pilot-Toano ranges lack extensive Oligocene intrusions and high-strain mylonitic fabrics.

The kinematics and conditions of the REH mylonitic shear zone were evaluated using field study, microstructural analysis and thermobarometry to understand the mechanisms controlling its development. Field observations indicates the 0.75-1 km-thick mylonite zone accommodated >80% attenuation of the originally 3.5 km-thick Neoproterozoic-Ordovician stratigraphic section. Microstructural analysis of REH mylonites indicates general shear strain at strain rates of 10^{-13} to 10^{-12} s^{-1} at temperatures of 400–600°C. Cross-cutting intrusions bracket mylonitic shear between 29 and 17 Ma, but thermochronology records cooling below the nominal temperature limit of quartz crystal plasticity (350 °C) by 23 Ma. The mylonite zone is thus ~10 Myr older than extensional exhumation of the range after 16 Ma. To explain these data, we argue 40-29 Ma magmatism and remobilization of Late Cretaceous leucogranitic melts enhanced mid-crustal buoyancy. Reduced viscosity due to thermal, melt and fluid-related weakening facilitated diapiric flow accommodated by attenuation of the mylonitic shear zone. This model is consistent with regional field relationships indicating minimal upper crustal extension prior to the Middle Miocene.

The key finding of this research is the protracted episode of Eocene-Oligocene melting within the Ruby Mountains-East Humboldt Range (REH) following initial ca. 39 Ma magmatism controlled the Oligocene development of the metamorphic core complex due to buoyancy driven crustal flow. Thus, the REH mylonite zone is not a result of a large-displacement low-angle normal fault. Pre-existing structures of the Late Jurassic thrust belt controlled the geometry of initial Early to Middle Miocene extensional faulting regionally, however the presence of high-strain mylonitic fabrics focused large-magnitude extension during Middle Miocene unroofing the REH metamorphic core complex. The Basin and Range metamorphic core complexes may thus be expressions of focused Eocene-Oligocene heating rather than records of initial collapse within the Sevier hinterland.

This dissertation is dedicated to my late grandparents Alan Levy and Anne Herstein.

ACKNOWLEDGEMENTS

My PhD has been an opportunity for me to pursue my interests in geology and grow into a scientist. The guidance and support of my advisor Dr. Andrew Zuza has allowed me to pursue that opportunity to the fullest extent. I have been able to explore many different topics and methods during my PhD, and despite his efferts to rein me in, he has backed me in all these endeavors. Andrew has been a dedicated mentor and made a consistent effort to help me hone my skills as a researcher and member of the geoscience community. Andrew and I graduated at the same ceremony at UCLA in 2016 -- him with his PhD and me with by BS. I started at UNR a year later as his first student, which was probably risky. However, I truly could not have asked for a better advisor, which is a testament to Andrew's brilliance as a scientist and mentor.

This experience at UNR would not be the same without the mentorship I received from Drs. Stacia Gordon, Wenrong Cao and Philipp Ruprecht. Their dedication to fostering a rigorous academic training ground for us students was constant, and consistently forced me to learn outside my comfort zone. Stacia has been a valued mentor and collaborator, and I owe my knowledge and interest in petrochronology to her. She has taught me to conduct my research with an acute attention to detail and high level of precision required in microanalytical studies, and these lessons have greatly influenced the scientists I have become. I am thankful to all the other faculty that acted as my teachers, including Chris Henry, Steve Wesnousky, Joel Scheingross, Mike Darin and Seth Dee.

Graduate school is much easier with "older siblings" to guide you along your path. Joel DesOrmeau helped me more than anyone through my PhD, and taught me an endless list of skills required to analyze rocks using electron beams and lasers. Peter Haproff and Margo Odlum have been great mentors and collaborators as I have grown into the scientists and am today, and their generosity is greatly appreciated.

I may not have started this journey to become a scientist if it were not for the teachers and professors that piqued my interest in the Earth and encouraged me along the way,

including Mark Robinson, John Tuberville, An Yin, Ray Ingersoll, Jon Aurnou and Sinan Akciz.

Thanks to all my fellow students who became the incredible group of friends that make grad school a fun and exciting time, including Mike Say, Colin Chupic, Scott Feehan, Heather Winslow, Jason Craig, Kurt Kraal, Ellyn Huggins, Ian Pierce, Josh Sturtevant, Emily Dektar, Ann Hanson, Gary McGaughey, Conni De Masi, Li Bing, Lizzie Langdon-Lassagne, and Sophie Rothman among many others.

I am truly grateful and fortunate to have had such a dedicated and supportive partner by my side these last five years. Haley has always been there to be my cheerleader and my voice of reason during challenging and stressful episodes of grad school. Her passion for science and nature is inspiring and motivates me to think beyond my bubble and appreciate the intricacies of the world around us. I am sure I never would have become interested in reptiles if it were not for her.

I acknowledge my funding sources that have offered generous support for this work, including Sigma Xi, the Geological Society of America, Earthscope, the Geological Society of Nevada, the University of Nevada Graduate Student Association, the United States Geological Survey and the National Science Foundation.

I want to thank my parents for the support they have given me to pursue my passions. They never once questioned my path or discouraged me. Lastly, I want to thank my Zach, Amanda, Tyler, Ari, and Rory for always being there to support me and cheer me on.

TABLE OF CONTENTS

LIST OF TABLES

LIST OF FIGURES

Chapter 1

Chapter 2

Chapter 1: Introduction to the dissertation

TECTONIC EVOLUTION OF A CORDILLERAN OROGENIC BELT

Earth's major mountain belts form at convergent plate margins during oceanic-continental subduction (accretionary) or continental collision (Dewey and Bird, 1970; Cawood et al., 2009). These mountain belts are generated through a history of continental deformation that varies from orogen to orogen, however, similar mechanisms of crustal thickening and eventual post-orogenic extension, or collapse, are applied to accretionary and collisional orogens (McQuarrie, 2002; McQuarrie et al., 2005; Zhao et al., 2011; Armijo et al., 2015; Zuza et al., 2019). Our analysis of crustal thickening in modern orogens is limited to surficial study and geophysical imaging of the crust (Clark and Royden, 2000; Yuan et al., 2000; McQuarrie et al., 2005; Zhao et al., 2011; Gao et al., 2013; Ye et al., 2015; Zuza et al., 2016). Similarly, investigations of orogenic collapse focus on ancient orogens of which the history of orogenic growth is often uncertain due to subsequent overprinting (e.g., Coney and Harms, 1984; Lister et al., 1984; Dewey, 1988; Malavieille, 1993; Fossen, 2000; Teyssier et al., 2005). These limitations in studying the full orogenic cycle inhibit our understanding of the diversity of crustal deformation mechanisms, and lead to poor analogies between modern and ancient orogens (e.g., Long, 2012).

The North American Cordillera has been a classic case study of the tectonic evolution of accretionary orogens and is often compared to the modern Andes (Allmendinger, 1992; DeCelles, 2004; DeCelles and Coogan, 2006). Furthermore, the Cordilleran metamorphic core complexes and Basin and Range province, located within the hinterland of the Cordillera, have been cited as examples of orogenic collapse analogous to the future Himalayan-Tibetan or Andean orogens (Molnar and Chen, 1983; Coney and Harms, 1984; Dewey, 1988). These comparisons rely on our knowledge of the timing and magnitude of crustal thickening, as well as the timing and mechanisms of initial post-orogenic extension. Whereas the Canadian Cordillera preserves a record of large-magnitude crustal shortening and thickening followed immediately by orogenic collapse and extensional exhumation of the deep crust (Vanderhaeghe and Teyssier, 1997; Teyssier et al., 2005; Gordon et al., 2008), the Sevier orogenic belt of the U.S. Cordillera records a different history where the magnitude and mechanisms of crustal thickening, and the relationship between crustal thickening and post-orogenic extension, remain uncertain (Fig. 1.1; Camilleri and

Chamberlain, 1997; Wells et al., 2012; Long et al., 2014, 2015; Long, 2015; Zuza et al., 2020, 2021). Reexamination of the tectonic evolution Sevier orogenic belt is warranted to better understand the mechanisms of crustal thickening and post-orogenic extension, and whether similar mechanisms should be expected between accretionary and collisional orogens.

The goal of this investigation is to understand timing and kinematics of Mesozoic crustal shortening within the Sevier hinterland, and the effect of pre-existing structures, metamorphism and magmatism on the timing and kinematics of post-orogenic extension and development of the Basin and Range. The results of this work will provide new insight into the tectonic evolution of the North American Cordillera, and broadly the interactions between shortening, thickening and extension within the retroarc of Cordilleran orogenic belts globally. Through geological mapping and structural analysis, geochronology and thermochronology, and metamorphic petrology, this study integrates information about the rheology of the crust and the thermal and mechanical controls on crustal deformation.

The first phase of this investigation concerns the kinematics of initial crustal shortening along southwestern Laurentia (i.e., ancestral North America) during the Late Paleozoic, and the mechanisms of subduction initiation. The Last Chance thrust system of east-central California is exposed within the exhumed normal fault blocks of the Death Valley region (Fig. 1.1). The kinematics of the thrust system indicate E to SE directed shortening, but the driver of margin-parallel shortening during the Late Paleozoic is uncertain. the Last Chance thrust system may therefore represent initial retroarc shortening, or transpressional crustal shortening during induced subduction initiation along the plate boundary transform. Elucidating the tectonic evolution of the Last Chance thrust system and the Late Paleozoic plate margin advances our understanding of the timing and mechanisms of initial Cordilleran subduction and initiation of the Cordilleran orogenic development.

The second phase of this investigation focuses on a region of the northern Basin and Range of northeast Nevada and northwest Utah, USA, that I informally term the Elko extensional domain, where deep to shallow crustal levels of the Mesozoic Sevier hinterland are exposed in fault blocks exhumed by Basin and Range normal faults (Fig. 1.1). I have

studied two localities within the Elko extensional domain that experienced different extensional exhumation styles despite their pre-extensional proximity. The Ruby Mountains-East Humboldt Range is a classic Cordilleran metamorphic core complex featuring migmatitic Neoproterozoic-Paleozoic passive margin metasedimentary rocks intruded by a pervasive Late Cretaceous leucogranite complex. The Ruby-East Humboldt mylonitic shear zone is considered a type example of mylonitic fabrics developed during large-magnitude extensional faulting. The Pilot-Toano ranges 60 km east expose the same metasedimentary stratigraphy, but the rocks only reached lower amphibolite facies conditions and were intruded by minimal Late Cretaceous leucogranites. The brittle Pilot Peak detachment fault juxtaposes a metamorphic footwall with unmetamorphosed strata in the hanging wall, yet mylonitic fabrics are absent below the detachment. These two localities preserve thick sections of the Mesozoic hinterland crust making it an ideal location to study the mechanisms of intracontinental deformation.

Each chapter of this dissertation after the introduction is written as a stand-alone paper. The second chapter, *Early Permian tectonic evolution of the Last Chance thrust system: An example of induced subduction initiation along a plate boundary transform*, was published in GSA Bulletin in 2021 (Levy et al., 2021). This study focuses on the Last Chance thrust system of northern Death Valley National Park, California, and applies 1:24,000-scale geological mapping, a balanced cross-section model and detrital zircon U-Pb geochronology to evaluate the timing and kinematics of subduction initiation along western North America during the Late Paleozoic. A regional structural analysis is presented using new and existing geological maps that illustrates the development of an out of sequence thrust system with slip direction that evolved through time to become margin parallel. This kinematic model illustrates the development of a partitioned transpressional system, which is consistent with the inferred Permian plate boundary setting along southwest Laurentia. These results integrate with recent investigations of Late Paleozoic tectonics in eastern California to illustrate a model of Early Permian induced subduction initiation along the nascent North American convergent plate margin.

The third chapter, *Mesozoic-Cenozoic thermal and kinematic evolution of the Sevier hinterland and the eastern Basin and Range*, will soon be submitted to Tectonics. This

work focuses on reconstructing the history of extensional and contractional faulting in the Elko extensional domain of northeast Nevada and northwest Utah to understand the thermal and kinematic evolution of the Sevier hinterland during the transition from Mesozoic shortening to Cenozoic Basin and Range extension. Geological mapping is used to construct regional retrodeformable cross sections to generate a kinematic model of hinterland shortening and multiple phases of extension during the Miocene. Argon thermochronology results place constraints on the timing of extensional exhumation. The results illustrate the controls of inherited structures and thermal history on the style of detachment faulting during initial Basin and Range extension.

The fourth chapter, *Buoyant doming generates metamorphic core complexes in the North American Cordillera*, was recently submitted to Geology and is currently in review. The paper builds on the results of Chapter 4 and presents microstructural analysis and Ti-in-quartz thermobarometry of quartzites within the Ruby Mountains-East Humboldt Range mylonitic shear zone to evaluate the role of buoyancy in core complex development. The results of these analyses are used to constrain the strain rate and conditions of ductile attenuation, which are used as parameters in an analytical model testing the rate of diapiric ascent due to thermal expansion or melt volume using Stokes flow and Rayleigh-Taylor instability formulations. We conclude the field, microstructural and thermobarometric data can be explained by a model of buoyant doming driven by enhanced melting and heating during the Eocene-Oligocene. The most significant conclusion is the Ruby Mountains-East Humboldt Range mylonitic shear zone developed prior to large-magnitude Middle Miocene extension, but the development of a strong preferred orientation fabric at mid-crustal depths localized brittle extensional faulting 10 Myr later.

The final chapter of the dissertation summarizes the implications of this research for our understanding of the evolution of the Sevier orogenic belt, and mechanisms of continental deformation globally. The results from my investigations of crustal thickening and post-orogenic extension in the Sevier Hinterland are synthesized in a model for the development of the Cordilleran metamorphic core complexes and the transition from Mesozoic shortening to the Cenozoic development of the Basin and Range province.

REFERENCES

Allmendinger, R.W., 1992, Fold and thrust tectonics of the western United States exclusive of the accreted terranes:, doi:10.1130/DNAG-GNA-G3.583.

Armijo, R., Lacassin, R., Coudurier-Curveur, A., and Carrizo, D., 2015, Coupled tectonic evolution of Andean orogeny and global climate: Earth-Science Reviews, v. 143, p. 1–35, doi:10.1016/j.earscirev.2015.01.005.

Camilleri, P.A., and Chamberlain, K.R., 1997, Mesozoic tectonics and metamorphism in the Pequop Mountains and Wood Hills region, northeast Nevada: Implications for the architecture and evolution of the Sevier orogen: GSA Bulletin, v. 109, p. 74–94, doi:10.1130/0016-7606(1997)109<0074:MTAMIT>2.3.CO;2.

Cawood, P.A., Kröner, A., Collins, W.J., Kusky, T.M., Mooney, W.D., and Windley, B.F., 2009, Accretionary orogens through Earth history: Geological Society, London, Special Publications, v. 318, p. 1–36, doi:10.1144/SP318.1.

Clark, M.K., and Royden, L.H., 2000, Topographic ooze: Building the eastern margin of Tibet by lower crustal flow: Geology, v. 28, p. 703–706, doi:10.1130/0091-7613(2000)28<703:TOBTEM>2.0.CO;2.

Coney, P.J., and Harms, T.A., 1984, Cordilleran metamorphic core complexes: Cenozoic extensional relics of Mesozoic compression: Geology, v. 12, p. 550–554, doi:10.1130/0091-7613(1984)12<550:CMCCCE>2.0.CO;2.

DeCelles, P.G., 2004, Late Jurassic to Eocene evolution of the Cordilleran thrust belt and foreland basin system, western U.S.A.: American Journal of Science, v. 304, p. 105–168, doi:10.2475/ajs.304.2.105.

DeCelles, P.G., and Coogan, J.C., 2006, Regional structure and kinematic history of the Sevier fold-and-thrust belt, central Utah: Geological Society of America Bulletin, p. 24.

Dewey, J.F., 1988, Extensional collapse of orogens: Tectonics, v. 7, p. 1123–1139, doi:10.1029/TC007i006p01123.

Dewey, J.F., and Bird, J.M., 1970, Mountain belts and the new global tectonics: Journal of Geophysical Research (1896-1977), v. 75, p. 2625–2647, doi:10.1029/JB075i014p02625.

Fossen, H., 2000, Extensional tectonics in the Caledonides: Synorogenic or postorogenic? Tectonics, v. 19, p. 213–224, doi:10.1029/1999TC900066.

Gao, R., Wang, H., Yin, A., Dong, S., Kuang, Z., Zuza, A.V., Li, W., and Xiong, X., 2013, Tectonic development of the northeastern Tibetan Plateau as constrained by high-resolution deep seismic-reflection data: Lithosphere, v. 5, p. 555–574, doi:10.1130/L293.1.

Gordon, S.M., Whitney, D.L., Teyssier, C., Grove, M., and Dunlap, W.J., 2008, Timescales of migmatization, melt crystallization, and cooling in a Cordilleran gneiss dome: Valhalla complex, southeastern British Columbia: TIMESCALE OF CORDILLERAN MIGMATIZATION: Tectonics, v. 27, p. n/a-n/a, doi:10.1029/2007TC002103.

Levy, D.A., Zuza, A.V., Haproff, P.J., and Odlum, M.L., 2021, Early Permian tectonic evolution of the Last Chance thrust system: An example of induced subduction initiation along a plate boundary transform: GSA Bulletin, v. 133, p. 1105–1127, doi:10.1130/B35752.1.

Lister, G.S., Banga, G., and Feenstra, A., 1984, Metamorphic core complexes of Cordilleran type in the Cyclades, Aegean Sea, Greece: Geology, v. 12, p. 221, doi:10.1130/0091-7613(1984)12<221:MCCOCT>2.0.CO;2.

Long, S.P., 2015, An upper-crustal fold province in the hinterland of the Sevier orogenic belt, eastern Nevada, U.S.A.: A Cordilleran Valley and Ridge in the Basin and Range: Geosphere, v. 11, p. 404–424, doi:10.1130/GES01102.1.

Long, S.P., 2012, Magnitudes and spatial patterns of erosional exhumation in the Sevier hinterland, eastern Nevada and western Utah, USA: Insights from a Paleogene paleogeologic map: , p. 21.

Long, S.P., Henry, C.D., Muntean, J.L., Edmondo, G.P., and Cassel, E.J., 2014, Early Cretaceous construction of a structural culmination, Eureka, Nevada, U.S.A.: Implications for out-of-sequence deformation in the Sevier hinterland: Geosphere, v. 10, p. 564–584, doi:10.1130/GES00997.1.

Long, S.P., Thomson, S.N., Reiners, P.W., and Di Fiori, R.V., 2015, Synorogenic extension localized by upper-crustal thickening: An example from the Late Cretaceous Nevadaplano: Geology, v. 43, p. 351–354, doi:10.1130/G36431.1.

Malavieille, J., 1993, Late Orogenic extension in mountain belts: Insights from the basin and range and the Late Paleozoic Variscan Belt: Tectonics, v. 12, p. 1115–1130, doi:10.1029/93TC01129.

McQuarrie, N., 2002, The kinematic history of the central Andean fold-thrust belt, Bolivia: Implications for building a high plateau: Geological Society of America Bulletin, v. 114, p. 950–963, doi:10.1130/0016-7606(2002)114<0950:TKHOTC>2.0.CO;2.

McQuarrie, N., Horton, B.K., Zandt, G., Beck, S., and DeCelles, P.G., 2005, Lithospheric evolution of the Andean fold–thrust belt, Bolivia, and the origin of the central Andean plateau: Tectonophysics, v. 399, p. 15–37, doi:10.1016/j.tecto.2004.12.013.

Molnar, P., and Chen, W.-P., 1983, Focal depths and fault plane solutions of earthquakes under the Tibetan Plateau: Journal of Geophysical Research: Solid Earth, v. 88, p. 1180–1196, doi:10.1029/JB088iB02p01180.

Teyssier, C., Ferré, E.C., Whitney, D.L., Norlander, B., Vanderhaeghe, O., and Parkinson, D., 2005, Flow of partially molten crust and origin of detachments during collapse of

the Cordilleran Orogen: Geological Society, London, Special Publications, v. 245, p. 39–64, doi:10.1144/GSL.SP.2005.245.01.03.

Vanderhaeghe, O., and Teyssier, C., 1997, Formation of the Shuswap metamorphic core complex during late-orogenic collapse of the Canadian Cordillera: Role of ductile thinning and partial melting of the mid-to lower crust: Geodinamica Acta, v. 10, p. 41–58, doi:10.1080/09853111.1997.11105292.

Wells, M.L., Hoisch, T.D., Cruz-Uribe, A.M., and Vervoort, J.D., 2012, Geodynamics of synconvergent extension and tectonic mode switching: Constraints from the Sevier-Laramide orogen: Tectonics, v. 31, doi:10.1029/2011TC002913.

Ye, Z., Gao, R., Li, Q., Zhang, H., Shen, X., Liu, X., and Gong, C., 2015, Seismic evidence for the North China plate underthrusting beneath northeastern Tibet and its implications for plateau growth: Earth and Planetary Science Letters, v. 426, p. 109–117, doi:10.1016/j.epsl.2015.06.024.

Yuan, X. et al., 2000, Subduction and collision processes in the Central Andes constrained by converted seismic phases: Nature, v. 408, p. 958–961, doi:10.1038/35050073.

Zhao, W. et al., 2011, Tibetan plate overriding the Asian plate in central and northern Tibet: Nature Geoscience, v. 4, p. 870–873, doi:10.1038/ngeo1309.

Zuza, A.V., Cheng, X., and Yin, A., 2016, Testing models of Tibetan Plateau formation with Cenozoic shortening estimates across the Qilian Shan–Nan Shan thrust belt: Geosphere, v. 12, p. 501–532, doi:10.1130/GES01254.1.

Zuza, A.V., Henry, C.D., Dee, S., Thorman, C.H., and Heizler, M.T., 2021, Jurassic–Cenozoic tectonics of the Pequop Mountains, NE Nevada, in the North American Cordillera hinterland: Geosphere, doi:10.1130/GES02307.1.

Zuza, A.V., Thorman, C.H., Henry, C.D., Levy, D.A., Dee, S., Long, S.P., Sandberg, C.A., and Soignard, E., 2020, Pulsed Mesozoic Deformation in the Cordilleran Hinterland and Evolution of the Nevadaplano: Insights from the Pequop Mountains, NE Nevada: Lithosphere, v. 2020, p. 8850336, doi:10.2113/2020/8850336.

Zuza, A.V., Wu, C., Wang, Z., Levy, D.A., Li, B., Xiong, X., and Chen, X., 2019, Underthrusting and duplexing beneath the northern Tibetan Plateau and the evolution of the Himalayan-Tibetan orogen: Lithosphere, v. 11, p. 209–231, doi:10.1130/L1042.1.

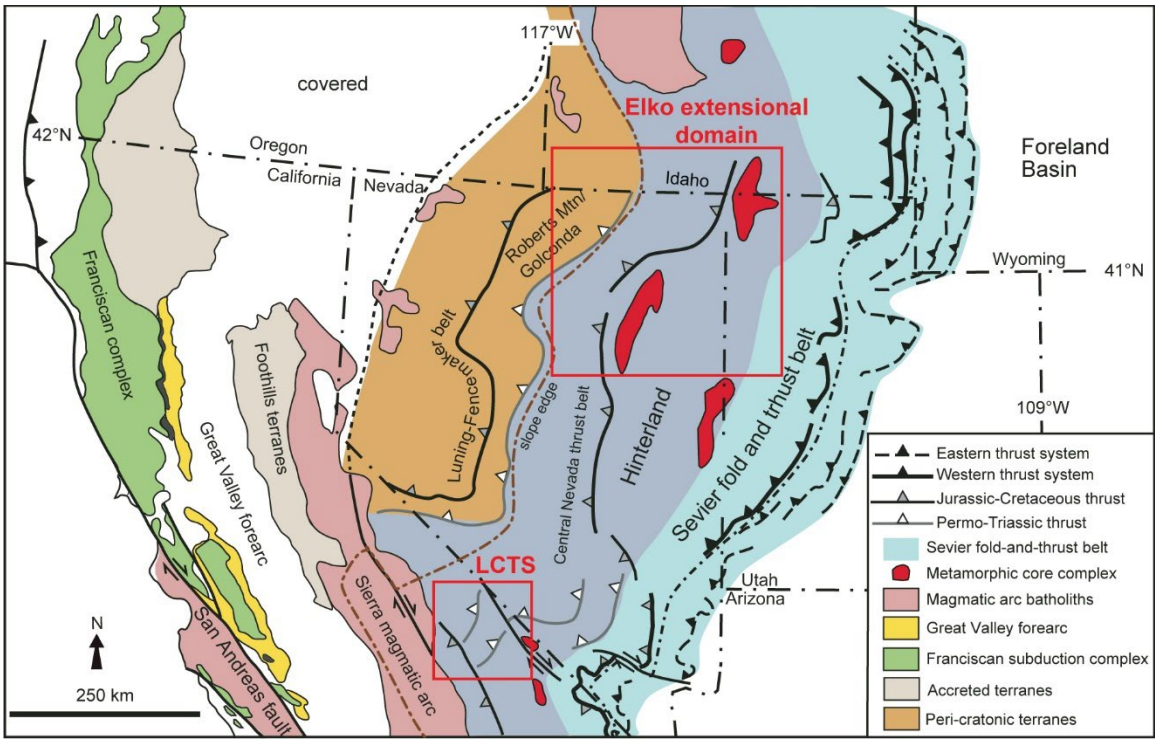

Figure 1.1. Simplified tectonic map of the western United States showing important features of the Sevier orogenic belt within the North American Cordillera. Modified from Gentry et al. (2018). Location of the Last Chance thrust system (LCTS) discussed in Chapter 2 is marked by the red box at the bottom. The locations of Chapter 3 and Chapter 4 study areas are located within the Elko extensional domain marked by the red box at the top.

Chapter 2: Early Permian tectonic evolution of the Last Chance thrust system: An example of induced subduction initiation along a plate boundary transform

Drew A. Levy[1]*, Andrew V. Zuza[1], Peter J. Haproff[2], Margaret L. Odlum[3]

[1]*Nevada Bureau of Mines and Geology, University of Nevada, Reno, NV, 89557, USA*
[2]*Department of Earth and Ocean Sciences, University of North Carolina, Wilmington, NC, 28403, USA*
[3]*Department of Geosciences, Utah State University, Logan, UT, 84322, USA*

This chapter has already been published and is included as part of this dissertation with permission from **GSA Bulletin, v. 133; no. 5/6; p. 1105-1127; doi.org/10.1130/B35752.1; 2021;**

ABSTRACT

We investigated the driving mechanism of the Permian Last Chance thrust system in southwest Laurentia to understand the transition from transform margin to subduction zone prior to the development of the Mesozoic Cordilleran arc. Here we present the results of new geological mapping, detrital zircon U-Pb geochronology, and a synthesis of regional tectonics to inform a kinematic model of the Last Chance thrust system and outline the Permian-Triassic tectonic evolution of the plate boundary during induced subduction initiation. The record of subduction initiation along an inferred late Paleozoic transform fault (the California-Coahuila transform, or CCt) is preserved by (1) Permian arc magmatism, (2) the onset of volcaniclastic sedimentation, and (3) the development of a regional transpressional system in present-day east-central California. The evolution of this transpressional system and subduction zone is recorded by development of the Last Chance thrust system of the Death Valley region. Geological mapping in the Last Chance Range, northern Death Valley National Park, and the Inyo Mountains reveals the east-directed Last Chance thrust system was constructed by repetitive out-of-sequence deformation consistent with transpressional strain. The Last Chance thrust system accommodated a minimum of >75 km (60%) shortening across these thrust faults, based on cross-section restorations guided by regional stratigraphic relationships and restoration of subsequent Mesozoic deformation. Large-magnitude shortening along the CCt accommodated a significant component of the convergent plate motion as the Panthalassan crust was thrust below the continental margin before initial slab sinking. Numerical models show the forces resisting subduction are greatest before initial slab sinking takes place, and compression is transmitted in board from the plate boundary. We argue the Last Chance thrust system developed in response to this compression. Early-middle Permian plutons and late Permian detrital zircons in coeval basins suggest subduction was well established by the early Permian. Collectively, the preservation of a thrust system, early arc magmatism, and syn-tectonic sedimentary basins, features typically destroyed by subduction magmatism and deformation, allow for the evaluation of subduction initiation mechanisms based on field observations.

INTRODUCTION

Understanding subduction zone initiation is critical for evaluating when and how plate tectonics initiated on Earth (Gurnis et al., 2004; Korenega, 2013; Gerya et al., 2015; Stern and Gerya, 2018). Subduction initiation models include spontaneous and induced mechanisms, which each make specific predictions for upper plate extension or compression, the geochemistry and geochronology of supra-subduction zone magmatism, and the tectonic setting at which that mechanism is favored (e.g., Stern, 2004). Although basic chronologies of initial slab sinking have been established using geochemistry and geochronology sampling from near subduction trenches (e.g., Reagan et al., 2010, Stern et al., 2012), these models are difficult to test from the continental geology record because subsequent magmatism destroys evidence of the initial stages of plate convergence. The paucity of actively initiating subduction systems on Earth today also limits study of the crustal response to subduction initiation. Numerical models, however, make predictions for the flexural behavior of the crust during these initial stages, such as the transmission of compression inboard from the plate boundary before initial slab sinking takes place (Gurnis et al., 2004), which would be expressed in the geologic record. Therefore, observations in the geologic record of crustal deformation associated and contemporaneous with subduction initiation can help guide geodynamic models of subduction initiation.

Initiation of the North American Cordilleran subduction system during the late Paleozoic-early Mesozoic remains enigmatic because of overprinting Mesozoic-Cenozoic magmatism and deformation along western North America (Fig. 1). During the Paleozoic, deformation along the western margin of Laurentia—present day Nevada and Idaho—was induced by the Antler and Sonoma orogenies, whereby pelagic strata were thrust onto the continental margin (Fig. 1A; Burchfiel and Davis, 1975; Wyld, 1991). This was not the case to the southwest, where transform faulting and shortening of the continental margin prevailed (Walker, 1988; Snow, 1992; Stevens and Stone, 2005a, 2005b; Lawton et al., 2017). In east-central California and southern Nevada, the Last Chance thrust system accommodated large-magnitude crustal shortening during Permian tectonism, yet the driver of deformation remains unclear (Fig. 1; e.g., Snow, 1992; Stevens et al., 1997; Stevens and Stone, 1988, 2005a, 2005b). Studies of Permian arc-magmatism along the

southwest Laurentian margin suggest subduction initiation was spatially and temporally related to transform tectonics and crustal shortening (Saleeby and Dunne, 2015; Attia et al., 2018; Cecil et al., 2019). A detailed analysis of Permian crustal shortening has yet to be examined in this context. Reexamination of late Paleozoic tectonic features in present-day east-central California using new geologic mapping, structural and tectonic analyses allows us to improve our understanding of the North American Cordilleran evolution. Specifically, the possible link between subduction initiation and the Last Chance thrust system has implications for understanding upper-plate strain during the inception of continental subduction.

To determine the driving mechanisms and tectonic significance of the Last Chance thrust system, we conducted local and regional geologic mapping and structural analysis. We focused on the Last Chance Range (Fig. 2), where the best exposure of the Last Chance thrust allows for the testing of the kinematic predictions of transpression or orthogonal convergence. To better constrain regional correlations and the pre-kinematic geometry of the stratigraphic framework deformed by the Last Chance thrust system, we conducted detrital zircon U-Pb geochronology of regionally extensive lower Cambrian clastic strata, as this interval best represents the passive margin geometry prior to initial Paleozoic deformation (i.e., the Devonian-Mississippian Antler Orogeny). These U-Pb ages are integrated with a growing database of detrital zircon data to improve our resolution of the paleogeography preceding late Paleozoic tectonism. Our geochronologic data and geological mapping allow us to develop a detailed kinematic model of deformation in the Last Chance thrust system. Taken together, we argue for a new model of Permian contraction during transform faulting, which further constrains the tectonic evolution of southwest Laurentia during the transition to a Cordilleran orogenic system.

GEOLOGIC CONTEXT AND STRUCTURAL SETTING

During the late Paleozoic assembly of Pangea, Laurentia was joined with Gondwana along the Ouchita-Marathon suture (Fig. 1A; Colpron and Nelson, 2009; Leary et al., 2018). By the Late Devonian, subduction of the Panthalassa Ocean beneath northwestern

Laurentia formed a series of island arc terranes that later accreted to the continent (e.g., Powerman et al., 2020). Oblique convergence at the southern tip of the subduction zone drove transpression along the southwest Laurentia transform margin (Lawton et al., 2017). This transpressional regime persisted until the late Paleozoic, driving the Late Devonian-Early Mississippian Antler Orogeny—recorded by emplacement of the Roberts Mountains thrust, and episodic Pennsylvanian-Permian contraction in central Nevada (Fig. 1A; e.g., Trexler et al., 2003, 2004; Cashman et al., 2011; Linde et al., 2016, 2017). The Permian-Triassic Sonoma orogeny resulted in closure of the Havallah oceanic back-arc basin and emplacement of basinal strata on the continental margin by the Golconda thrust (Fig. 1A; Wyld, 1991). By the Mesozoic, the southwestern margin had transitioned to a subduction zone, as indicated by observations of Permian plutons in the Mojave Desert and a belt of Triassic plutons between the northern Sierra Nevada and Mexico (Fig. 1B and 1C; Barth et al., 1997, 2011; Cecil et al., 2019).

Late Paleozoic transform motion along the southwest Laurentian margin is a crucial element to understanding the evolution of the Paleozoic-Mesozoic subduction system. The California-Coahuila transform is evidenced by the truncation and transport of passive margin blocks southeastward (Fig. 1; Walker, 1988; Dickinson and Lawton, 2001). This structure is compatible with the inferred kinematics of Laurentia during the late Paleozoic, whereby a transform structure is required to accommodate subduction of Panthalassan lithosphere in northwest Laurentia and Gondwana to the southeast (Fig. 1A; e.g., Dickinson and Lawton, 2001). The California-Coahuila transform is different from the proposed Jurassic Mojave-Sonora megashear, which is inferred to have a similar strike, and offset the same features from the Death Valley region to northern Mexico (e.g., Anderson and Silver, 2005). Geochronologic studies in the Caborca region of northern Mexico (Fig.1B) argue against the megashear hypothesis and posit the Proterozoic basement of the Cabroca Block was present in the region by 190 Ma (e.g., Amato et al., 2009; González-León et al., 2009).

The California-Coahuila transform was active between the Pennsylvanian (e.g., Stone and Stevens, 1988) and the early Triassic (e.g., Walker, 1988). The passive margin carbonate shelf shifted to a southeastward orientation during the Pennsylvanian, and

variations in subsidence and uplift patterns, expressed as facies changes or unconformity, respectively, in the Keeler and Darwin Basins throughout the Pennsylvanian-Permian suggests periodic switches from transtension to transpression along the transform (Stone and Stevens, 1988; Stevens et al., 1997, 2015). Despite the transform being obscured from the rock record, its location is inferred by the boundary between deep marine strata of the El Paso terrane and the Death Valley facies shelf strata (Fig. 1; Walker, 1988). Although assessment of transform-related deformation is hindered by limited exposures of the El Paso terrane (e.g., Walker, 1988), the Permian Last Chance thrust system is well exposed on the eastern side of the transform (e.g., Stevens and Stone, 2005a, 2005b).

The Death Valley thrust system is a series of east-vergent thrusts that generally place Cambrian-Ordovician strata atop Mississippian-Permian strata (Fig. 1C and 2A; Corbett, 1989; Snow, 1992; Stevens and Stone, 2005b). The thrust system developed during at least two periods of contraction. The first is recorded by the Last Chance thrust system, which includes the Eureka and Last Chance thrusts (Fig. 2A). The second period is indicated by a series of low magnitude thrusts that cut older contractional features; this includes the Hanging Rock, Marble Canyon and Lemoigne thrusts. Palinspastic reconstruction of Basin and Range extension in the Death Valley region revealed an original north trend of the Last Chance thrust system (Fig. 2B; Snow and Wernicke, 2000).

Thrust faults of the Sevier fold-thrust belt are also present in east-central California and southern Nevada (Fig. 1, 2). To the west of the Death Valley region (Fig. 2), the Jurassic-Early Cretaceous East Sierran thrust system is a narrow northwest-striking belt of thrust faults that place Paleozoic strata on Jurassic volcanic rocks (Dunne and Walker, 2004). To the east, the Jurassic-Cretaceous Wheeler Pass and Keystone thrusts place Neoproterozoic and Cambrian strata on Permian and Jurassic rocks, respectively (Fig. 2; e.g., Giallorenzo et al., 2018). Palinspastic reconstruction of this area indicates these thrusts are subparallel to thrusts of the Death Valley thrust system (Fig. 2B), and thus may reactivate older thrusts. We posit this is not the case, as the Wheeler Pass thrust exhumes deeper stratigraphy than the Death Valley system (e.g., Giallorenzo et al., 2018), indicating it likely roots at deeper stratigraphic levels.

The Last Chance thrust system is exposed regionally by Neogene normal and transtensional faulting (Fig. 3; Snow, 1992). Minimal Neogene-Quaternary faulting in the Last Chance Range preserves the original structural relationships of the Last Chance thrust (Levy et al., 2018). There, lower Cambrian strata are emplaced atop Mississippian rocks (Stewart et al., 1966; Corbett, 1989). To the west of Eureka Valley, the Eureka thrust is exposed at Jackass Flats, in the Inyo Mountains, where the thrust places Neoproterozoic-lower Cambrian strata over Mississippian strata of the Last Chance thrust hanging wall (Stewart et al., 1966; Corbett, 1989). The pre-Cenozoic tip of the Eureka thrust was likely above Eureka Valley before faulting and erosion concealed this relationship (Fig. 2 and 3; Snow and Wernicke, 2000). Pervasive late Cenozoic deformation in the Cottonwood Mountains largely obscures the Last Chance thrust system (Fig. 2A; Snow, 1992). In the Cottonwood Mountains, the hanging wall of the Last Chance thrust is down dropped into Racetrack Valley, where it forms the roof thrust of the Racetrack duplex system (Fig. 2 and 3; Snow, 1992). Thus, the original tip of the Last Chance thrust can be projected above the Cottonwood Mountains. In the southeastern Cottonwood Mountains, the Marble Canyon thrust places Ordovician Death Valley facies strata over the Permian Darwin Canyon Formation (Fig. 2; Snow, 1992; Stone et al., 2014). The Lemoigne thrust is geometrically similar to the Marble Canyon thrust, and places the middle Cambrian Bonanza King Formation over the Darwin Canyon Formation (Fig. 2; Snow, 1992; Stevens and Stone, 2005a). The Marble Canyon and Lemoigne thrusts do not accommodate a significant amount of shortening in the Death Valley thrust belt. Their regional extent and distinct structural style make these significant for interpreting the structural and tectonic evolution of the Death Valley thrust belt. In general, deformation youngs east (Corbett, 1989; Snow, 1992; Stevens and Stone, 2005a, 2005b). However, the Eureka thrust and minor cross-cutting thrusts throughout the Death Valley thrust system were emplaced out of sequence.

The tectonic setting in which the Last Chance thrust system developed is obscure. Early Permian strata deformed by the thrust system and middle and late Permian strata that overlap thrust system structures bracket the time of thrust system development between early Permian (ca. 300 Ma) and late Permian (ca. 260 Ma; Snow, 1992, Stevens and Stone, 2005a, 2005b). An Early Triassic pluton cross cuts the thrust system, which provides an

absolute timing constraint on deformation (245 Ma; Snow et al., 1991). These constraints preclude development during the Late Devonian-Early Mississippian Antler orogeny (Fig. 1A; Snow, 1992; Stevens and Stone, 2005b). Similarly, development during the Permian-Triassic Sonoma orogeny is incompatible, as the Golconda thrust exposed in the Sierra Nevada was active in the Middle Triassic (Stevens and Greene, 2000). Thus, the Last Chance thrust system likely developed during a localized contractional event not associated with the major Paleozoic orogenies of western North America. Alternatively, the thrust system may have developed during Pennsylvanian-Permian transform faulting. Transpressional fold-thrust development along the southeast-striking California-Coahuila transform offers a viable mechanism for the thrust system (Fig. 1; Stevens and Stone, 2005a, 2005b; Saleeby and Dunne, 2015; Lawton et al., 2017).

Further investigation is required to determine whether transpression can produce the reported 75-km of shortening (Corbett, 1989), or if orthogonal shortening is required. Both scenarios have implications for the evolution of plate margin strain evolution during subduction initiation.

GEOLOGIC MAPPING AND STRUCTURAL GEOLOGY OF THE LAST CHANCE RANGE

We focused new geological mapping in the northern Death Valley region, which is geomorphologically bounded on the west by Owens Valley and on the east by Death Valley (Fig. 3). Both valleys are bisected by right-slip faults that accommodate the majority of southern Walker Lane shear, or 25% of the relative Pacific-North American plate motion (Atwater and Stock, 1998; Faulds and Henry, 2008). Between these fault zones are a series of NE-striking, NW-extending normal faults defining prominent escarpments exposing Paleozoic-Mesozoic contractional structures (Fig. 3). Eureka Valley, which is bounded by the Last Chance Range and Inyo Mountains on the east and west, respectively, is a north trending actively extending basin that accommodates slip transfer from NE-striking normal faults in the Saline Range to the northern Death Valley fault.

We conducted detailed local and regional geological mapping to assess the structural relationships, deformation style, and kinematics. In the Last Chance Range, we mapped the Hanging Rock Canyon 7.5'-quadrangle at 1:24,000-scale (Fig. 3), and conducted $^{40}Ar/^{39}Ar$ dating of several volcanic units (methods in the Supplemental Materials). We made parallel observations via reconnaissance mapping at Jackass Flats (map drafted at 1:70,000-scale), in the Inyo Mountains, which elucidated regional variations in deformation style and kinematics between thrust sheets (Fig. 3). Field observations were supplemented with previous geological maps (McCoard, 1972; Casteel, 1986; Corbett, 1989; Wrucke and Corbett, 1990; Lawson, 2017) to construct a regional cross section and assess the structural geometry of the Last Chance thrust system.

Stratigraphy

The stratigraphy of the Death Valley region is primarily composed of sedimentary rocks of the Neoproterozoic-Paleozoic passive margin sequence (Stewart, 1970; Poole et al., 1992). This includes a Neoproterozoic-lower Cambrian section of sandstones, siltstone, and quartzite overlain by a thick upper Cambrian-Permian carbonate section, with siliciclastic beds present in the Ordovician Eureka Quartzite, and the Mississippian Perdido Formation and Rest Spring Shale (Fig. 4). Paleozoic strata in the northern Death Valley region are generally unmetamorphosed, except where locally intruded by Mesozoic plutons (Fig. 3; Sylvester et al., 1978; Nabelek and Morgan, 2012). The Paleozoic stratigraphy of the Last Chance Range is described by Stewart et al. (1966), McCoard (1972), and Casteel (1986) (Fig. 4). Detailed descriptions of the stratigraphy can be found in the Supplemental Materials.

The Paleozoic stratigraphy of the Last Chance Range is comprised of the lower Cambrian Wood Canyon Formation and the Zabriskie Quartzite, which are dominantly massive to cross-bedded sandstones (Fig. 4). The Carrara Formation consists of interbedded sandstone and shale, which transitions up section to limestone. The Bonanza King Formation is a 1-km-thick section of dolomite, with interbedded limestone near its top. The upper Cambrian through Devonian stratigraphy consists largely of marl and mottled limestone, with dolomite dominating the top of the section (Fig. 4). The

Dunderberg Shale member of the Cambrian Nopah Formation and the Ordovician Eureka Quartzite are distinct siliciclastic marker beds in this section. The Mississippian Perdido Formation is comprised of pebble conglomerate, sandstone and limestone. The highest unit in the section is the Mississippian Rest Spring Shale, which is typically a phylittic shale where exposed.

Field Relationships

Cenozoic Faults

The broad morphology of the Last Chance Range is controlled by late Miocene-Present normal faulting (Fig. 5). Eastward extensional rotation of the Last Chance Range is evidenced by the ~10°E dip of the 5.51 Ma bimodal volcanic sequence (see Supplementary Materials), and 10-20° E dip of uplifted fans and volcanic rocks along the western front of the range (Fig. 5). The range is cut by northeast-striking (*fa*) and north-striking (*fb, fc*) normal faults. *f*-notation for faults refers to exemplar faults in the Last Chance Range (Fig. 5) representative of each faulting episode discussed herein. The northeast-striking faults represent a period of middle-late Miocene faulting, and typically exhibit ~10s to ~100s of meters of offset (Fig. 5). Late Miocene to present extension is expressed by the north-striking normal faults, which decrease in displacement from ~100s to <1 m between the area east of Hanging Rock Canyon and the westernmost range front fault, indicating faults to the west are younger. An outcrop north of Hanging Rock Canyon displays the Bonanza King Formation in low-angle fault contact with the Mississippian Rest Spring Shale (*la*, Fig. 5). We interpret this as a late Neogene landslide block, similar to a landslide block in southern Eureka Valley (Watkins, 2015).

Late Paleozoic Faults

All thrust faults are characterized as late Paleozoic faults based on observed cross-cutting and older-over-younger relationships. Evidence for Mesozoic contraction in the region is limited to the East Sierran thrust system (Fig. 2 and 3). Within our study area, voluminous Jurassic plutons on the west side of Eureka Valley cross-cut Last Chance thrust system contractional structures in the Inyo Mountains (Fig. 3), and do not show evidence for post-emplacement deformation. This relationship only establishes the Last Chance

thrust system as pre-Jurassic in the study area, however we assume late Permian-Triassic strata that overlap Last Chance thrust system features in the southern Inyo Mountains indicate a late Paleozoic assignment is appropriate in the Last Chance Range.

Hanging Wall Ramp (f1) Paleozoic strata of the Last Chance Range generally strike ~340° and dip ~40°E (Fig. 5B and 6A). A component of this dip is due to ~10-20° eastward tilting of the range during the Cenozoic. The remaining dip is related to the hanging wall ramp geometry of the Last Chance thrust, which cuts up section across the map area (Fig. 5C). Rest Spring Shale is the highest footwall unit across the map area, suggesting a footwall flat underlies the Last Chance Range.

Last Chance thrust (f2, f3) The Last Chance thrust is best exposed 1 km east of Hanging Rock Canyon where the Carrara Formation is in contact with the Perdido Formation and the Rest Spring Shale (*f2*, Fig. 5 and 6B). Fault striations trend ~061° and kinematic indicators are consistent with top east shear (Fig. 6C -E). Local duplication of the Carrara Formation is common along this segment of the thrust (Fig. 5). The trace of the Last Chance thrust is obscured to the south by Cenozoic sedimentary deposits of the Crater Mine area (Fig. 5). The Last Chance thrust is also exposed along the southern range front (*f3*, Fig. 5), where the Wood Canyon Formation is thrust over a footwall duplex involving the Perdido Formation. This segment of the Last Chance thrust is in fault contact with an overturned section of the Last Chance thrust.

Hanging Rock Canyon thrust (f4, f5) Mississippian rocks of the Last Chance Range front are thrust over an overturned section of the Last Chance thrust by the Hanging Rock Canyon thrust (*f4*, Fig. 5). This relationship is well exposed along the southern range front, where overturned footwall strata lie above overturned hanging wall strata (Fig. 5D). The Hanging Rock Canyon thrust is reactivated by Cenozoic extension, and the hanging wall of this fault is down dropped along the range front (e.g., fault *f3* is a hanging wall block of the Hanging Rock Canyon thrust that has been down dropped during Cenozoic extension; Fig. 5D). Displacement on the Hanging Rock Canyon thrust is ~100s of m, decreasing to the south (Fig. 5D).

The Hanging Rock Canyon thrust is cut by range front normal faults in the south, but is continuously exposed in the north where a cross-sectional view of the fault is exposed in Hanging Rock Canyon (*f5*, Fig. 5A). The Hanging Rock Canyon thrust overturns the Last Chance thrust into an east-vergent, overturned syncline (Fig. 7), which is pervasively faulted with duplicated slices of Cambrian strata. A key marker bed in the Carrara Formation indicates which sections are upright or overturned within the fold, suggesting a complex faulting history following initial overturning of the fold (Fig. 7).

Structural Geology of the Last Chance Thrust System

Structures of the Last Chance thrust system can be classified into hanging wall or footwall domains. Rocks in the hanging wall strike north-northwest (~340°; *f1*, Fig. 5), and typically dip ~40° into the Last Chance thrust. A north-northwest-striking (320°) hanging wall ramp underlies the Last Chance Range, with the fault cutting up-section to the east (Fig. 5C; Snow, 1992). Footwall rocks tend to parallel the fault orientation, with local duplexing and pinching-out of the uppermost footwall units (*f3*, Fig. 5).

The Last Chance Range records multiple episodes of contraction: initial slip along the Last Chance thrust (*f2*, Fig. 5 and 6B) and a later episode of thrusting which folded and faulted the Last Chance thrust (*f4 and 5*, Fig. 5). The initial phase of contraction is characterized by the Cambrian Carrara Formation in fault contact with the Mississippian Rest Spring Shale and Perdido Formation (*f2*, Fig. 5 and 6B). Near the fault contact, beds in the hanging wall and footwall are sub-parallel (Fig. 6B). Structurally higher levels in the hanging wall are truncated by the thrust at an ~20-40° angle. The Mississippian Rest Spring Shale is strongly deformed and is in places absent from below the Last Chance thrust. This is likely due to pre-thrust folds being beheaded by the Last Chance thrust, and boudinage/pinching out of the Rest Spring Formation. The initial phase of thrusting is characterized by localized ductile shear in weak strata in the hanging wall (Fig. 6G) and strong shearing of footwall strata (Fig. 6E). Strain is generally weak in hanging wall strata. Quartzites of the Carrara Formation above the Last Chance thrust preserve primary detrital grain shape, and do not have a pervasive foliation. Evidence of crystal plastic deformation by dynamic recrystallization is absent. Where quartzite is interbedded with siltstone or

shale, cleavage is well developed in siltstone and shale beds between quartzite (Fig. 6F). Stratigraphically higher, shale and limestone of the Dunderberg Shale member display multiple generations of cleavage development and ductile flow, respectively. In the footwall, the initially fine-grained nature of the Mississippian shale, siltstone and pebble conglomerate makes investigation of deformation mechanisms challenging, but general ductilely deformed chert pebbles and foliation is present. Kinematic indicators in the Perdido Formation pebble conglomerate bed indicate top east simple shear (Fig. 6E). Similarly, upright to gently inclined folds of footwall strata are consistent with east vergence.

The second phase of contraction is challenging to evaluate, as distinct structural relationships are not obvious, and exposures of cross-cutting contractional structures are limited to the northern part of the Last Chance Range. The best location to observe cross-cutting relationships is in Hanging Rock Canyon (Fig. 5), where the Last Chance thrust is faulted and folded into an east vergent overturned syncline (Fig. 7). On the western front of the Last Chance Range, the Last Chance thrust is overturned, with overturned footwall strata juxtaposed above steep overturned hanging wall quartzites (*f4*, Fig. 5). Mississippian rocks exposed along the western piedmont are upright and thrust over the overturned portion of the Last Chance thrust footwall (Fig. 5D and 5E; Casteel, 1986).

The style of deformation during the second contractional phase is predominantly brittle thrust faulting, with folds developing in weak siltstones and limestones of the Cambrian Carrara Formation and Mississippian formations (Fig. 7). For example, at Hanging Rock Canyon, quartzites of the Zabriskie and Carrara formations are pervasively faulted and lie structurally above folded siltstone and limestone of the Carrara Formation (Fig. 7). South of Hanging Rock Canyon, the Mississippian Rest Spring Shale is pervasively folded at the meter to kilometer scale (Fig. 5). It is possible these folds are from the first phase of contraction and have been overprinted during the second phase, but their north to northwest trend suggests they record the second phase (Fig. 5B). Asymmetry of folds and the geometry of the overturned Last Chance thrust indicate the second phase of contraction was east- to east-northeast vergent (Fig. 7). Deformation is localized to the areas

immediately above and below the Hanging Rock Canyon thrust, and it is not apparent that the second phase involved a ramp-flat thrust geometry (Boyer and Elliot, 1982).

In summary, deformation in the Last Chance Range is generally characterized by brittle deformation, with subtle plastic flow localized to the footwall. The presence of Mississippian strata in the footwall of the Last Chance thrusts suggest an extensive footwall flat underlies the thrust panels. Kinematic indicators suggest east-directed transport of thrust sheets and folds consistent with the regional structural geometries prior to Basin and Range extension (Fig. 2B; Snow, 1992).

GEOLOGY OF JACKASS FLATS, INYO MOUNTAINS

Jackass Flats is a structural window in the Inyo Mountains where Mississippian and Devonian rocks are exposed beneath the Eureka thrust (Fig. 3 and 8). There, the Eureka thrust is expressed as a set of thrusts that place Neoproterozoic strata of White-Inyo affinity over Mississippian strata. In the northern Last Chance Range, the Eureka thrust sheet is thrust over the Last Chance thrust sheet (Fig. 3). Descriptions of the Jackass Flats stratigraphy follow those of Nelson (1962), Nelson (1976), Corbett (1989) and Chapman et al. (2015). Detailed descriptions of stratigraphy can be found in the Supplemental Materials.

Stratigraphy

The Neoproterozoic-Cambrian stratigraphy of the White-Inyo Mountains is lithologically distinct from that of the Last Chance Range to the east (Nelson, 1962; Corbett, 1989; Chapman et al., 2015). The lowest exposed unit is the Neoproterozoic Wyman Formation argillite (Fig. 8). The Reed Dolomite consists of dominantly dolomite, with a distinct lens of sandstone (Hines Tongue Member). The Deep Springs Formation is comprised limestone at its base, which transitions upward to sandstone and siltstone with a dolomite cap. The Campito Formation is a thick turbidite sequence of quartz sandstone, siltstone and shale. The Poleta Formation consists of dominantly limestone, with interbedded sandstone and siltstone. The Harkless Formation is primarily a phylittic shale,

and grades upward into the Saline Valley Formation, which is a massive quartz sandstone unit. The Mule Spring Limestone and the Monola Formation are comprised of primarily limestone, with interbedded siltstone and shale. The Monola Formation is overlain by the middle Cambrian Bonanza King Dolomite, which represents the bottom of the upper Cambrian-Mississippian stratigraphic section that is continuous across the Inyo Mountains and Last Chance Range.

Field Relationships

Jackass Flats consists of a set of Cenozoic half-grabens that have exhumed rocks within the footwall of the Eureka thrust (Fig. 8). These normal faults have down-to-the-west displacement of ~10s to ~100s of meters and expose Paleozoic structures in their footwall. The Paleozoic stratigraphy is folded into a north tending anticline that post-dates the Eureka thrust (Fig. 8B). There are two thrusts exposed at Jackass Flats. The structurally highest thrust places the Wyman Formation and Reed Dolomite on the Campito Formation (Fig. 8). This relationship is well exposed along the western flank of Jackass Flats. Below this thrust, the Campito Formation is thrust over the Perdido Formation. On the northeast side of Jackass Flats, this structurally lower thrust placed the Deep Springs Formation atop the Perdido Formation. We conclude the Campito Formation on the west side of Jackass Flats is a horse of a larger thrust duplex, and the roof thrust cuts up section to the east from the Wyman Formation to the Deep Springs Formation (Fig. 8B). To the south, a sliver of the Poleta and Harkless formations is exposed above the Perdido Formation and below the Deep Springs Formation. This is likely another horse of the thrust duplex horse below the main roof thrust.

Structural Geology

Rocks at Jackass Flats are generally more ductilely deformed than other rocks in the study area. For example, limestone layers are stretched around meter-scale boudinage of dolomite and pervasively folded limestone and strongly-foliated siltstone are common. Hanging wall clastic rocks are weakly to moderately foliated, with bedding and cross stratification well preserved. Sigma clasts are common between bedding planes, and generally show top east kinematics. The Eureka thrust continues to the north, where it cuts

the Last Chance thrust (Fig. 3). The continuation of the Eureka thrust in the south is uncertain, but it either dies out into the Lead Canyon Anticline (Fig. 3; Snow, 1992), or is correlated with the Fishhook thrust of the southern Inyo Mountains (Fig. 3; Stevens et al., 1997; Stone et al., 2009).

DETRITAL ZIRCON U-PB GEOCHRONOLOGY

White-Inyo and Death Valley facies

The Neoproterozoic-Paleozoic stratigraphy of eastern California is widely recognized for its continuity through the Neoproterozoic-Cambrian transition which has resulted in a detailed characterization of rocks in the White-Inyo Mountains and the Last Chance Range (Fig. 3; McAllister, 1952; Nelson, 1962, 1978; Stewart, 1965, 1970; Chapman et al., 2015). The Neoproterozoic-Cambrian White Inyo facies and Death Valley facies represent the respective outer and inner shelf strata. The Inyo Mountains and Saline Range are composed of the White-Inyo Mountains facies (Fig. 3), whereas the Last Chance Range and Cottonwood Mountains are composed of the Death Valley facies. The abrupt transition from White-Inyo to Death Valley facies across Eureka Valley (~10 km distance), in the context of the >150 km width of the modern western Atlantic passive margin shelf, suggests these assemblages are juxtaposed by the Eureka thrust (Corbett, 1989; Snow, 1992). Understanding the pre-deformation geometry of the passive margin and the spatial correlations between White-Inyo and Death Valley facies strata are important for evaluating the geometry and kinematics of thrust development.

Correlation of White-Inyo and Death Valley facies stratigraphy is based on the biostratigraphy of *Girvanella* stromalite and trilobite fossils (Supplemental Fig. S3; Nelson, 1976). Comparison of correlated lithologies indicates the White-Inyo strata represent the deeper-water equivalents of the Death Valley facies. In this study, we conducted detrital zircon U-Pb geochronology of Cambrian strata in the Inyo Mountains and the Last Chance Range to further correlate strata of the White-Inyo facies, the Death Valley facies, and the Snow Lake terrane (Fig. 1 and 3). The latter objective has implications in constraining the inferred reactivation of the Last Chance thrust in the Mesozoic (Chapman et al., 2015; Saleeby and Dunne, 2015). We also tested stratigraphic

correlations of the Death Valley facies and Cambrian siliciclastic strata of the Caborca block (Fig. 1; Stewart et al., 1984; Farmer et al., 2005), which has implications for estimating the amount of displacement across the California-Coahuila transform (e.g., Dickinson, 2000; Dickinson and Lawton, 2001).

Detrital Zircon U-Pb Geochronology Methods

We collected 7 samples in the White-Inyo Mountains and Last Chance Range for detrital zircon U-Pb geochronology (Fig. 3). U-Pb analyses were conducted at The University of Texas at Austin in the UT Chron LA-ICP-MS laboratory on the PhotonMachine Analyte G.2 Excimer laser with a large-volume Helex sample cell and a Thermo Element2 ICP-MS. Additional U-Pb analyses were performed at the Institute of Tibetan Plateau Research, Chinese Academy of Science on the Agilent 7500a Q-ICP-MS with an ArF laser-ablation system following the analytical procedures outlined in Xie et al. (2008). We randomly picked 100-200 grains from each sample for analysis (Gehrels et al., 2008; Gehrels, 2014). Detailed geochronology methods including sample preparation and instrument settings can be found in the Supplemental Materials. Data are displayed on a normalized relative probability plot using the program DZ Stats v2.3 (Saylor and Sundell, 2016).

A set of 24 detrital zircon U-Pb data sets were compiled from existing studies for comparison with our data (Table 1; Grasse et al., 2001; Barth et al., 2009; Maclean et al., 2009; Memeti et al., 2010; Schoenborn et al., 2012; Gehrels and Pecha 2014; Chapman et al., 2015; Attia et al., 2018). The compilation includes samples from four distinct Neoproterozoic-Cambrian sedimentary sequences in eastern California including the Snow Lake terrane—a group of metasedimentary roof pendants in the Sierra Nevada, the White-Inyo facies, the Death Valley facies, the Mojave facies—the southwestern extension of the Death Valley facies, and the Caborca Block—a sequence of Neoproterozoic-Cambrian inner shelf siliciclastic strata in northern Mexico (Fig. 1). These data were largely sourced from a compilation of 157 samples from Paleozoic-Mesozoic strata of western North America by Attia et al. (2018). Likewise, a thorough study of detrital zircon provenance and paleogeography of the Sierra Nevada–White-Inyo Mountains region by Chapman et

al. (2015) provides a foundation for our analysis of the White-Inyo and Death Valley facies. Data filtering and reporting follows the convention of the study in which the data was first reported. The similarities of detrital zircon age spectra were characterized by the multi-dimensional scaling algorithm using the MuDiSc v2.5 Matlab-GUI (Vermeesch, 2013).

U-Pb Data Results

White-Inyo Facies

Ten samples from the Neoproterozoic-Cambrian section of the White-Inyo facies show remarkably similar age populations (Fig. 9A). These data include minor age populations between 2.0 Ga and > 4.0 Ga. The major population in the White-Inyo facies is at 1.78 Ga, with a smaller subpeak at 1.7 Ga. The Andrews Mountain Member of the Campito Formation is an exception, with a major population at 1.1 Ga, and subsidiary populations up to 1.9 Ga.

Death Valley Facies

The Neoproterozoic-Cambrian section of the Death Valley facies show more variation than the White-Inyo age spectra (Fig. 9A). Age population peaks at 1.7–1.78 Ga are distinct, with a minor population—major in the Zabriskie Quartzite—1.8–1.9 Ga. Additional subpopulations at 1.0–1.2 Ga, and between the Paleoproterozoic and Archean are common.

Mojave Facies

Detrital zircon data from the Sterling Quartzite, Wood Canyon Formation, and the Zabriskie Quartzite of the Mojave Desert region show three primary peaks: 1.68–1.7 Ga, 1.4–1.45 Ga, and 1.09–1.21 Ga. Minor age populations in the Paleoproterozoic-Archean are present.

Snow Lake Terrane

Lithologic and detrital zircon age data from rocks of the Snow Lake terrane, preserved in roof pendants of the Sierra Nevada batholith (Fig. 1), have been used to suggest these rocks are related to the Death Valley facies (Grasse et al., 2001; Memeti et al., 2010;

Chapman et al., 2015). Ten samples from this group show broad similarity (Fig. 9A), with age peaks at 1.6–1.8 Ga, 1.35–1.48 Ga and ca. 1.1 Ga. Minor age populations in the Archean are also present.

Caborca Block

The Caborca Block of northern Mexico contains siliciclastic strata that are lithologically similar to the passive margin inner-shelf facies of the Death Valley and Mojave Desert regions (Fig. 1; Stewart et al., 1984; Farmer et al., 2005; Gehrels and Pecha, 2014). A data set from the Cambrian Proveedora Quartzite has a prominent population peak at 1.1 Ga with a subsidiary peak at 1.22, 1.44 Ga, and a broad population peak between 1.6 and 1.8 Ga.

DISCUSSION

Implications of Paleozoic Passive Margin Geometry on Last Chance Thrust System Models

Constraining the magnitude of shortening in the Last Chance thrust system is dependent on the passive margin geometry prior to juxtaposition of the outer and inner shelf facies and the extent to which subsequent deformation may have altered late Paleozoic structures. For example, the distance between the White-Inyo and Death Valley facies strata and the location of the Last Chance thrust footwall ramp during the early Paleozoic influence our understanding of Last Chance thrust system deformation and paleogeographic reconstructions prior and subsequent to the late Paleozoic. Below we discuss the implications of detrital zircon U-Pb data on our understanding of the continental margin configuration and Mesozoic overprinting of the Last Chance thrust system.

Multidimensional Scaling of Detrital Zircon U-Pb Age Data

The results of our MDS analysis show distinct and overlapping relationships between Neoproterozoic-Cambrian strata of the Mojave Desert, White-Inyo Mountains, Death Valley, and the Snow Lake terrane (Fig. 9B). Two distinct groups include the Mojave facies

and the Andrews Mountain Member-Wood Canyon paleochannel. Mojave facies samples are distinct due to a lower proportion of Paleoproterozoic and Archean grains relative to other groups. The Wood Canyon Formation of the Death Valley facies (Gehrels and Pecha, 2014) maps with the Andrews Mountain Member of the Campito Formation, which are both dominated by the 1.1 Ga peak. These units were likely deposited within a paleochannel that crossed the passive margin shelf (Chapman et al., 2015).

The Snow Lake terrane is characterized by a greater distribution of Neoproterozoic to Archean zircons relative to the other groups (Fig. 9). This group, while largely distinct, overlaps with the age spectra of White-Inyo and Death Valley strata. Definitive differences between the White-Inyo facies, the Death Valley facies and the Snow Lake terrane are apparent when mapped using MDS methods. Most notably, White-Inyo strata contain a lesser proportion of 1.0–1.4 Ga grains relative to the Death Valley facies. In contrast, the Snow Lake terrane contain a significant population of 1.0–1.4 Ga grains (Fig. 9A). These results are consistent with the MDS analysis of Chapman et al. (2015), which shows the White-Inyo facies is distinct from the Death Valley and Snow Lake terrane strata.

Lastly, the Proveedora Quartzite of the Caborca Block is similar to the Zabriskie Quartzite from the Snow Lake terrane (Fig. 9B). This supports previous interpretations of the Proveedora Quartzite being equivalent to the Zabriskie Quartzite, and the Caborca Block being a left laterally displaced block of Death Valley crust (Stewart et al., 1984).

Snow Lake Terrane

The metasedimentary roof pendant quartzites of the Snow Lake terrane show lithologic and detrital zircon provenance similar to the Death Valley facies (Fig. 9B; Chapman et al., 2015). Emplacement of the Snow Lake terrane is explained by ~400 km of right slip along the Snow Lake fault (Fig. 1; Lahren and Schweickert, 1989; Wyld and Wright, 2001), or extensional exhumation from the footwall of the Last Chance thrust (Chapman et al., 2015). Restoration of 65 km of late Cretaceous-Paleogene dextral displacement across the inferred Owens Valley shear zone (Fig. 1; Kylander-Clark et al., 2005; Bartley et al., 2007) results in rocks of the Snow Lake terrane lying adjacent to the Last Chance thrust system, and in alignment with a northwest-trending extensional shear zone exposed on the Kern Plateau

(Chapman et al., 2015; Saleeby and Dunne, 2015). This reconstructed geometry supports the model whereby the Snow Lake terrane was exhumed from the Last Chance thrust footwall by northeast-directed extension during the Early Jurassic (Chapman et al., 2015; Saleeby and Dunne, 2015). This model has implications for slip estimates on the Last Chance thrust, which could be magnified by extensional reactivation. Provided slip on a reactivated Last Chance thrust has a similar shear sense as the Permian faulting, discriminating between thrust and normal sense slip would be impractical.

To reconcile this issue, we note the Snow Lake terrane does not contain rocks younger than Ordovician (Memeti et al., 2010). Overlying the pendant rocks is a sequence of Early Jurassic marine turbidites, which were likely deposited in a supradetachment basin (Fig. 10; Saleeby and Dunne, 2015). Thus, Early Jurassic detachment faulting likely rooted in or below the footwall of the Last Chance thrust, and Silurian-Pennsylvanian rocks of the Death Valley facies were not exhumed along a reactivated thrust (Fig. 10).

The Snow Lake terrane exhumation model requires a certain magnitude of slip on the Last Chance thrust. Put simply, the Last Chance thrust footwall must have been far enough west to be exhumed by an extensional shear zone with a tip above the Sierra Nevada. In our cross-section of the Last Chance thrust system, the footwall ramp of the Last Chance thrust is located beneath the Inyo Mountains to create a geometry compatible with extensional exhumation of the Snow Lake terrane (Fig. 10).

Cross Section Model of the Last Chance Thrust System

A balanced cross section model of the Last Chance thrust system was constructed and restored to provide estimates of shortening and displacement, and demonstrate the viability of our interpreted kinematic evolution (Fig. 11). Local cross sections based on detailed and reconnaissance geologic mapping (Fig. 5 and 8) and field relationships were used to draft our regional cross section (see Fig. 3 for the section line). Deformation was restored via line-length balancing to estimate minimum shortening (Mitra and Namson, 1989). Unit thicknesses are based on observed thicknesses in mapped areas. The model does not constrain intra-unit deformation (e.g., cleavage development via pressure solution) or unit thickening, thus stratigraphic thicknesses are simplified to remain constant across the

model (Fig. 11A). Similarly, we assume stratigraphic thicknesses are uniform between the White-Inyo and Death Valley facies rocks, although the White-Inyo stratigraphic section is thicker than that observed in the Last Chance Range (Nelson, 1962; Stewart, 1965). A maximum of ~2 km extension across Eureka Valley is assumed in the construction of our model (Landreneau, 2019).

The most important feature controlling the amount of displacement on the Last Chance thrust is the location of the footwall ramp. The hanging wall ramp is fixed to the Last Chance Range (Fig. 5), therefore moving the footwall ramp increases or decreases the length of the footwall flat and the displacement of the thrust. We chose a location for the footwall ramp ~35 km west of the Last Chance Range below the Inyo Mountains (Fig. 11B). This geometry has been suggested by previous studies as the source of the White-Inyo Mountains anticlinorium (Fig. 3; Corbett, 1989; Morgan and Law, 1998). Similarly, a footwall ramp below the Inyo Mountains is required by our revised model of the exhumation of the Snow Lake terrane.

Displacement on the Last Chance thrust is also controlled by the depth of the thrust root. The Last Chance thrust likely roots into the Wood Canyon Formation, as this is the lowest hanging wall unit exposed in the Last Chance Range. The stratigraphic throw in the Last Chance Range is ~6 km. In the west, the Eureka thrust contains deeper strata in the hanging wall, suggesting the Eureka thrust soles deeper than the Last Chance thrust. We assume the root of the thrust is at a constant depth for our model, which provides a minimum shortening estimate. Based on the location of the footwall and hanging wall ramps, our model predicts ~50 km of displacement on the Last Chance thrust (Fig. 11B).

The geometry of the Eureka thrust requires lower-middle Cambrian strata of the White-Inyo facies to be located above the Death Valley facies strata along on the west side of Eureka Valley (Fig. 3). The slip must be such to place Cambrian strata in their west Eureka Valley location, while concealing the facies transition, which is achieved by placing the footwall ramp below the Inyo Mountains (Fig. 11C). Given our inferred locations of the hanging wall and footwall ramps, we estimate ~21 km slip along the Eureka thrust (Fig. 11C). This is consistent with estimates of previous studies (Corbett, 1989; Snow, 1992).

This geometry also generates an anticline at the present location of the White-Inyo Mountains anticlinorium (Fig. 3 and 11C; Morgan and Law, 1998). Total shortening at this stage of thrust system is >70 km.

Following emplacement of the Eureka thrust, the Hanging Rock Canyon thrust initiated and overturned the Last Chance thrust (Fig. 11D). Map relationships suggest the Hanging Rock Canyon thrust has a low displacement, as the Wood Canyon Formation is above the overturned footwall counterpart (*f3* and *f4*, Fig. 5), and the original Last Chance thrust hanging wall geometry is maintained in the central Last Chance Range (*f2*, Fig. 5). We model the geometry of the Hanging Rock Canyon thrust as a breached, overturned asymmetric anticline (Fig. 11D). This structure likely developed as a detachment fold that was subsequently breached during overturning of the fold. The overturned footwall syncline in our model maintains the geometry of the overturned syncline structure observed in Hanging Rock Canyon (Fig. 7). Field relationships show that the Hanging Rock Canyon thrust involved Mississippian strata in the already deformed Last Chance thrust footwall, which was presumably a mechanically weaker horizon just below (~100 m) the Last Chance thrust (Fig. 5D). Due to the scale of the model, we simplify this relationship in the cross section to show reactivation of the Last Chance thrust, which maintains the minimum slip estimation. The amount of slip on the Hanging Rock Canyon thrust is ~4.5 km.

The simplified structural geometry of the cross-section model adheres to our field observations, and successfully predicts the regional map relationships (Fig. 11D). Total minimum shortening accommodated by the Last Chance thrust system is 76 km.

Transpressional versus Retroarc thrusting of the Last Chance Thrust System

Retro-arc thrust belts generally strike parallel to the plate margin, which is perpendicular to convergence (DeCelles and Coogan, 2006; Anderson et al., 2018; Yonkee et al., 2019). In the proximal retro-arc, minimal shortening via relatively low-strain high-angle imbricate thrusting is expected (e.g., the East Sierran thrust system, Fig. 3; Dunne and Walker, 2004). In contrast, transpressional systems can produce fold-thrust belts when contraction and translation are partitioned in the crust (Tikoff and Teyssier, 1994; Bergh et al., 1997). The strike of thrust faults is typically oriented ~30-45° from the strike of the

transform fault, with full strain partitioning producing subparallel thrust and strike-slip faults (e.g., the San Andreas fault; Mount and Suppe, 1987; Bergh et al., 2019). The style of deformation in transpressional systems is typically characterized by out-of-sequence deformation at varying orientations (Bergh et al., 2019; Braathen et al., 1999). This is due to the sensitivity of transpressional thrust-belt style to convergence angle (Leever et al., 2011a), and a kinematic limitation on transpressional thrust belt propagation. For example, shortening of a typical thin-skinned retroarc fold-thrust belt is balanced at depth by basal detachment of the upper crust from the underlying basement (e.g., DeCelles and Coogan, 2006). In a transpressional system, thrust belts cannot propagate in the same manner, as the transform boundary condition prevents lateral displacement of the lower crust across a vertical plate boundary. Thus, transpressional thrust belts are expected to remain stationary relative to the transform fault, but the width of the deforming region can expand as a function of the convergence angle (Leever et al., 2011a). In this way, changes in the convergence angle, degree of strain partitioning and cumulative transform displacement control changes in fold-thrust geometry and kinematics manifested in out-of-sequence deformation (e.g., Bergh et al., 2019).

Assuming the strike of the California-Coahuila transform was ~140° (Fig. 1; Walker, 1988), the expected strike of a fold-thrust belt developed via orthogonal convergence is 140°, with vergence towards ~050°. The expected strike of structures formed during transpression along a strike-slip fault of this orientation is ~165±15° (Tikoff and Teyssier, 1994), with vergence towards ~075°. Folds in the Last Chance Range typically trend ~165°, with kinematic indicators showing east to east-northeast vergence (Fig. 5B). Similarly, palinspastic reconstructions of Cenozoic faulting in the Death Valley area indicate a north strike and east vergence of the Last Chance thrust system (Fig. 2; Corbett, 1989; Snow, 1992; Snow and Wernicke, 2000; Stevens and Stone, 2005a). This orientation and the style of episodic out-of-sequence thrusting are consistent with thrust development in a transpressional setting.

A comparable transpressional fol–thrust system is the Spitsbergen fold-thrust belt exposed at Svalbard in the North Atlantic (Bergh et al., 1997; Braathen et al., 1999). During the initial opening of the North Atlantic in the Paleocene, slip along an oceanic transform

boundary resulted in transpressional deformation as spreading initiated along western Greenland (Tessensohn and Piepjohn, 2000). The development of a fold-thrust belt on Spitsbergen during this transpressional regime is characterized by east-northeast vergent, thin-skinned thrusting and out-of-sequence truncation of local duplexes and thrust splays (Bergh et al., 1997). Analog modeling of the Spitsbergen fold-thrust belt shows the general thrust belt geometry and kinematics can be achieved with a convergence angle as low as ~15°, with thin-skinned fold-thrust structures rotated ~30° from the strike-slip zone (Leever et al., 2011a, 2011b). The above example is a simple shear dominated case, characterized by a low convergence angle (Tikoff and Teyssier, 1994). In a pure shear dominated case, the convergence angle is >20° and the trend of contractional structures is expected to be less than ~35° from the strike of the plate margin, as is the case with the Last Chance thrust system.

Late Paleozoic Tectonic Evolution of Southwest Laurentia

The transition from transform plate boundary to subduction zone along the southwest margin of Laurentia during the Pennsylvanian-Triassic is recorded by three domains exposed in California: the Last Chance thrust system and greater Death Valley region, the El Paso terrane, and the Foothills metamorphic belt (Fig. 1 and 12). Truncation of the southwest margin of Laurentia along the California-Coahuila transform initiated in the Middle Pennsylvanian with left slip displacement of the El Paso terrane and Caborca Block (Fig. 13). Outboard strands of the transform system transported fragments of the Shoo Fly terrane and Ordovician Kings-Kaweah ophiolite of the Foothills metamorphic belt to the southeast (Fig. 1, 12A and 13). Pennsylvanian mylonitic shear zones preserved in the Foothills metamorphic belt record left slip deformation at ca. 300 Ma (Saleeby, 2011). The early strain history of the California-Coahuila transform is inferred to be transtensional, as suggested by depositional patterns in the upper Pennsylvanian-lower Permian Keeler Basin (e.g., Stone and Stevens, 1988; Stevens et al., 2001).

Initiation of the Last Chance thrust system during the earliest Permian marks the onset of transpression along the California-Coahuila transform. The timing of this event is derived from the interruption of the margin parallel Keeler Basin (Fig. 12A and 13; Stevens

and Stone, 1988; Stevens et al., 2001). Strata of the upper Pennsylvanian-lower Permian Keeler Canyon Formation are carried in the hanging wall of the Last Chance thrust. Early Permian rocks of the upper Keeler Canyon Formation are in the footwall of the Racetrack duplex at Dry Mountain (Fig. 3). Global calibration of Pennsylvanian-early Permian conodont biostratigraphy using U-Pb zircon geochronology indicates the upper Keeler Canyon Formation was deposited by ca. 295 Ma (Schmitz and Davydov, 2014). Thus, the Last Chance thrust was not active before this time. Large magnitude displacement along the Last Chance thrust sheet was facilitated by localization in the Rest Spring Shale (Fig. 12A). Progressive transpression in the early Permian drove out-of-sequence emplacement of the Eureka thrust (Fig. 12B).

The thrust system expanded regionally with the development of the Hanging Rock Canyon thrust, and the Marble Canyon and Lemoigne thrusts (Fig. 12C). This episode occurred after deposition of the Permian Darwin Canyon Formation (ca. 290-285 Ma), which is overturned by the Marble Canyon thrust (Fig. 13; Stone et al., 2014; Vaughn, 2020). The style of deformation during this period is characterized by imbricate thrusting and tight footwall synclines, suggesting a different driving mechanism than the Last Chance thrust system.

Numerical models show the forces resisting subduction are greatest before initial slab sinking takes place, and compression is transmitted inboard from the plate boundary (Gurnis et al., 2004). This is likely the case for the Last Chance thrust system, which formed early in the subduction initiation process. Initial slab sinking by ca. 285 Ma is consistent with the (1) cessation of Last Chance thrust system, (2) distal flexural subsidence and formation of the Darwin Basin (Fig. 13; Vaughn, 2020), and (3) near-trench uplift and sediment recycling (Toth and Gurnis, 1998). Early Permian stratigraphy in the El Paso terrane record a transition from recycled, extra-regional sediment input to arc-derived volcaniclastic strata between ca. 280 and ca. 260 Ma (Rains et al., 2012; McDonald et al., 2018). A lag of at least 10 m.y. is expected between initial slab sinking and the development of a volcanic arc (Gurnis et al., 2004). Thus, 285 Ma is a reasonable estimate for the onset of slab sinking. More direct convergence of Panthalassa and Laurentia at ca. 280-270 Ma

likely drove regional expansion of the thrust system, including propagation of the Hanging Rock Canyon, Marble Canyon and Lemoigne thrusts (Domeier and Torsvik, 2014).

Middle Permian plutons in the El Paso terrane indicate localized arc magmatism was active by ca. 275 Ma (Fig. 12C and 13; Cecil et al., 2019). Local thrusts in the El Paso terrane indicate near-trench deformation in the late Permian. This time coincides with the observation of arc-derived detrital zircons in the sediment record. Upper Permian strata of the El Paso terrane contain a prominent ca. 265 Ma detrital zircon signature (McDonald et al., 2018). Similarly, ca. 265 Ma detrital zircons are present further from the trench to the east in upper Permian strata of the Lone Pine Basin (Fig. 13; Lodes et al., 2020). By the earliest Triassic, magmatism had spread north and south, and the ca. 245 Ma White Top Stock intrudes the Marble Canyon thrust (Fig. 12D and 13; Snow et al., 1991).

Late Permian evolution of the subduction zone includes underthrusting of the Foothills metamorphic belt within the upper plate of the subduction zone along the Foothills suture, and the ascent of ca. 255 Ma high-P metamorphic serpentinite diapirs into the Foothills ophiolitic mélange (Fig. 13; Saleeby, 2011). This suturing was contemporaneous with the Sonoma orogeny, which was driven by the accretion of island arc terranes to western Laurentia (Fig. 1; Miller, 1987; Wyld, 1991; Beranek and Mortensen, 2011; Powerman et al., 2020). Diffuse magmatism was established along the southwest Laurentian margin during the Triassic as the subduction zone expanded bilaterally (Fig. 12D; Chen and Moore, 1982; Barth and Wooden, 2006; Barth et al., 2011, 2018).

Implications for Induced Subduction Initiation

Subduction initiation has been grouped into two modes—spontaneous and induced—and more geologic observations of subduction initiation are required to advance our knowledge of this process (e.g., Stern 2004; Stern and Gerya, 2018). We propose that the late Paleozoic tectonic evolution of southwest Laurentia is consistent with the predictions of induced subduction initiation. This model predicts an evolution through compression, uplift and subsidence of the over-riding plate as subduction is established (Stern, 2004); the compressional phase is recorded by development of the Last Chance thrust system; near-trench uplift is indicated by the recycled sediment composition of Permian strata in

the El Paso terrane; the transition to subsidence coincides with cessation of the Last Chance thrust system and development of the Darwin basin. Once established, subduction dynamics were controlled by changes in the Panthalassa-Laurentia relative plate motion vector (Domeier and Torsvik, 2014; Saleeby, 2011). Near-orthogonal convergence in the middle Permian drove renewed thrusting in the upper plate, whereas oblique convergence in the middle Triassic accommodated rapid fore-arc extension and boninitic volcanism. Applying this model to southwest Laurentia helps explain the complex deformation and sedimentologic history of this region during the late Paleozoic. Similarly, it offers a case study for induced subduction initiation along continental-oceanic transforms as a potentially widespread process.

A well-studied, similar example comes from the Puysegur trench in southern New Zealand. There, Miocene subduction initiation along the southern tip of the dextral Alpine fault is recorded by regional uplift of the Fjordland region followed by subsidence of the near-trench Snares depression (Sutherland et al., 2006, 2009; Klepeis et al., 2019). Initial arc magmatism developed <25 Ma after subduction initiation, as evidenced by the Pleistocene Solander volcano (Reay and Parkinson, 1997). While the Puysegur subduction zone and the associated upper plate deformation are well characterized, a complex history of deformation and magmatism in Fjordland poses challenges to evaluating the crustal response to subduction initiation. Thus, the southwest Laurentia subduction initiation example is a prime candidate for further characterizing induced initiation using the rock record.

CONCLUSIONS

Our geologic mapping, detrital zircon U-Pb geochronology and structural analysis improves the current understanding of the structural evolution of the early Permian Last Chance thrust system and the tectonic evolution of southwest Laurentia. Geologic mapping in the Last Chance Range and Inyo Mountains reveals an east-vergent thrust system that accommodated shortening through repeated episodes of out-of-sequence deformation. The style of thrust deformation changes between thrust episodes suggesting an evolving plate

boundary stress field driving deformation. The style and kinematics of deformation are consistent with development in a transpressional setting.

The magnitude of shortening accommodated by the Last Chance thrust system is influenced by the original geometry of the Eureka and Last Chance thrust sheets, and the extent to which subsequent deformation has modified thrust geometries. Early Jurassic exhumation of the Snow Lake terrane from the Last Chance thrust footwall requires a footwall ramp below the Inyo Mountains. Using this geometry in our balanced cross section model we determined ~50 km of slip on the Last Chance thrust. The Eureka thrust slipped ~21 km east, which concealed the transition from the White-Inyo to Death Valley facies. Total shortening of the Last Chance thrust system is 76 km.

The initiation of subduction during the early to middle Permian coincides with the waning stages of thrust deformation. Nucleation of a subduction zone along an outer strand of the California-Coahuila transform is suggested by the distribution of early arc plutons in the El Paso terrane, which lies southwest of the main transform fault. The cessation of thrust system deformation is coeval with a shift of contraction southwestward towards the trench, and regional subsidence and basin formation in the Death Valley region. The record of evolving plate boundary stresses preserved in the structural and sedimentologic histories of this region is predicted by models of induced subduction initiation at a transform boundary.

Late Paleozoic features of the Death Valley region preserve a record of subduction initiation scarcely retained in the rock record, as subsequent subduction magmatism typically erases previous structures. The White-Inyo Mountains, Death Valley region and Mojave Desert provide an excellent location to study continental subduction initiation mechanisms in the field.

ACKNOWLEDGEMENTS

We are grateful to Death Valley National Park for providing a research permit to conduct this work (DEVA-2017-SCI-0027 and DEVA-2018-SCI-0044). This research was

supported by the U. S. Geological Survey, National Cooperative Geologic Mapping Program, under assistance Award No. G18AC00097. The views and conclusions contained in this document are those of the authors and should not be interpreted as necessarily representing the official policies, either expressed or implied, of the U.S. Government. Additional support came from Sigma-Xi Grant-in-Aid funding and a Geological Society of America Graduate Student Research Grant. Careful and thoughtful reviews by Alan Chapman and Jeff Amato greatly improved the clarity of this manuscript. Thanks to Michael Say, Kyle Armendariz, and Haley Moniz for assistance in the field, and Joel DesOrmeau for making a thin section of the Last Chance thrust fault gouge sample seen in Fig. 6D.

APPENDIX 1: DETRITAL ZIRCON U-PB GEOCHRONOLOGY METHODS

Samples analyzed at UT Austin

Rock samples were crushed and sent to GeoSep Services for zircon separation by conventional techniques. Zircons were poured onto double-sided tape, mounted in epoxy and polished in-house at UNR. Cathodoluminescence (CL) images of the mounts were collected to guide laser spot analyses.

The primary standard used was GJ1 (Jackson et al., 2004) and secondary standards include 91500 (238U/206Pb age of 1065 Ma), and Plesovice (238U/206Pb age of 337 Ma). Laser spot size was 30 micron for all magmatic samples. Laser energy was set to 4 mJ, with 300 analysis shots at 10 Hz. The fluence was set at 3.88 J/cm2.

Samples analyzed at the Institute for Tibetan Plateau Research

Samples were crushed using conventional jaw crusher and disk mill techniques, and zircons were separated using the Frantz magnetic separator and a standard heavy liquids protocol.

The zircon standards used were Plesovice and glass reference material NIST SRM 612 (Pearce et al., 1997). The first 15 s with the laser-off mode were used to collect the background values, and the following 40 s with the laser-on mode were employed to measure the peak intensities of the ablated material. A 25 micron laser spot size was used on all grains.

For zircon grains that are older than 1.0 Ga, 206Pb/207Pb age is reported. 206Pb/207Pb ages are preferred for older grains because the age uncertainty decreases with age for 206Pb/207Pb, and increases for 206Pb/238U. The uncertainty of young 206Pb/207Pb ages is due to the low abundance of 206Pb and difficulty in measuring 207Pb (Gehrels et al., 2008). 206Pb/207Pb ages (>1.0 Ga) that are >30% discordant are filtered out of the data set. Likewise, 206Pb/238U ages (<1.0 Ga) that are >30% discordant and have >10% error are excluded.

APPENDIX 2: 2. $^{40}AR/^{39}AR$ GEOCHRONOLOGY METHODS

Near-horizontal basalt flows within the Last Chance Range were dated to determine the extent of post-eruption tilting of the range. 40Ar/39Ar geochronology of basalt groundmass and sanidine from rhyolite tuff was conducted at the Nevada Isotope Geochronology Laboratory at the University of Nevada, Las Vegas.

The basalt groundmass experienced excess Ar complications, but an inverse isochron diagram provides an age of 5.528 ± 0.044 Ma with the 40Ar/36Ar intercept at 347. This is in agreement with a previously published K-Ar whole-rock age of 5.5 +- 0.2 Ma (Miller and Wrucke, 1995). Analysis of sanidine from the underlying rhyolite tuff return an age of 5.51 ± 0.03 Ma for 9 grains out of 14. These ages overlap within uncertainty, therefore we assign a general age of 5.51 Ma for the paleohorizontal marker.

LC 12B – Lapilli Tuff (sanidine) – 37.194371 N, -117.660864 W

LC 12A – Basalt (groundmass) – 37.194371 N, -117.660864 W

Nevada Isotope Geochronology Laboratory – Description and Procedures

Samples analyzed by the 40Ar/39Ar method at the University of Nevada Las Vegas were wrapped in Al foil and stacked in 6 mm inside diameter sealed fused silica tubes. Individual packets averaged 2 mm thick and neutron fluence monitors (FC-2, Fish Canyon Tuff sanidine) were placed every 5–10 mm along the tube. Synthetic K-glass and optical grade CaF2 were included in the irradiation packages to monitor neutron induced argon interferences from K and Ca. Loaded tubes were packed in an Al container for irradiation. Samples irradiated at the U. S. Geological Survey TRIGA Reactor, Denver, CO were in-core for 7 h in the 1 MW TRIGA type reactor. Correction factors for interfering neutron reactions on K and Ca were determined by repeated analysis of K-glass and CaF2 fragments. Measured (40Ar/39Ar)K values were 3.22 (±6.64%) × 10□2. Ca correction factors were (36Ar/37Ar)Ca = 2.33 (±0.83%) × 10□4 and (39Ar/37Ar)Ca = 6.82 (±0.65%) × 10□4. J factors were determined by fusion of 5–6 individual crystals of neutron fluence monitors which gave reproducibility's of 0.09% to 0.12% at each standard position. Variation in neutron fluence along the 100 mm length of the irradiation tubes was <4%.

Matlab curve fit was used to determine J and uncertainty in J at each standard position. No significant neutron fluence gradients were present within individual packets of crystals as indicated by the excellent reproducibility of the single crystal fluence monitor fusions.

Irradiated FC-2 sanidine standards together with CaF2 and K-glass fragments were placed in a Cu sample tray in a high vacuum extraction line and were fused using a 20 W CO2 laser.

Sample viewing during laser fusion was by a video camera system and positioning was via a motorized sample stage. Samples analyzed by the furnace step heating method utilized a double vacuum resistance furnace similar to the Staudacher et al. (1978) design. Reactive gases were removed by three GP-50 SAES getters prior to being admitted to a MAP 215–50 mass spectrometer by expansion. The relative volumes of the extraction line and mass spectrometer allow 80% of the gas to be admitted to the mass spectrometer for laser fusion analyses and 76% for furnace heating analyses. Peak intensities were measured using a Balzers electron multiplier by peak hopping through 7 cycles; initial peak heights were determined by linear regression to the time of gas admission. Mass spectrometer discrimination and sensitivity was monitored by repeated analysis of atmospheric argon aliquots from an online pipette system. Measured 40Ar/36Ar ratios were 286.52 ± 0.07% during this work, thus a discrimination correction of 1.0313 (4 AMU) was applied to measured isotope ratios. The sensitivity of the mass spectrometer was ~6×10^{-17} mol mV-1 with the multiplier operated at a gain of 36 over the Faraday. Line blanks averaged 2.52 mV for mass 40 and 0.01 mV for mass 36 for laser fusion analyses and 26.83 mV for mass 40 and 0.09 mV for mass 36 for furnace heating analyses.

Discrimination, sensitivity, and blanks were relatively constant over the period of data collection. Computer automated operation of the sample stage, laser, extraction line and mass spectrometer as well as final data reduction and age calculations were done using LabSPEC software written by B. Idleman (Lehigh University). An age of 28.02 Ma (Renne et al., 1998) was used for the Fish Canyon Tuff sanidine fluence monitor in calculating ages for samples.

For 40Ar/39Ar analyses a plateau segment consists of 3 or more contiguous gas fractions having analytically indistinguishable ages (i.e., all plateau steps overlap in age at ± 2σ analytical error) and comprising a significant portion of the total gas released (typically >50%). Total gas (integrated) ages are calculated by weighting by the amount of 39Ar released, whereas plateau ages are weighted by the inverse of the variance. For each sample inverse isochron diagrams are examined to check for the effects of excess argon. Reliable isochrons are based on the MSWD criteria of Wendt and Carl (1991) and, as for plateaus, must comprise contiguous steps and a significant fraction of the total gas released. All analytical data are reported at the confidence level of 1σ (standard deviation).

APPENDIX 3: STRATIGRAPHIC DESCRIPTIONS FOR THE LAST CHANCE RANGE AND JACKASS FLAT

Last Chance Range Stratigraphy

Paleozoic lithologic units

The oldest lithologic unit in the Last Chance Range is the Neoproterozoic-Cambrian Wood Canyon Formation (Fig. 4). This unit is characterized by thin- to medium bedded sandstone with minor shale and siltstone beds and a distinct limestone member separating the lower and upper clastic members. The base of the ~400-m-thick Wood Canyon Formation is not observed in the Last Chance Range. The upper contact with the Zabriskie Quartzite is gradational.

The Cambrian Zabriskie Quartzite is a distinct, ~300-m-tick massive quartz arenite with the lower section comprised of medium-bedded cross-bedded sandstone. The upper contact with Carrara Formation is gradational over ~10 m.

The Carrara Formation is an ~500-m-thick section of thin-to-medium bedded silt- and sandstone grading into a middle blue-green limestone member (Fig. 4). The upper tan limestone member is absent due to faulting in the northern map area (Fig. 5). A distinct white quartz sandstone and dark brown limestone are useful marker beds within the lower Carrara Formation. The white sandstone is the younger, stratigraphically higher unit. The unit is typically overturned in the northern Last Chance Range as indicated by cross bedding. The upper contact with the Bonanza King Formation is sharp.

The middle Cambrian bonanza King Formation is a cliff-forming, thick-bedded dolomite with infrequent buff-white limestone marker beds. Bed composition and texture varies significantly from marl to mottled dolomite, thin-bedded dolomite and shale, and massive limestone. The alternating white and grey beds form useful markers. The upper contact with the Dunderberg Shale member of the Nopah Formation is sharp.

The Dunderberg Shale, a classic marker bed across California and Nevada, is an ~50-m- thick shale with chert ribbons and a thin upper limestone bed. The thickness of the Dunderberg Shale varies across the Last Chance Range and is tectonically thinned in some

locations. The overlying member of the upper Cambrian Nopah Formation is a 450 m-thick, medium bedded limestone. The interbedded siltstones and marls grade up-section into dominantly limestone with an upper section of dolomite. The upper contact with the Pogonip Group is gradational and marked by the appearance of distinct chert nodules and limestone of the lower Pogonip Group.

The Ordovician Pogonip Group consists of the lower member, an ~900-m-thick medium bedded limestone with interbedded shale that grades up-section into massive limestone, and the Antelope Valley Limestone member, an ~450-m-thick, thin-bedded limestone with thin red siltstone and occasional marl beds (Fig. 4). This unit is distinguished from the lower Pogonip member by the thin red siltstone beds.

The overlying Ordovician Eureka Quartzite is another classic marker bed of California and Nevada (Fig. 4). In the Last Chance Range, an ~35-m-thick section of distinct pure white quartz sandstone with medium to massive bedding and occasional cross stratification is observed. The contact with the overlying Ely Springs Dolomite is sharp.

The upper Ordovician Ely Springs Dolomite is an ~300-m-thick, thin-bedded to massive fossiliferous dolomite with abundant chert nodules in the lower part of the section (Fig. 4). The upper contact is not observed in the Hanging Rock Canyon quadrangle.

The Silurian-Devonian Hidden Valley Dolomite had been placed atop the Ely Springs Dolomite by a fault (Fig. 4). The ~100-m-thick section of the Hidden Valley Dolomite consists of thin-bedded shale and dolomite with occasional medium marl beds. In the northeastern Last Chance Range, the Hidden Valley Dolomite is exposed as extensional klippen in the hanging wall of a low-angle fault over the Ely Springs Dolomite (Fig. 5). Tight meter-scale folds are abundant in the hanging wall adjacent to the fault. The upper contact of the unit is not observed.

The lower plate stratigraphy of the Last Chance thrust system is often difficult to distinguish due to extensive deformation (Fig. 4). The Devonian Lost Burro Dolomite is an ~20- 50-m-thick, massive dolomite exposed sporadically in the central Last Chance Range (Fig. 5). The dolomitic composition of this unit distinguishes it from the overlying Mississippian Perdido Formation.

The Mississippian Perdido Formation is a distinct footwall unit, comprised primarily of a sequence of shale, thin-bedded siltstone and cherty pebble conglomerate with interbeds of massive limestone near the top of the formation (Fig. 4). Foliation is commonly parallel to original bedding. In some locations, the pebble conglomerate is ductilely deformed to form an L- S tectonite. Unit thickness is variable owing to pervasive deformation, but it is ~55 m thick. The contact with the overlying Rest Spring Shale is gradational.

The Mississippian Rest Spring Shale is a locally phyllitic shale displaying pervasive internal deformation (Fig. 4). This unit is commonly folded and exhibits a strong foliation parallel to original bedding. Scattered thin white- to red-colored quartz sandstone beds are common. Rest Spring Shale is the youngest Paleozoic unit in the Last Chance Range and forms the stratigraphically highest footwall unit of the Last Chance thrust. The true stratigraphic thickness is unknown due to tectonic thinning, but the exposed thickness is ~30 m.

Jackass Flats Stratigraphy

The Neoproterozoic-Cambrian stratigraphy of the White-Inyo Mountains is lithologically distinct from that of the Last Chance Range to the east. The lowest exposed unit is the Neoproterozoic Wyman Formation (Fig. 8), which is a >2,700 m-thick succession of thin-bedded argillite, fine-grained quartzite, and siltstone interbedded with oolitic limestone lenses. The basal contact of the Wyman Formation is not exposed.

Unconformably overlying the Wyman Formation is the ~600-m-thick Reed Dolomite, which is subdivided into three members at Jackass Flats (Fig. 8). The lower member is a coarse- grained oolitic dolomite overlain by a >200-m-thick lens of quartzite and carbonaceous sandstone of the Hines Tongue Member. The upper member of the Reed Dolomite is a fine- grained dolomite. The contact with the overlying Deep Springs Formation is gradational.

The Deep Springs Formation is comprised of a >450-m-thick sequence divided into a lower fine-grained limestone, a middle member of quartzite overlain by interbedded limestone, shale and siltstone, and an upper member of quartz sandstone and siltstone

capped by a massive dolomite unit (Fig. 8). The contact with the overlying Campito Formation is sharp.

The Campito Formation consists of >1000 m of quartzite, siltstone, and shale (Fig. 8). The base of the formation is comprised of the Andrews Mountain Member, a >700-m-thick stack of massive quartz sandstone with interbedded siltstone and shale. The Andrews Mountain Member is overlain by shale with coarser-grained siltstone and sandstone of the Montenegro Member, which consists of grey shale with coarser grained interbeds of siltstone and sandstone.

Overlying the Campito Formation is the Poleta Formation (Fig. 8), which consists of >350 m of massive-to-thick bedded limestone, thin-bedded quartz sandstone and siltstone. The contact with the overlying Harkless Formation is abrupt.

The ~600-m-thick Harkless Formation is composed of phyllitic shale with interbeds of quartz sandstone, siltstone and distinct limestone marker beds (Fig. 8). The Harkless Formation grades into the massive quartzite of the >250-m-thick Saline Valley Formation. The upper contact of the Saline Valley Formation with the overlying Mule Spring Limestone is sharp.

The Mule Spring Limestone is an ~300-m-thick section of bedded limestone (Fig. 8). A sharp upper contact with the Monola Formation leads into ~380 m of shale and siltstone, massive limestone, and thin-bedded fine grained limestone interbedded with siltstone and shale. The overlying Bonanza King Formation is the oldest unit of an upper Cambrian-Ordovician carbonate succession that is continuous across the White-Inyo Mountains and Death Valley region.

REFERENCES

Anderson, T.H., and Silver, L.T., 2005, The Mojave-Sonora megashear—Field and analytical studies leading to the conception and evolution of the hypothesis, in Anderson, T.H., ed., The Mojave-Sonora Megashear Hypothesis: Development, Assessment, and Alternatives: Geological Society of America Special Paper 393, p. 1–50.

Anderson, R.B., Long, S.P., Horton, B.K., Thomson, S.N., Calle, A.Z., and Stockli, D.F., 2018, Orogenic wedge evolution of the central Andes, Bolivia (21°S): Implications for Cordilleran cyclicity: Tectonics, v. 37, p. 3577–3609.

Attia, S., Paterson, S.R., Cao, W., Chapman, A.D., Saleeby, J., Dunne, G.C., Stevens, C.H., and Memeti, V., 2018, Late Paleozoic tectonic assembly of the Sierra Nevada prebatholithic framework and western Laurentian provenance links based on synthesized detrital zircon geochronology, in Ingersoll, R.V., Lawton, T.F., and Graham, S.A., eds., Tectonics, Sedimentary Basins, and Provenance: A Celebration of William R. Dickinson's Career: Geological Society of America Special Paper 540.

Atwater, T., and Stock, J., 1998, Pacific – North America plate tectonics of the Neogene southwestern United States – An update: International Geology Reviews, v. 40, p. 375-402.

Barth, A.P., Tosdal, R.M., Wooden, J.L., and Howard, K.A., 1997, Triassic plutonism in southern California: Southward younging of arc initiation along a truncated continental margin: Tectonics, v. 16, no. 2, p. 290–304.

Barth, A.P. and Wooden, J.L., 2006, Timing of magmatism following initial convergence at a passive margin, southwestern US Cordillera, and ages of lower crustal magma sources: The Journal of Geology, v. 114, p.231-245.

Barth, A.P., Wooden, J.L., Coleman, D.S., and Vogel, M.B., 2009, Assembling and disassembling California: A zircon and monazite geochronologic framework for Proterozoic crustal evolution in southern California: The Journal of Geology, v. 117, p. 221–239.

Barth, A.P., Walker, J.D., Wooden, J.L., Riggs, N.R., and Schweickert, R.A., 2011, Birth of the Sierra Nevada magmatic arc: Early Mesozoic plutonism and volcanism in the east-central Sierra Nevada of California: Geosphere, v. 7, no. 4, p. 877–897.

Barth, A.P., Wooden, J.L., Riggs, N.R., Walker, J.D., Tani, K., Penniston-Dorland, S.C., Jacobson, C.E., Laughlin, J.A., and Hiramatsu, R., 2018, Marine volcaniclastic record of early arc evolution in the Eastern Ritter Range pendant, central Sierra Nevada, California: Geochemistry Geophysics Geosystems, v. 19, p. 2543–2559.

Bartley, J.M., Glazner, A.F., Coleman, D.S., Kylander-Clark, A., Mapes, R., and Friedrich, A.M., 2007, Large Laramide dextral offset across Owens Valley, California, and its possible relation to tectonic unroofing of the southern Sierra Nevada, in Roeske, S.M., Till, A.B., Foster, D.A., and Sample, J.C., eds., Exhumation Associated with

Continental Strike-Slip Fault Systems: Geological Society of America Special Paper 434, p. 129–148.

Beranek L.P. Mortensen J.K., 2011, The timing and provenance record of the Late Permian Klondike orogeny in northwestern Canada and arc-continent collision along western North America: Tectonics, v. 30, p. TC5017.

Bergh, S.G., Braathen, A., and Andresen, A., 1997, Interaction of basement-involved and thin-skinned tectonism in the Tertiary fold-and thrust belt of central Spitsbergen, Svalbard: American Association of Petroleum Geologists Bulletin, v. 81, p. 637–661.

Bergh, S.G., Sylvester, A.G., Damte, A. and Indrevær, K., 2019, Polyphase kinematic history of transpression along the Mecca Hills segment of the San Andreas fault, southern California: Geosphere, v. 15, p.901-934.

Boyer, S.E., and Elliott, D., 1982, Thrust systems: American Association of Petroleum Geologists Bulletin, v. 66, p. 1196–1230.

Braathen, A., Bergh, S.G., and Maher, H.D., Jr., 1999, Application of a critical wedge taper model to the Tertiary transpressional fold-thrust belt on Spitsbergen, Svalbard: Geological Society of America Bulletin, v. 111, p. 1468–1485.

Burchfiel, B.C., and Davis, G.A., 1975, Nature and controls of Cordilleran orogenesis, western United States: Extensions of an earlier synthesis: American Journal of Science, v. 275-A, p. 363–396.

Cashman, P.H., Villa, D.E., Taylor, W.J., Davydov, V.I., and Trexler, J.H., Jr., 2011, Late Paleozoic contractional and extensional deformation at Edna Mountain, Nevada: Geological Society of America Bulletin, v. 123, p. 651–668.

Cashman, P. H., Trexler, J. H. Jr., and Sturmer, D. M., 2016, Spatial and temporal distribution of late Paleozoic structures in Nevada: Progressive tectonic evolution of the western Laurentian margin: Geological Society of America Abstracts with Programs, v. 48, n. 7.

Casteel, M., 1986, Geology of a portion of the northwest Last Chance Range, south of Hanging Rock Canyon, Inyo County, California [M.S. thesis]: Fresno, California, California State University, 115 p.

Cecil, M.R., Ferrer, M.A., Riggs, N.R., Marsaglia, K., Kylander-Clark, A., Ducea, M.N. and Stone, P., 2019, Early arc development recorded in Permian− Triassic plutons of the northern Mojave Desert region, California, USA: Geological Society of America Bulletin, v. 131, p. 749-765.

Chapman, A.D., Ernst, W.G., Gottlieb, E., Powerman, V. and Metzger, E.P., 2015, Detrital zircon geochronology of Neoproterozoic–Lower Cambrian passive-margin strata of the White-Inyo Range, east-central California: Implications for the Mojave–Snow Lake fault hypothesis: Geological Society of America Bulletin, v. 127, p.926-944.

Chen, J.H., and Moore, J.G., 1982, Uranium-lead isotopic ages from the Sierra Nevada batholith, California: Journal of Geophysical Research, v. 87, p. 4761–4784.

Colpron, M., and Nelson, J.L., 2009, A Paleozoic Northwest Passage: Incursion of Caledonian, Baltican and Siberian terranes into eastern Panthalassa, and the early evolution of the North American Cordillera, *in* Cawood, P.A., and Kröner, A., eds., Earth Accretionary Systems in Space and Time: Geological Society, London, Special Publication 318, p. 273–307.

Corbett, K.P., 1989, Structural Geology of the Last Chance Thrust System, East-Central California [Ph.D. Thesis]: Los Angeles, California, University of California, Los Angeles, 245 pp.

DeCelles, P., and Coogan, J., 2006, Structural and kinematic history of the Sevier fold-and-thrust belt, central Utah: Geological Society of America Bulletin, v. 118, p. 841-864.

Dickinson, W.R., 2000, Geodynamic interpretation of Paleozoic tectonic trends oriented oblique to the Mesozoic Klamath-Sierran continental margin in California, in Soreghan, M.J., and Gehrels, G.E., eds., Paleozoic and Triassic Paleogeography and Tectonics of Western Nevada and Northern California: Geological Society of America Special Paper 347, p. 209–245.

Dickinson, W.R., and Lawton, T.F., 2001, Carboniferous to Cretaceous assembly and fragmentation of Mexico: Geological Society of America Bulletin, v. 113, p. 1142–1160.

Domeier, M., and Torsvik, T.H., 2014, Plate tectonics in the late Paleozoic: Geoscience Frontiers, v. 5, p. 303–350.

Farmer, G.L., Bowring, S.A., Matzel, J., Espinosa Maldonado, G., Fedo, C., and Wooden, J., 2005, Paleoproterozoic Mojave Province in northwestern Mexico? Isotopic and U-Pb zircon geochronologic studies of Precambrian and Cambrian crystalline and sedimentary rocks, Caborca, Sonora, in Anderson, T.H., Nourse, J.A., McKee, J.W., and Steiner, M.B., eds., The Mojave-Sonora Megashear Hypothesis: Development, Assessment, and Alternatives: Geological Society of America Special Paper 393, p. 183–198.

Faulds, J.E., and Henry, C.D., 2008, Tectonic influences on the spatial and temporal evolution of the Walker Lane: An incipient transform fault along the evolving Pacific–North American plate boundary, in Spencer, J.E., and Titley, S.R., eds., Ores and Orogenesis: Circum-Pacific Tectonics, Geologic Evolution, and Ore Deposits: Arizona Geological Society Digest 22, p. 437-470.

Gehrels, G.E., 2014, Detrital zircon U-Pb geochronology applied to tectonics: Annual Review of Earth and Planetary Sciences, v. 42, p. 127–149.

Gehrels, G., Valencia, V.A., and Ruiz, J., 2008, Enhanced precision, accuracy, efficiency, and spatial resolution of U-Pb ages by laser ablation– multicollector–inductively coupled plasma mass spectrometry: Geochemistry Geophysics Geosystems, v. 9, Q03017.

Gehrels, G. and Pecha, M., 2014, Detrital zircon U-Pb geochronology and Hf isotope geochemistry of Paleozoic and Triassic passive margin strata of western North America: Geosphere, v. 10, p.49-65.

Gerya, T.V., Stern, R.J., Baes, M., Sobolev, S.V. and Whattam, S.A., 2015, Plate tectonics on the Earth triggered by plume-induced subduction initiation: Nature, v. 527, p.221-225.

González-León, C.M., Valencia, V.A., Lawton, T.F., Amato, J.M., Gehrels, G.F., Leggett, W.J., Montijo-Contreras, O., Fernández, M.A., 2009, The Lower Mesozoic record of detrital zircon U-Pb geochronology of Sonora, Mexico and its paleogeographic implications: Revista Mexicana de Ciencias Geológicas, v. 26, no. 2, p. 301–314.

Grasse, S.W., Gehrels, G.E., Lahren, M.M., Schweickert, R.A., and Barth, A.P., 2001, U-Pb geochronology of detrital zircons from the Snow Lake pendant, central Sierra Nevada—Implications for Late Jurassic–Early Cretaceous dextral strike-slip faulting: Geology, v. 29, p. 307–310.

Gurnis, M., Hall, C., and Lavier, L., 2004, Evolving force balance during incipient subduction: Geochemistry, Geophysics, Geosystems, v. 5, p. 1-31.

Jackson, S.E., Pearson, N.J., Griffin, W.L., and Belousova, E.A., 2004, The application of laser ablation-inductively coupled plasma-mass spectrometry to in situ U-Pb zircon geochronology: Chemical Geology, v. 211, p. 47–69, https://doi.org/10.1016/j.chemgeo.2004.06.017.

Klepeis, K.A., Webb, L., Blatchford, H., Schwartz, J.J., Jongens, R., Turnbull, R., and Stowell, H.H., 2019, Deep slab collision during Miocene subduction causes uplift along crustalscale reverse faults in Fiordland, New Zealand: GSA Today, v. 29.

Knott, J.R., Wan, E., Deino, A.L., Casteel, M., Reheis, M.C., Phillips, M.C., Walkup, L., McCarty, K., Manoukian, D., and Nunez, E., 2018, Lake Andrei: A Pliocene Pluvial lake in Eureka Valley, Eastern California: Geological Society of America Abstracts with Programs, v. 50, n. 6.

Korenaga, J., 2013, Initiation and evolution of plate tectonics on Earth: theories and observations: Annual review of earth and planetary sciences, v. 41, p.117-151.

Kylander-Clark, A., Coleman, D.S., Glazner, A.F., and Bartley, J.M., 2005, Evidence for 65 km of dextral slip across Owens Valley, California, since 83 Ma: Geological Society of America Bulletin, v. 117, p. 962-968.

Landreneau, L.A., 2019, Structure and geometry of the Eureka Valley extensional basin, eastern California, from gravity modeling [M.S. Thesis]: Dallas, Texas, The University of Texas, 69 p.

Lahren, M.M., and Schweickert, R.A., 1989, Proterozoic and Lower Cambrian passive margin rocks of Snow Lake pendant, Yosemite-Emigrant Wilderness, Sierra Nevada, California: Evidence for major Early Cretaceous dextral translation: Geology, v. 17, p. 156–160.

Lawson, M., 2017, The Application of Luminescence to Tectonics: Improvements to Luminescent Dating and its Utilization in High-Energy Depositional Environments [Ph.D. Dissertation]: Los Angeles, California, University of California, 174 p.

Lawton, T.F., Cashman, P.H., Trexler, J.H. and Taylor, W.J., 2017, The late Paleozoic southwestern Laurentian borderland: Geology, v. 45, p.675-678.

Leary, R.J., Umhoefer, P., Smith, M.E. and Riggs, N., 2018, A three-sided orogen: A new tectonic model for Ancestral Rocky Mountain uplift and basin development: Geology, v. 45, p.735-738.

Leever, K.A., Gabrielsen, R.H., Sokoutis, D., and Willingshofer, E., 2011a, The effect of convergence angle on the kinematic evolution of strain partitioning in transpressional brittle wedges: Insight from analog modeling and high-resolution digital image analysis: Tectonics, v. 30, TC2013.

Leever, K.A., Gabrielsen, R.H., Faleide, J.I., and Braathen, A., 2011b, A transpressional origin for the West Spitsbergen fold-and-thrust belt: Insight from analog modeling: Tectonics, v. 30, TC2014.

Levy, D.A., Zuza, A.V., and Cashman, P.H., 2018, Tectonic Reconstruction of the Last Chance Thrust System, Death Valley National Park, California: Geological Society of America Abstracts with Programs, v. 50, no. 5.

Linde, G.M., Trexler, J.H., Cashman, P.H., Gehrels, G. and Dickinson, W.R., 2016, Detrital zircon U-Pb geochronology and Hf isotope geochemistry of the Roberts Mountains allochthon: New insights into the early Paleozoic tectonics of western North America: Geosphere, v. 12, p. 1016–1031

Linde, G.M., Trexler, J.H., Jr., Cashman, P.H., Gehrels, G., and Dickinson, W.R., 2017, Three-dimensional evolution of the early Paleozoic western Laurentian margin: New insights from detrital zircon U-Pb geochronology and Hf isotope geochemistry of the Harmony Formation of Nevada: Tectonics, v. 36, p. 2374–2369.

Lodes, E.B., Riggs, N.R., Smith, E.M., and Stone, P., 2020, Cordilleran subduction initiation: retro-arc timing and basinal response in the Inyo Mountains, eastern California: Lithosphere, *in* review.

MacLean, J.S., Sears, J.W., Chamberlain, K.R., Khudoley, A.K., Prokopiev, A.V., Kropachev, A.P., and Serkina, G.G., 2009, Detrital zircon geochronologic tests of the SE Siberia–SW Laurentia paleocontinental connection, *in* Stone, D.B., Fujita, K., Layer, P.W., Miller, E.L., Prokopiev, A.V., and Toro, J., eds., Geology, Geophysics and Tectonics of Northeastern Russia: A Tribute to Leonid Parfenov: Stephan Mueller Special Publication 4, p. 111–116.

McAllister, J. F., 1952, Rocks and structure of the Quartz Spring area, northern Panamint Range, California: California Division of Mines Special Report, 25-37 p.

McDonald, E.K., Cecil, M.R., Marsaglia, K.M., Riggs, N.R., and Heermance, R.V., 2018, Permian strata in the El Paso Mountains, southern California, record paleodrainage

reorganization in southwestern Laurentia and the emergence of the early Cordilleran arc; Geological Society of America Abstracts with Programs, v. 50, n. 5.

Memeti, V., Gehrels, G.E., Paterson, S.R., Thompson, J.M., Mueller, R., and Pignotta, M., 2010, Evaluating the Mojave–Snow Lake fault hypothesis and origins of central Sierran metasedimentary pendant strata using detrital zircon provenance analyses: Lithosphere, v. 2, p. 341–360.

Mitra, S., and Namson, J.S., 1989, Equal-area balancing: American Journal of Science, v. 289, no. 5, p. 563–599.

Miller, M.M., 1987, Dispersed remnants of a northeast Pacific fringing arc: Upper Paleozoic terranes of Permian McCloud faunal affinity, western US: Tectonics, v. 6, no. 6, p. 807–830.

Miller, R.J., and Wrucke, C.T., 1995, Age, chemistry, and geologic implications of Tertiary volcanic rocks in the Last Chance Range and part of the Saline Range, Northern Death Valley region, California: Isochron-West, v. 62, p. 30–36.

Morgan, S.S., and Law, R.D., 1998, An overview of Paleozoic–Mesozoic age structures developed in the central White-Inyo Range, eastern California: International Geology Review, v. 40, p. 245–256.

Mount, V. S., and Suppe, J., 1987, State of stress near the San Andreas fault: implications for wrench tectonics: Geology, v. 15, p. 1143-1146.

Nabelek, P.I., and Morgan, S.S., 2012, Metamorphism and fluid flow in the contact aureole of the Eureka Valley–Joshua Flat–Beer Creek (EJB) pluton, California: Geological Society of America Bulletin, v. 124, p. 228–239.

Nelson, C.A., 1962, Lower Cambrian–Precambrian succession White-Inyo Mountains, California: Geological Society of America Bulletin, v. 73, p. 139–144.

Nelson, C.A., 1971, Geologic map of the Waucoba Spring Quadrangle, Inyo County, California: United States Geological Survey Quadrangle Map GQ-921, scale 1:62500.

Nelson, C. A., 1976, Late Precambrian- Early Cambrian stratigraphic and faunal succession of eastern California and the Precambrian-Cambrian boundary, in Moore, J. N,, and Fritsche, A. E., eds., Depositional environments of lower Paleozoic rocks in the White-Inyo Mountains, Inyo County, California: Society of Economic Paleontologists and Mineralogists, Pacific Section, Pacific Coast Paleogeography Field Guide 1, p. 31-42.

Nelson, C.A., 1978, Late Precambrian–Early Cambrian stratigraphic and faunal succession of eastern California and the Precambrian-Cambrian boundary: Geological Magazine, v. 115, p. 121–126.

Pearce, N.J., Perkins, W.T., Westgate, J.A., Gorton, M.P., Jackson, S.E., Neal, C.R., and Chenery, S.P., 1997, A compilation of new and published major and trace element data for NIST SRM 610 and NIST SRM 612 glass reference materials: Geostandards Newsletter, v. 21, p. 115–144, https://doi.org/10.1111/j.1751-908X.1997.tb00538.x.

Poole, F.G., Stewart, J.H., Palmer, A.R., Sandberg, C.A., Madrid, R.J., Ross, R.J., Jr., Hintze, L.F., Miller, M.M., and Wrucke, C.T., 1992, Latest Precambrian to latest Devonian time; development of a continental margin, in Burchfiel, B.C., Lipman, P.W., and Zoback, M.L., eds., The Cordilleran Orogen: Conterminous U.S.: Boulder, Colorado, Geological Society of America, The Geology of North America, v. G-3, p. 9–56.

Powerman, V., Hanson, R., Nosova, A., Girty, G.H., Hourigan, J. and Tretiakov, A., 2020, Nature and timing of Late Devonian–early Mississippian island-arc magmatism in the Northern Sierra terrane and implications for regional Paleozoic plate tectonics: Geosphere, v. 16, p. 258-280.

Rains, J.L., Marsaglia, K.M., and Dunne, G.C., 2012, Stratigraphic record of subduction initiation in the Permian metasedimentary succession of the El Paso Mountains, California: Lithosphere, v. 4, no. 6, p. 533–552.

Reagan, M.K., Ishizuka, O., Stern, R.J., Kelley, K.A., Ohara, Y., Blichert-Toft, J., Bloomer, S.H., Cash, J., Fryer, P., Hanan, B.B., Hickey-Vargas, R., Ishii, T., Kimura, J.I., Peate, D.W., Rowe, M.C., Woods, M., 2010, Fore-arc basalts and subduction initiation in the Izu-Bonin-Mariana system: Geochemistry Geophysics Geosystems, v. 11, Q03X12.

Reay, A., and Parkinson, D.,1997, Adakites from Solander Island, New Zealand; New Zealand Journal of Geology and Geophysics, v. 40, p. 121-126.

Renne, P.R., Swisher, C.C., Deino, A.L., Karner, D.B., Owens, T.L., and DePaolo, D.J., 1998, Intercalibration of standards, absolute ages and uncertainties in 40Ar/39Ar dating: Chemical Geology, v. 145, p. 117–152, https://doi.org/10.1016/S0009-2541(97)00159-9.

Saleeby, J., 2011, Geochemical mapping of the Kings-Kaweah ophiolite belt, California—Evidence for progressive mélange formation in a large offset transform-subduction initiation environment, in Wakabayashi, J., and Dilek, Y., eds., Mélanges: Processes of Formation and Societal Significance: Boulder, Colorado, Geological Society of America Special Paper 480, p. 31–73, doi:10.1130/2011.2480(02)

Saleeby, J., and Dunne, G., 2015, Temporal and tectonic relations of early Mesozoic arc magmatism, southern Sierra Nevada, California, in Anderson, T.H., Didenko, A.N., Johnson, C.L., Khanchuk, A.I., and MacDonald Jr., J.H., eds., Late Jurassic Margin of Laurasia: A Record of Faulting Accommodating Plate Rotation: Geological Society of America Special Paper 513, p. 223-268.

Saylor, J.E., and Sundell, K.E., 2016, Quantifying comparison of large detrital geochronology data sets: Geosphere, v. 12, p. 203-220.

Schoenborn, W.A., Fedo, C.M., and Farmer, G.L., 2012, Provenance of the Neoproterozoic Johnnie Formation and Stirling Quartzite, southeastern California, determined by detrital zircon geochronology and Nd isotope geochemistry: Precambrian Research, v. 206–207, p. 182–199.

Schmitz, M.D., and Davydov, V.I., 2012, Quantitative radiometric and biostratigraphic calibration of the Pennsylvanian–Early Permian (Cisuralian) time scale and pan-Euramerican chronostratigraphic correlation: Geological Society of America Bulletin, v. 124, p. 549–577.

Snoke A.W. Tullis J., 1998, An overview of fault rocks, in Snoke A.W. Tullis J. Todd V.R., eds., Fault-related rocks: A photographic atlas: Princeton, New Jersey, Princeton University Press, p. 3–18.

Snow, J.K., Asmerom, Y., Lux, D.R., 1991, Permian-Triassic plutonism and tectonics, Death Valley region, California and Nevada: Geology, v. 19, p. 629-632.

Snow. J.K., 1992, Large-magnitude Permian shortening and continental-margin tectonics in the southern Cordillera: Geological Society of America Bulletin, v. 104, p. 80-105.

Snow, J.K., Wernicke, B., 2000, Cenozoic tectonism in the central Basin and Range: magnitude, rate, and distribution of upper crustal strain: American Journal of Science, v. 300, p. 659– 719.

Staudacher, T.H., Jessberger, E.K., Dorflinger, D., and Kiko, J., 1978, A refined ultrahigh-vacuum furnace for rare gas analysis: Journal of Physics. E, Scientific Instruments, v. 11, p. 781–784, https://doi.org/10.1088/0022-3735/11/8/019.

Stern, R.J., 2004, Subduction initiation: Spontaneous and induced: Earth and Planetary Science Letters, v. 226, p. 275–292.

Stern, R.J. and Gerya, T., 2018, Subduction initiation in nature and models: A review; Tectonophysics, v. 746, p.173-198.

Stern, R.J., Reagan, M., Ishizuka, O., Ohara, Y. and Whattam, S., 2012, To understand subduction initiation, study forearc crust: To understand forearc crust, study ophiolites: Lithosphere, v. 4, p.469-483.

Stevens, C.H., and Stone, P., 1988, Early Permian thrust faults in east-central California: Geological Society of America Bulletin, v. 100, p. 552-562.

Stevens, C.H., Stone, P., 2005a, Interpretation of the Last Chance thrust, Death Valley region, California, as an Early Permian décollement in a previously undeformed shale basin: Earth-Science Reviews, v. 73, p. 79-101.

Stevens, C.H., Stone, P., 2005b, Structure and regional significance of the Late Permian(?) Sierra Nevada–Death Valley thrust system, east-central California: Earth-Science Reviews, v. 73, p. 103-113.

Stevens, C.H., Stone, P., Dunne, G.C., Greene, D.C., Walker, J.D., Swanson, B.J., 1997, Paleozoic and Mesozoic evolution of east-central California: International Geology Review, v. 39, p. 788– 829.

Stevens, C.H., Stone, P., and Ritter, S.M., 2001, Conodont and fusulinid biostratigraphy and history of the Pennsylvanian to Lower Permian Keeler Basin, east-central California: Brigham Young University Geology Studies, v. 46, p. 99–142.

Stevens, C.H., Stone, P., and Magginetti, R.T., 2015, Regional implications of new chronostratigraphic and paleogeographic data from the Early Permian Darwin Basin, east-central California: Stratigraphy, v. 12, p. 149–166.

Stewart, J. H., 1965, Precambrian and Lower Cambrian strata in the Last Chance Range area, Inyo County, California: *in* Cohee, G. V., and Vest, V. S., Changes in stratigraphic nomenclature by the U.S. Geological Survey, 1964: U.S. Geological Survey Bulletin 1224-A, p. A60-A70.

Stewart, J.H., 1970, Upper Precambrian and Lower Cambrian strata in the southern Great Basin, California and Nevada: U.S. Geological Survey Professional Paper 620, 206 pp.

Stewart, J.H., Ross, D.C., Nelson, C.A., Burchfiel, B.C., 1966, Last Chance thrust—a major fault in the eastern part of Inyo County, California: U.S. Geological Survey Professional Paper 550-D, p. D23–D34.

Stewart, J.H., McMenamin, M.A.S., and Morales-Ramirez, J.M., 1984, Upper Proterozoic and Cambrian rocks in the Caborca region, Sonora, Mexico—Physical stratigraphy, biostratigraphy, paleocurrent studies, and regional relations: U.S. Geological Survey Professional Paper 1309, 36 p.

Stone, P., and Stevens, C.H., 1988, Pennsylvanian and Early Permian paleogeography of east-central California: Implications for the shape of the continental margin and the timing of continental truncation: Geology, v. 16, p. 330–333.

Stone, P., Swanson, Brian J., Stevens, Calvin H., Dunne, George C., and Priest, Susan S., 2009, Geologic map of the southern Inyo Mountains and vicinity, Inyo County, California (ver. 1.1, September, 2014): U.S. Geological Survey Scientific Investigations Map 3094, scale 1:24,000, 1 sheet, includes 22 p.

Stone, P., Stevens, C. H., Belasky, P., Montanez, I. P., Martin, L. G., Wardlaw, B. R., Sandberg, C. A., Wan, E., Olson, H. A. and Priest, S. S., 2014. Geologic map and upper Paleozoic stratigraphy of the Marble Canyon area, Cottonwood Canyon quadrangle, Death Valley National Park, Inyo County, California. Washington, DC: U.S. Geological Survey Scientific Investigations Map 3298, scale 1:24,000, 59 pp.

Sutherland, R., Barnes, P.M., and Uruski, C., 2006, Miocene–Recent deformation, surface elevation, and volcanic intrusion of the overriding plate during subduction initiation, offshore southern Fiordland, Puysegur margin, southwest New Zealand: New Zealand Journal of Geology and Geophysics, v. 49, p. 131–149.

Sutherland, R., Gurnis, M., Kamp, P.J.J., and House, M.A., 2009, Regional exhumation history of brittle crust during subduction initiation, Fiordland, southwest New Zealand, and implications for thermochronologic sampling and analysis strategies: Geosphere, v. 5, p. 409–425.

Sylvester, A.G., Oertel, G., Nelson, C.A., and Christie, J.M., 1978, Papoose Flat pluton: A granitic blister in the Inyo Mountains, eastern California: Geological Society of America Bulletin, v. 89, p. 1205-1219.

Tessensohn, F., and Piepjohn, K., 2000, Eocene compressive deformation in Arctic Canada, North Greenland and Svalbard and its plate tectonic causes: Polarforschung, v. 68, p. 121 – 124.

Tikoff, B., and Teyssier, C., 1994, Strain modeling of displacement-field partitioning in transpressional orogens: Journal of Structural Geology, v. 16, p. 1575–1588.

Toth, J., and Gurnis, M., 1998, Dynamics of subduction initiation at preexisting fault zones, Journal of Geophysical Research, v. 103, p. 18,053–18,067.

Trexler, J.H., Jr., Cashman, P.H., Cole, J.C., Snyder, W.S., Tosdal, R.M., and Davydov, V.I., 2003, Widespread effects of mid-Mississippian deformation in the Great Basin of western North America: Geological Society of America Bulletin, v. 115, p. 1278–1288.

Trexler, J.H., Jr., Cashman, P.H., Snyder, W.S., and Davydov, V.I., 2004, Late Paleozoic tectonism in Nevada: Timing, kinematics, and tectonic significance: Geological Society of America Bulletin, v. 116, p. 525–538.

Vaughn, L.M., 2020, Timing and Basin Response to Late Paleozoic Subduction Initiation Along the Southwestern Margin of Laurentia [M.S. Thesis]: Socorro, New Mexico, New Mexico Institute of Mining and Technology.

Vermeesch, P., 2013, Multi-sample comparison of detrital age distributions: Chemical Geology, v. 341, p. 140–146.

Walker, J.D., 1988, Permian and Triassic rocks of the Mojave Desert and their implications for timing and mechanisms of continental truncation: Tectonics, v. 7, p. 685–709.

Watkins, J.A., 2015, Tectonic and Aqueous Processes in the Formation of Mass-wasting Features on Mars and Earth [Ph.D. Dissertation]: Los Angeles, California, University of California, 230 p.

Wendt, I., and Carl, C., 1991, The statistical distribution of the mean squared weighted deviation: Chemical Geology, v. 86, p. 275–285.

Wrucke, C.T., Corbett, K.P., 1990, Geologic map of the Last Chance quadrangle, California and Nevada: U.S. Geological Survey Open-file Report 90-647-B, 1:62,500.

Wyld, S.J., 1991, Permo-Triassic tectonism in volcanic arc sequences of the western U.S. Cordillera and implications for the Sonoma orogeny: Tectonics, v. 10, p. 1007–1017.

Wyld, S.J., and Wright, J.E., 2001, New evidence for Cretaceous strike-slip faulting in the United States Cordillera and implications for terrane displacement, deformation patterns, and plutonism: American Journal of Science, v. 301, p. 150–181.

Xie, L., Zhang, Y., Zhang, H., Sun, J., and Wu, F., 2008, In situ simultaneous determination of trace elements, U-Pb and Lu-Hf isotopes in zircon and baddeleyite: Chinese Science Bulletin, v. 53, no. 10, p. 1565–1573.

Yonkee, W.A., Eleogram, B., Wells, M.L., Stockli, D.F., Kelley, S. and Barber, D.E., 2019, Fault Slip and Exhumation History of the Willard Thrust Sheet, Sevier Fold-Thrust Belt, Utah: Relations to Wedge Propagation, Hinterland Uplift, and Foreland Basin Sedimentation: Tectonics, v. 38, p. 2850-2893.

TABLE 2.1. SAMPLE DETAILS AND REFERENCES FOR DETRITAL ZIRCON U-PB DATA COMPILATION

Sample name	Formation	Terrane	Number of grains	Reference
SP-21	Carrara	Snow Lake	94	Memeti et al. (2010)
SLP-ZAB1	Zabriskie	Snow Lake	96	Grasse et al. (2001), Memeti et al. (2010)
SP-13	Wood Canyon	Snow Lake	95	Memeti et al. (2010)
SLP-STERLING1	Sterling Quartzite	Snow Lake	92	Grasse et al. (2001), Memeti et al. (2010)
BP-M-314	Benson Lake Pendant	Snow Lake	62	Memeti et al. (2010)
RE-242	Benson Lake Pendant	Snow Lake	75	Memeti et al. (2010)
SN7131	Quartzite Peak	Snow Lake	84	Memeti et al. (2010)
HE-8	Quartzite Mtn. Pendant	Snow Lake	87	Attia et al. (2018)
BCE-8, BC-31, 09-KK-6	Boyden Cave Pendant	Snow Lake	244 (82, 84, 78)	Attia et al. (2018)
SP-1	Crane Flat Area	Snow Lake	88	Attia et al. (2018)
SV	Saline Valley	White-Inyo	142	This study
HARK	Harkless	White-Inyo	32	This study
HAR* (12WI2)	Harkless	White-Inyo	85	Chapman et al. (2015)
POL* (12WI1)	Poleta	White-Inyo	82	Chapman et al. (2015)
CAMP* (611)	Campito–Monte Negro	White-Inyo	98	Chapman et al. (2015)
CAMP** (11IY1, WM101, 568)	Campito–Andrews Mountain	White-Inyo	247	Chapman et al. (2015)
DS* (12WI3, JSMD0301, JSMD0302)	Deep Spring	White-Inyo	143	Chapman et al. (2015), MacLean et al. (2009)
REED* (12WI6)	Reed Dolomite	White-Inyo	88	Chapman et al. (2015)
WY* (JSWI0301, WM 208, WM170, 12WI5, 1	Wyman	White-Inyo	395	Chapman et al. (2015), MacLean et al. (2009)
WY	Wyman	White-Inyo	166	This study
CAR	Carrara	Death Valley	141	This study
ZAB	Zabriskie Quartzite	Death Valley	140	This study
WC	Wood Canyon	Death Valley	143	This study
WC* (WC1)	Wood Canyon	Death Valley	204	Gehrels and Pecha (2014)
STIR* (JSPR0303)	Sterling Quartzite	Death Valley	40	MacLean et al. (2009)
STIR**CSSUPSTART CSSUPEND(NR9)	Sterling Quartzite	Death Valley	62	Schoenborn et al. (2012)
ZAB2	Zabriskie Quartzite	Mojave Desert	205	Gehrels and Pecha (2014)
WC2	Wood Canyon	Mojave Desert	197	Gehrels and Pecha (2014)
STIRLING1	Sterling Quartzite	Mojave Desert	60	Barth et al. (2009)
PROV	Proveedora Quartzite	Caborca block	146	Gehrels and Pecha (2014)

Note: Single and double asterisks denote separate detrital zircon data sets from the same formation.

Table 2.S1: Sanidine 40Ar/39Ar Geochronologic Data

Zuza-NBMG, LC 12b, Single Crystal Fusion, Sanidine, J = 0.00169 ± 0.42%

4 amu discrimination = 1.0190 ± 0.30% (crystals 1-9), 40/39K = 0.0322 ± 6.64%, 36/37Ca = 0.000233 ± 0.83%, 39/37Ca = 0.000682 ± 0.65%

4 amu discrimination = 1.0313 ± 0.07% (crystals 10-14)

Crystal	T (C)	t (min.)	36Ar	37Ar	38Ar	39Ar	40Ar	%40Ar*	Ca/K	40Ar*/39ArK	Age (Ma)	1s.d.
1	1600	1	0.027	0.51	1.082	82.6	159.6	94.6	0.027	1.8064	5.5	0.04
2	1600	1	0.024	1.493	0.88	69.9	134.8	94.1	0.093	1.8054	5.5	0.04
3	1601	1	0.014	0.266	0.457	34.9	68.0	94	0.033	1.8047	5.49	0.05
4	1602	1	0.015	0.446	0.843	63.4	121.9	95.7	0.031	1.8287	5.57	0.05
5	1603	1	0.016	0.213	0.487	33.1	59.9	91.3	0.028	1.6241	4.95	0.11
6	1604	1	0.016	0.213	0.487	37.2	75.8	96.9	0.025	1.9524	5.94	0.07
7	1605	1	0.014	0.179	0.311	23.2	46.1	97.1	0.034	1.882	5.73	0.05
8	1606	1	0.013	0.115	0.181	13.4	25.6	97.1	0.037	1.7698	5.39	0.14
9	1607	1	0.014	0.388	0.953	72.7	139.2	97.9	0.023	1.8666	5.68	0.04
10	1608	1	0.017	0.113	0.239	16.6	30.7	89.2	0.030	1.5488	4.72	0.09
11	1609	1	0.007	0.114	0.267	22.7	44.0	99.9	0.022	1.8521	5.64	0.08
12	1610	1	0.019	0.237	0.138	10.6	22.8	83.4	0.097	1.6527	5.03	0.17
13	1611	1	0.01	0.06	0.106	8.2	17.8	94.8	0.032	1.8541	5.64	0.12
14	1612	1	0.03	0.094	0.137	10.2	26.8	73.3	0.040	1.7945	5.46	0.12
note: isotope beams in mV rlsd = released, error in age includes J error, all errors 1 sigma										Mean ± s.d. =	5.45	0.33
(36Ar through 40Ar are measured beam intensities, corrected for decay in age calculations)										Mean ± s.d. =	5.5	0.27
										(fusion 10 omitted)		
										Wtd mean age =	5.51	0.03
										(9 fusions)		
										No isochron		

Table 2.S2: Basalt Groundmass 40Ar/39Ar Geochronologic Data

Zuza-NBMG, LC 12a, Basalt Groundmass, 26.59 mg, J = 0.00166 ± 0.40%

4 amu discrimination = 1.0313 ± 0.07%, 40/39K = 0.0322 ± 6.64%, 36/37Ca = 0.000233 ± 0.83%, 39/37Ca = 0.000682 ± 0.65%

step	T (C)	t (min.)	36Ar	37Ar	38Ar	39Ar	40Ar	%40Ar*	% 39Ar rlsd	Ca/K	40Ar*/39ArK	Age (Ma)	1s.d.
1	700	12	6.21	33.014	1.906	38.636	2166.42	18	6.8	3.76	10.15	30.15	0.43
2	770	12	0.585	18.735	0.728	41.809	285.282	43.9	7.4	1.97	2.82	8.44	0.1
3	840	12	0.997	25.464	0.951	48.293	452.716	38.5	8.5	2.32	3.49	10.43	0.1
4	890	12	0.774	34.802	0.841	42.75	344.28	38	7.5	3.58	2.93	8.74	0.08
5	940	12	0.42	26.96	0.868	40.813	229.772	51.7	7.2	2.91	2.64	7.89	0.11
6	990	12	0.23	20.013	0.978	42.63	167.217	67.8	7.5	2.07	2.31	6.91	0.07
7	1030	12	0.234	22.327	1.226	50.771	176.912	69.1	8.9	1.93	2.11	6.31	0.03
8	1070	12	0.24	25.526	1.454	58.494	184.066	69.5	10.3	1.92	1.93	5.77	0.04
9	1110	12	0.173	26.986	1.301	51.247	156.476	78	9	2.32	2.05	6.12	0.04
10	1150	12	0.111	43.353	0.729	30.384	95.077	99.7	5.3	6.29	2.23	6.67	0.11
11	1210	12	0.488	149.643	1.676	60.576	272.452	61.1	10.7	10.90	2.50	7.47	0.05
12	1400	12	0.551	185.201	1.752	62.235	291.218	63.3	10.9	13.14	2.48	7.42	0.07
							Cumulative %39Ar rlsd =		100		Total gas age =	8.97	0.03
note: isotope beams in mV, rlsd = released, error in age includes J error, all errors 1 sigma											No plateau		
(36Ar through 40Ar are measured beam intensities, corrected for decay for the age calculations)											No isochron		

Table 2.S3: Zircon U-Pb Geochronologic

Data Sample Name:								207/235		206/238		207/206		Best age		
Grain #	[U] ppm	U/Th	207/235	2σ error	206/238	2σ error	RHO	Age Ma	2σ error	Age (Ma)	2σ error	Age (Ma)	2σ error	(Ma)	2σ error	% Discordance*
DL_030118_1 – Saline Valley Formation - 37.059, -117.87046																
DL_030118_1_1	126.6	1.312	4.204	0.062	0.286	0.0036	0.70356	1674	12	1620	18	1744	20	1744	20	7.1
DL_030118_1_2	146.6	2.23	1.875	0.025	0.1796	0.0016	0.32962	1071	8.7	1064.8	8.9	1085	27	1085	27	1.9
DL_030118_1_3	175	1.267	4.543	0.075	0.301	0.0037	0.69871	1737	14	1695	18	1785	22	1785	22	5
DL_030118_1_4	281.1	2.046	4.308	0.053	0.3007	0.0032	0.78688	1693	10	1694	16	1698	14	1698	14	0.2
DL_030118_1_5	134	1.441	2.397	0.033	0.21	0.0022	0.57015	1239.8	9.9	1228	12	1259	23	1259	23	2.5
DL_030118_1_6	286.3	1.507	2.907	0.045	0.2358	0.0038	0.71337	1381	12	1364	20	1412	22	1412	22	3.4
DL_030118_1_7	332	1.882	1.771	0.026	0.1734	0.002	0.73308	1033.4	9.4	1030	11	1038	21	1038	21	0.8
DL_030118_1_8	155.9	2.685	3.154	0.04	0.2538	0.0025	0.45942	1444.5	9.7	1458	13	1426	24	1426	24	2.2
DL_030118_1_9	268	0.956	9.89	0.42	0.397	0.014	0.82428	2420	39	2153	64	2647	39	2647	39	18.7
DL_030118_1_10	104.9	1.431	17.39	0.26	0.5873	0.008	0.75277	2955	14	2976	32	2940	17	2940	17	1.2
DL_030118_1_11	173.3	1.739	4.365	0.062	0.3011	0.0037	0.66364	1703	12	1696	18	1706	20	1706	20	0.6
DL_030118_1_12	302	1.843	2.942	0.043	0.2302	0.003	0.64632	1393	11	1335	16	1478	22	1478	22	9.7
DL_030118_1_13	118.9	1.499	3.06	0.05	0.2451	0.0033	0.62151	1421	12	1413	17	1426	25	1426	25	0.9
DL_030118_1_14	122.2	0.2571	3.085	0.054	0.2437	0.0031	0.58642	1425	14	1405	16	1446	28	1446	28	2.8
DL_030118_1_15	341.7	4.83	7.88	0.12	0.4043	0.0047	0.77843	2216	13	2188	22	2238	17	2238	17	2.2
DL_030118_1_16	479	1.856	1.846	0.02	0.178	0.0016	0.66113	1062.9	7.7	1055.9	8.6	1069	18	1069	18	1.2
DL_030118_1_17	169.7	2.067	4.38	0.054	0.3003	0.0032	0.59352	1706	10	1692	16	1722	19	1722	19	1.7
DL_030118_1_18	275.1	2.157	4.417	0.052	0.3	0.0033	0.79841	1714	9.7	1690	16	1736	14	1736	14	2.6
DL_030118_1_19	195	1.198	13.82	0.18	0.5271	0.0065	0.69921	2735	12	2727	28	2737	16	2737	16	0.4
DL_030118_1_20	95	1.169	1.916	0.031	0.1834	0.0021	0.39131	1084	11	1085	11	1067	33	1067	33	1.7
DL_030118_1_21	120.1	1.237	2.071	0.044	0.1939	0.0032	0.72236	1135	15	1144	17	1118	29	1118	29	2.3
DL_030118_1_22	287.2	1.177	3.106	0.048	0.2485	0.0036	0.73351	1432	12	1430	18	1427	20	1427	20	0.2
DL_030118_1_23	325	0.8591	12.9	0.15	0.5145	0.0062	0.80532	2671	11	2678	27	2669	12	2669	12	0.3
DL_030118_1_24	142.1	1.105	12.1	0.21	0.5159	0.0072	0.69616	2607	16	2683	32	2544	21	2544	21	5.5
DL_030118_1_25	284.6	2.697	4.251	0.054	0.2979	0.0032	0.6803	1682	10	1680	16	1673	17	1673	17	0.4
DL_030118_1_26	236.8	2.277	4.589	0.06	0.3135	0.0039	0.74896	1747	11	1760	18	1730	18	1730	18	1.7
DL_030118_1_27	209.3	0.5653	15.15	0.23	0.5454	0.0074	0.80842	2822	15	2804	31	2830	15	2830	15	0.9

Sample Name:								207/235		206/238		207/206		Best age		
Grain #	[U] ppm	U/Th	207/235	2σ error	206/238	2σ error	RHO	Age Ma	2σ error	Age (Ma)	2σ error	Age (Ma)	2σ error	(Ma)	2σ error	% Discordance*
DL_030118_1_28	333	1.794	4.129	0.048	0.2892	0.0035	0.78222	1658.4	9.5	1639	18	1677	14	1677	14	2.3
DL_030118_1_29	56.3	1.027	3.074	0.058	0.2433	0.0036	0.52875	1422	14	1403	19	1444	31	1444	31	2.8
DL_030118_1_30	181.7	1.944	4.558	0.067	0.3115	0.0044	0.71097	1739	12	1747	22	1727	20	1727	20	1.2
DL_030118_1_31	329	1.654	4.616	0.04	0.31	0.0025	0.65804	1751.3	7.2	1740	12	1759	13	1759	13	1.1
DL_030118_1_32	205.4	0.96	3.11	0.036	0.2471	0.0023	0.61565	1433.6	8.8	1423	12	1440	18	1440	18	1.2
DL_030118_1_33	172.9	0.7241	16.01	0.19	0.562	0.0061	0.74194	2875	11	2876	26	2872	13	2872	13	0.1
DL_030118_1_34	214.4	2.014	4.82	0.058	0.3208	0.0039	0.77368	1786	10	1792	19	1777	16	1777	16	0.8
DL_030118_1_35	113.1	0.3734	12.23	0.15	0.489	0.0062	0.74459	2621	11	2564	27	2661	15	2661	15	3.6
DL_030118_1_36	242.1	1.538	3.154	0.048	0.2543	0.004	0.75589	1443	12	1459	21	1422	19	1422	19	2.6
DL_030118_1_37	121.7	1.174	5.274	0.079	0.3482	0.005	0.7404	1863	13	1924	24	1794	20	1794	20	7.2
DL_030118_1_38	80.5	0.829	2.162	0.042	0.1924	0.0025	0.58869	1168	14	1134	14	1224	33	1224	33	7.4
DL_030118_1_39	209.4	1.085	3.153	0.055	0.2542	0.004	0.67287	1443	13	1459	21	1418	26	1418	26	2.9
DL_030118_1_40	222.4	1.185	3.241	0.048	0.2565	0.0031	0.7041	1466	12	1471	16	1462	20	1462	20	0.6
DL_030118_1_41	231.6	1.343	1.918	0.033	0.1841	0.0025	0.77724	1088	11	1089	14	1087	21	1087	21	0.2
DL_030118_1_42	184.5	2.03	3.089	0.04	0.2463	0.0027	0.65111	1429.4	9.8	1419	14	1441	19	1441	19	1.5
DL_030118_1_43	153.9	1.468	4.232	0.064	0.298	0.0039	0.72381	1679	12	1683	19	1674	20	1674	20	0.5
DL_030118_1_44	146.3	1.329	1.995	0.032	0.1887	0.0022	0.56715	1112	11	1114	12	1109	26	1109	26	0.5
DL_030118_1_45	378.6	2.63	1.849	0.025	0.1812	0.0022	0.72801	1061.7	8.8	1073	12	1042	19	1042	19	3
DL_030118_1_46	94.6	1.73	4.78	0.082	0.3191	0.0049	0.69405	1778	14	1783	24	1774	23	1774	23	0.5
DL_030118_1_47	107.1	0.424	2.612	0.062	0.2208	0.0045	0.39332	1301	18	1286	24	1317	48	1317	48	2.4
DL_030118_1_48	149.9	1.494	4.187	0.08	0.2921	0.0055	0.79202	1668	16	1650	28	1687	23	1687	23	2.2
DL_030118_1_49	75.6	2.75	4.274	0.067	0.2974	0.004	0.65201	1687	13	1677	20	1706	22	1706	22	1.7
DL_030118_1_50	279	1.735	3.08	0.037	0.2439	0.0029	0.70485	1426	9.2	1406	15	1459	17	1459	17	3.6
DL_030118_1_51	289	1.176	2.84	0.03	0.225	0.0018	0.60114	1366	8.1	1307.9	9.2	1451	17	1451	17	9.9
DL_030118_1_52	375	3.04	4.201	0.06	0.29	0.0041	0.71851	1672	12	1640	21	1718	20	1718	20	4.5
DL_030118_1_53	196.5	0.876	2.976	0.052	0.2352	0.0036	0.63667	1399	13	1361	19	1465	26	1465	26	7.1
DL_030118_1_54	456	0.763	3.515	0.094	0.2447	0.0068	0.82435	1528	21	1419	39	1670	31	1670	31	15
DL_030118_1_55	326	0.943	2.573	0.049	0.2074	0.0035	0.77168	1290	13	1214	19	1416	23	1416	23	14.3
DL_030118_1_56	464	1.565	3.173	0.075	0.2192	0.0044	0.79552	1447	19	1277	23	1700	23	1700	23	24.9

Sample Name:								207/235		206/238		207/206		Best age		
Grain #	[U] ppm	U/Th	207/235	2σ error	206/238	2σ error	RHO	Age Ma	2σ error	Age (Ma)	2σ error	Age (Ma)	2σ error	(Ma)	2σ error	% Discordance*
DL_030118_1_57	274	2.36	5.06	0.16	0.3199	0.0088	0.67167	1824	27	1787	43	1867	45	1867	45	4.3
DL_030118_1_58	209.2	0.792	4.04	0.11	0.2817	0.0074	0.59298	1638	22	1598	37	1690	36	1690	36	5.4
DL_030118_1_59	134.9	1.681	4.08	0.11	0.279	0.0065	0.71754	1646	23	1585	33	1726	36	1726	36	8.2
DL_030118_1_60	189	1.566	2.924	0.069	0.2284	0.0045	0.69344	1385	18	1325	23	1476	34	1476	34	10.2
DL_030118_1_61	166.7	1.163	4.07	0.05	0.281	0.003	0.72445	1646	10	1596	15	1709	16	1709	16	6.6
DL_030118_1_62	459	6.09	4.451	0.068	0.2994	0.0041	0.83411	1719	13	1687	20	1757	16	1757	16	4
DL_030118_1_63	194.9	1.06	3.03	0.069	0.2381	0.0044	0.69644	1412	17	1376	23	1463	32	1463	32	5.9
DL_030118_1_64	240.8	0.846	11.82	0.19	0.4668	0.0072	0.75212	2586	15	2471	31	2683	17	2683	17	7.9
DL_030118_1_65	309	2.146	4.159	0.045	0.2854	0.0032	0.75871	1664.5	9	1618	16	1717	14	1717	14	5.8
DL_030118_1_66	225	1.052	11.48	0.15	0.4739	0.0061	0.80339	2560	12	2499	27	2599	13	2599	13	3.8
DL_030118_1_67	164	1.055	3.332	0.055	0.2412	0.0028	0.78833	1486	13	1392	14	1615	19	1615	19	13.8
DL_030118_1_68	586	2.306	3.084	0.068	0.216	0.0047	0.90616	1425	17	1260	25	1679	18	1679	18	25
DL_030118_1_69	599	0.87	2.428	0.038	0.1946	0.0028	0.85639	1250	11	1146	15	1428	16	1428	16	19.7
DL_030118_1_70	264.5	1.478	1.899	0.026	0.1751	0.0017	0.61681	1079.8	9.2	1040.1	9.4	1156	22	1156	22	10
DL_030118_1_71	470	2.07	10.38	0.24	0.406	0.011	0.93873	2473	24	2192	49	2723	19	2723	19	19.5
DL_030118_1_72	386	1.326	3.99	0.11	0.2702	0.0069	0.76683	1629	22	1540	35	1729	30	1729	30	10.9
DL_030118_1_73	548	2.276	4.156	0.079	0.2927	0.005	0.7781	1663	16	1654	25	1672	23	1672	23	1.1
DL_030118_1_74	306	0.724	3.556	0.095	0.2548	0.0073	0.80089	1541	22	1462	38	1623	37	1623	37	9.9
DL_030118_1_75	193	0.61	4.04	0.093	0.2759	0.0077	0.83025	1639	19	1568	39	1732	31	1732	31	9.5
DL_030118_1_76	248.9	1.866	4.144	0.088	0.2839	0.0059	0.81838	1659	17	1609	29	1721	22			
DL_030118_1_77	233.8	0.915	4.293	0.069	0.2974	0.0047	0.7932	1691	13	1677	23	1705	20	1705	20	1.6
DL_030118_1_78	243	1.758	4.074	0.051	0.2811	0.0034	0.75177	1647	10	1596	17	1711	16	1711	16	6.7
DL_030118_1_79	222	1.34	3.4	0.23	0.24	0.016	0.77686	1493	55	1382	83	1677	55	1677	55	17.6
DL_030118_1_80	289	1.91	3.93	0.14	0.2668	0.0079	0.84896	1614	30	1523	40	1732	37	1732	37	12.1
DL_030118_1_81	236.6	1.332	2.771	0.047	0.2272	0.0037	0.75389	1346	12	1319	20	1389	23	1389	23	5
DL_030118_1_82	282	1.821	4.178	0.07	0.2861	0.0043	0.70995	1667	14	1621	21	1722	26	1722	26	5.9
DL_030118_1_83	337	4.92	3.897	0.07	0.2712	0.0044	0.68573	1612	15	1546	22	1702	23	1702	23	9.2
DL_030118_1_84	605	1.069	2.96	0.1	0.2392	0.0072	0.7615	1395	26	1381	37	1409	46	1409	46	2
DL_030118_1_85	355	1.69	3.69	0.15	0.256	0.01	0.84717	1570	30	1467	52	1695	42	1695	42	13.5

Sample Name:								207/235		206/238		207/206		Best age		
Grain #	[U] ppm	U/Th	207/235	2σ error	206/238	2σ error	RHO	Age Ma	2σ error	Age (Ma)	2σ error	Age (Ma)	2σ error	(Ma)	2σ error	% Discordance*
DL_030118_1_86	181.3	1.937	4.275	0.057	0.2939	0.0032	0.64365	1688	11	1661	16	1719	19	1719	19	3.4
DL_030118_1_87	192.1	0.667	2.972	0.093	0.2275	0.0058	0.77358	1400	25	1320	30	1520	36	1520	36	13.2
DL_030118_1_88	108.4	1.084	3.173	0.046	0.2552	0.0031	0.53594	1448	11	1465	16	1425	21	1425	21	2.8
DL_030118_1_89	426	1.443	3.954	0.083	0.2712	0.0054	0.86102	1623	17	1546	28	1699	23	1699	23	9
DL_030118_1_90	212.5	1.383	3.98	0.06	0.2715	0.0039	0.75661	1630	13	1550	20	1731	19	1731	19	10.5
DL_030118_1_91	413	6.29	1.764	0.022	0.1658	0.002	0.75967	1032.1	8.2	988	11	1124	17	1124	17	12.1
DL_030118_1_92	305	1.224	2.998	0.051	0.2415	0.0039	0.79055	1405	13	1393	20	1425	21	1425	21	2.2
DL_030118_1_93	274.5	1.003	4.068	0.037	0.2772	0.0022	0.7182	1647.9	7.5	1577	11	1738	12	1738	12	9.3
DL_030118_1_94	206.6	0.966	4.366	0.056	0.2954	0.0033	0.71837	1704	11	1668	16	1752	16	1752	16	4.8
DL_030118_1_95	586	6.8	1.832	0.026	0.1762	0.0021	0.76169	1055.5	9.6	1046	12	1079	19	1079	19	3.1
DL_030118_1_96	392	1.961	3.246	0.036	0.2294	0.0025	0.77694	1467.3	8.7	1331	13	1662	14	1662	14	19.9
DL_030118_1_97	263.5	2.43	4.137	0.071	0.2912	0.0047	0.77902	1659	14	1646	23	1685	20	1685	20	2.3
DL_030118_1_98	213.4	1.629	2.848	0.056	0.2249	0.004	0.76683	1368	16	1307	21	1454	24	1454	24	10.1
DL_030118_1_99	216.8	2.385	3.066	0.04	0.2479	0.0028	0.66966	1422	10	1427	14	1419	19	1419	19	0.6
DL_030118_1_100	128.5	1.321	4.297	0.067	0.3	0.004	0.72499	1691	13	1690	20	1699	21	1699	21	0.5
DL_030118_1_101	231.4	1.394	3.707	0.054	0.2648	0.004	0.7734	1572	12	1513	20	1656	18	1656	18	8.6
DL_030118_1_102	201.4	1.087	3.059	0.04	0.2457	0.0027	0.75555	1420	10	1416	14	1430	16	1430	16	1
DL_030118_1_103	293	3.146	4.326	0.064	0.3016	0.004	0.78459	1696	12	1698	20	1695	18	1695	18	0.2
DL_030118_1_104	207.8	1.509	4.027	0.061	0.2812	0.0036	0.71679	1637	12	1596	18	1694	20	1694	20	5.8
DL_030118_1_105	72.6	0.973	4.071	0.06	0.2885	0.0035	0.70106	1647	12	1633	17	1670	19	1670	19	2.2
DL_030118_1_106	183.5	2.088	4.08	0.054	0.2852	0.0031	0.68491	1648	11	1617	15	1690	18	1690	18	4.3
DL_030118_1_107	174.7	1.483	1.857	0.025	0.1775	0.002	0.62277	1064.5	9.1	1053	11	1091	22	1091	22	3.5
DL_030118_1_108	372	1.201	2.772	0.031	0.2213	0.0021	0.72228	1346.6	8.3	1289	11	1438	15	1438	15	10.4
DL_030118_1_109	65.8	0.666	3.987	0.054	0.2701	0.0027	0.4699	1631	11	1541	14	1752	23	1752	23	12
DL_030118_1_110	187.1	0.5277	4.169	0.057	0.2915	0.0037	0.68751	1667	11	1648	18	1690	20	1690	20	2.5
DL_030118_1_111	136.9	0.924	3.072	0.047	0.2508	0.0033	0.75973	1423	12	1442	17	1398	19	1398	19	3.1
DL_030118_1_112	283	1.642	1.912	0.029	0.1829	0.0025	0.78345	1083	10	1082	14	1085	19	1085	19	0.3
DL_030118_1_113	246	2.133	3.003	0.049	0.2398	0.0034	0.7693	1406	12	1385	17	1437	20	1437	20	3.6
DL_030118_1_114	266	1.041	2.609	0.036	0.206	0.0024	0.73471	1303	10	1207	13	1459	18	1459	18	17.3

Sample Name:								207/235		206/238		207/206		Best age		
Grain #	[U] ppm	U/Th	207/235	2σ error	206/238	2σ error	RHO	Age Ma	2σ error	Age (Ma)	2σ error	Age (Ma)	2σ error	(Ma)	2σ error	% Discordance*
DL_030118_1_115	260.3	1.86	4.658	0.06	0.3081	0.0036	0.76555	1757	11	1730	18	1792	15	1792	15	3.5
DL_030118_1_116	147.6	0.891	4.18	0.064	0.291	0.0041	0.69755	1667	13	1645	21	1693	21	1693	21	2.8
DL_030118_1_117	487	3.85	4.504	0.053	0.304	0.0033	0.81975	1730	9.9	1710	16	1755	13	1755	13	2.6
DL_030118_1_118	324	3.179	2.994	0.046	0.239	0.003	0.75208	1404	12	1383	16	1434	19	1434	19	3.6
DL_030118_1_119	106.7	1.745	5.04	0.14	0.3132	0.0047	0.61845	1817	22	1755	24	1890	36	1890	36	7.1
DL_030118_1_120	373	1.018	1.869	0.022	0.1759	0.002	0.69636	1069	8.1	1044	11	1115	18	1115	18	6.4
DL_030118_1_121	209.9	0.3892	2.764	0.051	0.2203	0.0036	0.83065	1343	14	1282	19	1433	24	1433	24	10.5
DL_030118_1_122	166.2	1.522	3.02	0.038	0.2373	0.0026	0.6538	1412.2	9.5	1372	14	1474	20	1474	20	6.9
DL_030118_1_123	135.2	0.517	2.983	0.044	0.2347	0.0027	0.58251	1401	11	1359	14	1466	23	1466	23	7.3
DL_030118_1_124	289	3.97	1.599	0.019	0.1481	0.0016	0.74321	968.9	7.3	890.3	9	1146	21	1146	21	22.3
DL_030118_1_125	384.7	1.155	3.283	0.052	0.2294	0.0035	0.83936	1474	12	1330	18	1686	16	1686	16	21.1
DL_030118_1_126	197.4	1.488	4.093	0.057	0.2855	0.0038	0.79742	1652	12	1618	19	1691	16	1691	16	4.3
DL_030118_1_127	323	0.7083	11.17	0.14	0.4631	0.0052	0.77122	2535	12	2452	23	2601	14	2601	14	5.7
DL_030118_1_128	201.8	4.36	4.182	0.047	0.2892	0.0028	0.71505	1668.8	9.3	1637	14	1709	15	1709	15	4.2
DL_030118_1_129	167.8	1.514	4.219	0.053	0.29	0.0032	0.65856	1676	10	1641	16	1714	18	1714	18	4.3
DL_030118_1_130	280	0.824	2.642	0.034	0.2204	0.0024	0.70782	1310.8	9.6	1283	13	1351	18	1351	18	5
DL_030118_1_131	292	5.18	4.5	0.053	0.2978	0.0032	0.74912	1729.3	9.7	1680	16	1786	14	1786	14	5.9
DL_030118_1_132	510	5.41	1.764	0.022	0.1694	0.002	0.78462	1032.2	7.9	1008	11	1079	16	1079	16	6.6
DL_030118_1_133	132.1	1.155	4.291	0.058	0.2924	0.0033	0.69947	1691	11	1653	17	1733	18	1733	18	4.6
DL_030118_1_134	138.4	1.087	1.882	0.026	0.1728	0.0019	0.4873	1074.1	9.6	1027	10	1162	26	1162	26	11.6
DL_030118_1_135	271	2.819	3.008	0.032	0.2433	0.0026	0.67082	1408.4	8.2	1403	14	1414	17	1414	17	0.8
DL_030118_1_136	222.4	1.528	4.223	0.079	0.2773	0.0047	0.79709	1676	15	1577	23	1803	21	1803	21	12.5
DL_030118_1_137	378	2.474	3.825	0.066	0.2643	0.0045	0.80152	1596	14	1511	23	1708	20	1708	20	11.5
DL_030118_1_138	302.7	2.917	1.825	0.019	0.1733	0.0012	0.67417	1054.4	6.9	1029.9	6.9	1102	16	1102	16	6.5
DL_030118_1_139	179	0.87	4.034	0.037	0.2705	0.0023	0.55642	1640.1	7.5	1543	11	1759	15	1759	15	12.3
DL_030118_1_140	62.7	0.5044	15.55	0.19	0.5457	0.0064	0.73971	2847	12	2805	27	2875	13	2875	13	2.4
DL_030118_1_141	111.3	0.986	4.407	0.066	0.3034	0.0038	0.71459	1711	13	1707	19	1715	20	1715	20	0.5
DL_030118_1_142	418	1.194	4.145	0.041	0.2845	0.0025	0.86589	1662.1	8.2	1616	13	1723	12	1723	12	6.2
DL_030118_1_143	78.3	0.879	3.118	0.054	0.2468	0.004	0.64495	1434	13	1421	21	1458	27	1458	27	2.5

Sample Name:								207/235		206/238		207/206		Best age		
Grain #	[U] ppm	U/Th	207/235	2σ error	206/238	2σ error	RHO	Age Ma	2σ error	Age (Ma)	2σ error	Age (Ma)	2σ error	(Ma)	2σ error	% Discordance*

Sample Name:								207/235		206/238		207/206		Best age		
Grain #	[U] ppm	U/Th	207/235	2σ error	206/238	2σ error	RHO	Age Ma	2σ error	Age (Ma)	2σ error	Age (Ma)	2σ error	(Ma)	2σ error	% Discordance*
DL_271217 – Wood Canyon Formation -- 37.166405, -117.708913																
DL_271217_1	126.4	0.884	4.825	0.076	0.3165	0.0051	0.71913	1786	13	1771	25	1815	20	1815	20	2.4
DL_271217_2	281.8	1.191	4.311	0.068	0.2764	0.0039	0.62584	1694	13	1572	20	1845	19	1845	19	14.8
DL_271217_3	119.1	1.469	4.799	0.085	0.311	0.0055	0.65734	1784	15	1743	27	1842	26	1842	26	5.4
DL_271217_4	293	0.6824	2.404	0.031	0.2107	0.0028	0.76767	1242.1	9.2	1232	15	1259	17	1259	17	2.1
DL_271217_5	151.6	2.37	2.997	0.046	0.2372	0.0034	0.70007	1404	12	1371	18	1458	22	1458	22	6
DL_271217_6	503	1.426	14.59	0.17	0.5386	0.0058	0.74791	2789	11	2776	24	2796	13	2796	13	0.7
DL_271217_7	270.2	2.289	4.295	0.073	0.2927	0.0041	0.6757	1689	14	1654	21	1732	22	1732	22	4.5
DL_271217_8	419	1.81	2.426	0.059	0.1939	0.0043	0.88418	1248	18	1142	23	1441	22	1441	22	20.7
DL_271217_9	204.9	1.569	18.02	0.28	0.5664	0.0076	0.81649	2987	15	2890	31	3057	15	3057	15	5.5
DL_271217_10	155	0.705	13.28	0.18	0.5104	0.0069	0.70621	2699	13	2656	30	2733	18	2733	18	2.8
DL_271217_11	195	1.738	4.516	0.066	0.3047	0.0042	0.76357	1731	12	1716	21	1758	18	1758	18	2.4
DL_271217_12	69.2	2.02	4.106	0.054	0.286	0.0029	0.61557	1656	11	1621	14	1705	19	1705	19	4.9
DL_271217_13	247.1	2.142	4.221	0.057	0.2832	0.0033	0.70782	1676	11	1607	17	1771	17	1771	17	9.3
DL_271217_14	104	0.652	4.491	0.059	0.3023	0.0031	0.64008	1727	11	1702	15	1764	19	1764	19	3.5
DL_271217_15	138	0.869	4.913	0.086	0.3188	0.0055	0.77961	1801	15	1782	27	1837	21	1837	21	3
DL_271217_16	148.6	0.741	2.845	0.048	0.2311	0.0034	0.61021	1366	13	1340	18	1412	25	1412	25	5.1
DL_271217_17	60.5	1.236	4.688	0.068	0.3094	0.0037	0.64141	1762	12	1739	19	1798	21	1798	21	3.3
DL_271217_18	76.1	1.081	2.738	0.045	0.2285	0.003	0.5837	1338	13	1326	16	1372	27	1372	27	3.4
DL_271217_19	388.9	5.11	4.692	0.064	0.3105	0.0041	0.74617	1765	12	1742	20	1806	17	1806	17	3.5
DL_271217_20	122.6	1.026	3.041	0.043	0.2408	0.0032	0.69026	1417	11	1390	17	1469	24	1469	24	5.4
DL_271217_21	356.1	2.171	4.764	0.067	0.3182	0.0044	0.65648	1776	12	1779	22	1786	20	1786	20	0.4
DL_271217_22	75.01	3.58	4.905	0.071	0.3196	0.0039	0.57227	1801	12	1787	19	1831	22	1831	22	2.4
DL_271217_23	358	1.53	12.09	0.15	0.4979	0.0063	0.70802	2609	11	2607	28	2628	13	2628	13	0.8
DL_271217_24	117.4	1.67	2.888	0.05	0.2314	0.0031	0.51947	1376	13	1341	16	1442	28	1442	28	7
DL_271217_25	367	2.609	4.39	0.054	0.3053	0.0041	0.73243	1709	10	1717	20	1710	17	1710	17	0.4
DL_271217_26	75.4	2.06	3.75	0.19	0.2431	0.006	0.4928	1574	40	1401	31	1810	77	1810	77	22.6
DL_271217_27	281.8	2.169	4.71	0.085	0.3103	0.0051	0.87724	1768	15	1741	25	1810	16	1810	16	3.8
DL_271217_28	209	1.216	15.2	0.19	0.5432	0.0068	0.78041	2826	12	2795	28	2864	14	2864	14	2.4

Sample Name:								207/235		206/238		207/206		Best age		
Grain #	[U] ppm	U/Th	207/235	2σ error	206/238	2σ error	RHO	Age Ma	2σ error	Age (Ma)	2σ error	Age (Ma)	2σ error	(Ma)	2σ error	% Discordance*
DL_271217_29	189.3	0.916	9.55	0.13	0.4233	0.0052	0.857	2391	13	2274	24	2504	12	2504	12	9.2
DL_271217_30	451	2.167	4.758	0.07	0.3142	0.0034	0.66702	1775	12	1760	17	1799	20	1799	20	2.2
DL_271217_31	57.2	1.457	4.549	0.069	0.2983	0.0041	0.60327	1737	13	1681	20	1811	23	1811	23	7.2
DL_271217_32	121.9	1.17	5.11	0.082	0.3232	0.0041	0.66431	1834	13	1804	20	1885	21	1885	21	4.3
DL_271217_33	201.5	1.523	15.21	0.27	0.5222	0.0073	0.81015	2823	16	2706	31	2906	16	2906	16	6.9
DL_271217_34	237.9	0.861	12.54	0.15	0.5003	0.0065	0.79802	2643	11	2616	28	2680	13	2680	13	2.4
DL_271217_35	340	1.655	4.542	0.049	0.3056	0.0033	0.73539	1737.3	8.9	1718	16	1766	14	1766	14	2.7
DL_271217_36	145.4	0.815	3.984	0.07	0.2798	0.0043	0.67557	1627	14	1589	22	1687	26	1687	26	5.8
DL_271217_37	458	1.839	4.6	0.11	0.3082	0.0062	0.68347	1745	20	1731	31	1778	33	1778	33	2.6
DL_271217_38	259.7	1.547	4.954	0.058	0.3199	0.004	0.80119	1809.8	9.8	1788	19	1838	15	1838	15	2.7
DL_271217_39	437	2.173	4.484	0.047	0.3007	0.0027	0.69134	1727.1	8.7	1697	13	1768	15	1768	15	4
DL_271217_40	506	2.72	4.75	0.14	0.3142	0.0089	0.91284	1770	26	1759	44	1787	22	1787	22	1.6
DL_271217_41	385	1.301	3.972	0.048	0.2775	0.0029	0.81306	1628.2	9.4	1578	15	1690	13	1690	13	6.6
DL_271217_42	220.8	1.944	4.652	0.086	0.3143	0.0052	0.85486	1756	15	1760	26	1761	18	1761	18	0.1
DL_271217_43	685	15.43	4.348	0.053	0.2987	0.0037	0.7298	1701	10	1689	18	1722	15	1722	15	1.9
DL_271217_44	699	1.915	4.708	0.059	0.3161	0.0045	0.70985	1767	11	1772	22	1758	14	1758	14	0.8
DL_271217_45	938	6.265	4.054	0.08	0.2723	0.0051	0.63626	1642	16	1551	26	1741	19	1741	19	10.9
DL_271217_46	788	3.06	3.51	0.16	0.1555	0.0044	0.90735	1520	35	931	24	2471	37	DISC	DISC	62.3
DL_271217_47	396	0.933	4.493	0.071	0.275	0.0037	0.77321	1728	13	1565	19	1925	18	1925	18	18.7
DL_271217_48	570	2.85	5.206	0.087	0.2969	0.0048	0.7223	1852	14	1675	24	2048	20	2048	20	18.2
DL_271217_49	291.7	1.958	4.583	0.067	0.3014	0.004	0.70546	1743	12	1697	20	1799	21	1799	21	5.7
DL_271217_50	128.9	1.839	4.34	0.075	0.2921	0.0039	0.60334	1699	14	1651	20	1746	26			
DL_271217_51	76.9	0.973	13.71	0.19	0.5151	0.0064	0.80482	2728	13	2676	28	2765	13	2765	13	3.2
DL_271217_52	394	1.533	2.727	0.058	0.1919	0.0033	0.87499	1332	15	1131	18	1661	18	DISC	DISC	31.9
DL_271217_53	430	1.754	4.471	0.086	0.2831	0.0047	0.86211	1721	16	1608	23	1861	18	1861	18	13.6
DL_271217_54	367	1.71	4.313	0.075	0.2748	0.0048	0.80868	1695	15	1564	24	1851	18	1851	18	15.5
DL_271217_55	464	6.39	4.909	0.053	0.3156	0.0027	0.77126	1803.4	9	1768	13	1839	12	1839	12	3.9
DL_271217_56	173.9	1.076	4.637	0.068	0.3051	0.0042	0.77232	1753	12	1715	21	1788	20	1788	20	4.1
DL_271217_57	251	0.932	2.686	0.046	0.2228	0.0026	0.66001	1327	13	1296	14	1368	26	1368	26	5.3

Sample Name:								207/235		206/238		207/206		Best age		
Grain #	[U] ppm	U/Th	207/235	2σ error	206/238	2σ error	RHO	Age Ma	2σ error	Age (Ma)	2σ error	Age (Ma)	2σ error	(Ma)	2σ error	% Discordance*
DL_271217_58	260.9	1.253	4.51	0.063	0.3058	0.0043	0.76859	1730	12	1719	21	1745	18	1745	18	1.5
DL_271217_59	390.6	2.559	4.508	0.06	0.3034	0.0043	0.84639	1730	11	1707	21	1760	17	1760	17	3
DL_271217_60	348.4	1.909	4.542	0.048	0.2998	0.0028	0.63023	1740.2	8.3	1690	14	1783	13	1783	13	5.2
DL_271217_61	272	0.96	4.243	0.057	0.2943	0.0036	0.76063	1680	11	1664	18	1696	17	1696	17	1.9
DL_271217_62	111.8	1.032	5.305	0.074	0.3268	0.0043	0.604	1867	12	1822	21	1916	23	1916	23	4.9
DL_271217_63	239.7	0.797	11.59	0.14	0.4849	0.0052	0.81811	2571	11	2547	23	2586	12	2586	12	1.5
DL_271217_64	294	1.158	2.968	0.053	0.2347	0.0035	0.68705	1396	13	1358	18	1450	26	1450	26	6.3
DL_271217_65	591	1.32	5.066	0.071	0.3113	0.0041	0.62701	1829	12	1746	20	1918	21	1918	21	9
DL_271217_66	256.9	1.622	15.58	0.18	0.5494	0.0065	0.69175	2849	11	2824	26	2871	14	2871	14	1.6
DL_271217_67	92.8	1.043	4.59	0.055	0.3025	0.0032	0.56378	1746.8	9.7	1703	16	1788	20	1788	20	4.8
DL_271217_68	224	0.764	4.523	0.043	0.3006	0.0024	0.61934	1734	7.9	1694	12	1778	14	1778	14	4.7
DL_271217_69	354.3	1.011	10.58	0.25	0.4432	0.009	0.80625	2484	21	2363	40	2586	25	2586	25	8.6
DL_271217_70	130.5	1.485	10.49	0.17	0.4724	0.0083	0.8742	2475	15	2490	36	2464	13	2464	13	1.1
DL_271217_71	162.1	1.378	2.956	0.049	0.2329	0.0039	0.72941	1395	13	1349	21	1461	25	1461	25	7.7
DL_271217_72	95.8	1.031	2.836	0.07	0.2271	0.0052	0.66316	1362	19	1318	27	1441	38	1441	38	8.5
DL_271217_73	597	1.797	6.03	0.1	0.3483	0.006	0.76067	1979	15	1925	29	2030	22	2030	22	5.2
DL_271217_74	162.7	1.3	4.042	0.075	0.2843	0.0053	0.81138	1640	15	1611	26	1679	20	1679	20	4.1
DL_271217_75	146.2	1.698	4.327	0.065	0.3012	0.004	0.59446	1699	13	1696	20	1701	22	1701	22	0.3
DL_271217_76	223.7	1.33	4.434	0.056	0.297	0.0034	0.62727	1717	10	1676	17	1771	18	1771	18	5.4
DL_271217_77	192.1	1.297	4.535	0.046	0.2994	0.0027	0.57709	1737	8.7	1688	13	1794	17	1794	17	5.9
DL_271217_78	444	1.558	4.524	0.043	0.2968	0.003	0.64428	1734.2	7.9	1675	15	1808	14	1808	14	7.4
DL_271217_79	377	1.881	2.668	0.024	0.2251	0.0017	0.61151	1318.8	6.7	1308.6	9	1333	14	1333	14	1.8
DL_271217_80	85.3	0.4535	19.36	0.24	0.5881	0.0059	0.68066	3059	12	2983	24	3109	15	3109	15	4.1
DL_271217_81	82.4	1.012	5.587	0.075	0.3381	0.0038	0.68009	1912	12	1877	19	1949	19	1949	19	3.7
DL_271217_82	56	1.126	12.22	0.17	0.4816	0.0052	0.69507	2618	13	2533	22	2681	17	2681	17	5.5
DL_271217_83	309	1.278	7.71	0.16	0.3263	0.0061	0.87554	2195	19	1820	30	2568	17	2568	17	29.1
DL_271217_84	281.1	2.363	4.568	0.05	0.3051	0.0033	0.70296	1741.8	9.2	1716	16	1773	16	1773	16	3.2
DL_271217_85	824	1.292	3.582	0.061	0.2361	0.0037	0.91778	1542	13	1365	19	1795	12	1795	12	24
DL_271217_86	360	1.468	4.526	0.047	0.3034	0.003	0.61653	1734.7	8.6	1707	15	1767	16	1767	16	3.4

Sample Name:								207/235		206/238		207/206		Best age		
Grain #	[U] ppm	U/Th	207/235	2σ error	206/238	2σ error	RHO	Age Ma	2σ error	Age (Ma)	2σ error	Age (Ma)	2σ error	(Ma)	2σ error	% Discordance*
DL_271217_87	178.7	0.924	2.449	0.044	0.2021	0.0031	0.80366	1254	13	1186	16	1380	23	1380	23	14.1
DL_271217_88	76	0.636	2.86	0.049	0.2282	0.003	0.64354	1368	13	1324	16	1442	26	1442	26	8.2
DL_271217_89	287	2.58	4.012	0.056	0.2802	0.0031	0.78649	1634	11	1592	15	1690	16	1690	16	5.8
DL_271217_90	136.3	1.468	10.76	0.14	0.4584	0.0046	0.75853	2500	12	2431	21	2557	14	2557	14	4.9
DL_271217_91	85.7	1.135	18.39	0.21	0.5747	0.0066	0.8354	3008	11	2925	27	3065	11	3065	11	4.6
DL_271217_92	132.2	1.147	4.573	0.055	0.304	0.0032	0.6082	1744	10	1711	16	1788	19	1788	19	4.3
DL_271217_93	419	2.033	4.492	0.052	0.3018	0.0035	0.7867	1728.9	9.9	1702	18	1767	15	1767	15	3.7
DL_271217_94	123.7	1.985	2.915	0.043	0.231	0.0029	0.49646	1384	11	1339	15	1455	26	1455	26	8
DL_271217_95	336.6	0.768	15.28	0.19	0.5445	0.0075	0.87638	2832	12	2799	31	2858.7	9.6	2858.7	9.6	2.1
DL_271217_96	368	0.6494	11.84	0.12	0.4881	0.0045	0.77726	2589.9	9.7	2561	19	2616	11	2616	11	2.1
DL_271217_97	276.2	0.4	8.84	0.16	0.4218	0.0051	0.8612	2317	16	2267	23	2361	16	2361	16	4
DL_271217_98	177	0.869	4.49	0.055	0.3014	0.0032	0.6233	1727	10	1697	16	1769	18	1769	18	4.1
DL_271217_99	250	0.806	4.31	0.059	0.2895	0.0037	0.65609	1693	11	1638	19	1767	20	1767	20	7.3
DL_271217_100	481	3	3.89	0.16	0.262	0.01	0.89794	1606	32	1498	52	1770	27	1770	27	15.4
DL_271217_101	100.1	0.847	4.535	0.066	0.303	0.0039	0.71867	1735	12	1705	19	1780	19	1780	19	4.2
DL_271217_102	580	1.919	3.929	0.067	0.263	0.0041	0.81041	1619	13	1504	21	1778	18	1778	18	15.4
DL_271217_103	235	4.49	4.565	0.061	0.3036	0.0033	0.71549	1742	11	1708	16	1788	16	1788	16	4.5
DL_271217_104	400	1.395	4.561	0.066	0.3066	0.004	0.67704	1739	12	1723	20	1764	19	1764	19	2.3
DL_271217_105	86.4	2.126	3.991	0.059	0.2812	0.0042	0.63608	1630	12	1596	21	1685	22	1685	22	5.3
DL_271217_106	166.4	1.324	4.934	0.07	0.3139	0.004	0.63929	1805	12	1759	19	1867	21	1867	21	5.8
DL_271217_107	250.4	1.917	4.959	0.065	0.3185	0.0035	0.72115	1811	11	1782	17	1853	16	1853	16	3.8
DL_271217_108	203.8	1.289	14.9	0.23	0.5322	0.007	0.74066	2806	15	2749	29	2855	18	2855	18	3.7
DL_271217_109	668	2.222	4.639	0.067	0.3121	0.004	0.62636	1754	12	1750	20	1769	21	1769	21	1.1
DL_271217_110	181	0.562	4.423	0.068	0.2966	0.0038	0.79564	1717	13	1673	19	1771	17	1771	17	5.5
DL_271217_111	178.5	2.576	2.938	0.044	0.2412	0.0028	0.68461	1389	11	1392	14	1386	21	1386	21	0.4
DL_271217_112	149.3	0.957	2.744	0.042	0.2232	0.0024	0.62171	1338	11	1298	13	1398	23	1398	23	7.2
DL_271217_113	575	4.91	4.402	0.066	0.2874	0.0038	0.74003	1710	12	1630	19	1828	20	1828	20	10.8
DL_271217_114	131.8	1.174	3.016	0.055	0.2409	0.0038	0.62097	1408	14	1390	20	1448	27	1448	27	4
DL_271217_115	95.9	1.438	4.389	0.075	0.2993	0.0048	0.6955	1708	14	1686	24	1749	24	1749	24	3.6

Sample Name:								207/235		206/238		207/206		Best age		
Grain #	[U] ppm	U/Th	207/235	2σ error	206/238	2σ error	RHO	Age Ma	2σ error	Age (Ma)	2σ error	Age (Ma)	2σ error	(Ma)	2σ error	% Discordance*
DL_271217_116	186.1	1.429	1.868	0.025	0.1787	0.0022	0.61853	1068.2	9	1061	12	1093	23	1093	23	2.9
DL_271217_117	418	1.727	4.77	0.089	0.3095	0.0041	0.68654	1775	15	1737	20	1826	25	1826	25	4.9
DL_271217_118	170.9	5.4	5.148	0.054	0.3252	0.0029	0.71537	1842.6	8.8	1814	14	1879	13	1879	13	3.5
DL_271217_119	434	2.071	4.444	0.045	0.298	0.0028	0.66888	1719.3	8.3	1681	14	1763	13	1763	13	4.7
DL_271217_120	371	2.088	4.687	0.059	0.314	0.0039	0.69766	1763	11	1759	19	1771	15	1771	15	0.7
DL_271217_121	259	0.813	2.698	0.045	0.2161	0.0031	0.70518	1325	12	1261	17	1438	22	1438	22	12.3
DL_271217_122	140.4	1.439	2.977	0.038	0.2404	0.0028	0.66077	1399.9	9.8	1388	15	1424	20	1424	20	2.5
DL_271217_123	268	0.759	8.85	0.14	0.3641	0.0056	0.79598	2319	15	2000	26	2617	17	2617	17	23.6
DL_271217_124	896	2.904	3.741	0.055	0.2559	0.0039	0.77594	1577	12	1468	20	1730	18	1730	18	15.1
DL_271217_125	240.7	0.888	4.388	0.054	0.2977	0.0035	0.74513	1711	11	1681	18	1753	16	1753	16	4.1
DL_271217_126	137.3	2.541	2.963	0.042	0.238	0.0031	0.23889	1396	11	1377	16	1417	22	1417	22	2.8
DL_271217_127	334.7	0.874	2.69	0.033	0.2241	0.0025	0.75772	1324.1	9.1	1303	13	1357	15	1357	15	4
DL_271217_128	200	1.544	2.773	0.038	0.2294	0.0024	0.60319	1347	10	1331	13	1367	21	1367	21	2.6
DL_271217_129	95.4	2.81	11.5	0.16	0.456	0.0058	0.80024	2563	13	2421	26	2667	15	2667	15	9.2
DL_271217_130	79.6	1.61	5.08	0.062	0.3214	0.0033	0.57046	1831	10	1796	16	1867	19	1867	19	3.8
DL_271217_131	159	1.194	4.815	0.083	0.3142	0.0048	0.75841	1784	14	1760	24	1786	23	1786	23	1.5
DL_271217_132	168.8	1.915	4.592	0.052	0.3031	0.0032	0.67833	1747.2	9.7	1706	16	1784	17	1784	17	4.4
DL_271217_133	189.9	1.748	2.765	0.039	0.2202	0.0025	0.52821	1344	11	1282	13	1427	23	1427	23	10.2
DL_271217_134	173.9	1.241	11.28	0.12	0.4665	0.005	0.73834	2544.5	9.8	2467	22	2601	13	2601	13	5.2
DL_271217_135	82.1	0.5945	2.833	0.041	0.2294	0.0022	0.4379	1362	11	1331	11	1397	25	1397	25	4.7
DL_271217_136	67.6	0.992	2.98	0.061	0.2333	0.0042	0.11425	1398	16	1350	22	1461	33	1461	33	7.6
DL_271217_137	630	3.513	4.664	0.055	0.3128	0.0038	0.75477	1759.1	9.9	1753	19	1755	15	1755	15	0.1
DL_271217_138	103.7	1.16	4.413	0.089	0.2946	0.0047	0.56751	1712	16	1664	23	1761	32	1761	32	5.5
DL_271217_139	120.3	0.914	4.927	0.09	0.3158	0.0048	0.6717	1804	16	1768	24	1838	26	1838	26	3.8
DL_271217_140	324	2.72	4.604	0.044	0.3096	0.0026	0.63497	1749.4	8	1738	13	1759	15	1759	15	1.2
DL_271217_141	75.5	1.183	2.77	0.064	0.229	0.0056	0.69616	1345	17	1333	28	1366	36	1366	36	2.4
DL_271217_142	204.3	1.713	4.405	0.057	0.2993	0.0028	0.72766	1711	11	1687	14	1729	18	1729	18	2.4
DL_271217_143	341.4	1.658	4.478	0.064	0.299	0.0036	0.73629	1725	12	1686	18	1769	18	1769	18	4.7
DL_271217_144	212.9	3.245	1.985	0.029	0.1856	0.0021	0.64471	1110	10	1097	11	1126	23	1126	23	2.6

Sample Name:								207/235		206/238		207/206		Best age		
Grain #	[U] ppm	U/Th	207/235	2σ error	206/238	2σ error	RHO	Age Ma	2σ error	Age (Ma)	2σ error	Age (Ma)	2σ error	(Ma)	2σ error	% Discordance*
DL_271217_145	142.2	1.418	4.871	0.075	0.3131	0.0041	0.64061	1796	13	1755	20	1846	22	1846	22	4.9
DL_271217_146	353	1.752	4.636	0.057	0.3077	0.0035	0.76714	1756	10	1728	17	1783	14	1783	14	3.1

Sample Name:								207/235		206/238		207/206		Best age		
Grain #	[U] ppm	U/Th	207/235	2σ error	206/238	2σ error	RHO	Age Ma	2σ error	Age (Ma)	2σ error	Age (Ma)	2σ error	(Ma)	2σ error	% Discordance*
DL_040118_1 – Carrara Formation - 37.223652, -117.711052																
DL_040118_1_1	227	0.81	3.504	0.089	0.2442	0.0057	0.81136	1524	20	1407	30	1694	28	1694	28	16.9
DL_040118_1_2	142	0.657	2.608	0.061	0.2135	0.0052	0.75151	1300	17	1246	28	1390	34	1390	34	10.4
DL_040118_1_3	297	0.926	2.793	0.03	0.2303	0.0025	0.67787	1353.7	8.2	1335	13	1380	18	1380	18	3.3
DL_040118_1_4	132.9	0.3756	2.425	0.043	0.1841	0.0028	0.72308	1247	13	1089	15	1526	24	1526	24	28.6
DL_040118_1_5	190.6	5.01	4.821	0.044	0.3237	0.0029	0.57199	1787.5	7.7	1807	14	1761	15	1761	15	2.6
DL_040118_1_6	199.1	1.456	4.419	0.041	0.3057	0.0031	0.5774	1716	7.9	1719	15	1702	16	1702	16	1
DL_040118_1_7	189.1	0.956	2.61	0.029	0.2164	0.0019	0.50452	1302.2	8.3	1263	10	1361	20	1361	20	7.2
DL_040118_1_8	465.3	0.893	4.163	0.097	0.2789	0.0081	0.75022	1673	19	1584	41	1764	36	1764	36	10.2
DL_040118_1_9	232.2	0.756	4.439	0.069	0.2954	0.0032	0.67612	1719	13	1668	16	1783	21	1783	21	6.4
DL_040118_1_10	147.4	1.675	2.954	0.044	0.2315	0.0028	0.55339	1394	11	1342	15	1469	25	1469	25	8.6
DL_040118_1_11	270.8	1.51	4.247	0.048	0.2846	0.0032	0.70315	1681.7	9.4	1614	16	1767	14	1767	14	8.7
DL_040118_1_12	126.8	0.574	4.879	0.079	0.305	0.0055	0.65139	1797	14	1715	27	1880	27	1880	27	8.8
DL_040118_1_13	58.5	0.634	4.484	0.085	0.3063	0.0041	0.60309	1724	16	1722	20	1740	28	1740	28	1
DL_040118_1_14	156.9	1.508	4.552	0.047	0.3096	0.0028	0.52433	1739.3	8.6	1738	14	1737	17	1737	17	0.1
DL_040118_1_15	102.9	1.286	4.261	0.085	0.2974	0.0049	0.71814	1682	16	1677	24	1682	26	1682	26	0.3
DL_040118_1_16	289.9	0.717	2.193	0.027	0.1952	0.0022	0.65072	1177.7	8.5	1149	12	1225	20	1225	20	6.2
DL_040118_1_17	150	1.888	4.724	0.056	0.3167	0.0035	0.68681	1770	10	1773	17	1769	18	1769	18	0.2
DL_040118_1_18	193.9	0.715	11.91	0.13	0.4782	0.0049	0.71002	2595.7	9.8	2518	21	2654	13	2654	13	5.1
DL_040118_1_19	163.5	1.759	3.152	0.037	0.2499	0.0023	0.56009	1444	9	1438	12	1452	18	1452	18	1
DL_040118_1_20	145.4	1.976	4.646	0.049	0.3126	0.0026	0.43131	1756.2	8.9	1753	13	1756	19	1756	19	0.2
DL_040118_1_21	179	0.6408	18.09	0.16	0.5257	0.0051	0.7727	2993	8.7	2722	22	3179	10	3179	10	14.4
DL_040118_1_22	356	1.625	3.844	0.043	0.2699	0.0027	0.71992	1600.6	9.1	1540	14	1683	15	1683	15	8.5
DL_040118_1_23	173.7	2.024	4.331	0.038	0.3028	0.0029	0.56206	1698.3	7.3	1705	15	1693	17	1693	17	0.7
DL_040118_1_24	178.4	1.57	4.296	0.042	0.2991	0.0029	0.5439	1691.5	8	1686	14	1692	20	1692	20	0.4
DL_040118_1_25	177	1.829	3.056	0.035	0.2466	0.0024	0.60067	1420.5	8.8	1420	12	1414	19	1414	19	0.4
DL_040118_1_26	363	2.79	8.8	0.25	0.386	0.012	0.68725	2316	26	2104	56	2505	40	2505	40	16
DL_040118_1_27	311.4	0.991	7.39	0.17	0.3056	0.0056	0.86038	2157	21	1718	28	2604	20	DISC	DISC	34
DL_040118_1_28	83.36	2.811	3.069	0.041	0.249	0.0026	0.51522	1423	10	1433	13	1405	23	1405	23	2

Sample Name:								207/235		206/238		207/206		Best age		
Grain #	[U] ppm	U/Th	207/235	2σ error	206/238	2σ error	RHO	Age Ma	2σ error	Age (Ma)	2σ error	Age (Ma)	2σ error	(Ma)	2σ error	% Discordance*
DL_040118_1_29	402	1.479	15.68	0.34	0.532	0.013	0.88618	2854	21	2748	57	2927	19	2927	19	6.1
DL_040118_1_30	213.4	4.5	4.198	0.042	0.3008	0.0028	0.64912	1673.5	8	1696	14	1642	15	1642	15	3.3
DL_040118_1_31	95.9	1.106	4.478	0.052	0.3102	0.0026	0.50276	1725.4	9.6	1741	13	1704	20	1704	20	2.2
DL_040118_1_32	153.8	0.546	5.138	0.057	0.3283	0.0035	0.6815	1840.8	9.4	1830	17	1847	15	1847	15	0.9
DL_040118_1_33	96.3	1.215	2.558	0.037	0.2225	0.0027	0.43476	1288	11	1294	14	1275	28	1275	28	1.5
DL_040118_1_34	130	0.5457	14.9	0.21	0.5254	0.0071	0.77952	2807	13	2720	30	2872	14	2872	14	5.3
DL_040118_1_35	288	0.754	10.79	0.17	0.4393	0.0074	0.88085	2501	15	2345	33	2634	13	2634	13	11
DL_040118_1_36	231.2	1.397	4.628	0.044	0.3082	0.0028	0.74024	1753.2	7.9	1732	14	1780	12	1780	12	2.7
DL_040118_1_37	380	1.177	9.31	0.18	0.4222	0.0067	0.74116	2367	17	2268	30	2448	21	2448	21	7.4
DL_040118_1_38	510	2.41	3.077	0.039	0.2481	0.0031	0.89691	1425	10	1428	16	1426	14	1426	14	0.1
DL_040118_1_39	307	1.595	4.141	0.046	0.2886	0.0028	0.72775	1661	9.1	1634	14	1691	15	1691	15	3.4
DL_040118_1_40	423.9	0.872	20.87	0.3	0.6174	0.0089	0.76548	3130	14	3097	35	3147	13	3147	13	1.6
DL_040118_1_41	128.1	2.101	2.848	0.063	0.2378	0.0044	0.59428	1365	17	1374	23	1356	36	1356	36	1.3
DL_040118_1_42	150.3	2.32	4.384	0.047	0.305	0.0026	0.52315	1708	9	1716	13	1697	18	1697	18	1.1
DL_040118_1_43	374.2	1.261	3.057	0.051	0.2458	0.0036	0.86939	1421	13	1416	19	1428	16	1428	16	0.8
DL_040118_1_44	191.9	1.035	3.125	0.037	0.2484	0.0023	0.58301	1437.4	9.2	1430	12	1446	19	1446	19	1.1
DL_040118_1_45	405.4	2.2	3.108	0.03	0.2464	0.0021	0.62941	1433.8	7.4	1420	11	1452	14	1452	14	2.2
DL_040118_1_46	164.1	2.641	3.231	0.037	0.2567	0.0027	0.54084	1463.4	8.8	1472	14	1445	21	1445	21	1.9
DL_040118_1_47	212.2	1.84	4.267	0.083	0.3032	0.0052	0.70265	1685	17	1706	26	1658	26	1658	26	2.9
DL_040118_1_48	154.1	1.898	4.148	0.055	0.2889	0.0035	0.78724	1662	11	1635	18	1702	16	1702	16	3.9
DL_040118_1_49	278.8	2.929	4.449	0.043	0.3034	0.003	0.63564	1722.5	8.1	1708	15	1735	15	1735	15	1.6
DL_040118_1_50	76.2	1.016	2.814	0.043	0.2352	0.0026	0.56278	1357	11	1361	14	1340	26	1340	26	1.6
DL_040118_1_51	109.8	0.4358	2.294	0.036	0.2045	0.0028	0.45658	1208	11	1199	15	1223	30	1223	30	2
DL_040118_1_52	217.5	1.909	4.733	0.061	0.3143	0.003	0.59882	1772	10	1761	15	1788	21	1788	21	1.5
DL_040118_1_53	376.8	1.672	4.406	0.049	0.3039	0.0033	0.76535	1712	9	1710	16	1708	15	1708	15	0.1
DL_040118_1_54	257	3.66	4.545	0.048	0.316	0.003	0.54997	1737.9	8.6	1770	14	1707	18	1707	18	3.7
DL_040118_1_55	183.2	0.789	3.285	0.039	0.2576	0.0024	0.50889	1477.3	8.9	1477	12	1477	19	1477	19	0
DL_040118_1_56	230.4	1.5	3.07	0.033	0.2473	0.0024	0.60794	1424	8.2	1424	12	1421	18	1421	18	0.2
DL_040118_1_57	137.6	0.509	2.159	0.04	0.1761	0.0022	0.69421	1167	13	1045	12	1396	27	1396	27	25.1

Sample Name:								207/235		206/238		207/206		Best age		
Grain #	[U] ppm	U/Th	207/235	2σ error	206/238	2σ error	RHO	Age Ma	2σ error	Age (Ma)	2σ error	Age (Ma)	2σ error	(Ma)	2σ error	% Discordance*
DL_040118_1_58	311.1	1.484	3.044	0.044	0.2457	0.0035	0.55927	1418	11	1416	18	1414	27	1414	27	0.1
DL_040118_1_59	83.9	1.331	3.095	0.048	0.2476	0.0031	0.48671	1431	12	1425	16	1434	27	1434	27	0.6
DL_040118_1_60	151.7	1.535	3.097	0.036	0.247	0.0025	0.55983	1430.5	9	1422	13	1442	20	1442	20	1.4
DL_040118_1_61	271.9	1.456	3.06	0.037	0.2424	0.0028	0.77402	1421.3	9.3	1399	15	1449	14	1449	14	3.5
DL_040118_1_62	90.3	1.181	3.133	0.046	0.2489	0.0027	0.42709	1439	11	1432	14	1446	27	1446	27	1
DL_040118_1_63	453	5.12	3.52	0.055	0.256	0.0028	0.54146	1532	12	1469	14	1621	24	1621	24	9.4
DL_040118_1_64	215.9	2.621	4.764	0.047	0.3232	0.0028	0.56	1777.4	8.3	1805	14	1747	15	1747	15	3.3
DL_040118_1_65	230.1	1.316	3.081	0.06	0.2452	0.0036	0.623	1430	16	1413	19	1451	27	1451	27	2.6
DL_040118_1_66	250	1.855	4.736	0.044	0.3173	0.0026	0.64499	1772.6	7.7	1776	13	1765	13	1765	13	0.6
DL_040118_1_67	452	2.925	1.977	0.022	0.1871	0.0017	0.56094	1106.8	7.4	1105.3	9.4	1112	18	1112	18	0.6
DL_040118_1_68	175.7	0.89	12.78	0.12	0.5131	0.0051	0.6886	2663.7	8.8	2671	22	2660	13	2660	13	0.4
DL_040118_1_69	317.3	1.068	3.147	0.036	0.2525	0.0024	0.6619	1443	8.6	1451	12	1433	17	1433	17	1.3
DL_040118_1_70	164	0.931	4.186	0.059	0.2886	0.0035	0.74349	1669	12	1634	18	1715	18	1715	18	4.7
DL_040118_1_71	132.4	0.783	3.073	0.036	0.2456	0.0023	0.46988	1425.9	9.3	1416	12	1444	22	1444	22	1.9
DL_040118_1_72	120.3	1.475	1.918	0.03	0.181	0.0021	0.43275	1087	10	1072	11	1118	29	1118	29	4.1
DL_040118_1_73	286.2	1.215	3.756	0.067	0.2609	0.0045	0.86417	1581	15	1493	23	1704	17	1704	17	12.4
DL_040118_1_74	328	1.321	1.695	0.019	0.1651	0.0015	0.63269	1005.7	6.9	985.1	8.4	1057	20	1057	20	6.8
DL_040118_1_75	275.6	1.343	4.416	0.047	0.3034	0.0029	0.39835	1714	8.8	1707	14	1723	16	1723	16	0.9
DL_040118_1_76	317	3.32	4.319	0.051	0.2982	0.0034	0.78977	1695.4	9.7	1684	16	1711	14			
DL_040118_1_77	202.1	1.489	9.17	0.089	0.411	0.0042	0.71749	2355.1	9.1	2219	19	2478	12	2478	12	10.5
DL_040118_1_78	302.6	1.184	4.048	0.079	0.2805	0.0058	0.84858	1640	16	1592	29	1705	18	1705	18	6.6
DL_040118_1_79	403	1.542	2.962	0.034	0.2084	0.0022	0.77788	1396.6	8.6	1220	12	1681	13	1681	13	27.4
DL_040118_1_80	210.4	1.554	4.571	0.055	0.3025	0.0034	0.7504	1742	10	1703	17	1792	16	1792	16	5
DL_040118_1_81	262	3.44	4.594	0.087	0.3099	0.0054	0.60004	1744	16	1738	26	1754	30	1754	30	0.9
DL_040118_1_82	201.4	2.286	4.512	0.049	0.3125	0.0035	0.61394	1731.8	9.2	1752	17	1709	18	1709	18	2.5
DL_040118_1_83	164	0.974	4.293	0.052	0.2983	0.0032	0.5863	1690.3	9.8	1684	15	1705	19	1705	19	1.2
DL_040118_1_84	376.4	1.674	4.174	0.041	0.2898	0.0028	0.75619	1667.8	8	1642	15	1705	14	1705	14	3.7
DL_040118_1_85	236.5	1.149	3.189	0.035	0.2553	0.0026	0.68188	1454.4	8.7	1465	13	1440	17	1440	17	1.7
DL_040118_1_86	366.3	1.975	3.035	0.028	0.243	0.0018	0.65568	1415.7	6.9	1402	9.1	1433	14	1433	14	2.2

Sample Name:								207/235		206/238		207/206		Best age		
Grain #	[U] ppm	U/Th	207/235	2σ error	206/238	2σ error	RHO	Age Ma	2σ error	Age (Ma)	2σ error	Age (Ma)	2σ error	(Ma)	2σ error	% Discordance*
DL_040118_1_87	248.1	1.407	2.363	0.048	0.199	0.0036	0.75353	1232	15	1169	20	1354	28	1354	28	13.7
DL_040118_1_88	359	2.91	4.46	0.11	0.3054	0.0084	0.77266	1715	22	1713	42	1737	32	1737	32	1.4
DL_040118_1_89	268	2.632	4.44	0.055	0.3086	0.0035	0.65654	1718	10	1735	17	1701	19	1701	19	2
DL_040118_1_90	257.8	1.369	4.01	0.048	0.276	0.0033	0.6782	1636	10	1570	17	1725	18	1725	18	9
DL_040118_1_91	124.5	1.199	4.351	0.053	0.3032	0.0033	0.52143	1701	10	1706	16	1702	21	1702	21	0.2
DL_040118_1_92	331	2.01	4.308	0.062	0.2979	0.0041	0.77401	1696	12	1680	21	1717	17	1717	17	2.2
DL_040118_1_93	205.8	1.018	2.738	0.034	0.2206	0.0023	0.50264	1337.4	9.3	1285	12	1426	22	1426	22	9.9
DL_040118_1_94	162	2.308	4.471	0.055	0.3083	0.0034	0.57609	1724	10	1731	17	1709	18	1709	18	1.3
DL_040118_1_95	206.4	0.948	4.757	0.074	0.3132	0.0039	0.72857	1774	13	1756	19	1793	19	1793	19	2.1
DL_040118_1_96	708	3.569	4.929	0.04	0.3339	0.0033	0.68266	1806.5	6.8	1857	16	1748	13	1748	13	6.2
DL_040118_1_97	222.2	1.767	4.691	0.06	0.3122	0.0041	0.71921	1764	11	1753	21	1771	19	1771	19	1
DL_040118_1_98	524	1.06	3.643	0.054	0.2433	0.0036	0.80438	1557	12	1403	18	1765	14	1765	14	20.5
DL_040118_1_99	185.4	1.2	2.946	0.061	0.2389	0.0047	0.7465	1393	15	1380	24	1427	27	1427	27	3.3
DL_040118_1_100	207.3	1.193	3.188	0.05	0.2548	0.0033	0.52466	1452	12	1462	17	1434	26	1434	26	2
DL_040118_1_101	185.3	1.941	3.289	0.041	0.2561	0.0025	0.47655	1476.9	9.7	1469	13	1485	22	1485	22	1.1
DL_040118_1_102	161.2	2.54	3.117	0.036	0.2486	0.0023	0.48821	1435.4	8.9	1431	12	1440	20	1440	20	0.6
DL_040118_1_103	177.8	1.463	4.854	0.059	0.3215	0.0034	0.57261	1793	10	1797	17	1793	18	1793	18	0.2
DL_040118_1_104	336	2.168	1.839	0.023	0.1734	0.0027	0.70685	1058.4	8.5	1033	14	1105	22	1105	22	6.5
DL_040118_1_105	212.3	2.519	3.117	0.032	0.248	0.0023	0.51178	1436.8	7.7	1428	12	1446	18	1446	18	1.2
DL_040118_1_106	416.8	1.391	2.658	0.03	0.2117	0.002	0.61556	1316.6	8.5	1238	11	1439	19	1439	19	14
DL_040118_1_107	308.8	2.111	4.925	0.06	0.326	0.0036	0.70787	1805	10	1818	18	1791	16	1791	16	1.5
DL_040118_1_108	158.3	0.864	2.927	0.072	0.2386	0.0059	0.84083	1383	19	1381	31	1397	25	1397	25	1.1
DL_040118_1_109	206.7	1.695	4.439	0.06	0.307	0.0037	0.67544	1717	11	1725	18	1725	18	1725	18	0
DL_040118_1_110	147.8	2.709	4.977	0.067	0.3243	0.0034	0.6288	1813	11	1812	16	1820	19	1820	19	0.4
DL_040118_1_111	219.9	1.291	3.789	0.055	0.2618	0.0037	0.72192	1591	12	1498	19	1724	19	1724	19	13.1
DL_040118_1_112	76.8	1.091	3.207	0.048	0.2517	0.0029	0.46243	1458	11	1447	15	1470	26	1470	26	1.6
DL_040118_1_113	187.1	1.677	4.26	0.1	0.296	0.0065	0.86748	1681	20	1673	33	1702	20	1702	20	1.7
DL_040118_1_114	213.4	1.747	2.462	0.037	0.1969	0.0025	0.81209	1259	11	1158	14	1437	19	1437	19	19.4
DL_040118_1_115	264.2	1.563	4.45	0.11	0.3012	0.0059	0.68565	1716	21	1695	29	1741	34	1741	34	2.6

Sample Name:								207/235		206/238		207/206		Best age		
Grain #	[U] ppm	U/Th	207/235	2σ error	206/238	2σ error	RHO	Age Ma	2σ error	Age (Ma)	2σ error	Age (Ma)	2σ error	(Ma)	2σ error	% Discordance*
DL_040118_1_116	217.8	1.903	4.698	0.096	0.3082	0.0061	0.82987	1764	18	1733	31	1811	20	1811	20	4.3
DL_040118_1_117	266	1.399	1.438	0.036	0.1471	0.0033	0.51207	903	15	884	18	931	47	931	47	5
DL_040118_1_118	329	1.329	4.6	0.12	0.2987	0.0085	0.7393	1742	22	1687	41	1814	33	1814	33	7
DL_040118_1_119	73.6	1.26	4.37	0.085	0.3012	0.0045	0.71516	1702	16	1699	23	1707	26	1707	26	0.5
DL_040118_1_120	547	1.343	3.45	0.11	0.2461	0.0079	0.87341	1505	25	1414	40	1640	23	1640	23	13.8
DL_040118_1_121	311	3.321	4.598	0.049	0.3114	0.0032	0.62031	1747.6	8.9	1747	16	1741	17	1741	17	0.3
DL_040118_1_122	569	1.532	3.655	0.08	0.2579	0.0055	0.88361	1561	17	1478	28	1676	18	1676	18	11.8
DL_040118_1_123	348.9	1.996	4.939	0.06	0.3271	0.0043	0.61465	1810	10	1823	21	1791	20	1791	20	1.8
DL_040118_1_124	348	2.04	3.96	0.12	0.2777	0.0094	0.80138	1621	25	1577	47	1684	38	1684	38	6.4
DL_040118_1_125	583	2.293	4.363	0.084	0.3029	0.0054	0.7367	1701	16	1704	27	1705	24	1705	24	0.1
DL_040118_1_126	95.7	0.765	3.053	0.066	0.2116	0.0044	0.81169	1416	17	1236	23	1704	23	1704	23	27.5
DL_040118_1_127	76.1	1.39	4.769	0.063	0.3164	0.0037	0.52006	1777	11	1776	18	1782	21	1782	21	0.3
DL_040118_1_128	211	0.604	2.693	0.046	0.2236	0.0036	0.7477	1324	13	1300	19	1363	23	1363	23	4.6
DL_040118_1_129	174	1.848	4.217	0.083	0.2883	0.0059	0.7284	1677	17	1634	31	1731	29	1731	29	5.6
DL_040118_1_130	134.3	1.324	3.162	0.042	0.253	0.0024	0.51943	1446	10	1454	12	1433	20	1433	20	1.5
DL_040118_1_131	179.3	0.652	3.227	0.054	0.2321	0.0035	0.79555	1461	13	1345	18	1636	20	1636	20	17.8
DL_040118_1_132	92.7	0.774	3.96	0.12	0.2808	0.0061	0.66539	1624	24	1594	31	1661	42	1661	42	4
DL_040118_1_133	115.3	0.878	3.211	0.038	0.2516	0.0023	0.40331	1458.4	9.1	1446	12	1476	24	1476	24	2
DL_040118_1_134	186.5	1.918	3.114	0.034	0.248	0.0019	0.5542	1437	8.3	1427.9	9.7	1446	17	1446	17	1.3
DL_040118_1_135	244.8	1.154	3.198	0.041	0.2194	0.0023	0.61454	1455.3	9.9	1278	12	1730	18	1730	18	26.1
DL_040118_1_136	276	2.7	4.84	0.11	0.3182	0.0044	0.7349	1788	19	1780	22	1795	28	1795	28	0.8
DL_040118_1_137	183.1	1.111	2.995	0.038	0.239	0.0027	0.63477	1404.8	9.5	1381	14	1441	20	1441	20	4.2
DL_040118_1_138	154.3	1.06	16.22	0.16	0.5325	0.0047	0.71936	2888.1	9.6	2753	19	2985	12	2985	12	7.8
DL_040118_1_139	124.5	2.042	4.294	0.06	0.2982	0.003	0.56255	1691	11	1682	15	1699	21	1699	21	1
DL_040118_1_140	200	1.688	1.759	0.024	0.1718	0.0017	0.53715	1030.1	9.1	1021.7	9.3	1042	25	1042	25	1.9
DL_040118_1_141	272	1.022	1.97	0.025	0.1856	0.0019	0.70184	1104	8.6	1097	10	1112	20	1112	20	1.3
DL_040118_1_142	363	0.894	2.621	0.054	0.213	0.0043	0.81649	1303	15	1243	23	1409	23	1409	23	11.8
DL_040118_1_143	244	0.624	2.566	0.043	0.2057	0.0031	0.80009	1288	12	1205	17	1431	19	1431	19	15.8

Sample Name:								207/235		206/238		207/206		Best Age		
Grain #	[U] ppm	U/Th	207/235	1σ error	206/238	1σ error	RHO	Age Ma	1σ error	Age Ma	1σ error	Age Ma	1σ error	(Ma)	1σ error	% Discordance*
Zabriske6 – Zabriskie Quartzite – 37.228711, -117.710296																
Zabriskie6_1	132.2	1.048	6.058	0.053	0.3608	0.003	0.58218	1983.1	7.7	1986	14	1985	14	1985	14	0.1
Zabriskie6_2	186.2	1.373	5.404	0.049	0.3446	0.0027	0.53313	1884.3	7.7	1908	13	1865	14	1865	14	2.3
Zabriskie6_3	61.2	1.34	5.185	0.084	0.3306	0.0036	0.42091	1847	14	1841	17	1854	28	1854	28	0.7
Zabriskie6_4	155.7	0.646	5.014	0.046	0.3025	0.0024	0.57153	1820.7	7.8	1703	12	1958	15	1958	15	13
Zabriskie6_5	176.5	1.12	0.613	0.023	0.0775	0.0017	0.32875	484	14	481	10	489	78	481	10	0.6
Zabriskie6_6	40.4	0.728	12.67	0.26	0.5115	0.0088	0.66232	2653	19	2662	37	2658	28	2658	28	0.2
Zabriskie6_7	189.8	1.56	11.16	0.1	0.4819	0.0042	0.76824	2535.7	8.4	2535	18	2541	10	2541	10	0.2
Zabriskie6_8	68.7	1.238	4.954	0.076	0.3244	0.0042	0.55697	1813	13	1810	20	1815	26	1815	26	0.3
Zabriskie6_9	90.8	0.835	12.27	0.11	0.4978	0.0039	0.62949	2624.2	8.5	2603	17	2644	13	2644	13	1.6
Zabriskie6_10	62.8	0.907	4.959	0.061	0.322	0.0032	0.47368	1811	10	1799	16	1823	20	1823	20	1.3
Zabriskie6_11	279	0.73	0.803	0.038	0.0728	0.0014	0.1602	591	20	452.7	8.2	1180	110	DISC	DISC	23.4
Zabriskie6_12	68.9	0.858	4.922	0.072	0.3208	0.0037	0.56636	1806	13	1793	18	1826	23	1826	23	1.8
Zabriskie6_13	149.3	0.905	6.599	0.067	0.3771	0.0034	0.71621	2059	9.1	2062	16	2061	14	2061	14	0
Zabriskie6_14	55.7	0.831	5.462	0.095	0.3391	0.0042	0.54214	1892	15	1882	20	1913	27	1913	27	1.6
Zabriskie6_15	53.4	1.537	5.173	0.06	0.3314	0.003	0.42311	1846.5	9.9	1845	14	1856	21	1856	21	0.6
Zabriskie6_16	37.09	0.5858	12.52	0.13	0.5033	0.0057	0.65584	2642	10	2626	24	2657	15	2657	15	1.2
Zabriskie6_17	268.8	1.609	5.059	0.043	0.3297	0.0024	0.63087	1828.3	7.2	1837	12	1825	13	1825	13	0.7
Zabriskie6_18	25.23	0.4701	12.75	0.24	0.5084	0.0075	0.75095	2665	16	2647	32	2684	21	2684	21	1.4
Zabriskie6_19	124.5	0.813	12.86	0.14	0.512	0.005	0.75448	2668	10	2664	21	2676	12	2676	12	0.4
Zabriskie6_20	91.3	0.423	5.739	0.059	0.3512	0.0028	0.60844	1935.9	8.9	1942	14	1934	15	1934	15	0.4
Zabriskie6_21	177.8	1.157	5.587	0.047	0.3468	0.003	0.60905	1913.1	7.3	1919	14	1907	13	1907	13	0.6
Zabriskie6_22	120.6	1.688	4.302	0.042	0.2977	0.0027	0.44407	1692.9	8.1	1679	14	1709	16	1709	16	1.8
Zabriskie6_23	55.75	1.354	5.39	0.078	0.3454	0.004	0.74414	1882	12	1912	19	1857	19	1857	19	3
Zabriskie6_24	483	1.881	5.036	0.033	0.3324	0.0021	0.65997	1824.8	5.5	1851	10	1799.5	9.9	1799.5	9.9	2.9
Zabriskie6_25	190.2	1.332	11.696	0.094	0.5005	0.0036	0.78107	2580.3	7.3	2615	15	2557.7	8.7	2557.7	8.7	2.2
Zabriskie6_26	73.6	0.729	4.988	0.063	0.3251	0.0032	0.51034	1815	11	1814	15	1819	21			
Zabriskie6_27	107.8	0.759	5.63	0.065	0.3469	0.003	0.64457	1919	10	1919	14	1922	17	1922	17	0.2
Zabriskie6_28	109.3	1.259	13.64	0.16	0.5326	0.006	0.81514	2723	11	2754	25	2705	12	2705	12	1.8

Sample Name:								207/235		206/238		207/206		Best Age		
Grain #	[U] ppm	U/Th	207/235	1σ error	206/238	1σ error	RHO	Age Ma	1σ error	Age Ma	1σ error	Age Ma	1σ error	(Ma)	1σ error	% Discordance*
Zabriskie6_29	234.6	1.426	5.198	0.043	0.3345	0.0021	0.52225	1852.4	6.9	1860	10	1844	14	1844	14	0.9
Zabriskie6_30	249	1.128	5.077	0.051	0.3259	0.003	0.58028	1832.1	8.3	1818	14	1847	15	1847	15	1.6
Zabriskie6_31	193	1.849	5.91	0.2	0.3303	0.0036	0.32792	1953	29	1839	18	2071	56	2071	56	11.2
Zabriskie6_32	239.3	2.47	5.153	0.04	0.3354	0.0025	0.68983	1845	6.4	1864	12	1825.6	9.6	1825.6	9.6	2.1
Zabriskie6_33	55	1.213	5.109	0.07	0.3294	0.0036	0.5351	1837	11	1837	18	1835	22	1835	22	0.1
Zabriskie6_34	127.6	1.399	10.82	0.18	0.4704	0.0083	0.61297	2506	15	2484	36	2525	24	2525	24	1.6
Zabriskie6_35	117.8	1.435	5.11	0.049	0.3313	0.0027	0.64366	1837.8	8.4	1846	14	1835	16	1835	16	0.6
Zabriskie6_36	39.2	1.222	13.62	0.18	0.5292	0.0062	0.71084	2721	13	2736	26	2716	15	2716	15	0.7
Zabriskie6_37	68.1	1.083	5.045	0.059	0.3296	0.0031	0.56081	1825.2	9.9	1836	15	1816	18	1816	18	1.1
Zabriskie6_38	58.6	1.229	5.156	0.074	0.3332	0.0031	0.65602	1846	12	1853	15	1841	20	1841	20	0.7
Zabriskie6_39	38.74	1.401	11.7	0.14	0.4949	0.0056	0.61218	2579	11	2590	24	2571	16	2571	16	0.7
Zabriskie6_40	97.4	1.033	4.998	0.054	0.3216	0.0027	0.61484	1818.7	9	1799	13	1846	16	1846	16	2.5
Zabriskie6_41	69.9	1.024	5.641	0.066	0.3497	0.0033	0.57521	1920	10	1932	16	1908	17	1908	17	1.3
Zabriskie6_42	102.2	0.847	5.504	0.069	0.3417	0.004	0.61734	1902	10	1894	19	1903	19	1903	19	0.5
Zabriskie6_43	248.9	1.095	6.901	0.066	0.3842	0.0043	0.62333	2097.9	8.5	2095	20	2086	15	2086	15	0.4
Zabriskie6_44	161.7	0.3851	12.905	0.093	0.5195	0.0043	0.73934	2671.9	6.8	2696	18	2651	10	2651	10	1.7
Zabriskie6_45	93.9	1.351	4.787	0.066	0.3024	0.0034	0.63534	1780	12	1703	17	1870	19	1870	19	8.9
Zabriskie6_46	96.3	1.323	6.84	0.12	0.3837	0.0061	0.76531	2088	17	2092	29	2081	20	2081	20	0.5
Zabriskie6_47	136.3	0.7323	13.25	0.13	0.5282	0.0046	0.69152	2696	9.7	2733	19	2670	12	2670	12	2.4
Zabriskie6_48	77.7	0.1617	1.798	0.035	0.1738	0.0019	0.35883	1044	12	1033	11	1046	40	1046	40	1.2
Zabriskie6_49	798	1.703	4.487	0.08	0.2569	0.0044	0.80929	1726	15	1473	22	2048	18	2048	18	28.1
Zabriskie6_50	55.9	0.554	12.59	0.19	0.512	0.0076	0.73996	2646	14	2662	32	2634	18	2634	18	1.1
Zabriskie6_51	68.8	0.695	5.024	0.064	0.325	0.0037	0.61613	1823	11	1813	18	1832	18	1832	18	1
Zabriskie6_52	155.5	0.725	8.791	0.077	0.4368	0.0037	0.66457	2315.5	8	2338	16	2299	13	2299	13	1.7
Zabriskie6_53	76.1	0.4271	5.403	0.076	0.3376	0.0036	0.68	1883	12	1875	17	1891	19	1891	19	0.8
Zabriskie6_54	91.1	1.369	5.159	0.066	0.3325	0.0029	0.53922	1844	11	1850	14	1843	20	1843	20	0.4
Zabriskie6_55	30.9	0.514	13.17	0.2	0.5147	0.0068	0.59234	2690	14	2675	29	2700	21	2700	21	0.9
Zabriskie6_56	111.3	0.861	5.023	0.057	0.3202	0.0034	0.63081	1821.5	9.6	1790	17	1855	18	1855	18	3.5
Zabriskie6_57	99.9	1.212	6.621	0.073	0.3739	0.0037	0.50841	2060.8	9.7	2047	17	2072	19	2072	19	1.2

Sample Name:								207/235		206/238		207/206		Best Age		
Grain #	[U] ppm	U/Th	207/235	1σ error	206/238	1σ error	RHO	Age Ma	1σ error	Age Ma	1σ error	Age Ma	1σ error	(Ma)	1σ error	% Discordance*
Zabriskie6_58	99	0.978	4.968	0.056	0.3246	0.0028	0.51459	1812.4	9.5	1812	14	1813	19	1813	19	0.1
Zabriskie6_59	40.7	0.498	5.45	0.1	0.3353	0.0045	0.47214	1891	15	1863	22	1913	31	1913	31	2.6
Zabriskie6_60	55.2	1.091	5.485	0.086	0.3419	0.0038	0.54825	1897	14	1895	18	1895	24	1895	24	0
Zabriskie6_61	88	0.792	5.82	0.088	0.3456	0.0043	0.76046	1946	13	1916	21	1967	19	1967	19	2.6
Zabriskie6_62	156.2	1.366	4.908	0.046	0.3216	0.0026	0.59252	1802.6	8	1797	12	1809	14	1809	14	0.7
Zabriskie6_63	128.4	1.611	6.637	0.064	0.3765	0.0031	0.6287	2064	8.8	2059	14	2066	14	2066	14	0.3
Zabriskie6_64	107.1	0.578	5.201	0.057	0.3321	0.0031	0.5948	1851.2	9.4	1848	15	1851	17	1851	17	0.2
Zabriskie6_65	152.3	1.108	5.081	0.044	0.3296	0.0025	0.65147	1832	7.3	1836	12	1827	14	1827	14	0.5
Zabriskie6_66	132.1	1.444	5.054	0.087	0.3257	0.0054	0.63356	1827	15	1817	26	1833	23	1833	23	0.9
Zabriskie6_67	162.2	2.091	4.221	0.047	0.2932	0.0027	0.64703	1676.7	9.2	1657	13	1700	17	1700	17	2.5
Zabriskie6_68	259.7	1.515	6.53	0.077	0.3652	0.0047	0.67579	2049	10	2006	22	2088	18	2088	18	3.9
Zabriskie6_69	130.5	2.152	5.213	0.047	0.3283	0.0027	0.50489	1853.7	7.8	1830	13	1878	16	1878	16	2.6
Zabriskie6_70	211	1.848	11.994	0.08	0.4998	0.0033	0.62957	2603.2	6.3	2612	14	2591.7	9.8	2591.7	9.8	0.8
Zabriskie6_71	548	2.256	4.82	0.12	0.3078	0.0072	0.68527	1785	21	1729	36	1839	28	1839	28	6
Zabriskie6_72	282.8	0.8045	5.591	0.051	0.3407	0.0029	0.66446	1913.9	7.9	1890	14	1935	13	1935	13	2.3
Zabriskie6_73	181.1	0.912	5.232	0.046	0.3325	0.0027	0.55523	1856.9	7.4	1850	13	1855	15	1855	15	0.3
Zabriskie6_74	175	1.012	5.07	0.045	0.327	0.0027	0.54145	1831.2	7.8	1823	13	1838	16	1838	16	0.8
Zabriskie6_75	175.8	0.7879	5.596	0.055	0.3458	0.0028	0.58375	1914.2	8.5	1914	14	1909	15	1909	15	0.3
Zabriskie6_76	324.2	0.83	9.42	0.13	0.3804	0.0047	0.76488	2379	12	2078	22	2640	14	2640	14	21.3
Zabriskie6_77	406.6	1.809	6.142	0.056	0.3629	0.0029	0.55216	1997.2	8	1997	13	1992	14	1992	14	0.3
Zabriskie6_78	121.3	1.023	4.946	0.05	0.3175	0.0027	0.61655	1808.9	8.5	1777	13	1848	15	1848	15	3.8
Zabriskie6_79	81.3	0.814	5.169	0.061	0.3275	0.0034	0.69091	1846	10	1826	17	1868	16	1868	16	2.2
Zabriskie6_80	45.7	0.5943	5.537	0.071	0.3416	0.0036	0.36747	1904	11	1894	17	1917	23	1917	23	1.2
Zabriskie6_81	151	0.571	5.833	0.074	0.3531	0.0043	0.77183	1949	11	1951	20	1947	16	1947	16	0.2
Zabriskie6_82	148	1.476	4.637	0.059	0.3103	0.0031	0.67772	1754	11	1742	15	1767	18	1767	18	1.4
Zabriskie6_83	61.8	0.88	4.744	0.066	0.3161	0.0033	0.57901	1773	12	1770	16	1770	21	1770	21	0
Zabriskie6_84	229.5	1.136	6.715	0.051	0.3813	0.003	0.72546	2074.8	7	2082	14	2062	11	2062	11	1
Zabriskie6_85	75.3	1.333	4.771	0.07	0.3076	0.0037	0.69469	1777	12	1728	18	1831	19	1831	19	5.6
Zabriskie6_86	171.2	1.128	12.2	0.087	0.4989	0.0036	0.73817	2620	6.9	2608	16	2622.7	9	2622.7	9	0.6

Sample Name:								207/235		206/238		207/206		Best Age		
Grain #	[U] ppm	U/Th	207/235	1σ error	206/238	1σ error	RHO	Age Ma	1σ error	Age Ma	1σ error	Age Ma	1σ error	(Ma)	1σ error	% Discordance*
Zabriskie6_87	46.4	0.4246	5.485	0.068	0.3371	0.0037	0.49583	1896	11	1872	18	1918	21	1918	21	2.4
Zabriskie6_88	64.8	1.217	4.927	0.061	0.3208	0.003	0.56426	1805	10	1793	15	1819	19	1819	19	1.4
Zabriskie6_89	81.1	0.686	6.758	0.068	0.377	0.0032	0.5565	2080.2	8.6	2062	15	2096	16	2096	16	1.6
Zabriskie6_90	39.8	0.997	5.456	0.072	0.3359	0.0038	0.57567	1891	11	1866	18	1918	20	1918	20	2.7
Zabriskie6_91	36.1	0.554	12.97	0.17	0.509	0.0064	0.7013	2675	12	2650	28	2691	16	2691	16	1.5
Zabriskie6_92	47.6	1.238	5.091	0.077	0.3263	0.0035	0.62813	1832	13	1820	17	1843	21	1843	21	1.2
Zabriskie6_93	45.2	0.823	5.037	0.065	0.3234	0.0034	0.4523	1823	11	1806	17	1839	23	1839	23	1.8
Zabriskie6_94	87.8	0.944	13.54	0.13	0.525	0.0043	0.65448	2717	8.7	2720	18	2714	12	2714	12	0.2
Zabriskie6_95	134.9	1.82	5.02	0.044	0.325	0.0029	0.62317	1821.8	7.5	1813	14	1824	15	1824	15	0.6
Zabriskie6_96	87.2	0.902	12.59	0.11	0.5007	0.0041	0.63522	2648.3	8.4	2618	18	2668	12	2668	12	1.9
Zabriskie6_97	222.4	1.438	4.971	0.049	0.3196	0.0029	0.6496	1813.2	8.4	1787	14	1838	15	1838	15	2.8
Zabriskie6_98	97.9	0.921	4.982	0.052	0.3207	0.0025	0.52719	1815	8.8	1793	12	1834	17	1834	17	2.2
Zabriskie6_99	179.2	1.098	11.07	0.12	0.4681	0.0047	0.72607	2528	10	2474	21	2570	12	2570	12	3.7
Zabriskie6_100	52.2	1.016	5.35	0.13	0.3345	0.0047	0.32273	1871	19	1859	23	1873	33	1873	33	0.7
Zabriskie6_101	73.4	1.024	5.958	0.066	0.3528	0.0029	0.63647	1968.1	9.7	1947	14	1988	17	1988	17	2.1
Zabriskie6_102	167.7	1.07	6.454	0.055	0.3709	0.003	0.67911	2038.6	7.5	2033	14	2038	13	2038	13	0.2
Zabriskie6_103	61.6	1.365	4.879	0.058	0.3162	0.0029	0.61518	1797	10	1771	14	1826	17	1826	17	3
Zabriskie6_104	240.1	1.308	3.497	0.048	0.2269	0.0028	0.83611	1525	11	1318	15	1824	13	1824	13	27.7
Zabriskie6_105	88.2	0.968	4.948	0.058	0.3237	0.0029	0.58336	1810	9.7	1807	14	1809	18	1809	18	0.1
Zabriskie6_106	142.1	1.364	10.837	0.072	0.4724	0.0032	0.67528	2508.6	6.2	2493	14	2517	10	2517	10	1
Zabriskie6_107	158.4	1.638	5.125	0.049	0.315	0.0029	0.59893	1841.3	8.1	1767	13	1918	15	1918	15	7.9
Zabriskie6_108	52.9	0.4596	4.975	0.068	0.3148	0.0038	0.57306	1813	11	1763	19	1867	23	1867	23	5.6
Zabriskie6_109	64.9	0.5609	5.167	0.082	0.3221	0.0035	0.60019	1847	13	1799	17	1902	25	1902	25	5.4
Zabriskie6_110	189.9	0.85	5.051	0.052	0.3246	0.0031	0.5881	1826.6	8.8	1812	15	1841	16	1841	16	1.6
Zabriskie6_111	109.2	0.872	5.426	0.05	0.3351	0.0026	0.61161	1889.9	8.2	1863	13	1916	15	1916	15	2.8
Zabriskie6_112	146.6	1.603	5.014	0.043	0.3224	0.0027	0.63758	1821.8	7	1801	13	1840	13	1840	13	2.1
Zabriskie6_113	99.6	1.394	4.944	0.059	0.3219	0.0035	0.54296	1808	10	1798	17	1810	20	1810	20	0.7
Zabriskie6_114	300.4	0.54	5.115	0.083	0.3111	0.0042	0.767	1835	14	1745	21	1933	19	1933	19	9.7
Zabriskie6_115	227.7	1.6	4.073	0.044	0.2892	0.0027	0.733	1648.7	8.6	1637	14	1659	13	1659	13	1.3

Sample Name:								207/235		206/238		207/206		Best Age		
Grain #	[U] ppm	U/Th	207/235	1σ error	206/238	1σ error	RHO	Age Ma	1σ error	Age Ma	1σ error	Age Ma	1σ error	(Ma)	1σ error	% Discordance*
Zabriskie6_116	107	1.19	6.539	0.073	0.3704	0.0037	0.545	2049.9	9.8	2031	18	2068	18	2068	18	1.8
Zabriskie6_117	190.6	1.27	5.013	0.05	0.3247	0.0029	0.689	1820.2	8.5	1812	14	1828	14	1828	14	0.9
Zabriskie6_118	93.7	0.69	19.04	0.18	0.5988	0.0059	0.647	3042.5	9.1	3023	24	3051	13	3051	13	0.9
Zabriskie6_119	70.2	0.71	4.978	0.072	0.3211	0.0038	0.514	1814	12	1794	19	1832	23	1832	23	2.1
Zabriskie6_120	165	0.69	5.591	0.058	0.3441	0.0034	0.582	1914.5	8.7	1906	16	1916	16	1916	16	0.5
Zabriskie6_121	69.7	0.51	1.699	0.043	0.1567	0.0033	0.546	1006	16	938	18	1151	46	1151	46	18.5
Zabriskie6_122	132.9	1.79	5.044	0.06	0.3289	0.0033	0.555	1826.3	9.9	1832	16	1816	19	1816	19	0.9
Zabriskie6_123	48.2	0.62	13.86	0.17	0.5241	0.0053	0.726	2738	12	2715	22	2752	14	2752	14	1.3
Zabriskie6_124	46.9	1.21	5.149	0.075	0.3285	0.0034	0.475	1842	12	1830	17	1854	23	1854	23	1.3
Zabriskie6_125	55.3	0.68	5.44	0.11	0.3404	0.0055	0.329	1890	16	1888	27	1888	39	1888	39	0
Zabriskie6_126	100.7	0.68	9.71	0.15	0.436	0.0056	0.71	2405	14	2332	25	2465	18	2465	18	5.4
Zabriskie6_127	104.8	0.83	9.81	0.25	0.442	0.011	0.826	2414	23	2358	47	2460	25	2460	25	4.1
Zabriskie6_128	258.1	1.59	5.181	0.051	0.3299	0.0032	0.601	1848.4	8.4	1837	16	1862	15	1862	15	1.3
Zabriskie6_129	24.81	3.45	13.33	0.21	0.5233	0.008	0.697	2700	15	2714	35	2692	21	2692	21	0.8
Zabriskie6_130	96.8	0.53	11.49	0.19	0.4853	0.0074	0.81	2562	16	2549	32	2569	20	2569	20	0.8
Zabriskie6_131	73.2	0.96	5.139	0.063	0.3285	0.0029	0.492	1841	10	1830	14	1849	21	1849	21	1
Zabriskie6_132	115.8	0.41	0.619	0.014	0.07722	0.0009	0.108	487.9	8.6	479.4	5.4	509	51	479.4	5.4	1.7
Zabriskie6_133	45.9	0.76	4.984	0.068	0.3205	0.003	0.445	1814	11	1791	15	1839	24	1839	24	2.6
Zabriskie6_134	72.9	1.29	4.984	0.083	0.3123	0.0039	0.664	1813	14	1751	19	1881	22	1881	22	6.9
Zabriskie6_135	101.9	1.46	4.846	0.054	0.3179	0.003	0.513	1791.4	9.5	1779	14	1799	18	1799	18	1.1
Zabriskie6_136	54.4	0.66	5.183	0.069	0.3313	0.0031	0.447	1848	11	1844	15	1847	23	1847	23	0.2
Zabriskie6_137	38.4	0.8	5.054	0.081	0.3276	0.0037	0.465	1829	14	1828	18	1822	29	1822	29	0.3
Zabriskie6_138	102.7	0.74	11.89	0.1	0.4938	0.0039	0.554	2598.1	7.9	2586	17	2596	13	2596	13	0.4
Zabriskie6_139	123	1.23	5.028	0.066	0.3242	0.0037	0.595	1823	11	1810	18	1834	20	1834	20	1.3
Zabriskie6_140	59	0.84	6.58	0.16	0.3729	0.0071	0.794	2058	20	2042	33	2071	30	2071	30	1.4
Zabriskie6_141	58.3	0.57	6.545	0.069	0.3681	0.0035	0.43	2053	9.8	2020	17	2080	19	2080	19	2.9

Sample Name:								207/235		206/238		207/206		Best Age		
Grain #	[U] ppm	U/Th	207/235	1σ error	206/238	1σ error	RHO	Age Ma	1σ error	Age Ma	1σ error	Age Ma	1σ error	(Ma)	1σ error	% Discordance*
PH-7-11-13-1 - Wyman Fm. - N37°10'06.54" W118°11'39.70"																
PH-7-11-13-1-001		3.37	4.78814	0.04492	0.33301	0.00212	0.9	1783	8	1853	10	1705	9	1705	9	9.8
PH-7-11-13-1-002		0.95	17.61528	0.17661	0.55077	0.00439	0.9	2969	10	2828	18	3068	7	3068	7	-9.8
PH-7-11-13-1-003		2.34	4.81827	0.04988	0.33427	0.00223	0.9	1788	9	1859	11	1709	10	1709	10	10
PH-7-11-13-1-004		4.67	5.09896	0.04622	0.35696	0.00224	0.9	1836	8	1968	11	1692	8	1692	8	18.8
PH-7-11-13-1-005		3.46	4.65405	0.0538	0.32883	0.00231	0.9	1759	10	1833	11	1675	11	1675	11	10.7
PH-7-11-13-1-006		3.22	5.04753	0.04795	0.35097	0.00225	0.9	1827	8	1939	11	1704	9	1704	9	15.8
PH-7-11-13-1-007		4.24	4.64117	0.06105	0.32468	0.00246	0.9	1757	11	1813	12	1693	13	1693	13	8
PH-7-11-13-1-008		3.2	1.94098	0.04919	0.18982	0.00189	0.9	1095	17	1120	10	1048	35	1048	35	7.4
PH-7-11-13-1-009		2.41	5.40659	0.14125	0.35174	0.00463	0.9	1886	22	1943	22	1825	29	1825	29	7.3
PH-7-11-13-1-010		2.66	4.61783	0.04495	0.32311	0.00208	0.9	1752	8	1805	10	1692	9	1692	9	7.6
PH-7-11-13-1-011		3.75	3.03413	0.05063	0.2308	0.00192	0.9	1416	13	1339	10	1537	19	1537	19	-14.3
PH-7-11-13-1-012		2.04	9.47371	0.13529	0.44967	0.00416	0.9	2385	13	2394	18	2379	13	2379	13	0.7
PH-7-11-13-1-013		1.38	4.47104	0.05495	0.30024	0.00218	0.9	1726	10	1692	11	1767	12	1767	12	-4.9
PH-7-11-13-1-014		2.33	8.60013	0.10533	0.43399	0.0035	0.9	2297	11	2324	16	2274	11	2274	11	2.5
PH-7-11-13-1-015		2	4.93548	0.0721	0.33694	0.00274	0.9	1808	12	1872	13	1737	15	1737	15	8.9
PH-7-11-13-1-016		1.7	11.30927	0.15932	0.47494	0.00449	0.9	2549	13	2505	20	2585	12	2585	12	-3.8
PH-7-11-13-1-017		2.73	2.9236	0.06512	0.24912	0.00246	0.9	1388	17	1434	13	1319	28	1319	28	9.7
PH-7-11-13-1-018		2.02	5.09507	0.09339	0.35634	0.00344	0.9	1835	16	1965	16	1692	20	1692	20	18.7
PH-7-11-13-1-019		2.76	4.74822	0.06158	0.32497	0.00243	0.9	1776	11	1814	12	1732	13	1732	13	5.4
PH-7-11-13-1-020		50.43	4.38197	0.06524	0.30504	0.00247	0.9	1709	12	1716	12	1700	16	1700	16	1
PH-7-11-13-1-021		1.87	13.79301	0.12981	0.56479	0.00407	0.9	2736	9	2886	17	2626	7	2626	7	12.3
PH-7-11-13-1-022		1.28	1.06149	0.0366	0.11909	0.00132	0.9	735	18	725	8	763	54	725	8	-5.2
PH-7-11-13-1-023		2.2	10.56707	0.12698	0.49034	0.00403	0.9	2486	11	2572	17	2416	10	2416	10	7.8
PH-7-11-13-1-024		2.59	5.00512	0.05879	0.34221	0.00242	0.9	1820	10	1897	12	1733	12	1733	12	10.9
PH-7-11-13-1-025		5.15	4.78827	0.09852	0.32645	0.00342	0.9	1783	17	1821	17	1738	23	1738	23	5.5
PH-7-11-13-1-026		2.74	3.2399	0.0975	0.26444	0.00323	0.9	1467	23	1513	16	1401	39	1401	39	9
PH-7-11-13-1-027		4.59	3.2296	0.05382	0.26322	0.00214	0.9	1464	13	1506	11	1404	20	1404	20	8.2
PH-7-11-13-1-028		1.25	4.80174	0.15951	0.31909	0.00485	0.9	1785	28	1785	24	1785	38	1785	38	0.1

Sample Name:								207/235		206/238		207/206		Best Age		
Grain #	[U] ppm	U/Th	207/235	1σ error	206/238	1σ error	RHO	Age Ma	1σ error	Age Ma	1σ error	Age Ma	1σ error	(Ma)	1σ error	% Discordance*
PH-7-11-13-1-029		0.88	4.50522	0.08235	0.30527	0.00285	0.9	1732	15	1717	14	1749	20	1749	20	-2
PH-7-11-13-1-030		2.09	4.78198	0.08227	0.32443	0.00295	0.9	1782	14	1811	14	1747	18	1747	18	4.3
PH-7-11-13-1-031		1.45	14.36316	0.16901	0.56494	0.0048	0.9	2774	11	2887	20	2692	9	2692	9	9
PH-7-11-13-1-032		2.48	4.89948	0.06101	0.32934	0.00241	0.9	1802	11	1835	12	1764	12	1764	12	4.7
PH-7-11-13-1-033		2.17	11.88419	0.13558	0.51508	0.00414	0.9	2595	11	2678	18	2530	9	2530	9	7.2
PH-7-11-13-1-034		1.15	5.69771	0.08796	0.36882	0.0032	0.9	1931	13	2024	15	1832	16	1832	16	12.3
PH-7-11-13-1-035		0.63	11.69351	0.13217	0.51113	0.00407	0.9	2580	11	2661	17	2516	9	2516	9	7.1
PH-7-11-13-1-036		1.68	16.62013	0.22586	0.60164	0.00595	0.9	2913	13	3036	24	2828	11	2828	11	9.3
PH-7-11-13-1-037		3.43	13.55635	0.13637	0.5467	0.0041	0.9	2719	10	2811	17	2650	8	2650	8	7.6
PH-7-11-13-1-038		1.63	5.08981	0.13201	0.33681	0.0043	0.9	1834	22	1871	21	1792	29	1792	29	5.2
PH-7-11-13-1-039		2.16	16.01721	0.15084	0.56124	0.00412	0.9	2878	9	2872	17	2881	7	2881	7	-0.3
PH-7-11-13-1-040		3.36	5.01041	0.0651	0.34335	0.00258	0.9	1821	11	1903	12	1728	13	1728	13	11.8
PH-7-11-13-1-041		2.67	22.1234	0.31645	0.66968	0.00734	0.9	3189	14	3305	28	3116	11	3116	11	7.8
PH-7-11-13-1-042		6.35	4.33658	0.05951	0.31293	0.00237	0.9	1700	11	1755	12	1632	15	1632	15	8.7
PH-7-11-13-1-043		5.58	4.60892	0.07497	0.3276	0.00281	0.9	1751	14	1827	14	1660	18	1660	18	11.6
PH-7-11-13-1-044		1.82	4.78038	0.07955	0.32417	0.00287	0.9	1781	14	1810	14	1747	18	1747	18	4.2
PH-7-11-13-1-045		11.86	10.30673	0.10243	0.47827	0.0034	0.9	2463	9	2520	15	2415	8	2415	8	5.3
PH-7-11-13-1-046		2.22	4.86758	0.09357	0.3277	0.00324	0.9	1797	16	1827	16	1760	21	1760	21	4.5
PH-7-11-13-1-047		2.46	8.99307	0.21788	0.45363	0.00639	0.9	2337	22	2411	28	2272	23	2272	23	7.5
PH-7-11-13-1-048		2.18	17.13917	0.21522	0.58665	0.00547	0.9	2943	12	2976	22	2919	10	2919	10	2.5
PH-7-11-13-1-049		2.69	4.77614	0.05679	0.31196	0.0022	0.9	1781	10	1750	11	1815	12	1815	12	-4
PH-7-11-13-1-050		1.56	12.80791	0.21714	0.51981	0.00589	0.9	2666	16	2698	25	2639	14	2639	14	2.8
PH-7-11-13-1-051		2.28	5.22418	0.10208	0.34749	0.00353	0.9	1857	17	1923	17	1782	21	1782	21	9.3
PH-7-11-13-1-052		3.6	5.17711	0.0831	0.33641	0.00295	0.9	1849	14	1869	14	1824	17	1824	17	3
PH-7-11-13-1-053		2.63	8.82837	0.11447	0.44371	0.0037	0.9	2320	12	2367	17	2278	12	2278	12	4.8
PH-7-11-13-1-054		3.63	4.37234	0.06371	0.29618	0.00234	0.9	1707	12	1672	12	1748	15	1748	15	-4.8
PH-7-11-13-1-055		3.8	5.66887	0.12074	0.36479	0.00404	0.9	1927	18	2005	19	1842	23	1842	23	10.4
PH-7-11-13-1-056		2.03	9.29883	0.1013	0.37454	0.00283	0.9	2368	10	2051	13	2652	9	2652	9	-26.3
PH-7-11-13-1-057		1.22	16.09927	0.1944	0.58974	0.00522	0.9	2883	12	2988	21	2808	9	2808	9	8.2

Sample Name:								207/235		206/238		207/206		Best Age		
Grain #	[U] ppm	U/Th	207/235	1σ error	206/238	1σ error	RHO	Age Ma	1σ error	Age Ma	1σ error	Age Ma	1σ error	(Ma)	1σ error	% Discordance*
PH-7-11-13-1-058		1.47	5.28815	0.11574	0.32506	0.00367	0.9	1867	19	1814	18	1924	23	1924	23	-6.4
PH-7-11-13-1-059		7.63	4.98198	0.05965	0.33262	0.00235	0.9	1816	10	1851	11	1775	12	1775	12	5.1
PH-7-11-13-1-060		1.07	12.96918	0.16044	0.52922	0.00459	0.9	2677	12	2738	19	2630	10	2630	10	5.2
PH-7-11-13-1-061		6.07	4.42489	0.07457	0.30539	0.00267	0.9	1717	14	1718	13	1714	18	1714	18	0.4
PH-7-11-13-1-062		3.94	4.77437	0.06454	0.32228	0.00244	0.9	1780	11	1801	12	1754	14	1754	14	3.2
PH-7-11-13-1-063		2.16	4.19125	0.06908	0.30096	0.00255	0.9	1672	14	1696	13	1641	18	1641	18	4
PH-7-11-13-1-064		5.91	3.55809	0.0596	0.26443	0.0021	0.87	1540	13	1512	11	1579	35	1579	35	-4.7

Sample Name:								207/235		206/238		207/206		Best Age		
Grain #	[U] ppm	U/Th	207/235	1σ error	206/238	1σ error	RHO	Age Ma	1σ error	Age Ma	1σ error	Age Ma	1σ error	(Ma)	1σ error	% Discordance*
PH-7-16-13-3 - Wyman Fm. - N37°26.258 W118°10.062																
PH-7-16-13-3-001		2.04	7.85529	0.06056	0.40107	0.00239	0.9	2215	7	2174	11	2253	6	2253	6	-4.2
PH-7-16-13-3-002		6.6	4.24391	0.04004	0.29585	0.00183	0.9	1683	8	1671	9	1698	9	1698	9	-1.9
PH-7-16-13-3-003		2.7	4.07464	0.03944	0.28501	0.00177	0.9	1649	8	1617	9	1692	9	1692	9	-5.1
PH-7-16-13-3-004		4.53	4.26958	0.0365	0.29752	0.00176	0.9	1688	7	1679	9	1699	8	1699	8	-1.4
PH-7-16-13-3-005		2.25	4.63998	0.06295	0.30407	0.00234	0.9	1756	11	1711	12	1811	14	1811	14	-6.3
PH-7-16-13-3-006		2.89	4.11487	0.0584	0.28735	0.00222	0.9	1657	12	1628	11	1695	15	1695	15	-4.5
PH-7-16-13-3-007		3.62	3.73018	0.03467	0.26914	0.00163	0.9	1578	7	1536	8	1634	9	1634	9	-6.8
PH-7-16-13-3-008		1.63	3.7914	0.05524	0.27888	0.00216	0.9	1591	12	1586	11	1599	16	1599	16	-0.9
PH-7-16-13-3-009		2.02	4.29381	0.0419	0.30484	0.00191	0.9	1692	8	1715	9	1664	9	1664	9	3.4
PH-7-16-13-3-010		1.18	2.40477	0.05447	0.20968	0.002	0.9	1244	16	1227	11	1274	29	1274	29	-4.1
PH-7-16-13-3-011		4.05	1.88542	0.02955	0.18415	0.00132	0.9	1076	10	1090	7	1049	20	1049	20	4.1
PH-7-16-13-3-012		4.97	4.33254	0.04148	0.30054	0.00187	0.9	1700	8	1694	9	1707	9	1707	9	-0.9
PH-7-16-13-3-013		1.54	11.54544	0.09643	0.49306	0.00321	0.9	2568	8	2584	14	2557	6	2557	6	1.3
PH-7-16-13-3-014		2.79	2.84029	0.03894	0.23734	0.00168	0.9	1366	10	1373	9	1357	16	1357	16	1.3
PH-7-16-13-3-015		1.31	4.2967	0.07884	0.30207	0.0028	0.9	1693	15	1702	14	1683	20	1683	20	1.2
PH-7-16-13-3-016		1.29	4.47984	0.05222	0.31002	0.00215	0.9	1727	10	1741	11	1712	12	1712	12	1.9
PH-7-16-13-3-017		1.76	4.43327	0.04964	0.30705	0.00208	0.9	1719	9	1726	10	1710	11	1710	11	1
PH-7-16-13-3-018		1.27	10.72918	0.09179	0.48016	0.00314	0.9	2500	8	2528	14	2478	7	2478	7	2.4
PH-7-16-13-3-019		1.02	6.07029	0.10433	0.34297	0.00334	0.9	1986	15	1901	16	2076	17	2076	17	-9.8
PH-7-16-13-3-020		3.75	4.58884	0.05283	0.31582	0.00218	0.9	1747	10	1769	11	1722	11	1722	11	3.1
PH-7-16-13-3-021		1.4	4.84188	0.04338	0.32807	0.002	0.9	1792	8	1829	10	1750	8	1750	8	5.1
PH-7-16-13-3-022		1.3	4.43252	0.06112	0.31268	0.00239	0.9	1718	11	1754	12	1676	15	1676	15	5.2
PH-7-16-13-3-023		3.23	4.30627	0.04364	0.3029	0.00194	0.9	1695	8	1706	10	1682	10	1682	10	1.6
PH-7-16-13-3-024		1.2	2.92278	0.04796	0.24285	0.00192	0.9	1388	12	1401	10	1368	20	1368	20	2.7
PH-7-16-13-3-025		0.62	12.77212	0.10268	0.50145	0.00323	0.9	2663	8	2620	14	2696	6	2696	6	-3.5
PH-7-16-13-3-026		1.03	4.93128	0.12149	0.33284	0.00399	0.9	1808	21	1852	19	1757	28	1757	28	6.2
PH-7-16-13-3-027		0.81	9.95147	0.18795	0.45253	0.00532	0.9	2430	17	2406	24	2451	17	2451	17	-2.2
PH-7-16-13-3-028		1.32	4.5494	0.06054	0.31605	0.00238	0.9	1740	11	1770	12	1704	14	1704	14	4.4

Sample Name:								207/235		206/238		207/206		Best Age		
Grain #	[U] ppm	U/Th	207/235	1σ error	206/238	1σ error	RHO	Age Ma	1σ error	Age Ma	1σ error	Age Ma	1σ error	(Ma)	1σ error	% Discordance*
PH-7-16-13-3-029		2.54	4.37168	0.04448	0.31009	0.00199	0.9	1707	8	1741	10	1666	10	1666	10	5.1
PH-7-16-13-3-030		2	1.84824	0.03403	0.17798	0.00139	0.9	1063	12	1056	8	1078	24	1078	24	-2.2
PH-7-16-13-3-031		1.52	2.91037	0.06756	0.23674	0.00241	0.9	1385	18	1370	13	1408	29	1408	29	-3.1
PH-7-16-13-3-032		1.82	2.32244	0.08656	0.20824	0.00298	0.9	1219	26	1219	16	1220	51	1220	51	.
PH-7-16-13-3-033		1.93	4.34021	0.05432	0.30842	0.00221	0.9	1701	10	1733	11	1663	13	1663	13	4.8
PH-7-16-13-3-034		7.46	4.01463	0.04948	0.29602	0.00208	0.9	1637	10	1672	10	1594	13	1594	13	5.5
PH-7-16-13-3-035		1.56	4.29765	0.07632	0.30779	0.00277	0.9	1693	15	1730	14	1648	20	1648	20	5.6
PH-7-16-13-3-036		1.35	4.76195	0.0912	0.32069	0.00319	0.9	1778	16	1793	16	1762	21	1762	21	2
PH-7-16-13-3-037		8.6	3.84932	0.0301	0.27655	0.00156	0.9	1603	6	1574	8	1642	7	1642	7	-4.7
PH-7-16-13-3-038		2.37	4.26268	0.14349	0.29495	0.00428	0.9	1686	28	1666	21	1712	41	1712	41	-3.1
PH-7-16-13-3-039		2.33	10.62272	0.07748	0.47954	0.00285	0.9	2491	7	2525	12	2463	6	2463	6	3
PH-7-16-13-3-040		0.88	2.81778	0.06873	0.23292	0.0024	0.9	1360	18	1350	13	1378	31	1378	31	-2.3
PH-7-16-13-3-041		2.14	12.33361	0.10497	0.51415	0.00341	0.9	2630	8	2674	15	2597	7	2597	7	3.6
PH-7-16-13-3-042		3.31	4.33459	0.07443	0.30376	0.00244	0.87	1700	14	1710	12	1688	36	1688	36	1.5
PH-7-16-13-3-043		1.62	3.40279	0.04066	0.23764	0.00163	0.9	1505	9	1374	8	1695	12	1695	12	-21
PH-7-16-13-3-044		3.81	1.86261	0.04137	0.18385	0.00166	0.9	1068	15	1088	9	1028	30	1028	30	6.3
PH-7-16-13-3-045		0.6	3.74782	0.105	0.27648	0.00343	0.9	1582	22	1574	17	1593	34	1593	34	-1.4
PH-7-16-13-3-046		2.37	2.80464	0.04845	0.24139	0.00197	0.9	1357	13	1394	10	1299	21	1299	21	8
PH-7-16-13-3-047		2.67	4.70129	0.04442	0.32134	0.002	0.9	1767	8	1796	10	1734	9	1734	9	4.1
PH-7-16-13-3-048		4	4.62741	0.04837	0.31842	0.00209	0.9	1754	9	1782	10	1722	10	1722	10	3.9
PH-7-16-13-3-049		3.39	8.53168	0.10101	0.42617	0.00334	0.9	2289	11	2288	15	2291	10	2291	10	-0.2
PH-7-16-13-3-050		4.46	4.88001	0.09059	0.33129	0.0032	0.9	1799	16	1845	15	1747	20	1747	20	6.4
PH-7-16-13-3-051		0.89	4.68678	0.11726	0.31506	0.00377	0.9	1765	21	1766	18	1765	28	1765	28	.
PH-7-16-13-3-052		4.12	12.21227	0.21095	0.50401	0.00575	0.9	2621	16	2631	25	2614	15	2614	15	0.8
PH-7-16-13-3-053		2.31	3.05793	0.05003	0.26242	0.00207	0.9	1422	13	1502	11	1305	20	1305	20	16.9
PH-7-16-13-3-054		1.48	0.93027	0.0303	0.10815	0.0011	0.9	668	16	662	6	688	52	662	6	-4
PH-7-16-13-3-055		2.48	4.68378	0.05482	0.32168	0.00225	0.9	1764	10	1798	11	1725	12	1725	12	4.8
PH-7-16-13-3-056		6.24	4.18091	0.08285	0.30341	0.00299	0.9	1670	16	1708	15	1624	22	1624	22	5.9
PH-7-16-13-3-057		1.15	4.51119	0.07089	0.31988	0.00269	0.9	1733	13	1789	13	1667	17	1667	17	8.4

Sample Name:								207/235		206/238		207/206		Best Age		
Grain #	[U] ppm	U/Th	207/235	1σ error	206/238	1σ error	RHO	Age Ma	1σ error	Age Ma	1σ error	Age Ma	1σ error	(Ma)	1σ error	% Discordance*
PH-7-16-13-3-058		2.98	4.24575	0.07072	0.30899	0.00269	0.9	1683	14	1736	13	1618	18	1618	18	8.2
PH-7-16-13-3-059		1.91	3.63003	0.05816	0.27854	0.00227	0.9	1556	13	1584	11	1519	18	1519	18	4.8
PH-7-16-13-3-060		1.49	10.24972	0.19258	0.4689	0.00553	0.9	2458	17	2479	24	2441	17	2441	17	1.8
PH-7-16-13-3-061		0.81	10.00062	0.39627	0.45026	0.00776	0.91	2435	37	2396	34	2467	75	2467	75	-3.4
PH-7-16-13-3-062		1.69	4.70703	0.05812	0.32715	0.00236	0.9	1768	10	1825	11	1704	13	1704	13	8.1
PH-7-16-13-3-063		5.62	4.55582	0.06046	0.32154	0.00242	0.9	1741	11	1797	12	1675	14	1675	14	8.3
PH-7-16-13-3-064		1.21	8.11375	0.20512	0.36202	0.0041	0.89	2244	23	1992	19	2482	48	2482	48	-22.9
PH-7-16-13-3-065		3.65	4.60903	0.05898	0.31821	0.00235	0.9	1751	11	1781	11	1716	13	1716	13	4.3
PH-7-16-13-3-066		1.39	12.19462	0.20018	0.51809	0.00569	0.9	2619	15	2691	24	2565	14	2565	14	6
PH-7-16-13-3-067		3.97	12.11248	0.12087	0.50909	0.00375	0.9	2613	9	2653	16	2583	8	2583	8	3.2
PH-7-16-13-3-068		2.3	4.50292	0.04296	0.31524	0.00196	0.9	1732	8	1766	10	1690	9	1690	9	5.1
PH-7-16-13-3-069		3.24	4.46442	0.04447	0.31256	0.00199	0.9	1724	8	1753	10	1690	10	1690	10	4.2
PH-7-16-13-3-070		0.74	19.85286	0.21482	0.6121	0.00524	0.9	3084	10	3078	21	3089	8	3089	8	-0.5
PH-7-16-13-3-071		0.64	1.47842	0.03645	0.15765	0.00141	0.9	922	15	944	8	870	36	944	8	9.1
PH-7-16-13-3-072		1.91	3.62392	0.07002	0.27168	0.00218	0.88	1555	15	1549	11	1562	40	1562	40	-0.9
PH-7-16-13-3-073		2.89	3.11211	0.03541	0.22891	0.00136	0.88	1436	9	1329	7	1598	24	1598	24	-18.6
PH-7-16-13-3-074		2.05	2.68118	0.04021	0.22893	0.00169	0.9	1323	11	1329	9	1315	18	1315	18	1.1
PH-7-16-13-3-075		1.68	4.67222	0.04507	0.31473	0.00198	0.9	1762	8	1764	10	1761	9	1761	9	0.1
PH-7-16-13-3-076		2.94	4.395	0.10386	0.30599	0.00349	0.9	1711	20	1721	17	1700	27	1700	27	1.3
PH-7-16-13-3-077		1.64	5.51792	0.05387	0.33789	0.00219	0.9	1903	8	1877	11	1934	9	1934	9	-3.4
PH-7-16-13-3-078		2.19	11.2496	0.10239	0.47545	0.00303	0.9	2544	8	2507	13	2573	19	2573	19	-3.1
PH-7-16-13-3-079		1.7	4.1091	0.03962	0.28787	0.00179	0.9	1656	8	1631	9	1689	9	1689	9	-3.9
PH-7-16-13-3-080		2.38	5.7102	0.04708	0.34177	0.00204	0.9	1933	7	1895	10	1974	7	1974	7	-4.7
PH-7-16-13-3-081		2.63	4.30464	0.04586	0.29909	0.00196	0.9	1694	9	1687	10	1704	10	1704	10	-1.2
PH-7-16-13-3-082		2.98	2.80367	0.04035	0.23599	0.00171	0.9	1357	11	1366	9	1343	17	1343	17	1.9
PH-7-16-13-3-083		1.51	2.71042	0.03957	0.23	0.00168	0.9	1331	11	1334	9	1327	17	1327	17	0.6
PH-7-16-13-3-084		1.44	11.1283	0.08557	0.47818	0.00295	0.9	2534	7	2519	13	2546	6	2546	6	-1.3
PH-7-16-13-3-085		1.61	8.61216	0.09549	0.4141	0.00311	0.9	2298	10	2234	14	2356	9	2356	9	-6.2
PH-7-16-13-3-086		1.61	14.97218	0.20761	0.53144	0.00533	0.9	2813	13	2748	22	2862	11	2862	11	-4.9

Sample Name:								207/235		206/238		207/206		Best Age		
Grain #	[U] ppm	U/Th	207/235	1σ error	206/238	1σ error	RHO	Age Ma	1σ error	Age Ma	1σ error	Age Ma	1σ error	(Ma)	1σ error	% Discordance*
PH-7-16-13-3-087		0.81	10.66468	0.08017	0.46413	0.00282	0.9	2494	7	2458	12	2525	6	2525	6	-3.2
PH-7-16-13-3-088		12.8	4.23485	0.03124	0.29381	0.00164	0.9	1681	6	1661	8	1707	6	1707	6	-3.1
PH-7-16-13-3-089		1	10.69225	0.16874	0.46623	0.00478	0.9	2497	15	2467	21	2522	14	2522	14	-2.6
PH-7-16-13-3-090		5.75	4.28709	0.03365	0.30323	0.00173	0.9	1691	6	1707	9	1671	7	1671	7	2.4
PH-7-16-13-3-091		1.18	4.21092	0.04116	0.29437	0.00184	0.9	1676	8	1663	9	1693	9	1693	9	-2
PH-7-16-13-3-092		2.84	4.25531	0.04966	0.30628	0.0021	0.9	1685	10	1722	10	1639	12	1639	12	5.7
PH-7-16-13-3-093		1.33	11.15099	0.10088	0.46725	0.00319	0.9	2536	8	2471	14	2588	7	2588	7	-5.5
PH-7-16-13-3-094		0.91	11.8254	0.12493	0.49355	0.00378	0.9	2591	10	2586	16	2595	8	2595	8	-0.5
PH-7-16-13-3-095		2.55	13.76439	0.10495	0.51526	0.00306	0.9	2734	7	2679	13	2774	16	2774	16	-4.2
PH-7-16-13-3-096		2.52	9.09359	0.08183	0.43111	0.00285	0.9	2347	8	2311	13	2380	7	2380	7	-3.5
PH-7-16-13-3-097		1.99	3.08197	0.08172	0.24564	0.00284	0.9	1428	20	1416	15	1447	33	1447	33	-2.4
PH-7-16-13-3-098		3.05	4.21644	0.05277	0.2962	0.00212	0.9	1677	10	1672	11	1684	13	1684	13	-0.8
PH-7-16-13-3-099		1.14	3.92033	0.04077	0.28283	0.00181	0.9	1618	8	1606	9	1635	10	1635	10	-2
PH-7-16-13-3-100		2.34	2.41854	0.04035	0.21259	0.00164	0.9	1248	12	1243	9	1259	21	1259	21	-1.4

Sample Name:								207/235		206/238		207/206		Best Age		
Grain #	[U] ppm	U/Th	207/235	1σ error	206/238	1σ error	RHO	Age Ma	1σ error	Age Ma	1σ error	Age Ma	1σ error	(Ma)	1σ error	% Discordance*
PH-7-16-13-2A-2B - Harkless Fm. - N37°24.143 W118°13.548																
PH-7-16-13-2A-2B-001		0.91	4.5089	0.05461	0.31329	0.00222	0.9	1733	10	1757	11	1704	12	1704	12	3.5
PH-7-16-13-2A-2B-002		1.17	4.12856	0.04257	0.28269	0.00182	0.9	1660	8	1605	9	1731	10	1731	10	-8.3
PH-7-16-13-2A-2B-003		1.8	4.3702	0.03646	0.30652	0.00179	0.9	1707	7	1724	9	1687	8	1687	8	2.4
PH-7-16-13-2A-2B-004		1.26	4.23704	0.03155	0.29801	0.00166	0.9	1681	6	1681	8	1682	6	1682	6	-0.1
PH-7-16-13-2A-2B-005		1.08	4.25214	0.03931	0.29886	0.00182	0.9	1684	8	1686	9	1683	9	1683	9	0.1
PH-7-16-13-2A-2B-006		1.68	4.16008	0.0363	0.29486	0.00175	0.9	1666	7	1666	9	1668	8	1668	8	-0.2
PH-7-16-13-2A-2B-007		0.34	14.53594	0.12849	0.54009	0.00377	0.9	2785	8	2784	16	2787	7	2787	7	-0.2
PH-7-16-13-2A-2B-008		1.39	11.21857	0.08649	0.47686	0.00295	0.9	2541	7	2514	13	2564	6	2564	6	-2.4
PH-7-16-13-2A-2B-009		2.13	4.54133	0.04752	0.31676	0.00207	0.9	1739	9	1774	10	1697	10	1697	10	5.1
PH-7-16-13-2A-2B-010		2.51	4.27069	0.0346	0.29986	0.00173	0.9	1688	7	1691	9	1685	7	1685	7	0.4
PH-7-16-13-2A-2B-011		2.18	2.81971	0.03531	0.23583	0.00159	0.9	1361	9	1365	8	1355	14	1355	14	0.8
PH-7-16-13-2A-2B-012		1.95	4.25193	0.05439	0.3007	0.00219	0.9	1684	11	1695	11	1672	13	1672	13	1.5
PH-7-16-13-2A-2B-013		1.58	4.40227	0.05558	0.30436	0.0022	0.9	1713	10	1713	11	1713	13	1713	13	-0.1
PH-7-16-13-2A-2B-014		2.64	4.31023	0.04483	0.30435	0.00197	0.9	1695	9	1713	10	1675	10	1675	10	2.6
PH-7-16-13-2A-2B-015		1.54	4.00839	0.03898	0.28061	0.00175	0.9	1636	8	1594	9	1690	9	1690	9	-6.4
PH-7-16-13-2A-2B-016		5.88	4.30655	0.03142	0.30472	0.00169	0.9	1695	6	1715	8	1671	6	1671	6	3
PH-7-16-13-2A-2B-017		0.69	2.75434	0.05251	0.22827	0.00196	0.9	1343	14	1325	10	1373	23	1373	23	-3.8
PH-7-16-13-2A-2B-018		0.79	4.19134	0.03895	0.29114	0.00178	0.9	1672	8	1647	9	1705	9	1705	9	-3.9
PH-7-16-13-2A-2B-019		2.2	4.36901	0.03399	0.3047	0.00173	0.9	1706	6	1715	9	1697	7	1697	7	1.1
PH-7-16-13-2A-2B-020		1.93	4.33294	0.03527	0.3008	0.00174	0.9	1700	7	1695	9	1706	7	1706	7	-0.7
PH-7-16-13-2A-2B-021		3.55	4.47858	0.04107	0.31229	0.00191	0.9	1727	8	1752	9	1698	9	1698	9	3.6
PH-7-16-13-2A-2B-022		1.55	11.86055	0.10176	0.48644	0.00324	0.9	2593	8	2555	14	2624	7	2624	7	-3.2
PH-7-16-13-2A-2B-023		2.58	4.19445	0.03327	0.29508	0.00169	0.9	1673	7	1667	8	1681	7	1681	7	-1
PH-7-16-13-2A-2B-024		2.82	4.36483	0.03739	0.30995	0.00183	0.9	1706	7	1740	9	1664	8	1664	8	5.2
PH-7-16-13-2A-2B-025		3.65	4.46833	0.04003	0.31129	0.00188	0.9	1725	7	1747	9	1699	8	1699	8	3.2
PH-7-16-13-2A-2B-026		2.38	4.53021	0.04141	0.32226	0.00196	0.9	1737	8	1801	10	1661	9	1661	9	9.6
PH-7-16-13-2A-2B-027		3.5	4.5589	0.04701	0.31308	0.00204	0.9	1742	9	1756	10	1726	10	1726	10	2
PH-7-16-13-2A-2B-028		4.02	4.4388	0.04081	0.30681	0.00188	0.9	1720	8	1725	9	1714	9	1714	9	0.7

Sample Name:								207/235		206/238		207/206		Best Age		
Grain #	[U] ppm	U/Th	207/235	1σ error	206/238	1σ error	RHO	Age Ma	1σ error	Age Ma	1σ error	Age Ma	1σ error	(Ma)	1σ error	% Discordance*
PH-7-16-13-2A-2B-029		4.59	3.41771	0.03665	0.26485	0.00169	0.9	1508	8	1515	9	1501	11	1501	11	1
PH-7-16-13-2A-2B-030		2.72	4.15413	0.04601	0.29652	0.00198	0.9	1665	9	1674	10	1654	11	1654	11	1.3
PH-7-16-13-2A-2B-031		1.22	4.41449	0.04295	0.30499	0.00192	0.9	1715	8	1716	9	1715	9	1715	9	
PH-7-16-13-2A-2B-032		27.75	4.3455	0.03526	0.3024	0.00175	0.9	1702	7	1703	9	1701	7	1701	7	0.1

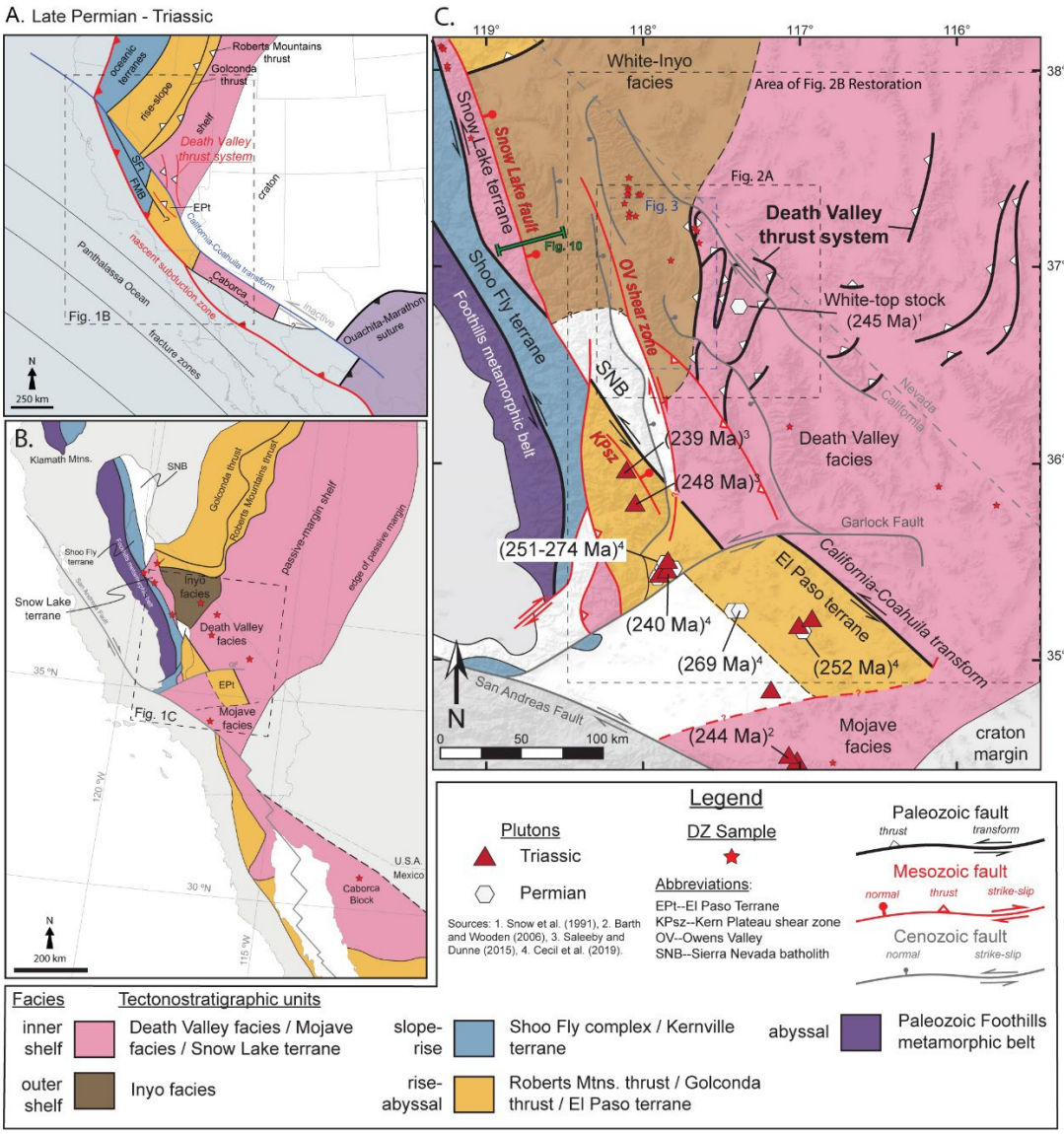

Figure 2.1. Simplified maps of key Paleozoic-Mesozoic domains and structures of the southwestern North American Cordillera. (A) Configuration of the southwest Laurentian margin during the late Permian-Triassic. Craton, shelf and rise-slope deposits represent Neoproterozoic-Devonian sediments of the Paleozoic passive margin sequence. Oceanic terranes include the Devonian-Mississippian island arc, Ordovician ophiolite, and mélange of the Foothills metamorphic belt (Saleeby, 2011; Powerman et al., 2020). Caborca is a block of passive margin shelf strata correlative with rocks in the Death Valley-Mojave Desert region. The Golconda thrust was emplaced at this time during the Sonoma Orogeny. Inset box shows location of Fig. 1B. DVts – Death Valley thrust system; Ept—El Paso terrane; FMB—Foothills metamorphic belt; SFt—Shoo Fly terrane. (B) Simplified regional map of late Paleozoic tectonostratigraphic units of southwest Laurentia (Attia et

al., 2018). The passive margin shelf includes siliciclastic and carbonate shallow water deposits. The Inyo facies is a subset of the shelf comprised of shelf-edge to slope carbonates and deep-water siliciclastic sediment. Rise-abyssal plain deposits of the Golconda and Roberts Mountains thrust sheets and the El Paso terrane (Ept) are characterized by deep marine siliciclastic rocks. The Sierra Nevada Batholith (SNB) is primarily a Jurassic-Cretaceous granitic batholith. The SNB underlies much of the Snow Lake terrane, Shoo-Fly complex and Foothills metamorphic belt. The Shoo-fly complex and Kernville terrane represent volcanic, sedimentary and magmatic rocks associated with a middle Devonian-Mississippian island arc. The Paleozoic oceanic assemblages of the Foothills metamorphic belt includes Ordovician ophiolite, Pennsylvanian-Permian serpentinite mélange, and Permian-Jurassic deep marine siliciclastic, volcaniclastic and igneous rocks. The Death Valley-correlative strata of the Caborca Block are displaced to the southeast by the California-Coahuila transform. Inset box shows location of Fig. 1C. (C) Tectonostratigraphic map of regions adjacent to the California-Coahuila transform (modified from Chapman et al., 2015 and Cecil et al., 2019). The cross section line of Figure 12 is shown in green. The inset boxes show the locations of Figure 2A, 2B, and 3.

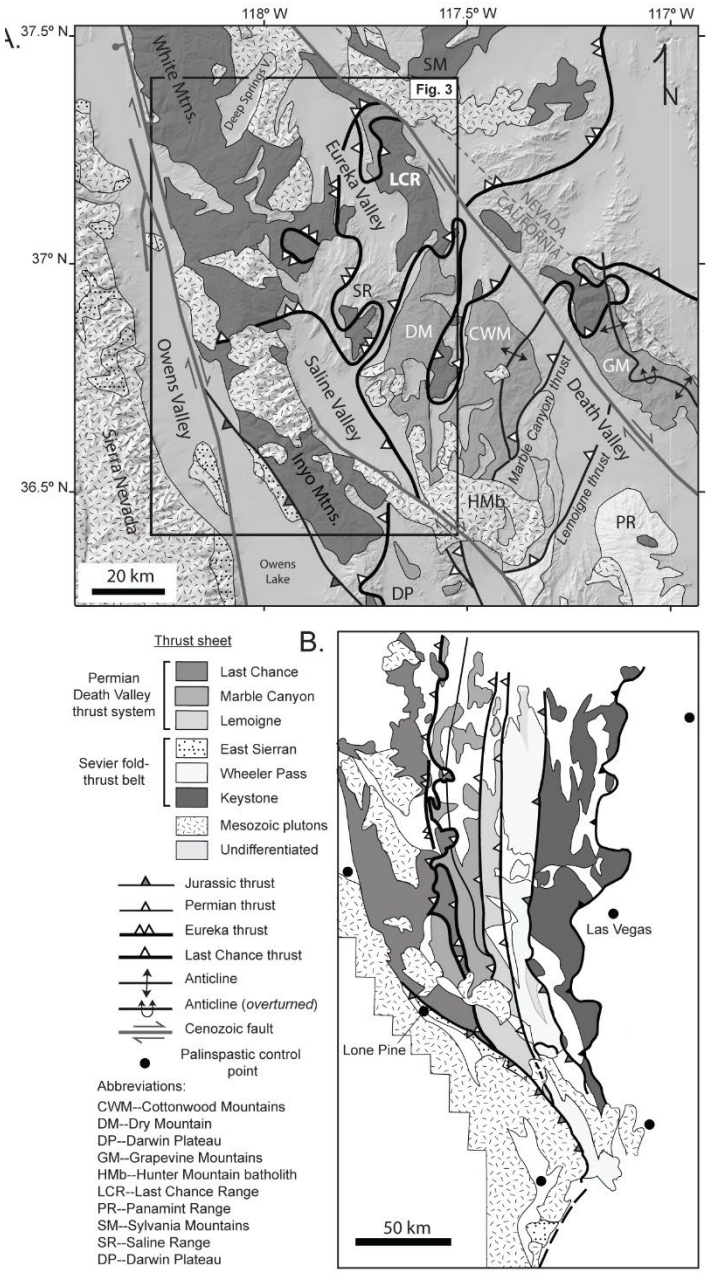

Figure 2.2. (A) Simplified tectonostratigraphic map of the White-Inyo-Mountains-Death Valley region, including the location of the Last Chance-Death Valley thrust system (Snow and Wernicke, 2000). Faults of the Last Chance thrust system are shown by thick black lines. Cenozoic strike-slip faults are shown as grey lines. The age of thrust faults is denoted by the hanging wall marker color. The hillshade basemap was made using the USGS 3D Elevation Program 1/3-arc second digital elevation model. Inset box shows location of Figure 3. CA—California. (B) Palinspastic reconstruction of Cenozoic extension in the Death Valley Region (Snow and Wernicke, 2000). The Cretaceous Keystone thrust is shown with black hanging wall markers.

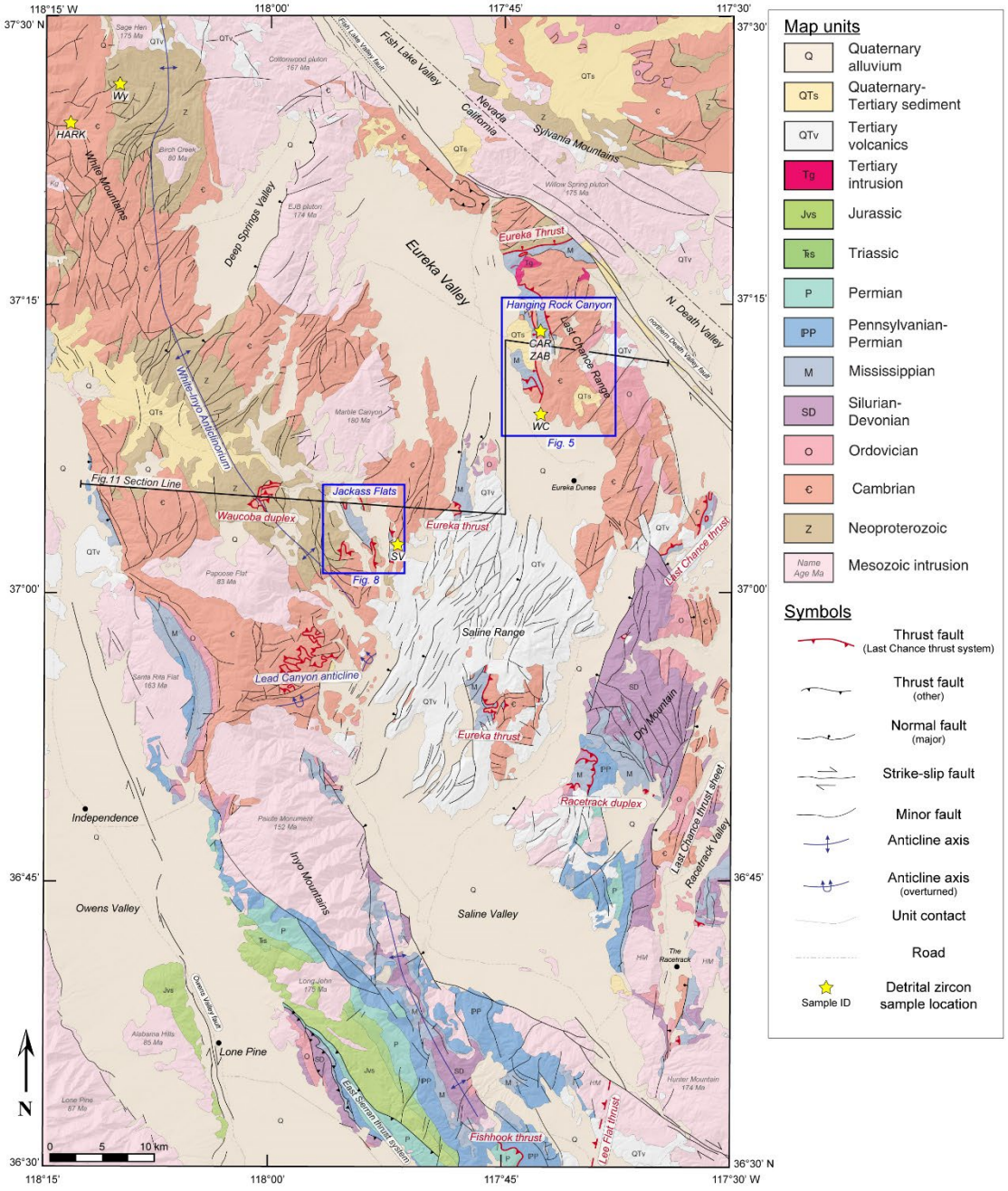

Figure 2.3. Generalized geological map of the White-Inyo Mountains and the northern Death Valley region (Ross, 1967). Inset boxes show location of Figure 5 and 8. The Fig. 13 cross section line is shown as a thick black line.The hillshade basemap was made using the USGS 3D Elevation Program 1/3-arc second digital elevation model.

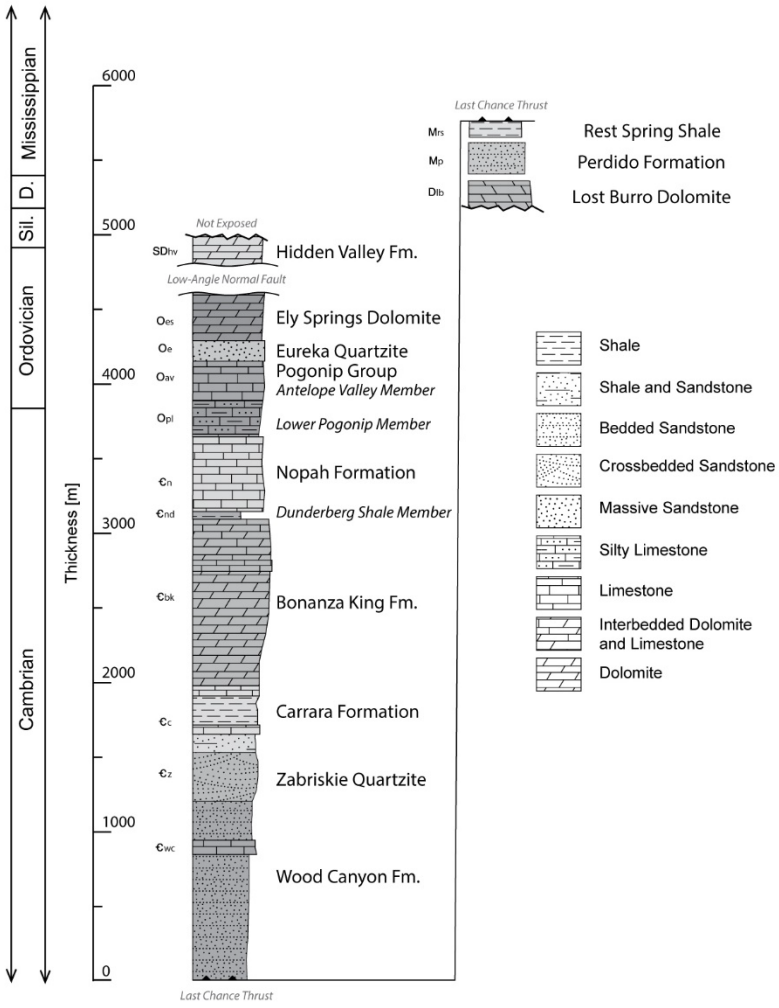

Figure 2.4. Stratigraphic column of the Last Chance Range based on Corbett (1989). In the Hanging Rock Canyon quadrangle, Ely Springs Dolomite is not observed in depositional contact with the Hidden Valley Formation. These units are conformable in the Dry Mountain area (Fig. 3). D—Devonian; Sil—Silurian.

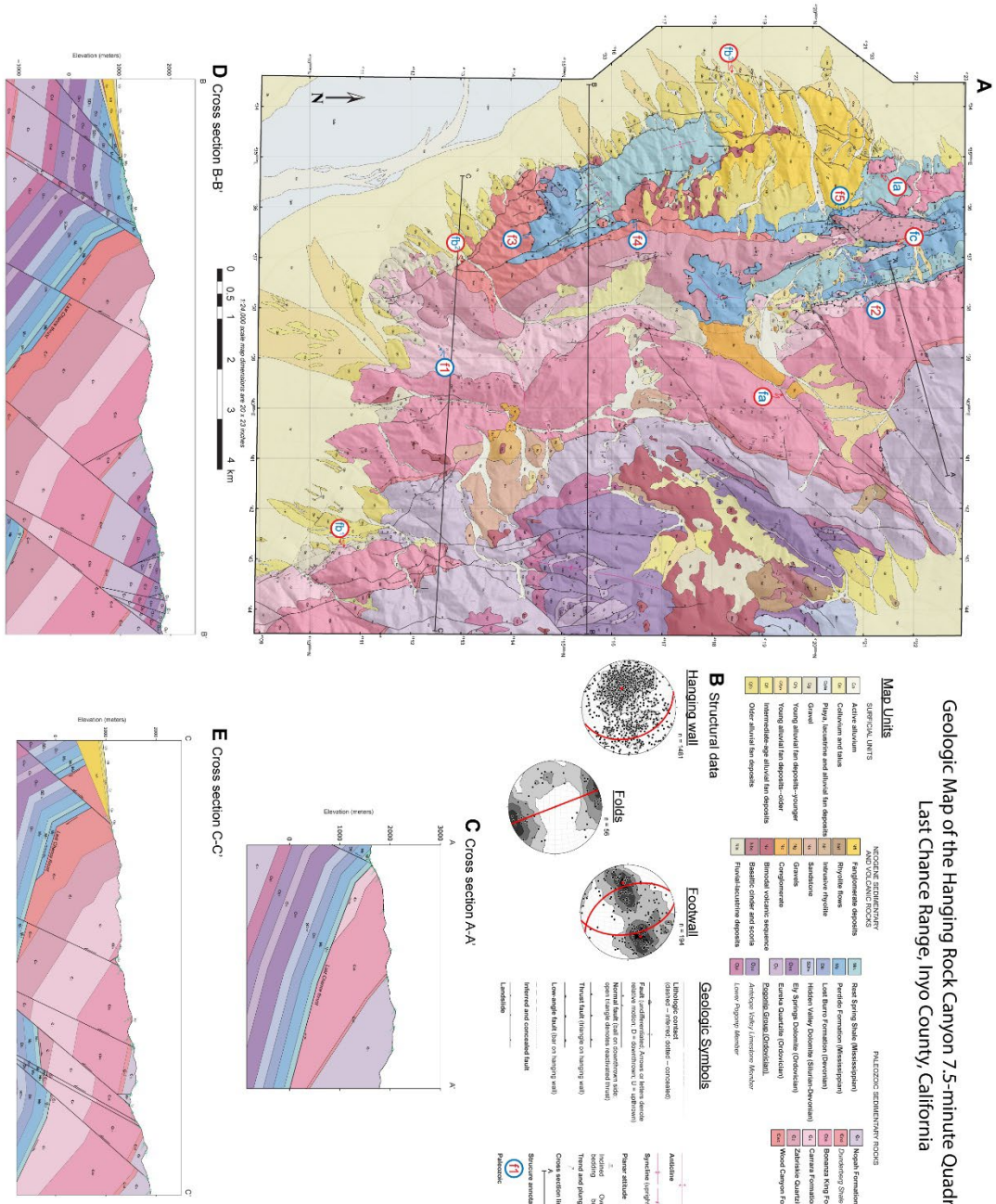

Figure 2.5. (A) Geologic map of the Hanging Rock Canyon 7.5'-quadrangle in the Last Chance Range (see Fig. 3 for location). 1:24,000 scale page dimensions are 20" long by 23" wide. Structural annotations shown as red and blue circles are referred to in text. (B) Lower hemisphere stereographic projections of bedding and fold attitudes from the map area. Red lines and dots indicate the average bedding orientation and fold axis. (C-E) Balanced cross sections across the Hanging Rock Canyon quadrangle. Double-headed half arrows indicate a normal-fault reactivated thrust.

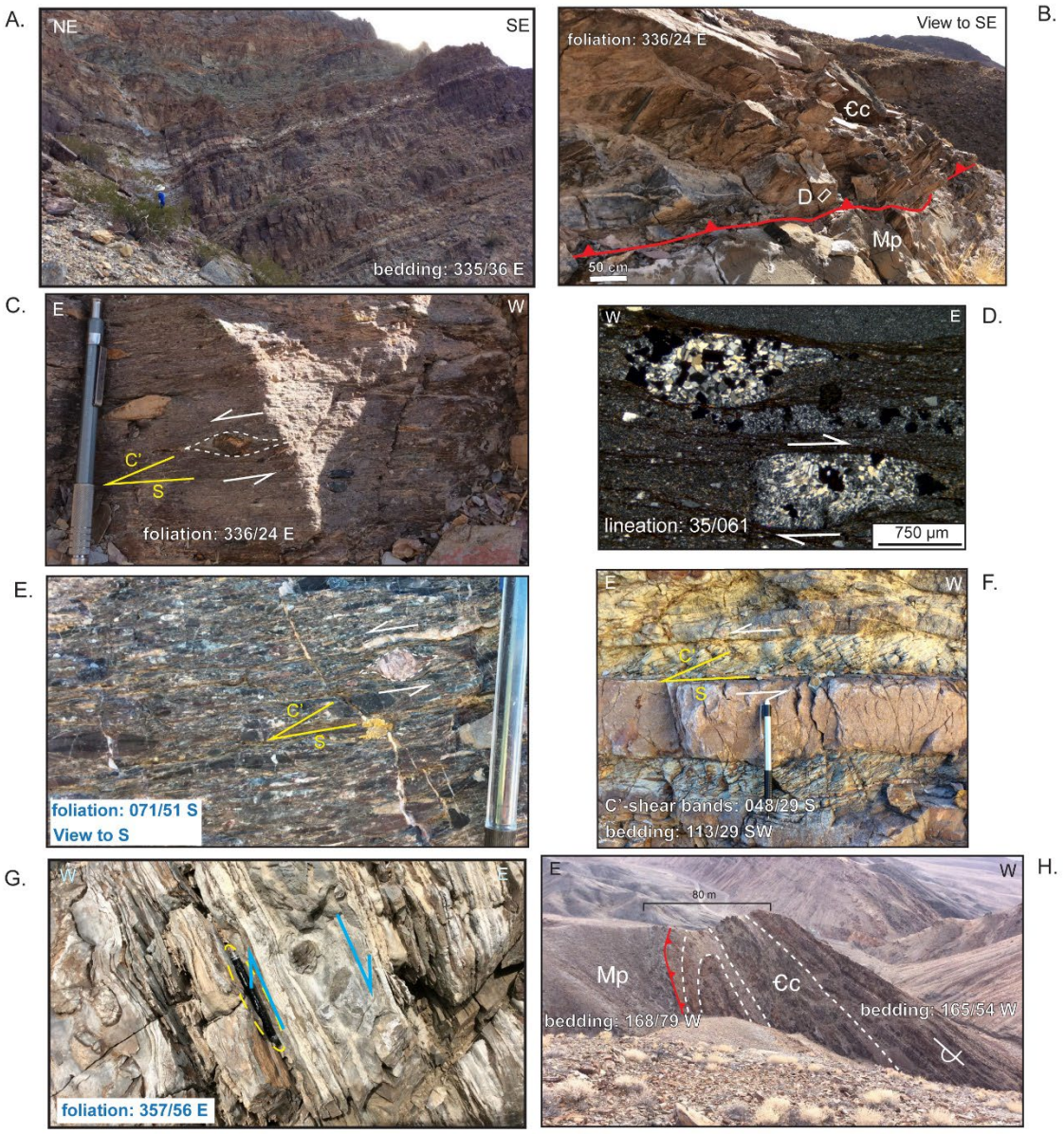

Figure 2.6. Field photographs displaying key structural relationships of the northern Last Chance Range. (A) East dipping Carrara Formation of the Last Chance thrust hanging wall in the southern Last Chance Range. (B) Exposure of the Last Chance thrust in the northern Last Chance Range (*f3* in Fig. 5). Inset boxes show location of Figure 6D. (C) Strongly foliated fault gouge below the Last Chance thrust. (D) Thin section cross-polarized photomicrograph of Last Chance thrust cataclasite. © Strongly deformed pebble conglomerate of the footwall Perdido Formation. (F) Preferential deformation of interbedded siltstone in the Last Chance thrust hanging wall. (G) Strongly deformed dolomite-bearing limestone of the Last Chance thrust hanging wall. Note pen for scale. (H) Deformation along a splay of the Hanging Rock Canyon out-of-sequence thrust. Overturned Carrara Formation is thrust eastward over the Perdido Formation.

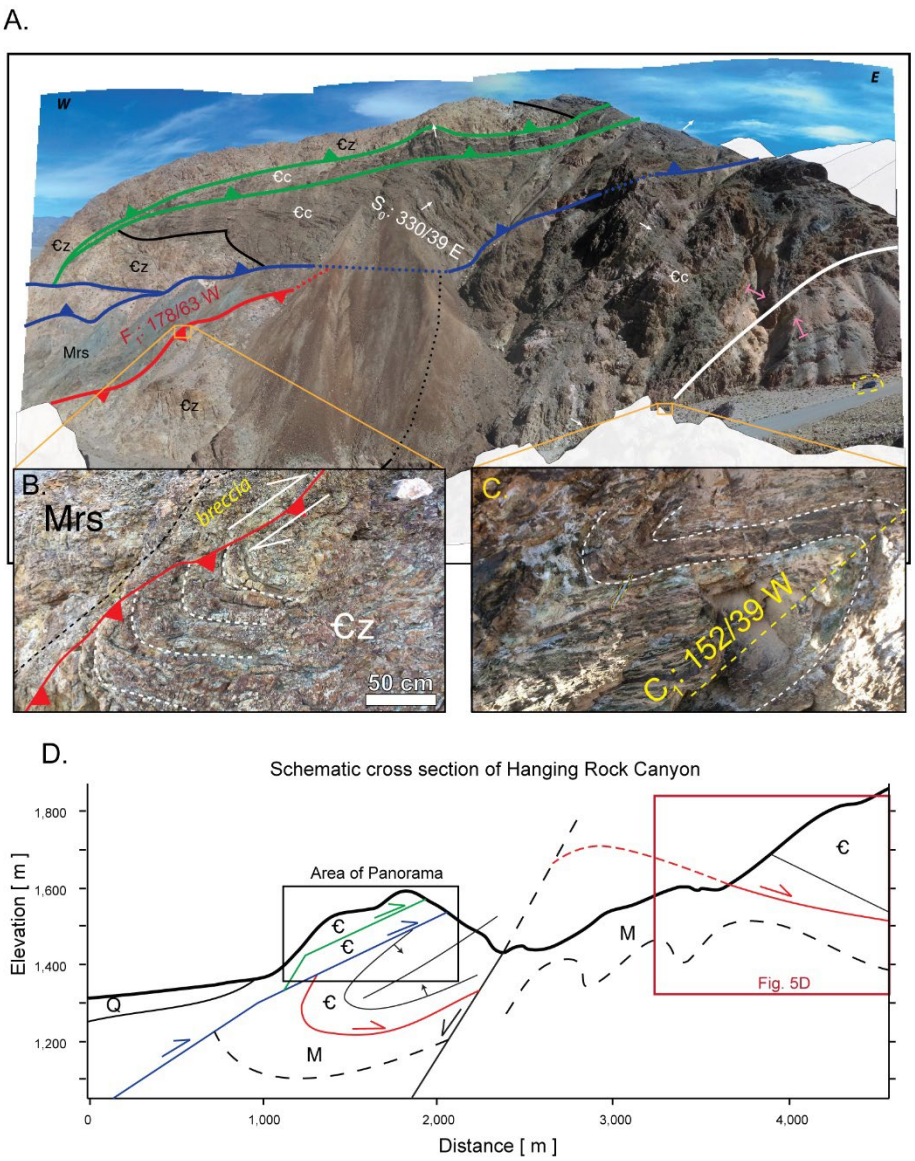

Figure 2.7. (A) Panorama photograph of the north wall of Hanging Rock Canyon. The lower half of the photograph shows the overturned Last Chance thrust (red fault) placing the Mississippian Rest Spring shale over the Zabriskie Quartzite. The hinge of the east vergent fold is shown on the right side of the photograph. The white-over-brown marker beds of the Carrara Formation are overturned, with the white arrow indicating the younging direction. The top half of the photograph shows duplexing of the Zabriskie Quartzite and Carrara Formation in the hanging wall of the Hanging Rock Canyon thrust. Note car on bottom right circled for scale. Pink arrows indicate younging direction of fold limbs. (B) Photograph of the overturned Last Chance thrust preserving original drag folds indicative of top-east shear sense. (C) Tight folds in the hinge zone of the overturned footwall syncline. (D) Schematic cross section across Hanging Rock Canyon. Blue and green lines denote faults splays of the Hanging Rock Canyon thrust. Black arrows indicate younging direction of fold limbs. Inset boxes show location of Fig. 5D and 7A.

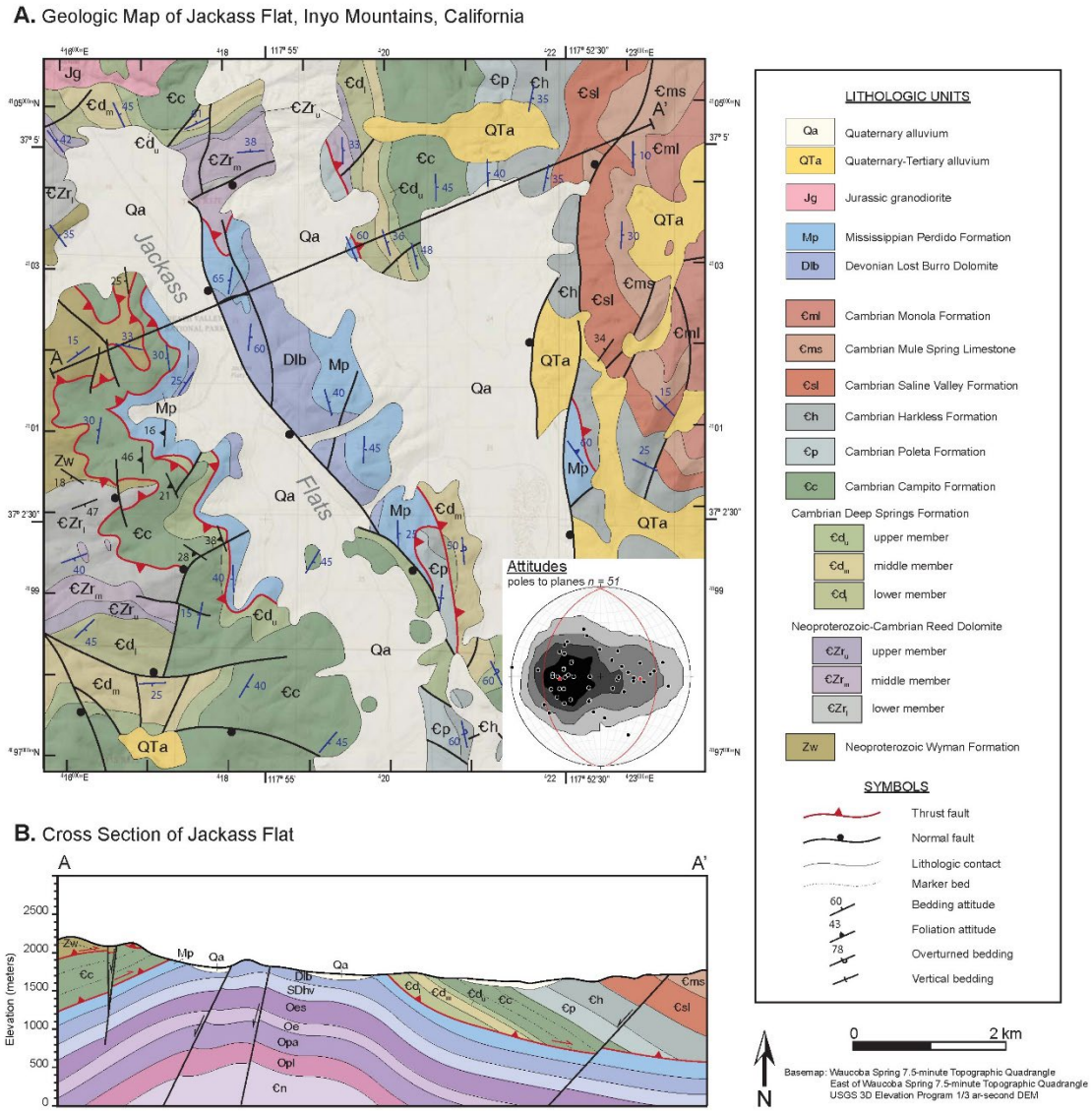

Figure 2.8. (A) Geologic map of Jackass Flats, Inyo Mountains, based on mapping of Stewart et al. (1966), Nelson (1971), Corbett (1989) and this study (see Fig. 3 for location). Structural attitudes from this study, Corbett (1989) and Nelson (1971). Inset lower hemisphere stereographic projection displays bedding attitudes in the map area. Bold black lines show average orientation of each fold limb. (B) Cross section across the Jackass Flats map area. Lower plate stratigraphy is the same as Figure 4 and 5. The thickness of Quaternary deposits and displacements on normal faults are inferred from field relationships.

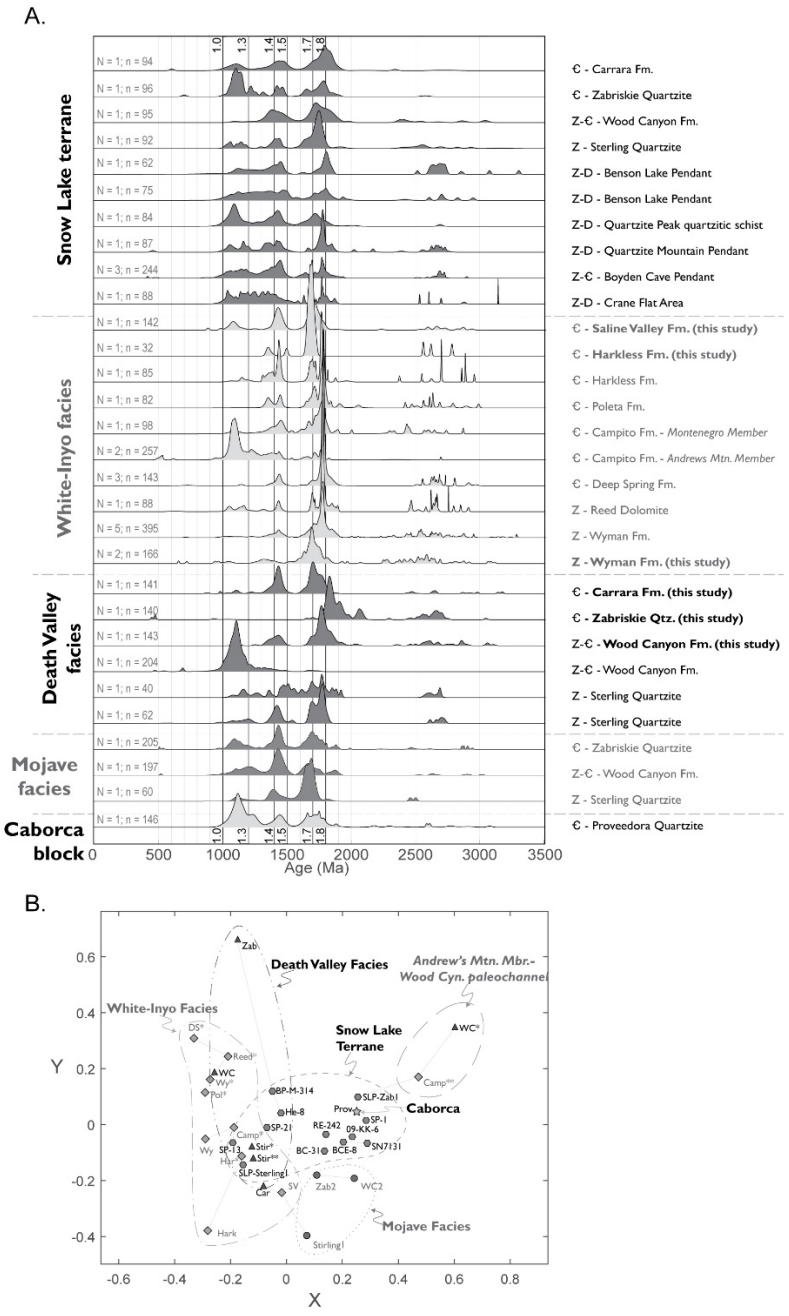

Figure 2.9. (A) Normalized probability plot of compiled detrital zircon U-Pb age data. Data are organized by tectonostratigraphic province (Fig. 1). Curve titles on the right indicate the age and name of the formation. N = number of samples. n = number of grains analyzed. See Table 1 for detailed sample information and references. (B) Two-dimensional multidimensional scaling map of detrital zircon U-Pb age data organized by tectonostratigraphic province. The distance between samples is a function of the Kolmogorov-Smirnov (i.e. increasing distance equals increasing dissimilarity) distances in two dimensions. Grey lines connecting points indicate nearest-neighbor pairs, or minimum K-S distances. Plot axes are dimensionless. See Table 1 for definitions of sample names.

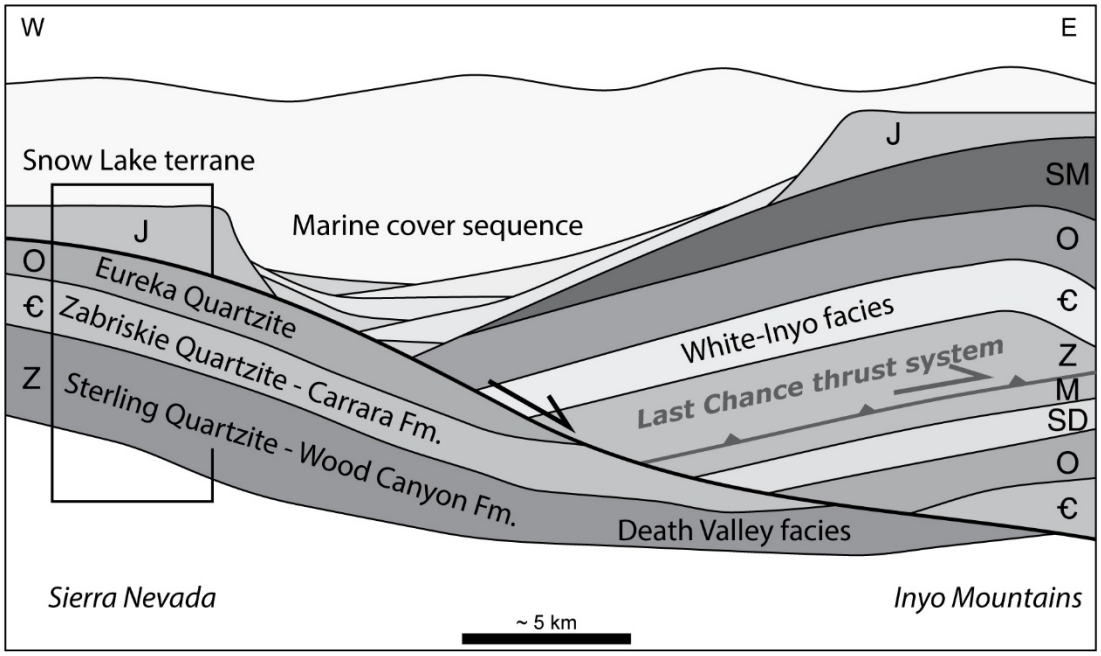

Figure 2.10. Schematic cross section showing the early Jurassic exhumation of the Snow Lake terrane (i.e., Neoproterozoic-Ordovician rocks of the Last Chance thrust footwall) in the footwall of a low-angle extensional complex. Exhumation in a submarine environment is evidenced by deposition of marine turbidites on the exhumed footwall rocks. The Last Chance thrust fault was not reactivated in the early Jurassic, thus preserving estimates of Permian fault slip. The inset black box indicates the stratigraphic sequence observed in the Snow Lake terrane. Abbreviations: Є-Cambrian; J–Jurassic; M–Mississippian; O–Ordovician; SD–Silurian-Devonian; SM–Silurian-Mississippian; Z–Neoproterozoic. Scale is approximate.

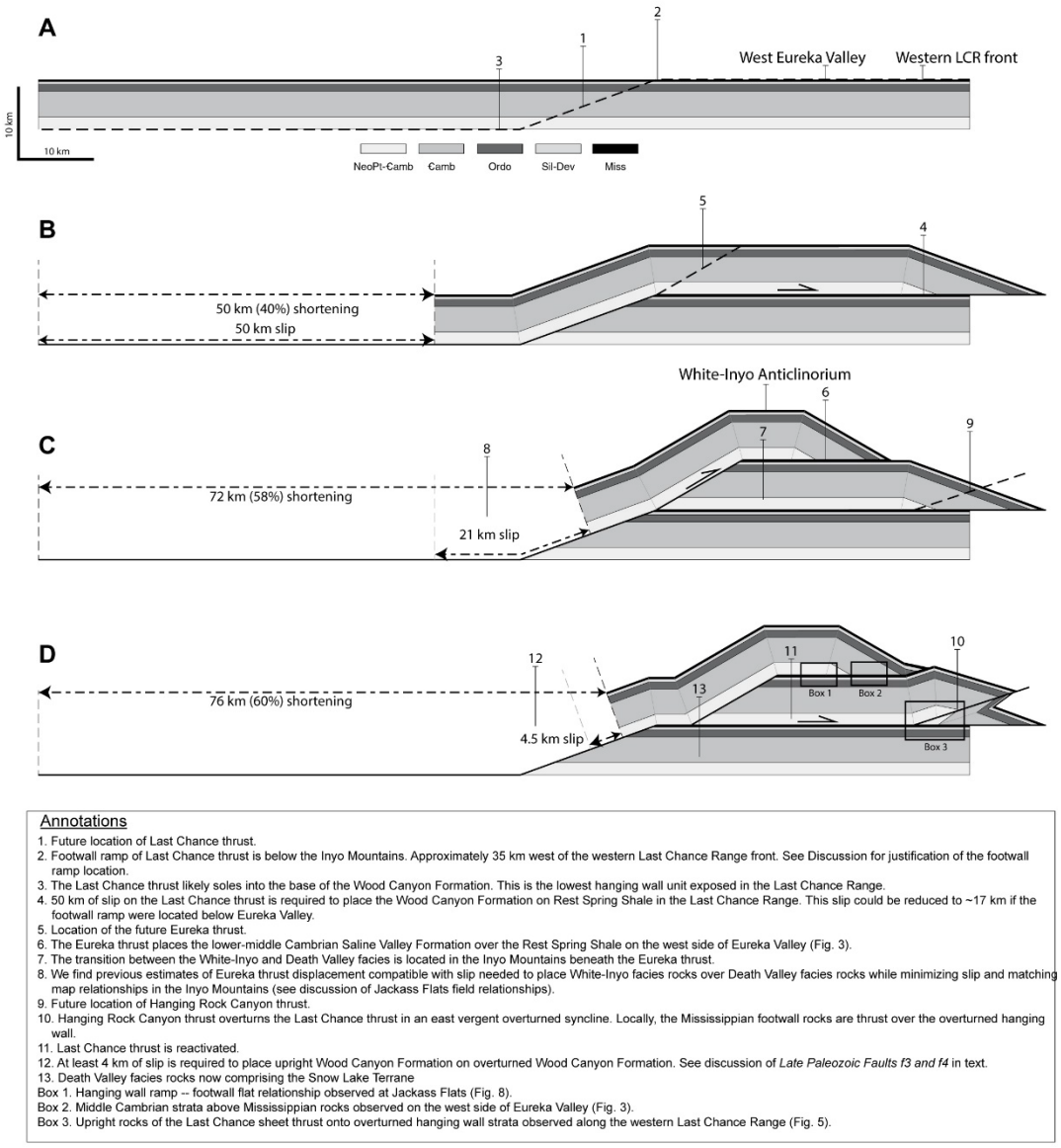

Annotations

1. Future location of Last Chance thrust.
2. Footwall ramp of Last Chance thrust is below the Inyo Mountains. Approximately 35 km west of the western Last Chance Range front. See Discussion for justification of the footwall ramp location.
3. The Last Chance thrust likely soles into the base of the Wood Canyon Formation. This is the lowest hanging wall unit exposed in the Last Chance Range.
4. 50 km of slip on the Last Chance thrust is required to place the Wood Canyon Formation on Rest Spring Shale in the Last Chance Range. This slip could be reduced to ~17 km if the footwall ramp were located below Eureka Valley.
5. Location of the future Eureka thrust.
6. The Eureka thrust places the lower-middle Cambrian Saline Valley Formation over the Rest Spring Shale on the west side of Eureka Valley (Fig. 3).
7. The transition between the White-Inyo and Death Valley facies is located in the Inyo Mountains beneath the Eureka thrust.
8. We find previous estimates of Eureka thrust displacement compatible with slip needed to place White-Inyo facies rocks over Death Valley facies rocks while minimizing slip and matching map relationships in the Inyo Mountains (see discussion of Jackass Flats field relationships).
9. Future location of Hanging Rock Canyon thrust.
10. Hanging Rock Canyon thrust overturns the Last Chance thrust in an east vergent overturned syncline. Locally, the Mississippian footwall rocks are thrust over the overturned hanging wall.
11. Last Chance thrust is reactivated.
12. At least 4 km of slip is required to place upright Wood Canyon Formation on overturned Wood Canyon Formation. See discussion of *Late Paleozoic Faults f3 and f4* in text.
13. Death Valley facies rocks now comprising the Snow Lake Terrane

Box 1. Hanging wall ramp -- footwall flat relationship observed at Jackass Flats (Fig. 8).
Box 2. Middle Cambrian strata above Mississippian rocks observed on the west side of Eureka Valley (Fig. 3).
Box 3. Upright rocks of the Last Chance sheet thrust onto overturned hanging wall strata observed along the western Last Chance Range (Fig. 5).

Figure 2.11. Palinspastic reconstruction of the Last Chance thrust system. The location of cross section line is shown in Fig. 3. Sections are scaled to 12.5% of the 1:24,000 scale cross sections in Fig. 5C-5E. (A) Undeformed stratigraphic section before the initiation of the Last Chance thrust. The original thickness of the stratigraphic section is 6.75 km. The locations of the western front of the Last Chance Range (LCR) and the western margin of Eureka Valley are marked. (B) ~50 km eastward slip along the Last Chance thrust. (C) Out-of-sequence initiation of the Eureka thrust atop the Last Chance thrust sheet to develop the White-Inyo anticlinorium. The spatial transition in strata from White-Inyo facies to Death Valley facies, located in the Last Chance thrust sheet, is concealed by the Eureka thrust sheet. (D) Initiation of the Hanging Rock Canyon thrust and overprinting of the Last Chance thrust. The inset boxes show locations of key structural relationships observed in the field.

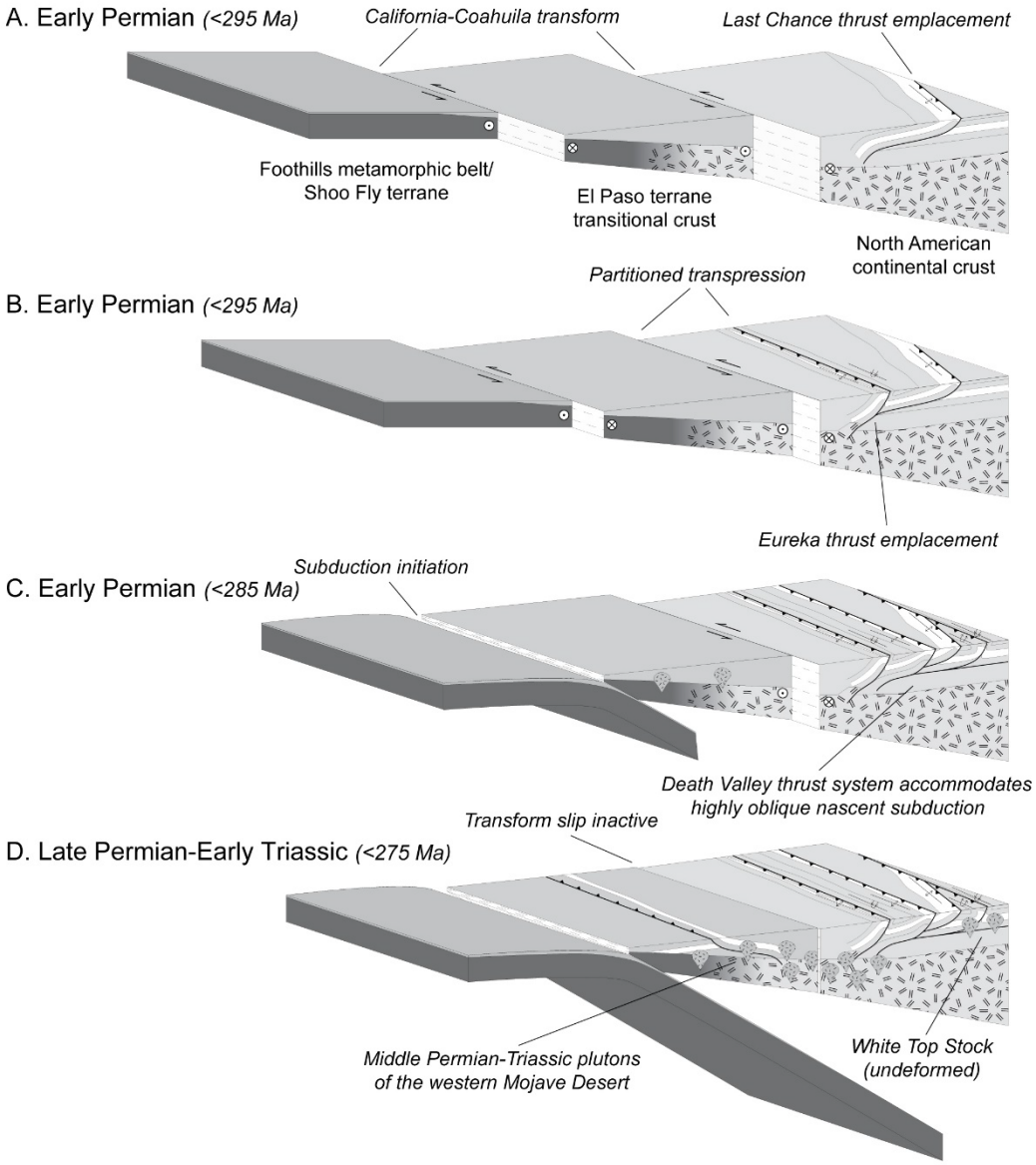

Figure 2.12. Block diagram showing the evolution of southwest Laurentia during the late Paleozoic. (A) Early-early Permian (<295 Ma) initiation of the Last Chance thrust system. California-Coahuila is already active by the beginning of the Permian. The Foothills metamorphic belt and Shoo Fly terrane are shown in dark grey, the El Paso terrane is shown in medium grey, and Laurentian continental crust is shown in light grey. (B) Late-early Permian (<295 Ma) out-of-sequence slip along the Eureka thrust occurred during continued slip along the California-Coahuila transform. Subduction initiates between the early and middle Permian (ca. 285 Ma). (C) Middle Permian (<285 Ma) development of the greater Death Valley thrust system. Transform faulting continues during the early stages of subduction. Early arc plutons intrude the El Paso terrane. (D) Cessation of contraction within the Death Valley thrust system and slip on the California-Coahuila transform. Local thrust faults develop in the El Paso terrane as arc magmatism expands laterally.

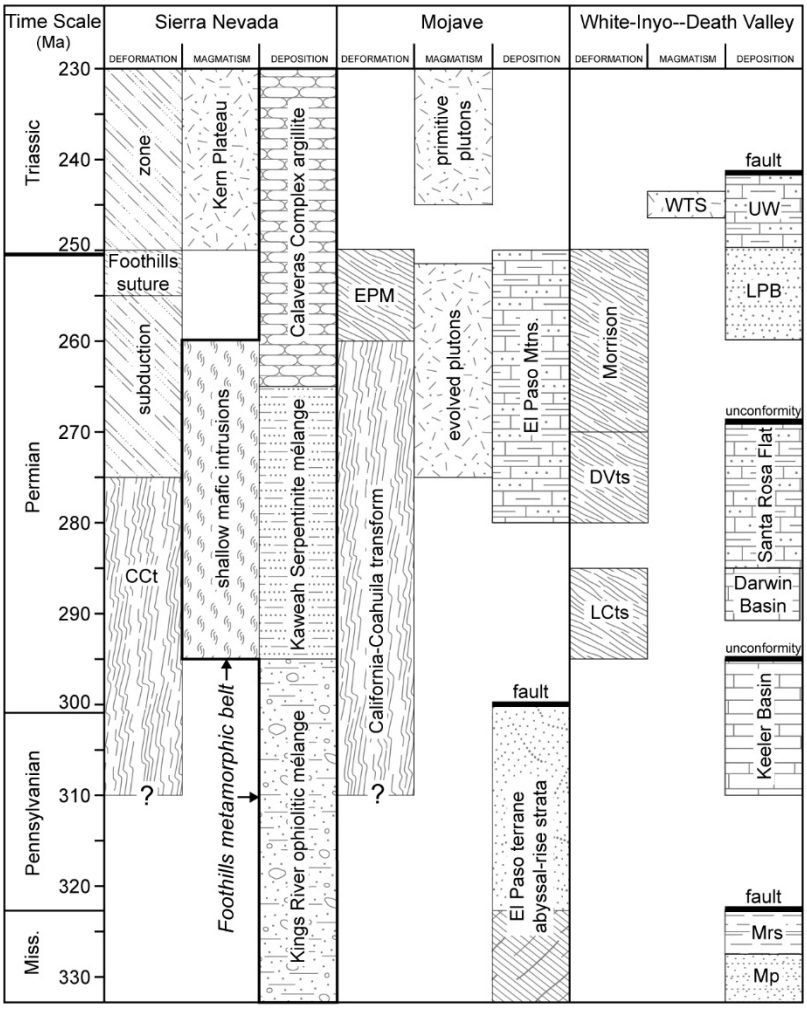

Figure 2.13. Time-space chart showing important deformation, magmatic and depositional events along southwest Laurentia between Mississippian and Triassic time. The Sierra Nevada, the Mojave Desert and the White-Inyo-Death Valley regions were separated by strands of the California-Coahuila transform (CCt) during the late Paleozoic. The western strand of the CCt develops into the Foothills suture during the late Permian. Abbreviations: DVts—Death Valley thrust system; EPM—El Paso Mountains; LCts—Last Chance thrust system; LPB—Lone Pine Basin; Miss—Mississippian; Mp—Mississippian Perdido Formation; Mrs—Mississippian Rest Spring Shale; UW—Union Wash Formation; WTS—White-Top Stock; See the text for references.

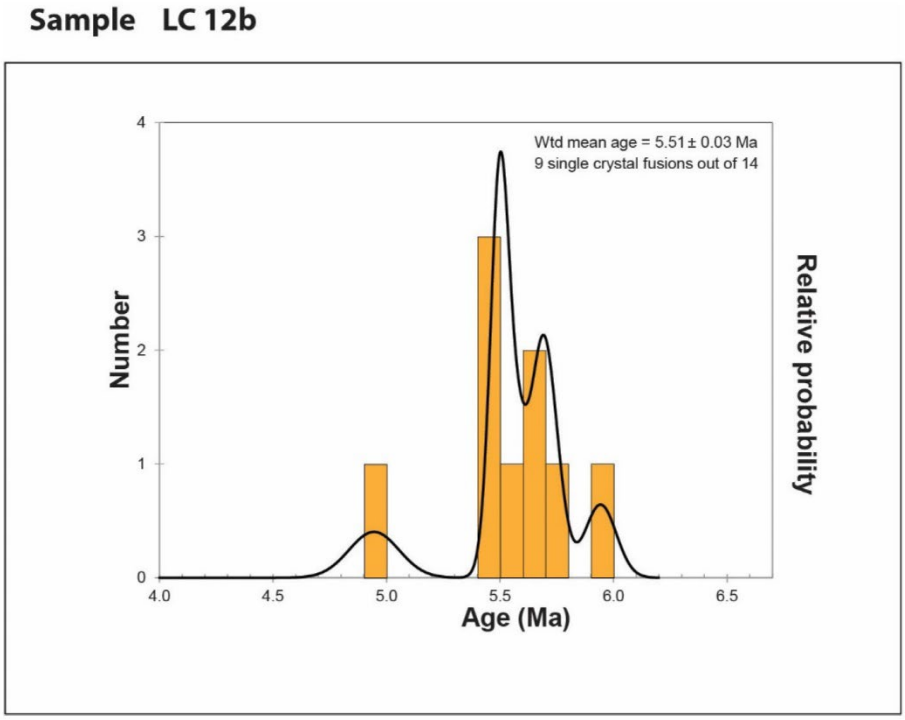

Figure 2.S1. Age probability distribution of sanidine $^{40}Ar/^{39}Ar$ ages.

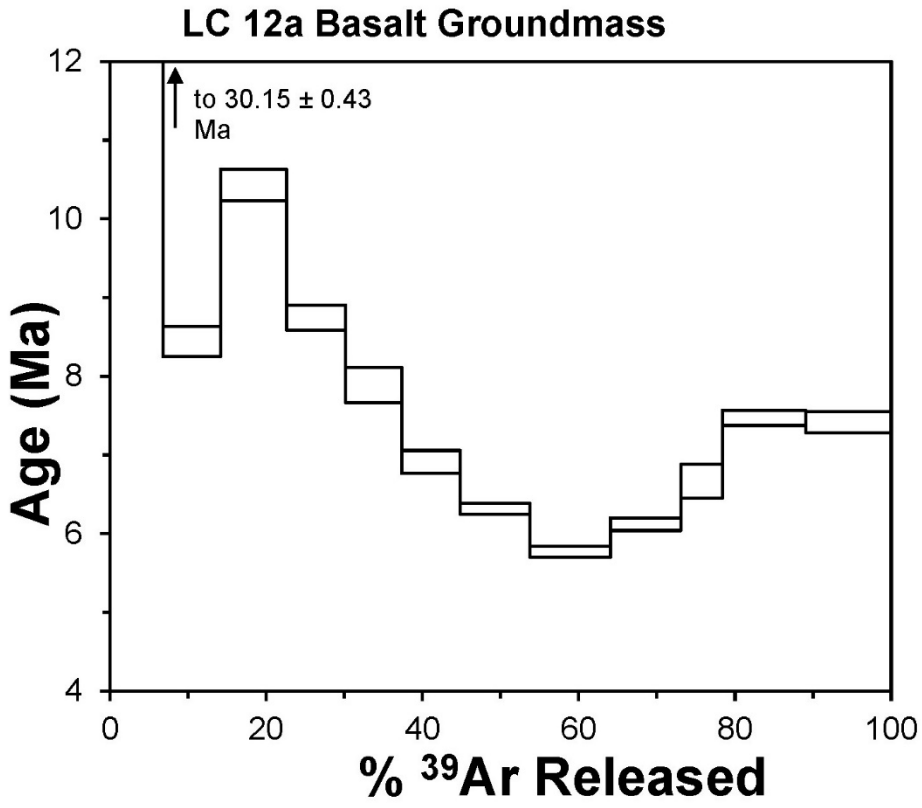

Figure 2.S2. $^{40}Ar/^{39}Ar$ Step-heating Age Spectrum for Basalt Groundmass.

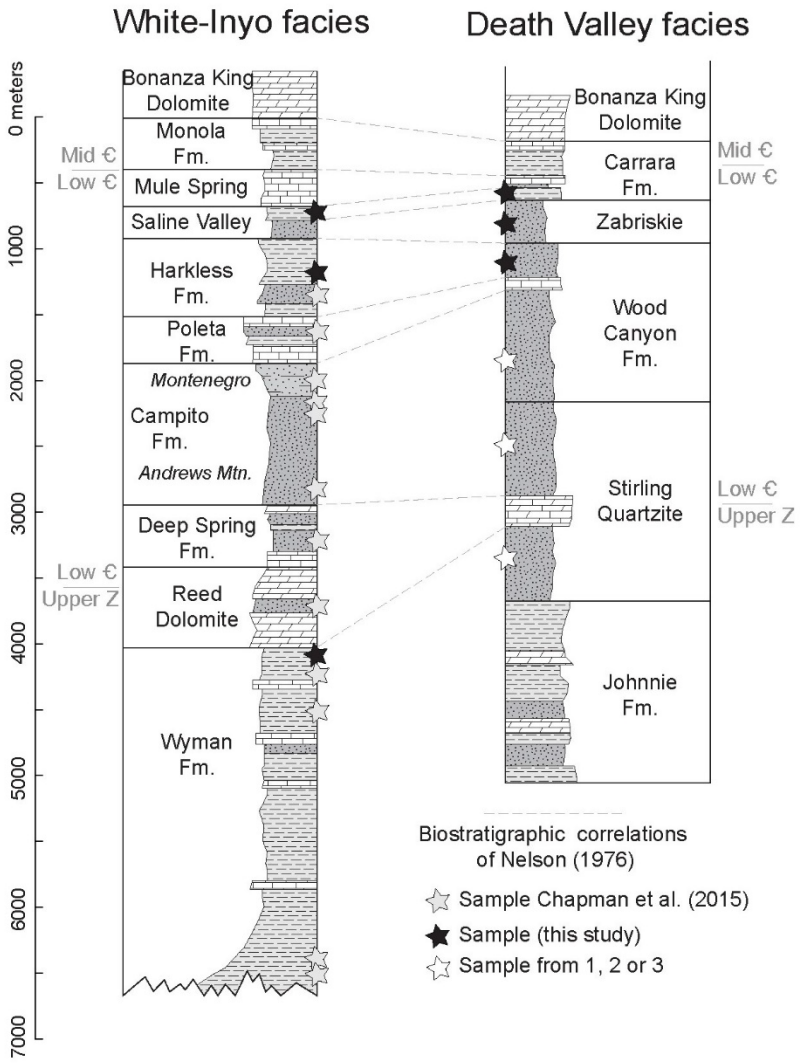

Figure 2.S3. Comparison of the Neoproterozoic-Cambrian strata of the White-Inyo facies and the Death Valley facies (modified from Nelson (1976 and Chapman et al. (2015)). Biostratigraphic correlation of facies by Nelson (1976) is shown with the gray dashed line. The stratigraphic location of detrital zircon samples compiled in this study are shown by colored stars. 1— Maclean et al., 2009; 2—Schoenborn et al., 2012; 3—Gehrels and Pecha, 2014. See text Table 1 for detailed sample information and references.

Chapter 3: Mesozoic-Cenozoic thermal and kinematic evolution of the Sevier hinterland and the eastern Basin and Range

Drew A. Levy[1]*, Matthew T. Heizler[2], Andrew V. Zuza[1], Christopher D. Henry[1], Joel W. DesOrmeau[3], Stacia M. Gordon[3]

[1]*Nevada Bureau of Mines and Geology, University of Nevada, Reno, NV, 89557, USA*

[2]*New Mexico Geochronology Research Laboratory, New Mexico Tech, Socorro, NM, 87801, USA*

[3]*Department of Geological Sciences and Engineering, University of Nevada, Reno, NV, 89557, USA*

ABSTRACT

Post-orogenic extension within the Basin and Range province was accommodated through ductile attenuation of the middle crust and brittle extension of the upper crust. The proximity of ductile and brittle domains suggests such domains experienced similar tectonic histories. Conventional models for the development of the Basin and Range province, such as redistribution of gravitational potential energy in overthickened crust, could not produce the spatiotemporal pattern of post-orogenic extension. Instead, we hypothesize the middle Cenozoic thermal structure of the crust was the primary control on the distribution of ductile and brittle extension. Here we test this hypothesis in the eastern Basin and Range, with study of the highly extended Elko extensional domain. Our study focuses on the brittle extensional system exposed in the Pequop, Toano and Pilot ranges. Systematic cross-section retrodeformation reveals the geometry and magnitude of Jurassic thrust belt that accommodated moderate (~12 km/~20%) shortening and minimal (<5 km) of thickening across the study area. Two generations of brittle normal faults accommodated ~30 km (~60%) of upper crustal extension.40Ar/39Ar thermochronology and zircon U-Pb geochronology reveal regional Late Jurassic, Late Cretaceous and Eocene magmatism and metamorphism across the study area. Paired muscovite-K feldspar multi-diffusion domain modeling records protracted cooling during the Late Cretaceous-Eocene followed by rapid cooling to <150 ℃ by the Late Miocene (ca. 9 Ma). Multi-diffusion domain modeling of muscovite in mylonitic quartzite exposed at the deepest structural level of the Pilot Range record rapid Oligocene cooling. The thermochronologic results suggest conductive cooling of the crust following peak Late Cretaceous metamorphism. Rapid cooling during the Middle Miocene resulted from extensional exhumation via the second generation of normal faults. Establishment of a background geothermal gradient of ~25℃/km by the Eocene promoted brittle extension across the study area. Oligocene mylonitic fabrics in the Pilot Range may represent the effects of regional crustal flow at that time, as observed in the adjacent metamorphic core complexes. Our findings suggest ductile extension within the Elko extensional domain resulted from Oligocene magmatism in the metamorphic core complexes and regionally elevated temperatures at deep structural levels in the Pilot Range. This was an important period of mid-crustal thinning; however, upper crustal extension

was limited. Brittle extension initiated across this domain during the Miocene, at which point the majority of crustal extension took place.

INTRODUCTION

The Basin and Range province is a region of distributed intracontinental extension superimposed on the Mesozoic North American Cordillera (e.g., Stewart, 1971; Wernicke, 1992; Dickinson, 2002). The locus of extensional deformation and evidence for lower crustal flow within the hinterland of the Cordilleran orogen has made the Basin and Range province a classic case study of orogenic collapse (e.g., Coney and Harms, 1984; Sonder et al., 1987; Bird, 1991; Malavielle, 1993; Sonder and Jones, 1999). The history of post-orogenic extension, defined as all crustal extension that occurred in the hinterland of the Cordillera, is protracted, with episodes documented during the Late Cretaceous (Hodges and Walker, 1992; Wells et al., 2008; Long et al., 2015; Druschke et al., 2009), Eocene-Oligocene (e.g., Gebelin et al., 2011; Long et al., 2018), and Miocene to present (e.g., Miller et al., 1999; Colgan and Henry, 2009). Throughout this time, kinematic boundary conditions, lithospheric rheology and internal body forces were evolving, which suggests the driver of extension shifted through time (e.g., Sonder and Jones, 1999). Post-orogenic extension has commonly been explained as a result of plate boundary shear or divergence (e.g., Atwater, 1970; Wernicke and Snow, 1998; Colgan and Henry, 2009), decoupling of the flat Farallon slab (e.g., Humphreys, 1995), asthenospheric upwelling (e.g., Gans et al., 1989), and/or the release of gravitational potential energy (e.g., Coney and Harms, 1984; Malavielle, 1993; Sonder and Jones, 1999). It is possible all these scenarios acted contemporaneously in varying proportions throughout the Cenozoic (e.g., Sonder and Jones, 1999). However, it is still unclear how the pre-existing crustal structure and the thermal evolution of the Cordilleran hinterland influenced widespread crustal extension. In particular, we seek to understand the spatiotemporal distribution of ductile versus brittle extension and the role of each in the development of the Basin and Range province.

To elucidate the spatial and temporal evolution of post-orogenic extension, we investigated the thermal evolution of the Elko extensional domain in the eastern Basin and Range (Fig. 3.1A). The eastern Basin and Range MCCs have been well-studied to understand Mesozoic metamorphism and the initiation of post-orogenic extension. However, multiple, complex deformation, metamorphic and magmatic events make distinguishing discrete extensional episodes uncertain. As such, thermochronological and

thermobarometric data, which have been interpreted to record extensional exhumation, often cannot be linked with observable structures. We seek to circumvent these challenges toward understanding post-orogenic extension through study of less deformed and metamorphosed rocks.

The Ruby-East Humboldt and Albion-Raft River-Grouse Creek MCCs located in northeast Nevada and northwest Utah expose extremely attenuated Archean basement and Neoproterozoic-Paleozoic stratigraphy metamorphosed to amphibolite facies conditions (Fig. 3.1A). The ranges located between these complexes expose a less attenuated section that is more conducive to structural reconstruction. This study focuses on these ranges, the Pequop, Toano and Pilot (PTP) ranges (Fig. 3.1B), which provide a well exposed record of Mesozoic crustal shortening, magmatism, metamorphism, and Cenozoic magmatism and crustal extension.

We reconstructed the extensional history of the PTP ranges via cross-section reconstructions and focused $^{40}Ar/^{39}Ar$ thermochronology and zircon U-Pb geochronology of igneous and metamorphic rocks in order to establish the spatiotemporal pattern of post-orogenic extension and the influence of thermal history on ductile versus brittle extension. Our cross-section reconstructions provide new constraints on the geometry, kinematics and magnitude of extension during individual episodes of deformation. We establish the timing of regional magmatism and metamorphism and cooling using zircon U-Pb geochronology of Jurassic and Eocene intrusions and $^{40}Ar/^{39}Ar$ thermochronology of hornblende, muscovite, biotite and K-feldspar. The novel application of multi-diffusion domain (MDD) modeling to muscovite and K-feldspar offer estimates of the timing and rate of cooling from ~450-150°C. We integrate these data sets to understand the thermal evolution of the PTP ranges and how that influenced the spatiotemporal pattern and magnitude of extension through time. These findings are compared to geological histories derived from the adjacent metamorphic core complexes to understand the influence of thermal history on the development of the Basin and Range province.

GEOLOGIC BACKGROUND

The northern Basin and Range geology consists of a ~15 km thick sedimentary sequence that was deposited on rifted Archean-Proterozoic basement during the Neoproterozoic-Paleozoic (e.g., Stewart, 1972; Poole, 1992; Dickinson, 2004; Whitmeyer and Karlstrom, 2007) and that has been variably metamorphosed, deformed, and altered by Mesozoic contraction, magmatism and metamorphism modified this region during Jurassic-Paleogene subduction (e.g., Armstrong, 1968; Burchfiel and Davis, 1975; DeCelles, 2004; Yonkee and Weil, 2015; Armstrong and Hansen, 1966; Miller and Gans, 1989; Miller and Hoisch, 1995). Cenozoic magmatism and extension thoroughly dismembered the pre-existing stratigraphic framework with deposition of thick volcanic deposits and extensional basins (e.g., Stewart, 1971; Gans et al., 1989; Dickinson, 2006). Our investigation centers on the Pequop, Toano and Pilot ranges (Fig. 3.1B), which preserve Jurassic thrust faults (e.g., Zuza et al., 2020), Jurassic, Late Cretaceous and Eocene intrusions (e.g., Wright and Wooden, 1991), Jurassic-Cretaceous-aged regional metamorphic fabrics (e.g., Miller and Hoisch, 1995), Eocene-Miocene volcanic rocks (e.g., Brooks et al., 1995), and Cenozoic normal faults (e.g., Henry et al., 2011).

Geology of the Pequop, Pilot and Toano Ranges

The eastern Basin and Range is underlain by a Neoproterozoic to Triassic stratigraphy that is remarkably consistent across the region. The base of the stratigraphic section is composed of the Neoproterozoic Trout Creek sequence, which consists of ~2 km of siliciclastic and diamictite-bearing strata overlying Neoarchean to Paleoproterozoic basement gneiss (e.g., Misch and Hazzard, 1962; Premo et al., 2008; Yonkee et al., 2014). Overlying the Trout Creek sequence is the Neoproterozoic McCoy Creek Group, a 2 km thick sequence of alternating quartzite and siltstone with lesser marble (e.g., Misch and Hazzard, 1962; Miller, 1984). The Cambrian stratigraphy is an ~ 4km-thick transgressive sequence that grades from massive quartzite through siltstone to a carbonate succession (e.g., McCollum and Miller, 1991). The Ordovician through Permian section (~5 km thick) is composed primarily of limestone and dolomite with lesser siliciclastic intervals (e.g., Thorman, 1970; Miller, 1984; Ketner, 1997). Triassic strata are preserved regionally in N-

S trending synclinoria (Fig. 3.1B), which contain an ~1 km-thick carbonate sequence overlain by siliciclastic sediment (e.g., Swenson, 1991). The Neoproterozoic-lower Cambrian stratigraphy is preserved in the Pilot Range, whereas a complete Cambrian-Triassic stratigraphic section is exposed in the Pequop Mountains (Fig. 3.1B). This ~14 km-thick crustal section is conducive to characterizing upper crustal deformation and metamorphism throughout the Jurassic-Neogene upper crust.

Neoproterozoic-Cambrian rocks across the study area are penetratively deformed and metamorphosed. In the Toano Range, the deepest structural level exposes amphibolite facies Neoproterozoic McCoy Creek Group quartzite and biotite-muscovite-garnet schist intruded by the Late Cretaceous Toano Spring two-mica granite (Fig. 3.2A-B). Along the margin of the granite, mineral assemblages formed during retrogression are synkinematic and concordant with the primary foliation in the range (Fig. 3.2D-E), which is cut by the Late Jurassic Silver Zone Pass granodiorite. Fresh mineral assemblages in paragneiss on the northern margin of the Toano Springs granite are not strongly foliated, suggesting a syn- to post-kinematic origin. The upper Cambrian section south of the Silver Zone Pass intrusion is composed of penetratively deformed upper Cambrian greenschist facies marble (Fig. 3.1B).

In the Pilot Range, similar metamorphic fabrics are preserved in the McCoy Creek Group rocks (Fig. 3.1B). The deepest section of the McCoy Creek Group is exposed in the central Pilot Range, where a mylonitic fabric is developed in quartzite and marble (Fig. 3.1B and 3.2J). These mylonites are separated from the non-mylonitic McCoy Creek Group (Fig. 3.2I) by a low-angle normal fault. Deformation of the non-mylonitic Neoproterozoic-Cambrian section is best expressed in the lower Cambrian Killian Springs Formation. Asymmetric east vergent folds and stretching lineations are interpreted as the result of E-SE Jurassic contraction (e.g., Miller and Hoisch, 1995). Top west S-C fabrics in Eocene granodiorite bodies indicate this section was overprinted by later deformation (Fig. 3.2C). Above the Pilot Peak detachment, unmetamorphosed Cambrian-Permian carbonates are moderately east tilted by west dipping normal faults that sole into the detachment.

The Pequop Mountains expose a continuous lower Cambrian-Permian stratigraphic section (Fig. 3.1B; Thorman, 1970; Camilleri and Chamberlain, 1997; Camilleri, 2010). The metamorphic grade decreases from amphibolite facies at the lowest part of the section to unmetamorphosed at the top, defining a peak geothermal gradient of ~45 °C/km (Zuza et al., 2020). This section is duplicated by the Independence thrust, which accommodated 7 km of shortening during the Jurassic (Fig. 3.1B; Zuza et al., 2020). A normal fault in the northern Pequop Mountains, the Pequop fault, truncates the Independence thrust and juxtaposes east tilted Pennsylvanian-Permian strata on top of sub-horizontal Ordovician rocks (Fig. 3.1B; Zuza et al., 2021). Restoration of slip on this fault, using the thrust as a piercing point, suggests 8 km of WNW directed slip, and an original position over the northern Toano Range (Zuza et al., 2021). Rare Late Cretaceous leucogranite dikes present throughout the lower Cambrian section (Bedell et al., 2010; Zuza et al., 2021) may be derived from the Toano Springs granite. This would imply the Pilot Peak detachment projects below the Pequop Mountains.

Cenozoic deposits are variably exposed across the study area (Fig. 3.1B), but they provide an important record of Paleogene volcanism and Neogene extensional basin development (e.g., Miller, 1984; Brooks et al., 1995; Mueller et al, 1999; Henry, 2008; Camilleri et al., 2017). During the Eocene, a regional pulse of magmatism swept across northeast Nevada depositing calc-alkaline volcanic rocks on Paleozoic bedrock. Regionally extensive sedimentation did not initiate until the Middle Miocene, at which point the Humboldt/Salt Lake formation was deposited in extensional basins (e.g., Lund-Snee et al., 2016; Zuza et al., 2021). The lack of regionally extensive, thick (>1 km) sedimentary basins before the Middle Miocene is interpreted to indicate the absence of regional crustal extension during the Late Cretaceous to Oligocene (e.g., Colgan and Henry, 2009).

Field Relationships

A system of east-directed thrust faults is exposed across the study area (Fig. 3.1B and 3.3A). In the Pequop Mountains, the Independence thrust is a sub-horizontal thrust fault that cuts up section to the east duplicating lower Cambrian through Ordovician strata (Fig. 3.1B and 3.3A). Along strike to the northeast, a system of east tilted imbricate thrust faults

that place upper Cambrian on Ordovician are exposed in the northern Toano Range. In the northern Pilot Range, Neoproterozoic-Cambrian metasedimentary rocks are folded into a tight, SE-vergent syncline (Fig. 3.1B). In the northern Silver Island Mountains, a steeply NW-dipping thrust juxtaposes Silurian-Devonian and Pennsylvanian-Permian strata. These thrust faults comprise a SE-directed fold-thrust system where shortening was accommodated through imbricate thrusting and folding in the upper crust.

There are two systems of low-angle normal faults exposed in the study area (Fig. 3.1B and 3.3A). The first is exposed in the Pequop Mountains, represented by the Pequop Fault, and the second is represented by the Pilot Peak detachment exposed in the Toano and Pilot Ranges (Fig. 3.1B and 3.3A). The Pequop Fault is exposed along the crest of the range, where it is subparallel to gently east-dipping Ordovician strata. The hanging wall of the fault contains Ordovician-Mississippian strata thrust over Pennsylvanian-Permian rocks. A potential continuation of this fault is exposed at Loray Pass placing Pennsylvanian-Permian limestone on Ordovician strata.

The Pilot Peak detachment (PPD) is a sub-horizontal fault exposed in the northern and southern Pilot Range and the northern Toano Range (Fig. 3.2F-H). The fault relationships are similar in both ranges, with Neoproterozoic-lower Cambrian rocks subparallel with the fault in the footwall, and east tilted upper Cambrian-Devonian rocks in the hanging wall. The similar stratigraphic position of the footwall in both ranges suggests the fault was active at depth at a very shallow angle (< 10°). The hanging wall features west dipping normal faults that are cut by the detachment, and rotate hanging wall strata to the east, which is consistent with a top-west extension direction.

The Pequop and Pilot Peak faults are relatively older than a final, third set of normal faults that are not exposed in the study area. The footwall of the Ruby-East Humboldt detachment fault includes the Ruby Mountains-East Humboldt Range, the Wood Hills and Pequop Mountains. The breakaway of this fault is likely located along the west side of the Pequop Mountains (e.g., Mueller and Snoke, 1993; Camilleri and Chamberlain, 1997).

Along the east side of Goshute Valley, Miocene-Pliocene sedimentary and volcanic rocks are deposited on Neoproterozoic-Cambrian rocks of the Pilot Peak detachment

footwall and hanging wall (Fig. 3.1B and 3.3A). This relationship highlights that the Toano Range was exhumed along a normal fault after slip on the Pilot Peak detachment before deposition of the 12.9 Ma rhyolite lava (Tv, Fig. 3.1B). This inferred structure is herein named the Goshute Valley fault.

High-angle normal faults are exposed along the Pequop Mountains and Pilot Range. The west dipping normal fault system along the Pequop Mountains juxtaposes Miocene-Pliocene sediment and Paleozoic bedrock. Along the Pilot Range, basin-ward stepping normal faults place Ordovician-Permian strata and Tertiary sediment on Neoproterozoic-Cambrian strata (Fig. 3.1B and 3.3A). Extensive Pleistocene-Holocene sediment from ancient Lake Bonneville is unfaulted along the eastern Toano Range, the Pilot Range and Silver Island Mountains, which suggests high-angle normal faults throughout these ranges were not rapidly slipping during this interval (e.g., Clark et al., 2020).

The geology beneath Goshute Valley, Pilot Creek Valley and Pilot Valley is poorly constrained, and we infer the subsurface geology using various lines of reasoning. First, we can estimate the maximum thickness of Cenozoic rocks based on the thickness observed in well holes regionally. The Oligocene-Miocene Humboldt Formation beneath Lamoille Valley (west side of the Ruby Mountains) is up to 5 km thick (Satarsuga and Johnson, 2000; Colgan et al., 2010). Wells drilled in the northern Pilot Creek Valley (Fig. 3.1B; Wilkins Ranch No. 2) 15 km west of the northern Pilot Range and in Goshute Valley (Fig. 3.1B; Shafter Federal No. 1) 15 km west of the Toano Range reached Mississippian and Permian rocks, respectively, at 1.3 km. We expect Tertiary basin fill to thicken towards range front normal faults, and therefore assume basin deposits are ~2 km deep. Second, the dip of strata in the subsurface is interpolated based on the orientation of rocks exposed on either side of the valley. A concealed normal fault was inferred beneath Pilot Creek Valley to account for similar dips of Ordovician rocks on either side of the valley. The breakaway of the PPD is inferred to be high-angle between the Pilot Range and Silver Island Mountains (Fig. 3.1B and 3.3A).

RECONSTRUCTION

Using published geological maps supplemented with our own field observations from these ranges, we drafted geologic cross sections of the Pequop Mountains and the Toano Range to the Silver Island Mountains (Fig. 3.3A; Pequop Mountains, Camilleri, 2010; Zuza et al., 2021; Silver Island Mountains, Schaeffer, 1960; Pilot Peak, Miller and Lush, 1994; Toano Range, Glick, 1987). These cross sections were constructed to illustrate the geometric relationships of extensional features, and to estimate the magnitude of extension. The geology of the modern cross section is simplified to represent average dips of stratigraphy and faults. Where stratigraphy is cut by a fault, cutoff angles are the same across the fault to maintain retrodeformability. Where fault offset is not directly observed, we assume minimal offset to produce observed relationships.

The effects of isostasy are ignored in our reconstruction of the PPD. This minimizes the effect of erosion on bedrock stratigraphy, and in places creates basins that are too deep (e.g., at the tip of the PPD; Fig. 3.3A). Extension magnitude is still minimized in this case, and observed field relationships are maintained in the cross section.

High-angle extension

Starting with the present day cross section, we first restore slip on high-angle normal faults (Fig. 3.3A-B). Restoration of offset on high-angle normal faults indicates 14 km, or 34%, of extension across the Toano and Pilot ranges, and 3.5 km, or 12%, across the Pequop Mountains. The Goshute Valley fault accommodates 4.3 km of the total extension and rotates the Toano Range ~15 degrees east. Normal faults on the west and east side of the Pilot Range accommodate 3.8 and 3.3 km of extension, respectively. The east dipping normal fault on the east side of the Silver Island Mountains accommodates 2 km of extension, and ~10 degrees of westward tilting of the range.

Detachment faulting

The Pequop fault and the Pilot Peak detachment are the main low-angle normal faults observed in the study area (Fig. 3.3A-B). Hanging wall cutoff relationships suggest these faults initiated at a high angle. The footwall flat preserved in the Toano and Pilot ranges

suggest the fault was low angle at depth during slip. Total extension across these normal fault systems is 15 km, or 39 % in the Toano and Pilot ranges, and 8 km, or 30% extension in the Pequop Mountains (Fig. 3.3B-C).

Thrust faulting

Restoring extension presents the geometry of the Jurassic thrust belt across the field area (Fig. 3.3C). The northern Toano Range thrusts are along strike equivalents of the Independence thrust in the Pequop Mountains (Fig. 3.1B; e.g., Zuza et al., 2021). These thrusts accommodated a minimum of ~3 km of shortening in the Toano Range (Fig. 3.3C). The Lost Canyon fault in the Silver Island Mountains accommodates ~4 km of shortening (Fig. 3.3C). In the Pequop Mountains, the Independence thrust accommodated ~7 km of shortening (Fig. 3.3C). A total of 16 km of shortening was accommodated across the study area (Fig. 3.3C-D).

Summary

The above reconstruction highlights two extensional episodes and one contractional event. Initial contractional deformation progressed from northwest to southeast across the study area with the development of southeast vergent folds and imbricate thrust faults. Our estimate of 16 km (~20%) shortening is consistent with published estimates from this area (e.g., Miller and Hoisch, 1995; Zuza et al., 2021). We estimate thrust faults across the study area soled into the lower-upper Cambrian contact, as the lowest exposed hanging wall unit of these thrusts is upper Cambrian. The next episode of deformation is represented by development of the Pilot Peak detachment at the onset of large magnitude extension. The fault initiated at a high-angle in the vicinity of Pilot Valley and likely exploited the pre-existing thrust decollement at depth allowing low-angle slip. Slip along the Pilot Peak detachment and Pequop faults account for 15 km (39%) of extension. In the waning stages of this extensional episode, a new set of normal faults developed in the west, possibly due to an unfavorable orientation of the Pilot Peak detachment for continued slip. Finally, high-angle normal faults accommodate modern extension and account for a minor component of extension across the study area.

GEO-THERMOCHRONOLOGY

Sample Selection

Thirty-one samples were collected for $^{40}Ar/^{39}Ar$ thermochronology from the Toano and Pilot ranges (Fig. 3.4 and 3.6-3.7). Samples were collected from Late Jurassic, Late Cretaceous and Eocene intrusions and metamorphic country rocks. Forty-nine $^{40}Ar/^{39}Ar$ dates were obtained from hornblende, muscovite, biotite or potassium feldspar (Table 3.S1). Where possible, multiple mineral systems were analyzed from a single sample to track cooling through time.

Zircon U-Pb geochronology was also applied to determine the crystallization age of six intrusions in the Toano and Pilot Ranges. Zircon U-Pb analyses were conducted at either the University of Nevada, Reno LA-ICP-MS laboratory using a *RESOlution M50* 193 nm excimer laser with an *Agilent 7700* quadrupole-ICPMS or the UC Santa Barbara ICP-MS facility using a *Photon Machines Analyte* 193 nm laser-ablation system and a *Nu Plasma* multicollector-ICPMS. Detailed U-Pb methods can be found in the supplemental materials. The difference between the zircon U-Pb age and hornblende or muscovite $^{40}Ar/^{39}Ar$ age gives an estimate of how quickly the intrusion cooled, which can be related to the ambient crustal temperature of the host rock at the time of intrusion. Analysis of metamorphic rocks adjacent to and distant from intrusions provides a measure of magmatic heating and resetting of previously cooled mineral systems.

Zircon U-Pb Results

We obtained new zircon U-Pb ages for five intrusions in the Pilot Range, and one intrusion in the Toano Range (Fig. 3.5). In the Pilot Range, we collected U-Pb dates from the McGinty Monzogranite (sample 070719-9), the Bettridge Creek Granodiorite (sample 100719-11), and two granodioritic intrusions in the southern Pilot Range (samples 090719-5 and 160719-13; Fig. 3.5). The $^{206}Pb/^{238}U$ zircon dates from these samples range from 40 to 37 Ma, which we interpret to record protracted zircon crystallization. A similar range of zircon U-Pb ages is observed in the Emigrant Pass plutonic complex in the southern Grouse Creek Mountains (Egger et al., 2003; Konstantinou et al., 2013). Two of the dated samples record Late Jurassic crystallization ages (Fig. 3.5). In the southern Pilot Range, zircons

from a gabbro intrusion (sample 090719-4) in the vicinity of the Miners Spring Granite yield a $^{206}Pb/^{238}U$ weighted mean age of 157 ± 3Ma (MSWD = 1.5; n = 32). Zircon dates from the Silver Zone Pass pluton (sample 180718-7) in the Toano Range vary from 168 to 152 Ma (Fig. 3.5). These crystallization ages indicate Late Jurassic magmas crystallized at ca. 160 Ma, and Eocene magmas intruded the study area at ca. 39 Ma.

$^{40}Ar/^{39}Ar$ Methods

All samples were crushed, sieved and rinsed with H_2O. Mineral separates were concentrated using a Frantz magnetic separator, and/or heavy liquids separation, followed by hand picking and a final ultrasonic bath in H_2O. $^{40}Ar/^{39}Ar$ analyses were conducted at the New Mexico Geochronology Research Laboratory following standard procedures outlined in Long et al. (2018) and Zuza et al. (2021). Detailed analytical methods can be found in the Appendix 3.1.

$^{40}Ar/^{39}Ar$ multi-diffusion domain (MDD) modeling was applied to select muscovite and K-feldspar samples to define the temperature-time path during cooling and exhumation. Extracting the thermal history of K-feldspar using the MDD method is well established (Lovera et al., 1989), and is an emerging technique in muscovite $^{40}Ar/^{39}Ar$ thermochronology (e.g., Long et al., 2018). To obtain MDD results, samples are step-heated in a temperature-controlled furnace and diffusion coefficients are determined based on fraction of ^{39}Ar released and the time of heating. Model kinetic parameters are determined from forward modeling of the fractional release of ^{39}Ar in conjunction with using an activation energy of 46 kcal/mol and 63 kcal/mol for K-feldspar and muscovite, respectively, to obtain the domain distribution. Biotite and hornblende age spectra are obtained by step-heating using a defocused diode laser. All samples were analyzed for argon isotopes using a *ThermoFisher Scientific Helix MC* multi-collector mass spectrometer.

$^{40}Ar/^{39}Ar$ Results

Hornblende

Hornblende was analyzed from 2 Eocene intrusions in the Pilot Range, and 1 Eocene intrusion from the northern Toano Range (Table 3.S1). Pilot Range samples 040719-2 and 160719-3 show complex age spectra with integrated ages older than the inferred intrusion ages . Both samples show a decrease in apparent age from ~75-50 Ma in the initial 60% of ^{39}Ar released with the data from the high-temperature steps oscillating between 45-40 Ma.

Sample 210719-2 from the Toano Range shows a continuous decrease in age from 44 to 41 Ma between the low- and high-temperature steps (Table 3.S1). These ages are older than the inferred intrusion age of ~38 Ma (correlated with McGinty Monzogranite in the Pilot Range; Fig. 3.5). It appears the hornblende data are impacted by both alteration and excess ^{40}Ar. Relatively poor isochron arrays (not shown) project to an initial trapped $^{40}Ar/^{36}Ar$ excess argon component. The generally complex hornblende data are consistent with the U/Pb zircon data and support intrusion of these granitoids in the Eocene around 38 Ma (Fig. 3.5 and 3.7).

Muscovite

Muscovite was analyzed from 7 intrusions and 8 metamorphic rocks in the Pequop, Pilot and Toano ranges (Fig. 3.6). The muscovite commonly show age gradients with most recording initial cooling during the Late Cretaceous, followed by protracted cooling through the Eocene. In contrast, six muscovite spectra from the central Pilot Range are much younger and record Oligocene-Miocene apparent ages (Fig. 3.6). Individual spectra are given in the supplementary materials where we assign a numerical date to each sample that is referred to as a “terminal” age (Table 3.S1). This date typically represents one or several steps that define the oldest apparent ages for the high temperature heating steps. These terminal ages record passage through a nominal closure temperature of ~400°C. Below we describe general characteristics of the muscovite spectra, but because they are not flat we avoid the using “plateau” terminology and assignment of a precise age of each sample.

Leucogranite dikes in the Pequop Mountains and the two-mica Toano Springs granite in the Toano Range show similar muscovite age spectra with 30-40 Ma apparent ages for the first 10% of ^{39}Ar released climbing to an overall flat spectrum at 80 Ma (Fig. 3.6; samples H18-23 and H17-23 and samples 020719-9 and 020719-13). Muscovite from a Jurassic lamprophyre dike in the Pequop Mountains shows an approximately flat spectrum at 75 Ma for 60% of the cumulative ^{39}Ar released, which then climbs to >100 Ma at the final heating steps (Fig. 3.6; sample H18-34). In the southern Pilot Range, a Jurassic(?) leucogranite dike shows a complex age spectrum climbing from 45 Ma to 80 Ma in the first 10% of ^{39}Ar released, followed by a decrease to 70 Ma at 60% before climbing to 75 Ma in the final heating steps (Fig. 3.6; sample 050719-23). In the central Pilot Range, a granodiorite dike shows a climbing age spectrum from 25 to 30 Ma (sample 180719-10).

Metamorphic rocks record variably shaped muscovite age spectra. Within the Cambrian Dunderberg Shale in the Pequop Mountains they record steeply climbing spectra from 20-25 Ma to 70-80 Ma (Fig. 3.6; samples H18-627 and H18-35). Lower in the stratigraphic section, muscovite in the Cambrian Morgan Pass Formation and the Cambrian-Neoproterozoic Prospect Mountain Quartzite record gently climbing spectrum from 75-85 Ma and 60-80 Ma, respectively (samples 61418(2) and H18-24). In the Toano Range, muscovite from the Cambrian Toano Formation shows a gently climbing spectra from 95 to 110 Ma (Fig. 3.6; sample 080719-18). Two samples from the top of the Neoproterozoic McCoy Creek Group record rapidly climbing spectra from ~20-45 Ma to 80 Ma (samples 010719-4 and 020719-5), whereas a third sample records a flat spectrum and an age of ca. 84 Ma (sample 080719-7). Prospect Mountain Quartzite from the southern Pilot Range record muscovite spectra that climb steeply from 40 to 75 Ma (Fig. 3.6; sample 090719-1) and 70 to 90 Ma (sample 160719-4). Muscovite from the Killian Springs Formation 5 km to the northeast show a steeply climbing spectrum from 40 to 95 Ma (sample 050719-16). The central Pilot Range exposes the lowest unit of the McCoy Creek Group (Fig. 3.1B). Muscovites from this unit record gently climbing spectra from 20 to 25 Ma (Fig. 3.6; samples 060719-7 and 200719-7) and 25 to 35 Ma (samples 060719-3 and 060719-5).

Biotite

Biotite was analyzed from 5 intrusions and 8 metamorphic rocks in the Pequop, Toano and Pilot ranges (Fig. 3.4 and 3.6). Biotite have overall flatter spectra in comparison to muscovite, but also do not form simple plateau type spectra. We report weighted mean ages for the dates within the spectra that yield a somewhat flat segment and suggest that this segment records cooling below ~300°C (Table 3.S1). In the southern Pilot Range, Jurassic and Eocene intrusions yield biotite $^{40}Ar/^{39}Ar$ cooling ages of 28-32 Ma (Fig. 3.4 and 3.6). An intrusion in the central Pilot Range records later closure at ~17 Ma (sample 180719-10). The McGinty Creek Monzogranite in the northern Pilot Range records biotite closure at 38 Ma (sample 070719-9), identical to biotite closure of the Eocene intrusion in the northern Toano Range (sample 210719-2). Biotite from metamorphic rocks record variable cooling ages in the Toano Range (Fig. 3.4). Samples on the southern and northern margin of the Late Cretaceous Toano Springs pluton record cooling at 44 Ma and 93 Ma, respectively (Fig. 3.6; samples 020719-5 and 080719-7). In the central Pilot Range, biotite from a pelitic schist records closure at 22 Ma (Fig. 3.4 and 3.6; sample 190719-3), while that from a mylonitic quartzite records closure at 10 Ma (sample 060719-3). Metamorphic rocks in the Pequop Mountains record Late Cretaceous biotite cooling ages (Fig. 3.4). Biotite from 3 samples show rapidly climbing age spectra from 20-30 Ma to 80-90 Ma (Fig. 3.6; samples H18-627, H18-35 and 61418(2)).

K-feldspar

K-feldspars reveal typical climbing age spectra for samples consisting of multiple diffusion domains experiencing complex and/or protracted cooling. K-feldspar from leucogranite in the Pequop Mountains shows a climbing age spectrum between 35 and 47 Ma (Fig. 3.6; sample H18-23). In the Toano Range, K-feldspar from the Toano Springs granite gives an age spectrum climbing between 20 and 40 Ma (Fig. 3.6; sample 020719-13). The Eocene Castle Park pluton K-feldspar in the northern Toano Range records a mostly flat age spectrum with steps giving ages near 39 Ma (Fig. 3.4 and 3.6; sample 210719-2). K-feldspar from igneous rocks in the Pilot Range show climbing spectra between 15 and 30-40 Ma (samples 050719-23 and 110719-3). Three samples return

disturbed age spectra which generally climb from 30 Ma to ages older than the emplacement age of those intrusions, which would imply some excess argon contamination.

MDD results

MDD modeling of muscovite and K-feldspar highlights cooling during the Late Cretaceous to Eocene and the Middle Miocene (Fig. 3.8). Coupled K-feldspar and muscovite models from leucogranite in the Pequop Mountains indicate Late Cretaceous cooling through about 400°C and reaching about 150°C in the Eocene (Fig. 3.8). Because the muscovite has an a youngest apparent age of ~60 Ma and the K-feldspar has an oldest age of ~45 Ma we cannot be certain of the thermal history between 60 and 45 Ma, however both minerals are compatible with a nearly isothermal segment of ~300°C during this time. Alternatively, the region could have cooled to well below 200°C by 60 Ma and then experience reheating (~300 °C) in the Eocene to explain the combined results. Composite MDD models from the Toano Range record protracted cooling from 400-200°C between 80 and 40 Ma, followed by cooling from 250-150°C between 30 and 17 Ma (Fig. 3.8). In the southern Pilot Range, muscovite MDD records cooling from 450-275°C between 80 and 40 Ma, whereas K-feldspar records cooling from 325-150°C between 30 and 12 Ma. Two muscovite MDD models from the central Pilot Range record cooling from 400-200°C between 40 and 18 Ma, with rapid cooling at 23 to 18 Ma (Fig. 3.8).

DISCUSSION

Structural Evolution of the Pilot-Toano ranges

The onset of Cordilleran deformation across the study area is represented by the east vergent thrust system, which accommodated ~ 20% (~12 km) shortening and accounted for <5 km of crustal thickening (Fig. 3.3C-D). Cross cutting relationships in the Pequop Mountains suggest this shortening took place during the Late Jurassic (Zuza et al., 2020). We do not observe evidence for Late Cretaceous or younger shortening.

We observe multiple generations of normal faults that accommodate ~60% (~30 km) extension across the study area (Fig. 3.3A-C). The Pilot Peak detachment was apparently

active at a low angle dip, which is consistent with footwall strata subparallel to the fault and the occurrence at similar stratigraphic levels in the footwall across the Toano and Pilot ranges (Fig. 3.3B). The fault likely reached the surface at a high-angle west of the Silver Island mountains creating a listric fault geometry. The continuation of the Pilot Peak detachment to the west is unclear, however map relationships in the Pequop Mountains and northern Toano range suggests the PPD cuts down-to-the-west below the thrust faults exposed in those ranges (Fig. 3.3A-B). This geometry places the Pequop Mountains in the hanging wall of the PPD. If the PPD continues at depth to the west, then it is plausible a regional decollement may have developed in the Miocene – possibly through reactivation of a Jurassic thrust decollement. In this framework, we think the down-to-the-west Pequop fault may have developed as a hanging wall splay of the PPD and similarly merged with this reactivated decollement at depth (Fig. 3.3B). Fault mechanics would support the development of hanging wall splays above a low-angle fault (i.e., the PPD) that is unfavorably oriented for continued slip.

The development of a kinematically linked detachment system across the study area does not necessarily coincide with rapid exhumation. The low-angle nature of the PPD and minimal stratigraphic omission across the fault implies minimal exhumation via that structure. To the west, the Pequop fault creates a greater stratigraphic omission, but it is unclear how much exhumation took place along that fault. It is clear that exhumation of Pequop, Toano and Pilot ranges took place during the second episode of extensional faulting.

Normal faults responsible for exhumation of the Pequop, Toano and Pilot ranges to the surface are poorly exposed across the study area, but map relationships reveal their geometry, kinematics and relative timing. In the Pequop Mountains, an active, west-dipping normal fault is well exposed along the western range front (Fig. 3.1B and 3.3A). The hanging wall of this fault contains Miocene sedimentary strata deposited on Permian bedrock underlain by the Pequop fault (Zuza et al., 2021). This relationship indicates ~ 3 km of down-west displacement after Pequop fault slip. Tephra dated at the base of the Miocene section suggests slip on this normal fault initiated by ca. 10 Ma, and possibly as early as ca. 15 Ma (Zuza et al., 2021). The Toano and Pilot ranges show similar

relationships with Eocene-Miocene sedimentary rocks in apparent fault contact with Paleozoic bedrock cut by the PPD (Fig. 3.1B and 3.3A). The magnitude of offset along these faults is not directly constrained, but the exposure of PPD footwall rocks requires ~6-8 km of exhumation. In the Toano Range, deposition of 12.9 Ma rhyolite lavas on PPD footwall rocks constrains this exhumation to pre-ca. 13 Ma (Fig. 3.1B). In the northern Pilot Range, ca. 10-8 Ma rhyolite and basalt lavas deposited across the trace of the range front normal fault bracket slip to pre-10 Ma (Fig. 3.1B).

Further constraints on the kinematics and timing of slip on the second generation of extensional faults are currently unavailable, and it is unclear if there is a kinematic link between these faults across the study area (i.e., merging with a regional decollement at depth). Activity on these faults during the interval 16-10 Ma is consistent with a regional pulse of extension across the northern Basin and Range (e.g., Miller et al., 1999; Wells, 2000; Colgan and Henry, 2009; Colgan et al., 2010; Konstantinou et al., 2012). Medium to low temperature thermochronology in the northern Basin and Range has been used to estimate the timing of extensional exhumation related cooling (e.g., Miller et al., 1999; Colgan et al., 2008, 2010).

Tectonothermal evolution of the Elko extensional domain

Late Cretaceous to Eocene metamorphism and cooling

The Middle to Late Jurassic was the primary episode of upper crustal shortening in eastern Nevada (e.g., Zuza et al., 2020, 2021). Thrusts faults exposed across the study area accommodated ~20 km of shortening and regionally <3 km of upper crustal thickening. Cross-cutting intrusions bracket the age of thrusting to before ~160 Ma magmatism. Lamprophyre dikes (ca. 160 Ma) intrude the Independence thrust in the Pequop Mountains indicating pre-Late Jurassic thrust faulting (Zuza et al., 2020). In the Toano Range, the Silver Zone Pass pluton cross cuts synkinematic greenschist facies metamorphic rocks. Late Jurassic magmatism enhanced regional metamorphism and amphibolite facies metamorphism was concentrated around Jurassic intrusions (e.g., Snoke and Miller, 1988; Miller and Hoisch, 1995). Syn-kinematic mineral assemblages are commonly retrogressed in the Toano and Pilot ranges, with garnet being replaced by chlorite. A fresh biotite-

muscovite-garnet-staurolite gneiss from the Toano Range is undeformed, suggesting further metamorphism after Jurassic tectonism. Similarly, a chlorite-muscovite-garnet schist from the Pilot Range exhibits a post-kinematic generation of garnet growth that overgrows a synkinematic assemblage. Muscovite from marble in the Toano Range and biotite from a lamprophyre dike in the Pequop Mountains record Early Cretaceous cooling ages, which we interpret as partial resetting of mica that formed in the Jurassic. These examples suggest the study area underwent Late Jurassic regional-contact metamorphism, at which point muscovite and biotite growth was widespread, followed by a subsequent thermal event that overprinted earlier assemblages.

The Late Cretaceous was a period of significant heating that resulted in widespread crustal melting and metamorphism (e.g., Snoke and Miller, 1988; Miller et al., 1988; Camilleri and Chamberlain, 1997; McGrew et al., 2000; Howard et al., 2011; Hallett and Spear, 2014, 2015). The cause of this thermal event is not clearly understood, but the result was an ~20 m.y. metamorphic event (ca. 90-70 Ma; Hallet and Spear, 2015) that resulted in the emplacement of pegmatitic leucogranite across the study area. In the Ruby-East Humboldt core complex, these intrusions occur as voluminous dikes throughout the Neoproterozoic-lower Paleozoic section (e.g., Howard et al., 2011). The Toano Springs two-mica granite (80-70 Ma $^{40}Ar/^{39}Ar$ muscovite) is the only known intrusion from this episode in the Toano and Pilot ranges. Muscovite and biotite from a post-kinematic pelitic gneiss 0.75 km from the pluton contact yields a muscovite age of 84 Ma and a 93 Ma biotite age. The cause of reverse discordance of muscovite and biotite ages is not known, but the data are consistent with regionally high Late Cretaceous temperatures. Muscovite from retrogressed pelitic schist <500 m from the contact record 70-80 Ma cooling ages. While the pattern of muscovite ages around the Toano Springs granite are consistent with variable resetting within a thermal aureole, the presence of Late Cretaceous muscovite ages and absence of leucogranite intrusions in the Pilot range suggests widespread heating and metamorphic overgrowth despite variability in the extent of crustal melting.

Muscovite and biotite from the Pequop Mountains, as well as muscovites from the Toano Range and southern Pilot Range, record cooling following the Late Cretaceous metamorphic event. Muscovite MDD model results from all three ranges indicate cooling

between 450 and 250 ℃ from ca. 80-45 Ma (Fig. 3.8). Results from the Pequop models suggest a cooling rate of 50 ℃/m.y., which is consistent with conductive cooling of the dike following emplacement into cooler country rock. Cooling rates from the Toano and Pilot Ranges are much slower at ~12 ℃/Ma Producing this cooling rate through extension would require 4.5 km of rock exhumation (225 ℃ cooling with a geothermal gradient of 45 ℃/km), however exhumation of this magnitude is precluded by the location of the regional Paleogene unconformity at shallow stratigraphic levels (e.g., Konstantinou et al., 2012). Therefore, we argue Late Cretaceous-Eocene cooling reflects generally adiabatic cooling of the crust to a background geothermal gradient of 20℃/km (e.g., Dumitru et al., 1991).

Eocene to Early Miocene ductile attenuation and brittle extension

The intrusion of monzogranitic plutons and eruption of calk-alkaline volcanics between 44 and 38 Ma is recorded across the study area (e.g., Miller et al., 1987; Wright and Wooden, 1991; Brooks et al., 1995; Henry, 2008). Plutons and dikes intruding the Pilot Range were emplaced at ambient crustal temperatures at or below the biotite closure temperature (~350 ℃), as recorded by 39-30 Ma biotite cooling ages (Fig. 3.6). In the northern Toano Range, hornblende, biotite and K-feldspar from a small Eocene pluton record synchronous cooling ages, suggesting emplacement at ca. 39 Ma below ~175 ℃ at ~ 7 km. These observations support the interpretation that Late Cretaceous-Eocene cooling was a result of regional conductive cooling and lowering of the geothermal gradient.

Paleovalleys in the Pequop Mountains and the Windemere Hills record the eastward transport of ash flow tuff erupted west of the study area (Henry, 2008; Henry and Thorman, 2015). Coeval volcanic rocks are poorly exposed and characterized in the Toano and Pilot ranges, but the trace of the paleovalleys suggest they continued past these ranges to the east. The continuity of strata within paleovalleys across the study area suggests minimal topography existed in the region at 40 Ma, which suggests major crustal extension did not take place before that time (Henry, 2008; Zuza et al., 2021).

In the Ruby-East Humboldt and Albion-Raft River-Grouse Creek metamorphic core complexes, Oligocene intrusions are associated with mylonitic fabrics (e.g., Wright and

Snoke, 1993; MacCready et al., 1997; Egger et al., 2003; Strickland et al., 2011a, 2011b; Konstantinou et al., 2013). Oligocene intrusions are not exposed in the Toano and Pilot ranges, but muscovite spectra from mylonitic quartzite in the central Pilot Range record rapid cooling from 30-20 Ma (Fig. 3.8). These mylonitic rocks are in the deepest section of the Pilot Range and are separated from non-mylonitic quartzites by an obscured low-angle fault contact (Fig. 3.1B and 3.2I-J; Miller et al., 1994). As this section is at least 2 km below the Pilot Peak detachment, it is apparent the two are unrelated. We interpret mylonitization in the Pilot Range records regional crustal flow in response to extreme ductile attenuation in the surrounding core complexes. The overlying low-angle fault accommodated differential motion between ductile deformation below and brittle deformation above; this fault is effectively the Oligocene brittle-ductile transition.

Middle Miocene to present brittle extension

Large magnitude extension initiated in the Middle Miocene, as recorded by rapid cooling in the Toano and Pilot Ranges (Fig. 3.8). The Pilot Peak detachment fault initiated as a high angle listric normal fault immediately west of Crater Island and the Silver Island Mountains (Fig. 3.1B). Initial syn-extensional sedimentation is represented by east tilted Miocene fanglomerate and lacustrine sediment in the northeast Pilot Range, which overlies Eocene tuffaceous sediment (Fig. 3.1B; Miller, 1984). This section is part of the regionally extensive Salt Lake and Humboldt formations, which were deposited in Middle Miocene syn-extensional basins (e.g., Mueller et al., 1999; Konstantinou et al., 2012; Lund-Snee et al., 2016; Camilleri et al., 2017; Zuza et al., 2021).

During progressive extension, west-dipping normal faults initiated in the hanging wall of the detachment and a new detachment, the Pequop fault (e.g., Zuza et al., 2021), initiated above the Toano Range (Fig. 3.3b). The Pequop fault is exposed in the Pequop Mountains, where Pennsylvanian-Permian strata are juxtaposed over Ordovician rocks. (e.g., Camilleri, 2010). The Ruby-East Humboldt detachment, the Mary's River Fault of Mueller and Snoke (1993) and Camilleri and Chamberlain (1997), initiated as a high angle normal fault above the Pequop Mountains and contributed to further unroofing. The Goshute Valley fault may be a footwall splay of the Ruby-Easy Humboldt detachment based on

initiation after the Pequop fault and rapid, large magnitude offset. Exhumation of the Toano Range to the surface along the Goshute Valley fault was completed by ca. 13 Ma. On the west side of the Toano Range, a 12.9 Ma rhyolite lava is deposited on Neoproterozoic rocks from the footwall of the Pilot Peak detachment (Miller, 1984; Glick, 1987).

Multi-diffusion domain model results for K-feldspar in the southern Pilot Range suggests cooling through 150 ℃ slightly later at ca. 8-10 Ma (Fig. 3.8). In our preferred model, this suggests the Pilot Peak detachment did not unroof the Pilot Range, which is reasonable considering the insignificant omission of stratigraphy along the detachment fault. Instead, we suggest the Pilot Range was exhumed contemporaneously with the Grouse Creek Mountains. The Grouse Creek fault is a west-dipping low-angle normal fault along the west side of the Grouse Creek Mountains 25 km northeast of the northern Pilot Range. We suggest the Pilot Valley fault is the southern continuation of the Grouse Creek fault; this correlation is similar to the correlation of the Northern Snake Range decollement and the Deep Creek fault (e.g., Miller et al., 1999). The Grouse Creek fault was active between 11.7 and 7.4 Ma (Compton, 1983; Wells et al., 2000), which coincides with rapid cooling in the Pilot Range (Fig. 3.8).

Modern high-angle normal faults are present across the study area, and are responsible for the modern topography of the Basin and Range (Fig. 3.3A). While high-angle extension is extensive across the modern Basin and Range, extensional slip rates are significantly lower than Middle Miocene rates [0.1-0.2 mm/yr for the modern Ruby-East Humboldt range front fault (Wesnousky and Willoughby, 2003) versus 2-4 mm/yr for the Ruby-East Humboldt detachment in the Middle Miocene (Colgan et al., 2010)]. Therefore, modern extension does not contribute significantly to post-orogenic extension of the Sevier hinterland.

Tectonothermal Evolution of the eastern Basin and Range

The structural and thermochronometric history of the Pequop, Toano and Pilot Ranges highlights the key episodes of the tectonothermal evolution of the eastern Basin and Range and offers new insight to regional patterns of extension. The Mesozoic contractional

evolution of the hinterland resulted in moderate upper crustal shortening and limited structural burial (e.g., Miller and Hoisch, 1995; Long et al., 2014; Di Fiori et al., 2020; Zuza et al., 2021). Jurassic amphibolite grade metamorphism was localized to zones of Late Jurassic magmatism (e.g., Miller et al., 1988; Snoke and Miller, 1988; Miller and Hoisch, 1995). Late Cretaceous metamorphism is more broadly identified through geochronology of metamorphic phases and $^{40}Ar/^{39}Ar$ cooling ages (e.g., Miller and Gans, 1989; Camilleri and Chamberlain, 1997; Wells et al., 2012; Hallett and Spear, 2015; this study. The latest Cretaceous to late Eocene was a tectonically quiescent period in the Sevier Hinterland, with regional cooling of the crust during flat slab subduction (e.g., Dumitru et al., 1991).

The arrival of the retreating flat slab in the eastern Basin and Range promoted widespread mantle-derived plutonism and volcanism (e.g., Best et al., 2009; Smith et al., 2014), as well as surface uplift in response to geodynamic effects of asthenospheric upwelling (e.g., Humphreys, 1995; Chamberlain et al., 2012; Smith et al., 2014, 2017; Cassel et al., 2018; Lund-Snee and Miller, 2021). Late Eocene extension is documented across most of the eastern Basin and Range (see Long et al., 2018, for a review), however the persistence of a low-relief volcanic plateau through the Oligocene suggests any extension was local in extent and of a lesser magnitude than the primary Middle Miocene event (e.g., Henry, 2008; Colgan and Henry, 2009; Cassel et al., 2014, 2018). Plutonism continued during the Eocene-Oligocene in the Ruby-East Humboldt and the Albion-Raft River-Grouse Creek metamorphic core complexes (e.g., Wright and Snoke, 1993; Egger et al., 2003; Konstantinou et al., 2013). Oligocene intrusions in these complexes represent chemically and isotopically evolved magmas generated through continued incorporation of crustal melts in late Eocene magma chambers. Such continued melting suggests localized mid-crustal “hot zones” persisted through the Oligocene, and likely contributed to the ductile attenuation of the country rock (e.g., Annen et al., 2006; Konstantinou et al., 2013). The known extent of Oligocene plutons is local to these major metamorphic core complexes, but ductile attenuation distant from these intrusions may reflect a broad thermal influence during melting (i.e., Pilot Range mylonites).

Large magnitude Oligocene upper crustal extension is best expressed in the brittle Grant Range detachment system. Extension in the Grant Range is expressed in a system of low-angle normal faults which accommodated ~24 km of top-west extension between 28-31 and 15-19 Ma (Long and Walker, 2015; Long et al., 2018). The Grant Range system is interpreted as forming in response to decreased interplate coupling during Eocene-Oligocene slab rollback and represents one of the few large magnitude extensional systems active during this interval (Long et al., 2018).

In contrast, Oligocene extension in the Ruby-East Humboldt core complex is expressed as ductile attenuation of footwall rocks bracketed by mylonitization of ca. 29 Ma monzogranite intrusions and cooling through $^{40}Ar/^{39}Ar$ biotite closure temperatures at ca. 23 Ma (Dallmeyer et al., 1986; Wright and Snoke, 1993; McGrew and Snee, 1994). Similarly, the Albion-Raft River-Grouse Creek core complex experienced footwall attenuation during Oligocene magmatism (e.g., Todd, 1980; Egger et al., 2003; Strickland et al., 2011a, 2011b; Konstantinou et al., 2012, 2013). In both core complexes, however, evidence of contemporaneous upper crustal extension of the same order of magnitude as footwall strain is lacking, which has been attributed to decoupling between upper and mid-crustal strain (e.g., Konstantinou et al., 2012; Lee et al., 2017).

Rapid Middle Miocene cooling recorded across the eastern Basin and Range is attributed to Middle Miocene extensional exhumation of footwall rocks from ~5-10 km depth to the surface in ca. 5 Ma Modes of extensional exhumation vary between metamorphic core complexes, which exhibit exhumation along low-angle normal faults (e.g., Wells, 2000; Konstantinou et al., 2012; Snoke, 1980; Haines and van der Pluijm, 2010; Miller et al., 1999; Gébelin et al., 2011) and highly-extended upper crustal blocks, which generally exhibit exhumation via domino-style faulting and block rotation (e.g., Proffett, 1977; Surpless et al., 2002; Colgan and Henry, 2009). An exceptional feature of the extensional systems which exhume the metamorphic core complexes (i.e., Ruby-East Humboldt, Albion-Raft River-Grouse Creek and Snake Range) is the along strike variability in footwall deformation style. For example, the Ruby detachment fault was continuous for ~150 km along the western Ruby-East Humboldt core complex (e.g., Colgan et al., 2010). Along the northern half of this fault trace, the footwall is composed

of mylonitic metasedimentary rocks and orthogneiss dipping gently to the west. To the south, unmetamorphosed Paleozoic strata are moderately east tilted as a coherent footwall block. A very similar configuration is recorded at the Snake Range core complex. The Snake Range décollement can be traced for ~150 km along the eastern flank of the Snake Range and Deep Creek Range. The central segment of the fault overlies gently east dipping mylonitic metasedimentary rocks and lesser orthogneiss (e.g., Miller et al., 1999). Along the Deep Creek Range to the north, the footwall is composed on non-mylonitic Neoproterozoic-Paleozoic metasedimentary rocks west tilted as a coherent block (e.g., Rodgers, 1987). As with the Ruby-East Humboldt core complex, where footwall rocks are non-mylonitic the footwall rotates opposite the sense of shear and exhibits a lower apparent magnitude of fault slip. This point emphasizes the importance of localized magmatic and metamorphic events on mid-crustal ductile attenuation and core complex development. Ductile attenuation may have been a primary cause of footwall exhumation rather than large magnitude extensional exhumation. In either case, pre-Middle Miocene mylonitic fabrics may have offered a weak horizon for Middle Miocene extensional reactivation and rapid fault slip.

CONCLUSION

Structural and thermochronologic data from the Pequop-Toano-Pilot extensional system in northeast Nevada-northwest Utah provide new constraints on the space-time pattern of post-orogenic extension in the Basin and Range. The kinematics and magnitude of extension across the Pequop, Toano and Pilot ranges is constrained through field structural observations and cross section retrodeformation. Detachment faulting across the study area accommodated 23 km of extension, and is likely kinematically linked to the adjacent metamorphic core complexes. Restored offset on normal faults reveals the pre-Eocene structure, which is composed of a system of southeast vergent folds and thrust faults. These contractional structures accommodated 12 km, or 23%, shortening during the middle Jurassic.

Zircon U-Pb geochronology and $^{40}Ar/^{39}Ar$ thermochronology were conducted to constrain the thermal evolution of the Pequop, Pilot and Toano Ranges. Zircon U-Pb dating

of intrusive rocks in the Toano and Pilot Ranges constrains episodes of Late Jurassic (155-160 Ma) and late Eocene (39 Ma) magmatism. $^{40}Ar/^{39}Ar$ thermochronology of igneous and metamorphic rocks from the Pequop, Pilot and Toano ranges record a history of protracted cooling between the Late Jurassic and Miocene. Muscovite $^{40}Ar/^{39}Ar$ ages from all three ranges record Late Cretaceous to Eocene cooling. In the central Pilot Range, mylonitic quartzite at the lowest structural level in the study area records rapid cooling from ~450°C between 20-30 Ma. K-feldspar $^{40}Ar/^{39}Ar$ ages record rapid cooling of the Toano and Pilot Ranges at 18 and 12 Ma.

We integrate these data into the following tectonic evolution. Mesozoic crustal shortening and magmatism promoted regional-contact metamorphism across the study area. Late Cretaceous muscovite $^{40}Ar/^{39}Ar$ ages suggest metamorphism ceased with ~30 m.y. of tectonic quiescence and conductive cooling of the upper crust. Cryptic normal faulting during this time is expressed in the Toano and Pilot ranges, however the kinematics and magnitude of extension are poorly constrained. Rollback of the flat Farallon slab promoted widespread magmatism across the eastern Basin and Range, which is expressed through late Eocene intrusions and volcanic rocks across the study area. Localized reheating of metamorphic country rocks is inferred from biotite and K-feldspar $^{40}Ar/^{39}Ar$ spectra that reveal partial argon loss. Detachment faulting initiated during the early Miocene(?) with development of the Pilot Peak detachment system, which evolved with time to become kinematically linked to the Ruby-East Humboldt and Albion-Raft River-Grouse Creek metamorphic core complex. Final unroofing of the Toano Range was complete by ~13 Ma, whereas the Pilot Range was unroofed slightly later by ~10 Ma.

New constraints on the spatial and temporal evolution of extension within the eastern Basin and Range improve our understanding of post-orogenic extension in the North American Cordillera. Our observations are consistent with previous studies that show extensional thinning of the Sevier Hinterland was minimal before the Middle Miocene. We highlight the influence of pre-existing structures in localizing large magnitude extension, such as the development of mylonitic fabrics during Oligocene magmatism, which facilitated detachment faulting during the Middle Miocene.

ACKNOWLEDGEMENTS

We greatly acknowledge support from the Earthscope AGeS2 Program (EAR-1759200, -1759353, -1759201), USGS STATEMAP (G14AC00237, G16AC00186, G17AC00212, G18AC00198, G19AC00383), Geological Society of Nevada, and the Tectonics Program of the National Science Foundation (EAR 1830139). The views and conclusions contained in this document are those of the authors and should not be interpreted as necessarily representing the official policies, either expressed or implied, of the U.S. Government.

APPENDIX 3.1: $^{40}Ar/^{39}Ar$ methods and data

The analytical data are organized to comply with FAIR data reporting norms (see for instance Schaen et al., 2020). Excel workbooks are provided with data formatted within a variety of worksheets to facilitate ease of data viewing. Data are presented in isotope ratio format. Raw intensity data available upon request. Each workbook also has a worksheet with summary age information.

The minerals were separated from the samples using standard magnetic, heavy liquid and hand-picking techniques. Samples were irradiated at Oregon State University in either the CLOCIT or CLICIT positions for between 10 and 14 hours along with neutron flux monitor Fish Canyon sanidine (FC-2). Neutron flux gradients were measured using Fish Canyon sanidine placed in holes of known geometry in the Al disks. All ages and J-factors are calculated using and age of 28.201 Ma (Kuiper et al., 2008) and a total ^{40}K decay constant of 5.463e-10 /a (Min et al., 2000). Typically, 6 single crystals from each position were analyzed to determine the J-value. Mean values for each location were fit with a sine curve and J-values for unknowns were extrapolated based on their geometric relation. J-factor errors are determined at 0.1 to 0.2% (1σ). Correction factors for interfering reactions were measured using CaF_2 and K-glass included with the samples during irradiation. The K-feldspar multiple diffusion domain (MDD) analytical methods follow those presented in detail in Sanders et al. (2006) with additional details presented here for the samples in this study.

Muscovite and K-feldspar were step heated in a double vacuum molybdenum resistance furnace, where as the biotite and hornblende was heated with a diode laser. Both the K-feldspar and muscovite separates were wrapped in Cu-foil and heated with high resolution (30-39 steps) heating schedules. The furnace samples were cleaned during heating with a cold SAES GP-50 getter heating and additionally reacted with a hot SAES GP-50 (2.1 A) in a second stage for 60 seconds before isotope analysis using a Thermo Scientific Helix MC mass spectrometer. The furnace thermocouple was calibrated by melting Cu-foil and true furnace temperature was ~ 50°C lower than the thermocouple temperature. Heating

schedules were adjusted by this amount, and corrected sample temperatures are reported in data tables.

Furnace blank and background values were determined by running a 10 or 20 minute, cold blank prior to each analysis and these blank values are included in the table for each analysis. The cold blank underestimates the blanks for steps above 1200°C, but because the samples are relatively old with high K the signal to blank value remains high and age calculations are not impacted by the slight underestimation of the blank values.

The biotite and hornblende samples were heated with 10 to 15 increments, each for a duration of 45 seconds, and the evolved gas was gettered with a hot SAES GP-50 getter during heating and reacted for an additional 60 seconds before gas inlet into the mass spectrometer. Gas was also exposed to a cold finger operated at -140°C. Isotope measurement was the same as for the furnace samples.

Integrated ages are reported for all of the samples and are calculated by summing the isotopes for all heating steps and the error is calculated as the quadratic sum of the errors for each heating step. Weighted mean ages (inverse variance, Taylor, 1992) were determined for steps comprising the flattest part of the age spectrum, however most spectra show excess scatter and thus MSWD values are quite elevated. Weighted mean age errors are increased by the square root of the MSWD for MSWD values greater than one. Because this study does not require ultra precise comparison of individual samples the assigned ages delineate large differences between mineral ages rather than scrutiny of small variations. Terminal ages are defined for samples that have climbing spectra where in some instances the final heating step is used to define these terminal ages. Multiple heating steps can define terminal ages and when so, the reported terminal age is the weighted mean of the included steps.

The MDD thermal histories were obtained using the basic procedures of Lovera et al. (1989), Sanders et al. (2006) and Long et al. (2018). For MDD modeling diffusion coefficients are calculated based on the fractional release of ^{39}Ar and plotted on the Arrhenius plots. $Log(r/r_0)$ plots were obtained by using an activation energy of 46 kcal/mol for K-feldspar (Lovera et al., 1997) and 63 kcal/mol for muscovite (Harrison et al., 2009)

and using the convention of placing the reference Arrhenius law (r_o) to pass through the first heating step such that the $\log(r/r_o)$ value is zero for the first increment of gas release. The $\log(r/r_o)$ plots have a form consistent with a multi-domain behavior with inflections that closely correlate to inflections within the age spectra. The Arrhenius data were forward modeled with equal activation energy for each domain and yield model fits that closely match the measured data. Fitting the measured age spectrum with acceptable fits determined by a Chebyshev's approximation derives the model thermal histories. A minimum of 20 successful model fits is used to determine a mean and 90% confidence interval for the thermal histories that only allow cooling from and initially high temperature.

REFERENCES

Armstrong, R.L., 1968, Sevier orogenic belt in Nevada and Utah: Geological Society of America Bulletin, v. 79, p. 429–458, doi: 10 .1130 /0016 -7606(1968) 79 [429: SOBINA]2 .0 .CO;2.

Armstrong, R. L., and Hansen, E. C, 1966, Cordilleran infrastructure in the eastern Great Basin: American Journal of Science, v. 264, p. 2-27.

Atwater, T., 1970, Implications of plate tectonics for the Cenozoic evolution of North America: Geological Society of America Bulletin, v. 81, p. 3513–3536, https://doi .org /10 .1130 /0016 -7606 (1970)81 [3513: IOPTFT]2.0 .CO;2 .

Bedell, R., Struhsacker, E., Craig, L., Miller, M., Coolbaugh, M., Smith, J., Parratt, R.L., and Goldfarb, R.J., 2010, The Pequop mining district, Elko County, Nevada: An evolving new gold district: Society of Economic Geologists, p. 29-56.

Best, M.G., Barr, D.L., Christiansen, E.H., Gromme, S., Deino, A.L., and Tingey, D.G., 2009, The Great Basin Altiplano during the middle Cenozoic ignimbrite flareup: Insights from volcanic rocks: International Geology Review, v. 51, p. 589–633, https:// doi .org /10.1080 /00206810902867690 .

Brooks, W.E., Thorman, W.E., and Snee, L.W., 1995a, The 40Ar/39Ar ages and tectonic setting of the middle Eocene northeast Nevada volcanic field: Journal of Geophysical Research, v. 100, p. 10,403–10,416, doi:10.1029/94JB03389.

Burchfiel, B.C., and Davis, G.A., 1975, Nature and controls of Cordilleran orogenesis, western United States—Extension of an earlier synthesis: American Journal of Science, v. 275A, p. 363–396.

Camilleri, P. A., and Chamberlin, K. R., 1997, Mesozoic tectonics and metamorphism in the Pequop Mountains and Wood Hills region, northeast Nevada: Implications for the architecture and evolution of the Sevier orogen: Geological Society of America Bulletin, v. 109, p. 74–94.

Camilleri, P., 2010a, Geologic map of the northern Pequop Mountains, Elko County, Nevada: Nevada Bureau of Mines and Geology Map, v. 171.

Camilleri, P.A., Deibert, J., and Perkins, M.E., 2017, Middle Miocene to Holocene tectonics, basin evolution, and paleogeography along the southern margin of the Snake River Plain in the Knoll Mountain-Ruby-East Humboldt Range region, northeastern Nevada and south- central Idaho: Geosphere, v. 13, p. 1901–1948, doi:10.1130/GES01318.1.

Cassel, E.J., Breecker, D.O., Henry, C.D., Larson, T.E., and Stockli, D.F., 2014, Profile of a paleo-orogen: High topography across the present-day Basin and Range from 40 to 23 Ma: Geology, v. 42, p. 1007–1010, https:// doi .org /10 .1130 /G35924 .1 .

Cassel, E.J., Smith, M.E., and Jicha, B.R., 2018, The impact of slab rollback on Earth's surface: Uplift and extension in the hinterland of the North American Cordillera:

Geophysical Research Letters, v. 45, no. 20, p. 10,996– 11,004, https:// doi .org /10 .1029 /2018GL079887.

Chamberlain, C.P., Mix, H.T., Mulch, A., Hren, H.T., Kent-Corson, M.L., Davis, S.J., Horton, T.W., and Graham, S.A., 2012, Cenozoic climatic and topographic evolution of the western North America Cordillera: American Journal of Science, v. 312, p. 213–262.

Clark, D.L., Oviatt, C.G., Hardwick, C.L., and Page, D., 2020, Interim geologic map of the Bonneville Salt Flats and east part of the Wendover 30' x 60' quadrangles, Tooele County, Utah—year 3: Utah Geological Survey Open-File Report 731, 30 p., 2 plates, scale 1:62.500, https://doi.org/10.34191/OFR-731.

Colgan, J.P., and Henry, C.D., 2009, Rapid middle Miocene collapse of the Mesozoic orogenic plateau in north-central Nevada: International Geology Review, v. 51, p. 920–961, doi: 10 .1080 /00206810903056731 .

Colgan, J.P., Howard, K.A., Fleck, R.J., and Wooden, J.L., 2010, Rapid middle Miocene extension and unroofi ng of the southern Ruby Mountains, Nevada: Tectonics, v. 29, p. TC6022, doi:10.1029/2009TC002655.

Compton, R.R., 1983, Displaced Miocene rocks on the west flank of the Raft River–Grouse Creek core complex, Utah; tectonic and stratigraphic studies in the eastern Great Basin, in Miller, D.M., et al., eds., Tectonic and stratigraphic studies in the eastern Great Basin: Geological Society of America Memoir 157, p. 271–279.

Coney, P.J., and Harms, T., 1984, Cordilleran metamorphic core complexes; Cenozoic extensional relics of Mesozoic compression: Geology, v. 12, p. 550–554.

Dallmeyer, R.D., Snoke, A., and McKee, E.H., 1986, The Mesozoic–Cenozoic tectonothermal evolution of the Ruby Mountains, East Humboldt Range, Nevada: A Cordilleran metamorphic core complex: Tectonics, v. 5, p. 931–954, doi: 10 .1029 /TC005i006p00931 .

DeCelles, P.G., 2004, Late Jurassic to Eocene evolution of the Cordilleran thrust belt and foreland basin system, western U.S.A.: American Journal of Science, v. 304, p. 105–168, https:// doi .org /10 .2475 /ajs .304 .2 .105 .

Dewey, J.F., 1988, Extensional collapse of orogens: Tectonics, v. 7, no. 6, p. 1123–1139, https://doi.org/10.1029 /TC007i006p01123.

Di Fiori, R.V., Long, S.P., Fetrow, A.C., Snell, K.E., Bonde, J.W., and Vervoort, J., 2020, Syncontractional deposition of the Cretaceous Newark Canyon Formation, Diamond Mountains, Nevada: Implications for strain partitioning within the U.S. Cordillera: Geosphere, v. 16, no. 2, p. 546– 566, https://doi.org /10.1130 /GES02168.1.

Dickinson, W.R., 2004, Evolution of the North American Cordillera: Annual Review of Earth and Planetary Sciences, v. 32, p. 13–45, https:// doi .org /10 .1146 /annurev.earth .32 .101802 .120257 .

Dickinson, W.R., 2006, Geotectonic evolution of the Great Basin: Geosphere, v. 2, p. 353–368, https:// doi .org /10.1130 /GES00054 .1 .

Druschke, P., Hanson, A.D., Wells, M.L., Rasbury, T., Stockli, D.F., and Gehrels, G., 2009a, Synconvergent surface-breaking normal faults of Late Cretaceous age within the Sevier hinterland, east-central Nevada: Geology, v. 37, p. 447–450, https:// doi .org /10 .1130/G25546A .1 .

Dumitru, T.A., Gans, P.B., Foster, D.A., and Miller, E.L., 1991, Refrigeration of the western Cordilleran lithosphere during Laramide shallow-angle subduction: Geology, v. 19, p. 1145–1148.

Egger, A.E., Dumitru, T.A., Miller, E.L., Savage, C.F.I., and Wooden, J.L., 2003, Timing and nature of Tertiary plutonism and extension in the Grouse Creek Mountains, Utah: International Geology Review, v. 45, p. 497–532, doi:10.2747/0020-6814.45.6.497.

Gans, P.B., Mahood, G.A., and Schermer, E., 1989, Synextensional Magmatism in the Basin and Range Province: A Case Study from the Eastern Great Basin: Geological Society of America Special Paper 223, 53 p.

Gébelin, A., Mulch, A., Teyssier, C., Heizler, M., Vennemann, T., and Seaton, N.C.A., 2011, Oligo-Miocene extensional tectonics and fluid flow across the northern Snake Range detachment system, Nevada: Tectonics, v. 30, TC5010, doi: 10 .1029 /2010TC002797.

Glick, L. L., 1987, Structural geology of the northern Toano Range, Elko County, Nevada [M.S. thesis]: San Jose, California, San Jose State University, 141 p.

Haines, S.H., and van der Pluijm, B., 2010, Dating the detachment fault system of the Ruby Mountains, Nevada: Signifi cance for the kinematics of low-angle normal faults: Tectonics, v. 29, p. TC4028, doi:10.1029/2009TC002552.

Hallett, B.W., and Spear, F.S., 2014, The P-T history of anatectic pelites of the northern East Humboldt Range, Nevada: Evidence for tectonic loading, decompression, and anatexis: Journal of Petrology, v. 55, p. 3–36.

Hallett, B.W., Spear, F.S., 2015, Monazite, zircon, and garnet growth in migmatitic pelites as a record of metamorphism and partial melting in the East Humboldt Range, Nevada: American Mineralogist, v. 100, p. 951-972.

Harrison, T.M., Heizler, M.T., Haviv, I., Avouac, J.P., 2009. Continuous thermal histories from muscovite 40Ar/39Ar age spectra. Geochimica Et Cosmochimica Acta 73, A497.

Henry, C.D., 2008, Ash-flow tuffs and paleovalleys in northeastern Nevada: Implications for Eocene paleogeography and extension in the Sevier hinterland, northern Great Basin: Geosphere, v. 4, p. 1–35, doi: 10 .1130 /GES00122 .1.

Henry, C.D., and Thorman, C.H., 2015, Preliminary geologic map of the Pequop Summit quadrangle, Elko County, Nevada: Nevada Bureau of Mines and Geology Open File Report 15-8, scale 1:24,000, 12 p.

Howard, K.A., Wooden, J.L., Barnes, C.G., Premo, W.R., Snoke, A.W., and Lee, S.Y., 2011, Episodic growth of a Late Cretaceous and Paleogene intrusive complex of pegmatitic leucogranite, Ruby Mountains core complex, Nevada, USA: Geosphere, v. 7, no. 5, p. 1220-1248.

Humphreys, E.D., 1995, Post-Laramide removal of the Farallon slab, western United States: Geology, v. 23, p. 987–990, https:// doi .org /10 .1130 /0091 -7613 (1995)023 <0987:PLROTF>2 .3 .CO;2 .

Ketner, K.B., Day, W.C., Elrick, M., Vaag, M.K., Zimmerman, R.A., Snee, L.W., Saltus, R.W., Wardlaw, B.R., Taylor, M.E., and Harris, A.G., 1998, An outline of tectonic, igneous, and metamorphic events in the Goshute-Toano range between Silver Zone pass and White Horse pass, Elko county, Nevada: a history of superposed contractional and extensional deformation: US Geological Survey, no. 1593, 12 p.

Konstantinou, A., Strickland, A., Miller, E.L., and Wooden, J.W., 2012, Multi-stage Cenozoic extension of the Albion–Raft River–Grouse Creek metamorphic core complex: Geochronologic and stratigraphic constraints: Geosphere, v. 8, p. 1429-1466.

Konstantinou, A, Strickland, A., Miller, E., Vervoort, J., Fisher, C.M., Wooden, J., and Valley, J., 2013, Synextensional magmatism leading to crustal flow in the Albion-Raft River-Grouse Creek metamorphic core complex, northeastern Basin and Range: Tectonics, v. 32, 1384–1403.

Kuiper, K. F., Deino A., Hilgen, F. J., Krijgsman, W., Renne, P. R., and Wijbrans, J. R. (2008) Synchronizing the rock clocks of Earth history. Science 320, 500–504.

Langenheim, V.E., Athens, N.D., Chuchel, B.A., Willis, H., Knepprath, N.E., Rosario, J., Roza, J., Kraushaar, S.M., and Hardwick, C.L., 2013, Preliminary Isostatic Residual Gravity Map of the Newfoundland Mountains and East Part of the Wells 30′ x 60′ Quadrangles, Box Elder County, Utah: Utah Geological Survey Miscellaneous Publication 13-4, 1 plate, scale 1:100,000.

Lee, J., Blackburn, T., and Johnston, S., 2017, Timing of mid-crustal ductile extension in the northern Snake Range metamorphic core complex, Nevada: Evidence from U/Pb zircon ages: Geosphere, v. 13, p. 439-459.

Long, S.P., 2018, Geometry and magnitude of extension in the Basin and Range Province (39° N), Utah, Nevada, and California, USA: Constraints from a province-scale cross section: GSA Bulletin, v. 131, no. 1-2, p. 99-119.

Long, S.P., and Walker, J.P., 2015, Geometry and kinematics of the Grant Range brittle detachment system, eastern Nevada, U.S.A.: An end-member style of upper-crustal extension: Tectonics, v. 34, p. 1837–1862, https:// doi.org /10 .1002 /2015TC003918 .

Long, S.P., Henry, C.D., Muntean, J.L., Edmondo, G.P., and Cassel, E.J., 2014, Early Cretaceous construction of a structural culmination, Eureka, Nevada, U.S.A.: Implications for out-of-sequence deformation in the Sevier hinterland: Geosphere, v. 10, p. 564–584, https:// doi.org /10 .1130 /GES00997 .1 .

Long, S.P., Thomson, S.N., Reiners, P.W., and Di Fiori, R.V., 2015, Synorogenic extension localized by upper-crustal thickening: An example from the Late Cretaceous Nevadaplano: Geology, v. 43, p. 351–354, https:// doi .org/10 .1130 /G36431 .1 .

Long, S.P., Heizler, M.T., Thomson, S.N., Reiners, P.W., and Fryxell, J.E., 2018, Rapid Oligocene to early Miocene extension along the Grant Range detachment system,

Nevada, USA: Insights from multipart cooling histories of footwall rocks: Tectonics, v. 2037 37, no. 12, p. 4752-4779.

Lovera, O.M., Grove, M., Harrison, T.M., 1997, Systematic analysis of K-feldspar 40Ar/39Ar step heating results; I, Significance of activation energy determination: Geochimica et Cosmochimica Acta, v. 61, no. 15, p. 3171-3192.

Lovera, O.M., Richter, F.M., and Harrison, T.M., (1989), The 40Ar/39Ar geothermometry for slowly cooled samples having a distribution of diffusion domain sizes, J. Geophys. Res. 94, 17,917-17,935.

Lund-Snee, J.E., and Miller, E.L., 2020, Cenozoic Magmatism, Migrating Topography, and the Onset of Basin and Range Faulting: Geological Society of Nevada 2020 Symposium Proceedings.

Lund-Snee, J.-E., Miller, E.L., Grove, J., Hourigan, J.K., and Konstantinou, A., 2016, Cenozoic paleogeographic evolution of the Elko Basin and surrounding region, northeast Nevada, Geosphere, v. 12, p. 464–500.

MacCready, T., Snoke, A.W., Wright, J.E., and Howard, K.A., 1997, Mid-crustal fl ow during Tertiary extension in the Ruby Mountains core complex, Nevada: Geological Society of America Bulletin, v. 109, p. 1576–1594, doi:10.1130/0016-7606(1997)109<1576: MCFDTE>2.3.CO;2.

Malavieille, J., 1987, Extensional shearing deformation and kilometer-scale “a”-type folds in a Cordilleran Metamorphic Core Complex (Raft River Mountains, northwestern Utah): Tectonics, v. 6, no. 4, p. 423-448.

McGrew, A.J., and Snee, L.W., 1994, $^{40}Ar/^{39}Ar$ thermochronologic constraints on the tectonothermal evolution of the Northern East Humboldt range metamorphic core complex, Nevada; Tectonophysics, v. 238, p. 425-450.

McGrew, A.J., Peters, M.T., and Wright, J.E., 2000, Thermobarometric constraints on the tectonothermal evolution of the East Humboldt Range metamorphic core complex, Nevada: Bulletin of the Geological Society of America, v. 112, p. 45–60, doi:10.1130/0016-7606(2000)112<45:TCOTTE>2.0.CO;2.

Miller, D.M., 1984, Sedimentary and Igneous Rocks of the Pilot Range and Vicinity, Utah and Nevada: Utah Geological Association, v. 13, p. 45-63.

Miller, D. M., and Schneyer, J. D., 1985, Geologic map of the Tecoma quadrangle, Box Elder County, Utah, and Elko County, Nevada: Utah Geological and Mineral Survey Map 77,8 p., scale 1:24,000.

Miller, D. M., Hillhouse, W. C., Zartman, R. E., and Lanphere, M. A., 1987, Geochronology of intrusive and metamorphic rocks in the Pilot Range, Utah and Nevada, and comparison with regional patterns: Geological Society of America Bulletin, v. 99, p. 866-879.

Miller, D. M., Nakata, J. K., and Glick, L. L., 1990, K-Ar ages of Jurassic to Tertiary plutonic and metamorphic rocks, northwestern Utah and northeastern Nevada: U.S. Geological Survey Bulletin 1906, 18 p.

Miller, D.M., Jordan, T.E., and Allmendinger, R.W., 1990b, Geologic map of the Crater Island Quadrangle, Box Elder County, Utah: Utah Geological and Mineral Survey Map 125, 16 p. of text and 2 map sheets, scale 1:24,000.

Miller, D.M., Lush, A.P., and Schneyer, J.D., 1993, Geologic map of the Patterson Pass quadrangle, Box Elder County, Utah, and Elko County, Nevada: Utah Geological Survey Map 160, 1:24,000.

Miller, D.M., Lush, A.P., 1994, Geologic map of the Pilot Peak quadrangle, Box Elder County, Utah, and Elko County, Nevada: Utah Geological Survey Map 144, 1:24,000.

Miller, D.M., Hoisch, T.D., 1995, Jurassic tectonics of northeastern Nevada and northwestern Utah from the perspective of barometric studies in Miller, D.M., and Busby, C., Jurassic Magmatism and Tectonics of the North American Cordillera: Society of America Special Paper 299.

Miller, E.M., Gans, P.B., 1989, Cretaceous crustal structure and metamorphism in the hinterland of the Sevier thrust belt, western U.S. Cordillera; Geology, v. 17, p. 59-62.

Miller, E.L., Gans, P.B., Wright, J.E., and Sutter, J . F, 1988, Metamorphic history of the east central Basin and Range province: Tectonic setting and relationship to magmatism, in Ernst, W.G., ed., Metamorphism and crustal evolution, western conterminous United States (Rubey Volume VII): Englewood Cliffs, New Jersey, Prentice-Hall, p. 649-682.

Miller, E.L., Dumitru, T.A., Brown, R.W., and Gans, P.B., 1999, Rapid Miocene slip on the Snake Range–Deep Creek Range fault system, east-central Nevada: Geological Society of America Bulletin, v. 111, p. 886–905, https:// doi .org /10 .1130 /0016 -7606 (1999)111<0886: RMSOTS>2 .3 .CO;2 .

Min, K., Mundil, R., Renne, P. R., and Ludwig, K. R., 2000, A test for systematic errors in 40Ar/39Ar geochronology through comparison with U/Pb analysis of a 1.1 Ga rhyolite: Geochim. Cosmochim. Acta, v. 64, p. 73-98.

Molnar, P., and Lyon-Caen, H., 1988, Some simple aspects of the support, structure and evolution of mountain belts, in Clark, S.P., Jr., Burchfiel, B.C., and Suppe, J., eds., Processes in Continental Lithosphere Deformation: Geological Society of America Special Paper 218, p. 179–207, https:// doi .org /10 .1130 /SPE218 -p179 .

Mueller, K. J., and Snoke, A. W., 1993, Progressive overprinting of normal fault systems and their role in Tertiary exhumation of the East Humboldt–Wood Hills metamorphic complex, northeast Nevada: Tectonics, v. 12, p. 361–371.

Mueller, K.J., Cerveny, P.K., Perkins, M.E., and Snee, L.W., 1999, Chronology of polyphase extension in the Windermere Hills, northeast Nevada: Geological Society of America Bulletin, v. 111, p. 11–27, doi:10.1130/0016-7606(1999)111<0011:COPEIT>2.3.CO;2.

Proffett, J.M., Jr., 1977, Cenozoic geology of the Yerington district, Nevada, and implications for the nature and origin of Basin and Range faulting: Geological Society of America Bulletin, v. 88, p. 247–266, https:// doi .org /10.1130 /0016 -7606 (1977)88 <247: CGOTYD>2 .0 .CO;2 .

Rey, P., Vanderheaghe, O., and Teyssier, C., 2001, Gravitational collapse of continental crust: Defi nition, regimes, and modes: Tectonophysics, v. 342, p. 435–449, doi: 10.1016/S0040-1951(01)00174-3.

Rodgers, D.W., 1987, Thermal and structural evolution of the southern Deep Creek Range, west-central Utah and east-central Nevada [Ph.D. thesis]: Stanford, California, Stanford University, 184 p.

Sanders, R.E., Heizler, M.T. and Goodwin, L.B., 2006, 40Ar/39Ar thermochronology constraints on the timing of Proterozoic basement exhumation and fault ancestry, southern Sangre de Cristo Range, New Mexico. Geol. Soc. of Am. Bull., 118, 11, 1489-1506.

Satarugsa, P., and Johnson, R.A., 2000, Cenozoic tectonic evolution of the Ruby Mountains metamorphic core complex and adjacent valleys, northeastern Nevada: Rocky Mountain Geology, v. 35, p. 205–230, doi: 10 .2113 /35 .2 .205 .

Schaeffer, F. E., ed., 1960, Geology of the Silver Island Mountains, Box Elder and Tooele Counties, Utah, and Elko County, Nevada: Utah Geological Society Guidebook to the Geology of Utah, no. 15, 185 p.

Schaen, A.J., Jicha, B.R., Hodges, K.V., Vermeesch, P., Stelten, M.E., Mercer, C.M., Phillips, D., Rivera, T.A., Jourdan, F., Matchan, E.L., Hemming, S.R., Morgan L.E., Kelley, S.P., Cassata, W.S., Heizler, M.T., Vasconcelos, P.M., Koppers, A.A.P., Mark, D.F., Niespolo, E.M., Sprain, C.J., Benowitz, J.A., Hames, W.E., Kuiper, K.F., Turrin, B.D., Renne, P.R., Ross, J., Nomade, S., Guillou, H., Laura E. Webb, L.E., Cohen, B.A., Calvert, A.T., Joyce, N., Morgan Ganderød, M., Wijbrans, J., Ishizuka, O., He, H., Ramirez, A., Pfänder, J.A., Lopez-Martínez, M., Huaning Qiu, H., Brad S. Singer, B.S., 2020, On the reporting and interpretation of 40Ar/39Ar geochronologic data, Geol. Soc. Am. Bull., 133 (3-4), DOI:10.1130/B35560.1

Smith, M.E., Carroll, A.R., Jicha, B.J., Cassel, E.J., and Scott, J.J., 2014, Paleogeographic record of Eocene Farallon slab rollback beneath western North America: Geology, v. 42, p. 1039–1042, https:// doi .org /10 .1130 /G36025 .1.

Smith, M.E., Cassel, E.J., Jicha, B.R., Singer, B.S., and Canada, A.S., 2017, Hinterland drainage closure and lake formation in response to middle Eocene Farallon slab removal, Nevada, USA: Earth and Planetary Science Letters, v. 479, p. 156-169.

Snoke, A.W., 1980, Transition from infrastructure to suprastructure in the northern Ruby Mountains, Nevada, *in* Crittenden, M.D., Coney, P.J., and Davis, G.H., eds., Cordilleran Metamorphic Core Complexes: Geological Society of America Memoir, v. 153, p. 287-334.

Snoke, A. W., and Miller, D. M., 1988, Metamorphic and tectonic history of the northeastern Great Basin, in Ernst, W. G., ed., Metamorphism and crustal evolution of the western United States (Rubey Volume VII): Englewood Cliffs, New Jersey, Prentice-Hall, p. 608–648.

Sonder, L.J., and Jones, C.H., 1999, Western United States extension: How the West was widened: Annual Review of Earth and Planetary Sciences, v. 27, p. 417–462, https:// doi .org /10 .1146 /annurev .earth .27 .1 .417 .

Stewart, J.H., 1971, Basin and Range structure—A system of horsts and grabens produced by deep-seated extension: Geological Society of America Bulletin, v. 82, p. 1019–1043, https:// doi .org /10 .1130 /0016 -7606(1971)82 [1019: BARSAS]2 .0 .CO;2 .

Stewart, J.H., 1972, Initial deposits in the Cordilleran geosyncline: Evidence of a Late Precambrian (<850 m.y.) continental separation: Geological Society of America Bulletin, v. 83, p. 1345-1360.

Strickland, A., Miller, E.L., and Wooden, J., 2011a, The timing of Tertiary metamorphism and deformation in the Albion–Raft River–Grouse Creek metamorphic core complex, Utah and Idaho: Journal of Geology, v. 119, p. 185–206, doi:10.1086/658294.

Strickland, A., Miller, E.L., Wooden, J., Kozdon, R., and Valley, J.W., 2011b, Syn-extensional plutonism and peak metamorphism in the Albion–Raft River–Grouse Creek metamorphic core complex: American Journal of Science, v. 311, p. 261–314, doi:10.2475/04.2011.01.

Surpless, B.E., Stockli, D.F., Dumitru, T.A., and Miller, E.L., 2002, Two-phase westward encroachment of Basin and Range extension into the northern Sierra Nevada: Tectonics, v. 21, no. 1, https:// doi .org /10 .1029/2000TC001257 .

Taylor, J.R., 1982. An Introduction to Error Analysis: The Study of Uncertainties in Physical Measurements, Univ. Sci. Books, Mill Valley, Calif., 270 p.

Teyssier, C., Ferré, E.C., Whitney, D.L., Norlander, B., Vanderhaeghe, O., and Parkinson, D., 2005, Flow of partially molten crust and origin of detachments during collapse of the Cordilleran orogen, in Bruhn, D., and Burlini, L., eds., High-strain zones: Structure and physical properties: Geological Society of London Special Publication 245, p. 39–64, doi: 10.1144/GSL.SP.2005.245.01.03.

Todd, V.R., 1980, Structure and petrology of a Tertiary gneiss complex in northwestern Utah, *in* Crittenden, M.D., Jr., et al., eds., Cordilleran metamorphic core complexes: Geological Society of America Memoir 153, p. 349–383

Wells, M.L., 1997, Alternating contraction and extension in the hinterlands of orogenic belts; an example from the Raft River Mountains, Utah: Geological Society of America Bulletin, v. 109, p. 107–126, doi:10.1130/0016-7606(1997)109<0107:ACAEIT>2.3.CO;2.

Wells, M.L., Snee, L.W., and Blythe, A.E., 2000, Dating of major normal fault systems using thermochronology; an example from the Raft River detachment, Basin and Range, western United States: Journal of Geophysical Research, v. 105, no. B7, p. 16303–16327, doi:10.1029/2000JB900094.

Wells, M.L., and Hoisch, T.D., 2008, The role of mantle delamination in widespread Late Cretaceous extension and magmatism in the Cordilleran orogen, western United States:

Geological Society of America Bulletin, v. 120, p. 515–530, https:// doi .org /10 .1130 /B26006 .1 .

Wells, M.L., Hoisch, T.D., Cruz-Aribe, A.M., and Vervoort, J.D., 2012, Geodynamics of synconvergent extension and tectonic mode switching: Constraints from the Sevier-Laramide orogeny: Tectonics, v. 31, TC1002, https:// doi .org /10 .1029 /2011TC002913 .

Wernicke, B., and Snow, J.K., 1998, Cenozoic tectonism in the central Basin and Range: Motion of the Sierran–Great Valley block: International Geology Review, v. 40, p. 403–410.

Wesnousky, S. G., and Willoughby, C. H., 2003, Neotectonic note: The Ruby–East Humboldt Range, northeastern Nevada: Bulletin of the Seismological Society of America, v. 93, no. 3, p. 1345-1354.

Whitmeyer, S.J., and Karlstrom, K.E., 2007, Tectonic model for the Proterozoic growth of North America: Geosphere, v. 3, p. 220–259, doi: 10.1130 /GES00055.1.

Wright, J. E., and Wooden, J. L., 1991, New Sr, Nd, and Pb isotopic data from plutons in the northern Great Basin: Implications for crustal structure and granite petrogenesis in the hinterland of the Sevier thrust belt: Geolo©r, v. 19, p. 457-460.

Wright, J.E., and Snoke, A.W., 1993, Tertiary magmatism and mylonitization in the Ruby-East Humboldt metamorphic core complex, northeastern Nevada: U-Pb geochronology and Sr, Nd, and Pb isotope geochemistry: Geological Society of America Bulletin, v. 105, no. 7, p. 935-952.

Yonkee, W.A., and Weil, A.B., 2015, Tectonic evolution of the Sevier and Laramide belts within the North American Cordillera orogenic system: Earth-Science Reviews, v. 150, p. 531–593.

Yonkee, W.A., Dehler, C.D., Link, K., Balgord, E.A., Keeley, J.A., Hayes, D.S., Fanning, C.M., Wells, M.L., Johnston, S.M., 2014. Tectono-stratigraphic framework of Neoproterozoic to Cambrian strata, west-central U.S.: protracted rifting, glaciation, and evolution of the North American Cordilleran margin. Earth-Sci. Rev. 136, 59–95.

Zuza, A.V., Thorman, C.H., Henry, C.D., Levy, D.A., Dee, S., Long, S.P., Sandberg, C.A., and Soignard, E., 2020, Pulsed Mesozoic deformation in the Cordilleran hinterland and evolution of the Nevadaplano: Insights from the Pequop Mountains, NE Nevada: Lithosphere.

Zuza, A. V., Henry, C. D., Dee, S., Thorman, C. H., & Heizler, M. T., 2021, Records of pulsed intracontinental plateau growth and subsequent collapse in the North American Cordilleran hinterland: Jurassic-Cenozoic tectonics of the Pequop Mountains, NE Nevada: Geosphere.

Table 3.S1. Summary of $^{40}Ar/^{39}Ar$ results

								Preferred Age						TGA			
Sample	Unit	Location	L#	Irrad	min	analysis	n	$\%^{39}Ar$	MSWD	Age(Ma)	±	2σ	n	Age(Ma)	±	1σ
61418(2)ms		Pequop	66829-01	NM-303C	Muscovite	Terminal	1	3.2	NA	87.04	±	0.32	32	78.493	±	0.028
61418(2)bt		Pequop	66837-01	NM-303D	Biotite	Plateau	8	96.2	131	78.20	±	0.35	11	77.821	±	0.048
H15-35M		Pequop	66827-01	NM-303C	Muscovite	Terminal	2	8.8	2.55	84.3	±	1.3	12	74.62	±	0.18
H15-35B		Pequop	66835-01	NM-303C	Biotite	Plateau	2	39.7	73.2	82.94	±	0.49	11	77.964	±	0.049
H17-23		Pequop	66820-01	NM-303C	Muscovite	Terminal	4	18.6	26.8	76.96	±	0.23	33	74.277	±	0.032
H18-23M		Pequop	66822-01	NM-303C	Muscovite	Terminal	1	7.1	NA	70.92	±	0.07	33	67.860	±	0.020
H18-23K		Pequop	66866-01	NM-303F	K-Feldspar	Terminal	3	26.5	7.16	46.72	±	0.04	33	41.917	±	0.013
H18-24		Pequop	66824-01	NM-303C	Muscovite	Terminal	1	4.7	NA	76.16	±	0.24	33	69.772	±	0.031
H18-34		Pequop	66826-01	NM-303C	Muscovite	Terminal	4	12.8	7.23	94.80	±	0.58	14	82.072	±	0.061
H18-40M		Pequop	66825-01	NM-303C	Muscovite	Terminal	2	14.4	50.7	75.85	±	0.27	31	73.061	±	0.027
H18-40K		Pequop	66862-01	NM-303F	K-Feldspar	Terminal	3	21.2	482	51.59	±	0.31	35	45.123	±	0.012
H18-627B		Pequop	66828-01	NM-303C	Muscovite	Plateau	7	50.9	25.9	80.29	±	0.63	14	76.13	±	0.12
H18-627B		Pequop	66836-01	NM-303D	Biotite	Plateau	4	48.4	52.5	91.85	±	0.34	12	87.700	±	0.055
H18-648		Pequop	66834-01	NM-303C	Biotite	TGA							10	136.31	±	0.36
040719-2		Pilot	67502-01	NM-309E	Hornblende	Plateau	9	36.2	349	39.9	±	1.0	14	49.700	±	0.064
040719-2		Pilot	67460-01	NM-309B	Ksp/Plag	TGA							31	82.74	±	0.37
050719-16		Pilot	67507-01	NM-309F	Muscovite	Terminal	1	17.1	NA	96.581	±	0.060	30	86.790	±	0.034
050719-23		Pilot	67472-01	NM-309C	Muscovite	Terminal	5	26.6	3191	71.11	±	0.52	39	70.550	±	0.027
050719-23		Pilot	67461-01	NM-309B	K-Feldspar	Terminal	3	20.5	1435	36.04	±	0.47	34	30.721	±	0.012
060719-3		Pilot	67504-01	NM-309E	Biotite	Plateau	10	50.0	3.89	10.77	±	0.20	13	9.49	±	0.12
060719-3		Pilot	67510-01	NM-309F	Muscovite	Terminal	1	5.7	NA	36.83	±	0.17	31	27.010	±	0.051
060719-5		Pilot	67471-01	NM-309C	Muscovite	Terminal	8	42,4	2080	37.92	±	0.23	38	34.401	±	0.017
060719-7		Pilot	67517-01	NM-309F	Muscovite	Terminal	3	13.2	6.52	27.52	±	0.15	30	22.586	±	0.032
070719-9		Pilot	67317-01	NM-306F	Biotite	Plateau	6	64.2	290	37.88	±	0.16	15	36.629	±	0.011
090719-1		Pilot	67515-01	NM-309F	Muscovite	Terminal	1	5.2	NA	76.22	±	0.27	35	62.306	±	0.073
090719-5		Pilot	67487-01	NM-309D	Biotite	TGA							15	29.358	±	0.053
090719-5		Pilot	67463-01	NM-309B	Ksp/Plag	TGA							35	87.76	±	0.10
110719-3		Pilot	67464-01	NM-309B	Ksp	Terminal	3	25.2	6133	31.33	±	0.57	35	23.116	±	0.009
160719-4		Pilot	67505-01	NM-309F	Muscovite	Terminal	1	14.7	NA	89.29	±	0.11	29	110.03	±	0.17
160719-13		Pilot	67499-01	NM-309E	Hornblende	Plateau	3	13.2	5.43	37.04	±	0.37	14	58.594	±	0.093
160719-13		Pilot	67459-01	NM-309B	Ksp/Plag	Plateau							31	233.17	±	0.26
180719-10		Pilot	67500-01	NM-309E	Biotite	Plateau	8	33.1	5.90	17.94	±	0.17	15	16.914	±	0.063
180719-10		Pilot	67513-01	NM-309F	Muscovite	Terminal	4	16.7	3.61	30.61	±	0.10	34	28.287	±	0.031
190719-3		Pilot	67498-01	NM-309E	Biotite	Plateau	12	68.7	39.2	22.90	±	0.24	15	21.483	±	0.050
190818-3		Pilot	67321-01	NM-306F	Biotite	Plateau	4	49.3	327	31.62	±	0.29	14	32.975	±	0.016
200719-7		Pilot	67497-01	NM-309E	Biotite	Plateau	3	15.1	5.85	11.70	±	0.44	14	9.31	±	0.10
200719-7		Pilot	67514-01	NM-309F	Muscovite	Terminal	3	8.9	18.5	25.31	±	0.17	34	22.966	±	0.018
010719-4		Toano	67511-01	NM-309F	Muscovite	Terminal	1	4.0	0.54	75.82	±	0.17	31	62.934	±	0.027
020719-5		Toano	67488-01	NM-309D	Biotite	Plateau	10	54.3	29.4	44.7	±	1.0	12	39.36	±	0.18
020719-5		Toano	67508-01	NM-309F	Muscovite	Terminal	3	17.6	35.2	79.87	±	0.34	29	74.241	±	0.039
020719-9		Toano	67311-01	NM-306E	Muscovite	Terminal	6	24.0	140	77.22	±	0.14	37	75.006	±	0.013
020719-13		Toano	67312-01	NM-306E	Muscovite	Terminal	2	14.3	4.99	73.934	±	0.040	37	70.400	±	0.012

								Preferred Age						TGA			
Sample	Unit	Location	L#	Irrad	min	analysis	n	$\%^{39}Ar$	MSWD	Age(Ma)	±	2σ	n	Age(Ma)	±	1σ
020719-13		Toano	67457-01	NM-309B	Ksp	Terminal	1	3.3	NA	38.988	±	0.051	36	30.432	±	0.022
080719-7		Toano	67503-01	NM-309E	Biotite	Plateau	7	77.2	29.4	92.161	±	0.094	15	92.114	±	0.029
080719-7		Toano	67506-01	NM-309F	Muscovite	Plateau	29	100.0	7.51	84.17	±	0.15	29	83.793	±	0.071
080719-18		Toano	67318-01	NM-306F	Muscovite	Terminal	5	10.5	20.0	110.80	±	0.25	33	104.952	±	0.021
210719-2		Toano	67322-01	NM-306F	Hornblende	Plateau	7	35.7	5.11	40.76	±	0.14	14	45.672	±	0.056
210719-2		Toano	67323-01	NM-306F	Biotite	Plateau	5	80.3	102	39.017	±	0.066	13	38.483	±	0.009
210719-2		Toano	67456-01	NM-309B	Ksp	Terminal	1	3.4	NA	41.646	±	0.068	36	39.189	±	0.020

Table 3.S2. $^{40}Ar/^{39}Ar$ isotopic ratio data

	ID	Power/Temp (Watts/°C)	$^{40}Ar/^{39}Ar$	$^{37}Ar/^{39}Ar$	$^{36}Ar/^{39}Ar$ (x 10^{-3})	$^{39}Ar_K$ (x 10^{-15} mol)	K/Ca	$^{40}Ar^*$ (%)	^{39}Ar (%)	Age (Ma)	±1s (Ma)	Time (min)
	61418(2)ms, Muscovite, 4.16 mg, J=0.0014882±0.02%, IC=0.9983056±0.0003725, NM-303C, Lab#=66829-01											
X	A	450	142.5	-0.0573	399.8	0.2	-	17.1	0.1	65.2	3.1	20
X	B	500	39.75	-0.1214	47.84	0.1	-	64.4	0.2	68.4	3.6	20
X	C	540	32.06	0.2423	22.33	0.2	2.1	79.5	0.4	68.1	1.9	20
X	D	570	32.14	0.2514	14.21	0.4	2.0	87.0	0.6	74.7	1.3	20
X	E	600	30.14	0.1480	8.169	0.6	3.4	92.0	1.0	74.06	0.76	20
X	F	630	29.78	0.0334	6.462	0.9	15.3	93.6	1.7	74.40	0.53	20
X	G	650	29.20	0.0300	4.761	1.0	17.0	95.2	2.5	74.20	0.42	20
X	H	680	29.28	0.0008	4.152	1.6	635.8	95.8	3.7	74.87	0.30	20
X	I	700	29.31	-0.0096	3.149	1.8	-	96.8	4.9	75.71	0.27	20
X	J	710	29.10	0.0135	3.039	1.4	37.7	96.9	6.0	75.26	0.29	20
X	K	720	29.64	0.0191	4.158	1.4	26.7	95.9	7.0	75.82	0.32	20
X	L	730	29.87	0.0099	4.120	1.4	51.8	95.9	8.0	76.45	0.35	20
X	M	740	29.88	0.0105	5.111	1.5	48.6	94.9	9.1	75.70	0.32	20
X	N	750	30.95	0.0116	7.340	1.8	44.1	93.0	10.4	76.77	0.29	20
X	O	760	31.04	0.0046	5.211	2.9	109.8	95.0	12.5	78.64	0.18	20
X	P	770	31.03	0.0024	3.994	4.5	215.8	96.2	15.7	79.55	0.12	20
X	Q	780	30.30	0.0083	2.086	5.9	61.2	98.0	20.0	79.119	0.091	20
X	R	790	30.00	0.0045	1.436	6.0	112.8	98.6	24.4	78.856	0.090	20
X	S	800	29.72	-0.0115	1.138	5.5	-	98.9	28.4	78.329	0.098	20
X	T	810	29.68	-0.0056	1.243	4.7	-	98.8	31.8	78.14	0.11	20
X	U	820	29.76	0.0010	1.253	4.5	510.9	98.8	35.0	78.36	0.11	20
X	V	840	29.69	0.0029	1.325	5.4	178.5	98.7	39.0	78.130	0.096	20
X	W	860	29.62	0.0003	1.627	5.9	1734.8	98.4	43.2	77.700	0.083	20
X	X	880	29.38	0.0059	1.713	6.1	86.6	98.3	47.7	77.014	0.085	20
X	Y	900	29.28	0.0034	1.850	6.3	148.7	98.1	52.2	76.652	0.086	20
X	Z	920	29.04	0.0033	1.772	7.0	152.6	98.2	57.3	76.089	0.072	20
X	AA	950	28.85	0.0063	1.360	9.9	81.5	98.6	64.4	75.903	0.055	20
X	AB	1000	29.71	0.0045	1.453	12.7	113.6	98.6	73.6	78.089	0.048	20
X	AC	1050	30.63	0.0026	1.169	24.3	197.3	98.9	91.2	80.697	0.030	20
X	AD	1100	30.85	0.0018	1.069	3.6	288.7	99.0	93.8	81.34	0.14	3
X	AE	1200	31.22	0.0193	2.252	4.2	26.4	97.9	96.8	81.39	0.13	3
	AF	1600	86.51	0.0602	182.0	4.5	8.5	37.8	100.0	87.04	0.32	3
	Integrated age ± 1s			n=32		138.1	70.6		K2O=8.57%	78.493	0.028	
	Terminal age ± 1s		step AF	n=1		4.457			3.2	87.04	0.32	
	61418(2)bt, Biotite, 1.3 mg, J=0.0015594±0.04%, IC=0.9924642±0.0020102, NM-303D, Lab#=66837-01											
X	A	0.5	61.00	0.1396	165.4	0.2	3.7	19.9	0.4	34.3	1.6	
X	B	0.8	26.78	0.2916	18.54	0.6	1.7	79.6	1.6	59.90	0.71	
X	C	1.0	29.43	0.1461	9.479	1.1	3.5	90.5	3.8	74.51	0.43	
	D	1.5	29.57	0.1601	7.967	2.7	3.2	92.1	9.5	76.14	0.18	
	E	2.0	29.41	0.1897	4.858	4.5	2.7	95.2	18.9	78.22	0.11	
	F	2.5	29.25	0.2061	3.487	4.6	2.5	96.5	28.5	78.89	0.11	
	G	3.0	29.47	0.0323	3.153	4.8	15.8	96.8	38.6	79.70	0.10	
	H	3.5	29.63	0.0093	3.009	4.9	54.9	97.0	48.9	80.27	0.11	
	I	5.0	28.47	0.0019	1.623	9.5	266.6	98.3	68.9	78.190	0.058	
	J	7.0	28.09	0.0054	1.161	9.8	93.7	98.8	89.6	77.549	0.053	
	K	15.0	28.10	0.0579	1.242	4.9	8.8	98.7	100.0	77.51	0.10	
	Integrated age ± 1s			n=11		47.4	7.8		K2O=8.98%	77.821	0.048	
	Plateau ± 1s		steps D-K	n=8	MSWD=131	45.592			96.2	78.20	0.35	
	H15-35M, Muscovite, 1.26 mg, J=0.0014996±0.02%, IC=0.9947317±0.000765, NM-303C, Lab#=66827-01											
X	A	0.4	40.51	2.987	106.3	0.2	0.17	23.1	2.8	25.5	1.1	
X	B	0.6	24.30	6.290	18.38	0.2	0.081	79.7	5.6	52.6	1.4	
X	C	0.8	26.59	4.688	9.037	0.4	0.11	91.4	10.1	65.70	0.98	
X	D	1.0	27.45	2.031	4.619	0.6	0.25	95.6	17.7	70.75	0.59	
X	E	1.2	27.65	1.227	3.455	0.8	0.42	96.7	27.4	72.02	0.49	
X	F	1.5	28.10	0.7077	3.107	1.2	0.72	96.9	41.8	73.32	0.34	
X	G	2.0	28.73	0.4741	2.914	2.0	1.1	97.1	65.0	75.08	0.26	
X	H	3.0	29.75	0.4869	2.350	2.0	1.0	97.8	88.8	78.19	0.24	
	I	4.0	31.83	1.026	2.065	0.6	0.50	98.3	95.7	84.02	0.81	
	J	5.0	34.15	1.374	3.068	0.2	0.37	97.7	97.6	89.4	3.3	
X	K	8.0	45.15	2.842	4.957	0.1	0.18	97.3	99.1	116.9	5.2	
X	L	15.0	53.99	2.973	7.804	0.1	0.17	96.2	100.0	137.5	9.5	
	Integrated age ± 1s			n=12		8.5	0.41		K2O=1.72%	74.62	0.18	
	Plateau ± 1s		steps I-J	n=2	MSWD=2.55	0.744			8.8	84.33	1.250	
	H15-35B, Biotite, 1.31 mg, J=0.0015393±0.02%, IC=0.9924642±0.0020102, NM-303C, Lab#=66835-01											
X	A	0.5	39.16	-0.0318	108.8	0.5	-	17.9	1.2	19.69	0.75	
X	B	0.8	32.38	0.0420	46.74	1.4	12.1	57.3	4.4	51.59	0.36	
X	C	1.0	33.14	0.0464	29.01	1.5	11.0	74.1	7.9	67.97	0.32	
X	D	1.5	33.07	0.0303	23.41	2.7	16.9	79.1	14.0	72.26	0.21	
X	E	2.0	33.62	0.0271	20.09	3.8	18.8	82.3	22.7	76.38	0.16	
X	F	2.5	34.34	0.0246	21.21	4.1	20.7	81.8	32.1	77.44	0.16	
X	G	3.0	33.86	0.0225	16.74	4.3	22.7	85.4	42.0	79.71	0.14	
X	H	3.5	33.60	0.0123	13.35	4.6	41.5	88.3	52.6	81.70	0.14	
	I	5.0	33.42	0.0133	10.64	9.6	38.2	90.6	74.6	83.379	0.077	
	J	7.0	33.42	0.0268	11.89	7.7	19.0	89.5	92.3	82.388	0.087	
X	K	15.0	33.76	0.0385	20.62	3.4	13.3	82.0	100.0	76.35	0.18	
	Integrated age ± 1s			n=11		43.4	21.9		K2O=8.27%	77.964	0.049	
	Plateau ± 1s		steps I-J	n=2	MSWD=73.2	17.235			39.7	82.94	0.49	
	H17-23, Muscovite, 6.53 mg, J=0.0015471±0.02%, IC=0.9983056±0.0003725, NM-303C, Lab#=66820-01											
X	A	400	1189.4	0.3417	3635.7	0.2	1.5	9.7	0.2	299.9	8.8	20
X	B	450	269.3	0.4070	714.4	0.1	1.3	21.6	0.3	158.0	7.1	20
X	C	500	109.9	0.3624	244.2	0.2	1.4	34.3	0.4	103.9	3.6	20
X	D	540	50.72	0.6645	90.67	0.5	0.77	47.3	0.8	66.7	1.0	20
X	E	570	36.33	0.7693	43.65	0.7	0.66	64.7	1.4	65.39	0.73	20

	ID	Power/Temp (Watts/°C)	$^{40}Ar/^{39}Ar$	$^{37}Ar/^{39}Ar$	$^{36}Ar/^{39}Ar$ (x 10^{-3})	$^{39}Ar_K$ (x 10^{-15} mol)	K/Ca	$^{40}Ar^*$ (%)	^{39}Ar (%)	Age (Ma)	±1s (Ma)	Time (min)
X	F	600	32.53	0.4824	30.99	1.0	1.1	72.0	2.1	65.14	0.50	20
X	G	630	31.51	0.2235	28.02	1.4	2.3	73.8	3.2	64.68	0.34	20
X	H	650	30.68	0.1643	24.27	1.4	3.1	76.7	4.3	65.44	0.34	20
X	I	680	30.93	0.1336	22.01	2.3	3.8	79.0	6.1	67.94	0.22	20
X	J	700	30.09	0.0995	18.30	2.6	5.1	82.0	8.2	68.61	0.20	20
X	K	710	29.07	0.0860	13.26	2.5	5.9	86.5	10.2	69.89	0.21	20
X	L	720	29.35	0.0926	13.49	2.5	5.5	86.4	12.2	70.48	0.21	20
X	M	730	28.73	0.0605	10.98	2.8	8.4	88.7	14.5	70.80	0.18	20
X	N	740	28.29	0.0575	9.633	2.9	8.9	90.0	16.8	70.69	0.16	20
X	O	750	28.41	0.0430	9.556	3.3	11.9	90.1	19.5	71.08	0.14	20
X	P	760	28.54	0.0385	9.619	3.6	13.2	90.1	22.3	71.37	0.15	20
X	Q	770	28.99	0.0331	10.10	4.1	15.4	89.7	25.6	72.22	0.14	20
X	R	780	28.25	0.0249	7.605	4.6	20.5	92.1	29.3	72.20	0.11	20
X	S	790	28.35	0.0349	7.072	4.8	14.6	92.6	33.1	72.91	0.11	20
X	T	800	28.09	0.0236	6.165	4.8	21.6	93.5	36.9	72.93	0.11	20
X	U	810	28.05	0.0310	5.867	4.7	16.5	93.8	40.7	73.05	0.12	20
X	V	820	28.35	0.0361	6.088	4.6	14.1	93.7	44.4	73.69	0.12	20
X	W	840	28.49	0.0394	6.178	5.6	12.9	93.6	48.9	74.008	0.094	20
X	X	860	28.58	0.0349	6.331	6.4	14.6	93.5	54.0	74.123	0.089	20
X	Y	880	28.73	0.0334	6.703	6.5	15.3	93.1	59.3	74.226	0.090	20
X	Z	900	29.15	0.0354	7.240	5.7	14.4	92.7	63.8	74.942	0.100	20
X	AA	920	29.51	0.0405	7.750	5.2	12.6	92.2	68.0	75.51	0.11	20
X	AB	950	29.71	0.0551	7.641	6.0	9.3	92.4	72.9	76.158	0.093	20
X	AC	1000	29.40	0.0541	7.036	10.7	9.4	92.9	81.4	75.790	0.062	20
	AD	1050	29.28	0.0304	5.238	15.3	16.8	94.7	93.7	76.909	0.046	20
	AE	1100	30.24	0.0335	5.297	1.5	15.2	94.8	94.9	79.48	0.32	3
	AF	1200	34.09	0.3451	22.49	2.5	1.5	80.6	96.9	76.20	0.26	3
	AG	1600	64.73	0.5181	124.2	3.9	0.98	43.4	100.0	77.82	0.32	3
Integrated age ± 1s				n=33		125.0	6.4		K2O=4.75%	74.277	0.032	
Plateau ± 1s			steps AD-AG	n=4	MSWD=26.82	23.239			18.6	76.96	0.23	
H18-23M, Muscovite, 7.89 mg, J=0.0015461±0.02%, IC=0.9983056±0.0003725, NM-303C, Lab#=66822-01												
X	A	400	242.5	-0.0056	792.7	0.4	-	3.4	0.1	23.1	2.1	20
X	B	450	53.44	0.1613	135.3	0.2	3.2	25.2	0.2	37.8	1.8	20
X	C	500	34.94	0.0523	52.46	0.3	9.8	55.6	0.3	54.2	1.4	20
X	D	540	27.84	0.0907	23.22	0.4	5.6	75.4	0.5	58.44	0.86	20
X	E	570	26.24	-0.0066	15.23	0.6	-	82.8	0.7	60.52	0.66	20
X	F	600	26.62	0.0070	14.78	0.8	72.7	83.6	0.9	61.92	0.50	20
X	G	630	26.59	0.0459	13.97	1.1	11.1	84.5	1.4	62.49	0.37	20
X	H	650	26.86	-0.0034	14.78	1.3	-	83.7	1.8	62.58	0.35	20
X	I	680	27.33	-0.0142	15.83	2.0	-	82.9	2.5	63.00	0.23	20
X	J	700	26.71	0.0167	12.51	2.3	30.6	86.2	3.3	63.99	0.21	20
X	K	710	26.14	0.0081	9.962	2.2	62.8	88.7	4.1	64.50	0.21	20
X	L	720	25.61	0.0130	7.170	2.4	39.3	91.7	5.0	65.31	0.18	20
X	M	730	25.51	0.0043	5.959	2.8	119.8	93.1	6.0	66.02	0.18	20
X	N	740	25.05	0.0072	4.527	3.3	71.0	94.7	7.1	65.91	0.14	20
X	O	750	25.03	0.0072	3.865	4.0	71.1	95.4	8.6	66.38	0.11	20
X	P	760	24.76	0.0111	2.674	5.0	45.9	96.8	10.3	66.623	0.089	20
X	Q	770	24.83	0.0038	2.421	6.3	135.5	97.1	12.6	67.014	0.078	20
X	R	780	25.00	0.0062	2.822	7.5	82.9	96.7	15.3	67.144	0.066	20
X	S	790	24.94	0.0046	2.225	8.6	110.4	97.4	18.4	67.453	0.057	20
X	T	800	24.99	0.0005	1.199	11.6	1076.8	98.6	22.6	68.428	0.044	20
X	U	810	24.81	0.0038	0.8938	12.3	134.0	98.9	27.0	68.191	0.040	20
X	V	820	33.43	0.0069	32.54	11.5	73.9	71.2	31.1	66.178	0.085	20
X	W	840	24.43	0.0036	0.7526	14.7	140.6	99.1	36.4	67.262	0.036	20
X	X	860	24.35	0.0054	0.8837	13.8	95.2	98.9	41.4	66.928	0.040	20
X	Y	880	24.37	0.0008	1.007	14.3	655.1	98.8	46.5	66.892	0.036	20
X	Z	900	24.38	0.0004	1.038	13.7	1440.0	98.7	51.4	66.884	0.038	20
X	AA	920	24.46	-0.0021	1.042	12.4	-	98.7	55.9	67.114	0.041	20
X	AB	950	24.67	0.0028	1.055	13.9	179.9	98.7	60.9	67.672	0.040	20
X	AC	1000	24.98	0.0020	1.148	21.1	250.6	98.6	68.4	68.437	0.028	20
X	AD	1050	25.24	0.0006	0.8652	42.2	858.9	99.0	83.6	69.367	0.017	20
X	AE	1100	25.38	-0.0022	0.5940	10.2	-	99.3	87.2	69.974	0.051	3
X	AF	1200	25.36	0.0015	0.6202	15.7	348.0	99.3	92.9	69.902	0.033	3
	AG	1550	37.19	0.0033	39.40	19.8	156.7	68.7	100.0	70.923	0.067	3
Integrated age ± 1s				n=33		278.5	169.2		K2O=8.77%	67.860	0.020	
Terminal age ± 1s			step AG	n=1		19.850			7.1	70.923	0.067	
H18-23K, K-Feldspar, 14.38 mg, J=0.0015142±0.03%, IC=0.9989127±0.0007362, NM-303F, Lab#=66866-01												
X	A	450	167.6	0.0036	341.5	2.8	141.4	39.8	0.4	176.11	0.59	10
X	B	450	24.86	-0.0081	46.76	2.3	-	44.4	0.7	30.35	0.21	20
X	C	500	15.77	0.0088	15.64	5.3	58.0	70.7	1.5	30.633	0.084	10
X	D	500	13.40	0.0010	7.355	8.8	505.4	83.8	2.7	30.855	0.048	20
X	E	550	14.08	0.0015	4.848	12.8	350.8	89.8	4.6	34.711	0.032	10
X	F	550	13.59	0.0042	3.013	16.8	120.7	93.5	7.0	34.863	0.025	20
X	G	600	13.78	0.0024	2.479	20.7	210.2	94.7	9.9	35.813	0.022	10
X	H	600	13.43	0.0002	1.304	24.7	2831.3	97.1	13.4	35.795	0.016	20
X	I	650	13.71	0.0007	1.380	24.7	710.5	97.0	17.0	36.500	0.016	10
X	J	650	13.64	0.0039	0.8029	29.6	131.1	98.3	21.2	36.786	0.015	20
X	K	700	13.94	0.0010	1.131	24.4	514.3	97.6	24.7	37.341	0.017	10
X	L	700	13.96	0.0029	0.7864	23.6	177.2	98.3	28.0	37.647	0.016	20
X	M	750	14.20	0.0002	0.9037	16.5	2700.9	98.1	30.4	38.205	0.021	10
X	N	750	14.33	0.0005	1.146	19.3	966.8	97.6	33.1	38.378	0.020	20
X	O	800	14.41	0.0035	0.8766	15.5	145.9	98.2	35.4	38.797	0.024	10
X	P	800	14.44	0.0005	0.7886	19.5	1050.2	98.4	38.1	38.951	0.019	20
X	Q	850	14.67	-0.0027	1.051	16.3	-	97.9	40.5	39.380	0.024	10
X	R	850	14.64	0.0037	0.7404	21.5	137.9	98.5	43.5	39.542	0.017	20
X	S	900	15.05	0.0022	1.473	14.3	234.9	97.1	45.6	40.079	0.027	10
X	T	900	15.12	0.0012	1.124	14.4	433.5	97.8	47.6	40.539	0.026	20
X	U	950	15.72	0.0032	2.531	10.2	157.6	95.2	49.1	41.026	0.038	10
X	V	950	16.01	0.0072	2.807	10.7	71.2	94.8	50.6	41.593	0.036	20

	ID	Power/Temp (Watts/°C)	$^{40}Ar/^{39}Ar$	$^{37}Ar/^{39}Ar$	$^{36}Ar/^{39}Ar$ (x 10^{-3})	$^{39}Ar_K$ (x 10^{-15} mol)	K/Ca	$^{40}Ar^*$ (%)	^{39}Ar (%)	Age (Ma)	±1s (Ma)	Time (min)
X	W	1000	16.52	0.0097	4.240	9.5	52.6	92.4	52.0	41.837	0.044	10
X	X	1000	16.78	0.0051	4.389	12.3	100.4	92.3	53.7	42.429	0.036	20
X	Y	1050	17.38	0.0120	5.528	10.5	42.5	90.6	55.2	43.146	0.043	10
X	Z	1050	17.30	0.0104	4.848	15.0	49.0	91.7	57.4	43.473	0.034	20
X	BA	1100	17.94	0.0083	6.148	13.0	61.5	89.9	59.2	44.141	0.042	10
X	BB	1100	17.80	0.0057	6.032	19.9	89.5	90.0	62.1	43.865	0.030	20
X	BC	1100	17.73	0.0027	5.631	37.3	188.1	90.6	67.4	44.009	0.022	60
X	BD	1100	18.14	0.0021	6.604	42.9	243.2	89.2	73.5	44.337	0.021	120
	BG	1250	18.93	0.0004	6.294	150.5	1139.6	90.2	95.0	46.721	0.013	4
	BH	1450	28.31	0.0026	38.17	31.0	195.9	60.2	99.4	46.617	0.057	4
	BI	1600	213.6	-0.0130	668.1	4.3	-	7.6	100.0	44.36	0.71	4
Integrated age ± 1s				n=33		701.0	219.7		K2O=12.37%	41.917	0.013	
Plateau ± 1s			steps BG-BI	n=3	MSWD=7.16	185.843			26.5	46.72	0.036	
H18-24, Muscovite, 4.41 mg, J=0.0015295±0.02%, IC=0.9983056±0.0003725, NM-303C, Lab#=66824-01												
X	A	400	213.7	0.1918	693.0	0.2	2.7	4.2	0.2	24.7	2.6	20
X	B	450	101.6	-0.1154	289.5	0.1	-	15.8	0.3	44.5	4.8	20
X	C	500	38.57	0.0901	68.73	0.2	5.7	47.4	0.4	50.5	2.0	20
X	D	540	28.53	0.0557	32.22	0.2	9.2	66.6	0.5	52.5	1.9	20
X	E	570	26.97	0.0967	17.89	0.4	5.3	80.4	0.9	59.74	0.97	20
X	F	600	24.92	0.1003	11.27	0.5	5.1	86.7	1.3	59.49	0.77	20
X	G	630	23.71	-0.0175	7.370	0.7	-	90.8	1.9	59.32	0.51	20
X	H	650	23.90	0.0168	4.980	0.8	30.4	93.8	2.6	61.73	0.53	20
X	I	680	23.98	0.0259	4.684	1.2	19.7	94.2	3.6	62.19	0.33	20
X	J	700	23.57	0.0367	3.627	1.3	13.9	95.5	4.6	61.93	0.32	20
X	K	710	23.85	0.0108	3.646	1.1	47.4	95.5	5.6	62.67	0.35	20
X	L	720	23.95	0.0179	3.321	1.1	28.5	95.9	6.5	63.20	0.37	20
X	M	730	24.37	-0.0055	3.974	1.2	-	95.2	7.6	63.80	0.32	20
X	N	740	25.47	-0.0044	5.101	1.4	-	94.1	8.8	65.88	0.31	20
X	O	750	25.39	0.0405	4.438	1.7	12.6	94.8	10.3	66.22	0.25	20
X	P	760	25.63	0.0101	3.254	2.0	50.3	96.3	11.9	67.80	0.23	20
X	Q	770	25.97	-0.0204	3.504	2.3	-	96.0	13.9	68.51	0.20	20
X	R	780	25.89	0.0022	2.646	2.7	229.2	97.0	16.2	68.97	0.16	20
X	S	790	25.97	-0.0029	2.036	3.2	-	97.7	18.9	69.68	0.14	20
X	T	800	25.84	-0.0091	1.452	3.5	-	98.3	21.8	69.78	0.12	20
X	U	810	25.83	-0.0099	1.292	3.7	-	98.5	25.0	69.88	0.13	20
X	V	820	25.83	0.0018	1.273	3.8	288.8	98.5	28.2	69.91	0.12	20
X	W	840	25.57	-0.0011	1.097	5.8	-	98.7	33.0	69.346	0.088	20
X	X	860	25.31	0.0022	1.016	7.1	227.4	98.8	39.1	68.717	0.070	20
X	Y	880	25.10	-0.0024	1.188	9.2	-	98.6	46.8	68.008	0.054	20
X	Z	900	25.33	-0.0034	1.188	10.6	-	98.6	55.8	68.637	0.048	20
X	AA	920	25.73	0.0020	1.114	10.0	252.8	98.7	64.3	69.757	0.051	20
X	AB	950	26.18	0.0001	1.104	10.9	5353.7	98.8	73.5	70.983	0.050	20
X	AC	1000	26.73	-0.0020	0.9976	13.8	-	98.9	85.1	72.563	0.039	20
X	AD	1050	27.35	0.0040	1.136	9.6	126.6	98.8	93.2	74.100	0.057	20
X	AE	1100	27.81	0.0097	1.917	1.1	52.5	98.0	94.2	74.73	0.42	3
X	AF	1200	28.73	0.0382	5.048	1.3	13.3	94.8	95.3	74.73	0.34	3
	AG	1600	67.75	0.0222	135.3	5.6	22.9	41.0	100.0	76.16	0.24	3
Integrated age ± 1s				n=33		118.2	155.1		K2O=6.73%	69.772	0.031	
Terminal age ± 1s			step AG	n=1		5.608			4.7	76.16	0.24	
H18-34, Muscovite, 3.05 mg, J=0.001507±0.02%, IC=0.9947317±0.000765, NM-303C, Lab#=66826-01												
X	A	0.4	348.0	1.228	762.3	0.2	0.42	35.3	0.6	311.1	7.2	
X	B	0.6	51.77	3.494	75.62	0.3	0.15	57.4	1.6	80.4	1.7	
X	C	0.8	29.90	3.033	22.77	0.7	0.17	78.3	3.5	63.61	0.61	
X	D	1.0	28.98	1.686	10.22	1.0	0.30	90.0	6.5	70.69	0.45	
X	E	1.2	28.35	0.6105	3.957	1.8	0.84	96.0	11.9	73.64	0.25	
X	F	1.5	28.20	0.1258	1.997	3.7	4.1	97.9	23.0	74.65	0.12	
X	G	2.0	28.18	0.0836	1.537	6.8	6.1	98.4	43.2	74.937	0.070	
X	H	3.0	28.96	0.1070	1.720	8.7	4.8	98.3	69.2	76.879	0.062	
X	I	4.0	34.08	0.2599	4.473	5.5	2.0	96.2	85.5	88.29	0.11	
	J	5.0	36.71	0.3204	5.471	2.1	1.6	95.7	91.9	94.43	0.25	
	K	6.0	36.85	0.3334	5.902	0.9	1.5	95.3	94.8	94.46	0.57	
	L	7.0	37.83	0.2797	5.757	0.7	1.8	95.6	97.0	97.13	0.72	
	M	8.0	38.32	0.2922	6.038	0.5	1.7	95.4	98.4	98.2	1.1	
X	N	15.0	44.81	0.5604	10.62	0.6	0.91	93.1	100.0	111.6	1.1	
Integrated age ± 1s				n=14		33.4	1.5		K2O=2.79%	82.072	0.061	
Plateau ± 1s			steps J-M	n=4	MSWD=7.23	4.286			12.8	94.80	0.579	
H18-40M, Muscovite, 4.27 mg, J=0.0015208±0.03%, IC=0.9983056±0.0003725, NM-303C, Lab#=66825-01												
X	A	500	30.56	-0.1586	32.14	0.2	-	68.9	0.2	57.7	1.5	20
X	B	540	25.92	0.1387	16.97	0.4	3.7	80.7	0.4	57.33	0.93	20
X	C	570	26.55	0.2422	13.47	0.5	2.1	85.1	0.8	61.84	0.80	20
X	D	600	25.97	0.2292	10.54	0.7	2.2	88.1	1.2	62.59	0.59	20
X	E	630	25.79	0.1793	7.705	1.0	2.8	91.2	1.9	64.37	0.44	20
X	F	650	26.57	0.0115	8.382	1.1	44.3	90.7	2.7	65.87	0.39	20
X	G	680	28.01	0.0020	10.87	1.7	260.9	88.5	3.9	67.77	0.28	20
X	H	700	28.56	-0.0170	10.86	2.0	-	88.8	5.3	69.25	0.24	20
X	I	710	28.80	0.0015	9.060	1.7	338.3	90.7	6.5	71.31	0.26	20
X	J	720	28.72	0.0001	8.375	1.8	5606.6	91.4	7.7	71.64	0.29	20
X	K	730	28.76	0.0090	6.566	2.0	56.6	93.3	9.1	73.17	0.23	20
X	L	740	28.09	0.0096	5.132	2.4	52.9	94.6	10.8	72.51	0.20	20
X	M	750	27.66	0.0102	3.846	2.8	50.1	95.9	12.7	72.39	0.18	20
X	N	760	27.74	0.0069	4.095	3.3	74.4	95.6	15.1	72.41	0.14	20
X	O	770	27.45	0.0071	3.494	3.8	71.8	96.2	17.7	72.11	0.12	20
X	P	780	27.45	0.0040	2.858	4.4	126.6	96.9	20.8	72.61	0.11	20
X	Q	790	27.91	-0.0011	2.579	7.4	-	97.3	26.0	74.053	0.073	20
X	R	800	27.41	0.0011	1.281	7.9	447.9	98.6	31.6	73.742	0.067	20
X	S	810	27.08	0.0061	1.234	6.5	83.4	98.7	36.1	72.898	0.080	20
X	T	820	26.91	0.0101	1.256	5.8	50.4	98.6	40.2	72.425	0.082	20
X	U	840	26.83	0.0003	1.466	6.9	1679.4	98.4	45.1	72.038	0.075	20

	ID	Power/Temp (Watts/°C)	$^{40}Ar/^{39}Ar$	$^{37}Ar/^{39}Ar$	$^{36}Ar/^{39}Ar$ (x 10^{-3})	$^{39}Ar_K$ (x 10^{-15} mol)	K/Ca	$^{40}Ar^*$ (%)	^{39}Ar (%)	Age (Ma)	±1s (Ma)	Time (min)
X	V	860	26.79	0.0002	1.434	7.0	3027.9	98.4	50.0	71.966	0.076	20
X	W	880	26.76	0.0054	1.717	7.1	93.6	98.1	54.9	71.673	0.069	20
X	X	900	26.94	0.0034	2.255	6.2	150.3	97.5	59.3	71.710	0.079	20
X	Y	920	27.07	0.0032	2.144	5.8	157.9	97.7	63.3	72.159	0.088	20
X	Z	950	27.37	-0.0020	2.256	5.9	-	97.6	67.5	72.877	0.089	20
X	AA	1000	27.80	-0.0005	2.403	9.6	-	97.4	74.3	73.897	0.058	20
X	AB	1050	28.09	0.0044	2.136	13.6	115.4	97.8	83.8	74.900	0.043	20
X	AC	1100	28.32	0.0041	2.619	2.6	125.6	97.3	85.6	75.13	0.21	3
	AD	1200	28.30	0.0015	1.720	14.6	350.7	98.2	95.8	75.789	0.039	3
	AE	1600	53.09	0.0052	83.92	5.9	98.0	53.3	100.0	77.12	0.18	3
Integrated age ± 1s				n=31		142.3	82.9		K2O=8.41%	73.061	0.027	
Plateau ± 1s			steps AD-AE	n=2	MSWD=50.7	20.482			14.4	75.85	0.27	
H18-40K, K-Feldspar, 16.07 mg, J=0.0015541±0.02%, IC=0.9989127±0.0007362, NM-303F, Lab#=66862-01												
X	A	450	274.5	0.0149	734.9	2.8	34.2	20.9	0.3	156.34	0.85	10
X	B	450	25.58	-0.0099	37.24	4.8	-	57.0	0.9	41.01	0.14	20
X	C	500	16.56	0.0481	15.87	0.8	10.6	71.7	1.0	33.47	0.35	10
X	D	500	13.49	0.0050	4.853	14.9	102.3	89.4	2.8	33.982	0.032	20
X	E	550	13.56	0.0045	3.357	15.5	114.1	92.7	4.7	35.399	0.028	10
X	F	550	13.08	0.0051	1.761	22.2	100.0	96.0	7.4	35.398	0.020	20
X	G	600	13.53	0.0079	1.680	21.6	64.3	96.3	10.0	36.708	0.019	10
X	H	600	13.35	0.0051	1.038	26.7	100.9	97.7	13.2	36.737	0.016	20
X	I	650	13.64	0.0016	1.030	19.9	319.9	97.8	15.6	37.561	0.019	10
X	J	650	13.66	0.0007	0.8374	28.8	742.4	98.2	19.1	37.772	0.014	20
X	K	700	13.87	0.0052	0.8360	18.1	98.0	98.2	21.3	38.350	0.021	10
X	L	700	13.90	-0.0015	0.6047	23.9	-	98.7	24.1	38.614	0.016	20
X	M	750	14.08	0.0024	0.5719	16.7	215.0	98.8	26.2	39.146	0.020	10
X	N	750	14.19	-0.0004	0.5030	20.5	-	99.0	28.6	39.526	0.017	20
X	O	800	14.44	-0.0004	0.6495	17.0	-	98.7	30.7	40.097	0.023	10
X	P	800	14.53	0.0022	0.5194	21.1	235.8	98.9	33.2	40.458	0.017	20
X	Q	850	14.76	0.0017	0.6326	18.3	291.8	98.7	35.4	41.001	0.020	10
X	R	850	14.87	-0.0031	0.4787	22.5	-	99.0	38.2	41.416	0.018	20
X	S	900	15.12	0.0047	0.6913	17.0	108.5	98.7	40.2	41.946	0.021	10
X	T	900	15.30	0.0010	0.5679	23.1	527.5	98.9	43.0	42.539	0.018	20
X	U	950	15.77	0.0035	1.001	16.8	144.9	98.1	45.0	43.506	0.024	10
X	V	950	16.12	0.0008	1.283	21.0	655.2	97.6	47.6	44.242	0.022	20
X	W	1000	16.87	0.0039	2.460	14.6	131.4	95.7	49.3	45.359	0.031	10
X	X	1000	16.82	0.0031	1.350	20.4	164.1	97.6	51.8	46.122	0.023	20
X	Y	1050	17.72	0.0044	2.046	16.4	117.2	96.6	53.8	48.061	0.027	10
X	Z	1050	17.81	0.0016	2.074	22.9	320.1	96.6	56.5	48.293	0.023	20
X	BA	1100	18.24	0.0047	2.538	19.3	108.4	95.9	58.9	49.102	0.027	10
X	BB	1100	18.14	0.0030	2.410	27.9	168.1	96.1	62.2	48.927	0.020	20
X	BC	1100	18.39	0.0022	3.071	51.2	230.9	95.1	68.4	49.058	0.016	60
X	BD	1100	19.09	0.0000	4.775	55.8	22575	92.6	75.1	49.621	0.017	120
X	BE	1150	20.17	-0.0029	6.311	4.0	-	90.8	75.6	51.34	0.10	4
X	BF	1200	19.52	-0.0017	5.553	26.0	-	91.6	78.8	50.174	0.027	4
	BG	1250	20.73	0.0006	7.676	109.1	792.7	89.1	91.9	51.776	0.015	4
	BH	1450	26.42	0.0018	28.34	62.8	291.4	68.3	99.5	50.622	0.035	4
	BI	1600	366.4	0.0103	1188.4	4.1	49.3	4.1	100.0	42.7	1.1	4
Integrated age ± 1s				n=35		828.5	264.6		K2O=12.74%	45.123	0.012	
Plateau ± 1s			steps BG-BI	n=3	MSWD=482	175.981			21.2	51.59	0.31	
H18-627B, Muscovite 1.61 mg, J=0.0014933±0.02%, IC=0.9947317±0.000765, NM-303C, Lab#=66828-01												
X	A	0.4	57.32	1.574	166.6	0.2	0.32	14.3	1.8	22.4	1.3	
X	B	0.6	28.89	3.624	38.61	0.2	0.14	61.5	3.4	48.0	1.3	
X	C	0.8	29.50	2.637	18.79	0.5	0.19	81.9	6.7	65.00	0.80	
X	D	1.0	29.09	2.082	9.137	0.6	0.25	91.3	11.5	71.28	0.60	
X	E	1.2	28.53	1.183	4.705	0.9	0.43	95.5	18.2	73.04	0.44	
X	F	1.5	28.41	0.5381	2.797	1.6	0.95	97.2	29.7	74.02	0.27	
X	G	2.0	29.02	0.3304	2.414	2.7	1.5	97.6	49.1	75.87	0.16	
	H	3.0	31.09	0.3037	2.562	3.3	1.7	97.6	73.4	81.17	0.16	
	I	4.0	30.02	0.4237	2.421	2.1	1.2	97.7	88.4	78.51	0.23	
	J	5.0	31.00	0.5835	5.276	0.9	0.87	95.1	95.1	78.92	0.57	
	K	6.0	31.64	0.7522	4.774	0.3	0.68	95.7	97.4	81.0	1.6	
	L	7.0	33.13	0.5896	3.754	0.2	0.87	96.8	98.8	85.7	2.5	
	M	8.0	36.67	1.321	3.281	0.1	0.39	97.6	99.3	95.4	8.0	
	N	15.0	56.07	0.7701	25.46	0.1	0.66	86.7	100.0	128.3	7.0	
Integrated age ± 1s				n=14		13.7	0.74		K2O=2.19%	76.13	0.12	
Plateau ± 1s			steps H-N	n=7	MSWD=25.86	6.984			50.9	80.29	0.633	
H18-627B, Biotite, 1.43 mg, J=0.0015578±0.04%, IC=0.9924642±0.0020102, NM-303D, Lab#=66836-01												
X	A	0.5	35.09	0.0203	90.55	0.7	25.2	23.7	1.3	23.60	0.59	
X	B	0.8	29.67	0.0510	27.34	1.3	10.0	72.8	3.9	60.55	0.34	
X	C	1.0	33.01	0.0310	14.92	1.7	16.5	86.7	7.2	79.80	0.31	
X	D	1.5	33.73	0.0375	12.30	3.3	13.6	89.2	13.6	83.88	0.17	
X	E	2.0	34.19	0.0244	11.16	4.4	20.9	90.4	22.2	86.03	0.14	
X	F	2.5	34.34	0.0238	10.32	4.6	21.5	91.1	31.2	87.12	0.14	
X	G	3.0	34.51	0.0130	9.999	5.0	39.3	91.4	41.0	87.85	0.13	
X	H	3.5	34.67	0.0106	8.243	5.4	48.3	93.0	51.6	89.68	0.12	
	I	5.0	34.77	0.0277	6.462	10.0	18.4	94.5	71.0	91.400	0.071	
	J	7.0	35.88	0.0207	9.203	11.6	24.7	92.4	93.7	92.210	0.065	
	K	9.0	35.69	0.0246	7.194	2.3	20.7	94.0	98.1	93.29	0.27	
	L	15.0	34.34	0.0765	9.671	1.0	6.7	91.7	100.0	87.66	0.55	
Integrated age ± 1s				n=12		51.1	21.0		K2O=8.82%	87.700	0.055	
Plateau ± 1s			steps I-L	n=4	MSWD=52.45	24.772			48.4	91.85	0.344	
H18-648, Biotite, .19 mg, J=0.0015319±0.02%, IC=0.9924642±0.0020102, NM-303C, Lab#=66834-01												
X	A	0.5	93.21	0.3673	165.1	0.2	1.4	47.7	2.2	120.6	4.4	
X	B	0.8	65.45	0.6584	24.85	0.3	0.77	88.9	7.0	156.3	2.8	
X	C	1.0	61.96	0.3286	10.49	0.4	1.6	95.0	12.2	158.1	2.4	
X	D	1.5	57.76	0.0771	8.051	0.7	6.6	95.9	21.8	149.1	1.2	

	ID	Power/Temp (Watts/°C)	$^{40}Ar/^{39}Ar$	$^{37}Ar/^{39}Ar$	$^{36}Ar/^{39}Ar$ (x 10^{-3})	$^{39}Ar_K$ (x 10^{-15} mol)	K/Ca	$^{40}Ar^*$ (%)	^{39}Ar (%)	Age (Ma)	±1s (Ma)	Time (min)
X	E	2.0	53.01	0.0348	7.290	0.7	14.6	95.9	31.9	137.3	1.1	
X	F	2.5	50.51	0.0651	6.567	0.7	7.8	96.2	41.3	131.4	1.2	
X	G	3.0	49.95	0.0271	6.438	0.6	18.8	96.2	49.7	130.0	1.3	
X	H	5.0	48.47	0.3423	4.954	1.5	1.5	97.0	71.8	127.39	0.46	
X	I	7.0	49.92	0.1943	3.029	1.0	2.6	98.2	85.6	132.60	0.81	
X	J	15.0	52.04	0.2484	2.135	1.0	2.1	98.8	100.0	138.83	0.82	
Integrated age ± 1s				n=10		7.0	2.4		K2O=9.23%	136.31	0.36	
No Plateau												
010719-4, Muscovite, 2.01 mg, J=0.0037056±0.01%, IC=1.029171±0.0012136, NM-309F, Lab#=67511-01												
X	A	455	34.55	0.0430	107.0	1.1	11.9	8.5	0.9	19.8	1.1	20
X	B	500	9.767	0.0049	13.01	0.8	103.9	60.7	1.5	39.75	0.70	20
X	C	550	8.661	0.0117	5.854	1.4	43.7	80.0	2.6	46.42	0.38	20
X	D	600	8.550	0.0178	4.248	2.7	28.6	85.3	4.8	48.83	0.20	20
X	E	650	8.262	0.0092	2.380	4.5	55.2	91.5	8.3	50.57	0.13	20
X	F	680	8.360	0.0017	1.280	4.5	296.0	95.5	11.9	53.36	0.11	20
X	G	695	8.516	0.0023	0.8500	3.7	225.9	97.1	14.8	55.22	0.14	20
X	H	710	8.645	-0.0074	0.7302	3.6	-	97.5	17.7	56.30	0.14	20
X	I	720	8.736	0.0031	0.7641	3.4	165.7	97.4	20.3	56.83	0.15	20
X	J	730	8.898	0.0103	0.5891	3.1	49.6	98.1	22.8	58.24	0.16	20
X	K	740	8.994	0.0149	0.6153	3.3	34.2	98.0	25.3	58.83	0.15	20
X	L	750	9.095	0.0133	0.5946	3.4	38.3	98.1	28.0	59.53	0.15	20
X	M	755	9.208	-0.0019	0.6145	3.2	-	98.0	30.5	60.22	0.16	20
X	N	760	9.298	-0.0032	0.7081	2.9	-	97.7	32.8	60.63	0.18	20
X	O	765	9.351	0.0047	0.6085	2.8	109.2	98.1	35.0	61.18	0.19	20
X	P	770	9.374	0.0029	0.5946	2.7	173.3	98.1	37.1	61.36	0.19	20
X	Q	780	9.489	0.0010	0.5670	2.9	514.0	98.2	39.4	62.16	0.18	20
X	R	790	9.600	0.0064	0.6085	3.0	79.6	98.1	41.7	62.81	0.17	20
X	S	800	9.661	0.0092	0.5930	3.4	55.4	98.2	44.4	63.24	0.15	20
X	T	820	9.783	0.0112	0.4908	4.6	45.6	98.5	48.1	64.24	0.11	20
X	U	840	10.01	0.0057	0.8103	5.8	89.5	97.6	52.6	65.136	0.100	20
X	V	860	10.14	0.0059	0.5600	6.8	86.8	98.4	58.0	66.435	0.085	20
X	W	890	10.19	0.0071	0.5701	9.2	71.6	98.4	65.3	66.737	0.066	20
X	X	920	10.26	0.0062	0.7579	10.6	82.7	97.8	73.6	66.828	0.062	20
X	Y	950	10.31	0.0103	0.5404	10.5	49.5	98.5	81.9	67.570	0.059	20
X	Z	980	10.52	0.0162	0.6223	8.0	31.4	98.3	88.2	68.781	0.080	20
X	AA	1010	10.83	0.0194	0.6858	6.0	26.2	98.1	92.9	70.70	0.11	20
X	AB	1030	11.20	0.0287	0.9299	3.9	17.8	97.6	96.0	72.63	0.15	20
	AC	1070	11.07	0.0571	-0.7515	0.7	8.9	102.0	96.5	75.06	0.76	3
	AD	1110	11.99	0.0808	1.928	1.4	6.3	95.3	97.6	75.89	0.44	3
	AE	1150	11.64	0.0679	0.7655	3.0	7.5	98.1	100.0	75.86	0.19	3
Integrated age ± 1s				n=31		126.9	45.5		K2O=6.55%	62.934	0.027	
Plateau ± 1s			steps AC-AE	n=3	MSWD=0.54	5.108			4.02416497	75.8230628	0.17369023	
020719-5, Biotite, J=0.0037389±0.01%, IC=1.03261±0.0045346, NM-309D, Lab#=67488-01												
X	A	0.5	17.84	0.0326	46.03	5.1	15.6	23.8	24.3	28.79	0.54	
X	B	0.8	12.54	0.0298	23.61	4.5	17.1	44.4	45.7	37.69	0.34	
	C	1.0	12.72	0.0260	21.42	2.0	19.6	50.3	55.0	43.24	0.45	
	D	1.5	12.73	0.0345	21.20	2.6	14.8	50.8	67.3	43.74	0.39	
	E	1.8	12.39	0.0189	19.91	1.7	27.1	52.5	75.5	43.99	0.46	
	F	2.0	12.28	0.0110	18.82	0.9	46.3	54.7	80.0	45.39	0.70	
	G	2.5	12.42	0.0508	20.35	1.1	10.0	51.6	85.2	43.33	0.58	
	H	2.8	11.54	0.0512	18.58	0.5	10.0	52.4	87.5	40.95	0.99	
	I	3.0	11.54	0.0492	18.84	0.4	10.4	51.8	89.1	40.5	1.3	
	J	3.5	11.64	0.0661	18.24	0.4	7.7	53.7	91.0	42.3	1.2	
	K	6.0	12.63	0.0222	18.38	1.2	23.0	57.0	96.5	48.62	0.63	
	L	12.0	13.01	-0.0393	16.48	0.7	-	62.5	100.0	54.82	0.77	
Integrated age ± 1s				n=12		21.1	17.8			39.36	0.18	
Plateau ± 1s			steps C-L	n=10	MSWD=29.44	11.431			54.3	44.66	1.026	
020719-5, Muscovite, 2.11 mg, J=0.0036975±0.02%, IC=1.029742±0.0011289, NM-309F, Lab#=67508-01												
X	A	455	70.00	0.0789	214.0	1.3	6.5	9.7	1.1	45.2	1.7	20
X	B	500	16.64	0.1284	34.86	0.9	4.0	38.2	1.8	42.52	0.94	20
X	C	550	13.24	0.1287	22.84	1.5	4.0	49.1	3.1	43.47	0.58	20
X	D	600	11.10	0.0474	12.81	2.4	10.8	65.9	5.1	48.90	0.36	20
X	E	650	10.43	0.0274	7.715	3.1	18.6	78.2	7.6	54.34	0.26	20
X	F	680	10.62	0.0077	5.073	2.7	66.4	85.9	9.9	60.73	0.27	20
X	G	695	10.80	0.0382	3.452	2.2	13.3	90.6	11.8	65.05	0.31	20
X	H	710	11.00	0.0311	2.486	2.1	16.4	93.3	13.5	68.18	0.32	20
X	I	720	11.10	0.0168	2.074	2.1	30.3	94.5	15.2	69.62	0.32	20
X	J	730	11.17	0.0140	1.650	2.0	36.5	95.6	16.8	70.91	0.34	20
X	K	740	11.32	-0.0006	1.437	2.3	-	96.3	18.7	72.33	0.29	20
X	L	750	11.38	0.0173	1.266	2.5	29.5	96.7	20.7	73.04	0.28	20
X	M	755	11.47	0.0097	1.135	2.4	52.6	97.1	22.7	73.87	0.29	20
X	N	760	11.62	0.0134	1.292	2.4	38.0	96.7	24.7	74.52	0.29	20
X	O	765	11.60	0.0149	1.102	2.5	34.3	97.2	26.8	74.75	0.27	20
X	P	770	11.68	0.0056	0.9262	2.6	91.0	97.7	28.9	75.59	0.27	20
X	Q	780	11.78	-0.0037	0.8951	3.0	-	97.8	31.5	76.29	0.22	20
X	R	790	11.85	-0.0029	0.7916	3.9	-	98.0	34.7	76.94	0.18	20
X	S	800	11.85	0.0027	0.8209	4.5	187.7	98.0	38.4	76.95	0.16	20
X	T	820	11.91	0.0049	0.7217	6.4	103.8	98.2	43.7	77.48	0.12	20
X	U	840	11.88	0.0042	0.7006	7.4	121.6	98.3	49.9	77.32	0.10	20
X	V	860	11.88	-0.0003	0.7665	7.9	-	98.1	56.4	77.205	0.099	20
X	W	890	11.91	-0.0022	0.8185	9.5	-	98.0	64.4	77.333	0.083	20
X	X	920	11.98	-0.0013	0.9791	8.8	-	97.6	71.7	77.476	0.089	20
X	Y	950	12.07	0.0021	1.118	7.2	242.5	97.3	77.7	77.76	0.11	20
X	Z	980	12.14	0.0058	1.043	5.6	87.6	97.5	82.4	78.38	0.14	20
	AA	1030	12.24	-0.0018	0.9688	7.9	-	97.7	89.0	79.19	0.10	20
	AB	1070	12.17	0.0538	0.1977	1.5	9.5	99.6	90.2	80.25	0.44	3
	AC	1150	12.35	0.0024	0.7787	11.8	209.6	98.1	100.0	80.216	0.072	3
Integrated age ± 1s				n=29		120.5	53.1		K2O=5.93%	74.241	0.039	

	ID	Power/Temp (Watts/°C)	$^{40}Ar/^{39}Ar$	$^{37}Ar/^{39}Ar$	$^{36}Ar/^{39}Ar$ (x 10^{-3})	$^{39}Ar_K$ (x 10^{-15} mol)	K/Ca	$^{40}Ar^*$ (%)	^{39}Ar (%)	Age (Ma)	±1s (Ma)	Time (min)
	Plateau ± 1s		steps AA-AC	n=3	MSWD=35.24	21.239			17.6	79.87	0.344	
	020719-9, Muscovite, 10.92 mg, J=0.0037782±0.01%, IC=1.041266±0.0013036, NM-306E, Lab#=67311-01											
X	A	450	60.85	0.0622	196.6	3.6	8.2	4.6	0.3	19.1	1.1	20
X	B	500	13.71	0.1376	34.40	2.6	3.7	26.0	0.6	24.46	0.46	20
X	C	550	19.98	0.5760	55.11	4.9	0.89	18.7	1.1	25.68	0.46	20
X	D	600	10.62	0.7739	16.41	7.1	0.66	54.9	1.7	39.95	0.20	20
X	E	650	14.01	0.3942	21.70	9.4	1.3	54.5	2.6	52.06	0.21	20
X	F	680	14.16	0.0946	16.13	10.2	5.4	66.4	3.6	63.91	0.16	20
X	G	695	13.53	0.0264	10.88	9.5	19.3	76.3	4.5	70.01	0.15	20
X	H	710	13.51	0.0168	7.778	12.0	30.3	83.0	5.7	75.98	0.12	20
X	I	720	12.80	0.0044	4.675	13.4	116.1	89.2	7.0	77.315	0.093	20
X	J	730	19.19	0.0078	27.38	15.8	65.7	57.8	8.5	75.20	0.18	20
X	K	740	12.23	0.0088	2.466	18.9	57.7	94.0	10.3	77.896	0.064	20
X	L	750	12.05	0.0071	2.134	23.7	72.3	94.8	12.6	77.321	0.054	20
X	M	755	11.75	0.0048	1.682	22.1	106.9	95.8	14.7	76.243	0.053	20
X	N	760	11.66	0.0081	1.453	21.9	63.4	96.3	16.8	76.064	0.046	20
X	O	765	11.53	0.0049	1.147	22.9	104.6	97.1	19.0	75.820	0.045	20
X	P	770	11.55	0.0033	1.391	21.3	154.3	96.4	21.0	75.489	0.049	20
X	Q	780	11.55	-0.0016	1.291	26.5	-	96.7	23.5	75.668	0.044	20
X	R	790	11.48	0.0016	1.057	27.8	314.6	97.3	26.2	75.676	0.039	20
X	S	800	11.48	0.0007	0.8168	34.1	782.2	97.9	29.5	76.122	0.033	20
X	T	820	11.50	0.0017	0.6809	59.3	308.7	98.3	35.1	76.498	0.021	20
X	U	840	11.33	0.0036	0.6869	54.6	143.3	98.2	40.4	75.368	0.023	20
X	V	860	11.32	0.0012	0.9061	44.6	433.4	97.6	44.6	74.886	0.029	20
X	W	875	11.36	0.0016	1.097	36.5	317.4	97.1	48.1	74.792	0.032	20
X	X	890	11.41	0.0034	1.177	34.3	149.3	97.0	51.4	74.918	0.035	20
X	Y	905	11.41	0.0005	1.143	33.8	1011.1	97.0	54.7	75.042	0.034	20
X	Z	920	11.42	0.0015	1.046	31.1	345.3	97.3	57.6	75.286	0.036	20
X	AA	935	11.44	-0.0007	0.9689	32.2	-	97.5	60.7	75.557	0.035	20
X	AB	950	11.45	0.0004	0.8810	34.0	1356.6	97.7	64.0	75.779	0.034	20
X	AC	965	11.48	0.0000	0.8333	37.9	-	97.9	67.6	76.065	0.031	20
X	AD	980	11.50	0.0016	0.7944	40.1	323.0	98.0	71.4	76.269	0.029	20
X	AE	1000	11.56	0.0005	0.8281	48.1	1001.4	97.9	76.0	76.598	0.027	20
	AF	1030	11.60	0.0007	0.8532	72.6	767.0	97.8	83.0	76.877	0.022	20
	AG	1050	11.54	0.0011	0.5098	69.1	454.4	98.7	89.6	77.093	0.020	20
	AH	1070	11.47	-0.0008	0.0947	8.1	-	99.8	90.4	77.501	0.094	3
	AI	1100	11.57	0.0010	0.2709	11.6	503.0	99.3	91.5	77.818	0.071	3
	AJ	1150	11.49	0.0044	0.0864	27.7	116.8	99.8	94.2	77.595	0.033	3
	AK	1600	11.94	0.0011	1.625	61.0	479.2	96.0	100.0	77.601	0.027	3
	Integrated age ± 1s			n=37		1044	33.3		K2O=9.72%	75.006	0.013	
	Plateau ± 1s		steps AF-AK	n=6	MSWD=140	250.157			24.0	77.22	0.140	
	020719-13, Muscovite, 10.18 mg, J=0.0037856±0.01%, IC=1.033525±0.001543, NM-306E, Lab#=67312-01											
X	A	450	95.98	0.0346	295.7	2.2	14.8	9.0	0.2	58.6	1.7	20
X	B	500	12.41	0.0217	26.20	1.8	23.5	37.6	0.4	32.08	0.52	20
X	C	550	7.942	0.0212	9.420	3.3	24.0	65.0	0.7	35.41	0.24	20
X	D	600	9.827	0.0067	13.98	6.2	76.7	58.0	1.3	39.06	0.20	20
X	E	650	12.53	0.0033	20.24	10.6	153.7	52.2	2.3	44.80	0.18	20
X	F	680	12.26	0.0090	13.85	15.1	56.7	66.6	3.7	55.76	0.14	20
X	G	695	10.40	0.0034	4.497	13.8	151.2	87.2	5.0	61.811	0.083	20
X	H	710	10.76	0.0017	3.532	15.3	296.5	90.3	6.4	66.144	0.077	20
X	I	720	11.20	0.0018	3.570	16.4	284.2	90.6	8.0	69.014	0.085	20
X	J	730	11.05	-0.0007	2.158	19.6	-	94.2	9.8	70.771	0.080	20
X	K	740	11.01	0.0023	1.719	23.0	226.5	95.4	12.0	71.355	0.049	20
X	L	750	10.86	0.0033	1.061	28.1	156.9	97.1	14.6	71.684	0.039	20
X	M	755	10.77	0.0007	0.7460	26.5	719.6	98.0	17.1	71.669	0.036	20
X	N	760	10.72	0.0039	0.5532	27.3	131.4	98.5	19.7	71.746	0.034	20
X	O	765	10.72	0.0012	0.5479	25.7	426.2	98.5	22.1	71.721	0.037	20
X	P	770	10.67	0.0029	0.4402	24.4	177.0	98.8	24.4	71.634	0.036	20
X	Q	780	10.74	0.0004	0.5529	28.2	1260.7	98.5	27.0	71.831	0.035	20
X	R	790	10.69	0.0006	0.3999	29.6	897.9	98.9	29.8	71.850	0.032	20
X	S	800	10.64	0.0018	0.3514	31.8	289.1	99.0	32.8	71.615	0.031	20
X	T	810	10.57	-0.0001	0.3538	29.9	-	99.0	35.6	71.146	0.031	20
X	U	820	10.53	0.0034	0.4179	27.2	149.9	98.8	38.2	70.714	0.035	20
X	V	830	10.47	0.0019	0.4352	24.7	275.6	98.8	40.5	70.304	0.035	20
X	W	840	10.47	0.0019	0.5868	23.2	262.5	98.3	42.7	69.998	0.039	20
X	X	860	10.38	0.0020	0.5199	29.4	252.4	98.5	45.4	69.514	0.032	20
X	Y	875	10.34	0.0029	0.5642	30.5	178.9	98.4	48.3	69.173	0.032	20
X	Z	890	10.33	0.0039	0.5756	30.6	129.5	98.4	51.2	69.065	0.033	20
X	AA	905	10.35	0.0003	0.5457	30.5	1574.2	98.4	54.0	69.246	0.032	20
X	AB	920	10.41	-0.0020	0.5395	34.6	-	98.5	57.3	69.691	0.030	20
X	AC	935	10.46	0.0031	0.4948	37.2	165.8	98.6	60.8	70.116	0.052	20
X	AD	950	10.52	0.0011	0.4720	38.6	477.7	98.7	64.4	70.588	0.055	20
X	AE	975	10.59	0.0001	0.4699	48.7	6516.0	98.7	69.0	71.009	0.057	20
X	AF	1000	10.67	0.0011	0.4587	58.9	481.0	98.7	74.5	71.549	0.021	20
X	AG	1030	10.79	0.0001	0.4059	78.2	4689.4	98.9	81.9	72.452	0.017	20
X	AH	1070	10.86	0.0051	0.3037	17.3	100.8	99.2	83.5	73.183	0.047	3
X	AI	1100	10.94	0.0057	0.3306	23.5	89.7	99.1	85.7	73.611	0.037	3
	AJ	1150	10.93	0.0005	0.1536	45.4	967.0	99.6	90.0	73.901	0.023	3
	AK	1650	11.65	0.0015	2.559	106.9	334.5	93.5	100.0	73.981	0.027	3
	Integrated age ± 1s			n=37		1064.3	276.0		K2O=10.61%	70.400	0.012	
	Terminal age ± 1s		steps AJ-AK	n=2	MSWD=4.99	152.255			14.3	73.93	0.040	
	020719-13, K-Feldspar, 11.2 mg, J=0.0037424±0.02%, IC=1.029598±0.0015691, NM-309B, Lab#=67457-01											
X	B	450.0	233.5	0.0386	633.0	8.6	13.2	19.9	0.8	293.2	1.9	10
X	C	450	21.67	0.0323	63.28	5.7	15.8	13.7	1.3	20.27	0.42	20
X	D	500	17.87	0.0497	43.25	9.9	10.3	28.5	2.2	34.58	0.30	10
X	E	500	7.954	0.0079	17.89	12.9	64.3	33.5	3.4	18.19	0.16	20
X	F	550	12.46	-0.0084	28.23	18.7	-	33.1	5.1	28.01	0.18	10

	ID	Power/Temp (Watts/°C)	$^{40}Ar/^{39}Ar$	$^{37}Ar/^{39}Ar$	$^{36}Ar/^{39}Ar$ (x 10^{-3})	$^{39}Ar_K$ (x 10^{-15} mol)	K/Ca	$^{40}Ar^*$ (%)	^{39}Ar (%)	Age (Ma)	±1s (Ma)	Time (min)
X	G	550	4.994	0.0040	7.711	19.4	128.0	54.4	6.8	18.509	0.083	20
X	H	600	9.821	0.0017	19.99	23.5	295.9	39.8	8.9	26.61	0.13	10
X	I	600	3.967	0.0016	4.234	21.2	325.4	68.5	10.9	18.510	0.057	20
X	J	650	8.287	0.0025	14.71	23.6	202.0	47.5	13.0	26.79	0.10	10
X	K	650	3.399	0.0054	2.661	20.7	94.1	76.9	14.9	17.814	0.046	20
X	L	700	6.728	0.0159	10.77	15.9	32.1	52.7	16.3	24.14	0.10	10
X	M	700	3.421	0.0083	2.508	17.2	61.1	78.4	17.9	18.270	0.050	20
X	N	750	5.241	-0.0156	7.628	12.9	-	57.0	19.1	20.339	0.099	10
X	O	750	3.325	0.0148	1.979	16.8	34.4	82.4	20.6	18.684	0.046	20
X	P	800	4.885	0.0088	6.169	13.9	58.1	62.7	21.9	20.864	0.091	10
X	Q	800	3.283	0.0034	1.571	16.4	152.0	85.9	23.4	19.207	0.042	20
X	R	850	4.046	0.0102	3.678	14.3	49.9	73.2	24.6	20.164	0.061	10
X	S	850	3.439	-0.0020	1.655	18.7	-	85.8	26.3	20.099	0.039	20
X	T	900	4.294	0.0047	3.750	16.7	109.6	74.2	27.9	21.694	0.062	10
X	U	900	3.535	-0.0011	1.373	21.6	-	88.5	29.8	21.310	0.034	20
X	V	950	3.750	-0.0034	1.881	17.2	-	85.2	31.4	21.751	0.043	10
X	W	950	3.748	0.0034	1.606	21.5	151.0	87.3	33.3	22.286	0.036	20
X	X	1000	4.140	0.0048	2.580	16.0	105.3	81.6	34.8	22.997	0.054	10
X	Y	1000	4.326	0.0045	2.865	21.2	113.7	80.4	36.7	23.681	0.050	20
X	Z	1050	5.155	-0.0038	4.875	15.7	-	72.1	38.1	25.268	0.073	10
X	AA	1050	5.843	0.0058	6.620	20.8	88.3	66.5	40.0	26.436	0.073	20
X	AB	1100	7.623	0.0215	10.90	16.1	23.7	57.8	41.5	29.919	0.096	10
X	AC	1100	8.162	0.0055	12.09	27.5	93.6	56.2	44.0	31.184	0.086	20
X	AD	1100	7.377	-0.0004	9.748	86.9	-	60.9	51.9	30.543	0.054	120
X	AE	1100	7.259	0.0029	9.159	117.9	174.2	62.7	62.6	30.928	0.044	240
X	AF	1150	6.741	0.0084	8.031	13.2	60.6	64.8	63.8	29.68	0.10	10
X	AG	1200	6.738	0.0074	8.241	36.3	69.4	63.9	67.1	29.245	0.063	4
X	AH	1250	6.896	0.0025	7.554	241.4	203.9	67.6	89.0	31.672	0.032	4
X	AI	1350	6.633	0.0042	4.842	83.3	120.3	78.4	96.6	35.297	0.036	4
	AJ	1550	7.458	0.0048	5.773	36.8	105.7	77.1	99.9	38.988	0.051	4
X	AK	1680	67.02	0.0447	194.7	1.2	11.4	14.2	100.0	63.9	1.6	4
Integrated age ± 1s				n=36		1101	120.1		K2O=10.09%	30.432	0.022	
Terminal age ± 1s				step AJ					3.3	38.988	0.051	
040719-2, Hornblende, 5.42 mg, J=0.0037292±0.02%, IC=1.03261±0.0045346, NM-309E, Lab#=67502-01												
X	A	1.5	37.16	1.343	78.16	4.4	0.38	38.1	5.8	94.37	0.81	
X	B	2.0	12.20	4.984	13.94	6.6	0.10	69.6	14.4	57.24	0.21	
X	C	2.5	9.268	5.411	6.173	13.2	0.094	85.1	31.7	53.238	0.098	
X	D	3.0	8.217	5.305	4.394	14.9	0.096	89.5	51.3	49.677	0.083	
X	E	3.5	7.711	5.016	4.411	9.6	0.10	88.4	63.8	46.104	0.097	
	F	4.0	6.564	4.312	3.385	5.4	0.12	90.1	70.8	40.05	0.12	
	G	4.5	6.072	3.778	3.158	6.3	0.14	89.7	79.1	36.90	0.10	
	H	5.0	7.123	4.725	3.933	3.6	0.11	89.1	83.8	42.95	0.17	
	I	5.5	6.969	4.758	3.990	2.2	0.11	88.6	86.8	41.83	0.22	
	J	6.0	6.888	4.189	4.263	1.1	0.12	86.7	88.2	40.41	0.42	
	K	6.5	7.273	4.567	3.460	4.3	0.11	91.1	93.8	44.80	0.14	
	L	7.0	6.276	3.796	2.999	2.1	0.13	90.8	96.5	38.60	0.22	
	M	10.0	6.103	3.418	3.138	2.6	0.15	89.4	99.9	36.94	0.18	
	N	15.0	10.21	4.732	13.98	0.1	0.11	63.3	100.0	43.7	4.2	
Integrated age ± 1s				n=14		76.2	0.11		K2O=1.45%	49.700	0.064	
Plateau ± 1s			steps F-N	n=9	MSWD=349	27.560			36.2	39.93	1.03	
040719-2, K-Feldspar/Plag, 1.27 mg, J=0.0037443±0.03%, IC=1.037825±0.0008778, NM-309B, Lab#=67460-01												
X	A	500	361.1	1.402	1197.3	0.4	0.36	2.1	3.1	50.2	4.1	10
X	B	500	62.37	4.187	196.2	0.2	0.12	7.6	4.6	32.4	2.3	20
X	C	600	56.10	1.194	175.3	0.6	0.43	7.8	8.7	29.9	1.3	10
X	D	600	34.28	1.361	105.5	0.3	0.37	9.3	10.9	21.8	1.3	20
X	E	650	42.25	4.360	132.6	0.3	0.12	8.1	12.9	23.3	1.8	10
X	F	650	21.38	0.7127	63.26	0.3	0.72	12.8	14.8	18.7	1.3	20
X	G	700	22.53	1.393	64.96	0.2	0.37	15.3	16.3	23.5	1.5	10
X	H	700	14.59	-1.1863	41.38	0.3	-	15.5	18.2	15.5	1.1	20
X	I	750	18.62	4.175	51.26	0.2	0.12	20.5	19.8	26.1	1.5	10
X	J	750	10.40	0.2572	26.33	0.3	2.0	25.4	21.6	18.0	1.1	20
X	K	800	17.51	1.216	48.65	0.2	0.42	18.5	23.2	22.1	1.4	10
X	L	800	9.514	1.935	22.78	0.2	0.26	30.9	24.9	20.1	1.2	20
X	M	850	46.40	0.1859	144.2	0.3	2.7	8.2	27.0	25.8	1.7	10
X	N	850	21.91	0.4966	63.83	0.4	1.0	14.1	29.7	21.1	1.1	20
X	O	900	42.63	1.274	124.4	0.6	0.40	14.0	33.9	40.4	1.1	10
X	P	900	11.92	-0.0915	27.14	0.5	-	32.6	37.2	26.47	0.76	20
X	Q	950	24.90	1.882	63.11	0.4	0.27	25.7	39.8	43.5	1.2	10
X	R	950	14.23	-0.4450	36.06	0.4	-	24.9	42.7	24.11	0.87	20
X	S	1000	19.21	0.9174	51.89	0.4	0.56	20.6	45.5	26.88	0.99	10
X	T	1000	18.16	1.380	49.54	0.5	0.37	20.0	49.3	24.80	0.79	20
X	U	1050	22.37	1.312	60.17	0.5	0.39	21.0	53.0	31.93	0.89	10
X	V	1050	23.68	0.9400	64.85	0.6	0.54	19.4	57.3	31.24	0.83	20
X	W	1100	26.68	0.6754	69.42	0.6	0.76	23.3	61.7	42.16	0.91	10
X	X	1100	32.06	1.617	84.86	0.7	0.32	22.2	66.5	48.18	0.95	20
X	Y	1100	53.09	1.530	150.4	1.0	0.33	16.5	73.3	59.25	0.98	60
X	Z	1100	120.4	1.631	368.2	0.8	0.31	9.7	78.7	78.5	1.7	120
X	AA	1200	182.7	2.047	587.4	0.9	0.25	5.1	84.8	62.9	2.0	4
X	AB	1250	154.3	2.314	438.1	0.6	0.22	16.2	89.3	164.2	2.4	4
X	AC	1350	194.2	3.806	518.4	1.0	0.13	21.3	96.6	264.0	2.2	4
X	AD	1550	209.4	8.607	356.6	0.3	0.059	50.0	99.1	608.6	10.3	4
X	AE	1680	700.3	7.028	2083.2	0.1	0.073	12.2	100.0	509.4	21.9	4
Integrated age ± 1s				n=31		14.2	0.29		K2O=1.15%	82.74	0.37	
No Plateau												
050719-16, Muscovite, 1.92 mg, J=0.0036976±0.02%, IC=1.029742±0.0011289, NM-309F, Lab#=67507-01												
X	A	435	36.14	0.1270	106.0	0.7	4.0	13.4	0.4	32.5	1.7	20
X	B	480	13.68	0.0292	22.27	0.4	17.5	51.9	0.7	47.4	1.6	20

	ID	Power/Temp (Watts/°C)	$^{40}Ar/^{39}Ar$	$^{37}Ar/^{39}Ar$	$^{36}Ar/^{39}Ar$ (x 10^{-3})	$^{39}Ar_K$ (x 10^{-15} mol)	K/Ca	$^{40}Ar^*$ (%)	^{39}Ar (%)	Age (Ma)	±1s (Ma)	Time (min)
X	C	530	12.87	0.0550	16.80	0.8	9.3	61.5	1.2	52.75	0.88	20
X	D	580	13.42	0.0219	11.73	1.4	23.3	74.2	2.1	66.19	0.53	20
X	E	630	12.41	0.0351	5.806	2.6	14.5	86.2	3.8	70.99	0.30	20
X	F	660	11.90	0.0209	3.502	3.0	24.5	91.3	5.8	72.08	0.26	20
X	G	675	11.78	0.0297	2.815	2.6	17.2	93.0	7.5	72.65	0.27	20
X	H	690	12.01	0.0218	2.847	2.9	23.4	93.0	9.4	74.08	0.25	20
X	I	700	12.07	0.0171	2.419	2.8	29.8	94.1	11.2	75.27	0.27	20
X	J	710	12.71	0.0071	3.283	3.0	71.4	92.4	13.2	77.81	0.26	20
X	K	720	13.16	0.0181	3.566	3.3	28.1	92.0	15.3	80.20	0.24	20
X	L	730	13.83	0.0094	2.948	3.9	54.1	93.7	17.9	85.65	0.21	20
X	M	735	13.94	-0.0007	2.365	4.2	-	95.0	20.6	87.48	0.20	20
X	N	740	13.91	0.0145	1.900	4.5	35.1	96.0	23.6	88.20	0.18	20
X	O	745	13.84	0.0090	1.682	4.2	56.8	96.4	26.3	88.13	0.19	20
X	P	750	13.64	0.0073	1.395	3.6	70.2	97.0	28.7	87.44	0.22	20
X	Q	760	13.56	0.0005	1.337	4.1	989.7	97.1	31.4	87.02	0.18	20
X	R	770	13.51	0.0045	1.230	4.3	114.6	97.3	34.2	86.89	0.18	20
X	S	780	13.39	0.0003	1.425	4.1	1527.1	96.9	36.9	85.75	0.20	20
X	T	800	13.40	0.0072	1.469	5.2	70.6	96.8	40.3	85.74	0.16	20
X	U	820	13.33	0.0041	1.672	5.3	123.8	96.3	43.8	84.88	0.15	20
X	V	840	13.13	0.0055	1.879	5.7	92.8	95.8	47.5	83.20	0.14	20
X	W	870	13.01	0.0071	1.928	6.6	71.9	95.6	51.8	82.31	0.13	20
X	X	900	13.13	0.0040	2.023	6.8	128.9	95.5	56.2	82.95	0.12	20
X	Y	930	13.55	0.0054	2.092	6.2	94.5	95.4	60.3	85.52	0.14	20
X	Z	960	13.91	0.0025	2.039	6.8	204.0	95.7	64.7	87.94	0.13	20
X	AA	1010	14.37	0.0066	1.898	11.3	76.9	96.1	72.1	91.181	0.091	20
X	AB	1050	14.43	0.0174	1.022	1.9	29.3	97.9	73.3	93.21	0.43	3
X	AC	1130	14.79	0.0075	1.759	14.6	68.0	96.5	82.9	94.141	0.075	3
	AD	1580	15.90	0.0142	4.242	26.1	35.8	92.1	100.0	96.581	0.060	3
Integrated age ± 1s				n=30		152.7	49.3		K2O=8.26%	86.790	0.034	
Terminal age ± 1s			step AD	n=1	MSWD=NA	26.078			17.1	96.581	0.060	
050719-23, Muscovite, 10.35 mg, J=0.003749±0.04%, IC=1.042355±0.0005192, NM-309C, Lab#=67472-01												
X	A	500	49.58	0.2164	142.2	2.5	2.4	15.3	0.3	51.21	0.55	20
X	B	550	11.64	0.0916	18.00	2.2	5.6	54.4	0.5	42.92	0.24	20
X	C	580	13.35	0.1189	23.21	2.3	4.3	48.7	0.8	44.10	0.26	20
X	D	610	11.46	0.0866	15.63	3.2	5.9	59.8	1.1	46.40	0.19	20
X	E	640	11.57	0.0885	14.85	4.4	5.8	62.2	1.6	48.71	0.15	20
X	F	670	10.04	0.1220	7.891	6.2	4.2	76.9	2.3	52.24	0.10	20
X	G	700	10.99	0.0073	8.831	8.6	70.2	76.3	3.2	56.657	0.085	20
X	H	730	11.34	-0.0437	7.574	12.1	-	80.2	4.6	61.413	0.068	20
X	I	740	11.72	0.0599	7.443	11.4	8.5	81.3	5.8	64.222	0.067	20
X	J	730	10.82	-0.1294	4.033	6.8	-	88.9	6.6	64.819	0.094	20
X	K	740	11.39	0.0456	5.150	8.0	11.2	86.7	7.5	66.530	0.087	20
X	L	750	12.07	-0.0294	5.822	10.6	-	85.7	8.7	69.688	0.076	20
X	M	760	12.75	0.0245	4.613	21.4	20.9	89.3	11.0	76.510	0.045	20
X	N	770	12.60	-0.0094	3.063	45.3	-	92.8	16.1	78.510	0.026	20
X	O	775	12.03	0.0058	2.015	53.1	88.3	95.1	21.9	76.832	0.021	20
X	P	780	11.50	-0.0089	1.280	47.1	-	96.7	27.1	74.757	0.024	20
X	Q	785	11.21	-0.0030	1.079	38.8	-	97.2	31.4	73.222	0.024	20
X	R	790	11.04	0.0204	1.055	31.6	25.1	97.2	34.9	72.180	0.026	20
X	S	800	10.86	-0.0043	1.002	30.9	-	97.3	38.4	71.083	0.026	20
X	T	810	10.74	0.0116	1.044	29.4	43.8	97.1	41.6	70.228	0.027	20
X	U	820	10.68	0.0146	1.106	26.1	34.9	96.9	44.5	69.684	0.031	20
X	V	830	10.63	0.0243	1.227	24.0	21.0	96.6	47.2	69.175	0.033	20
X	W	840	10.61	0.0039	1.419	22.1	129.9	96.1	49.6	68.650	0.035	20
X	X	850	10.58	0.0017	1.570	19.2	299.5	95.6	51.7	68.163	0.038	20
X	Y	860	10.54	-0.0384	1.736	17.7	-	95.1	53.7	67.509	0.041	20
X	Z	870	10.53	0.0022	1.976	16.2	228.4	94.5	55.5	67.025	0.043	20
X	AA	880	10.56	0.0032	2.215	15.9	160.4	93.8	57.3	66.730	0.046	20
X	AB	900	10.64	0.0449	2.430	17.7	11.4	93.3	59.2	66.898	0.043	20
X	AC	930	10.85	0.0481	2.740	21.0	10.6	92.6	61.5	67.674	0.040	20
X	AD	960	11.06	0.0109	2.801	23.7	46.6	92.5	64.2	68.931	0.037	20
X	AE	990	11.21	0.0019	2.761	26.6	269.5	92.7	67.1	70.005	0.036	20
X	AF	1030	11.37	-0.0049	2.632	34.5	-	93.2	70.9	71.280	0.030	20
	AG	1060	11.43	0.0019	2.299	45.8	265.5	94.1	76.0	72.339	0.023	20
	AH	1090	11.15	-0.0056	1.457	75.4	-	96.1	84.4	72.101	0.017	20
	AI	1120	10.68	0.0118	0.7140	88.7	43.4	98.0	94.2	70.497	0.014	20
	AJ	1150	10.50	0.0230	0.3510	10.5	22.2	99.0	95.3	69.981	0.059	3
	AK	1230	10.33	-0.0021	0.3114	19.9	-	99.1	97.6	68.958	0.033	3
X	AL	1430	9.152	-0.0014	1.617	10.9	-	94.8	98.8	58.579	0.053	3
X	AM	1630	13.81	0.0117	7.221	11.3	43.8	84.6	100.0	78.454	0.078	3
Integrated age ± 1s				n=39		902.8	76.8		K2O=8.94%	70.550	0.027	
Plateau ± 1s			steps AG-AK	n=5	MSWD=3191	240.288			26.6	71.11	0.52	
050719-23, K-Feldspar, 9.23 mg, J=0.0037479±0.02%, IC=1.029598±0.0015691, NM-309B, Lab#=67461-01												
X	A	505	83.37	0.0091	163.8	16.1	55.8	41.9	1.4	225.36	0.56	10
X	B	505	7.328	0.0469	14.16	3.0	10.9	42.9	1.7	21.46	0.28	20
X	C	550	4.262	0.0024	5.749	7.7	211.9	60.1	2.3	17.50	0.11	10
X	D	550	3.518	-0.0354	4.524	12.3	-	61.9	3.4	14.879	0.079	20
X	E	600	5.864	0.0187	10.47	13.6	27.3	47.3	4.6	18.92	0.11	10
X	F	600	2.663	0.0097	1.828	22.8	52.5	79.7	6.5	14.510	0.034	20
X	G	650	4.016	0.0019	4.635	24.0	272.0	65.9	8.6	18.066	0.052	10
X	H	650	2.462	0.0115	0.9494	30.6	44.3	88.6	11.3	14.912	0.024	20
X	I	700	2.690	0.0084	1.200	29.4	60.7	86.8	13.8	15.957	0.025	10
X	J	700	2.548	0.0110	0.8197	34.9	46.2	90.5	16.8	15.759	0.021	20
X	K	750	3.002	0.0187	1.614	23.1	27.3	84.2	18.8	17.250	0.037	10
X	L	750	2.590	0.0081	0.5805	29.7	63.2	93.4	21.4	16.518	0.021	20
X	M	800	3.891	0.0123	1.128	18.3	41.5	91.5	23.0	24.253	0.037	10
X	N	800	3.010	0.0094	0.7896	22.9	54.5	92.3	25.0	18.954	0.028	20
X	O	850	3.647	0.0033	1.567	16.3	153.6	87.3	26.4	21.718	0.042	10
X	P	850	2.994	0.0177	0.7986	23.1	28.9	92.2	28.4	18.836	0.026	20

	ID	Power/Temp (Watts/°C)	$^{40}Ar/^{39}Ar$	$^{37}Ar/^{39}Ar$	$^{36}Ar/^{39}Ar$ (x 10^{-3})	$^{39}Ar_K$ (x 10^{-15} mol)	K/Ca	$^{40}Ar^*$ (%)	^{39}Ar (%)	Age (Ma)	±1s (Ma)	Time (min)
X	Q	900	3.513	0.0104	1.437	20.2	49.0	87.9	30.1	21.069	0.035	10
X	R	900	2.995	0.0078	0.6939	28.4	65.8	93.2	32.6	19.041	0.021	20
X	S	950	3.729	0.0170	1.604	24.8	30.0	87.3	34.7	22.204	0.034	10
X	T	950	3.272	0.0116	0.6959	31.4	44.1	93.7	37.5	20.921	0.020	20
X	U	1000	3.979	0.0173	1.919	25.6	29.4	85.8	39.7	23.268	0.037	10
X	V	1000	3.962	-0.0035	1.257	28.7	-	90.6	42.2	24.468	0.030	20
X	W	1050	4.859	0.0327	2.112	21.1	15.6	87.2	44.0	28.843	0.044	10
X	X	1050	5.237	0.0048	2.485	25.6	106.2	86.0	46.2	30.634	0.043	20
X	Y	1100	6.170	0.0123	3.729	20.9	41.5	82.2	48.0	34.447	0.056	10
X	Z	1100	5.777	0.0209	3.663	31.5	24.4	81.3	50.7	31.935	0.045	20
X	AA	1150	6.314	0.0223	4.290	32.1	22.9	79.9	53.5	34.306	0.047	10
X	AB	1150	5.750	0.0121	3.336	51.3	42.3	82.9	58.0	32.400	0.033	20
X	AC	1150	5.441	0.0066	2.168	107.7	77.8	88.2	67.3	32.642	0.021	60
X	AD	1150	5.501	0.0046	2.066	134.9	110.3	88.9	79.0	33.246	0.017	120
	AE	1200	5.755	0.0023	1.906	22.0	223.3	90.2	80.9	35.277	0.040	10
	AF	1300	6.024	0.0025	2.133	157.3	200.6	89.5	94.5	36.634	0.017	4
	AG	1400	5.596	-0.0023	1.360	57.0	-	92.8	99.4	35.290	0.021	4
X	AH	1550	10.85	0.0368	12.97	6.6	13.9	64.7	100.0	47.56	0.19	4
Integrated age ± 1s				n=34		1155	62.2		K2O=12.82%	30.721	0.012	
Plateau ± 1s			steps AE-AG	n=3	MSWD=1434	236.285			20.5	36.04	0.473	
060719-3, Biotite, .83 mg, J=0.003722±0.02%, IC=1.03261±0.0045346, NM-309E, Lab#=67504-01												
X	A	0.5	15.69	0.0136	49.82	14.3	37.5	6.2	18.3	6.62	0.49	
X	B	0.8	7.752	0.0109	21.81	16.7	46.9	16.9	39.6	8.89	0.23	
X	C	1.0	7.119	0.0092	19.23	8.1	55.7	20.2	50.0	9.77	0.26	
	D	1.5	6.718	0.0119	17.43	12.7	43.0	23.4	66.2	10.66	0.21	
	E	1.8	6.671	0.0079	17.41	8.9	65.0	22.9	77.6	10.38	0.22	
	F	2.0	6.624	0.0133	17.08	5.0	38.3	23.8	84.0	10.73	0.27	
	G	2.5	6.637	0.0094	17.31	3.9	54.1	23.0	89.0	10.35	0.28	
	H	2.8	6.341	0.0013	16.43	1.2	389.4	23.4	90.6	10.09	0.46	
	I	3.0	6.351	0.0153	16.10	0.8	33.2	25.1	91.5	10.83	0.66	
	J	3.5	7.093	0.0259	18.30	1.1	19.7	23.8	93.0	11.45	0.53	
	K	4.0	6.725	0.0159	17.11	2.1	32.1	24.8	95.7	11.34	0.39	
	L	5.0	6.419	0.0153	15.91	3.0	33.3	26.8	99.4	11.67	0.31	
	M	6.0	7.344	-0.0361	17.63	0.4	-	29.0	100.0	14.47	0.96	
Integrated age ± 1s				n=13		78.3	45.4		K2O=9.73%	9.49	0.12	
Plateau ± 1s			steps D-M	n=10	MSWD=3.89	39.1			50.0	10.77	0.20	
060719-3, Muscovite, 5.01 mg, J=0.0037018±0.01%, IC=1.029171±0.0012136, NM-309F, Lab#=67510-01												
X	A	455	120.4	0.0455	288.8	0.6	11.2	29.1	1.1	223.1	3.2	20
X	B	500	15.76	0.0015	29.32	0.4	340.3	45.0	1.9	47.5	1.3	20
X	C	550	13.89	0.0498	19.02	0.9	10.3	59.6	3.5	55.25	0.77	20
X	D	600	9.559	0.0004	14.37	1.4	1378.2	55.6	6.1	35.65	0.40	20
X	E	650	4.722	0.0113	5.508	2.1	45.2	65.6	9.9	20.86	0.26	20
X	F	680	3.989	0.0285	3.481	2.0	17.9	74.3	13.5	19.96	0.21	20
X	G	695	3.755	-0.0007	2.324	1.6	-	81.7	16.4	20.67	0.21	20
X	H	710	3.497	0.0006	1.918	1.5	868.6	83.8	19.1	19.76	0.23	20
X	I	720	3.475	-0.0061	1.530	1.3	-	87.0	21.4	20.36	0.26	20
X	J	730	3.493	0.0344	1.525	1.2	14.8	87.2	23.7	20.52	0.26	20
X	K	740	3.562	0.0186	1.778	1.2	27.4	85.3	25.9	20.47	0.27	20
X	L	750	3.505	-0.0114	1.485	1.3	-	87.5	28.2	20.65	0.25	20
X	M	755	3.521	0.0189	1.307	1.2	27.0	89.1	30.4	21.13	0.26	20
X	N	760	3.532	0.0206	1.410	1.1	24.8	88.3	32.3	21.00	0.30	20
X	O	765	3.509	0.0031	1.335	1.0	162.5	88.8	34.2	20.99	0.32	20
X	P	770	3.615	-0.0084	1.234	1.0	-	89.9	36.1	21.89	0.30	20
X	Q	780	3.534	0.0117	1.211	1.1	43.7	89.9	38.1	21.40	0.27	20
X	R	790	3.677	-0.0069	1.507	1.1	-	87.9	40.2	21.76	0.28	20
X	S	800	3.638	0.0127	1.359	1.3	40.3	89.0	42.5	21.81	0.24	20
X	T	820	3.751	0.0031	1.753	1.8	163.9	86.2	45.8	21.78	0.18	20
X	U	840	3.693	0.0029	1.444	2.0	178.3	88.4	49.4	22.00	0.18	20
X	V	860	3.761	-0.0026	1.606	2.5	-	87.4	54.0	22.14	0.15	20
X	W	890	3.796	0.0046	1.785	3.3	112.0	86.1	60.0	22.02	0.12	20
X	X	920	3.783	0.0024	1.669	3.8	208.9	87.0	66.9	22.16	0.11	20
X	Y	950	3.917	0.0104	1.885	3.7	49.0	85.8	73.7	22.63	0.11	20
X	Z	980	4.301	0.0157	2.171	3.2	32.6	85.1	79.4	24.64	0.13	20
X	AA	1030	4.552	0.0233	2.142	3.9	21.9	86.1	86.4	26.37	0.11	20
X	AB	1070	4.569	0.0083	0.6289	0.5	61.7	95.9	87.4	29.47	0.60	3
X	AC	1110	5.909	0.0102	5.041	0.9	50.1	74.8	89.0	29.71	0.46	3
X	AD	1150	5.248	0.0161	2.818	3.0	31.7	84.2	94.3	29.68	0.15	3
	AE	1200	6.565	0.0063	3.638	3.1	81.3	83.6	100.0	36.83	0.17	3
Integrated age ± 1s				n=31		55.0	51.6		K2O=1.14%	27.010	0.051	
Terminal age ± 1s			Steps AE	n=1		3.115			5.7	36.83	0.17	
060719-5, Muscovite, 9.51 mg, J=0.0037659±0.05%, IC=1.042355±0.0005192, NM-309C, Lab#=67471-01												
X	A	520	33.43	0.1942	108.7	3.2	2.6	4.0	0.4	9.10	0.52	20
X	B	570	8.911	0.0676	20.92	2.2	7.5	30.7	0.6	18.76	0.23	20
X	C	600	7.547	-0.0313	15.36	2.7	-	39.8	0.9	20.60	0.18	20
X	D	630	8.583	-0.0316	18.43	3.5	-	36.5	1.3	21.47	0.17	20
X	E	660	9.134	0.0275	19.15	5.2	18.6	38.1	2.0	23.82	0.14	20
X	F	690	9.600	0.0270	18.96	8.4	18.9	41.7	2.9	27.36	0.11	20
X	G	720	9.445	0.0149	13.85	18.3	34.3	56.7	5.1	36.543	0.062	20
X	H	750	7.281	-0.0051	4.242	53.9	-	82.8	11.3	41.084	0.022	20
X	I	755	5.301	0.0077	1.637	43.2	65.8	90.9	16.4	32.914	0.016	20
X	J	760	4.796	0.0135	1.172	35.3	37.9	92.8	20.5	30.428	0.018	20
X	K	770	4.634	0.0072	0.9311	33.9	70.6	94.1	24.4	29.806	0.016	20
X	L	775	4.341	-0.0087	0.6990	27.2	-	95.2	27.6	28.278	0.018	20
X	M	780	4.238	0.0065	0.6999	22.9	78.9	95.1	30.2	27.583	0.020	20
X	N	785	4.167	-0.0173	0.6215	18.5	-	95.6	32.4	27.246	0.022	20
X	O	790	4.159	-0.0001	0.6704	17.5	-	95.2	34.4	27.099	0.024	20
X	P	800	4.212	-0.0077	0.6807	16.8	-	95.2	36.4	27.435	0.025	20

	ID	Power/Temp (Watts/°C)	$^{40}Ar/^{39}Ar$	$^{37}Ar/^{39}Ar$	$^{36}Ar/^{39}Ar$ (x 10^{-3})	$^{39}Ar_K$ (x 10^{-15} mol)	K/Ca	$^{40}Ar^*$ (%)	^{39}Ar (%)	Age (Ma)	±1s (Ma)	Time (min)
X	Q	810	4.265	-0.0349	0.7300	17.8	-	94.9	38.4	27.680	0.023	20
X	R	820	4.343	-0.0084	0.7767	16.4	-	94.7	40.3	28.132	0.026	20
X	S	830	4.455	0.0083	0.8862	14.9	61.6	94.1	42.1	28.685	0.028	20
X	T	840	4.601	-0.0062	0.9855	12.9	-	93.7	43.6	29.464	0.032	20
X	U	850	4.767	-0.0103	1.114	13.9	-	93.1	45.2	30.332	0.032	20
X	V	860	4.954	-0.0210	1.194	12.0	-	92.8	46.6	31.432	0.037	20
X	W	870	5.138	-0.0153	1.271	12.4	-	92.7	48.0	32.530	0.036	20
X	X	880	5.298	-0.0069	1.319	12.2	-	92.6	49.5	33.523	0.039	20
X	Y	890	5.451	0.0149	1.334	12.2	34.3	92.8	50.9	34.537	0.038	20
X	Z	900	5.574	-0.0170	1.331	11.5	-	92.9	52.2	35.359	0.039	20
X	AA	920	5.665	0.0230	1.250	15.9	22.1	93.5	54.1	36.157	0.033	20
X	AB	950	5.781	0.0173	1.218	25.1	29.4	93.8	57.0	37.004	0.022	20
	AC	980	5.879	-0.0115	1.139	33.6	-	94.3	60.9	37.806	0.019	20
	AD	1010	5.936	0.0155	1.069	47.8	32.9	94.7	66.5	38.348	0.016	20
	AE	1050	5.976	-0.0007	1.011	95.0	-	95.0	77.5	38.722	0.010	20
	AF	1080	5.704	0.0028	0.5980	112.1	184.8	96.9	90.6	37.710	0.009	20
	AG	1110	5.534	-0.0070	0.3540	60.0	-	98.1	97.5	37.046	0.011	20
	AH	1140	5.515	-0.0123	-0.0074	5.2	-	100.0	98.1	37.631	0.074	3
	AI	1170	5.541	-0.0955	-0.0025	6.3	-	99.9	98.9	37.749	0.060	3
	AJ	1250	5.607	-0.0926	0.0189	4.4	-	99.8	99.4	38.155	0.088	3
X	AK	1450	7.710	0.0218	4.895	1.7	23.4	81.3	99.6	42.69	0.25	3
X	AL	1650	19.58	0.0317	43.01	3.6	16.1	35.1	100.0	46.76	0.26	3
	Integrated age ± 1s			n=38		859.8	4035.6		K2O=9.22%	34.401	0.017	
	Plateau ± 1s		steps AC-AJ	n=8	MSWD=2080	364.463			42.4	37.92	0.232	
	060719-7, Muscovite, 1.06 mg, J=0.0037142±0.02%, IC=1.029171±0.0012136, NM-309F, Lab#=67517-01											
X	A	455	50.32	0.0423	166.8	0.7	12.1	2.0	0.8	7.0	2.0	20
X	B	500	7.766	0.0313	18.04	0.4	16.3	31.4	1.3	16.5	1.0	20
X	C	550	6.648	0.0290	13.50	0.7	17.6	40.0	2.2	18.00	0.67	20
X	D	600	6.263	0.0163	11.69	1.2	31.3	44.8	3.6	19.00	0.45	20
X	E	650	4.851	0.0044	6.867	2.0	116.7	58.2	6.0	19.08	0.26	20
X	F	680	4.180	0.0031	4.596	1.9	162.5	67.5	8.2	19.08	0.23	20
X	G	710	3.866	0.0054	3.082	2.5	95.2	76.5	11.2	19.98	0.17	20
X	H	730	3.780	0.0100	2.506	2.4	51.0	80.4	14.1	20.55	0.17	20
X	I	750	3.737	-0.0001	2.074	2.9	-	83.6	17.6	21.12	0.14	20
X	J	755	3.756	0.0001	1.705	2.2	3964.3	86.6	20.2	21.98	0.17	20
X	K	760	3.886	0.0197	1.858	2.2	25.9	85.9	22.9	22.56	0.17	20
X	L	765	3.872	-0.0031	1.592	2.1	-	87.8	25.5	22.98	0.17	20
X	M	770	3.868	0.0253	1.323	1.8	20.2	89.9	27.7	23.50	0.19	20
X	N	780	3.896	0.0153	1.419	2.2	33.3	89.3	30.3	23.49	0.16	20
X	O	790	3.897	0.0019	1.411	2.2	269.1	89.3	32.9	23.51	0.17	20
X	P	800	3.792	0.0017	1.225	2.3	297.0	90.5	35.8	23.17	0.15	20
X	Q	820	3.792	-0.0141	1.188	3.3	-	90.7	39.8	23.24	0.11	20
X	R	840	3.716	0.0036	1.145	4.0	143.2	90.9	44.7	22.819	0.096	20
X	S	860	3.650	-0.0065	1.110	4.1	-	91.0	49.6	22.441	0.093	20
X	T	890	3.573	0.0014	1.215	5.6	359.6	90.0	56.4	21.719	0.075	20
X	U	915	3.507	0.0103	1.185	5.5	49.5	90.0	63.0	21.343	0.077	20
X	V	920	3.486	0.0076	1.287	3.8	67.6	89.1	67.6	21.00	0.10	20
X	W	950	3.591	0.0156	1.471	4.1	32.8	87.9	72.5	21.343	0.099	20
X	X	980	3.749	-0.0019	1.538	4.1	-	87.9	77.4	22.26	0.11	20
X	Y	1000	3.941	0.0083	1.769	3.4	61.6	86.7	81.4	23.10	0.12	20
X	Z	1030	4.127	0.0142	1.706	3.6	35.9	87.8	85.8	24.48	0.12	20
X	AA	1070	3.951	0.0792	0.5444	0.8	6.4	96.1	86.8	25.63	0.40	3
	AB	1110	6.051	0.0509	6.644	1.2	10.0	67.6	88.2	27.61	0.40	3
	AC	1150	4.394	0.0078	1.213	4.3	65.0	91.9	93.4	27.238	0.097	3
	AD	1250	4.310	0.0073	0.7079	5.4	70.2	95.2	100.0	27.674	0.072	3
	Integrated age ± 1s			n=30		82.9	67.8		K2O=8.09%	22.586	0.032	
	Plateau ± 1s		steps AB-AD	n=3	MSWD=6.52	10.943			13.2	27.52	0.147	
	070719-9, Biotite, 4.93 mg, J=0.0037856±0.02%, IC=1.028619±0.0009457, NM-306F, Lab#=67317-01											
X	A	0.5	12.17	0.0232	23.98	7.1	22.0	41.8	1.2	34.92	0.22	
X	B	0.8	7.927	0.0160	20.25	10.3	31.9	24.5	2.9	13.42	0.16	
X	C	1.0	7.067	0.0173	12.36	10.5	29.5	48.3	4.7	23.52	0.14	
X	D	1.5	6.256	0.0085	5.273	25.1	59.9	75.1	8.8	32.269	0.055	
X	E	1.7	6.244	0.0073	4.029	29.9	69.8	80.9	13.8	34.693	0.046	
X	F	1.9	6.121	0.0063	2.823	33.1	81.6	86.4	19.3	36.280	0.037	
X	G	2.0	6.156	0.0072	2.641	30.7	70.4	87.3	24.5	36.877	0.036	
X	H	2.1	6.061	0.0059	1.892	31.1	86.4	90.8	29.7	37.737	0.030	
X	I	2.5	6.165	0.0074	2.081	37.1	68.5	90.0	35.8	38.066	0.031	
	J	3.0	6.162	0.0083	2.004	43.5	61.7	90.4	43.1	38.198	0.028	
	K	3.5	6.144	0.0119	1.987	49.3	43.0	90.5	51.3	38.115	0.025	
	L	5.0	6.095	0.0312	1.770	91.0	16.3	91.5	66.5	38.227	0.017	
	M	6.0	6.168	0.0375	2.315	88.9	13.6	89.0	81.3	37.631	0.020	
	N	7.0	6.147	0.0586	2.241	65.2	8.7	89.3	92.1	37.647	0.024	
	O	15.0	6.148	0.2547	2.508	47.1	2.0	88.3	100.0	37.239	0.027	
	Integrated age ± 1s			n=15		600.0	12.4		K2O=12.35%	36.629	0.011	
	Plateau ± 1s		steps J-O	n=6	MSWD=290.4	384.952			64.2	37.88	0.156	
	080719-7, Biotite, 1.48 mg, J=0.0037231±0.02%, IC=1.03261±0.0045346, NM-309E, Lab#=67503-01											
X	A	0.5	21.29	0.0113	27.52	4.8	45.1	61.8	2.9	87.57	0.38	
X	B	0.8	14.10	0.0044	1.883	20.2	115.1	96.1	14.9	90.035	0.051	
	C	1.0	14.02	0.0072	0.6589	17.6	70.8	98.6	25.3	91.857	0.052	
	D	1.5	14.01	0.0095	0.5467	33.9	53.6	98.9	45.5	92.002	0.030	
	E	1.8	14.02	0.0092	0.4874	26.1	55.3	99.0	61.1	92.182	0.036	
	F	2.0	14.00	0.0100	0.4204	17.7	50.8	99.1	71.6	92.223	0.046	
	G	2.5	14.01	0.0121	0.3992	19.1	42.3	99.2	83.0	92.337	0.044	
	H	2.8	14.07	0.0179	0.3885	8.7	28.6	99.2	88.2	92.702	0.085	
	I	3.0	14.11	0.0246	0.4081	6.6	20.7	99.2	92.1	92.95	0.10	
X	J	3.5	14.21	0.0423	0.3805	4.8	12.1	99.2	94.9	93.67	0.14	
X	K	4.0	14.23	0.0431	0.1730	1.7	11.8	99.7	96.0	94.19	0.37	

	ID	Power/Temp (Watts/°C)	$^{40}Ar/^{39}Ar$	$^{37}Ar/^{39}Ar$	$^{36}Ar/^{39}Ar$ (x 10^{-3})	$^{39}Ar_K$ (x 10^{-15} mol)	K/Ca	$^{40}Ar^*$ (%)	^{39}Ar (%)	Age (Ma)	±1s (Ma)	Time (min)
X	L	5.0	14.26	0.0302	0.4263	2.0	16.9	99.1	97.2	93.91	0.33	
X	M	6.0	14.68	0.0824	0.4033	2.3	6.2	99.2	98.5	96.66	0.28	
X	N	7.0	15.52	0.0749	0.1900	1.0	6.8	99.7	99.1	102.48	0.68	
X	O	12.0	15.90	0.0665	0.4890	1.5	7.7	99.1	100.0	104.36	0.47	
Integrated age ± 1s				n=15		168.0	37.9		K2O=11.71%	92.114	0.029	
Plateau ± 1s			steps C-I	n=7	MSWD=29.40	129.740			77.2	92.16	0.094	
080719-7, Muscovite, .99 mg, J=0.0036993±0.02%, IC=1.029742±0.0011289, NM-309F, Lab#=67506-01												
	A	455	125.4	0.1100	390.5	0.2	4.6	8.0	0.3	66.5	6.4	20
	B	500	529.2	-0.1347	1849.8	0.1	-	-3.3	0.4	-121.9	17.9	20
	C	550	21.10	0.2515	28.54	0.2	2.0	60.1	0.7	83.9	4.0	20
	D	600	18.93	0.1222	20.47	0.4	4.2	68.1	1.3	85.3	2.0	20
	E	650	17.66	0.0542	17.86	0.7	9.4	70.1	2.3	82.0	1.0	20
	F	680	16.81	0.0210	13.81	0.8	24.2	75.7	3.5	84.24	0.96	20
	G	695	16.94	-0.0263	15.40	0.8	-	73.1	4.7	82.0	1.0	20
	H	710	17.09	0.0006	15.33	0.8	900.6	73.5	5.9	83.11	0.95	20
	I	720	22.80	0.0144	34.28	0.9	35.4	55.6	7.1	83.8	1.1	20
	J	730	24.13	0.0145	38.92	1.3	35.2	52.3	9.0	83.61	0.83	20
	K	740	16.24	0.0076	11.71	3.2	66.9	78.7	13.6	84.53	0.31	20
	L	750	14.45	0.0063	5.690	5.3	80.7	88.4	21.1	84.51	0.18	20
	M	755	13.55	-0.0039	2.977	5.0	-	93.5	28.3	83.82	0.18	20
	N	760	13.32	0.0074	2.140	4.2	68.9	95.3	34.2	83.99	0.19	20
	O	765	13.21	-0.0090	1.842	3.5	-	95.9	39.2	83.84	0.22	20
	P	770	13.21	0.0235	1.840	2.9	21.7	95.9	43.4	83.81	0.27	20
	Q	780	13.23	0.0019	1.907	3.1	268.7	95.7	47.8	83.81	0.24	20
	R	790	13.23	0.0036	1.788	3.1	141.4	96.0	52.2	84.08	0.25	20
	S	800	13.24	0.0075	2.073	3.1	67.9	95.4	56.6	83.54	0.26	20
	T	820	13.33	-0.0005	2.204	3.5	-	95.1	61.6	83.90	0.24	20
	U	840	13.43	-0.0066	2.387	4.1	-	94.7	67.4	84.19	0.20	20
	V	860	13.58	-0.0003	2.800	3.7	-	93.9	72.8	84.38	0.22	20
	W	890	13.84	0.0036	3.695	3.7	140.3	92.1	78.0	84.34	0.24	20
	X	920	14.27	-0.0017	5.253	2.9	-	89.1	82.1	84.12	0.30	20
	Y	950	14.88	-0.0028	7.043	2.3	-	86.0	85.3	84.70	0.37	20
	Z	980	15.11	0.0325	7.223	2.2	15.7	85.9	88.5	85.85	0.38	20
	AA	1030	14.93	0.0167	7.067	3.0	30.5	86.0	92.8	84.96	0.29	20
	AB	1070	14.54	0.0164	5.165	0.5	31.2	89.5	93.4	86.1	1.6	3
	AC	1150	14.27	0.0092	5.029	4.6	55.5	89.6	100.0	84.60	0.19	3
Integrated age ± 1s				n=29		69.9	78.0		K2O=7.33%	83.793	0.071	
Plateau ± 1s			steps A-AC	n=29	MSWD=7.51	69.9			100.0	84.175	0.150	
080719-18, Muscovite, 9.84 mg, J=0.0037825±0.01%, IC=1.033525±0.001543, NM-306F, Lab#=67318-01												
X	A	500	72.61	0.7780	189.8	3.0	0.66	22.9	0.4	111.5	1.2	20
X	B	500	18.21	2.431	32.17	1.3	0.21	48.9	0.6	60.73	0.75	20
X	C	550	19.02	5.473	23.82	3.4	0.093	65.3	1.0	84.40	0.41	20
X	D	600	22.68	8.058	18.92	5.9	0.063	78.2	1.7	119.55	0.29	20
X	E	650	16.35	2.805	8.549	11.7	0.18	85.9	3.2	94.99	0.13	20
X	F	680	14.54	0.1821	3.531	12.4	2.8	92.9	4.8	91.251	0.100	20
X	G	695	14.49	0.0721	2.581	10.6	7.1	94.8	6.2	92.72	0.10	20
X	H	710	14.74	0.0469	2.426	11.2	10.9	95.2	7.6	94.620	0.100	20
X	I	720	14.99	0.0383	2.173	10.4	13.3	95.7	8.9	96.79	0.11	20
X	J	730	15.38	0.0417	2.113	10.9	12.2	96.0	10.3	99.44	0.10	20
X	K	740	15.59	0.0281	1.819	12.4	18.1	96.6	11.9	101.381	0.093	20
X	L	750	15.86	0.0180	1.671	15.3	28.3	96.9	13.9	103.402	0.077	20
X	M	755	15.85	0.0165	1.362	15.9	30.9	97.5	15.9	103.93	0.12	20
X	N	760	16.14	0.0140	2.002	16.1	36.5	96.3	18.0	104.64	0.11	20
X	O	765	16.08	0.0096	1.192	19.0	53.2	97.8	20.4	105.803	0.067	20
X	P	770	16.09	0.0116	1.098	17.2	43.9	98.0	22.6	106.03	0.10	20
X	Q	790	16.01	0.0101	0.7273	29.5	50.6	98.7	26.4	106.201	0.044	20
X	R	800	15.92	0.0066	0.6912	29.0	77.7	98.7	30.1	105.720	0.044	20
X	S	820	15.91	0.0040	0.6470	40.9	126.3	98.8	35.3	105.717	0.036	20
X	T	840	15.70	0.0056	0.5859	41.4	91.6	98.9	40.6	104.494	0.034	20
X	U	860	15.42	0.0094	0.5831	31.8	54.5	98.9	44.7	102.652	0.040	20
X	V	875	15.34	0.0112	0.6044	23.8	45.5	98.8	47.8	102.102	0.051	20
X	W	890	15.39	0.0094	0.5775	21.4	54.1	98.9	50.5	102.434	0.089	20
X	X	920	15.48	0.0082	0.5722	30.5	62.0	98.9	54.4	103.061	0.051	20
X	Y	950	15.63	0.0089	0.5017	40.5	57.1	99.1	59.6	104.172	0.070	20
X	Z	980	15.77	0.0059	0.3766	55.1	86.9	99.3	66.6	105.340	0.029	20
X	AA	1000	15.94	0.0039	0.2421	68.5	129.6	99.6	75.4	106.684	0.070	20
X	AB	1030	16.15	0.0027	0.1731	110.2	188.5	99.7	89.5	108.191	0.032	20
	AC	1050	16.49	0.0059	0.1602	65.3	87.0	99.7	97.9	110.465	0.073	20
	AD	1070	16.73	0.0262	0.5016	13.7	19.5	99.1	99.6	111.392	0.092	20
	AE	1110	16.70	0.1479	0.9595	0.9	3.4	98.4	99.7	110.4	1.0	3
	AF	1150	16.23	0.2540	0.6335	1.4	2.0	99.0	99.9	107.99	0.68	3
	AG	1150	16.45	0.4351	0.2865	0.5	1.2	99.7	100.0	110.2	1.8	3
Integrated age ± 1s				n=33		781.2	3.5		K2O=8.06%	104.952	0.021	
Plateau ± 1s			steps AC-AG	n=5	MSWD=20.00	81.931			10.5	110.80	0.254	
090719-1, Muscovite, J=0.0037156±0.02%, IC=1.029171±0.0012136, NM-309F, Lab#=67515-01												
X	A	455	117.8	0.2630	342.1	0.3	1.9	14.2	0.7	110.6	4.2	20
X	B	500	31.19	0.4436	76.37	0.1	1.2	27.8	1.0	58.0	4.9	20
X	C	550	16.64	0.2892	27.49	0.2	1.8	51.3	1.5	57.2	2.4	20
X	D	600	11.23	0.1266	14.07	0.5	4.0	63.1	2.6	47.56	0.98	20
X	E	650	8.143	0.0102	7.089	1.0	49.9	74.3	4.8	40.69	0.49	20
X	F	680	7.665	0.0518	4.284	1.0	9.8	83.5	6.9	43.04	0.46	20
X	G	695	7.652	0.0737	3.609	0.7	6.9	86.1	8.6	44.29	0.56	20
X	H	710	7.644	-0.0275	3.170	0.8	-	87.7	10.3	45.05	0.56	20
X	I	720	7.926	0.0804	2.783	0.7	6.3	89.7	11.8	47.73	0.63	20
X	J	730	8.071	-0.0338	2.888	0.7	-	89.4	13.3	48.43	0.66	20
X	K	740	8.183	0.0361	2.672	0.7	14.1	90.4	14.9	49.63	0.59	20
X	L	750	8.379	-0.0564	2.857	0.8	-	89.9	16.6	50.51	0.56	20

	ID	Power/Temp (Watts/°C)	$^{40}Ar/^{39}Ar$	$^{37}Ar/^{39}Ar$	$^{36}Ar/^{39}Ar$ (x 10^{-3})	$^{39}Ar_K$ (x 10^{-15} mol)	K/Ca	$^{40}Ar^*$ (%)	^{39}Ar (%)	Age (Ma)	±1s (Ma)	Time (min)
X	M	755	8.587	0.0432	2.667	0.7	11.8	90.9	18.3	52.31	0.59	20
X	N	760	8.640	-0.0078	2.462	0.7	-	91.6	19.7	53.04	0.69	20
X	O	765	8.761	0.0139	2.818	0.7	36.7	90.5	21.4	53.15	0.64	20
X	P	770	9.101	0.0133	2.857	0.7	38.4	90.7	22.9	55.32	0.64	20
X	Q	780	9.297	0.0353	2.532	0.9	14.5	92.0	24.9	57.26	0.57	20
X	R	790	9.526	0.0125	2.112	1.0	40.8	93.5	27.1	59.58	0.49	20
X	S	800	9.682	0.0055	2.318	1.1	92.4	92.9	29.5	60.19	0.45	20
X	T	820	9.979	0.0065	2.308	1.6	78.2	93.2	33.1	62.17	0.34	20
X	U	840	9.990	-0.0058	1.711	2.1	-	94.9	37.7	63.40	0.26	20
X	V	860	9.867	0.0248	1.751	2.3	20.6	94.8	42.9	62.52	0.23	20
X	W	890	9.873	0.0031	1.374	3.0	166.7	95.9	49.5	63.29	0.18	20
X	X	905	9.868	0.0070	1.429	2.6	72.6	95.7	55.2	63.15	0.21	20
X	Y	920	10.03	0.0094	1.519	2.3	54.2	95.5	60.4	64.05	0.24	20
X	Z	935	10.13	-0.0124	1.655	1.9	-	95.2	64.7	64.39	0.27	20
X	AA	950	10.28	0.0062	1.824	1.8	82.7	94.8	68.8	65.10	0.29	20
X	AB	965	10.47	0.0246	1.984	1.8	20.8	94.4	72.8	66.04	0.31	20
X	AC	980	10.65	0.0118	2.072	1.6	43.3	94.3	76.5	67.04	0.32	20
X	AD	1000	10.81	-0.0027	2.119	1.7	-	94.2	80.2	67.96	0.33	20
X	AE	1030	10.89	-0.0302	2.110	2.2	-	94.3	85.0	68.54	0.27	20
X	AF	1070	10.72	0.0641	1.442	0.5	8.0	96.1	86.1	68.7	1.1	3
X	AG	1110	11.77	0.0339	4.215	0.9	15.1	89.4	88.2	70.27	0.57	3
X	AH	1150	11.18	0.0175	1.057	2.9	29.2	97.2	94.8	72.47	0.15	3
	Al	1250	12.09	0.0145	2.194	2.3	35.2	94.6	100.0	76.22	0.27	3
	Integrated age ± 1s			n=35		44.7	32.5			62.306	0.073	
	Terminal age ± 1s		step Al	n=1	MSWD=NA	2.322			5.2	76.22	0.27	
	090719-5, Biotite, 1.79 mg, J=0.0037426±0.01%, IC=1.03261±0.0045346, NM-309D, Lab#=67487-01											
X	A	0.5	40.91	0.0261	123.8	7.2	19.6	10.6	3.7	29.4	1.2	
X	B	0.8	10.64	0.0121	20.54	16.1	42.0	43.0	11.9	31.08	0.23	
X	C	1.0	7.278	0.0109	9.118	17.4	46.7	63.0	20.7	31.14	0.11	
X	D	1.5	6.257	0.0121	6.292	31.6	42.2	70.3	36.8	29.885	0.078	
X	E	1.8	5.851	0.0194	5.445	24.4	26.4	72.5	49.2	28.843	0.073	
X	F	2.0	5.452	0.0342	4.514	18.8	14.9	75.6	58.7	28.013	0.069	
X	G	2.5	5.318	0.0590	4.121	24.8	8.7	77.2	71.4	27.910	0.063	
X	H	2.8	5.212	0.2053	3.515	18.3	2.5	80.4	80.7	28.483	0.062	
X	I	3.0	5.147	0.1834	3.129	12.6	2.8	82.3	87.1	28.806	0.070	
X	J	3.5	5.150	0.2479	2.624	12.6	2.1	85.3	93.5	29.866	0.061	
X	K	4.0	5.263	0.3585	2.507	5.8	1.4	86.5	96.5	30.926	0.096	
X	L	5.0	5.012	0.1432	2.040	3.9	3.6	88.2	98.4	30.04	0.12	
X	M	6.0	4.933	0.1612	1.793	1.9	3.2	89.5	99.4	30.01	0.21	
X	N	7.0	5.234	0.1953	2.232	0.8	2.6	87.7	99.8	31.19	0.48	
X	O	12.0	5.714	0.1502	4.292	0.4	3.4	78.0	100.0	30.29	0.85	
	Integrated age ± 1s			n=15		196.7	6.3		K2O=11.28%	29.358	0.053	
	No Plateau											
	090719-5, K-Feldspar, 11.54 mg, J=0.0037509±0.02%, IC=1.029598±0.0015691, NM-309B, Lab#=67463-01											
X	A	500	377.1	0.5824	1123.8	5.0	0.88	11.9	1.8	285.7	3.3	10
X	B	500	54.49	0.3405	166.2	2.4	1.5	9.9	2.7	36.8	1.1	20
X	C	550	56.26	0.4527	163.7	1.0	1.1	14.1	3.1	53.6	1.7	10
X	D	550	28.08	0.5486	83.81	3.0	0.93	12.0	4.2	22.96	0.70	20
X	E	600	75.05	0.9952	214.0	0.7	0.51	15.9	4.5	80.0	2.2	10
X	F	600	25.13	0.8313	71.93	3.7	0.61	15.7	5.8	26.92	0.58	20
X	G	650	59.48	0.9921	172.9	3.3	0.51	14.2	7.0	57.26	0.87	10
X	H	650	23.55	1.064	70.08	4.6	0.48	12.4	8.7	20.00	0.53	20
X	I	700	29.03	1.360	80.75	1.0	0.38	18.2	9.1	35.9	1.2	10
X	J	700	17.67	1.316	46.16	4.9	0.39	23.4	10.9	28.22	0.37	20
X	K	750	33.56	1.284	85.93	3.2	0.40	24.6	12.1	55.97	0.70	10
X	L	750	6.553	0.8635	13.53	6.9	0.59	40.1	14.6	17.94	0.18	20
X	M	800	18.72	0.7787	45.43	4.1	0.66	28.6	16.1	36.42	0.45	10
X	N	800	6.008	0.6652	11.65	5.4	0.77	43.6	18.1	17.90	0.19	20
X	O	850	23.04	0.6326	65.89	6.4	0.81	15.7	20.5	24.70	0.46	10
X	P	850	9.946	0.5515	24.68	7.1	0.93	27.1	23.1	18.43	0.23	20
X	Q	900	23.50	0.4105	67.00	10.1	1.2	15.9	26.8	25.44	0.39	10
X	R	900	8.288	0.3795	17.40	10.2	1.3	38.3	30.6	21.69	0.17	20
X	S	950	16.45	0.5431	36.50	10.0	0.94	34.7	34.2	38.79	0.26	10
X	T	950	8.546	0.4256	17.76	8.8	1.2	39.0	37.5	22.75	0.19	20
X	U	1000	12.18	0.3645	28.75	8.0	1.4	30.5	40.4	25.35	0.25	10
X	V	1000	10.15	0.2865	24.76	10.8	1.8	28.2	44.4	19.54	0.21	20
X	W	1050	11.53	0.2393	28.82	12.7	2.1	26.3	49.1	20.73	0.21	10
X	X	1050	12.35	0.2054	31.80	18.5	2.5	24.0	55.9	20.24	0.19	20
X	Y	1100	14.13	0.2781	34.25	17.0	1.8	28.5	62.2	27.47	0.20	10
X	Z	1100	16.77	0.3239	41.25	19.8	1.6	27.5	69.4	31.37	0.22	20
X	AA	1150	21.91	0.4174	47.48	14.0	1.2	36.1	74.6	53.60	0.25	10
X	AB	1150	26.64	0.3432	64.21	17.3	1.5	28.9	81.0	52.10	0.30	20
X	AC	1150	40.42	0.4411	101.1	25.9	1.2	26.2	90.5	71.22	0.38	60
X	AD	1150	70.23	0.8104	154.1	12.9	0.63	35.2	95.2	162.6	0.61	120
X	AE	1200	163.2	2.182	255.2	0.7	0.23	53.9	95.5	522.6	4.9	10
X	AF	1300	182.5	4.532	253.2	0.1	0.11	59.2	95.5	624.2	37.2	4
X	AG	1400	238.7	6.248	322.6	0.0	0.082	60.3	95.5	792.8	126	4
X	AH	1550	192.1	4.012	197.2	11.2	0.13	69.8	99.7	747.6	0.69	4
X	Al	1700	307.7	7.935	324.9	0.9	0.064	69.0	100.0	1077	6.2	4
	Integrated age ± 1s			n=35		271.7	0.77		K2O=2.41%	87.76	0.10	
	No Plateau											
	110719-3, K-Feldspar, 9.46 mg, J=0.0037448±0.03%, IC=1.037825±0.0008778, NM-309B, Lab#=67464-01											
X	A	450	82.05	0.0546	128.6	6.0	9.3	53.7	0.5	279.50	0.43	10
X	B	450	5.533	0.0877	9.631	5.2	5.8	48.7	0.9	18.37	0.10	20
X	C	500	4.345	-0.0088	5.589	9.6	-	62.0	1.8	18.361	0.057	10
X	D	500	2.885	0.0237	2.938	14.8	21.5	70.0	3.0	13.786	0.035	20

	ID	Power/Temp (Watts/°C)	$^{40}Ar/^{39}Ar$	$^{37}Ar/^{39}Ar$	$^{36}Ar/^{39}Ar$ (x 10^{-3})	$^{39}Ar_K$ (x 10^{-15} mol)	K/Ca	$^{40}Ar^*$ (%)	^{39}Ar (%)	Age (Ma)	±1s (Ma)	Time (min)
X	E	550	3.075	-0.0155	2.286	20.7	-	78.0	4.7	16.364	0.027	10
X	F	550	2.417	0.0062	1.342	23.7	82.6	83.6	6.7	13.802	0.019	20
X	G	600	2.593	0.0211	1.217	26.8	24.1	86.2	9.0	15.253	0.017	10
X	H	600	2.303	0.0116	0.7351	32.1	43.9	90.6	11.7	14.244	0.013	20
X	I	650	2.459	-0.0091	0.9179	31.3	-	88.9	14.3	14.926	0.014	10
X	J	650	2.241	0.0058	0.4926	35.6	87.3	93.5	17.3	14.313	0.010	20
X	K	700	2.330	0.0362	0.5691	26.1	14.1	92.9	19.5	14.780	0.013	10
X	L	700	2.216	0.0225	0.4047	32.5	22.7	94.7	22.2	14.323	0.010	20
X	M	750	2.310	0.0037	0.5783	24.0	138.5	92.6	24.2	14.605	0.014	10
X	N	750	2.232	0.0099	0.4312	27.3	51.7	94.3	26.5	14.375	0.013	20
X	O	800	2.323	0.0096	0.5809	22.2	53.2	92.6	28.4	14.692	0.015	10
X	P	800	2.263	0.0179	0.4326	26.4	28.5	94.4	30.6	14.587	0.013	20
X	Q	850	2.338	-0.0076	0.5131	25.8	-	93.5	32.7	14.923	0.014	10
X	R	850	2.315	0.0175	0.3733	33.7	29.1	95.3	35.6	15.061	0.011	20
X	S	900	2.416	0.0260	0.4800	25.3	19.6	94.2	37.7	15.540	0.014	10
X	T	900	2.459	0.0051	0.4657	31.7	100.8	94.4	40.4	15.844	0.012	20
X	U	950	2.649	-0.0094	0.7262	23.4	-	91.9	42.3	16.606	0.016	10
X	V	950	2.740	-0.0035	0.7369	29.4	-	92.0	44.8	17.203	0.014	20
X	W	1000	3.035	0.0087	1.227	24.9	58.8	88.1	46.9	18.232	0.018	10
X	X	1000	3.082	0.0143	1.059	30.6	35.7	89.9	49.5	18.889	0.015	20
X	Y	1050	3.426	0.0288	1.571	27.3	17.7	86.5	51.7	20.207	0.019	10
X	Z	1050	3.485	-0.0038	1.412	36.7	-	88.0	54.8	20.907	0.016	20
X	AA	1100	3.815	0.0176	1.926	29.4	29.0	85.1	57.3	22.127	0.020	10
X	AB	1100	3.930	0.0040	1.889	41.1	126.6	85.8	60.7	22.969	0.016	20
X	AC	1100	4.134	0.0083	1.859	68.4	61.6	86.7	66.5	24.412	0.013	60
X	AD	1100	4.513	0.0038	2.020	67.2	134.9	86.8	72.1	26.653	0.014	120
X	AE	1150	4.918	-0.0185	2.269	11.0	-	86.3	73.1	28.874	0.042	10
X	AF	1200	5.195	-0.0072	2.668	20.8	-	84.8	74.8	29.959	0.029	4
	AG	1250	5.480	0.0022	2.395	107.5	233.7	87.1	83.8	32.427	0.012	4
	AH	1350	5.206	0.0016	2.292	138.5	316.0	87.0	95.4	30.781	0.011	4
	AI	1550	5.256	0.0004	2.534	54.3	1280.0	85.8	100.0	30.640	0.017	4
Integrated age ± 1s				n=35		1191	73.4		K2O=12.92%	23.116	0.009	
Plateau ± 1s			steps AG-AI	n=3	MSWD=6133	300.225			25.2	31.33	0.569	
160719-4, Muscovite, 1.07 mg, J=0.0037012±0.02%, IC=1.029742±0.0011289, NM-309F, Lab#=67505-01												
X	A	500	2888.3	-0.0158	8008.6	0.8	-	18.1	0.8	1969	13.7	20
X	B	550	17.27	0.0110	24.75	0.5	46.4	57.7	1.3	66.2	1.4	20
X	C	600	14.64	0.0214	14.95	1.0	23.8	69.8	2.3	67.99	0.79	20
X	D	650	13.49	0.0036	8.539	1.7	142.2	81.3	4.0	72.81	0.46	20
X	E	680	13.29	0.0305	6.051	1.8	16.8	86.6	5.8	76.35	0.44	20
X	F	695	13.94	0.0143	5.622	1.5	35.8	88.1	7.3	81.39	0.51	20
X	G	710	14.31	0.0278	5.360	1.6	18.3	88.9	8.8	84.25	0.50	20
X	H	720	14.52	0.0118	4.591	1.5	43.1	90.7	10.3	87.06	0.52	20
X	I	730	15.01	-0.0012	4.889	1.5	-	90.4	11.8	89.65	0.54	20
X	J	740	14.86	0.0001	4.659	1.4	5046.5	90.7	13.2	89.15	0.54	20
X	K	750	14.60	-0.0098	4.340	1.7	-	91.2	14.9	88.07	0.46	20
X	L	755	14.08	-0.0178	3.361	1.6	-	92.9	16.5	86.57	0.48	20
X	M	760	13.75	0.0085	3.521	1.5	59.7	92.4	18.0	84.17	0.48	20
X	N	765	13.64	0.0448	3.294	1.4	11.4	92.9	19.4	83.91	0.53	20
X	O	770	13.59	0.0167	2.946	1.3	30.5	93.6	20.8	84.19	0.53	20
X	P	780	13.56	0.0341	2.606	1.7	14.9	94.3	22.4	84.71	0.44	20
X	Q	790	13.40	0.0063	2.729	1.9	80.5	94.0	24.3	83.41	0.39	20
X	R	800	13.38	-0.0081	2.669	2.0	-	94.1	26.4	83.35	0.37	20
X	S	820	13.49	0.0071	2.760	3.0	71.5	94.0	29.4	83.93	0.25	20
X	T	840	13.38	-0.0022	2.377	4.2	-	94.7	33.6	83.90	0.19	20
X	U	860	13.20	0.0016	2.446	4.6	312.6	94.5	38.2	82.66	0.17	20
X	V	890	13.09	0.0051	2.356	5.8	100.2	94.7	44.1	82.07	0.14	20
X	W	920	13.04	0.0009	2.437	7.1	589.6	94.5	51.2	81.59	0.12	20
X	X	950	13.03	0.0004	2.315	8.0	1159.6	94.8	59.2	81.81	0.12	20
X	Y	980	13.15	0.0039	2.210	7.4	130.9	95.0	66.6	82.75	0.12	20
X	Z	1030	13.33	0.0034	2.240	9.2	149.0	95.0	75.8	83.877	0.094	20
X	AA	1070	13.35	0.0174	1.684	1.5	29.4	96.3	77.3	85.09	0.48	3
X	AB	1150	13.80	0.0014	2.574	8.1	369.2	94.5	85.3	86.26	0.12	3
	AC	1600	16.73	0.0054	10.90	14.7	94.4	80.8	100.0	89.29	0.11	3
Integrated age ± 1s				n=29		100.1	102.3		K2O=9.71%	110.03	0.17	
Terminal age ± 1s			Step AC	n=1		14.672			14.7	89.29	0.11	
160719-13, Hornblende, 3.34 mg, J=0.0037343±0.03%, IC=1.03261±0.0045346, NM-309E, Lab#=67499-01												
X	A	1.5	103.9	5.882	192.5	1.0	0.087	45.7	2.6	299.9	2.8	
X	B	2.0	14.95	5.506	21.07	2.3	0.093	61.4	8.8	61.86	0.45	
X	C	2.5	10.68	5.477	7.811	7.6	0.093	82.6	29.2	59.53	0.15	
X	D	3.0	8.469	5.268	4.449	8.1	0.097	89.5	50.9	51.30	0.11	
X	E	3.5	8.454	5.457	4.979	5.3	0.094	87.9	65.1	50.26	0.15	
X	F	4.0	8.215	5.370	5.220	2.8	0.095	86.6	72.6	48.14	0.21	
	G	4.5	6.392	4.277	4.060	1.8	0.12	86.7	77.4	37.60	0.26	
	H	5.0	6.065	3.647	3.494	1.2	0.14	87.9	80.6	36.16	0.35	
	I	5.5	6.232	3.076	3.489	1.9	0.17	87.5	85.8	36.97	0.25	
X	J	6.0	7.986	5.906	5.263	1.9	0.086	86.6	90.9	46.84	0.28	
X	K	6.5	8.559	5.061	5.171	1.1	0.10	87.0	93.9	50.36	0.44	
X	L	7.0	6.838	3.092	4.584	0.5	0.17	83.9	95.2	38.87	0.81	
X	M	10.0	10.02	5.714	6.400	1.0	0.089	85.8	98.0	58.02	0.51	
X	N	15.0	12.60	6.802	6.405	0.7	0.075	89.4	100.0	75.73	0.77	
Integrated age ± 1s				n=14		37.3	0.098		K2O=1.15%	58.594	0.093	
Plateau ± 1s			steps G-I	n=3	MSWD=5.43	4.932			13.2	37.04	0.374	
160719-13, Ksp/Plag, 5.49 mg, J=0.0037424±0.03%, IC=1.029598±0.0015691, NM-309B, Lab#=67459-01												
X	A	500	1065.2	1.653	2937.0	1.0	0.31	18.5	1.6	1014	8.8	10
X	B	500	87.01	1.607	214.8	0.5	0.32	27.2	2.4	155.5	3.2	20
X	C	550	94.55	1.181	259.2	0.5	0.43	19.1	3.3	119.6	2.9	10
X	D	550	33.25	1.654	84.95	0.7	0.31	24.9	4.5	55.9	1.6	20

	ID	Power/Temp (Watts/°C)	$^{40}Ar/^{39}Ar$	$^{37}Ar/^{39}Ar$	$^{36}Ar/^{39}Ar$ (x 10^{-3})	$^{39}Ar_K$ (x 10^{-15} mol)	K/Ca	$^{40}Ar^*$ (%)	^{39}Ar (%)	Age (Ma)	±1s (Ma)	Time (min)
X	E	600	96.73	1.499	216.4	0.9	0.34	34.0	6.0	212.7	2.4	10
X	F	600	23.76	1.588	60.31	0.9	0.32	25.5	7.4	41.2	1.1	20
X	G	650	71.29	1.289	148.6	0.9	0.40	38.5	8.9	179.3	2.0	10
X	H	650	22.44	1.724	56.10	1.2	0.30	26.8	10.8	40.74	0.89	20
X	I	700	55.80	1.718	113.1	1.1	0.30	40.3	12.6	148.3	1.5	10
X	J	700	13.73	1.441	23.37	1.2	0.35	50.5	14.6	46.97	0.60	20
X	K	750	65.91	1.172	126.0	1.2	0.44	43.7	16.6	187.4	1.5	10
X	L	750	12.81	1.204	19.07	1.3	0.42	56.8	18.7	49.18	0.56	20
X	M	800	50.88	1.268	84.12	1.3	0.40	51.3	20.9	170.9	1.3	10
X	N	800	10.36	1.059	16.42	1.3	0.48	54.0	23.2	37.97	0.51	20
X	O	850	29.82	0.7949	56.83	1.5	0.64	43.9	25.6	87.57	0.83	10
X	P	850	9.177	0.7221	14.39	1.7	0.71	54.3	28.4	33.84	0.40	20
X	Q	900	33.71	0.7921	68.04	2.3	0.64	40.6	32.1	91.39	0.75	10
X	R	900	9.961	0.5190	17.93	2.1	0.98	47.2	35.6	31.96	0.38	20
X	S	950	24.46	1.141	46.18	2.1	0.45	44.6	39.0	73.31	0.63	10
X	T	950	12.25	0.8044	21.50	1.7	0.63	48.7	41.9	40.40	0.50	20
X	U	1000	16.91	0.7329	30.05	1.5	0.70	47.9	44.4	54.65	0.60	10
X	V	1000	13.89	0.5974	24.78	2.1	0.85	47.6	48.0	44.77	0.44	20
X	W	1050	19.18	0.7227	31.05	2.1	0.71	52.5	51.5	67.69	0.52	10
X	X	1050	17.07	0.8240	28.46	2.4	0.62	51.1	55.5	58.87	0.45	20
X	Y	1100	22.52	0.9397	32.24	2.8	0.54	58.0	60.1	87.46	0.46	10
X	Z	1100	25.23	0.9155	36.22	2.8	0.56	57.9	64.6	97.44	0.52	20
X	AA	1150	28.47	0.8207	38.95	3.5	0.62	59.8	70.3	113.15	0.47	10
X	AB	1150	38.97	0.9070	59.81	3.2	0.56	54.8	75.6	140.93	0.59	20
X	AC	1300	122.1	2.853	176.1	4.9	0.18	57.6	83.6	428.20	0.95	4
X	AD	1400	162.4	4.771	163.7	6.0	0.11	70.5	93.5	654.35	0.90	4
X	AE	1700	159.2	5.331	205.2	3.9	0.096	62.2	100.0	578.6	1.2	4
Integrated age ± 1s				n=31		60.7	0.28		K2O=1.14%	233.17	0.26	
No Plateau												
180719-10, Biotite, 2.19 mg, J=0.0037353±0.02%, IC=1.03261±0.0045346, NM-309E, Lab#=67500-01												
X	A	0.5	26.79	0.0123	83.51	10.6	41.3	7.9	4.5	14.40	0.81	
X	B	0.8	7.517	0.0070	17.99	27.4	73.0	29.3	16.0	14.98	0.18	
X	C	1.0	7.067	0.0058	15.73	21.4	88.3	34.2	25.0	16.47	0.17	
X	D	1.5	7.262	0.0066	16.13	30.9	77.4	34.4	38.0	17.00	0.16	
X	E	1.8	7.650	0.0050	17.61	24.0	101.3	32.0	48.1	16.65	0.18	
X	F	2.0	7.427	0.0075	16.61	21.6	67.9	33.9	57.2	17.14	0.18	
X	G	2.5	7.588	0.0062	17.14	23.1	81.8	33.3	66.9	17.18	0.18	
	H	2.8	6.758	0.0075	13.88	16.6	68.1	39.3	73.9	18.08	0.16	
	I	3.0	6.790	0.0065	13.65	12.6	79.1	40.6	79.2	18.75	0.17	
	J	3.5	7.053	0.0076	14.85	14.6	66.8	37.8	85.3	18.13	0.18	
	K	4.0	7.154	0.0086	15.58	10.6	59.4	35.7	89.8	17.36	0.20	
	L	5.0	7.394	0.0129	16.24	8.0	39.6	35.1	93.2	17.66	0.23	
	M	6.0	7.299	0.0077	16.04	5.7	66.5	35.1	95.6	17.43	0.25	
	N	7.0	7.007	0.0093	15.07	2.3	55.0	36.4	96.6	17.37	0.33	
	O	12.0	6.682	0.0083	13.78	8.2	61.4	39.1	100.0	17.76	0.21	
Integrated age ± 1s				n=15		237.7	70.4		K2O=11.16%	16.914	0.063	
Plateau ± 1s			steps H-O	n=8	MSWD=5.90	78.703			33.1	17.94	0.174	
180719-10, Muscovite, J=0.0037121±0.01%, IC=1.029171±0.0012136, NM-309F, Lab#=67513-01												
X	A	455	59.23	0.0442	185.9	0.7	11.5	7.3	0.6	29.1	2.1	20
X	B	500	12.53	-0.0945	30.53	0.4	-	27.9	1.0	23.6	1.2	20
X	C	550	8.970	0.0116	20.54	0.9	44.2	32.4	1.7	19.62	0.68	20
X	D	600	7.188	0.0176	13.12	1.6	29.0	46.1	3.0	22.37	0.39	20
X	E	650	6.209	-0.0037	9.867	2.7	-	53.0	5.1	22.24	0.34	20
X	F	680	4.981	0.0029	5.391	2.7	173.3	68.0	7.3	22.88	0.20	20
X	G	695	5.519	-0.0003	6.871	2.4	-	63.2	9.2	23.55	0.24	20
X	H	710	5.074	0.0116	4.976	2.1	44.0	71.0	10.8	24.33	0.24	20
X	I	720	5.009	0.0209	4.391	2.1	24.4	74.1	12.5	25.06	0.23	20
X	J	730	5.251	0.0017	4.802	2.0	304.1	73.0	14.1	25.86	0.25	20
X	K	740	5.529	0.0099	5.801	2.0	51.6	69.0	15.8	25.75	0.25	20
X	L	750	5.691	-0.0179	5.934	2.1	-	69.2	17.4	26.55	0.25	20
X	M	755	5.748	-0.0085	5.816	2.3	-	70.1	19.3	27.17	0.22	20
X	N	760	6.604	-0.0012	8.083	2.4	-	63.8	21.2	28.42	0.24	20
X	O	765	6.078	0.0049	6.297	2.5	103.7	69.4	23.3	28.43	0.23	20
X	P	770	5.566	-0.0082	4.235	2.4	-	77.5	25.2	29.08	0.21	20
X	Q	780	5.793	0.0024	4.882	3.5	209.9	75.1	28.1	29.33	0.17	20
X	R	790	5.539	0.0047	3.974	4.1	109.7	78.8	31.4	29.42	0.14	20
X	S	800	5.393	-0.0005	3.566	4.2	-	80.5	34.8	29.25	0.13	20
X	T	820	5.292	-0.0028	3.134	6.5	-	82.5	40.0	29.425	0.095	20
X	U	840	5.086	0.0038	2.633	7.1	133.9	84.7	45.7	29.042	0.088	20
X	V	860	5.064	0.0026	2.850	6.9	199.4	83.4	51.3	28.465	0.092	20
X	W	875	5.146	-0.0045	3.294	5.5	-	81.1	55.7	28.14	0.11	20
X	X	890	5.311	0.0064	3.815	5.0	80.1	78.8	59.7	28.21	0.12	20
X	Y	905	5.472	0.0109	4.374	4.5	46.9	76.4	63.4	28.19	0.13	20
X	Z	920	5.615	0.0104	4.849	4.1	49.1	74.5	66.7	28.21	0.16	20
X	AA	950	5.686	0.0071	5.290	4.9	72.0	72.5	70.6	27.80	0.14	20
X	AB	980	5.841	0.0102	5.347	5.3	49.9	73.0	74.9	28.73	0.13	20
X	AC	1000	5.846	-0.0043	5.070	4.5	-	74.4	78.6	29.30	0.15	20
X	AD	1030	5.891	0.0063	4.830	5.9	81.5	75.8	83.3	30.09	0.12	20
	AE	1070	5.816	0.0140	4.360	1.3	36.5	77.9	84.4	30.52	0.32	3
	AF	1110	6.290	0.0039	5.781	3.0	130.3	72.8	86.8	30.87	0.18	3
	AG	1150	5.622	0.0025	3.552	7.8	205.8	81.3	93.1	30.807	0.092	3
	AH	1250	4.994	0.0003	1.595	8.6	1818.3	90.6	100.0	30.473	0.067	3
Integrated age ± 1s				n=34		124.1	176.4			28.287	0.031	
Plateau ± 1s			steps AE-AH	n=4	MSWD=3.61	20.716			16.7	30.61	0.097	
190719-3, Biotite, 1.09 mg, J=0.003732±0.03%, IC=1.03261±0.0045346, NM-309E, Lab#=67498-01												
X	A	0.5	16.18	0.0803	50.69	10.1	6.4	7.5	7.2	8.22	0.51	
X	B	0.8	6.359	0.0850	10.88	19.5	6.0	49.6	21.0	21.41	0.13	

	ID	Power/Temp (Watts/°C)	$^{40}Ar/^{39}Ar$	$^{37}Ar/^{39}Ar$	$^{36}Ar/^{39}Ar$ (x 10^{-3})	$^{39}Ar_K$ (x 10^{-15} mol)	K/Ca	$^{40}Ar^*$ (%)	^{39}Ar (%)	Age (Ma)	±1s (Ma)	Time (min)
X	C	1.0	5.645	0.0401	8.354	14.5	12.7	56.3	31.3	21.60	0.11	
	D	1.5	5.323	0.0357	6.552	21.0	14.3	63.7	46.2	23.013	0.088	
	E	1.8	5.304	0.0313	6.510	15.3	16.3	63.8	57.0	22.965	0.099	
	F	2.0	5.340	0.0332	6.771	11.9	15.4	62.6	65.5	22.69	0.10	
	G	2.5	5.199	0.0330	5.801	14.3	15.5	67.1	75.6	23.668	0.094	
	H	2.8	5.260	0.0449	6.282	7.7	11.4	64.8	81.1	23.13	0.13	
	I	3.0	5.348	0.0506	7.189	5.1	10.1	60.4	84.8	21.92	0.15	
	J	3.5	5.531	0.0603	7.963	5.1	8.5	57.5	88.4	21.61	0.16	
	K	4.0	5.459	0.0579	7.788	5.0	8.8	57.9	92.0	21.48	0.17	
	L	5.0	5.269	0.0593	5.769	4.4	8.6	67.7	95.1	24.22	0.16	
	M	6.0	5.327	0.0361	6.785	3.1	14.1	62.4	97.3	22.57	0.20	
	N	7.0	5.378	0.0417	6.233	2.1	12.2	65.8	98.8	24.02	0.24	
	O	12.0	6.298	0.0472	11.71	1.7	10.8	45.1	100.0	19.31	0.37	
Integrated age ± 1s				n=15		141.0	10.4		K2O=13.32%	21.483	0.050	
Plateau ± 1s			steps D-O	n=12	MSWD=39.18	96.892			68.7	22.90	0.237	
190818-3, Biotite, 1.75 mg, J=0.0037855±0.01%, IC=1.028619±0.0009457, NM-306F, Lab#=67321-01												
X	B	0.8	23.54	0.0218	43.88	2.4	23.4	44.9	1.2	71.88	0.51	
X	C	1.0	11.86	0.0179	14.16	4.1	28.6	64.7	3.3	52.41	0.23	
X	D	1.5	8.027	0.0096	6.337	10.2	53.4	76.7	8.5	42.16	0.10	
X	E	1.7	5.746	0.0060	2.872	12.6	85.5	85.2	14.9	33.626	0.062	
X	F	1.9	5.298	0.0087	2.277	12.9	58.4	87.3	21.4	31.777	0.051	
X	G	2.0	5.189	0.0094	2.204	10.2	54.5	87.5	26.6	31.184	0.063	
X	H	2.1	5.081	0.0125	2.035	8.1	41.0	88.2	30.7	30.785	0.069	
X	I	2.5	5.098	0.0379	2.187	10.9	13.5	87.4	36.2	30.614	0.061	
X	J	3.0	5.131	0.0370	2.366	13.5	13.8	86.4	43.0	30.478	0.053	
X	K	3.5	5.130	0.0618	2.248	15.0	8.3	87.1	50.7	30.721	0.051	
	L	5.0	5.097	0.1518	1.871	27.3	3.4	89.4	64.5	31.304	0.029	
	M	6.0	5.115	0.1838	1.924	23.6	2.8	89.2	76.5	31.338	0.036	
	N	7.0	5.013	0.1678	1.643	17.9	3.0	90.6	85.5	31.201	0.037	
	O	15.0	5.137	0.1466	1.474	28.6	3.5	91.8	100.0	32.372	0.029	
Integrated age ± 1s				n=14		197.4	5.6		K2O=11.45%	32.975	0.016	
Plateau ± 1s			steps L-O	n=4	MSWD=327.23	97.410			49.3	31.62	0.290	
200719-7, Biotite, 1.57 mg, J=0.0037308±0.03%, IC=1.03261±0.0045346, NM-309E, Lab#=67497-01												
Xi	A	0.5	17.82	0.0232	58.36	12.5	22.0	3.2	9.8	3.95	0.57	
Xi	B	0.8	10.06	0.0169	30.36	18.9	30.2	10.9	24.5	7.45	0.31	
Xi	C	1.0	9.142	0.0171	26.42	11.0	29.9	14.6	33.0	9.10	0.30	
Xi	D	1.5	8.799	0.0156	24.60	16.1	32.7	17.4	45.5	10.42	0.26	
Xi	E	1.8	8.750	0.0167	24.49	12.9	30.6	17.3	55.6	10.31	0.27	
Xi	F	2.0	8.653	0.0152	24.43	8.8	33.6	16.6	62.4	9.78	0.29	
Xi	G	2.5	8.693	0.0168	24.27	9.4	30.3	17.5	69.7	10.37	0.29	
Xi	H	2.8	9.235	0.0178	26.51	5.0	28.6	15.2	73.6	9.55	0.37	
Xi	I	3.0	9.367	0.0182	26.94	4.6	28.0	15.0	77.2	9.59	0.37	
Xi	J	3.5	9.125	0.0153	25.87	5.5	33.4	16.2	81.4	10.10	0.34	
Xi	K	4.0	8.881	0.0136	24.73	4.4	37.7	17.7	84.9	10.73	0.37	
	L	5.0	8.450	0.0136	22.85	5.2	37.6	20.1	88.9	11.57	0.34	
	M	7.0	8.752	0.0167	24.11	7.7	30.5	18.6	94.9	11.08	0.29	
	N	12.0	9.188	0.0158	24.86	6.5	32.3	20.1	100.0	12.55	0.32	
Integrated age ± 1s				n=14		128.6	30.2		K2O=8.43%	9.311	0.100	
Plateau ± 1s			steps L-N	n=3	MSWD=5.85	19.5			15.1	11.70	0.44	
200719-7, Muscovite, 2.57 mg, J=0.003714±0.02%, IC=1.029171±0.0012136, NM-309F, Lab#=67514-01												
X	A	455	29.11	0.0449	93.48	3.3	11.4	5.1	1.5	10.13	0.67	20
X	B	500	9.287	0.0293	21.80	1.9	17.4	30.7	2.4	19.26	0.42	20
X	C	550	8.695	0.0122	17.78	2.6	41.8	39.6	3.7	23.26	0.33	20
X	D	600	6.891	0.0138	12.30	3.9	37.0	47.3	5.5	22.01	0.23	20
X	E	650	4.558	0.0086	5.804	5.5	59.1	62.4	8.1	19.23	0.13	20
X	F	680	3.690	-0.0055	2.834	5.6	-	77.3	10.7	19.287	0.096	20
X	G	695	3.563	-0.0013	2.053	4.7	-	83.0	12.9	19.987	0.098	20
X	H	710	3.636	0.0072	2.049	4.7	71.0	83.4	15.1	20.493	0.098	20
X	I	720	3.726	0.0081	2.088	4.2	62.8	83.5	17.1	21.02	0.11	20
X	J	730	3.724	0.0044	1.661	4.6	115.6	86.8	19.3	21.851	0.096	20
X	K	740	3.865	0.0068	1.578	4.4	74.9	87.9	21.3	22.961	0.099	20
X	L	750	4.003	0.0054	1.436	5.7	95.3	89.4	24.0	24.170	0.081	20
X	M	755	4.047	0.0006	1.152	6.1	870.5	91.6	26.9	25.026	0.072	20
X	N	760	4.001	0.0025	0.9544	5.8	204.7	93.0	29.6	25.111	0.072	20
X	O	765	3.971	0.0048	0.9625	5.2	105.4	92.8	32.1	24.894	0.077	20
X	P	770	3.929	0.0017	0.8910	5.1	297.0	93.3	34.5	24.754	0.074	20
X	Q	780	3.923	0.0004	0.9111	5.5	1368.9	93.1	37.1	24.676	0.070	20
X	R	790	3.939	0.0099	1.068	5.8	51.6	92.0	39.8	24.474	0.072	20
X	S	800	3.868	0.0030	0.8245	5.7	168.4	93.7	42.5	24.475	0.071	20
X	T	820	3.882	0.0029	0.9690	7.4	178.9	92.6	46.0	24.282	0.056	20
X	U	840	3.846	0.0040	1.067	9.0	126.6	91.8	50.2	23.849	0.055	20
X	V	860	3.803	0.0014	1.157	11.2	363.1	91.0	55.5	23.384	0.047	20
X	W	890	3.741	0.0023	1.284	13.1	226.7	89.9	61.7	22.715	0.043	20
X	X	900	3.711	0.0054	1.406	9.2	95.2	88.8	66.1	22.273	0.059	20
X	Y	920	3.706	-0.0008	1.470	9.3	-	88.3	70.4	22.109	0.057	20
X	Z	935	3.765	0.0117	1.585	8.1	43.6	87.6	74.3	22.279	0.066	20
X	AA	950	3.806	0.0069	1.628	7.9	73.9	87.4	78.0	22.469	0.067	20
X	AB	980	3.844	-0.0018	1.509	8.2	-	88.4	81.8	22.957	0.066	20
X	AC	1000	3.885	0.0042	1.501	8.2	122.1	88.6	85.7	23.251	0.061	20
X	AD	1030	3.985	0.0061	1.388	9.8	83.3	89.7	90.3	24.149	0.053	20
X	AE	1070	3.854	0.0077	1.035	1.8	66.5	92.1	91.1	23.97	0.18	3
	AF	1110	4.323	0.0065	2.073	2.7	78.6	85.8	92.4	25.06	0.15	3
	AG	1150	4.041	0.0033	0.8931	9.5	155.2	93.5	96.9	25.499	0.050	3
	AH	1250	4.083	0.0111	1.293	6.6	45.9	90.7	100.0	24.995	0.070	3
Integrated age ± 1s				n=34		212.1	99.9		K2O=8.54%	22.966	0.018	
Plateau ± 1s			steps AF-AH	n=3	MSWD=18.53	18.773			8.9	25.31	0.170	

	ID	Power/Temp (Watts/°C)	$^{40}Ar/^{39}Ar$	$^{37}Ar/^{39}Ar$	$^{36}Ar/^{39}Ar$ (x 10^{-3})	$^{39}Ar_K$ (x 10^{-15} mol)	K/Ca	$^{40}Ar^*$ (%)	^{39}Ar (%)	Age (Ma)	±1s (Ma)	Time (min)
210719-2, Hornblende, 3.48 mg, J=0.0037905±0.01%, IC=1.028619±0.0009457, NM-306F, Lab#=67322-01												
X	A	1.5	41.56	1.671	77.27	2.2	0.31	45.4	4.3	126.52	0.85	
X	B	2.0	9.798	0.9178	13.09	3.3	0.56	61.3	10.8	41.22	0.25	
X	C	2.5	8.043	3.095	6.444	3.8	0.16	79.5	18.1	43.91	0.18	
X	D	3.0	7.456	4.948	5.111	4.7	0.10	85.2	27.2	43.68	0.14	
X	E	3.5	7.145	4.996	4.294	5.6	0.10	87.9	38.1	43.23	0.12	
X	F	4.0	6.848	4.622	3.607	6.7	0.11	89.9	51.0	42.37	0.10	
X	G	4.5	6.726	3.749	3.243	6.8	0.14	90.3	64.3	41.769	0.093	
	H	5.0	6.573	3.273	3.023	4.7	0.16	90.5	73.5	40.89	0.12	
	I	5.5	6.763	3.308	3.428	2.8	0.15	89.0	79.0	41.39	0.17	
	J	6.0	6.803	4.597	3.994	1.3	0.11	88.2	81.5	41.28	0.31	
	K	6.5	6.457	5.295	3.427	1.6	0.096	91.0	84.5	40.47	0.27	
	L	7.0	6.340	6.685	3.586	1.3	0.076	91.9	87.0	40.16	0.32	
	M	10.0	6.257	4.584	2.542	4.9	0.11	94.0	96.5	40.47	0.10	
	N	15.0	6.837	5.683	4.557	1.8	0.090	87.1	100.0	41.01	0.25	
Integrated age ± 1s				n=14		51.4	0.13		K2O=1.50%	45.672	0.056	
Plateau ± 1s			steps H-N	n=7	MSWD=5.11	18.333			35.7	40.76	0.144	
210719-2, K-Feldspar, 11.15 mg, J=0.0037386±0.02%, IC=1.029598±0.0015691, NM-309B, Lab#=67456-01												
X	A	450	435.8	0.2844	1500.5	1.9	1.8	-1.8	0.2	-53.0	5.8	10
X	B	450	68.06	0.2583	214.8	0.7	2.0	6.8	0.2	31.2	2.2	20
X	C	500	49.01	-0.0360	148.2	0.5	-	10.6	0.3	35.3	2.0	10
X	D	500	28.12	0.1412	78.09	3.0	3.6	18.0	0.6	34.25	0.69	20
X	E	550	25.45	0.2199	67.16	3.5	2.3	22.1	0.9	38.09	0.58	10
X	F	550	11.72	0.2018	21.61	4.1	2.5	45.7	1.3	36.26	0.29	20
X	G	600	19.04	0.2712	45.07	5.3	1.9	30.2	1.8	38.91	0.38	10
X	H	600	8.749	0.1326	11.10	6.6	3.8	62.6	2.4	37.13	0.16	20
X	I	650	12.98	0.2015	24.58	7.5	2.5	44.2	3.1	38.82	0.22	10
X	J	650	7.528	0.1589	6.632	8.8	3.2	74.1	3.9	37.80	0.12	20
X	K	700	9.532	0.1547	13.14	9.4	3.3	59.4	4.8	38.34	0.15	10
X	L	700	6.684	0.1602	3.746	11.4	3.2	83.6	5.9	37.862	0.077	20
X	M	750	8.110	0.1605	8.304	10.4	3.2	69.9	6.9	38.39	0.11	10
X	N	750	6.485	0.1401	3.036	11.7	3.6	86.3	8.0	37.927	0.064	20
X	O	800	8.817	0.1168	10.67	11.0	4.4	64.3	9.0	38.43	0.12	10
X	P	800	6.401	0.1034	2.670	11.2	4.9	87.8	10.1	38.065	0.067	20
X	Q	850	10.54	0.1110	16.46	9.8	4.6	53.9	11.0	38.49	0.16	10
X	R	850	6.999	0.0632	4.765	11.6	8.1	80.0	12.1	37.901	0.084	20
X	S	900	13.21	0.0362	24.73	12.4	14.1	44.7	13.3	39.97	0.20	10
X	T	900	7.522	0.0494	6.452	11.3	10.3	74.7	14.3	38.061	0.096	20
X	U	950	14.71	0.0560	30.47	16.9	9.1	38.8	15.9	38.70	0.18	10
X	V	950	8.433	0.0362	9.395	15.7	14.1	67.1	17.4	38.33	0.10	20
X	W	1000	14.01	0.0433	28.02	24.4	11.8	40.9	19.7	38.79	0.15	10
X	X	1000	9.590	0.0463	13.27	22.5	11.0	59.1	21.8	38.41	0.10	20
X	Y	1050	12.50	0.0330	22.85	39.6	15.5	46.0	25.6	38.94	0.11	10
X	Z	1050	10.06	0.0547	14.52	32.3	9.3	57.4	28.6	39.069	0.091	20
X	AA	1100	10.54	0.0476	16.02	39.7	10.7	55.1	32.4	39.336	0.093	10
X	AB	1100	9.821	0.0445	13.62	57.9	11.5	59.1	37.8	39.272	0.072	20
X	AC	1100	9.308	0.0314	11.90	118.9	16.3	62.3	49.1	39.236	0.051	60
X	AD	1100	8.910	0.0212	10.58	144.4	24.1	64.9	62.7	39.172	0.046	120
X	AE	1150	8.753	0.0110	9.645	59.4	46.5	67.4	68.3	39.961	0.057	10
X	AF	1200	8.621	0.0085	9.218	145.1	59.7	68.4	82.0	39.922	0.042	4
X	AG	1250	8.794	0.0105	9.932	121.5	48.5	66.6	93.4	39.669	0.046	4
X	AH	1350	9.073	0.0739	10.21	31.5	6.9	66.8	96.4	41.029	0.077	4
	AI	1550	8.768	0.0518	8.855	36.0	9.8	70.2	99.8	41.646	0.068	4
X	AJ	1680	44.74	0.0712	127.0	1.9	7.2	16.1	100.0	48.8	1.0	4
Integrated age ± 1s				n=36		1060	12.0		K2O=9.77%	39.189	0.020	
Terminal age ± 1s			Step AI	n=1	MSWD=NA	35.990			3.4	41.646	0.068	
210719-2, Biotite, 5.35 mg, J=0.0037941±0.01%, IC=1.028619±0.0009457, NM-306F, Lab#=67323-01												
X	C	1.0	13.96	0.0336	39.61	3.2	15.2	16.2	0.5	15.65	0.41	
X	D	1.5	10.48	0.0193	22.59	9.0	26.4	36.4	1.8	26.28	0.19	
X	E	1.7	7.438	0.0097	7.639	12.9	52.6	69.7	3.7	35.634	0.095	
X	F	1.9	6.790	0.0098	4.602	15.2	51.9	80.0	6.0	37.336	0.066	
X	G	2.0	6.854	0.0117	5.126	15.5	43.7	77.9	8.3	36.718	0.070	
X	H	2.1	6.610	0.0078	3.651	15.0	65.8	83.7	10.5	38.023	0.063	
X	I	2.5	6.416	0.0108	2.773	25.4	47.0	87.2	14.3	38.464	0.042	
X	J	3.0	6.388	0.0102	2.630	36.1	49.8	87.8	19.7	38.567	0.034	
	K	3.5	6.271	0.0124	2.141	47.4	41.3	89.9	26.7	38.752	0.028	
	L	5.0	6.123	0.0194	1.561	98.0	26.3	92.5	41.3	38.914	0.016	
	M	6.0	6.165	0.0326	1.721	104.5	15.6	91.8	56.9	38.890	0.017	
	N	7.0	6.113	0.0356	1.524	101.7	14.3	92.7	72.0	38.934	0.016	
	O	15.0	5.946	0.0455	0.8536	188.1	11.2	95.8	100.0	39.149	0.009	
Integrated age ± 1s				n=13		672.0	17.5		K2O=12.72%	38.483	0.009	
Plateau ± 1s			steps K-O	n=5	MSWD=102	539.697			80.3	39.02	0.066	

Notes:

Isotopic ratios corrected for blank, radioactive decay, and mass discrimination, not corrected for interfering reactions.
Errors quoted for individual analyses include analytical error only, without interfering reaction or J uncertainties.
Integrated age calculated by summing isotopic measurements of all steps.
Integrated age error calculated by quadratically combining errors of isotopic measurements of all steps.
Plateau age is inverse-variance-weighted mean of selected steps.
Plateau age error is inverse-variance-weighted mean error (Taylor, 1982) times root MSWD where MSWD>1.
Plateau error is weighted error of Taylor (1982).
Terminal age generally last a last few steps of a climbing spectrum
Isotopic abundances after Steiger and Jäger (1977).
X preceding sample ID denotes analyses excluded from plateau age calculations.
Weight percent K_2O calculated from ^{39}Ar signal, sample weight, and instrument sensitivity.

ID	Power/Temp (Watts/°C)	$^{40}Ar/^{39}Ar$	$^{37}Ar/^{39}Ar$	$^{36}Ar/^{39}Ar$ (x 10^{-3})	$^{39}Ar_K$ (x 10^{-15} mol)	K/Ca	$^{40}Ar^*$ (%)	^{39}Ar (%)	Age (Ma)	±1s (Ma)	Time (min)

Ages calculated relative to FC-2 Fish Canyon Tuff sanidine interlaboratory standard at 28.201 Ma
Decay Constant (LambdaK (total)) = 5.463e-10/a
Correction factors:

NM-303	NM-306 and NM-309
$(^{39}Ar/^{37}Ar)_{Ca}$ = 0.0006926 ± 0.000016	$(^{39}Ar/^{37}Ar)_{Ca}$ = 0.000679 ± 0.000001
$(^{36}Ar/^{37}Ar)_{Ca}$ = 0.0002702 ± 0.0000010	$(^{36}Ar/^{37}Ar)_{Ca}$ = 0.0002757 ± 0.0000015
$(^{38}Ar/^{39}Ar)_K$ = 0.0121±0.00005	$(^{38}Ar/^{39}Ar)_K$ = 0.01208±0.00002
$(^{40}Ar/^{39}Ar)_K$ = 0.000129 ± 8e-05	$(^{40}Ar/^{39}Ar)_K$ = 0.000129 ± 8e-05

Table 3.S3. Zircon U-Pb Metadata - University of Nevada, Reno

Laboratory and Sample Preparation	
Laboratory Name	University of Nevada, Reno
Sample type/mineral	Igneous zircons
Sample preparation	Standard mineral-separation techniques, mounted in 1-inch epoxy rounds, and polished to expose the approximate center of the grains;
Imaging	CL images of the zircon were collected at 10 kV on the JEOL JSM-7100FT field emission scanning electron microscope (FE-SEM) at the UNR with a 12 mm working distance.
Laser Ablation System	
Make, Model, Type	Resonetics RESOlution M-50 E (ATL laser)
Ablation cell and volume	Laurin Technic M-50A dual volume
Laser wavelength (nm)	Excimer, 193 nm
Pulse width (ns)	20 ns
Fluence (J cm^{-2})	~3-4 J cm^{-2}
Repetition Rate (Hz)	7 Hz
Ablation duration (s)	30 s
Ablation pit depth/ablation rate	~10-12 um
Spot diameter (microns)	25 um
Sampling mode/pattern	Static spot ablation
Carrier gas	He carrier gas mixed with N_2 for increased sensitivity
Cell carrier gas flow (l min^{-1})	0.85 L/min (He), 0.0045 L/min (N_2)
ICP-MS Instrument	
Make, Model, Type	Agilent 7700 quadrupole ICP-MS
Sample Introduction	dry plasma
RF Power (W)	1350 W
Make-up gas flow (l min^{-1})	0.85 L/min
Detection System	Pulse mode
Masses measured	204, 206, 207, 208, 232, 238
Integration time per peak/dwell times (ms)	0.01 s for ^{208}Pb; 0.025 s for ^{232}Th; 0.04 s for ^{238}U and ^{204}Pb; 0.08 s for ^{206}Pb and 0.11 s for ^{207}Pb
Total integration time per output data point (s)	0.305 sec
Sensitivity' as useful yield (%, element)	NA
IC Dead time (ns)	NA
Data Processing	
Gas blank	NA
Calibration strategy	91500 used as primary reference material, Plešovice & Temora-2 used as secondary/validation
Reference Material Information	91500 (Wiedenback et al., 1995), Plešovice (Sláma et al., 2008), Temora-2 (Black et al., 2004)
Data processing package used/Correction for LIEF	MassHunter v.4.5 time resolved analysis mode and Iolite v3/4
Mass discrimination	Standard sample bracketing wrt to primary reference material
Common-Pb correction, composition and uncertainty	NA
Uncertainty level and propagation	Data was reduced using Iolite v3 or v4 (Paton et al., 2010). Uncertainties were calculated using a least squares method of the error given in Iolite and extra error was added based on whether all the individual ratios and ages of the secondary standard revealed a single population assessed by the mean square weighted deviation (MSWD). If they did not, the extra uncertainty required to make the ratio or age measurements a single population was added to all of the unknown measurements.
Quality Control/Validation	

Table 3.S4. Zircon U-Pb Data - University of Nevada, Reno

March, 2021, Dept. of Geological Sciences and Engineering, University of Nevada, Reno

				Isotopic Compositions							Isotopic Dates								
Sample	Spot	Rim / Core	Notes	207Pb/ 206Pb	± 2σ %	207Pb/ 235U	± 2σ %	206Pb/ 238U	± 2σ %	Rho	206Pb/ 238U (Ma)	± 2σ abs	207Pb/ 235U (Ma)	± 2σ abs	207Pb/ 206Pb (Ma)	± 2σ abs	BestAge*	± 2σ abs	Concordance
160719-3 [41.002548, -114.106831] - granodiorite																			
	z1			0.050	7.7	0.041	8.0	0.0059	2.4	0.30	38.0	0.9	40.6	3.3	193.2	14.8	37.9	3.7	0.94
	z2			0.049	5.2	0.036	6.1	0.0054	3.3	0.53	34.8	1.1	36.1	2.2	122.7	6.4	34.7	2.3	0.96
	z3			0.051	5.7	0.041	6.1	0.0058	2.4	0.39	37.4	0.9	40.8	2.5	246.2	13.9	37.1	2.7	0.92
	z4			0.050	6.6	0.041	7.2	0.0059	2.9	0.40	38.2	1.1	40.7	2.9	191.8	12.7	38.0	3.2	0.94
	z5			0.070	6.6	0.057	7.2	0.0059	3.0	0.41	37.7	1.1	56.1	4.0	932.6	61.2	36.6	3.1	0.67
	z6			0.064	11.0	0.054	11.4	0.0061	3.0	0.26	39.0	1.2	53.3	6.1	754.9	83.1	38.1	5.4	0.73
	z7			0.059	5.4	0.049	6.4	0.0060	3.5	0.55	38.7	1.4	48.9	3.1	583.9	31.3	38.1	2.6	0.79
	z8			0.085	3.9	1.041	14.9	0.0889	14.3	0.96	548.8	78.6	724.4	107.6	1314.6	51.5	530.5	27.9	0.76
	z9			0.097	2.5	3.032	3.6	0.2271	2.7	0.73	1319.3	35.0	1415.6	51.6	1563.7	39.0	1564.5	483.1	0.93
	z10			0.054	7.1	0.046	7.9	0.0062	3.3	0.42	39.6	1.3	45.3	3.6	359.6	25.7	39.2	3.6	0.87
	z11			0.050	7.9	0.047	9.7	0.0068	5.8	0.59	43.6	2.5	46.2	4.5	181.8	14.3	43.4	4.3	0.94
	z12			0.055	10.1	0.048	10.8	0.0063	3.9	0.36	40.7	1.6	47.7	5.2	413.7	41.7	40.3	5.2	0.85
	z13			0.067	7.8	0.056	8.4	0.0060	2.9	0.35	38.9	1.1	55.2	4.6	838.6	65.7	37.9	3.9	0.70
	z14			0.043	7.3	0.035	7.8	0.0060	2.9	0.37	38.3	1.1	35.4	2.8	-157.9	11.5	38.5	3.5	1.08
	z15			0.047	10.2	0.039	10.7	0.0060	3.3	0.31	38.8	1.3	38.8	4.1	34.6	3.5	38.8	5.0	1.00
	z16			0.047	8.4	0.038	9.1	0.0059	3.5	0.39	37.8	1.3	37.7	3.4	30.7	2.6	37.8	4.0	1.00
	z17			0.063	6.6	0.051	7.2	0.0059	2.9	0.40	37.8	1.1	50.3	3.6	699.4	46.2	37.0	3.2	0.75
	z18			0.049	6.9	0.040	7.4	0.0059	2.6	0.36	38.0	1.0	40.0	2.9	160.9	11.1	37.9	3.3	0.95
	z19			0.060	13.6	0.052	14.1	0.0062	3.9	0.27	39.9	1.5	51.1	7.2	612.1	83.3	39.2	6.9	0.78
	z20			0.047	7.3	0.039	8.2	0.0060	3.8	0.46	38.3	1.4	38.6	3.2	61.3	4.5	38.2	3.5	0.99
	z21			0.045	7.2	0.039	8.5	0.0062	4.5	0.53	39.8	1.8	38.6	3.3	-31.4	2.3	39.8	3.6	1.03
	z22			0.047	8.0	0.039	9.0	0.0060	4.1	0.45	38.5	1.6	38.5	3.5	36.8	2.9	38.5	3.9	1.00
	z23			0.051	6.8	0.042	7.9	0.0060	4.0	0.51	38.7	1.5	41.9	3.3	234.3	16.0	38.5	3.3	0.92
	z24			0.056	11.5	0.047	12.3	0.0061	4.3	0.35	39.2	1.7	46.4	5.7	439.0	50.6	38.7	5.7	0.84
	z25			0.053	9.0	0.045	9.9	0.0062	4.2	0.42	39.7	1.7	44.5	4.4	315.9	28.5	39.4	4.5	0.89
	z26			0.068	8.8	0.061	10.3	0.0066	5.3	0.52	42.1	2.2	60.4	6.2	863.0	76.0	41.0	4.7	0.70
	z27			0.131	15.4	0.120	16.3	0.0067	5.2	0.32	42.8	2.2	115.5	18.8	2114.3	326.6	38.2	8.4	0.37
	z28			0.117	15.3	0.098	16.0	0.0061	4.5	0.28	39.3	1.8	95.2	15.2	1904.8	291.8	35.8	7.6	0.41
	z29			0.045	7.5	0.039	9.4	0.0063	5.7	0.61	40.6	2.3	38.7	3.6	-80.1	6.0	40.7	3.8	1.05
	z30			0.371	11.0	0.624	13.3	0.0122	7.6	0.57	78.1	5.9	492.4	65.6	3796.5	416.8	46.1	11.1	0.16
	z31			0.054	7.6	0.046	9.3	0.0061	5.3	0.57	39.5	2.1	45.2	4.2	363.0	27.8	39.1	3.8	0.87

				Isotopic Compositions							Isotopic Dates								
Sample	Spot	Rim / Core	Notes	207Pb/ 206Pb	± 2σ %	207Pb/ 235U	± 2σ %	206Pb/ 238U	± 2σ %	Rho	206Pb/ 238U (Ma)	± 2σ abs	207Pb/ 235U (Ma)	± 2σ abs	207Pb/ 206Pb (Ma)	± 2σ abs	BestAge*	± 2σ abs	Concordance
090719-5 [40.99928, -114.069551] - granodiorite																			
	z1			0.054	6.0	0.046	6.5	0.0061	2.6	0.40	39.4	1.0	45.4	3.0	373.0	22.4	39.0	3.0	0.87
	z2			0.051	9.3	0.042	9.8	0.0060	3.2	0.32	38.6	1.2	42.0	4.1	242.4	22.5	38.4	4.5	0.92
	z3			0.045	7.4	0.037	7.9	0.0060	2.8	0.35	38.7	1.1	36.9	2.9	-79.6	5.9	38.8	3.6	1.05
	z4			0.060	7.2	0.054	7.7	0.0066	2.7	0.34	42.1	1.1	53.4	4.1	592.2	42.9	41.4	3.9	0.79
	z5			0.051	8.5	0.043	9.1	0.0061	3.3	0.36	39.5	1.3	42.7	3.9	227.8	19.3	39.3	4.2	0.92
	z6			0.047	8.1	0.038	8.7	0.0059	3.0	0.34	37.6	1.1	38.0	3.3	59.4	4.8	37.6	3.9	0.99
	z7			0.047	7.2	0.040	8.2	0.0062	3.9	0.48	39.9	1.6	39.8	3.2	32.0	2.3	39.9	3.6	1.00
	z8			0.058	6.9	0.047	7.3	0.0059	2.3	0.32	37.7	0.9	46.7	3.4	540.8	37.2	37.1	3.3	0.81
	z9			0.062	8.8	0.099	18.8	0.0115	16.7	0.88	73.6	12.3	95.6	18.0	686.4	60.3	72.2	8.2	0.77
	z10			0.055	8.6	0.048	9.0	0.0063	2.7	0.30	40.4	1.1	47.2	4.3	410.1	35.2	39.9	4.4	0.86
	z11			0.047	7.6	0.039	7.9	0.0060	2.3	0.29	38.9	0.9	38.8	3.1	31.6	2.4	38.9	3.7	1.00
	z12			0.044	8.3	0.037	8.7	0.0062	2.4	0.28	39.9	1.0	37.2	3.2	-138.3	11.5	40.1	4.2	1.07
	z13			0.046	5.2	0.039	5.6	0.0062	2.0	0.36	39.7	0.8	39.1	2.2	4.9	0.3	39.7	2.6	1.01
	z14			0.053	10.1	0.044	10.5	0.0061	2.9	0.28	39.0	1.1	44.1	4.6	328.5	33.3	38.7	5.0	0.89
	z15			0.050	9.5	0.040	9.9	0.0058	3.0	0.30	37.5	1.1	39.7	3.9	174.1	16.5	37.3	4.5	0.94
	z16			0.051	6.3	0.041	6.7	0.0058	2.2	0.34	37.6	0.8	41.1	2.7	255.1	16.0	37.3	3.0	0.91
	z17			0.057	8.5	0.052	9.2	0.0065	3.4	0.37	42.1	1.4	51.2	4.7	501.1	42.7	41.5	4.5	0.82
	z18			0.045	7.1	0.037	7.8	0.0060	3.1	0.40	38.8	1.2	36.9	2.9	-83.2	5.9	38.9	3.5	1.05
	z19			0.077	2.8	0.206	4.5	0.0194	3.5	0.79	124.1	4.4	190.1	8.6	1116.8	31.1	119.7	4.4	0.65
	z20			0.045	10.3	0.038	10.8	0.0061	3.3	0.30	38.9	1.3	37.5	4.1	-52.9	5.5	39.0	5.1	1.04
	z21			0.043	9.7	0.035	10.5	0.0059	4.0	0.38	37.7	1.5	35.0	3.7	-152.5	14.8	37.9	4.6	1.08
	z22			0.047	7.0	0.040	7.7	0.0061	3.1	0.40	39.0	1.2	39.6	3.0	73.1	5.1	39.0	3.5	0.99
	z23			0.061	10.3	0.054	10.8	0.0063	3.3	0.31	40.7	1.3	53.1	5.7	654.7	67.2	40.0	5.3	0.77
	z24			0.050	6.8	0.042	7.4	0.0062	3.0	0.41	39.7	1.2	41.9	3.1	171.6	11.7	39.6	3.4	0.95
	z25			0.083	6.4	0.069	7.0	0.0061	2.8	0.40	39.0	1.1	68.2	4.8	1269.6	81.6	37.2	3.2	0.57
	z26			0.070	11.9	0.061	12.6	0.0063	4.2	0.33	40.7	1.7	60.6	7.6	940.2	111.7	39.5	6.1	0.67
	z27			0.045	8.2	0.038	8.7	0.0060	3.0	0.35	38.9	1.2	37.7	3.3	-38.1	3.1	38.9	4.0	1.03
	z28			0.063	10.7	0.053	11.1	0.0061	3.3	0.29	39.1	1.3	52.2	5.8	707.8	75.4	38.3	5.3	0.75
	z29			0.067	9.8	0.083	11.0	0.0090	5.1	0.46	57.6	2.9	80.7	8.9	831.8	81.3	56.2	7.1	0.71
	z30			0.159	8.0	0.157	8.9	0.0072	4.0	0.44	46.1	1.8	148.2	13.3	2443.8	195.9	39.5	4.7	0.31
100719-11 [41.058084, -114.020882] - granodiorite																			
	z31			0.044	9.8	0.037	10.3	0.0060	3.1	0.30	38.5	1.2	36.5	3.8	-92.5	9.1	38.6	4.8	1.05
	z32			0.046	7.4	0.038	7.9	0.0059	2.8	0.36	38.2	1.1	37.6	3.0	0.4	0.0	38.2	3.6	1.02

				Isotopic Compositions							Isotopic Dates								
Sample	Spot	Rim / Core	Notes	207Pb/ 206Pb	± 2σ %	207Pb/ 235U	± 2σ %	206Pb/ 238U	± 2σ %	Rho	206Pb/ 238U (Ma)	± 2σ abs	207Pb/ 235U (Ma)	± 2σ abs	207Pb/ 206Pb (Ma)	± 2σ abs	BestAge*	± 2σ abs	Concordance
	z33			0.054	6.7	0.042	7.1	0.0057	2.4	0.34	36.6	0.9	41.8	3.0	350.5	23.5	36.3	3.1	0.88
	z34			0.051	10.8	0.043	11.1	0.0061	2.6	0.23	39.4	1.0	42.5	4.7	223.7	24.2	39.2	5.4	0.93
	z35			0.051	8.5	0.043	8.8	0.0060	2.2	0.26	38.7	0.9	42.3	3.7	251.0	21.2	38.5	4.1	0.92
	z36			0.047	8.5	0.040	9.0	0.0061	2.8	0.31	39.5	1.1	39.6	3.5	43.4	3.7	39.5	4.3	1.00
	z37			0.067	14.8	0.058	15.2	0.0063	3.3	0.22	40.6	1.3	57.2	8.7	824.8	122.1	39.6	7.6	0.71
	z38			0.062	9.9	0.051	10.2	0.0059	2.4	0.24	37.8	0.9	50.1	5.1	686.7	68.0	37.0	4.7	0.75
	z39			0.047	6.0	0.038	6.8	0.0059	3.2	0.47	37.8	1.2	37.8	2.6	33.7	2.0	37.8	2.9	1.00
	z40			0.061	24.2	0.050	25.1	0.0059	6.5	0.26	38.1	2.5	49.3	12.4	634.1	153.5	37.5	11.7	0.77
	z41			0.045	6.2	0.039	6.8	0.0062	2.8	0.42	40.1	1.1	38.9	2.6	-37.0	2.3	40.2	3.1	1.03
	z42			0.047	9.5	0.039	10.1	0.0061	3.2	0.32	39.0	1.3	38.9	3.9	31.5	3.0	39.0	4.7	1.00
	z43			0.064	14.2	0.056	14.9	0.0064	4.4	0.30	41.0	1.8	55.2	8.2	725.2	102.8	40.2	7.4	0.74
	z44			0.048	8.5	0.040	9.0	0.0061	2.9	0.32	39.1	1.1	40.0	3.6	94.1	8.0	39.0	4.2	0.98
	z45			0.108	14.0	0.095	14.5	0.0064	3.5	0.24	40.9	1.4	92.2	13.3	1771.6	248.6	37.7	7.3	0.44
	z46			0.158	15.6	0.169	16.9	0.0078	6.4	0.38	49.9	3.2	158.7	26.8	2432.5	380.5	42.9	9.9	0.31
	z47			0.043	8.1	0.036	8.6	0.0060	3.0	0.34	38.7	1.1	35.6	3.1	-169.4	13.7	38.9	4.0	1.09
	z48			0.048	6.9	0.041	7.8	0.0063	3.6	0.47	40.4	1.5	41.1	3.2	81.8	5.6	40.3	3.5	0.98
	z49			0.047	7.9	0.042	8.7	0.0064	3.5	0.40	40.9	1.4	41.3	3.6	63.5	5.1	40.9	4.1	0.99
	z50			0.046	6.9	0.039	7.7	0.0061	3.3	0.43	39.5	1.3	38.9	3.0	4.6	0.3	39.5	3.4	1.01
	z51			0.072	13.8	0.061	14.1	0.0062	2.9	0.21	39.8	1.1	60.6	8.5	986.5	136.1	38.5	6.9	0.66
	z52			0.096	9.2	0.088	9.6	0.0066	2.8	0.29	42.4	1.2	85.3	8.2	1552.6	142.5	39.8	4.9	0.50
	z53			0.047	7.0	0.040	7.8	0.0061	3.5	0.45	39.3	1.4	39.7	3.1	64.1	4.5	39.3	3.5	0.99
	z54			0.050	8.5	0.043	9.0	0.0061	3.0	0.33	39.5	1.2	42.3	3.8	204.9	17.5	39.3	4.3	0.93
	z55			0.055	7.3	0.047	7.9	0.0062	3.0	0.37	40.1	1.2	47.1	3.7	416.8	30.5	39.7	3.7	0.85
	z56			0.086	8.1	0.074	8.8	0.0063	3.6	0.41	40.2	1.5	72.3	6.4	1329.1	107.0	38.2	4.1	0.56
	z57			0.063	4.2	0.145	7.1	0.0166	5.7	0.80	106.4	6.1	137.1	9.7	708.6	30.0	104.4	5.7	0.78
	z58			0.046	9.2	0.039	9.8	0.0061	3.3	0.34	39.4	1.3	39.0	3.8	16.2	1.5	39.4	4.6	1.01
	z59			0.049	7.8	0.042	8.3	0.0061	2.9	0.35	39.4	1.1	41.5	3.4	164.7	12.8	39.3	3.9	0.95
	z60			0.068	8.6	0.055	9.2	0.0059	3.1	0.34	38.0	1.2	54.4	5.0	855.6	73.9	37.0	4.1	0.70

*BestAge is 207Pb-corrected 206Pb/238U date for analyses < 1000 Ma and 207Pb/206Pb for analyses > 1000 Ma. 207Pb/206Pb = 0.84 is used for 207Pb corrected date calculation.

Table 3.S5. Zircon U-Pb Metadata - University of California, Santa Barbara

Laboratory and Sample Preparation	
Laboratory name	Dept of Earth Science, University of California, Santa Barbara
Sample type/mineral	Igneous zircons
Sample preparation	Standard mineral-separation techniques, mounted in 1-inch epoxy rounds, and polished to expose the approximate center of the grains
Imaging	CL images of the zircon were collected at 10 kV on the JEOL JSM-7100FT field emission scanning electron microscope (FE-SEM) at the UNR with a 12 mm working distance.
Laser ablation system	
Make, Model and type	Photon Machines Excite Excimer laser
Ablation cell and volume	HeLex dual volume cell
Laser wavelength (nm)	193 nm
Pulse width (ns)	4 ns
Fluence (J cm^{-2})	~1 J cm^{-2}
Repetition rate (Hz)	5 Hz
Ablation duration (s)	12 s
Ablation pit depth / ablation rate	~0.08 mm/pulse
Spot diameter (mm) nominal/actual	20 mm
Sampling mode / pattern	Static spot ablation
Carrier gas	100% He in the cell, Ar make-up gas combined with a mixing bulb after ~50 cm
Cell carrier gas flow (l min^{-1})	0.1 and 0.02 l min^{-1} in the cell and cup, respectively
ICP-MS Instrument	
Make, Model and type	Nu Instruments, Nu Plasma HR, MC-ICP-MS and Agilent 7700x quadrupole ICP-MS
Sample introduction	Ablation aerosol
RF power (W)	1300 W
Make-up gas flow (l min^{-1})	Sourced from a MFC on each ICP-MS, with a total of ~2.4 l min^{-1} Ar.
Detection system	Nu Plasma HR: mixed Faraday-multiple ion counting array; Agilent 7700x: single Dual-mode detector
Masses measured	Nu Plasma HR: 204, 206, 207, 208 232, 238;
Integration time per peak/dwell times (ms); quadrupole settling time between mass jumps	Nu Plasma HR: 500 ms for each isotope; Agilent 7700x: 500 ms per sweep
Total integration time per output data point (s)	~ 0.5 s
'Sensitivity' as useful yield (%, element)	0.4% U ((#ions detected/#atoms sampled)*100; Schaltegger *et al.* 2015)
IC Dead time (ns)	6, 9 and 7 ns IC0, IC1 and IC2 resp.
Data Processing	
Gas blank	20 s on-peak zero subtracted
Calibration strategy	91500 used as primary reference material, Plesovice, and GJ used as secondaries/validation
Reference Material info	91500 (Wiedenbeck *et al* . 1995) Plešovice (Slama *et al* . 2008) GJ (Jackson et al., 2004)
Data processing package used / Correction for LIEF	Iolite v3.5 (Paton et al., 2010)
Mass discrimination	
Common-Pb correction, composition and uncertainty	No common-Pb correction applied to the data.
Uncertainty level and propagation	Ages are quoted at 2*s* absolute, propagation is by quadratic addition. Reproducibility and age uncertainty of reference material and common-Pb composition uncertainty are propagated where appropriate.
Quality control / Validation	Plešovice – Wtd ave $^{206}Pb/^{238}U$ age = 338 ± 3 (2*s* , MSWD = 0.9, n = 8) GJ-1 – Wtd ave $^{206}Pb/^{238}U$ age = 602 ± 5 (2*s* , MSWD = 1.1, n = 7) Systematic uncertainty for propagation is 2% (2*s*).

Table 3.S6: Zircon U-Pb data - University of California, Santa Barbara

2-3 November, 2020, Dept. of Earth Science, University of California, Santa Barabara

				Elemental Composition				Isotopic Compositions											Isotopic Dates									
Sample	Spot	Rim / Core	Notes	Pb (ppm)	U (ppm)	Th (ppm)	Th/U	238U/ 206Pb	± 2σ abs	207Pb/ 206Pb	± 2σ abs	Rho	207Pb/ 235U	± 2σ abs	206Pb/ 238U	± 2σ abs	Rho	208Pb/ 232Th	± 2σ abs	206Pb/ 238U (Ma)	± 2σ abs	208Pb/ 232Th (Ma)	± 2σ abs	207Pb/ 235U (Ma)	± 2σ abs	207Pb/ 206Pb (Ma)	± 2σ abs	BestAge	± 2σ abs	Concordance
090719_4 [40.999756, -114.069553] - gabbro																													
090719_4-1		core		171	2475	2332	0.94	40.58	0.88	0.0494	0.0010	0.35	0.1684	0.0036	0.0246	0.0005	0.87	0.00797	0.00017	156.9	3.4	160.4	3.5	158.0	3.3	167.0	12.5	156.9	3.4	0.99
090719_4-2		core		103	2944	1381	0.47	40.13	0.85	0.0491	0.0010	0.01	0.1695	0.0037	0.0249	0.0005	0.90	0.00808	0.00018	158.7	3.4	162.6	3.6	159.0	3.4	153.0	9.5	158.7	3.4	1.00
090719_4-3		core		315	4636	4268	0.92	40.31	0.92	0.0497	0.0010	0.29	0.1707	0.0038	0.0248	0.0006	0.95	0.00802	0.00019	158.0	3.6	161.4	3.8	160.0	3.5	179.5	8.7	157.9	3.6	0.99
090719_4-4		core		78	2348	1059	0.45	39.97	0.89	0.0493	0.0010	-0.39	0.1702	0.0040	0.0250	0.0006	0.93	0.00801	0.00019	159.3	3.5	161.2	3.9	159.6	3.7	159.0	11.5	159.3	3.5	1.00
090719_4-5		core		155	2110	1970	0.93	41.15	0.93	0.0492	0.0010	-0.27	0.1647	0.0037	0.0243	0.0006	0.84	0.00856	0.00018	154.8	3.5	172.2	3.7	154.8	3.4	154.8	9.6	154.8	3.5	1.00
090719_4-6		core		200	3265	2640	0.81	40.36	0.89	0.0492	0.0010	0.14	0.1680	0.0037	0.0248	0.0005	0.89	0.00831	0.00020	157.8	3.5	167.2	4.1	157.7	3.5	155.0	8.7	157.8	3.5	1.00
090719_4-7		core		379	4725	4950	1.05	40.27	0.92	0.0498	0.0010	0.26	0.1716	0.0038	0.0248	0.0006	0.92	0.00834	0.00019	158.1	3.6	167.8	3.9	160.8	3.5	183.3	9.9	158.0	3.6	0.98
090719_4-8		core		358	5580	4860	0.87	40.03	0.90	0.0494	0.0010	0.40	0.1705	0.0037	0.0250	0.0006	0.96	0.00810	0.00019	159.1	3.6	163.1	3.9	159.8	3.5	163.2	7.5	159.0	3.5	0.99
090719_4-9		core		510	4414	6930	1.57	40.32	0.99	0.0494	0.0010	0.52	0.1686	0.0038	0.0248	0.0006	0.96	0.00804	0.00019	157.9	3.8	161.9	4.0	158.2	3.5	167.0	10.5	157.9	3.8	1.00
090719_4-10		core		230	3240	3138	0.97	40.60	1.03	0.0501	0.0012	-0.57	0.1689	0.0049	0.0246	0.0006	0.86	0.00807	0.00026	156.9	4.0	162.4	5.4	158.4	4.4	198.0	31.3	156.7	3.9	0.99
090719_4-11		core		50	1074	677	0.63	40.52	1.06	0.0491	0.0010	0.23	0.1675	0.0044	0.0247	0.0006	0.95	0.00814	0.00020	157.2	4.1	163.9	4.1	157.2	4.0	152.1	9.9	157.2	4.1	1.00
090719_4-12		core		186	3341	2578	0.77	40.65	0.98	0.0493	0.0010	-0.29	0.1675	0.0041	0.0246	0.0006	0.97	0.00795	0.00019	156.7	3.8	160.1	3.9	157.2	3.8	162.4	7.1	156.6	3.7	1.00
090719_4-13		core		658	5910	8941	1.51	40.39	0.91	0.0495	0.0010	0.31	0.1691	0.0038	0.0248	0.0006	0.93	0.00805	0.00018	157.7	3.5	162.1	3.6	158.6	3.5	174.0	11.5	157.6	3.5	0.99
090719_4-14		core		382	5280	5300	1.00	40.42	0.98	0.0496	0.0010	-0.05	0.1691	0.0041	0.0247	0.0006	0.98	0.00791	0.00019	157.6	3.8	159.2	3.8	158.6	3.8	174.1	5.9	157.5	3.8	0.99
090719_4-15		core		240	4314	3300	0.76	40.72	1.01	0.0496	0.0010	-0.01	0.1682	0.0040	0.0246	0.0006	0.96	0.00793	0.00018	156.4	3.9	159.7	3.7	157.9	3.7	173.0	11.5	156.3	3.9	0.99
090719_4-16		core		620	6450	8606	1.33	40.45	0.94	0.0497	0.0010	-0.07	0.1695	0.0039	0.0247	0.0006	0.96	0.00786	0.00017	157.4	3.6	158.2	3.5	159.0	3.6	182.7	8.3	157.3	3.6	0.99
090719_4-17		core		389	7440	5307	0.71	40.26	0.87	0.0498	0.0010	0.19	0.1701	0.0037	0.0248	0.0005	0.93	0.00802	0.00017	158.1	3.4	161.4	3.5	159.5	3.4	184.1	10.2	158.1	3.4	0.99
090719_4-18		core		236	5642	3296	0.58	40.14	0.88	0.0495	0.0010	-0.25	0.1691	0.0037	0.0249	0.0005	0.96	0.00788	0.00018	158.6	3.5	158.7	3.7	158.6	3.4	172.6	7.0	158.5	3.5	1.00
090719_4-19		core		281	4820	3800	0.79	39.90	1.22	0.0497	0.0010	-0.53	0.1723	0.0059	0.0251	0.0008	0.99	0.00816	0.00028	159.5	4.8	164.3	5.8	161.4	5.3	180.5	9.1	159.5	4.8	0.99
090719_4-20		core		360	4829	4932	1.02	40.52	0.98	0.0499	0.0010	0.39	0.1686	0.0040	0.0247	0.0006	0.96	0.00803	0.00017	157.1	3.8	161.7	3.4	158.2	3.6	188.4	8.0	157.0	3.8	0.99
090719_4-21		core		177	3040	2394	0.79	40.50	0.98	0.0498	0.0010	0.04	0.1688	0.0042	0.0247	0.0006	0.90	0.00806	0.00020	157.2	3.8	162.3	4.1	158.4	3.8	183.0	12.5	157.1	3.8	0.99
090719_4-22		core		518	3630	6960	1.92	39.89	0.98	0.0497	0.0010	0.05	0.1708	0.0044	0.0251	0.0006	0.97	0.00817	0.00022	159.6	3.9	164.6	4.4	160.1	3.9	181.0	11.6	159.5	3.9	1.00
090719_4-23		core		365	5540	5000	0.90	40.18	0.95	0.0496	0.0010	-0.09	0.1693	0.0040	0.0249	0.0006	0.98	0.00799	0.00020	158.5	3.7	160.8	4.0	158.8	3.7	175.7	7.5	158.4	3.7	1.00
090719_4-24		core		221	3343	3022	0.90	40.72	0.96	0.0499	0.0010	0.06	0.1676	0.0041	0.0246	0.0006	0.95	0.00797	0.00018	156.4	3.7	160.5	3.7	157.3	3.7	189.3	8.5	156.3	3.7	0.99
090719_4-25		core		100	2341	1383	0.59	40.60	0.89	0.0498	0.0010	0.25	0.1677	0.0036	0.0246	0.0005	0.93	0.00784	0.00017	156.8	3.4	157.9	3.5	157.4	3.4	184.5	10.2	156.7	3.4	1.00
090719_4-26		core		1060	9200	14970	1.63	40.42	0.85	0.0502	0.0010	0.14	0.1697	0.0036	0.0247	0.0005	0.96	0.00779	0.00017	157.5	3.3	156.7	3.4	159.2	3.3	201.0	7.6	157.4	3.3	0.99
090719_4-27		core		360	19100	37000	1.94	109.89	77.32	0.5400	0.2103	-0.98	0.0660	0.0460	0.0091	0.0064	1.00	0.00290	0.00200	58.0	41.0	59.0	40.7	61.0	43.0	3200.0	1201.7	21.9	22.0	0.90
090719_4-29		core		191	3080	2660	0.86	40.70	0.98	0.0498	0.0010	-0.06	0.1671	0.0041	0.0246	0.0006	0.97	0.00781	0.00020	156.5	3.8	157.3	4.0	156.9	3.7	185.5	8.7	156.3	3.7	1.00
090719_4-30		core		542	5900	7462	1.26	40.16	0.93	0.0507	0.0010	-0.11	0.1723	0.0041	0.0249	0.0006	0.95	0.00787	0.00018	158.5	3.6	158.5	3.7	161.4	3.7	224.6	10.9	158.3	3.6	0.98
090719_4-31		core		510	7430	7090	0.95	40.72	0.92	0.0515	0.0012	0.17	0.1727	0.0042	0.0246	0.0006	0.67	0.00775	0.00017	156.4	3.5	156.0	3.5	161.7	3.9	261.0	23.6	156.0	3.5	0.97
090719_4-32		core		126	3130	1740	0.56	39.84	1.92	0.0500	0.0010	0.03	0.1714	0.0082	0.0251	0.0012	0.99	0.00810	0.00055	159.9	7.7	163.0	11.7	160.5	7.2	194.0	11.7	159.7	7.6	0.99
090719_4-33		core		206	4252	2828	0.67	40.62	0.87	0.0498	0.0010	-0.13	0.1678	0.0036	0.0246	0.0005	0.93	0.00787	0.00016	156.8	3.4	158.5	3.3	157.5	3.4	186.3	7.0	156.7	3.3	1.00
090719_4-34		core		609	7320	8469	1.16	40.57	0.96	0.0499	0.0010	0.00	0.1680	0.0040	0.0247	0.0006	0.95	0.00772	0.00018	157.0	3.7	155.4	3.6	157.7	3.7	190.2	10.3	156.8	3.7	1.00
090719_4-35		core		296	5354	4140	0.77	41.65	1.03	0.0563	0.0016	0.11	0.1858	0.0063	0.0240	0.0006	0.54	0.00769	0.00020	153.0	3.8	154.8	4.1	173.0	5.6	460.0	49.9	151.6	3.7	0.88
070719_9 [41.186779, -114.011723] - monzogranite																													
070719_9-1		core		5	596	282	0.47	167.14	3.79	0.0478	0.0012	-0.25	0.0393	0.0012	0.0060	0.0001	0.68	0.00205	0.00006	38.5	0.9	41.3	1.3	39.1	1.2	87.0	34.0	38.4	0.9	0.98
070719_9-2		rim		49	5810	2653	0.46	164.47	3.60	0.0475	0.0010	0.20	0.0398	0.0009	0.0061	0.0001	0.75	0.00199	0.00004	39.1	0.9	40.1	0.9	39.6	0.9	75.0	20.1	39.0	0.9	0.99
070719_9-3		core		2	138	101	0.73	167.08	3.83	0.0486	0.0020	0.37	0.0399	0.0016	0.0060	0.0001	-0.11	0.00197	0.00007	38.5	0.9	39.7	1.5	39.7	1.5	123.0	82.0	38.4	0.9	0.97
070719_9-4		core		3	196	162	0.82	166.94	4.73	0.0471	0.0022	0.35	0.0384	0.0015	0.0060	0.0002	0.10	0.00197	0.00005	38.5	1.1	39.9	1.1	38.3	1.5	55.0	95.0	38.5	1.1	1.01
070719_9-5		core		8	879	434	0.49	166.94	3.61	0.0486	0.0012	0.26	0.0400	0.0010	0.0060	0.0001	0.25	0.00197	0.00005	38.5	0.8	39.7	1.0	39.9	1.0	126.0	32.1	38.4	0.8	0.97
070719_9-6		rim		67	8640	3690	0.43	165.15	3.55	0.0476	0.0010	0.40	0.0396	0.0009	0.0061	0.0001	0.64	0.00195	0.00004	38.9	0.8	39.4	0.9	39.5	0.9	76.0	18.1	38.9	0.8	0.99
070719_9-7		core		2	112	98	0.86	171.23	6.05	0.0477	0.0037	0.24	0.0383	0.0030	0.0058	0.0002	0.14	0.00187	0.00010	37.5	1.3	37.7	2.1	38.2	2.9	70.0	160.0	37.5	1.3	0.98
070719_9-8		rim		49	10230	2808	0.27	172.03	3.63	0.0482	0.0010	-0.19	0.0387	0.0009	0.0058	0.0001	0.88	0.00188	0.00004	37.4	0.8	38.0	0.8	38.6	0.8	110.0	13.2	37.3	0.8	0.97
070719_9-9		core		9	415	472	1.14	166.67	3.85	0.0461	0.0011	0.04	0.0383	0.0010	0.0060	0.0001	0.56	0.00201	0.00005	38.6	0.9	40.7	1.0	38.2	1.0	2.0	27.0	38.6	0.9	1.01
070719_9-10		core		2	360	127	0.35	157.73	8.56	0.0476	0.0021	-0.17	0.0417	0.0031	0.0063	0.0003	0.84	0.00199	0.00008	40.8	2.3	40.1	1.5	41.5	3.0	77.0	87.0	40.7	2.2	0.98
070719_9-11		rim		1	89	65	0.72	160.08	3.61	0.0477	0.0035	0.33	0.0412	0.0029	0.0062	0.0001	-0.14	0.00222	0.00010	40.1	0.9	44.8	2.2	41.8	2.5	80.0	150.0	40.1	0.9	0.98
070719_9-12		core		15	3520	1131	0.32	164.69	3.64	0.0505	0.0012	0.33	0.0424	0.0010	0.0061	0.0001	0.43	0.00137	0.00007	39.0	0.9	27.6	1.1	42.1	1.0	218.0	28.3	38.8	0.9	0.93
070719_9-13		rim		6	656	320	0.49	169.78	3.65	0.0479	0.0016	-0.28	0.0392	0.0012	0.0059	0.0001	0.53	0.00192	0.00005	37.9	0.8	38.7	1.0	39.1	1.2	93.0	59.0	37.8	0.8	0.97
070719_9-14		core		8	628	444	0.71	169.75	3.47	0.0470	0.0014	-0.10	0.0382	0.0012	0.0059	0.0001	0.28	0.00199	0.00005	37.9	0.8	40.2	1.0	38.1	1.2	50.0	52.0	37.9	0.8	0.99
070719_9-15		core		23	539	242	0.45	90.17	6.99	0.1480	0.0133	0.45	0.2240	0.0205	0.0111	0.0009	0.17	0.01040	0.00132	71.1	5.5	210.0	76.9	205.0	16.5	2340.0	138.2	62.1	5.0	0.35
070719_9-16		core		2	159	83	0.52	169.49	4.83	0.0469	0.0028	0.04	0.0392	0.0028	0.0059	0.0002	0.36	0.00204	0.00007	37.9	1.1	41.3	1.5	39.1	2.7	50.0	120.0	37.9	1.1	0.97
070719_9-17		rim		7	1003	375	0.37	169.64	3.77	0.0477	0.0013	0.49	0.0388	0.0009	0.0059	0.0001	0.16	0.00202	0.00005	37.9	0.8	40.7	1.0	38.6	0.9	82.0	40.0	37.8	0.8	0.98
070719_9-18		rim		21	1438	1141	0.79	171.23	4.02	0.0474	0.0011	0.00	0.0380	0.0011	0.0058	0.0001	0.60	0.00202	0.00005	37.5	0.9	40.7	1.0	37.9	1.1	70.0	26.0	37.5	0.9	0.99

				Elemental Composition				Isotopic Compositions											Isotopic Dates									
Sample	Spot	Rim / Core	Notes	Pb (ppm)	U (ppm)	Th (ppm)	Th/U	238U/ 206Pb	± 2σ abs	207Pb/ 206Pb	± 2σ abs	Rho	207Pb/ 235U	± 2σ abs	206Pb/ 238U	± 2σ abs	Rho	208Pb/ 232Th	± 2σ abs	206Pb/ 238U (Ma)	± 2σ abs	208Pb/ 232Th (Ma)	± 2σ abs	207Pb/ 235U (Ma)	± 2σ abs	207Pb/ 206Pb (Ma)	± 2σ abs	BestAge	± 2σ abs	Concordance
070719_9-19		core		5	550	259	0.47	168.78	3.98	0.0481	0.0014	-0.10	0.0396	0.0014	0.0059	0.0001	0.66	0.00204	0.00007	38.1	0.9	41.2	1.5	39.4	1.4	104.0	50.0	38.0	0.9	0.97
070719_9-20		core		10	599	538	0.90	161.08	4.03	0.0478	0.0014	0.28	0.0409	0.0012	0.0062	0.0002	0.44	0.00204	0.00005	39.9	1.0	41.3	1.1	40.7	1.2	85.0	48.0	39.8	1.0	0.98
070719_9-21		rim		24	4730	1612	0.34	162.02	3.44	0.0476	0.0010	0.46	0.0407	0.0009	0.0062	0.0001	0.56	0.00157	0.00004	39.7	0.8	31.8	0.7	40.5	0.9	79.0	16.1	39.6	0.8	0.98
070719_9-22		rim		9	1085	479	0.44	159.44	3.34	0.0466	0.0011	-0.25	0.0402	0.0010	0.0063	0.0001	0.64	0.00206	0.00005	40.3	0.8	41.6	1.0	40.0	1.0	30.0	28.0	40.3	0.8	1.01
070719_9-23		core		7	3192	394	0.12	166.56	3.69	0.0474	0.0011	-0.10	0.0394	0.0010	0.0060	0.0001	0.73	0.00201	0.00005	38.6	0.9	40.5	1.0	39.2	1.0	69.0	29.0	38.6	0.9	0.98
070719_9-24		core		14	1842	775	0.42	169.26	3.81	0.0468	0.0011	0.36	0.0380	0.0009	0.0059	0.0001	0.37	0.00191	0.00004	38.0	0.9	38.5	0.9	37.9	0.9	39.0	31.0	38.0	0.9	1.00
070719_9-25		core		2	125	122	0.98	169.41	4.31	0.0457	0.0031	0.40	0.0369	0.0023	0.0059	0.0002	-0.12	0.00203	0.00005	37.9	1.0	41.0	1.0	36.8	2.3	-10.0	-140.0	38.0	1.0	1.03
070719_9-26		core		3	298	145	0.48	161.63	3.94	0.0521	0.0027	0.55	0.0445	0.0021	0.0062	0.0002	-0.27	0.00229	0.00007	39.8	1.0	46.2	1.7	44.2	2.0	280.0	110.1	39.5	1.0	0.90
070719_9-27		rim		43	4443	2292	0.52	162.58	3.36	0.0473	0.0010	-0.54	0.0401	0.0009	0.0062	0.0001	0.88	0.00204	0.00004	39.5	0.8	41.2	0.9	40.0	0.9	62.0	14.1	39.5	0.8	0.99
070719_9-28		core		7	326	392	1.20	169.52	3.80	0.0468	0.0013	0.52	0.0382	0.0010	0.0059	0.0001	-0.04	0.00193	0.00005	37.9	0.8	38.9	1.0	38.1	1.0	36.0	44.0	37.9	0.9	1.00
070719_9-29		core		2	197	102	0.52	166.22	3.85	0.0467	0.0018	0.07	0.0387	0.0015	0.0060	0.0001	0.29	0.00203	0.00008	38.7	0.9	41.0	1.6	38.5	1.4	38.0	73.0	38.7	0.9	1.00
070719_9-30		rim		45	4510	2276	0.50	164.77	3.49	0.0474	0.0010	0.05	0.0397	0.0009	0.0061	0.0001	0.77	0.00213	0.00005	39.0	0.8	43.1	1.0	39.5	0.9	69.0	18.1	39.0	0.8	0.99
070719_9-31		core		5	1320	245	0.19	163.67	4.21	0.0474	0.0011	-0.47	0.0398	0.0013	0.0061	0.0002	0.89	0.00207	0.00008	39.3	1.0	41.8	1.6	39.6	1.3	67.0	28.0	39.2	1.0	0.99
070719_9-32		rim		5	198	281	1.42	168.46	4.35	0.0476	0.0018	0.07	0.0396	0.0020	0.0059	0.0002	0.29	0.00199	0.00006	38.2	1.0	40.2	1.3	39.4	1.9	76.0	73.0	38.1	1.0	0.97
070719_9-33		rim		11	831	588	0.71	170.01	3.53	0.0473	0.0015	-0.41	0.0385	0.0012	0.0059	0.0001	0.63	0.00197	0.00005	37.8	0.8	39.8	1.0	38.3	1.2	63.0	53.0	37.8	0.8	0.99
070719_9-34		core		73	244	110	0.45	4.36	0.11	0.0909	0.0019	0.02	2.8790	0.0763	0.2294	0.0060	0.98	0.07100	0.00186	1331.0	33.3	1387.0	36.7	1376.0	30.4	1444.2	30.1	1445.1	39.1	0.97
070719_9-35		core		5	771	271	0.35	169.06	3.73	0.0472	0.0013	0.25	0.0387	0.0011	0.0059	0.0001	0.35	0.00205	0.00006	38.0	0.8	41.5	1.4	38.5	1.1	58.0	44.0	38.0	0.8	0.99
070719_9-36		rim		43	4180	2223	0.53	164.61	3.35	0.0555	0.0017	0.43	0.0467	0.0014	0.0061	0.0001	-0.21	0.00207	0.00005	39.0	0.8	41.9	1.1	46.3	1.4	429.0	51.7	38.6	0.8	0.84
070719_9-37		core		2	650	102	0.16	170.27	3.64	0.0474	0.0016	-0.03	0.0385	0.0013	0.0059	0.0001	0.35	0.00215	0.00012	37.8	0.8	43.3	2.7	38.4	1.3	87.0	68.0	37.7	0.8	0.98
070719_9-38		rim		17	2780	810	0.29	152.93	3.56	0.0471	0.0010	0.08	0.0423	0.0010	0.0065	0.0002	0.87	0.00226	0.00006	42.0	1.0	45.6	1.2	42.1	1.0	54.0	21.0	42.0	1.0	1.00
070719_9-39		rim		80	11410	4551	0.40	170.47	3.96	0.0473	0.0010	-0.27	0.0383	0.0010	0.0059	0.0001	0.92	0.00188	0.00004	37.7	0.9	37.9	0.9	38.1	0.9	61.0	15.0	37.7	0.9	0.99
070719_9-40		core		23	760	1216	1.60	168.66	4.36	0.0476	0.0015	0.21	0.0389	0.0013	0.0059	0.0002	0.41	0.00199	0.00005	38.1	1.0	40.2	0.9	38.8	1.2	77.0	55.0	38.1	1.0	0.98
070719_9-41		core		8	4220	424	0.10	168.75	4.01	0.0479	0.0010	0.03	0.0390	0.0010	0.0059	0.0001	0.87	0.00204	0.00006	38.1	0.9	41.1	1.3	38.8	0.9	92.0	17.1	38.0	0.9	0.98
070719_9-42		rim		17	2780	834	0.30	161.86	3.50	0.0468	0.0010	0.21	0.0396	0.0009	0.0062	0.0001	0.53	0.00218	0.00006	39.7	0.9	44.0	1.2	39.5	0.9	40.0	22.0	39.7	0.9	1.01
070719_9-43		core		6	1311	299	0.23	163.43	3.51	0.0484	0.0012	-0.12	0.0405	0.0010	0.0061	0.0001	0.62	0.00215	0.00006	39.3	0.8	43.4	1.3	40.3	1.0	118.0	33.1	39.2	0.8	0.97
070719_9-44		rim		17	4730	929	0.20	168.41	3.69	0.0470	0.0010	0.19	0.0383	0.0008	0.0059	0.0001	0.81	0.00199	0.00004	38.2	0.8	40.2	0.9	38.2	0.8	49.0	15.0	38.2	0.8	1.00
070719_9-45		rim		3	178	181	1.02	168.69	3.83	0.0489	0.0021	0.13	0.0392	0.0015	0.0059	0.0001	0.23	0.00195	0.00006	38.1	0.9	39.4	1.2	39.1	1.5	136.0	90.0	38.0	0.9	0.98
070719_9-46		rim		5	661	235	0.36	161.26	3.53	0.0459	0.0013	0.51	0.0395	0.0011	0.0062	0.0001	-0.07	0.00208	0.00007	39.9	0.9	41.9	1.4	39.4	1.1	-2.0	-45.0	39.9	0.9	1.01
070719_9-47		core		6	318	297	0.94	169.12	3.82	0.0476	0.0018	0.11	0.0389	0.0015	0.0059	0.0001	0.27	0.00211	0.00005	38.0	0.9	42.6	1.1	38.8	1.5	77.0	73.0	38.0	0.9	0.98
070719_9-48		rim		22	2066	1131	0.55	161.21	3.60	0.0530	0.0031	0.57	0.0448	0.0023	0.0062	0.0001	-0.14	0.00207	0.00009	39.9	0.9	41.8	1.8	44.5	2.2	310.0	120.2	39.6	0.9	0.90
070719_9-49		core		56	1407	3026	2.15	170.42	3.81	0.0547	0.0028	-0.45	0.0437	0.0022	0.0059	0.0001	0.56	0.00197	0.00005	37.7	0.8	39.7	1.1	43.5	2.2	390.0	110.3	37.3	0.8	0.87
070719_9-50		rim		104	10597	6010	0.57	168.07	3.64	0.0472	0.0010	-0.24	0.0388	0.0009	0.0060	0.0001	0.85	0.00186	0.00005	38.2	0.8	37.5	0.9	38.6	0.9	59.0	12.1	38.2	0.8	0.99
070719_9-51		core		6	820	325	0.40	169.00	3.59	0.0468	0.0013	0.28	0.0386	0.0012	0.0059	0.0001	0.13	0.00200	0.00005	38.0	0.8	40.4	1.0	38.4	1.1	40.0	45.0	38.0	0.8	0.99
070719_9-52		rim		23	8840	665	0.08	171.91	3.97	0.0564	0.0016	0.00	0.0453	0.0013	0.0058	0.0001	0.43	0.00373	0.00025	37.4	0.9	75.3	9.8	44.9	1.3	464.0	44.0	36.9	0.9	0.83
070719_9-53		core		22	8824	1194	0.14	169.32	3.53	0.0474	0.0010	0.22	0.0385	0.0008	0.0059	0.0001	0.73	0.00198	0.00004	38.0	0.8	39.9	0.9	38.4	0.8	67.0	12.1	37.9	0.8	0.99
070719_9-54		core		5	852	253	0.30	167.50	4.75	0.0471	0.0013	-0.14	0.0384	0.0012	0.0060	0.0002	0.78	0.00206	0.00006	38.3	1.1	41.5	1.3	38.3	1.1	54.0	40.0	38.4	1.1	1.00
070719_9-55		core		8	358	413	1.15	167.03	3.72	0.0457	0.0016	-0.41	0.0372	0.0016	0.0060	0.0001	0.66	0.00199	0.00004	38.5	0.9	40.1	0.9	37.1	1.6	-14.0	-62.0	38.5	0.9	1.04
070719_9-56		core		2	144	125	0.87	168.69	4.13	0.0504	0.0033	0.18	0.0414	0.0026	0.0059	0.0001	0.09	0.00211	0.00006	38.1	0.9	42.6	1.3	41.2	2.5	200.0	140.1	37.9	0.9	0.93
070719_9-57		core		19	6000	1022	0.17	167.11	3.75	0.0472	0.0010	0.21	0.0390	0.0009	0.0060	0.0001	0.71	0.00200	0.00005	38.5	0.9	40.3	0.9	38.8	0.9	58.0	20.0	38.4	0.9	0.99
070719_9-59		core		6	771	272	0.35	165.56	4.86	0.0493	0.0016	-0.20	0.0417	0.0016	0.0060	0.0002	0.73	0.00221	0.00008	38.8	1.1	44.5	1.8	41.4	1.5	176.0	62.1	38.7	1.1	0.94
070719_9-60		rim		23	4780	1162	0.24	165.65	3.89	0.0474	0.0010	-0.26	0.0395	0.0010	0.0060	0.0001	0.88	0.00211	0.00005	38.8	0.9	42.6	1.1	39.4	1.0	69.0	19.1	38.8	0.9	0.99
070719_9-61		core		3	285	152	0.53	161.73	3.84	0.0487	0.0023	-0.11	0.0417	0.0021	0.0062	0.0001	0.38	0.00212	0.00008	39.7	0.9	42.7	1.8	41.5	2.1	128.0	98.0	39.6	0.9	0.96
070719_9-62		rim		9	1131	484	0.43	165.95	3.80	0.0484	0.0013	-0.94	0.0400	0.0014	0.0060	0.0001	0.96	0.00202	0.00005	38.7	0.9	40.8	1.0	39.8	1.4	117.0	39.1	38.7	0.9	0.97
070719_9-63		core		4	394	223	0.57	169.32	3.88	0.0478	0.0014	-0.33	0.0390	0.0013	0.0059	0.0001	0.65	0.00215	0.00006	38.0	0.9	43.4	1.2	38.8	1.3	88.0	48.0	37.9	0.9	0.98
070719_9-64		rim		18	1906	881	0.46	155.81	3.35	0.0473	0.0011	0.00	0.0416	0.0009	0.0064	0.0001	0.60	0.00223	0.00005	41.2	0.9	45.0	1.1	41.4	0.9	62.0	25.0	41.2	0.9	1.00
070719_9-65		core		4	134	181	1.36	160.00	4.10	0.0928	0.0058	-0.38	0.0804	0.0056	0.0063	0.0002	0.55	0.00286	0.00013	40.1	1.0	53.7	3.4	78.5	5.3	1470.0	113.9	37.8	1.0	0.51
070719_9-66		core		1	97	63	0.65	166.50	3.69	0.0473	0.0022	-0.95	0.0392	0.0021	0.0060	0.0001	0.97	0.00203	0.00019	38.6	0.9	41.0	4.2	39.1	2.1	63.0	95.0	38.6	0.9	0.99
070719_9-67		rim		2	261	127	0.49	162.60	4.73	0.0481	0.0015	-0.17	0.0405	0.0018	0.0062	0.0002	0.66	0.00207	0.00007	39.5	1.1	41.8	1.4	40.3	1.8	82.0	67.0	39.5	1.1	0.98
070719_9-68		rim		46	8600	2593	0.30	169.61	3.61	0.0474	0.0010	-0.05	0.0385	0.0009	0.0059	0.0001	0.75	0.00188	0.00004	37.9	0.8	38.0	0.8	38.4	0.9	66.0	19.0	37.9	0.8	0.99
070719_9-69		core		16	5125	882	0.17	168.72	3.90	0.0470	0.0011	-0.07	0.0384	0.0010	0.0059	0.0001	0.76	0.00199	0.00005	38.1	0.9	40.1	1.0	38.3	1.0	48.0	26.0	38.1	0.9	0.99
070719_9-70		core		9	271	477	1.76	173.31	4.79	0.0480	0.0016	-0.13	0.0386	0.0018	0.0058	0.0002	0.58	0.00194	0.00005	37.1	1.0	39.1	1.0	38.5	1.7	95.0	64.0	37.0	1.0	0.96
070719_9-72		core		3	300	66	0.22	142.65	11.16	0.0810	0.0101	-0.45	0.0780	0.0141	0.0070	0.0005	0.75	0.00459	0.00056	45.0	3.5	93.0	22.8	76.0	13.1	1160.0	261.0	43.1	3.4	0.59
070719_9-73		core		15	6680	791	0.12	166.67	3.64	0.0469	0.0010	-0.16	0.0389	0.0009	0.0060	0.0001	0.81	0.00202	0.00005	38.6	0.8	40.7	1.0	38.8	0.9	42.0	19.0	38.6	0.8	0.99
070719_9-74		rim		20	6400	781	0.12	164.99	3.61	0.0530	0.0018	-0.65	0.0443	0.0015	0.0061	0.0001	0.77	0.00280	0.00025	39.0	0.8	56.5	6.9	44.0	1.5	326.0	61.3	38.6	0.8	0.89
070719_9-75		core		5	352	284	0.81	168.92	4.13	0.0468	0.0018	0.23	0.0384	0.0015	0.0059	0.0001	0.29	0.00205	0.00008	38.1	0.9	41.4	1.6	38.2	1.4	38.0	72.0	38.0	0.9	0.99
070719_9-76		core		2	175	122	0.70	169.66	4.10	0.0467	0.0017	0.54	0.0385	0.0010	0.0059	0.0001	-0.06	0.00205	0.00008	37.9	0.9	41.3	1.7	38.3	1.0	35.0	65.0	37.9	0.9	0.99
070719_9-77		core		2	341	125	0.37	168.92	4.81	0.0476	0.0020	0.35	0.0391	0.0016	0.0059	0.0002	0.22	0.00209	0.00007	38.0	1.1	42.3	1.6	38.9	1.6	76.0	86.0	38.0	1.1	0.98

				Elemental Composition				Isotopic Compositions											Isotopic Dates									
Sample	Spot	Rim / Core	Notes	Pb (ppm)	U (ppm)	Th (ppm)	Th/U	238U/ 206Pb	± 2σ abs	207Pb/ 206Pb	± 2σ abs	Rho	207Pb/ 235U	± 2σ abs	206Pb/ 238U	± 2σ abs	Rho	208Pb/ 232Th	± 2σ abs	206Pb/ 238U (Ma)	± 2σ abs	208Pb/ 232Th (Ma)	± 2σ abs	207Pb/ 235U (Ma)	± 2σ abs	207Pb/ 206Pb (Ma)	± 2σ abs	BestAge	± 2σ abs	Concordance
070719_9-78		rim		23	3360	1173	0.35	159.74	3.67	0.0471	0.0010	0.18	0.0405	0.0010	0.0063	0.0001	0.81	0.00210	0.00005	40.2	0.9	42.5	1.0	40.3	0.9	51.0	22.0	40.2	0.9	1.00
070719_9-79		core		6	1590	348	0.22	177.62	5.67	0.0480	0.0012	0.45	0.0374	0.0012	0.0056	0.0002	0.67	0.00191	0.00005	36.2	1.1	38.6	1.0	37.3	1.2	96.0	39.0	36.1	1.2	0.97
070719_9-80		rim		36	3430	2459	0.72	161.11	3.51	0.0511	0.0012	0.24	0.0437	0.0010	0.0062	0.0001	0.33	0.00154	0.00004	39.9	0.9	31.2	0.7	43.4	1.0	242.0	26.4	39.7	0.9	0.92
070719_9-81		core		9	274	471	1.72	170.18	4.39	0.0479	0.0018	-0.04	0.0389	0.0016	0.0059	0.0002	0.48	0.00195	0.00005	37.8	1.0	39.5	1.1	38.7	1.6	92.0	70.0	37.7	1.0	0.97
070719_9-82		rim		8	1056	454	0.43	166.09	3.74	0.0482	0.0012	-0.50	0.0397	0.0013	0.0060	0.0001	0.80	0.00201	0.00004	38.7	0.9	40.7	0.9	39.5	1.2	105.0	32.1	38.6	0.9	0.98
070719_9-83		core		5	192	246	1.28	163.40	3.88	0.0466	0.0022	0.37	0.0397	0.0020	0.0061	0.0001	0.00	0.00207	0.00007	39.3	0.9	41.8	1.4	39.5	2.0	30.0	95.0	39.3	0.9	0.99
070719_9-84		rim		39	4080	1877	0.46	163.61	3.91	0.0472	0.0010	0.00	0.0398	0.0010	0.0061	0.0001	0.91	0.00221	0.00005	39.3	0.9	44.5	1.1	39.6	1.0	57.0	18.0	39.3	0.9	0.99
070719_9-86		core		12	1660	650	0.39	171.38	3.64	0.0491	0.0012	-0.04	0.0398	0.0011	0.0058	0.0001	0.58	0.00202	0.00005	37.5	0.8	40.8	0.9	39.7	1.1	150.0	32.1	37.4	0.8	0.95
070719_9-87		core		7	2050	315	0.15	162.34	3.61	0.0483	0.0011	-0.38	0.0410	0.0010	0.0062	0.0001	0.84	0.00224	0.00006	39.6	0.9	45.1	1.2	40.8	1.0	114.0	28.1	39.5	0.9	0.97
070719_9-88		core		6	900	303	0.34	168.27	3.86	0.0480	0.0013	0.26	0.0394	0.0010	0.0059	0.0001	0.33	0.00202	0.00006	38.2	0.9	40.8	1.3	39.2	1.0	82.0	44.0	38.1	0.9	0.97
070719_9-89		core		8	667	379	0.57	166.78	3.96	0.0599	0.0016	-0.05	0.0496	0.0013	0.0060	0.0001	0.64	0.00222	0.00006	38.5	0.9	44.8	1.2	49.2	1.3	596.0	38.9	37.9	0.9	0.78
070719_9-90		rim		6	999	319	0.32	169.95	4.00	0.0467	0.0011	0.13	0.0379	0.0011	0.0059	0.0001	0.68	0.00193	0.00005	37.8	0.9	38.9	0.9	37.8	1.1	36.0	29.0	37.8	0.9	1.00
070719_9-91		core		2	302	120	0.40	166.11	4.15	0.0464	0.0017	0.11	0.0384	0.0017	0.0060	0.0002	0.41	0.00208	0.00006	38.7	1.0	42.0	1.2	38.2	1.7	23.0	64.0	38.7	1.0	1.01
070719_9-92		rim		6	1102	319	0.29	163.13	4.38	0.0469	0.0013	0.09	0.0396	0.0014	0.0061	0.0002	0.88	0.00206	0.00005	39.4	1.1	41.5	1.1	39.5	1.4	44.0	42.0	39.4	1.1	1.00
070719_9-93		core		50	2070	2854	1.38	172.21	3.99	0.0469	0.0011	-0.23	0.0378	0.0009	0.0058	0.0001	0.81	0.00186	0.00004	37.3	0.9	37.6	0.9	37.6	0.9	42.0	25.0	37.3	0.9	0.99
070719_9-94		core		3	603	175	0.29	171.03	4.32	0.0477	0.0013	-0.08	0.0388	0.0013	0.0058	0.0001	0.73	0.00202	0.00008	37.6	0.9	40.8	1.7	38.6	1.3	84.0	42.0	37.5	0.9	0.97
070719_9-95		core		2	122	104	0.86	167.22	4.36	0.0487	0.0027	0.07	0.0402	0.0022	0.0060	0.0002	0.19	0.00205	0.00006	38.4	1.0	41.4	1.2	40.0	2.2	130.0	110.0	38.3	1.0	0.96
070719_9-96		rim		13	2212	694	0.31	167.84	3.91	0.0466	0.0011	-0.17	0.0383	0.0011	0.0060	0.0001	0.68	0.00204	0.00006	38.3	0.9	41.2	1.2	38.2	1.1	27.0	33.0	38.3	0.9	1.00
070719_9-97		core		2	110	105	0.96	171.53	6.81	0.0485	0.0032	0.29	0.0389	0.0024	0.0058	0.0002	0.26	0.00195	0.00010	37.5	1.5	39.4	2.0	38.7	2.3	110.0	140.0	37.4	1.5	0.97
070719_9-98		rim		5	916	260	0.28	170.21	4.20	0.0477	0.0013	0.36	0.0386	0.0010	0.0059	0.0001	0.40	0.00204	0.00007	37.8	0.9	41.3	1.6	38.5	1.0	81.0	44.0	37.7	0.9	0.98
070719_9-100		rim		8	2119	422	0.20	166.33	3.59	0.0465	0.0012	0.19	0.0382	0.0009	0.0060	0.0001	0.44	0.00202	0.00005	38.6	0.8	40.8	1.1	38.1	0.9	25.0	37.0	38.7	0.8	1.01
070719_9-101		core		1	80	47	0.58	167.17	4.02	0.0496	0.0032	0.48	0.0407	0.0023	0.0060	0.0001	-0.25	0.00215	0.00010	38.5	0.9	43.4	2.1	40.5	2.3	160.0	130.0	38.3	0.9	0.95
070719_9-102		core		5	753	239	0.32	170.82	4.27	0.0480	0.0018	0.05	0.0388	0.0015	0.0059	0.0001	0.46	0.00205	0.00007	37.6	0.9	41.4	1.4	38.6	1.5	99.0	72.0	37.6	0.9	0.97
180818_7 [40.908338, -114.307611] - granodiorite																													
180818_7-1		rim		13	565	175	0.31	40.24	0.91	0.0488	0.0011	-0.08	0.1666	0.0039	0.0249	0.0006	0.79	0.00817	0.00021	158.2	3.5	164.4	4.3	156.5	3.7	137.0	24.2	158.3	3.6	1.01
180818_7-2		core		9	447	124	0.28	40.70	0.91	0.0491	0.0012	0.38	0.1673	0.0040	0.0246	0.0006	0.52	0.00798	0.00022	156.5	3.5	160.8	4.4	157.1	3.7	152.0	32.1	156.5	3.5	1.00
180818_7-3		core		11	482	99	0.21	23.15	2.14	0.0624	0.0030	-0.98	0.3770	0.0486	0.0432	0.0040	1.00	0.01052	0.00063	273.0	24.6	212.0	10.2	323.0	36.6	705.0	86.2	269.0	24.6	0.84
180818_7-4		rim		23	580	295	0.51	39.56	0.94	0.0488	0.0011	0.04	0.1709	0.0041	0.0253	0.0006	0.74	0.00829	0.00023	160.9	3.8	166.9	4.6	160.2	3.8	136.0	25.1	161.0	3.8	1.00
180818_7-5		rim		13	354	160	0.45	39.32	1.04	0.0501	0.0013	0.40	0.1748	0.0049	0.0254	0.0007	0.48	0.00847	0.00020	161.9	4.3	170.6	4.2	163.6	4.4	198.0	40.2	161.7	4.3	0.99
180818_7-6		rim		11	296	138	0.46	39.48	1.09	0.0490	0.0012	-0.26	0.1724	0.0051	0.0253	0.0007	0.86	0.00846	0.00026	161.3	4.4	170.2	5.5	161.5	4.6	143.0	34.1	161.3	4.4	1.00
180818_7-8		core		24	671	260	0.39	38.90	0.92	0.0498	0.0011	0.08	0.1768	0.0046	0.0257	0.0006	0.75	0.00992	0.00028	163.7	3.8	199.4	6.4	165.3	4.1	182.0	27.2	163.6	3.8	0.99
180818_7-9		core		38	911	462	0.51	38.91	0.92	0.0496	0.0011	0.34	0.1758	0.0043	0.0257	0.0006	0.70	0.00890	0.00021	163.6	3.9	179.1	4.4	164.4	4.0	174.0	20.3	163.5	3.9	0.99
180818_7-10		core		49	166	686	4.14	40.47	0.96	0.0490	0.0012	0.00	0.1651	0.0043	0.0247	0.0006	0.60	0.00772	0.00018	157.4	3.7	155.5	3.6	155.1	3.9	146.0	32.1	157.4	3.7	1.01
180818_7-11		core		43	937	990	1.06	40.27	1.01	0.0502	0.0011	0.46	0.1732	0.0046	0.0248	0.0006	0.79	0.00590	0.00140	158.1	4.0	120.0	21.4	162.2	4.2	203.0	26.3	157.9	4.0	0.97
180818_7-12		core		272	2420	3742	1.55	41.19	0.88	0.0499	0.0010	-0.08	0.1668	0.0037	0.0243	0.0005	0.88	0.00785	0.00018	154.6	3.3	158.0	3.7	156.6	3.5	188.0	12.6	154.5	3.3	0.99
180818_7-13		core		77	207	87	0.42	2.85	0.15	0.1960	0.0040	-0.77	9.5000	0.5442	0.3510	0.0184	1.00	0.09510	0.00554	1938.0	92.5	1836.0	98.1	2398.0	65.1	2792.4	56.2	2793.2	33.4	0.81
180818_7-14		rim		30	1260	409	0.32	40.73	0.91	0.0496	0.0011	-0.19	0.1686	0.0044	0.0246	0.0006	0.86	0.00795	0.00019	156.3	3.5	160.1	3.9	158.2	4.0	174.0	22.3	156.3	3.5	0.99
180818_7-15		rim		5	209	71	0.34	40.14	0.93	0.0489	0.0012	0.25	0.1690	0.0045	0.0249	0.0006	0.60	0.00834	0.00022	158.6	3.6	167.9	4.5	158.5	4.0	143.0	35.1	158.7	3.7	1.00
180818_7-16		core		4	101	57	0.56	39.90	0.92	0.0487	0.0016	0.28	0.1690	0.0059	0.0251	0.0006	0.15	0.00828	0.00024	159.5	3.7	166.7	5.0	158.5	5.3	129.0	59.1	159.7	3.7	1.01
180818_7-17		core		21	1245	269	0.22	40.23	0.95	0.0491	0.0010	-0.37	0.1689	0.0046	0.0249	0.0006	0.93	0.00822	0.00020	158.3	3.7	165.5	4.2	158.5	4.2	150.0	17.3	158.3	3.7	1.00
180818_7-18		core		26	763	326	0.43	39.78	0.96	0.0490	0.0010	-0.15	0.1690	0.0039	0.0251	0.0006	0.93	0.00860	0.00020	160.1	3.9	173.0	4.1	158.5	3.6	147.0	12.4	160.1	3.8	1.01
180818_7-19		rim		16	734	204	0.28	39.82	0.91	0.0494	0.0011	0.14	0.1720	0.0043	0.0251	0.0006	0.77	0.00837	0.00022	159.9	3.7	168.5	4.5	161.1	3.9	167.0	23.2	159.8	3.6	0.99
180818_7-20		rim		6	303	78	0.26	39.03	0.91	0.0497	0.0011	0.14	0.1752	0.0042	0.0256	0.0006	0.66	0.00864	0.00023	163.1	3.8	173.9	4.7	163.9	3.8	180.0	18.4	163.0	3.8	0.99
180818_7-21		core		72	1311	975	0.74	40.68	1.08	0.0501	0.0010	0.21	0.1695	0.0045	0.0246	0.0007	0.89	0.00805	0.00019	156.5	4.1	162.0	3.8	159.0	4.1	200.0	14.6	156.3	4.1	0.98
180818_7-22		core		25	222	111	0.50	33.90	2.73	0.1320	0.0401	-0.97	0.5800	0.2203	0.0295	0.0024	0.99	0.02460	0.00871	188.0	14.5	490.0	443.2	430.0	130.3	1770.0	561.1	168.0	16.5	0.40
180818_7-23		core		336	3372	4595	1.36	40.50	0.92	0.0491	0.0010	0.15	0.1677	0.0037	0.0247	0.0006	0.94	0.00784	0.00016	157.2	3.6	157.9	3.3	157.4	3.4	150.1	10.2	157.3	3.5	1.00
180818_7-24		core		60	860	860	1.00	41.93	1.16	0.0510	0.0014	-0.65	0.1672	0.0061	0.0239	0.0007	0.90	0.00732	0.00038	151.9	4.2	147.3	7.5	157.0	5.4	240.0	39.3	151.6	4.2	0.97
180818_7-25		core		46	500	600	1.20	40.31	0.92	0.0491	0.0011	-0.13	0.1677	0.0040	0.0248	0.0006	0.77	0.00826	0.00020	158.0	3.6	166.3	4.1	157.4	3.6	151.0	23.2	158.0	3.6	1.00
180818_7-26		core		3	77	38	0.50	39.84	0.94	0.0501	0.0026	0.13	0.1734	0.0090	0.0251	0.0006	0.14	0.00837	0.00030	159.8	3.8	168.5	6.3	162.3	7.9	190.0	110.1	159.6	3.8	0.98
180818_7-27		rim		4	181	54	0.30	40.27	0.86	0.0477	0.0015	0.53	0.1634	0.0050	0.0248	0.0005	-0.21	0.00822	0.00021	158.1	3.3	165.4	4.3	153.6	4.5	83.0	59.0	158.4	3.4	1.03
180818_7-28		core		8	165	102	0.62	40.21	0.93	0.0479	0.0013	0.15	0.1640	0.0043	0.0249	0.0006	0.38	0.00842	0.00023	158.4	3.6	169.5	4.7	154.2	3.9	90.0	42.0	158.6	3.7	1.03
180818_7-29		core		24	276	70	0.25	10.63	0.64	0.0804	0.0018	-0.77	1.0420	0.0721	0.0941	0.0056	0.99	0.03660	0.00260	579.0	33.1	727.0	63.2	723.0	36.9	1205.0	31.3	564.4	33.0	0.80
180818_7-30		rim		18	508	246	0.48	41.05	1.11	0.0495	0.0012	-0.43	0.1652	0.0051	0.0244	0.0007	0.87	0.00810	0.00021	155.1	4.2	163.2	4.2	155.2	4.6	171.0	31.2	155.1	4.2	1.00
180818_7-31		core		62	843	796	0.94	40.16	1.03	0.0492	0.0010	0.04	0.1695	0.0047	0.0249	0.0006	0.88	0.00831	0.00021	158.5	4.0	167.3	4.3	159.0	4.2	157.0	17.3	158.6	4.0	1.00
180818_7-32		rim		24	620	320	0.52	39.67	0.94	0.0489	0.0011	-0.11	0.1699	0.0050	0.0252	0.0006	0.77	0.00830	0.00022	160.5	3.8	167.1	4.5	159.3	4.5	139.0	27.1	160.6	3.8	1.01
180818_7-33		core		18	426	239	0.56	40.62	0.94	0.0489	0.0011	-0.26	0.1670	0.0048	0.0246	0.0006	0.76	0.00807	0.00018	156.8	3.6	162.5	3.6	156.8	4.3	140.0	27.1	156.8	3.6	1.00

				Elemental Composition				Isotopic Compositions										Isotopic Dates									
Sample	Spot	Rim / Core	Notes	Pb (ppm)	U (ppm)	Th (ppm)	Th/U	238U/ 206Pb	± 2σ abs	207Pb/ 206Pb	± 2σ abs	Rho	207Pb/ 235U	± 2σ abs	206Pb/ 238U	± 2σ abs	Rho	208Pb/ 232Th	± 2σ abs	206Pb/ 238U (Ma)	± 2σ abs	208Pb/ 232Th (Ma)	± 2σ abs	207Pb/ 235U (Ma)	± 2σ abs	207Pb/ 206Pb (Ma)	± 2σ abs	BestAge	± 2σ abs	Concordance
180818_7-34		core		62	935	810	0.87	39.92	1.19	0.0494	0.0011	0.11	0.1707	0.0050	0.0251	0.0007	0.88	0.00826	0.00025	159.5	4.7	166.3	5.3	160.0	4.5	165.0	22.2	159.5	4.7	1.00
180818_7-35		core		36	680	411	0.60	38.71	0.91	0.0494	0.0012	-0.62	0.1760	0.0056	0.0258	0.0006	0.89	0.00934	0.00026	164.4	3.8	187.9	5.6	164.6	5.0	165.0	33.2	164.4	3.8	1.00
180818_7-36		core		159	126	114	0.91	1.95	0.05	0.1815	0.0037	-0.42	12.7800	0.3126	0.5128	0.0125	0.96	0.14840	0.00429	2668.0	61.2	2796.0	80.3	2663.0	54.8	2665.5	53.9	2666.4	34.1	1.00
180818_7-37		rim		12	471	155	0.33	39.65	0.95	0.0495	0.0011	0.00	0.1722	0.0044	0.0252	0.0006	0.85	0.00846	0.00024	160.6	3.8	170.3	5.0	161.3	4.0	169.0	19.3	160.5	3.8	1.00
180818_7-38		rim		19	469	150	0.32	29.15	1.25	0.0685	0.0022	-0.83	0.3260	0.0210	0.0343	0.0015	0.97	0.01324	0.00082	217.6	9.5	266.0	20.3	266.0	16.1	881.0	53.0	212.5	9.0	0.76
180818_7-39		rim		10	434	134	0.31	39.62	0.94	0.0498	0.0011	-0.38	0.1730	0.0050	0.0252	0.0006	0.82	0.00824	0.00022	160.7	3.8	165.8	4.5	162.0	4.5	186.0	25.3	160.6	3.8	0.99
180818_7-40		rim		97	1384	1212	0.88	38.11	0.97	0.0497	0.0010	-0.50	0.1807	0.0056	0.0262	0.0007	0.95	0.00850	0.00021	166.9	4.2	171.0	4.2	168.7	5.0	178.0	14.4	166.9	4.2	0.99
180818_7-41		rim		15	361	187	0.52	39.95	0.91	0.0520	0.0012	-0.04	0.1803	0.0050	0.0250	0.0006	0.71	0.00863	0.00024	159.4	3.6	173.7	5.1	168.3	4.5	282.0	30.5	158.8	3.6	0.95
180818_7-42		core		21	780	276	0.35	39.86	1.39	0.0492	0.0010	0.03	0.1701	0.0057	0.0251	0.0009	0.98	0.00831	0.00047	159.7	5.5	167.2	9.7	159.5	5.1	157.0	16.3	159.7	5.5	1.00
180818_7-43		rim		10	324	114	0.35	37.99	0.89	0.0497	0.0013	0.14	0.1793	0.0047	0.0263	0.0006	0.51	0.00910	0.00026	167.5	3.9	183.1	5.6	167.4	4.2	176.0	39.2	167.4	3.9	1.00
180818_7-44		core		53	961	658	0.68	39.89	1.16	0.0494	0.0011	0.37	0.1701	0.0045	0.0251	0.0007	0.90	0.00836	0.00026	159.6	4.6	168.2	5.4	159.5	4.1	170.0	24.2	159.6	4.6	1.00
180818_7-45		core		11	539	137	0.25	39.62	1.02	0.0493	0.0011	0.38	0.1716	0.0044	0.0252	0.0007	0.80	0.00843	0.00023	160.7	4.1	169.6	4.6	160.8	4.0	160.0	23.2	160.7	4.1	1.00
180818_7-46		core		29	1310	374	0.29	40.58	0.99	0.0492	0.0010	-0.50	0.1674	0.0045	0.0246	0.0006	0.95	0.00830	0.00021	156.9	3.8	167.0	4.4	157.1	4.1	157.0	14.3	156.9	3.8	1.00
180818_7-47		core		46	788	530	0.67	37.76	0.96	0.0492	0.0011	-0.19	0.1807	0.0050	0.0265	0.0007	0.86	0.00926	0.00028	168.5	4.3	186.4	6.0	168.7	4.4	154.0	25.2	168.5	4.2	1.00
180818_7-48		core		121	1730	1510	0.87	38.46	2.07	0.0495	0.0010	-0.70	0.1774	0.0100	0.0260	0.0014	0.99	0.00894	0.00087	165.1	8.9	180.0	18.9	165.7	8.8	189.0	15.4	165.4	8.8	1.00
180818_7-49		core		13	389	174	0.45	39.35	0.88	0.0491	0.0011	0.11	0.1716	0.0042	0.0254	0.0006	0.66	0.00830	0.00023	161.7	3.6	167.0	4.8	160.8	3.8	152.0	22.2	161.8	3.6	1.01
180818_7-50		core		15	817	189	0.23	39.18	1.15	0.0490	0.0010	0.03	0.1732	0.0053	0.0255	0.0008	0.91	0.00862	0.00028	162.4	4.7	173.5	5.8	162.2	4.8	147.0	17.3	162.5	4.7	1.00
180818_7-51		core		22	606	285	0.47	38.83	0.98	0.0487	0.0011	0.28	0.1729	0.0044	0.0258	0.0007	0.82	0.00847	0.00020	163.9	4.1	170.5	4.1	161.9	4.0	131.0	23.1	164.0	4.1	1.01
180818_7-52		core		26	723	318	0.44	39.59	0.97	0.0493	0.0011	0.45	0.1712	0.0042	0.0253	0.0006	0.87	0.00881	0.00025	160.8	4.0	177.3	5.3	160.5	3.9	163.0	19.3	160.8	3.9	1.00
180818_7-53		core		30	711	374	0.53	40.27	0.97	0.0503	0.0011	0.19	0.1720	0.0046	0.0248	0.0006	0.74	0.00863	0.00020	158.1	3.8	173.7	4.2	161.2	4.2	205.0	20.4	157.9	3.8	0.98

*BestAge is 207Pb-corrected 206Pb/238U date for analyses < 1000 Ma and 207Pb/206Pb for analyses > 1000 Ma. 207Pb/206Pb = 0.84 is used for 207Pb corrected date calculation.

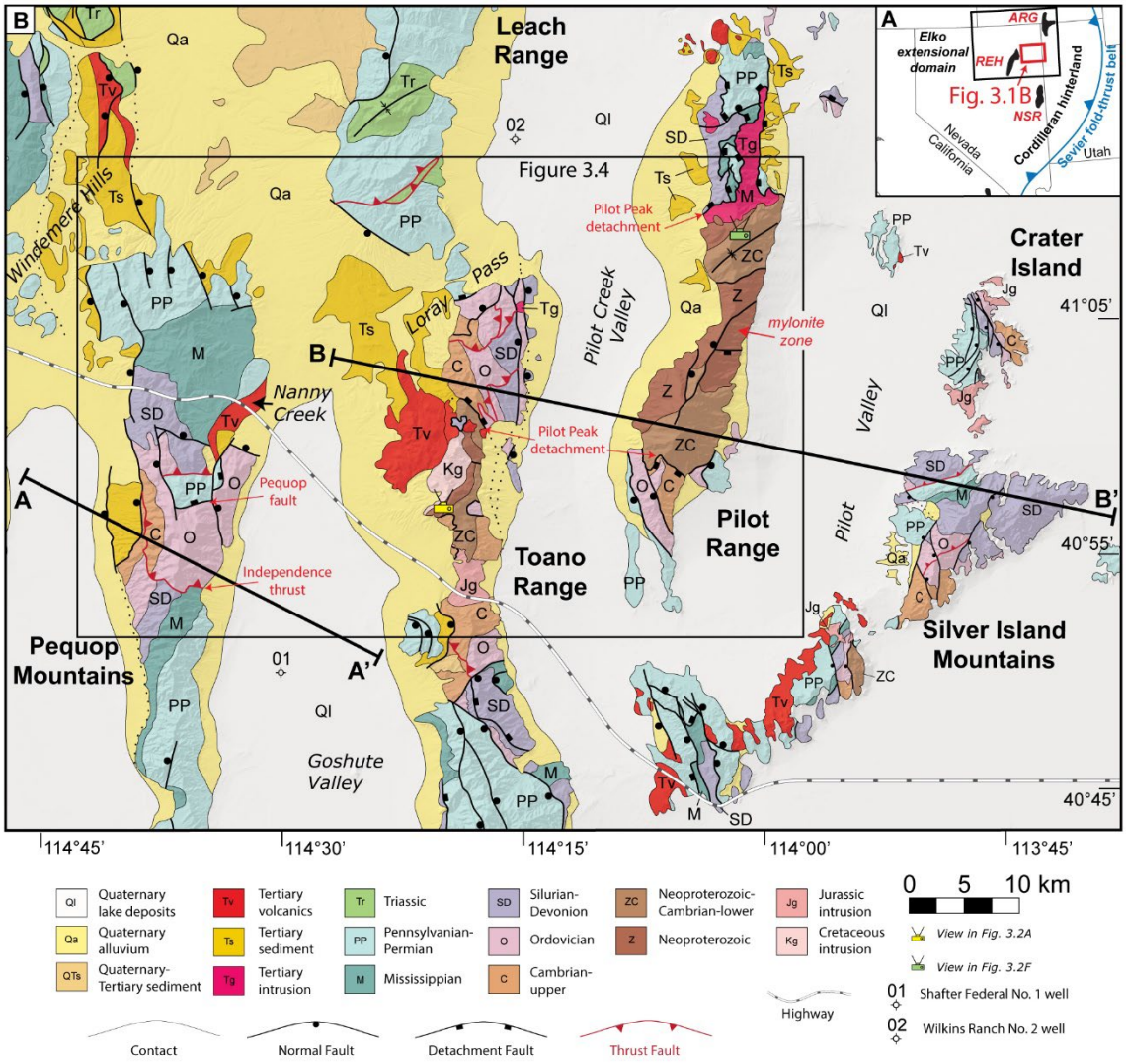

Figure 3.1. (A) Geographic map showing location of the Elko extensional domain and the eastern Basin and Range metamorphic core complexes (MCC). Inset box shows location of Fig. 3.1B. ARG – Albion-Raft River-Grouse Creek MCC. NSR – Northern Snake Range MCC. REH – Ruby-East Humboldt MCC. (B) Simplified geological map of the study area in northeast Nevada-northwest Utah after Coats (1987), Doelling (1980) and Moore and Sorenson (1979). Inset map shows location of Fig. 3.4. Figure 3.3 cross section lines are indicated by A-A' and B-B'.

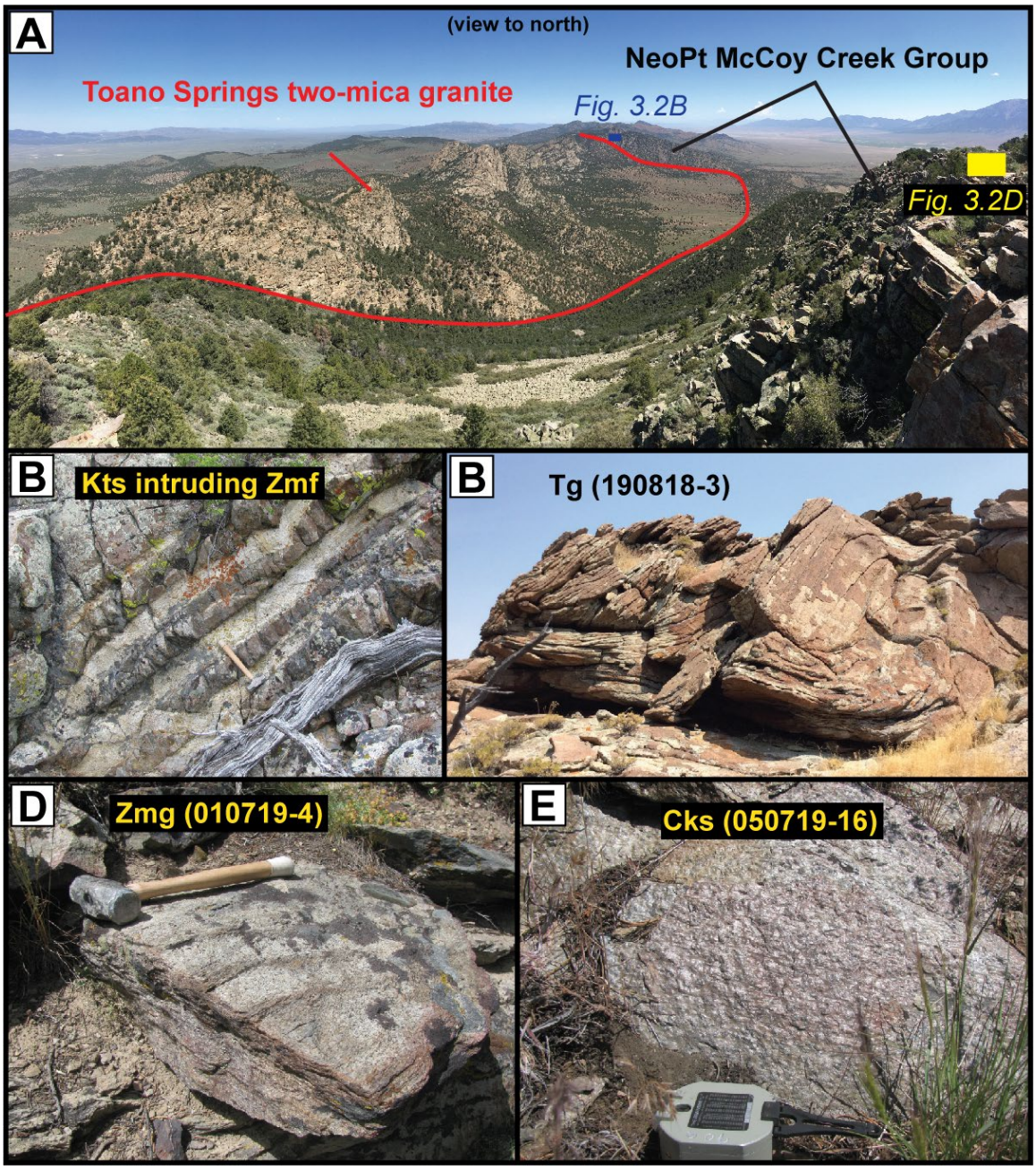

Figure 3.2. Photographs of key lithologic units and important structural relationships in the Toano and Pilot Ranges. (A) Late Cretaceous Toano Springs granite intruded into the Neoproterozoic McCoy Creek Group. The locations of Fig. 3.2B and 3.2D are shown as blue and yellow boxes, respectively. (B) Toano Springs granite intruded and cross cut the foliation of Neoproterozoic country rock. (C) Outcrop-scale S-C fabric within Eocene granodiorite in the Pilot Range – intrudes the Cambrian Killian Springs formation. Sample 190818-3. Top-west kinematics. This rock does not show evidence of pervasive sub-solidus ductile deformation in thin section. (D) Foliated pelitic schist along the contact of the Toano Springs granite. Sample 010719-4. Muscovite and biotite are part of the

synkinematic garnet (retrogressed to chlorite) bearing mineral assemblage. Location in 2A. (E) Pelitic schist in the Cambrian Killian Springs formation, Pilot Range. Muscovite, grown discordant to the foliation and within pseudomorphed garnet, is part of the post-kinematic retrograde mineral assemblage. (F) Overview of the northern Pilot Range highlighting the Pilot Peak detachment fault. The hanging wall features east tilted Silurian-Devonian strata juxtaposed with Mississippian strata by a low-angle normal fault. This sequence was intruded by a correlative of the Eocene McGinty Monzogranite. The footwall of the fault at this location includes the main body of the McGinty Monzogranite and the metasedimentary Neoproterozoic rocks (foreground) it intrudes. The Albion-Raft River-Grouse Creek metamorphic core complex is seen in the upper right background. (G) View of the Pilot Peak detachment fault in the southern Pilot Range, where Cambro-Ordovician Notch Peak limestone is juxtaposed above Neoproterozoic-lower Cambrian metasedimentary rocks. The locations of Fig. 3.2H and 3.2I are shown as yellow boxes. (H) Plastically deformed Cambrian marble beneath the detachment fault. Quartz sigma clasts show top west kinematics. (I) Photomicrograph of Prospect Mountain quartzite below the Pilot Peak detachment fault exhibiting static recrystallization of quartz. Compare with Fig. 3.2J, which is a finely recrystallized quartz mylonite. Location in 3.2G. (J) Mylonitic quartzite from McCoy Creek Unit A in the central Pilot Range – the deepest structural level in the range. This sample is at least 2 km structurally below the Pilot Peak detachment.

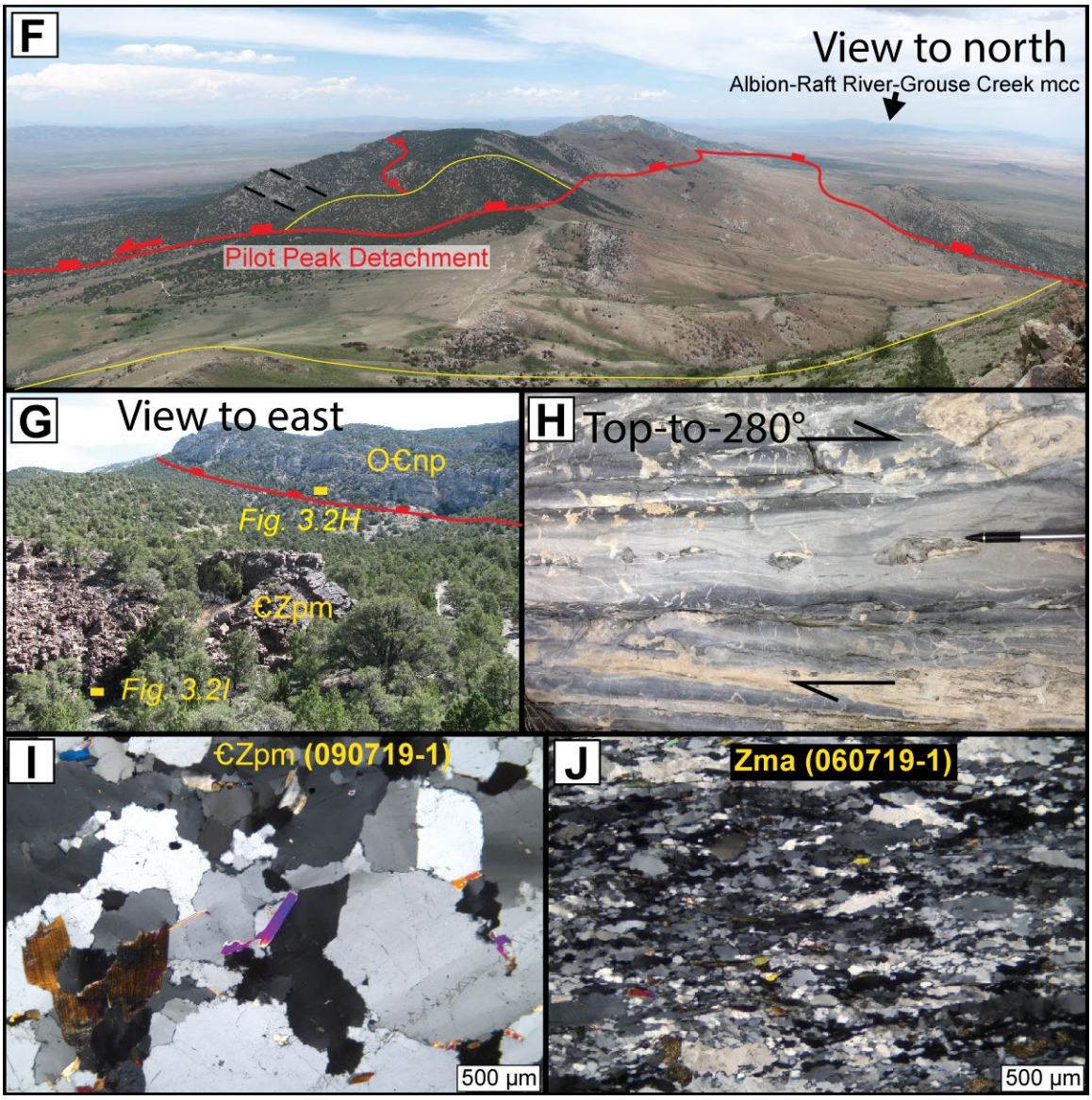

Figure 3.2. *(continued)*

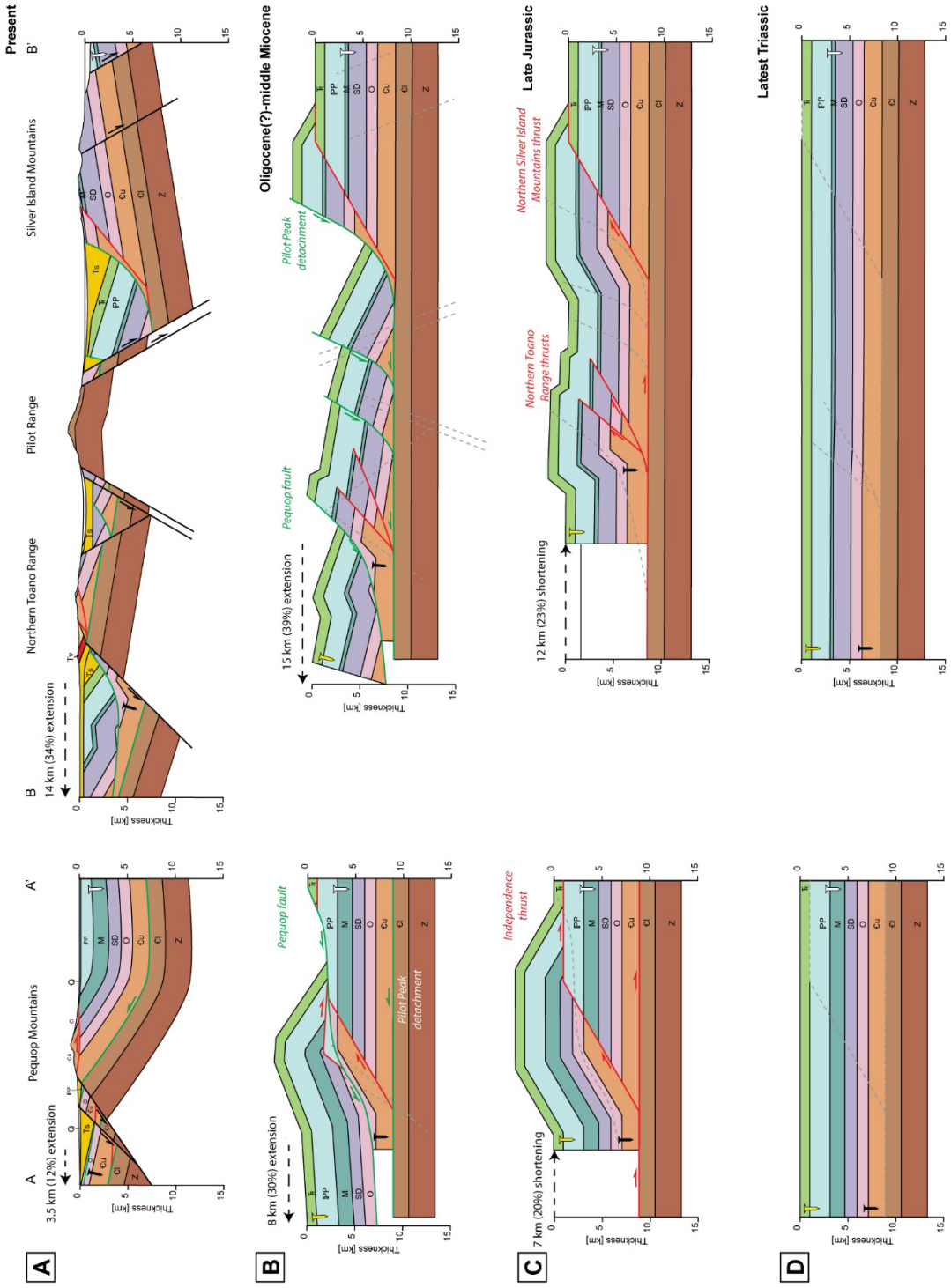

Figure 3.3. Schematic cross section reconstruction showing Late Triassic to Present tectonic history of the Pequop, Pilot and Toano Ranges. Cross section drafted along line A-A' and B-B' in Fig. 3.1. See text for details.

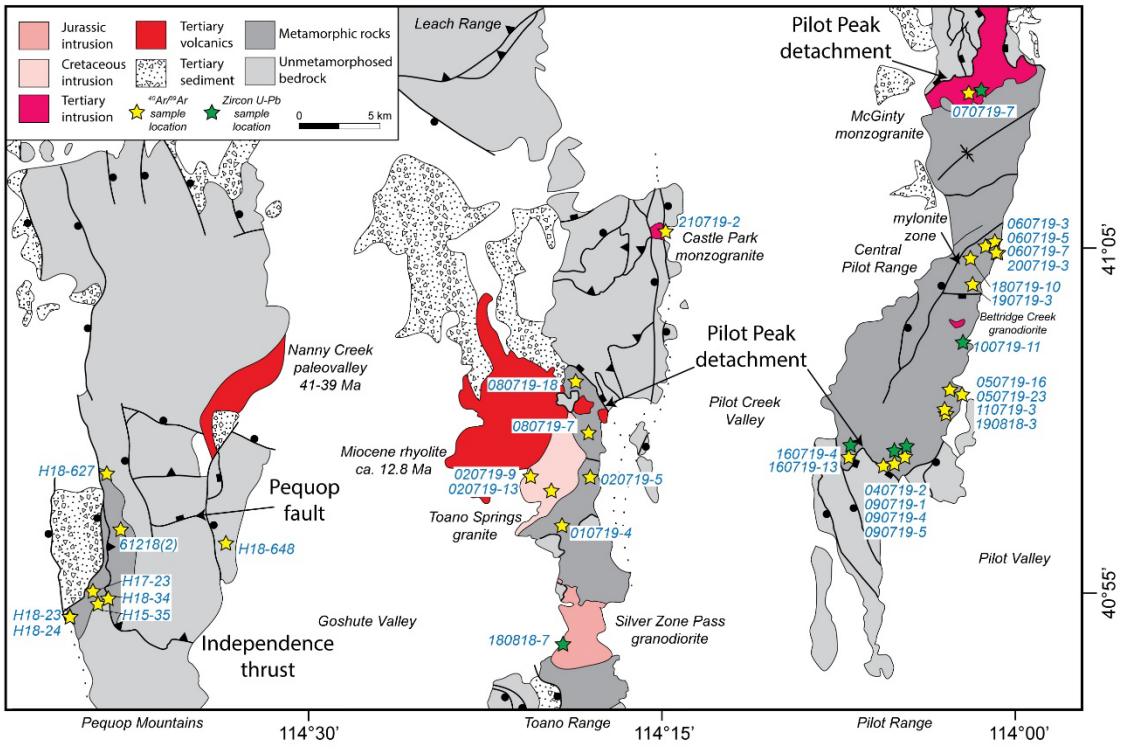

Figure 3.4. Simplified geological map showing the location of $^{40}Ar/^{39}Ar$ and zircon U-Pb samples analyzed in this study. See Supplemental Table S8 for samples coordinates.

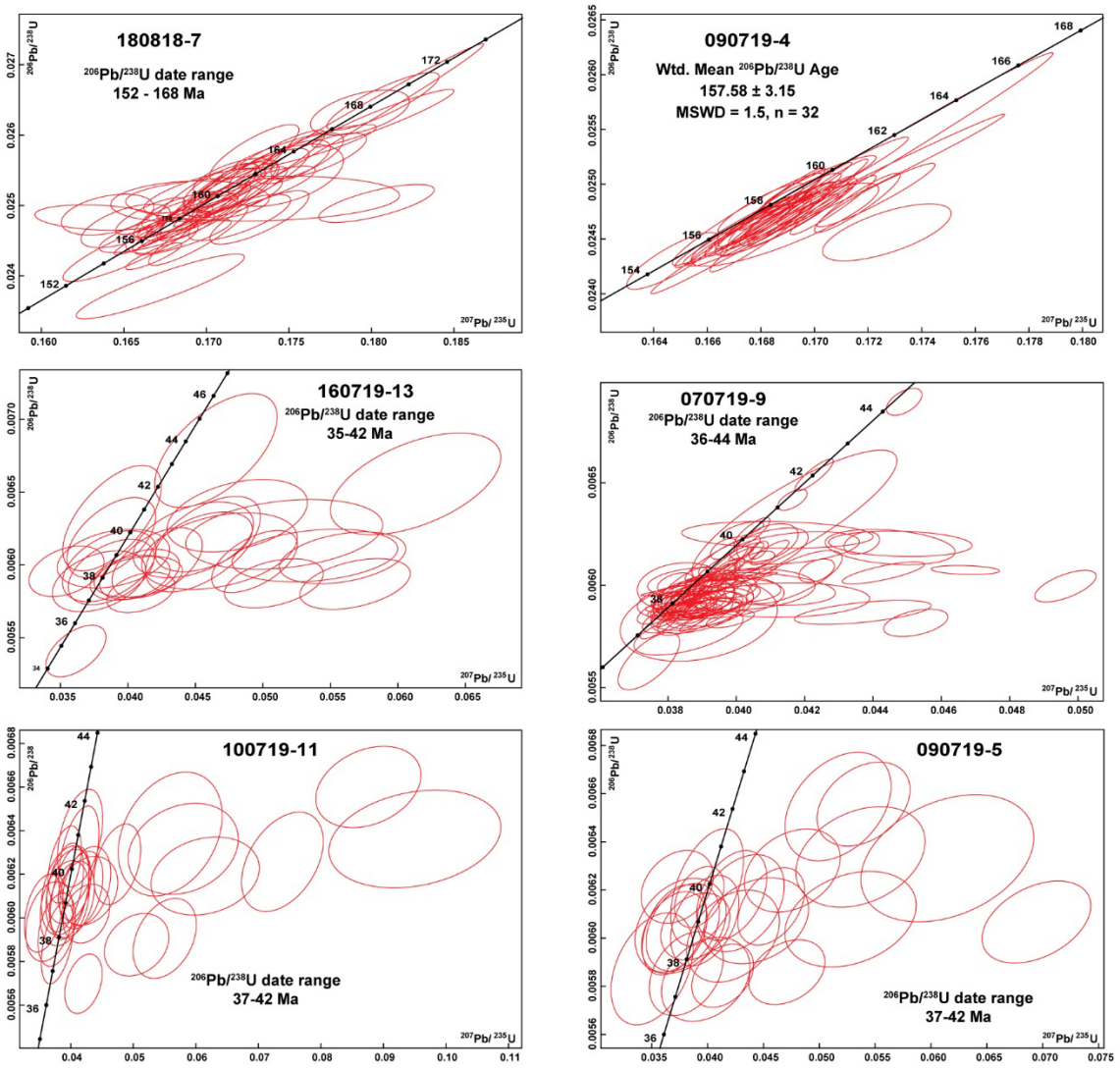

Figure 3.5. Zircon U-Pb Wetherill Concordia diagrams for Late Jurassic and Eocene intrusions dated in this study. See Supplementary Tables 3.S5 and 3.S7 for full datasets.

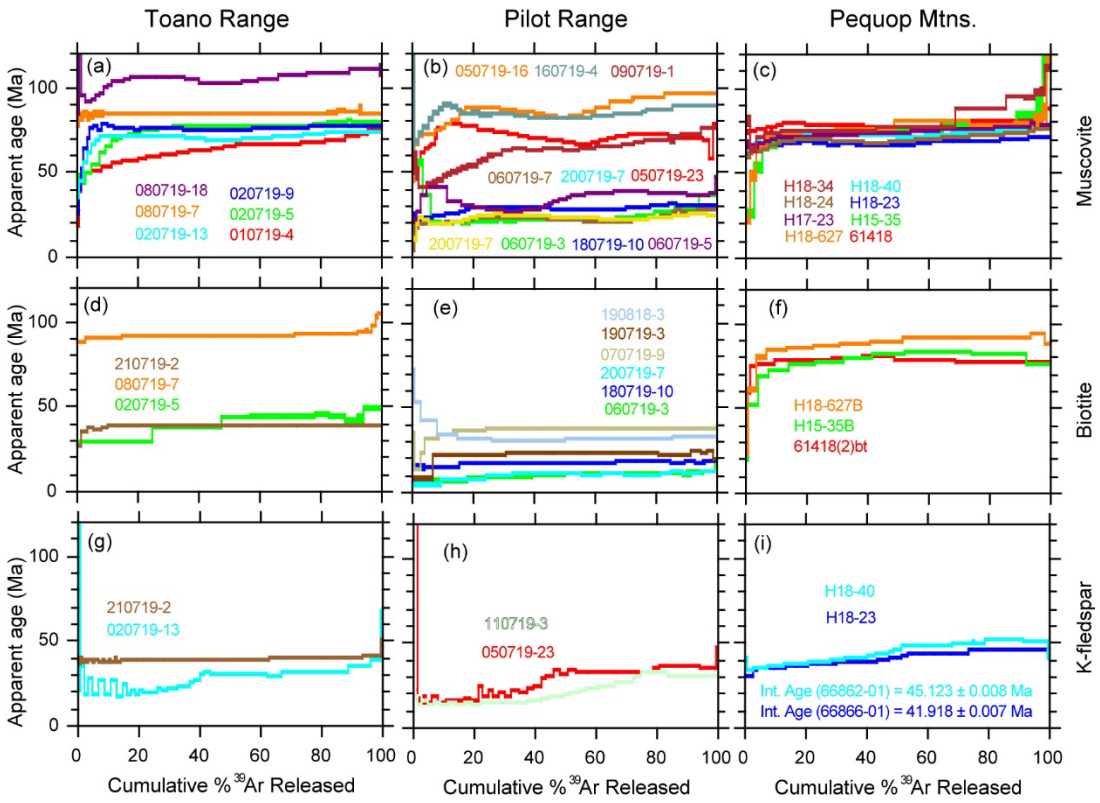

Figure 3.6. $^{40}Ar/^{39}Ar$ age spectra for each phase analyzed in this study. See Supplemental Table 3.S2 for full dataset.

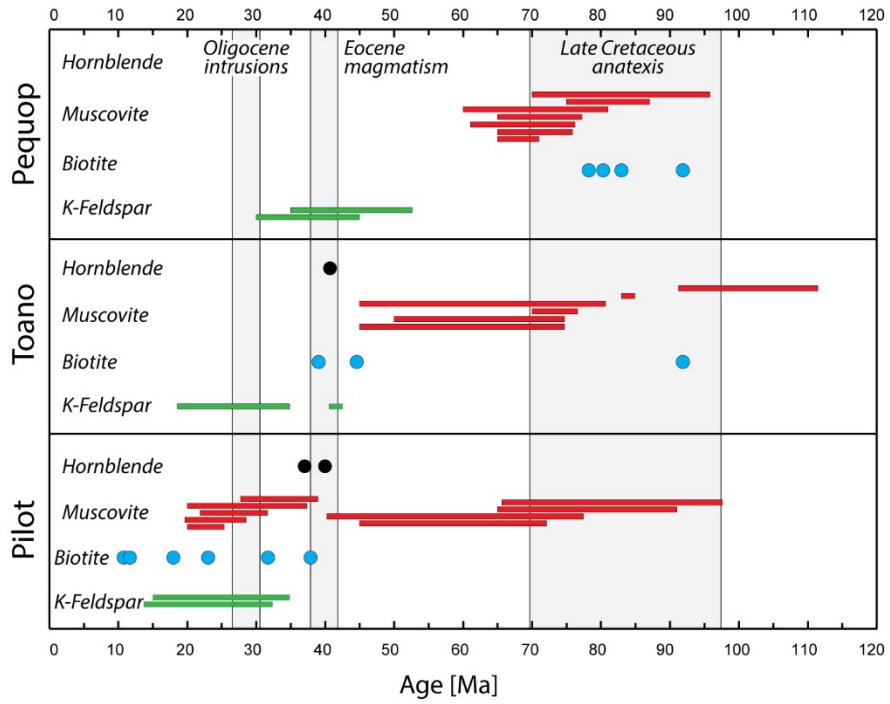

Figure 3.7. Summary of $^{40}Ar/^{39}Ar$ cooling ages grouped by location. Hornblende and biotite markers show interpreted cooling age based on plateau age, integrated age or weighted mean average of consecutive gas fractions. Muscovite and K-feldspar ages are represented by bars that span the lower and upper age range of climbing spectra.

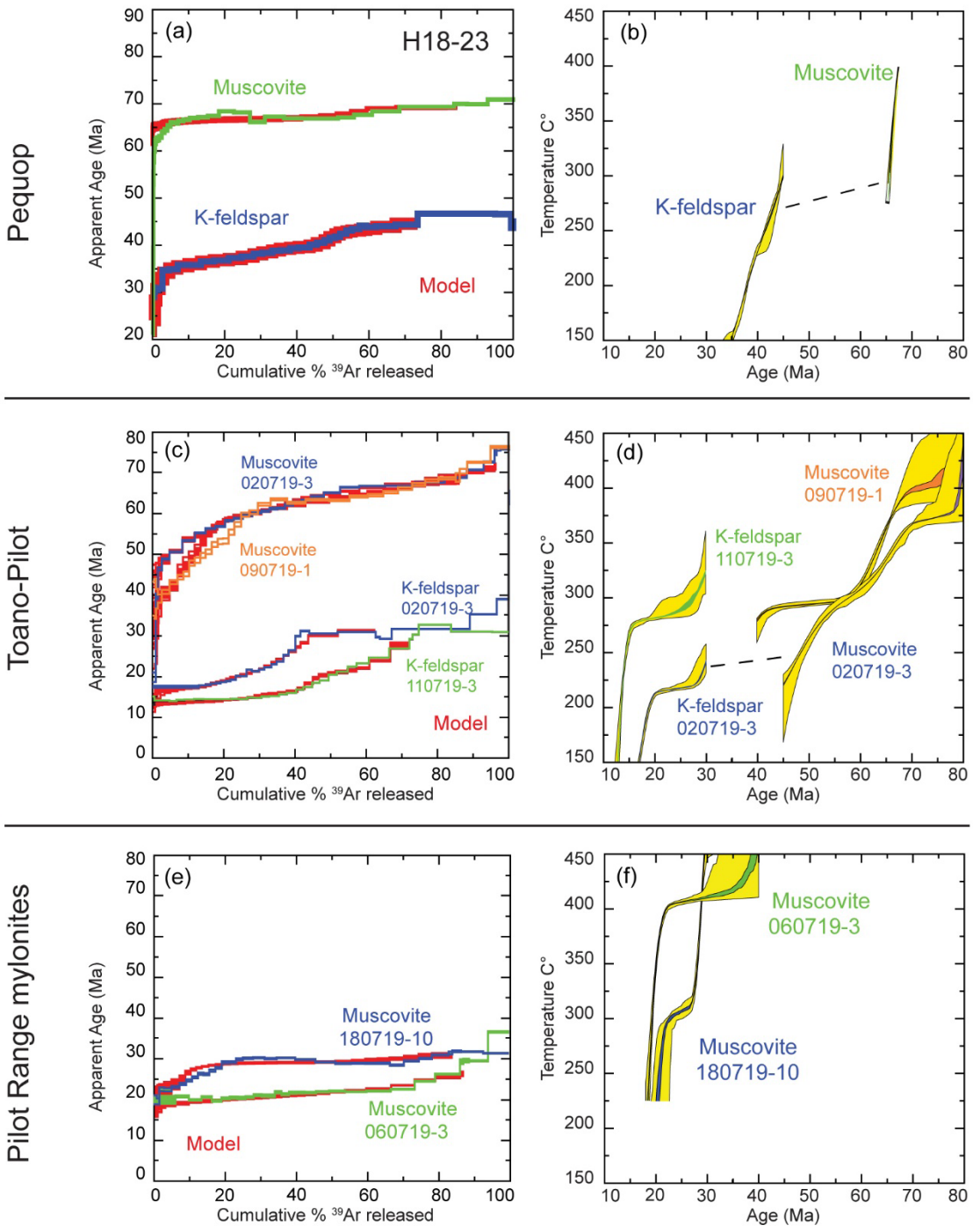

Figure 3.8. $^{40}Ar/^{39}Ar$ muscovite and K-feldspar MDD model results. Plots in the left column show measured and modeled $^{40}Ar/^{39}Ar$ age spectra. Plots in the right column show modeled cooling history of each sample.

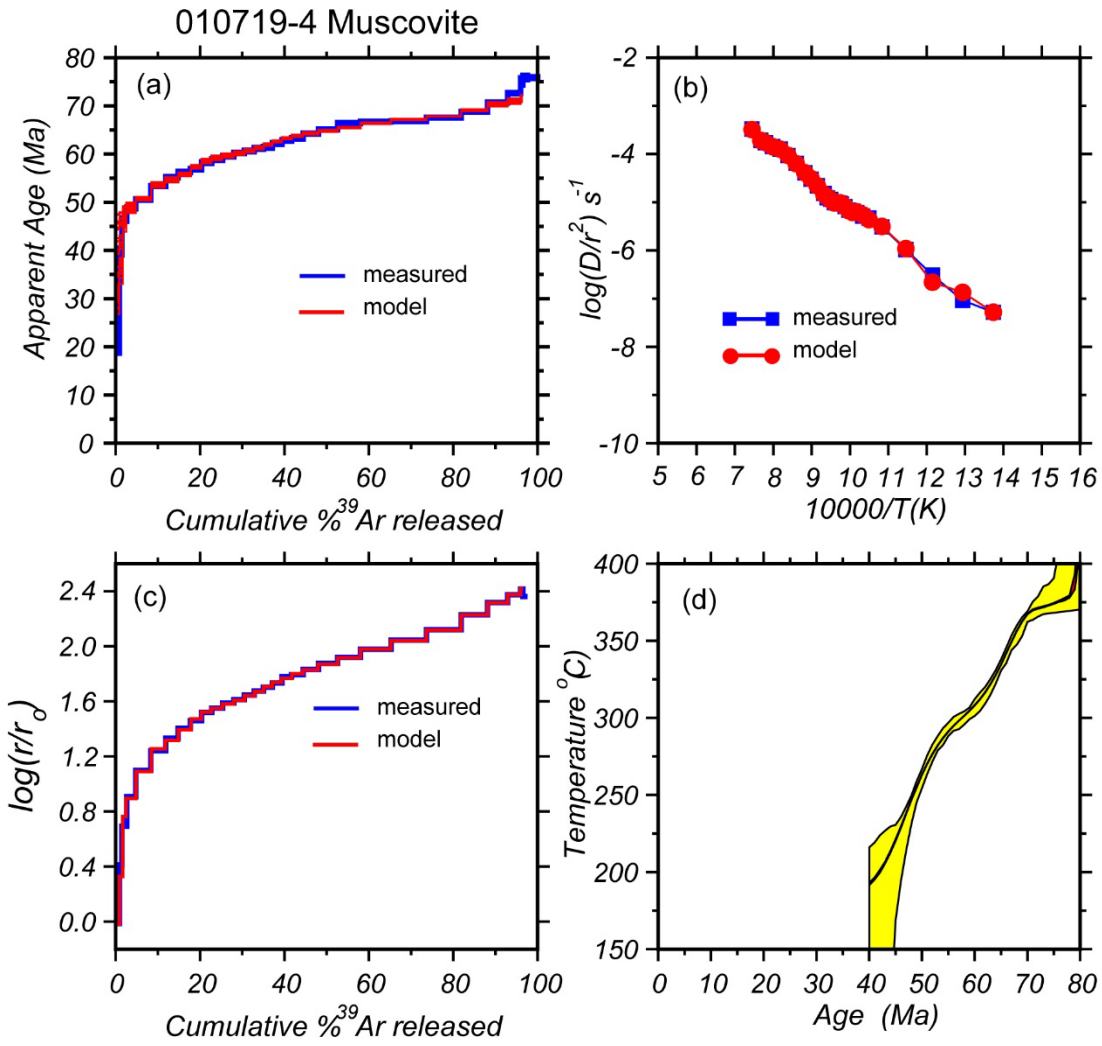

Figure 3.S1. $^{40}Ar/^{39}Ar$ muscovite and K-feldspar MDD model results for all samples modeled in this study. The plot in the top left panel shows measured and modeled $^{40}Ar/^{39}Ar$ age spectra. The bottom left panel shows the $\log(r/r_o)$ plot. The top right panel shows the Arrhenius plot for measured and modeled data. The bottom right panel shows the modeled cooling history of each sample.

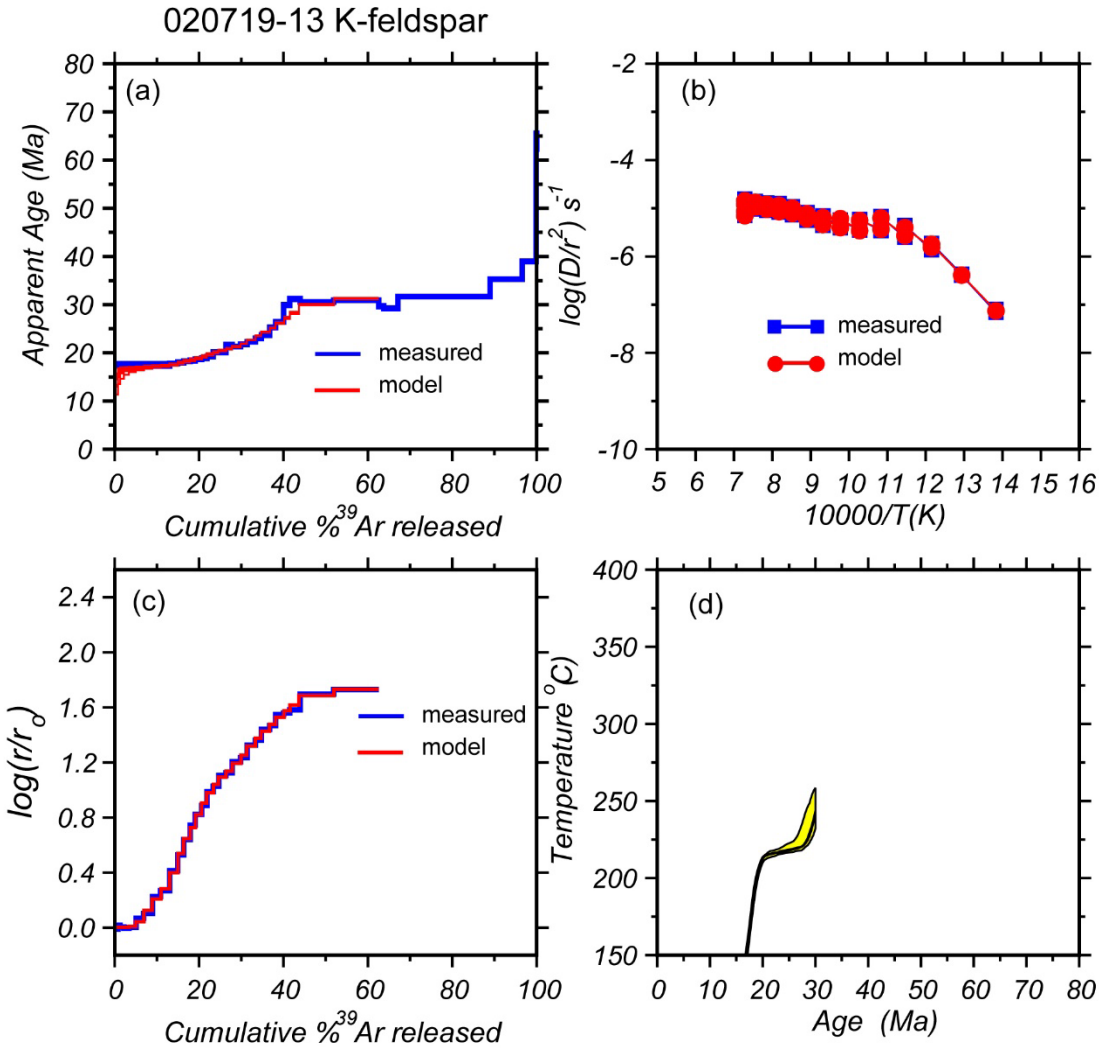

Figure 3.S1. *(continued)*

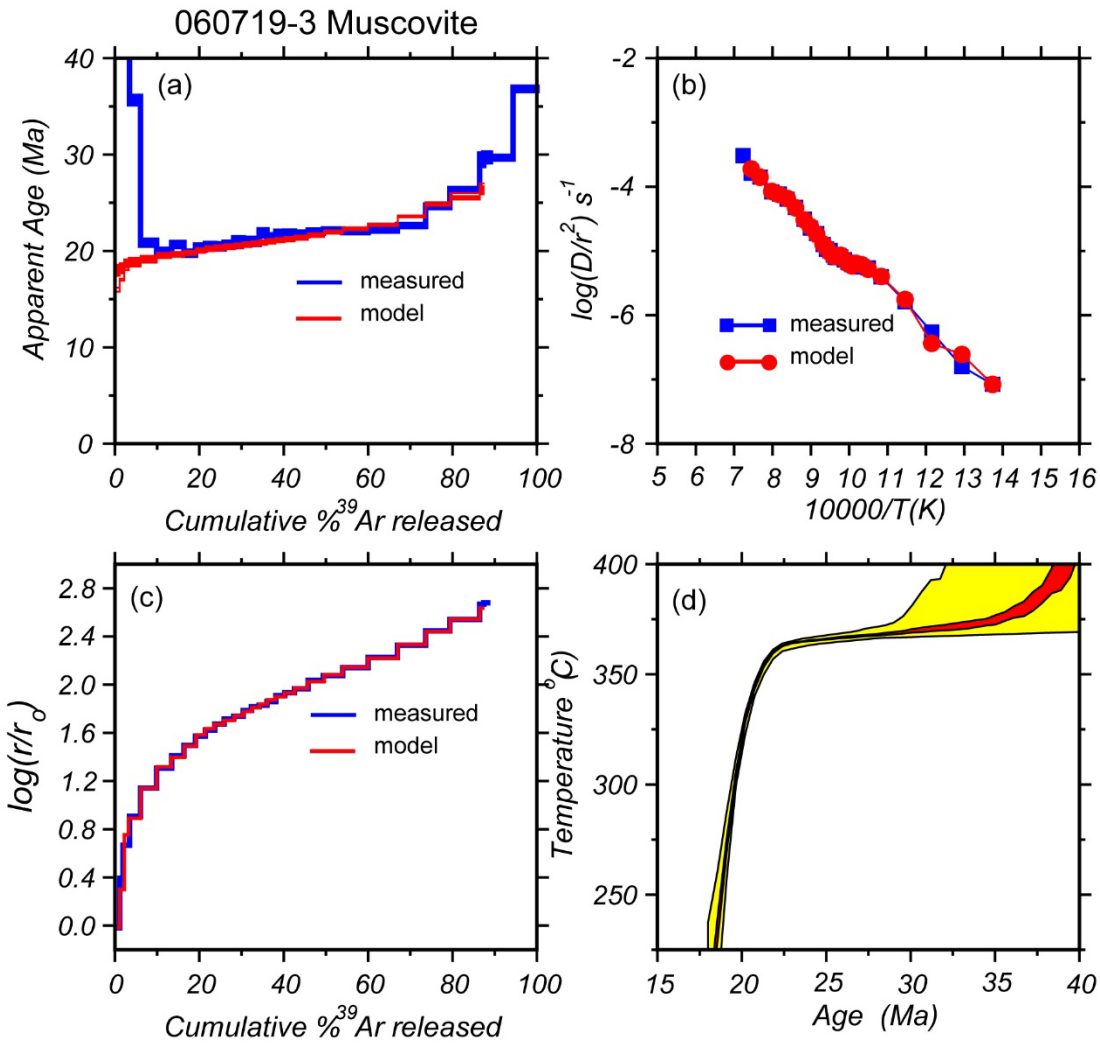

Figure 3.S1. *(continued)*

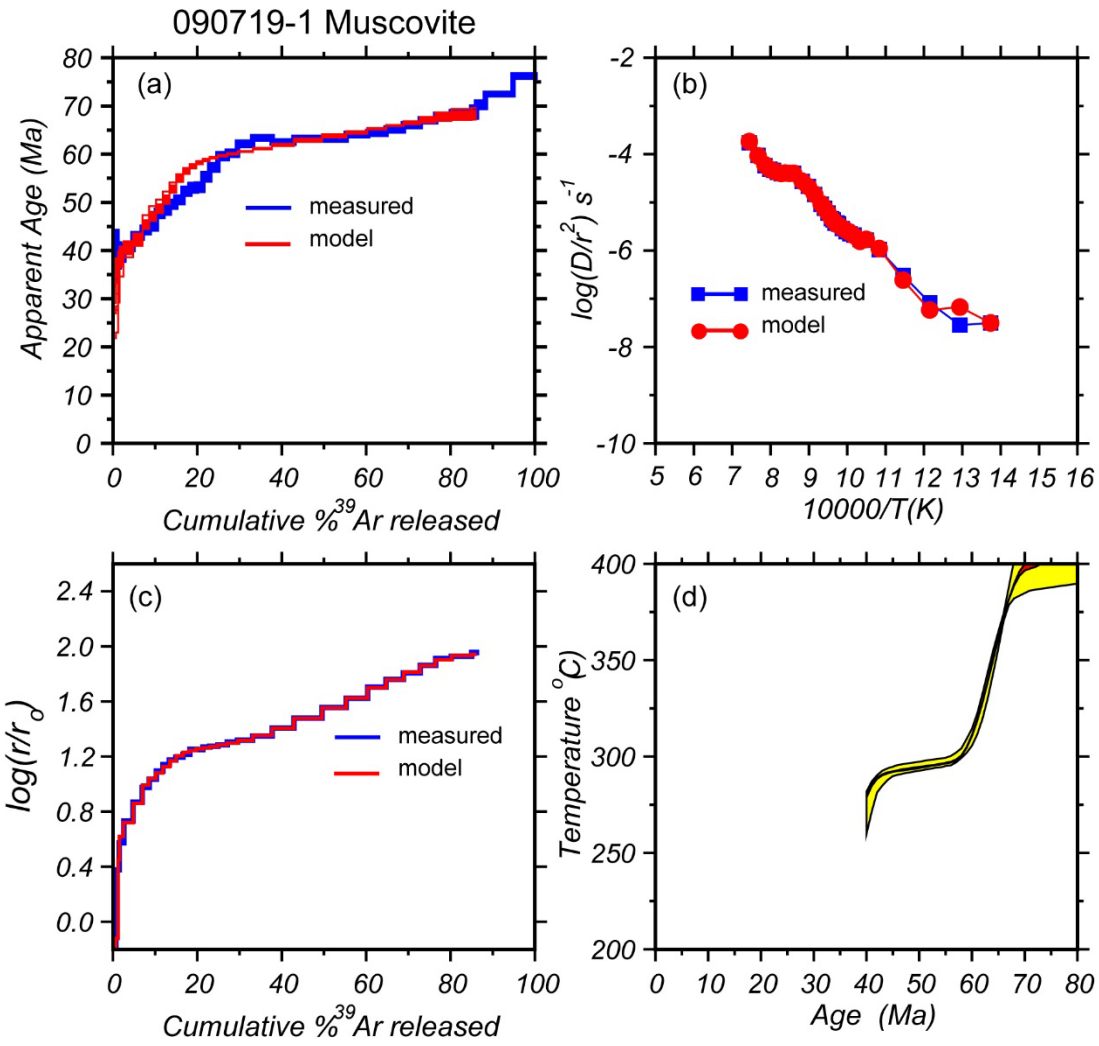

Figure 3.S1. *(continued)*

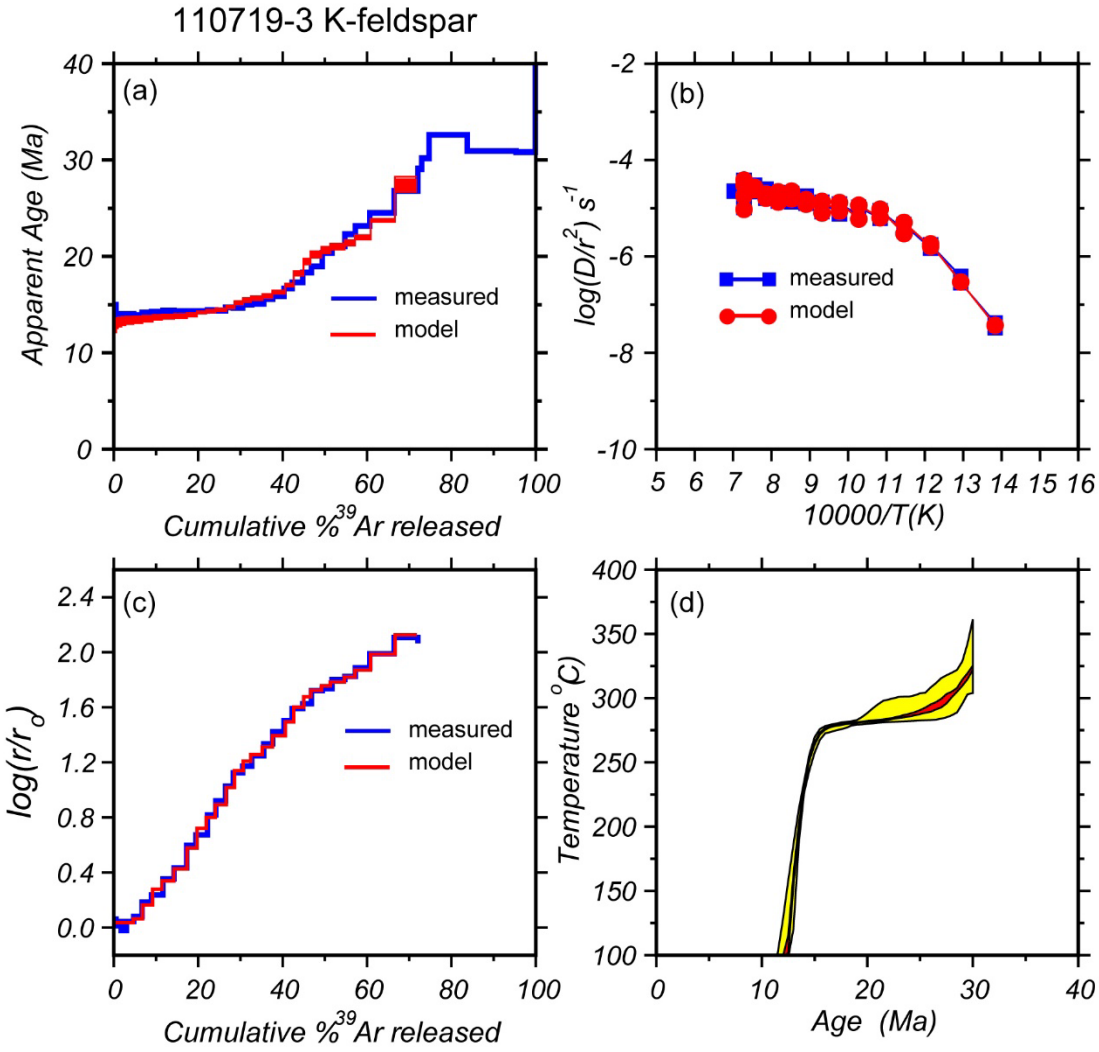

Figure 3.S1. *(continued)*

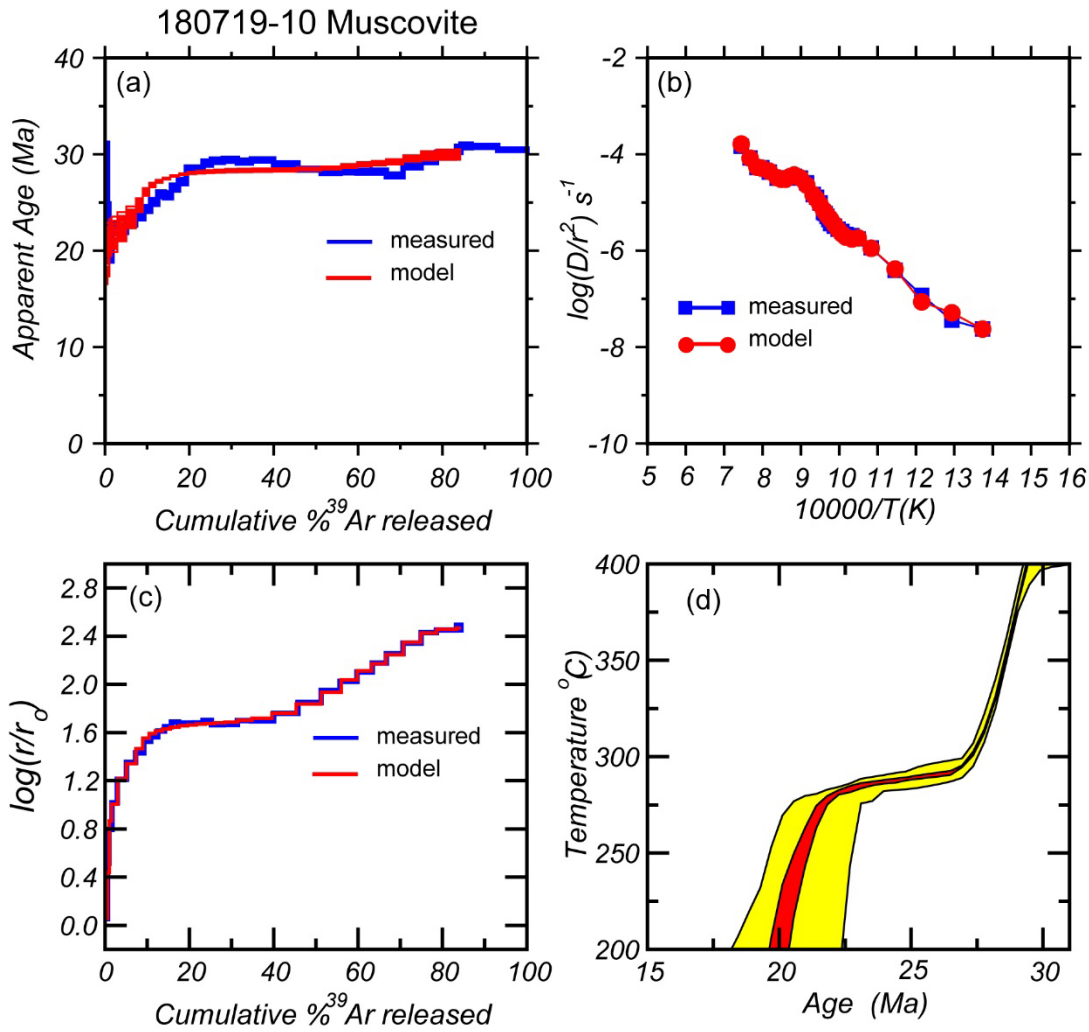

Figure 3.S1. *(continued)*

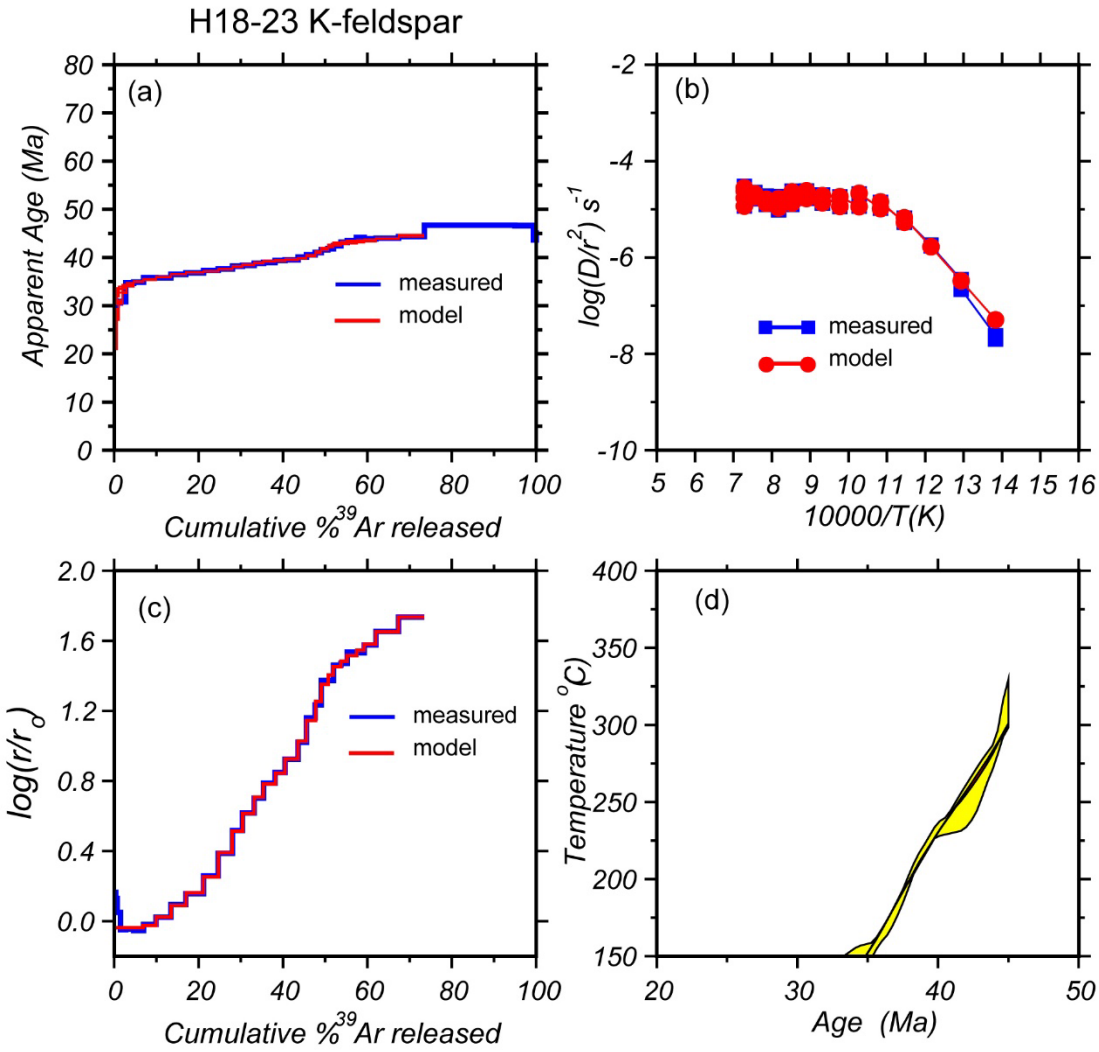

Figure 3.S1. *(continued)*

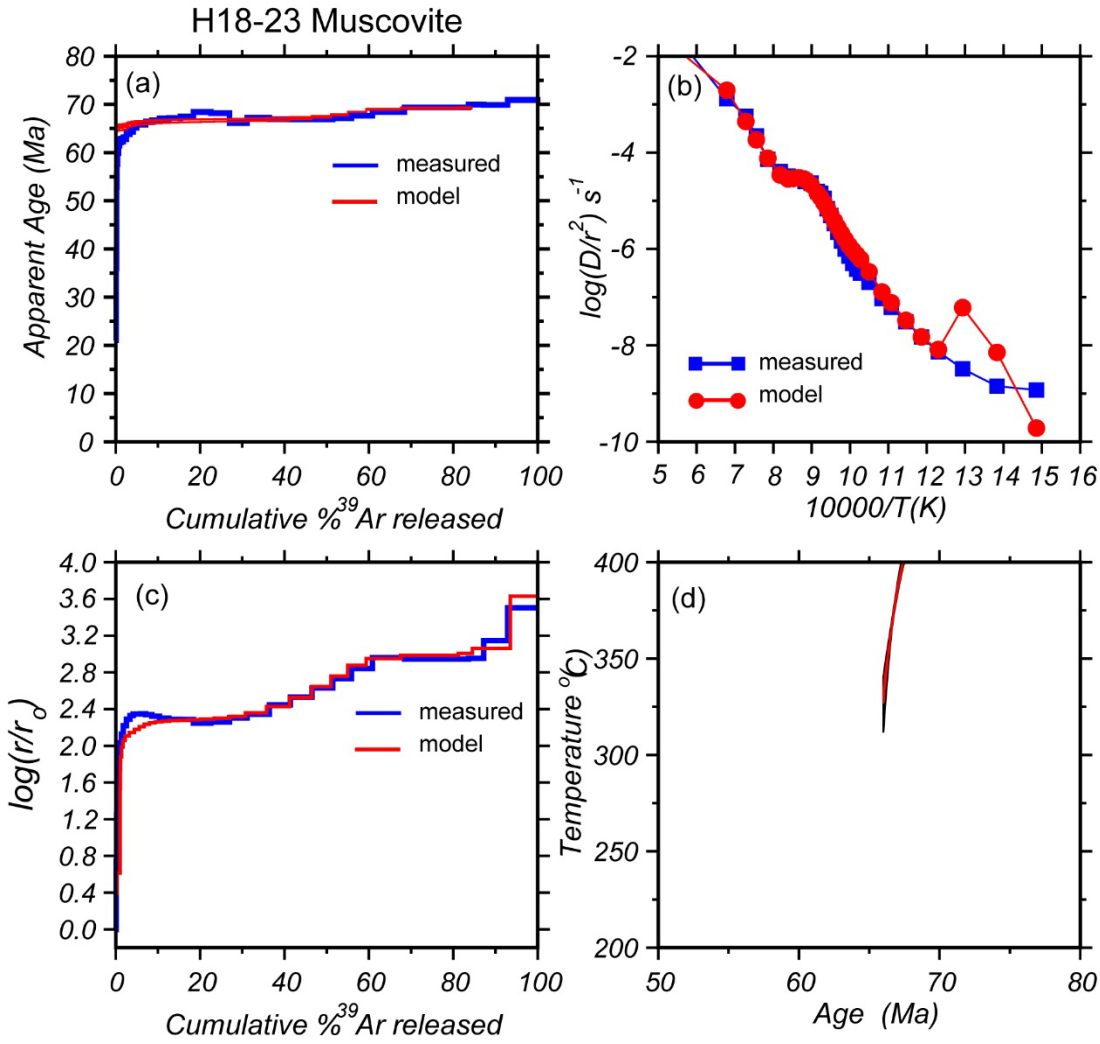

Figure 3.S1. *(continued)*

Chapter 4: Buoyant doming generates metamorphic core complexes in the North American Cordillera

Drew A. Levy[1*], Andrew V. Zuza[1], Zachary D. Michels[2], Joel W. DesOrmeau[3]

[1]*Nevada Bureau of Mines and Geology, University of Nevada, Reno, NV, 89557, USA*

[2]*Department of Geosciences, University of Arizona, Tucson, AZ, 85721, USA*

[3]*Department of Geological Sciences and Engineering, University of Nevada, Reno, NV, 89557, USA*

ABSTRACT

Continental metamorphic core complexes (MCCs) are considered a hallmark of large-magnitude crustal extension, with their characteristic high-strain mylonitic fabrics attributed to simple-shear strain along the down-dip continuation of a detachment fault. However, some MCCs exhibit pure-shear-dominated mylonitic fabrics temporally decoupled from regional extension, which may be related to magmatically-enhanced buoyant doming of the lower crust. Here we test the viability of buoyant doming for the formation of MCCs in the North American Cordillera by investigating the timing, kinematics, and conditions of mylonitic shear in the Ruby Mountains-East Humboldt Range (REH) MCC. Field observations and geochronology demonstrate an ~10 Myr gap between mid-crustal attenuation and regional extension. Mylonites in the REH record general shear strain with >80% attenuation at strain rates of 10^{-13} to 10^{-12} s^{-1} at temperatures of 400–600°C. The REH mylonites developed during protracted 40–29 Ma magmatism involving mantle-derived mafic intrusions and remobilized Late Cretaceous leucogranitic melts, well before post-17 Ma detachment faulting. We demonstrate that diapirism driven by observed temperatures and partial melt abundances can generate mylonitic shear zones at our estimated strain rates. Characteristics of the buoyant doming model are expressed in many low- to moderate-melt fraction MCCs globally, and the pre-extensional high-strain mylonitic fabrics may therefore be an important mechanism for localizing temporally decoupled brittle detachment faulting.

INTRODUCTION

Metamorphic core complexes (MCCs) impact the thermal, mechanical, and chemical evolution of the lithosphere as they accommodate efficient vertical mass and heat transfer through the crust (e.g., Crittenden et al., 1980; Teyssier and Whitney, 2002; Whitney et al., 2013). It remains unclear whether MCC development is driven primarily by extensional boundary conditions or magmatic-metamorphic processes in the lower crust. The density of the lower crust may be reduced by magmatism, partial melting, and protracted heating, which can cause buoyant diapiric exhumation of magmatic or migmatitic gneiss domes (Fig. 4.1A; Eskola, 1948). This "buoyant doming" model predicts pure-shear stretching accommodates significant (>50%) wall rock attenuation above the rising dome (e.g., Miller et al., 1983; Rey et al., 2009). Conversely, MCCs can develop via low-angle normal faulting, hanging wall removal, and isostatic footwall exhumation during large-magnitude (>100%) regional extension driven by plate-boundary forces (Wernicke and Axen, 1988). This classic "extensional exhumation" model links brittle detachment faulting with a mylonitic simple-shear zone at depth (Fig. 4.1B; Davis, 1983). Isostatically driven footwall exhumation may cause decompression melting that results in positive buoyancy feedbacks that increase exhumation rates (Fig. 4.1C; e.g., Teyssier and Whitney, 2002).

The MCCs spanning the North American Cordillera exhibit a range of exhumation and strain characteristics (Fig. 4.1D; Crittenden et al., 1980; Whitney et al., 2013). Many of the southern MCCs show deformation kinematics compatible with extensional exhumation, including brittle detachment faults that juxtapose Tertiary volcanics on mylonitic footwall rocks, temporally overlapping detachment fault and mylonite ages, and simple-shear strain conditions that are interpreted in the context large-displacement normal faults driving footwall isostatic rebound (e.g., Davis, 1983; Spencer and Reynolds, 1991;). Conversely, central MCCs developed diachronously with lower plate mylonitic fabrics pre-dating regional extension by ~10 Myr (e.g., Colgan et al., 2010; Konstantinou et al., 2012; Lee et al., 2017).

Syn-magmatic mylonitic fabrics, finite strain patterns exhibiting pure-shear flattening, and magmatic gneiss domes have been interpreted as records of late Eocene-Oligocene buoyant doming preceding Miocene detachment faulting in the central MCCs (e.g., Armstrong, 1968; Howard, 1980; Snoke, 1980; Todd, 1980; Miller et al., 1983; Lee et al., 1987; Konstantinou et al., 2012). The role of buoyancy in the development of the central MCCs and vertical flow of the deep crust, or infrastructure (Armstrong and Hansen, 1966), is often overlooked despite potential controls on the thermal and rheologic evolution of the Cordilleran orogen and localization of large-magnitude post-orogenic extension. Further investigation of the mechanisms driving ductile attenuation and crustal mass transfer is warranted to explain the diachroneity of regional extension and mylonitic fabrics. Here we investigate the timing, kinematics and conditions of ductile attenuation in the Ruby Mountains-East Humboldt Range (REH) MCC to understand the potential role of buoyancy forces in MCC development and deep crustal exhumation.

RUBY MOUNTAINS-EAST HUMBOLDT RANGE MCC

The REH MCC in the hinterland of the Sevier orogenic belt in northeast Nevada contains migmatitic Archean-Paleozoic metasediments pervasively intruded by Jurassic-Paleogene granitic dikes and sills representative of the Cordilleran infrastructure (Fig. 4.1D, 4.2A; Armstrong and Hansen, 1966; Howard, 1980). Peak metamorphism at 100–65 Ma is marked by partial melting and emplacement of voluminous pegmatitic leucogranite (McGrew et al., 2000; Howard et al., 2011; Hallett and Spear, 2015). Late Cretaceous(?)–Paleogene km-scale recumbent folding points to lower-crust mobility facilitated by magmatism and sustained mid-crustal temperatures >600 °C until ca. 30 Ma (McGrew and Snee, 1994; MacCready et al., 1997).

Post-Laramide magmatism at ca. 41 Ma led to the emplacement of Eocene mantle-derived mafic-intermediate intrusions, observed as voluminous sills of quartz diorite deformed in the upper mylonite zone (Fig. 4.2A; Wright and Snoke, 1993). Mylonitic 31–29 Ma monzogranite, derived from hybridization of basaltic and crustal melts at depth, are cut by moderately foliated leucogranite dikes indicating the generation of diorite and

monzogranite magmas included new and/or remobilized leucogranitic melts (Howard et al., 2011).

The upper 1 km of the infrastructure is deformed in a top-WNW mylonitic shear zone (Snoke, 1980; Hacker et al., 1990). The mylonitic Neoproterozoic to Ordovician section is ~0.75 km thick in the northern REH (Fig. 4.2A, 4.S1A); The same stratigraphy in adjacent ranges is 3.5 km thick indicating >80% vertical attenuation (Colgan et al., 2010; Zuza et al., 2021). The shear zone developed 29–22 Ma based on mylonitic monzogranite, 26–23 Ma zircon and titanite fission-track ages, and 22–21 Ma muscovite and biotite $^{40}Ar/^{39}Ar$ dates (Dokka et al., 1986; Wright and Snoke, 1993; McGrew and Snee, 1994).

The shear zone was cut by a west-directed brittle detachment fault that accommodated negligible stratigraphic omission, as Mississippian rocks are juxtaposed across it (Fig. 4.2A, 4.S1; Snoke, 1980). Non-deformed ca. 17 Ma basalt dikes with chilled margins crosscut the mylonitic fabric and are truncated by the detachment fault (Fig. 4.2A, 4.S1B; Snoke, 1980; Zuza et al., 2021). Large-magnitude extension and unroofing of the infrastructure initiated ca. 16–12 Ma based on low-temperature thermochronology (Colgan et al., 2010), ca. 16–12 Ma deposition of the >2 km thick sedimentary and volcanic Humboldt Formation (Lund Snee et al., 2016), and ca. 13–11 Ma clay gouge dates from the REH detachment fault (Haines and van der Pluijm, 2010).

MICROSTRUCTURE AND KINEMATIC OBSERVATIONS

We conducted microstructural analysis and Ti-in-quartz thermobarometry to investigate mylonite kinematics, deformation conditions, and strain rates to test between modes of MCC exhumation. Oriented samples of quartzite were collected across and below the mylonite zone for petrographic examination to establish kinematics, dynamic crystallization regime and target locations for electron backscatter diffraction (EBSD) analysis (Fig. 4.S1A). Asymmetric plagioclase porphyroclasts, mica fish and S–C and C' fabrics indicate top-west kinematics (Fig. 4.S2). Quartz recrystallization textures are indicative of grain boundary migration at the base of the mylonite zone grading to subgrain rotation at the top with most of the mylonites showing similar dynamic recrystallization

microstructures. EBSD data collected from 15 samples indicate similar quartz crystallographic preferred orientations consistent with top-west asymmetry and activity of the prism <a> and rhomb <a> slip systems (Figs. 4.2B, 4.S3).

The relative contributions of stretching strain and rotational flow in a shear zone can be quantified by the kinematic vorticity number, W_k, where perfect simple shear is $W_k = 1$ and pure shear is $W_k = 0$. To estimate W_k, we apply the oblique grain shape fabric method to recrystallized quartz grains to characterize the final increment of ductile strain (e.g., Wallis, 1995). This approach requires an estimate of the angle between the instantaneous stretching axis (ISA) and shear plane from the primary foliation, δ and β respectively (Fig. 4.S4). We used EBSD grain-boundary maps to fit grain shapes with ellipses, and the mean ellipse long axis is assumed to represent ISA. Shear plane orientations are determined using the best-fit to all quartz c- and a-axis orientations (Fig. 4.S4). The results indicate kinematic vorticity numbers of 0.15–0.85 with an interquartile range of 0.32–0.77, or ~45–75% pure shear (Fig. 4.2C). Theses vorticity estimates are indicative of general shear deformation.

Mean recrystallized grain size was determined from EBSD maps of each sample (Methods in Appendix 2). We observe a decrease in the root-mean-square mean recrystallized grain size from 115 μm at the base of the mylonite zone to 4 μm at the top (Fig. 4.2D), which corresponds to differential stress estimates between 23 MPa and 194 MPa (e.g., Cross et al., 2017).

Deformation temperatures were derived from Ti-in-quartz thermobarometry (S4). Temperature estimates decrease from 587 (+71/-77) ℃ in the structurally deepest sample to 373 (+31/-69) ℃ in the structurally highest sample (Fig. 4.3). Qualitative temperature estimates of 500 ± 50 ℃ based on quartz subgrain rotation dynamic recrystallization textures were assumed for the remaining samples (Fig. 4.S2).

DEVELOPMENT OF THE RUBY MOUNTAINS-EAST HUMBOLDT RANGE MCC

Available timing constraints demonstrate ca. 29–22 Ma mylonitization occurred prior to post-17 Ma regional extensional exhumation. Extensional basin development is a

ubiquitous trait of large-magnitude extension across the Basin and Range (e.g., Friedmann and Burbank, 1995), and the absence of thick, coarse-clastic pre-middle Miocene deposits in the REH region precludes significant extensional exhumation during the Eocene-Oligocene (Colgan et al., 2010; Zuza et al., 2021). Significant attenuation (>80%) of the Neoproterozoic-Ordovician section, minimal stratigraphic omission across the REH detachment, and a median kinematic vorticity number estimate of 0.53 are consistent with pure-shear dominated attenuation of the middle crust. Therefore, the REH mylonite zone was not related to extensional exhumation along a brittle detachment fault.

Deformation temperatures were integrated with differential stress to estimate strain rates with a wet quartzite flow law (Tokle et al., 2019). Our observations suggest strain rates of 10^{-13} to 10^{-12} s^{-1}, with the structurally highest two samples yielding strain rates of 10^{-11} s^{-1} consistent with previous estimates from the REH (Fig. 4.3; Hacker et al., 1990).

We argue field, geochronologic, and microstructural observations from the REH are compatible with the buoyant-doming model for MCC development. We posit the REH represents the western flank of an elongate north-south dome tilted ~40°E during Miocene to present normal faulting (Fig. 4.4; Colgan et al., 2010; Zuza et al., 2021). Oligocene domal upwelling dynamically supported surface elevations, thus explaining the lack of syn-kinematic Oligocene basin deposits (Lund Snee et al., 2016).

BUOYANT DOMING DRIVEN BY EOCENE-OLIGOCENE MAGMATISM

Crustal-scale buoyant doming requires mantle-derived magmatism, protracted heating, or crustal melting to reduce the density and viscosity of the lower crust and drive upwelling. Eocene intrusion of mantle-derived basaltic melts into the lower crust initiated heating, remobilization of Late Cretaceous granites, and hybridization with crustal melts to form the suite of Oligocene monzogranites (e.g., Howard et al., 2011). The migration of granitic melts to mid-crustal levels contributed to further heating and decreased density due to thermal expansion and increased lower-density melt volume (e.g., Rey et al., 2009), which activated diapiric ascent of the middle crust and development of the mylonitic shear zone (Fig. 4.4).

To test the viability of buoyant doming, we calculate the ascent velocity of a spherical diapir using a Stokes flow solution (Turcotte and Schubert, 2002; Methods in Appendix 5). Increased temperatures within the diapir will lead to lower intra-diapir density due to thermal expansion and increased melt fraction during partial melting. The formation and ascent of a buoyant gneiss dome can also be described analytically as a Rayleigh-Taylor instability (e.g., Ramberg, 1981), which yields comparable results to the Stokes flow solution (Appendix 5). Ascent velocity U is given by (Turcotte and Schubert, 2002):

$$U = \frac{a^2 g}{\mu_h}\gamma \quad (1)$$

where a is the sphere radius, g is the acceleration due to gravity, and μ_h is the viscosity of the host crust. The γ parameter quantifies density changes due to thermal expansion γ_e or partial melting γ_m, defined as:

$$\gamma_m = \rho_h - M(\rho_h - \rho_d) \quad (2)$$

$$\gamma_e = \rho_h \alpha (T_d - T_h) \quad (3)$$

where ρ_h is the density of the host crust, $\rho_d$is the density of the diapir, *M* is melt fraction, and α is the coefficient of thermal expansion. Using reasonable parameters and observations of mylonite zone width, deformation temperature and melt fraction estimates (Appendix 5), we calculate ascent velocities between 1–100 mm/yr. These velocities result in strain rates along the edge of a rising dome of ~10^{-14} to 10^{-12} s^{-1} at ΔT = 200°C and μ_h = 10^{18}–10^{20} Pa·s (Figs. 4.S9, 4.S10). These modeled strain rates agree with quartz microstructures and thermometry data from the REH (Fig. 4.3), and supports our interpretation that buoyant doming could have generated general shear in the REH mylonite zone.

THE ROLE OF BUOYANCY IN MCC DEVELOPMENT

The buoyant doming model highlights the capacity for magmas to sufficiently heat the crust, enhance density contrasts, and create positive buoyancy in the middle crust. Buoyancy may be secondary to isostasy during syn-extensional exhumation (Rey et al., 2009), but feedbacks between heating, partial melting and crustal flow demonstrate the

impact of buoyancy forces increases with melt fraction (Fig. 4.S10). The central MCCs show characteristics consistent with buoyant doming during Eocene-Oligocene magmatism despite lower melt fractions than the northern MCCs (Fig. 4.1A; Todd, 1980; Miller et al., 1983; Konstantinou et al., 2012). This may fundamentally differ from the southern MCCs where detachment slip is apparently coupled with mylonite generation (Fig. 4.1B), or these may represent hybrid cases (Fig. 4.1C). The domal geometry of central belt MCCs was subsequently overprinted by Basin and Range faulting, thus modifying their map geometries.

High-strain shear zones in MCCs are generally assumed to represent the down-dip continuation of a brittle detachment fault. Here we have shown the characteristic high-strain zone in MCCs can form in the absence of large-magnitude extension, with crustal advection driven solely from mantle-derived heat and magmatism. Such interpretations influence models of orogenic collapse, or post-orogenic extension, where mylonites in MCCs are commonly used as evidence for large-magnitude extension (Coney and Harms, 1984) when they may instead reflect crustal heat/mass redistribution. The development of pre-extensional shear zones likely creates a weak zone that localizes later extensional faulting leading to the apparent kinematic coupling between detachment faults and mylonitic shear zones in MCCs (Fig. 4.4B).

ACKNOWLEDGEMENTS

Research was supported by the Geological Society of Nevada, Geological Society of America, and the USGS National Cooperative Geologic Mapping Program via State Map awards (G19AC00383, G20AS00006). We thank B. Monteleone for assistance with SIMS data collection.

APPENDIX 1: EBSD data collection details and grain size analysis

Electron backscatter diffraction (EBSD) analysis was conducted with 15 samples at the University of Nevada, Reno using the JEOL JSM-7100FT field-emission scanning electron microscope with an Oxford NordlysMax2 EBSD detector (Table 4.S1, Fig. 4.S2). Thin sections for each sample were polished using a vibratory polisher with 0.05 μm colloidal silica for 6–8 hours. EBSD data was collected at a working distance of 25 mm and 70° tilt using a beam energy of 25–30 kV and probe current of 18. EBSD maps were collected at a step size of 0.2–6 μm depending on the estimated size of recrystallized grains. For select samples, maps were collected at a larger and smaller step size to capture a large area of the fabric and to resolve small grains, respectively. EBSD data was processed using Oxford Instruments Channel 5 software to correct for wild spikes and a 7 nearest neighbor zero solutions correction. For select samples wild spikes and zero solutions corrections were conducted using the MTEX toolbox (5.7.0; https://mtex-toolbox.github.io/) (Bachmann et al., 2010) for MATLAB. Quartz crystallographic axes are plotted as one-point-per-grain lower-hemisphere pole figures (Fig. 4.S3). In Fig. 4.S6, all quartz crystallographic axes are plotted in lower-hemisphere pole figures for kinematic vorticity analysis. Fabric parameters M and PGR provide a measure of fabric strength (M) and the shape of the CPO (P – point; G – girdle; R – random) (Table 4.S2). The M-index is calculated in MTEX using the function calcMIndex.m following the code of Mainprice et al. (2015) and the method of Skemer et al. (2005). Higher M-index values corresponding to a stronger CPO than lower M-index values. PGR values were calculated using the code of Mainprice et al. (2015) following the method Vollmer (1990). Values close to 1, e.g., P = 0.9, indicates the CPO is dominated by a point geometry. Due to a low proportion of quartz in sample AZ 8-19-19 (2), it has been omitted from our grain size and kinematic vorticity analysis.

Recrystallized grain size analysis was conducted following the protocol of Cross et al. (2017) using the *RexRelict.m* script (https://doi.org/10.1002/2017GL073836) (Table 4.S2, Fig. 4.S3). We do not apply the GOS-threshold to distinguish recrystallized versus relict grains, as we assume the quartz in our samples is all recrystallized. Our analysis

follows the same data input and initial grain calculation scheme, as well as grain size estimation scheme. Grain size is determined by the area-equivalent diameter. No stereological correction is used. The mean grain size is given by the root mean square of the recrystallized grain population. Differential stress estimates from mean recrystallized grain size estimates were calculated using the paleopiezometric calibration of Cross et al. (2017) (Table 4.S2).

The quartz c-axis fabric opening angle thermometer (e.g., Law, 2014; Faleiros et al., 2016) was applied to sample AZ 8-4-18 (3), which displayed a nice c-axis girdle with an opening angle of 65° (Fig. 4.S3). Applying the opening angle thermometer calibration of Faleiros et al. (2016), we estimate a deformation temperature of 496 °C.

To evaluate strain rate, we apply the wet quartzite flow law of Tokle et al. (2019). The form of the flow law is:

$$\dot{\varepsilon} = A\sigma^n f_{H2O}^r e^{-\frac{Q}{RT}} \quad (4.A1.1)$$

where A = 1.75 x10^{-12} (MPa^{-n}s^{-1}), n = 4, r = 1, Q = 1.25 x10^5 Jmol^{-1}, R = gas constant, T = temperature, and f_{H2O} = 50 MPa. Water fugacity was calculated using T. Withers' fugacity calculator (https://publish.uwo.ca/~awither5/fugacity/index.htm).

APPENDIX 2: Kinematic vorticity calculations

To estimate kinematic vorticity of our quartz mylonite samples, we apply the oblique grain shape fabric method (Fig. 4.S4; e.g., Wallis, 1995; see Xypolias (2010) for a review of the method). This approach requires an estimate of the angle between the instantaneous stretching axis (ISA) and shear plane from the primary foliation, δ and β respectively (Fig. 4.S4). EBSD grain-boundary maps were fit by ellipses, and the mean ellipse long axis was assumed to represent ISA (Fig. 4.S6). Shear plane orientations were determined directly from c-axis pole figure plots by calculating the angle between a best fit line through the quartz CPO and the vertical axis of the pole figure (Fig. 4.S6).

Vorticity analysis was conducting using the MTEX toolbox (5.7.0; https://mtex-toolbox.github.io/) (Bachmann et al., 2010). We fit ellipses to all grains to estimate ISA. All grain boundaries were smoothed using the *smooth.m* function. The *fitEllipse.m* function was used for ellipse fitting. Grains with an aspect ratio less than 1.4 were removed from the subset. The mean ISA was determined using a kernel density estimate of ellipse axes with the maxima defining the mean vector. The best fit vector of quartz c-axes was computed using the all c-axis orientation. The best fit vector was estimated as the mean plane orthogonal to c-axis vectors. The angle between the best fit vector and the horizontal is the parameter β.

Ellipse and c-axis fits were inspected visually to validate the results. Where the c-axis best fit was visually misaligned with the bulk shape of the CPO or inclined towards the ISA, a best fit line was determined manually, or the a-axis fit was used. Quartz a-axes were fit manually to provide a second measure of β (e.g., Little et al., 2016). Quartz a-axes commonly form a conjugate pattern across the X plane (Fig. 4.S5). The strength of either conjugate pair may vary depending on the components of coaxial and non-coaxial strain (e.g., Law, 1990). In the samples we have analyzed, we note fitting the dominant a-axis maxima generates estimates of β much greater than the value acquired from fitting the c-axis maxima. If instead the center of the a-axis conjugate pair is fit, the β value will match the c-axis maxima derived value well. The quality of a-axis fits was checked against the m-pole maxima, which should be orthogonal to the c-axis maxima. The MTEX c-axis best

fit method does a poor job fitting samples with symmetric quartz c-axis girdles. The c-axis best fit was determined manually as a line through the center of the girdle. Both manual and MTEX β values are listed in Table 4.S3. The kinematic vorticity number is given by:

$$W_k = \sin\left(2 * (\beta + \delta)\right) \tag{4.A2.1}$$

The best W_k values are calculated as the mean of W_k calculated from MTEX and manually determined β values. If either the c- or a-axis best fit lines were uncertain, the fit with higher confidence was used. An uncertainty of ±5° was assigned to each W_k estimate. Figure 4.S6 shows the results of the vorticity analysis for each sample.

APPENDIX 3: Secondary ion microprobe analytical details

Seven samples representative of different structural levels of the mylonite zone were selected for Ti-in-quartz thermometry (Table 4.S4). Zones displaying representative microstructures within the thin section of each sample were cut into ~5x5 mm squares using a slow speed saw. EBSD and cathodoluminescence maps were collected for each sample to guide spot placement on recrystallized grains.

Ti concentrations were measured on a Cameca IMS 1280 ion probe at the Northeast National Ion Microprobe Facility (Woods Hole Oceanographic Institution). A 250 pA 16O- primary beam was accelerated at 12kV and focused to a diameter of 5 μm. Secondary ions of 30Si+, 40Ca+, 48Ti+, and 49Ti+ were extracted at a 10kV voltage potential. Entrance and exit slit widths were set to achieve a mass resolving power >6500, sufficient to separate 48Ti+ from 48Ca+ and 49Ti+ from 48Ti1H+ and 48Ca1H+. After 300 seconds of pre-sputtering, each mass was measured on an ETP electron multiplier (EM) for count times ranging from 3-10 seconds within each measurement cycle, over a total of 5 cycles, and ratios were derived using 30Si as the reference mass. Electron multiplier background was determined by measurement at 29.7 within each cycle and was ~0.01 CPS. An maximum estimate of 48Ca+ contribution to the 48Ti+ measurement (assuming complete peak overlap) was calculated by multiplying the measured 40Ca/30Si by the naturally occurring 48Ca/40Ca ratio (1.93E-3). However, good agreement between concentrations derived by measuring uncorrected 48Ti/30Si and 49Ti/30Si demonstrate that a correction for potential 48Ca+ interference was not required. Two linear calibrations for Ti concentration, plotting Ti (μg/g) vs. 48Ti/30Si and 49Ti/30Si were obtained by analyzing four synthetic quartz crystals with Ti concentrations ranging from 21 to 813 μg/g (Thomas et al. 2010, Ashley et al., 2013, Nachlas et al., 2014). Data processing for each measurement utilized in-house matlab codes, and included EM deadtime correction, time interpolation within each cycle, and two sigma filtering of cycle ratios. ^{48}Ti and ^{49}Ti normalized to ^{30}Si were measured over 10 cycles for each analysis, of which the mean and standard deviation were calculated. These data were corrected for drift in the standards measurements. The mean and standard deviation of the corrected values were used to calculate the ^{30}Si normalized concentrations of ^{48}Ti and ^{49}Ti. The concentrations of ^{48}Ti are used for thermometry.

Ti concentrations were measured from at least 12 spots in each sample (Table 4.S4, Fig. 4.S7). The mean and standard deviation was calculated for each sample. In some cases, outlier values were omitted from the mean and standard deviation calculations. Our mean concentrations were then used to calculate temperature estimates using the calibration of Thomas et al. (2010). We calculated temperature estimates of the mean Ti concentration, as well as the upper and lower standard deviation values ([Ti] + 2 SD, [Ti] – 2 SD). The Thomas et al. (2010) calibration depends on a_{TiO2} and pressure. The a_{TiO2} is not independently constrained in this study, however a value of 0.25 is assumed. We consider this a reasonable assumed value for a_{TiO2} based on the absence of Ti-bearing phases (i.e., rutile, titanite, ilmenite), and the estimation of a_{TiO2} in chemically comparable quartz mylonites in previous studies (e.g., Lusk and Platt, 2020). We assume pressures between 3 and 4 kbar for our calculations. These values are based on thermobarometry of rocks within the Ruby-East Humboldt mylonite zone (e.g., Hurlow et al., 1991).

Additionally, there is uncertainty associated with the calibration of the Ti-in-quartz thermobarometer of Thomas et al. (2010). The uncertainties in the calibration constants are incorporated into our results through calculation of total quantified uncertainty, which combines uncertainty in individual measurements and the calibration. We do so by calculating temperature as a function of [Ti] + 2SD using calibration constants + error to get T_{hi}. The opposite is done to calculate T_{lo} ([Ti] - 2SD using calibration constants – error). The final total quantified uncertainty is calculated as +Total Error = T_{hi} – T and -Total Error = T – T_{lo}.

APPENDIX 4: Analytical model of diapir ascent velocity details

Stokes flow solution

The steady-state velocity of a spherical diapir can be modeled using the Stokes flow solution. In this formulation, velocity is given by:

$$U = \frac{a^2 g(\rho_h - \rho_d)}{3\mu_h} \quad (4.A4.1)$$

where U is velocity, a is diapir radius, g is acceleration due to gravity, ρ_h is host density, ρ_d is diapir density, and μ_h is host viscosity (Turcotte and Schubert, 2002). Diapir velocity scales with density difference. Conceptually, the density difference we model is due to magmatism and partial melting, and the accompanying conductive heat loss to the host would lower the host viscosity allowing diapir rise. Diapir density is calculated as a function of melt fraction expressed as:

$$\rho_d = \rho_h - M * (\rho_h - \rho_{d^*}) \quad (4.A4.2)$$

where M is melt fraction, and ρ_{d^*} is the density of the melt when solid (Gerya, 2010). This formulation is the density-driven case.

Diapir ascent velocity can also be formulated as a function of thermal expansion and temperature (i.e., temperature-driven case) given by:

$$U = \frac{a^2 g \rho_h \alpha (T_d - T_h)}{\mu_h} \quad (4.A4.3)$$

and

$$(\rho_h - \rho_d) = \rho_h \alpha (T_d - T_h) \quad (4.A4.4)$$

where α is the coefficient of thermal expansion, T_d is the diapir temperature, and T_h is the host temperature. The values of T_h and T_d are estimated based on the mylonite deformation temperatures (~500–600 °C) determined by Ti-in-quartz thermometry (T_h) and a near-solidus temperature range for Eocene monzogranites of the Harrison Pass pluton in the southern Ruby Mountains (~700–800 °C; Barnes et al., 2001; T_d). The full list of parameters and sources are listed in Table 4.S5.

For the temperature-driven case, a temperature difference of 200–300°C results in ascent velocities from 83–166 km/m.y. at a host viscosity of 10^{18} Pa·s, 8–16 km/m.y. at 10^{19} Pa·s, and 0.8–1.6 km/m.y. at 10^{20} Pa·s (Fig. 4.S9A). For the density-driven case, a melt fraction of 0.2–0.4 results in ascent velocities from 411–823 km/m.y. at a host viscosity of 10^{18} Pa·s, 41–82 km/m.y. at 10^{19} Pa·s, and 4–8 km/m.y. at 10^{20} Pa·s (Fig. 4.S10A).

To relate the ascent velocities to strain rates derived from microstructural observations, we use the geometry of simple- and pure-shear zones located along the margin of the ascending diapir to calculate shear zone parallel strain rates (Fig. 4.S8). For each shear zone model, the zone is dipping 45° tangential to the diapir. In the simple shear zone, we apply a width (w) and calculate the shear zone parallel component of the diapir velocity (U_{sx}). The quotient of U_{sx} and w is the shear zone parallel strain rate ($\dot{\gamma_{sx}}$) (Fig. 4.S8A). In the pure shear zone, strain rate is calculated using the pure shear deformation matrix of Tikoff and Fossen (1993), where the diagonals S_1 and S_2 describe the x and y stretch given by:

$$S_1 = \varepsilon_{xx} + 1 \tag{4.A4.5}$$

$$S_2 = \varepsilon_{yy} + 1 \tag{4.A4.6}$$

where ε_{xx} and ε_{yy} are the x and y components of strain. Stretch is related to related to strain rate through the equation:

$$S_1 = e^{\dot{\varepsilon_x} t} \tag{4.A4.7}$$

$$S_2 = e^{\dot{\varepsilon_y} t} \tag{4.A4.8}$$

where t is the time duration of deformation, and $\dot{\varepsilon_x}$ and $\dot{\varepsilon_y}$ are the x and y components of strain rate (Fig. 4.S8B). The duration of deformation is calculated as the quotient of the vertical displacement and velocity of the diapir. The vertical displacement of the diapir is estimated as the difference between the original and final thickness of a 5 km thick stratigraphic section.

For the temperature-driven case where (T_d - T_h) = 200–300 °C, pure shear strain rates are 2–3 x10^{-12} s^{-1} for a host viscosity of 10^{18} Pa·s, 2–3 x10^{-13} s^{-1} at 10^{19} Pa·s, and 2–3 x10^{-14} s^{-1} at 10^{20} Pa·s (Fig. 4.S9C). Simple shear strain rates derived from the temperature-driven case are 3–5.5 x10^{-12} s^{-1} for a host viscosity of 10^{18} Pa·s, 3–5.5 x10^{-13} s^{-1} at 10^{19} Pa·s, and 3–5.5 x10^{-14} s^{-1} at 10^{20} Pa·s (Fig. 4.S9B).

Pure shear strain rates derived from the density-driven case are 5 x10^{-12} to 1 x10^{-11} s^{-1} for a host viscosity of 10^{18} Pa·s, 5 x10^{-13} to 1 x10^{-12} s^{-1} at 10^{19} Pa·s, and 5 x10^{-14} to 1 x10^{-13} s^{-1} at 10^{20} Pa·s (Fig. 4.S10C). Simple shear strain rates derived from the density-driven case at melt fractions of 0.2–0.4 are 9 x10^{-11} to 1.8 x10^{-10} s^{-1} for a host viscosity of 10^{18} Pa·s, 9 x10^{-13} to 1.8 x10^{-12} s^{-1} at 10^{19} Pa·s, and 9 x10^{-14} to 1.8 x10^{-13} s^{-1} at 10^{20} Pa·s (Fig. 4.S10B).

These results highlight that for melt fractions consistent with the observed melt volume in the Ruby Mountains-East Humboldt Range MCC (> 50%; Howard et al., 2011) or temperature gradients consistent with estimated deformation and magmatic intrusion temperatures, shear zone parallel strain rates are in the range of 10^{-11} to 10^{-14} s^{-1}.

Rayleigh-Taylor instability

A rising diapir can be described as a Rayleigh-Taylor instability originating from decreased lower crustal density during partial melting. As the density of the lower layer in a stratified system decreases (Fig. 4.S11A), the Rayleigh number grows until the critical Rayleigh number is reached at which point fluid motion initiates if a disturbance is present (Turcotte and Schubert, 2002). The Rayleigh number is given by:

$$Ra = \frac{\Delta\rho g h^3}{\mu\kappa} \tag{4.A4.9}$$

where $\Delta\rho$ is the density difference between layers, h is the layer thickness, μ is viscosity and κ is the thermal diffusivity. The ascent of a basement-derived gneiss dome was modeled as a Rayleigh-Taylor instability by Ramberg (1981). This work placed early gneiss domes studies (e.g., Eskola, 1949) within a simple theoretical framework that is still

applicable. In the formulation herein, we simplify our model geometry to a two-layer system representing an ~30 km-thick section of the lower crust (Fig. 4.S11A). The two layers have same initial density and viscosity. The lower layer (layer 2) has a melt fraction between 0–0.75, which decreases the layer 2 density by 5%. The vertical velocity of the interface between the layers is the vertical velocity of the growing dome given by the following equation.

$$\frac{\partial w}{\partial t} = \frac{(\rho_1-\rho_2)gh}{4\mu} * \frac{\left(\left(\frac{\lambda}{2\pi h}\right)^2 \tanh\left(\frac{2\pi h}{\lambda}\right) - \frac{1}{\sinh\left(\frac{2\pi h}{\lambda}\right)\cosh\left(\frac{2\pi h}{\lambda}\right)}\right)}{\left(\frac{\lambda}{2\pi h} + \frac{1}{\sinh\left(\frac{2\pi h}{\lambda}\right)\cosh\left(\frac{2\pi h}{\lambda}\right)}\right)} w \tag{4.A4.10}$$

where ρ_2 is given by:

$$\rho_2 = \rho_1 - M * (\rho_1 - \rho_{2^*}) \tag{4.A4.11}$$

We can also calculate the time for the instability to grow given by:

$$t = \ln\left(\frac{w}{w_o}\right) * \tau_a \tag{4.A4.12}$$

where the growth time of a disturbance (τ_a) is:

$$\tau_a = \frac{4\mu}{(\rho_1-\rho_2)gh} * \frac{\left(\frac{\lambda}{2\pi h} + \frac{1}{\sinh\left(\frac{2\pi h}{\lambda}\right)\cosh\left(\frac{2\pi h}{\lambda}\right)}\right)}{\left(\left(\frac{\lambda}{2\pi h}\right)^2 \tanh\left(\frac{2\pi h}{\lambda}\right) - \frac{1}{\sinh\left(\frac{2\pi h}{\lambda}\right)\cosh\left(\frac{2\pi h}{\lambda}\right)}\right)} \tag{4.A4.13}$$

The parameters for the above equations are listed in Table 4.S6.

For melt fractions between 0.2–0.4, a Rayleigh-Taylor diapir rises at 59–118 km/m.y. at a layer 1 viscosity of 10^{18} Pa·s, 5.9–11.8 km/m.y. at 10^{19} Pa·s, and 0.59–1.18 km/m.y. at 10^{20} Pa·s (Fig. 4.S12A). The growth time for the diapir is 0.3–0.15 m.y. at a layer 1 viscosity of 10^{18} Pa·s, 3.1–1.5 m.y. at 10^{19} Pa·s, and 31–15 m.y. at 10^{20} Pa·s (Fig. 4.S12B).

Using the same simple- and pure-shear zone geometries as the Stokes flow spherical diapir calculations, we derive shear zone parallel strains rates for zones dipping 45° tangential to the diapir (Fig. 4.S11). For the pure shear zone, we compute shear zone parallel strain rates of 0.7–1.5 x10^{-12} s^{-1} at a layer 1 viscosity of 10^{18} Pa·s, 0.7–1.5 x10^{-13} s^{-}

^{1} at 10^{19} Pa·s, and 0.7–1.5 x10^{-14} s^{-1} at 10^{20} Pa·s (Fig. 4.S12D).For the simple shear case at melt fractions of 0.2–0.4, we compute strain rates of 1.3–2.6 x10^{-12} s^{-1} at a layer 1 viscosity of 10^{18} Pa·s, 1.3–2.6 x10^{-13} s^{-1} at 10^{19} Pa·s, and 1.3–2.6 x10^{-14} s^{-1} at 10^{20} Pa·s (Fig. 4.S12C).

These results highlight that for a Rayleigh-Taylor diapir that develops due to an increased melt fraction consistent with the observed melt volume in the Ruby Mountains-East Humboldt Range (REH) MCC (> 50%; Howard et al., 2011), the resultant ascent velocity drives shear zone strain rates within the range of 10^{-12} to 10^{-14} s^{-1}. This Rayleigh-Taylor formulation does not account for a viscosity difference between layers 1 and 2, which would realistically result from an increase in molten rock in layer 2 and heating of layer 1. This simplified case illustrates to first-order the deformation rates, length scales and timescales observed in the REH MCC can be described as the result of a Rayleigh-Taylor instability.

REFERENCES

Armstrong, R.L., 1968, Mantled Gneiss Domes in the Albion Range, Southern Idaho: Geological Society of America Bulletin, v. 79, p. 1295, doi:10.1130/0016-7606(1968)79[1295:MGDITA]2.0.CO;2.

Armstrong, R.L., and Hansen, E., 1966, Cordilleran infrastructure in the eastern Great Basin: American Journal of Science, v. 264, p. 112–127, doi:10.2475/ajs.264.2.112.

Ashley, K.T., Webb, L.E., Spear, F.S. and Thomas, J.B., 2013, P-T-D histories from quartz: A case study of the application of the TitaniQ thermobarometer to progressive fabric development in metapelites: Geochemistry, Geophysics, Geosystems, v. 14, p.3821-3843.

Bachmann, F., Hielscher, R. and Schaeben, H., 2010, Texture analysis with MTEX–free and open source software toolbox: Solid State Phenomena, v. 160, p. 63-68.

Barnes, C.G., Burton, B.R., Burling, T.C., Wright, J.E., and Karlsson, H.R., 2001, Petrology and geochemistry of the Late Eocene Harrison Pass pluton, Ruby Mountains core complex, northeastern Nevada: Journal of Petrology, v. 42, p. 901–929, doi: 10.1093/petrology/42.5.901.

Colgan, J.P., Howard, K.A., Fleck, R.J., and Wooden, J.L., 2010, Rapid middle Miocene extension and unroofing of the southern Ruby Mountains, Nevada: SOUTH RUBY MOUNTAINS: Tectonics, v. 29, p. n/a-n/a, doi:10.1029/2009TC002655.

Coney, P.J., and Harms, T.A., 1984, Cordilleran metamorphic core complexes: Cenozoic extensional relics of Mesozoic compression: Geology, v. 12, p. 550–554, doi:10.1130/0091-7613(1984)12<550:CMCCCE>2.0.CO;2.

Crittenden, M.D., Coney, P.J., and Davis, G.H. (Eds.), 1980, Cordilleran metamorphic core complexes: Boulder, Colo, Geological Society of America, Memoir - The Geological Society of America 153, 490 p.

Cross, A.J., Prior, D.J., Stipp, M., and Kidder, S., 2017, The recrystallized grain size piezometer for quartz: An EBSD-based calibration: EBSD-Based Quartz Grain Size Piezometer: Geophysical Research Letters, v. 44, p. 6667–6674, doi:10.1002/2017GL073836.

Davis, G.H., 1983, Shear-zone model for the origin of metamorphic core complexes: Geology, v. 11, p. 342, doi:10.1130/0091-7613(1983)11<342:SMFTOO>2.0.CO;2.

Dokka, R.K., Mahaffie, M.J., and Snoke, A.W., 1986, Thermochronologic evidence of major tectonic denudation associated with detachment faulting, Northern Ruby Mountains - East Humboldt Range, Nevada: Tectonics, v. 5, p. 995–1006, doi:10.1029/TC005i007p00995.

Eskola, P.E., 1948, The problem of mantled gneiss domes: Quarterly Journal of the Geological Society, v. 104, p. 461–476, doi:10.1144/GSL.JGS.1948.104.01-04.21.

Faleiros, F.M., Moraes, R.D., Pavan, M. and Campanha, G.D.C., 2016, A new empirical calibration of the quartz c-axis fabric opening-angle deformation thermometer: Tectonophysics, v. 671, p.173-182.

Friedmann, S.J., and Burbank, D.W., 1995, Rift basins and supradetachment basins: intracontinental extensional end-members: Basin Research, v. 7, p. 109–127, doi:10.1111/j.1365-2117.1995.tb00099.x.

Hacker, B.R., Yin, A., Christie, J.M., and Snoke, A.W., 1990, Differential stress, strain rate, and temperatures of mylonitization in the Ruby Mountains, Nevada: Implications for the rate and duration of uplift: Journal of Geophysical Research, v. 95, p. 8569, doi:10.1029/JB095iB06p08569.

Haines, S.H., and van der Pluijm, B.A., 2010, Dating the detachment fault system of the Ruby Mountains, Nevada: Significance for the kinematics of low-angle normal faults: FAULT GOUGE AGES FOR RUBY MOUNTAINS: Tectonics, v. 29, p. n/a-n/a, doi:10.1029/2009TC002552.

Hallett, B.W., and Spear, F.S., 2015, Monazite, zircon, and garnet growth in migmatitic pelites as a record of metamorphism and partial melting in the East Humboldt Range, Nevada: American Mineralogist, v. 100, p. 951–972, doi:10.2138/am-2015-4839.

Howard, K.A., 1980, Metamorphic infrastructure in the northern Ruby Mountains, Nevada:, doi:10.1130/MEM153-p335.

Howard, K.A., Wooden, J.L., Barnes, C.G., Premo, W.R., and Snoke, A.W., 2011, Episodic growth of a Late Cretaceous and Paleogene intrusive complex of pegmatitic leucogranite, Ruby Mountains core complex, Nevada, USA: Geosphere, v. 7, p. 29.

Hurlow, H. A., Snoke, A. W., & Hodges, K. V., 1991, Temperature and pressure of mylonitization in a Tertiary extensional shear zone, Ruby Mountains-East Humboldt Range, Nevada: Tectonic implications: Geology, v. 19, p. 82-86.

Konstantinou, A., Strickland, A., Miller, E.L., and Wooden, J.P., 2012, Multistage Cenozoic extension of the Albion–Raft River–Grouse Creek metamorphic core complex: Geochronologic and stratigraphic constraints: Geosphere, v. 8, p. 1429–1466, doi:10.1130/GES00778.1.

Law, R.D., 1990, Crystallographic fabrics: a selective review of their applications to research in structural geology; Geological Society, London, Special Publications, v. 54, p.335-352.

Law, R.D., 2014, Deformation thermometry based on quartz c-axis fabrics and recrystallization microstructures: A review: Journal of structural Geology, v. 66, p.129-161.

Law, R.D., Searle, M.P. and Simpson, R.L., 2004, Strain, deformation temperatures and vorticity of flow at the top of the Greater Himalayan Slab, Everest Massif, Tibet: Journal of the Geological Society, v. 161, p.305-320.

Lee, J., Blackburn, T., and Johnston, S., 2017, Timing of mid-crustal ductile extension in the northern Snake Range metamorphic core complex, Nevada: Evidence from U/Pb zircon ages: Geosphere, v. 13, p. 439–459, doi:10.1130/GES01429.1.

Lee, J., Miller, E.L., and Sutter, J.F., 1987, Ductile strain and metamorphism in an extensional tectonic setting: a case study from the northern Snake Range, Nevada, USA: Geological Society, London, Special Publications, v. 28, p. 267–298, doi:10.1144/GSL.SP.1987.028.01.18.

Little, T.A., Prior, D.J. and Toy, V.G., 2016, Are quartz LPOs predictably oriented with respect to the shear zone boundary?: A test from the Alpine Fault mylonites, New Zealand. Geochemistry, Geophysics, Geosystems, v. 17, p.981-999.

Lund Snee, J.-E., Miller, E.L., Grove, M., Hourigan, J.K., and Konstantinou, A., 2016, Cenozoic paleogeographic evolution of the Elko Basin and surrounding region, northeast Nevada: Geosphere, v. 12, p. 464–500, doi:10.1130/GES01198.1.

MacCready, T., Snoke, A.W., Wright, J.E., and Howard, K.A., 1997, Mid-crustal flow during Tertiary extension in the Ruby Mountains core complex, Nevada: Geological Society of America Bulletin, v. 109, p. 1576–1594, doi:10.1130/0016-7606(1997)109<1576:MCFDTE>2.3.CO;2.

Mainprice, D., Bachmann, F., Hielscher, R. and Schaeben, H., 2015, Descriptive tools for the analysis of texture projects with large datasets using MTEX: strength, symmetry and components: Geological Society, London, Special Publications, v. 409, p.251-271.

McGrew, A.J., Peters, M.T., and Wright, J.E., 2000, Thermobarometric constraints on the tectonothermal evolution of the East Humboldt Range metamorphic core complex, Nevada: Geological Society of America Bulletin, v. 112, p. 45–60, doi:10.1130/0016-7606(2000)112<45:TCOTTE>2.0.CO;2.

McGrew, A.J., and Snee, L.W., 1994, 40Ar/39Ar thermochronologic constraints on the tectonothermal evolution of the Northern East Humboldt range metamorphic core complex, Nevada: Tectonophysics, v. 238, p. 425–450, doi:10.1016/0040-1951(94)90067-1.

Miller, E.L., Gans, P.B., and Garing, J., 1983, The Snake Range Décollement: An exhumed Mid-Tertiary ductile-brittle transition: Tectonics, v. 2, p. 239–263, doi:10.1029/TC002i003p00239.

Nachlas, W.O., Whitney, D.L., Teyssier, C., Bagley, B. and Mulch, A., 2014, Titanium concentration in quartz as a record of multiple deformation mechanisms in an extensional shear zone: Geochemistry, Geophysics, Geosystems, v. 15, p.1374-1397.

Ramberg, H., 1981, The role of gravity in orogenic belts: Geological Society, London, Special Publications, v. 9, p. 125–140, doi:10.1144/GSL.SP.1981.009.01.11.

Rey, P.F., Teyssier, C., and Whitney, D.L., 2009, Extension rates, crustal melting, and core complex dynamics: Geology, v. 37, p. 391–394, doi:10.1130/G25460A.1.

Skemer, P., Katayama, I., Jiang, Z. and Karato, S.I., 2005, The misorientation index: Development of a new method for calculating the strength of lattice-preferred orientation: Tectonophysics, v. 411, p.157-167.

Snoke, A.W., 1980, Transition from infrastructure to suprastructure in the northern Ruby Mountains, Nevada:, doi:10.1130/MEM153-p287.

Teyssier, C., and Whitney, D.L., 2002, Gneiss domes and orogeny: Geology, v. 30, p. 1139, doi:10.1130/0091-7613(2002)030<1139:GDAO>2.0.CO;2.

Thomas, J.B., Watson, E.B., Spear, F.S., Shemella, P.T., Nayak, S.K. and Lanzirotti, A., 2010, TitaniQ under pressure: the effect of pressure and temperature on the solubility of Ti in quartz: Contributions to Mineralogy and Petrology, v. 160, p.743-759.

Tikoff, B., & Fossen, H.. 1993, Simultaneous pure and simple shear: the unifying deformation matrix: Tectonophysics, v. 217, p. 267-283.

Todd, V.R., 1980, Structure and petrology of a Tertiary gneiss complex in northwestern Utah:, doi:10.1130/MEM153-p349.

Tokle, L., Hirth, G., and Behr, W.M., 2019, Flow laws and fabric transitions in wet quartzite: Earth and Planetary Science Letters, v. 505, p. 152–161, doi:10.1016/j.epsl.2018.10.017.

Turcotte, D.L., and Schubert, G., 2002, Geodynamics: Cambridge University Press, 484 p.

Vollmer, F.W., 1990, An application of eigenvalue methods to structural domain analysis: Geological Society of America Bulletin, v. 102, p.786-791.

Wallis, S., 1995, Vorticity analysis and recognition of ductile extension in the Sanbagawa belt, SW Japan: Journal of Structural Geology, v. 17, p.1077-1093.

Wernicke, B., and Axen, G.J., 1988, On the role of isostasy in the evolution of normal fault systems: Geology, v. 16, p. 848, doi:10.1130/0091-7613(1988)016<0848:OTROII>2.3.CO;2.

Whitney, D.L., Teyssier, C., Rey, P., and Buck, W.R., 2013, Continental and oceanic core complexes: GSA Bulletin, v. 125, p. 273–298, doi:10.1130/B30754.1.

Wright, J.E., and Snoke, A.W., 1993, Tertiary magmatism and mylonitization in the Ruby-East Humboldt metamorphic core complex, northeastern Nevada: U-Pb geochronology and Sr, Nd, and Pb isotope geochemistry: Geological Society of America Bulletin, v. 105, p. 935–952, doi:10.1130/0016-7606(1993)105<0935:TMAMIT>2.3.CO;2.

Xypolias, P., 2010, Vorticity analysis in shear zones: A review of methods and applications: Journal of Structural Geology, v. 32, p. 2072–2092.

Zuza, A.V., Henry, C.D., Dee, S., Thorman, C.H., and Heizler, M.T., 2021, Jurassic–Cenozoic tectonics of the Pequop Mountains, NE Nevada, in the North American Cordillera hinterland: Geosphere, v. 17, p. 2078–2122, doi:10.1130/GES02307.1.

TABLE 4.S1. Sample locations

		Location		
Sample	Structural Position	Latitude	Longitude	Unit
AZ 10-8-19 (1a)	1	40.83177	-115.14803	Mdp
AZ 7-1-20 (1)	2	40.93692	-115.23821	Oe
200718-6	3	40.86394	-115.24889	Ocm
AZ8-19-19-(2)	4	40.95774	-115.19940	Tmg
AZ8-19-19-(4)	5	40.95701	-115.17796	CZpm
AZ8-19-19-(5)	6	40.95703	-115.17836	CZpm
AZ 6-30-20 (2)	7	40.94923	-115.21765	CZpm
AZ 8-4-18 (3)	8	40.84163	-115.13982	CZpm
AZ 8-4-18 (1)	9	40.84158	-115.13997	CZpm
020619-2	10	40.86344	-115.24653	CZpm
200718-4	11	40.86350	-115.24592	CZpm
200718-3a	12	40.86369	-115.24514	CZpm
020619_5	13	40.86400	-115.24389	CZpm
020619-4	14	40.86456	-115.24300	CZpm
020619-3	15	40.86433	-115.24258	CZpm
AZ 7-2-20 (4)	16	40.94657	-115.15773	Zmu

Table 4.S2: Microstructural data

		EBSD	Fabric parameters				Paleopiezometry			
Sample	Structural Position	Step size (µm)	M	P	G	R	Mean recrystallized grain size (µm)	1SD (µm)	Differential stress (MPa)	uncertainty (+ / -)
AZ 10-8-19 (1a)	1	0.5	0.03	0.12	0.25	0.63	-	-	-	-
"		0.2	0.03	0.13	0.16	0.71	3.8	1.8	193.5	98.7/42.3
AZ 7-1-20 (1)	2	1	0.90	0.26	0.29	0.44	13.1	8.7	89.2	88.1/24.5
200718-6	3	3	0.05	0.16	0.28	0.56	14.1	6.0	85.4	35.8/17.1
AZ8-19-19-(4)	5	5	0.40	0.68	0.25	0.07	44.6	31.1	41.4	46.6/11.7
AZ8-19-19-(5)	6	5	0.50	0.80	0.16	0.04	55.7	43.1	36.0	55.7/10.9
AZ 6-30-20 (2)	7	3	0.34	0.61	0.38	0.02	44.8	32.1	41.2	49.7/11.9
AZ 8-4-18 (3)	8	5	0.36	0.66	0.26	0.08	-	-	-	-
"		2	0.42	0.72	0.24	0.03	44.0	36.7	41.7	87.4/13.2
AZ 8-4-18 (1)	9	5	0.38	0.61	0.30	0.09	-	-	-	-
"		2	0.32	0.53	0.37	0.09	32.7	24.5	50.3	69.7/14.9
020619-2	10	3	0.38	0.68	0.17	0.15	35.8	17.8	47.5	25.7/10.7
200718-4	11	5	0.30	0.56	0.32	0.12	34.9	20.3	48.3	35.3/12.1
200718-3a	12	2	0.35	0.63	0.31	0.62	55.3	29.3	36.1	21.9/8.5
020619_5	13	5	0.28	0.51	0.39	0.09	38.5	25.2	45.4	43.4/12.3
020619-4	14	2	0.20	0.42	0.37	0.21	37.3	25.2	46.3	48.0/12.9
020619-3	15	2	0.25	0.43	0.49	0.09	45.4	33.4	40.9	53.2/12.0
AZ 7-2-20 (4)	16	6	0.57	0.80	0.14	0.07	115.1	96.5	22.8	49.0/7.3

Table 4.S3: Kinematic vorticity data

			Kinematic vorticity					
Sample	Structural Position	δ MTEX	β *MTEX*	β *manual*[b]	Wk *MTEX*	Wk *manual*	Wk best	uncertainty[d]
AZ 10-8-19 (1a)	1	-	-	-	-	-	-	-
AZ 7-1-20 (1)	2	0.0	5.5[a]	3.0	0.19	0.10	0.15[c]	0.17
200718-6	3	-	-	-	-	-	-	-
AZ8-19-19-(4)	4	20.8	8.40	9.6[e]	0.85	-	0.85	0.17
AZ8-19-19-(5)	5	7.7	2[e]	8.6	0.33	0.54	0.54	0.17
AZ 6-30-20 (2)	6	4.7	14.5	1.0	0.62	0.20	0.41[c]	0.17
AZ 8-4-18 (3)	7	2.8	3.20	4.4	0.21	0.25	0.23[c]	0.17
AZ 8-4-18 (1)	8	15.0	1.60	0	0.55	0.50	0.52[c]	0.17
020619-2	9	1.7	14.8[e]	4	0.55	0.20	0.2[c]	0.17
200718-4	10	12.3	9.4	0	0.69	0.41	0.41	0.17
200718-3a	11	18.5	14.2	1.8	0.91	0.65	0.78[c]	0.17
020619_5	12	15.3	14.0	8.6	0.85	0.74	0.80[c]	0.17
020619-4	13	19.0	3.60	5.6	0.71	0.76	0.73[c]	0.17
020619-3	14	17.3	8.4	7.0	0.78	0.75	0.76[c]	0.17
AZ 7-2-20 (4)	15	-	-	-	-	-	-	-

[a] - β from girdle axis

[b] - β from <a> axes

[c] - average of Wk estimates

[d] - 5° uncertainty

[e] - fit uncertain

Table 4.S4: SIMS Ti-in-Quartz data

Sample	Structural Position	n	[Ti] (ppm)	2 SD	aTiO2	P (kbar)	Temperature (°C)	-2SD (°C)	+2SD (°C)	-TotErr (°C)	+TotErr (°C)
AZ 10-8-19 (1)	1	16	1.91	1.6	0.25	3	405	93	37	122	73
AZ 7-1-20 (1)	2	23	5.42	3.4	0.25	3	471	63	35	97	74
200718-6	3	14	0.31	0.1	0.1	3	373	23	17	69	32
AZ 6-30-20 (2)	7	16	11.83	3.3	0.25	4	551	26	21	65	62
AZ 8-14-18 (1)	9	9	5.21	3.8	0.25	4	488	83	41	116	80
200718-3	12	12	13.31	6.0	0.25	4	558	46	37	125	121
AZ 7-2-20 (4)	16	20	17.86	6.1	0.25	4	587	36	27	77	71

Table 4.S5. Material properties used for diapir ascent models

Parameter	Value	Reference
a [m]	10,000	Half width of presently exposed mylonite zone (This study)
ρ_h [kg m^{-3}]	2,700	Average density of gneiss (Turcotte and Schubert, 2002)
ρ_{d^*} [kg m^{-3}]	2,500	Density of molten granite/felsic crust (Gerya, 2010)
M	0-0.75	Range of lower crust melt fractions (Rey et al., 2009)
ρ_d [kg m^{-3}]	2,700-2,550	$\rho_d = \rho_h - M * (\rho_h - \rho_{d^*})$ (Gerya, 2010)
μ_h [Pa s]	10^{18}-10^{20}	Range of lower crustal viscosities (Rey et al., 2009)
α [K^{-1}]	3 x10^{-5}	Turcotte and Schubert (2002)
T_d [℃]	700-800	Near-solidus temperature of monzogranite (Barnes et al., 2001)
T_h [℃]	500-600	Quartz mylonite deformation conditions (This study)

Table 4.S6. Model parameters for Rayleigh-Taylor instability

Parameter	Value	Reference
h [km]	16	Layer thickness to achieve w = 4 km
w [km]	0.1 * λ	Amplitude of the instability where w << λ (Ramberg, 1972)
w_o [km]	0.01 * w	Amplitude of the initial disturbance (assume low w_o ; Ramberg, 1972)
λ [km]	2.568 * h	Wavelength that gives shortest timescale
ρ_1 [kg m^{-3}]	2,700	Average density of gneiss (Turcotte and Schubert, 2002)
ρ_{2^*} [kg m^{-3}]	2,500	Density of molten granite/felsic crust (Gerya, 2010)
M	0-0.75	Range of lower crust melt fractions (Rey et al., 2009)
ρ_2 [kg m^{-3}]	2,700-2,550	$\rho_d = \rho_h - M * (\rho_h - \rho_{d^*})$ (Gerya, 2010)
μ [Pa s]	10^{18}-10^{20}	Range of lower crustal viscosities (Rey et al., 2009)

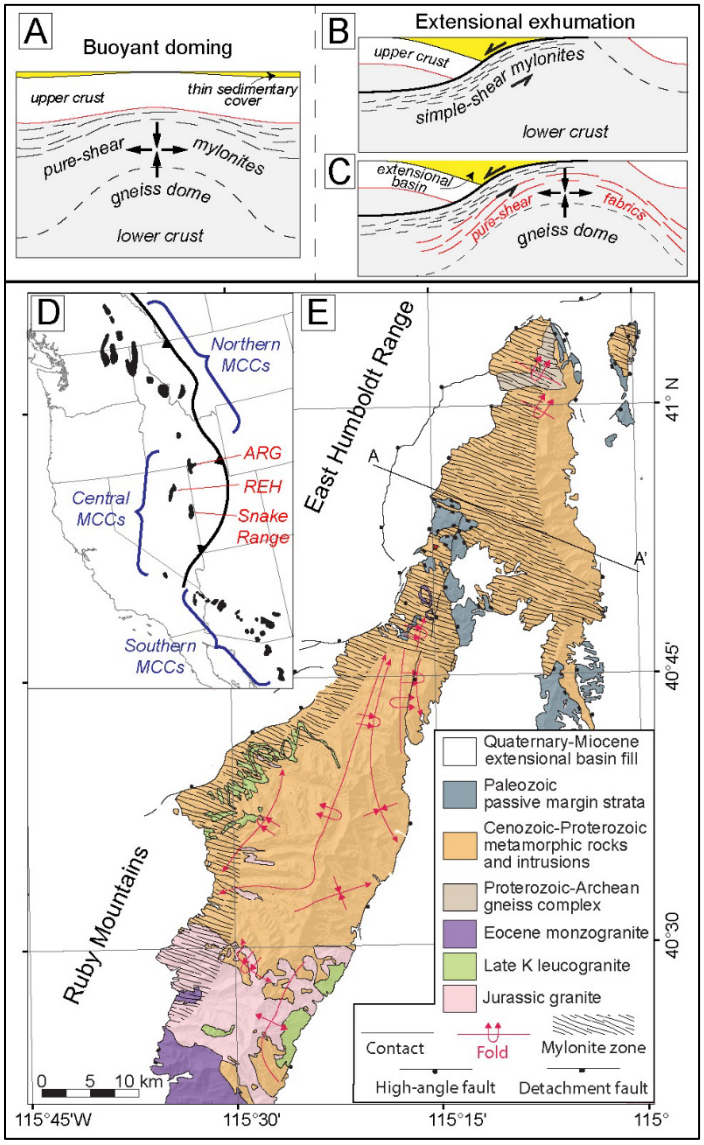

Figure 4.1. Illustrations of (A) a pure shear zone developed during buoyancy-driven exhumation, (B) a simple shear zone developed during isostatically-driven exhumation, and (C) a gneiss dome formed during isostatically-induced decompression melting. (D) Map of the western United States showing the distribution of metamorphic core complexes (MCCs; Whitney et al. (2013). ARG – Albion-Raft River-Grouse Creek. REH – Ruby Mountains-East Humboldt Range. (E) Geological map of the REH after Wright and Snoke (1993). Fig. 4.2 cross section line shown between A-A'.

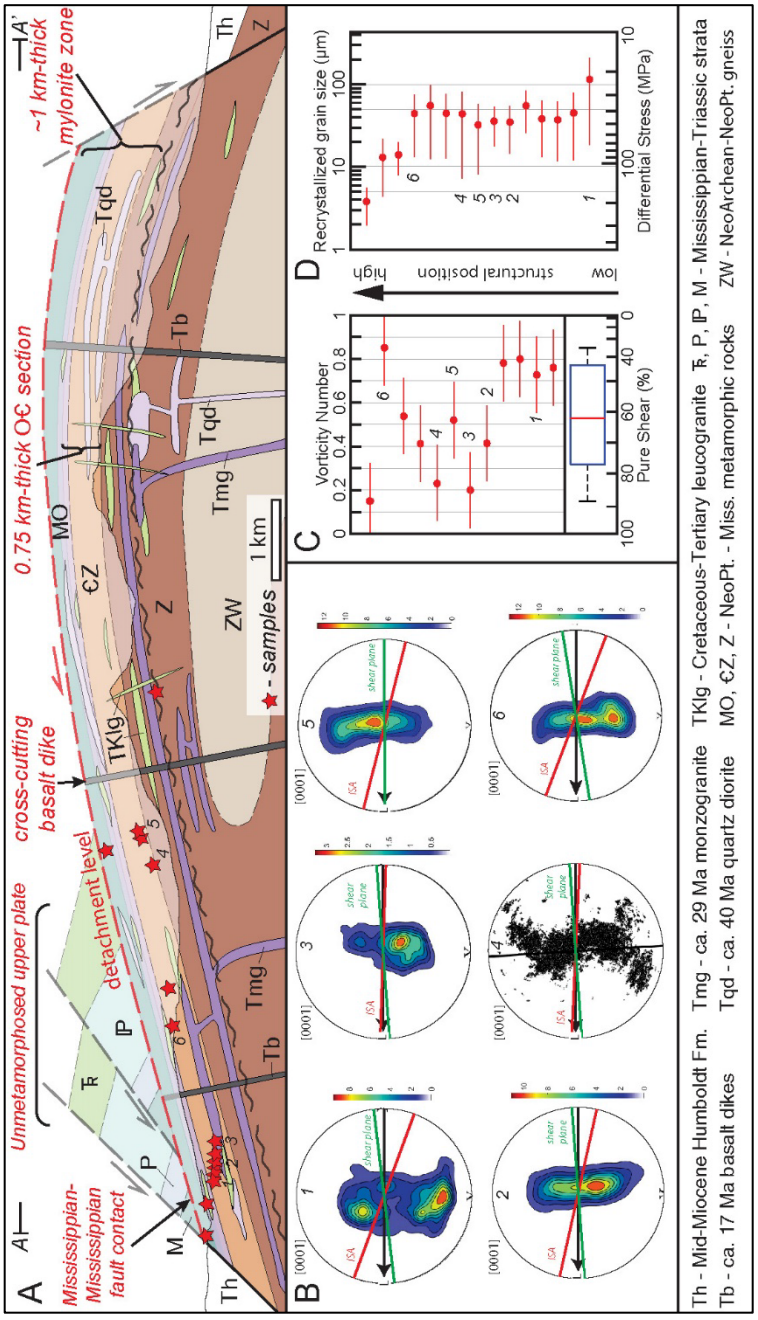

Figure 4.2. (A) Cross section showing the geometry and key structural relationships of the REH MCC. (B) Quartz c-axis pole figures from representative samples. Lineation (L), shear plane (green), foliation (black), and instantaneous stretching axis (ISA – red) are shown. Color bars show multiples of uniform density. (C) Results of kinematic vorticity analysis showing the component of pure shear for each sample. Box plot shows the median (red bar) and interquartile range (blue box) of vorticity number estimates. (D) Results of mean recrystallized grain size measurements and the corresponding differential stress value.

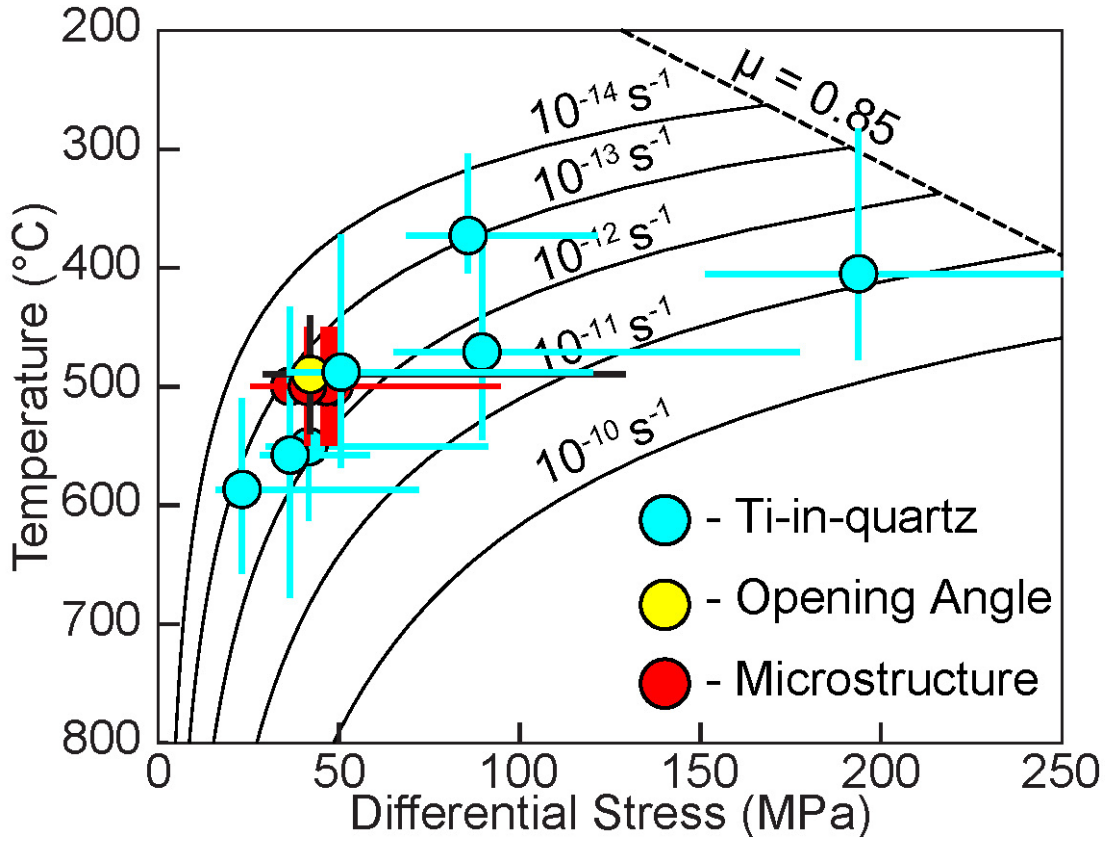

Figure 4.3. Temperature-stress plot showing strain rate estimates for each sample. Differential stress estimates come from paleopiezometry (Fig. 4.2D). Temperature estimates are based on the thermometric techniques applied to recrystallized quartz grains. Dashed black line shows Byerlee's friction law.

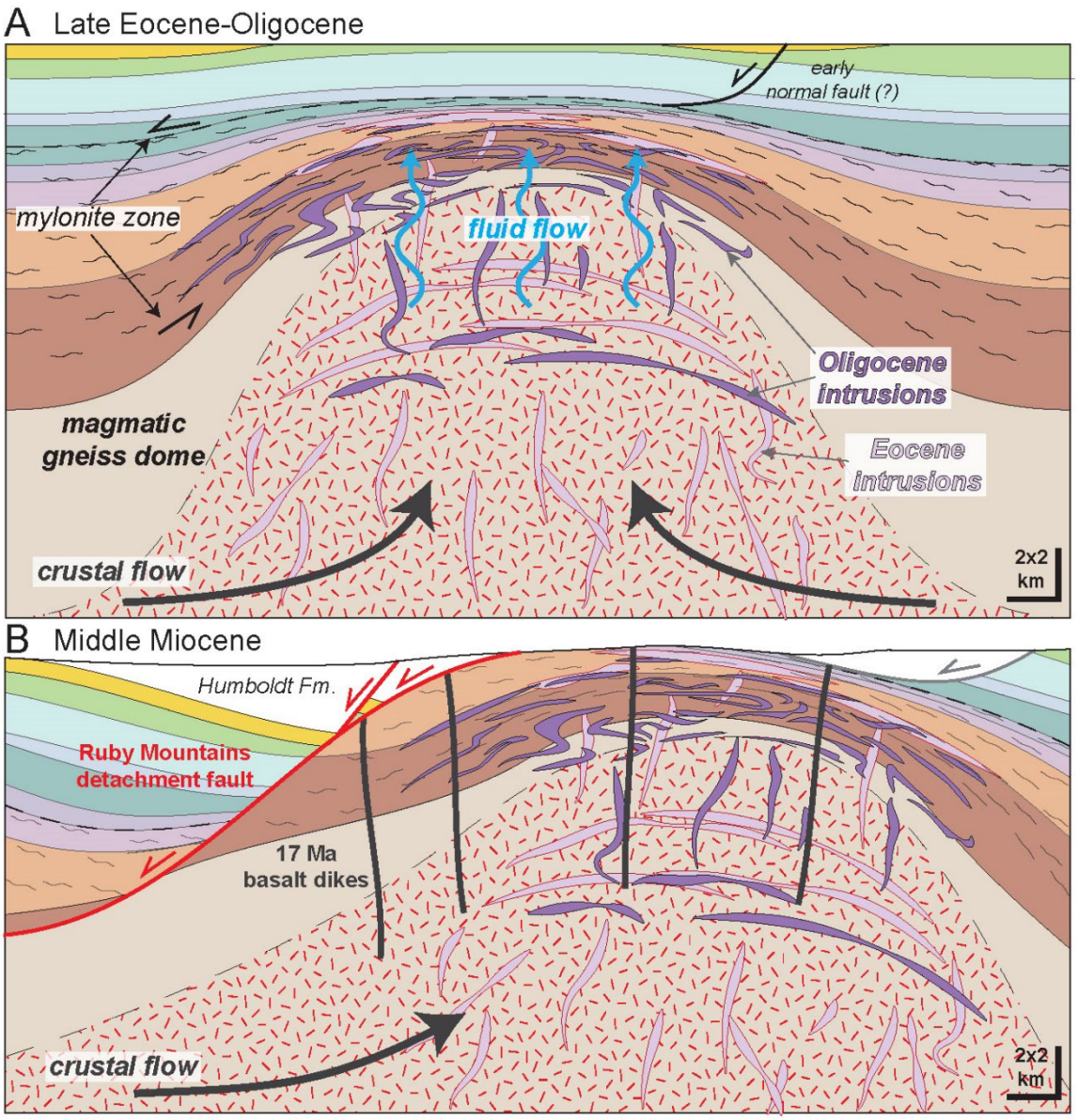

Figure 4.4. Schematic cross sections showing (A) Eocene-Oligocene and (B) Miocene development of the REH.

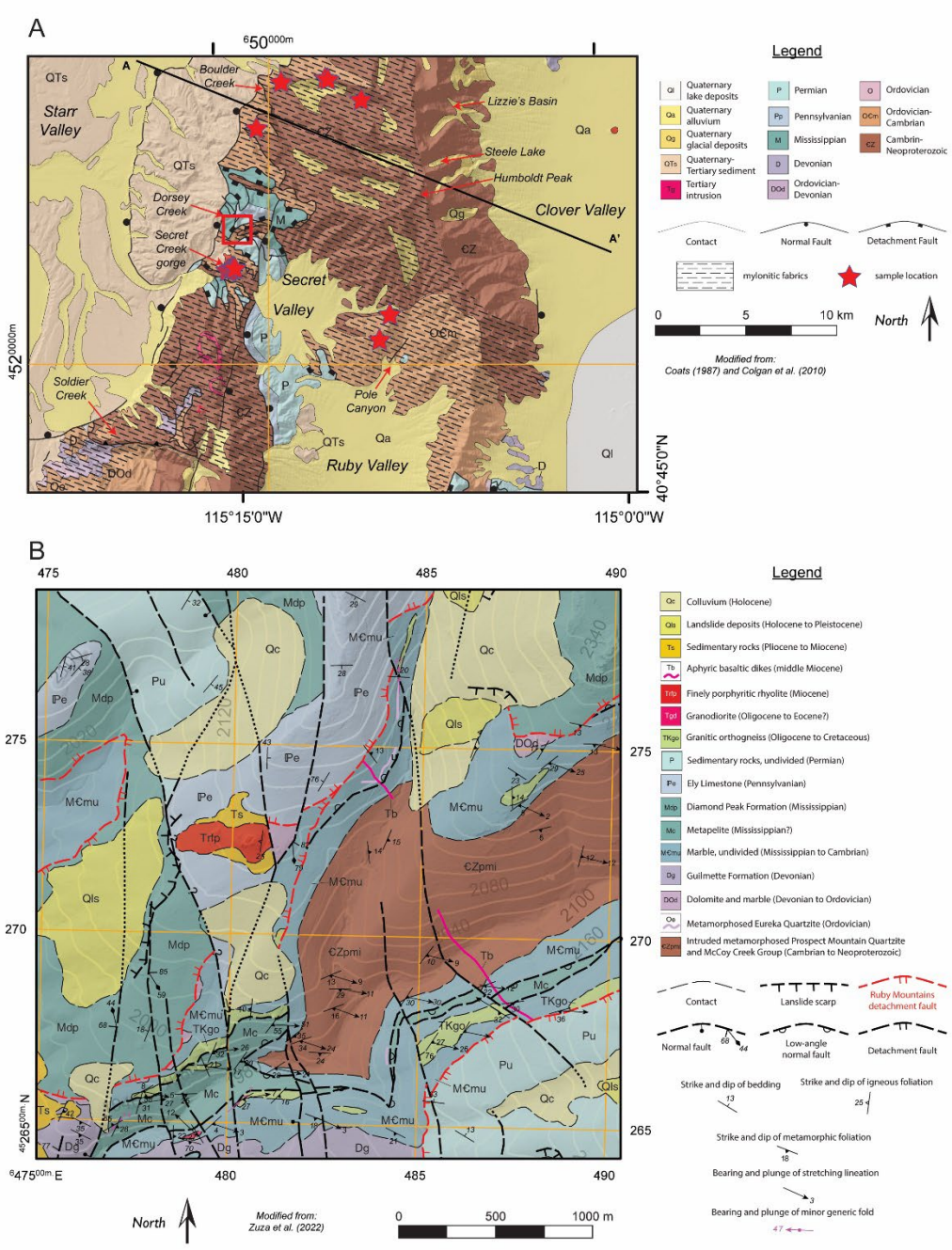

Figure 4.S1. A) Geological map of the northern Ruby Mountains-East Humboldt Range study area. B) Detailed geological map of the Dorsey Creek area. Middle Miocene basalt dikes (Tb) that crosscut the mylonitic fabric are truncated by the Ruby Mountains detachment fault.

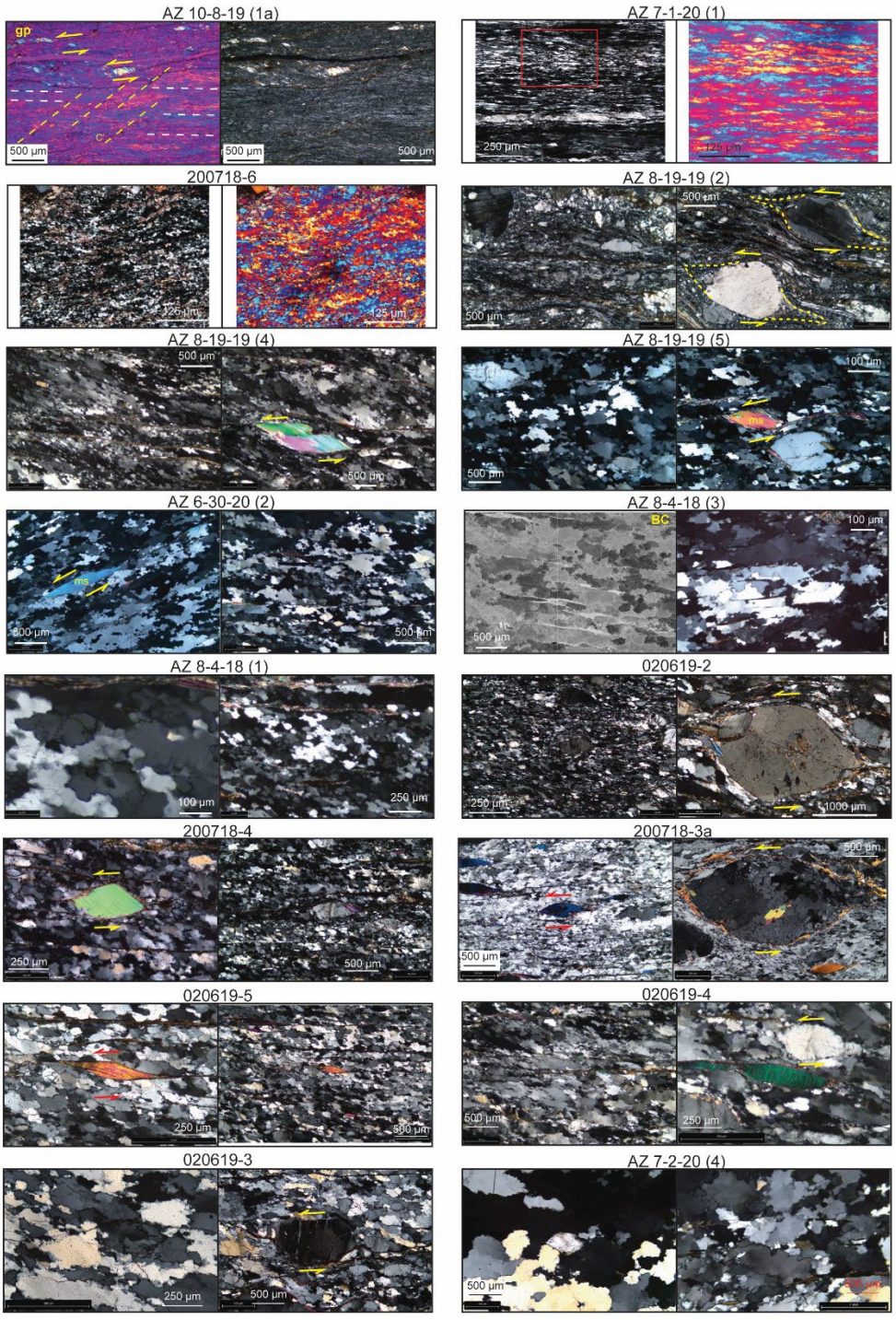

Figure 4.S2. Photomicrographs of each sample analyzed in this study showing characteristic microstructures. Photos are oriented left to west.

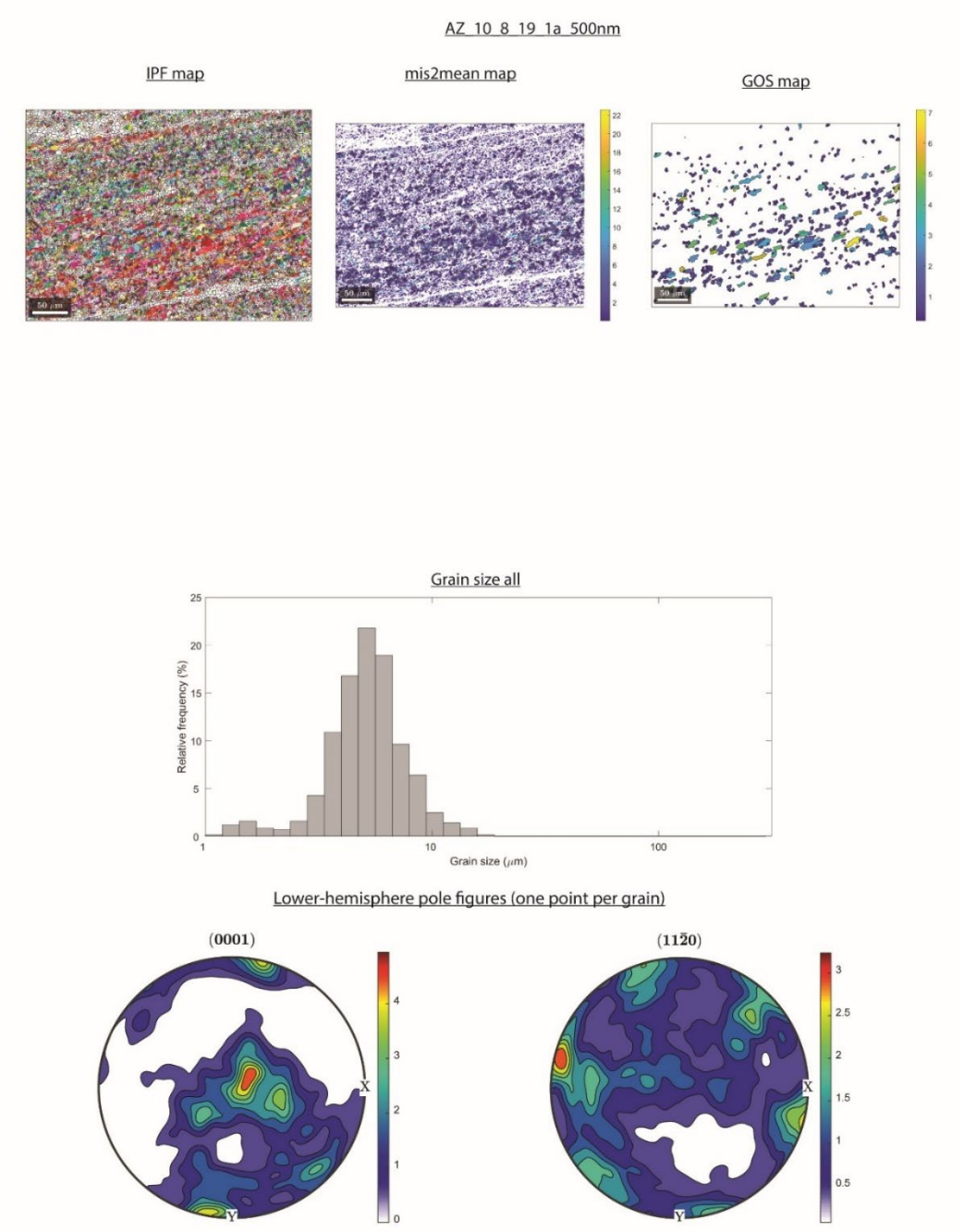

Figure 4.S3. EBSD maps showing inverse pole figure (IPF) map, misorientation to the mean (mis2mean) map, and the grain orientation spread (GOS) map. The mis2mean and GOS map scales are in units of degrees. The histogram shows the distribution of grain sizes. The lower-hemisphere pole figures display the quartz crystallographic preferred orientation. The pole figure color scales are multiples of uniform density (M.U.D.).

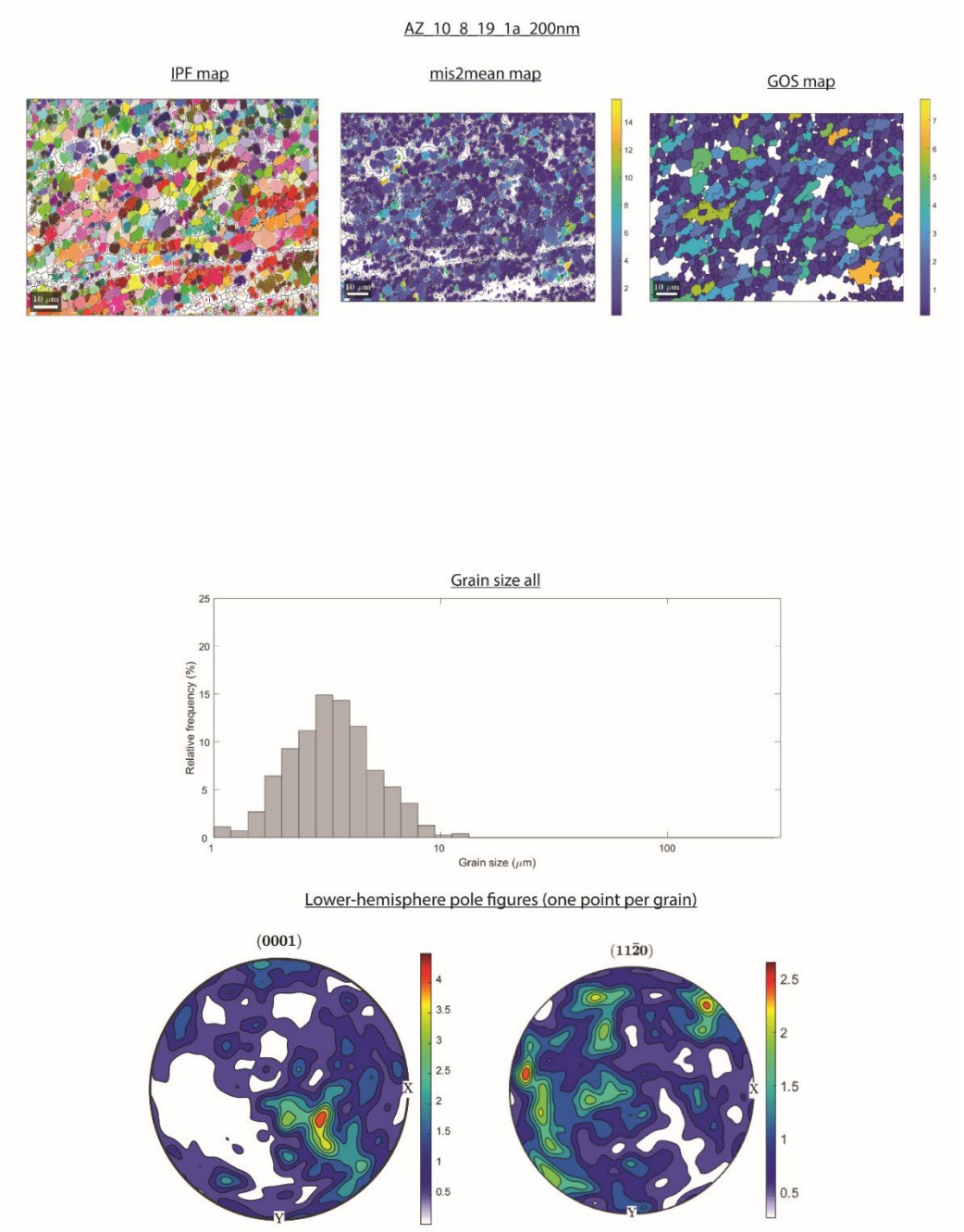

Figure 4.S3. (*continued*)

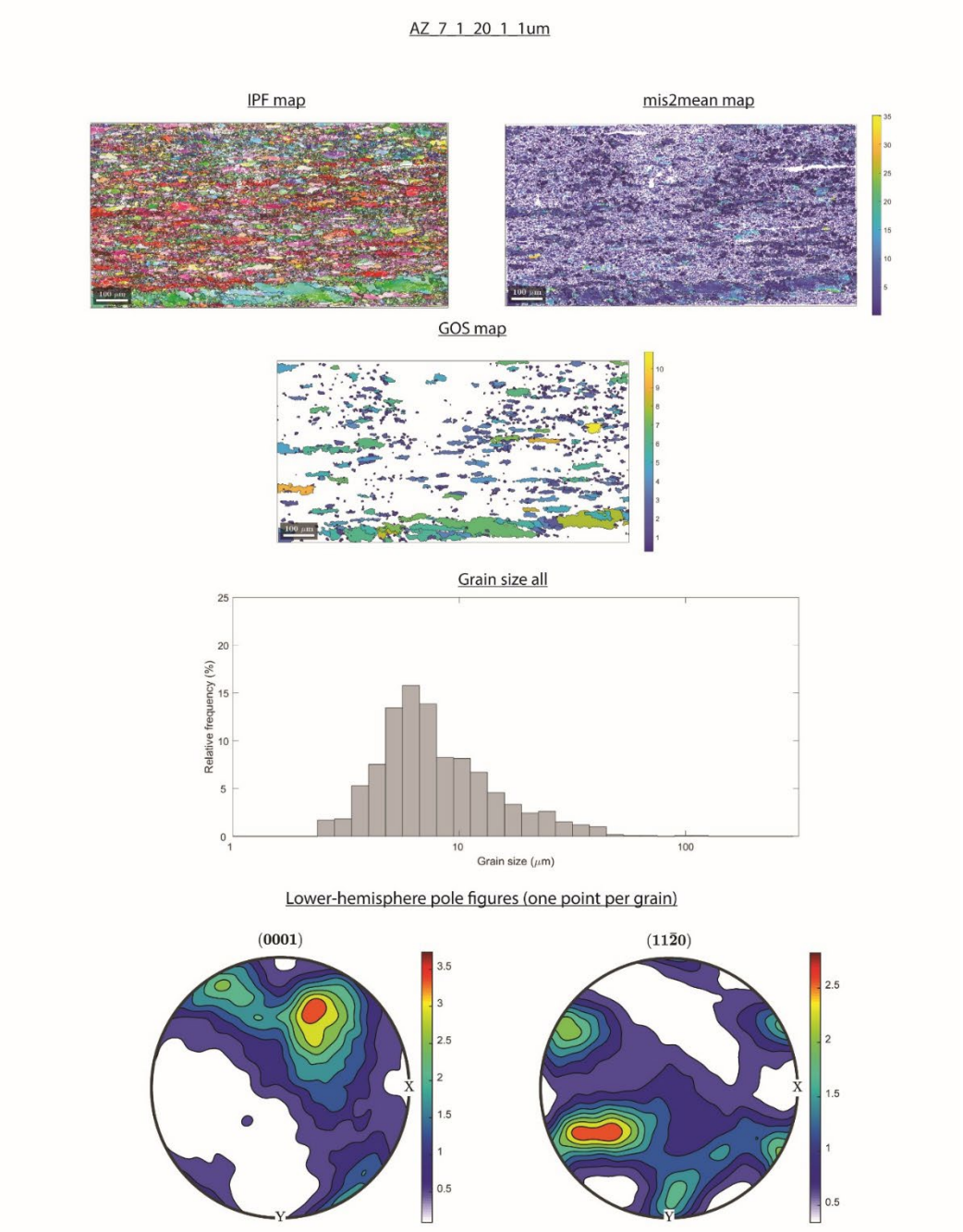

Figure 4.S3. (*continued*)

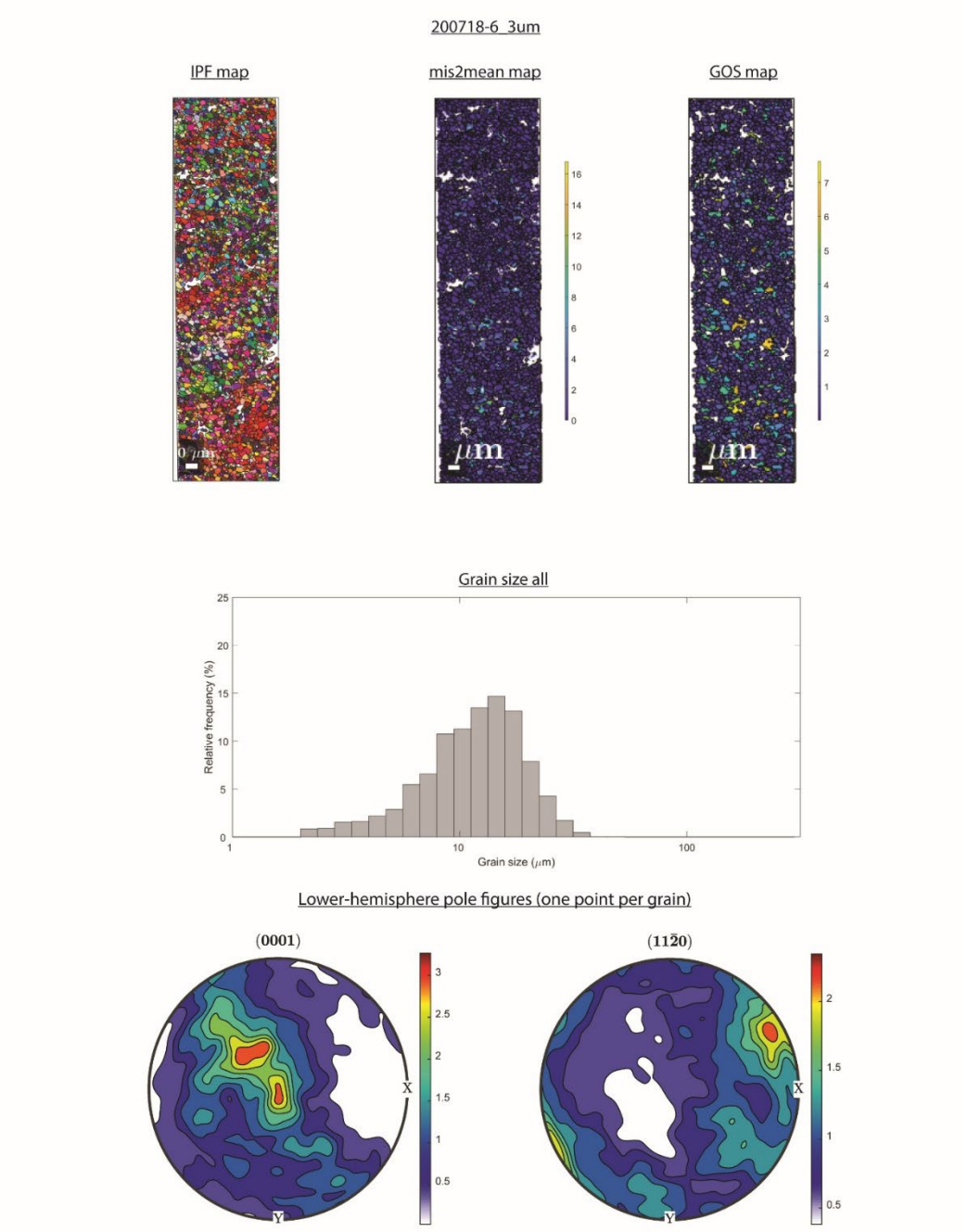

Figure 4.S3. (*continued*)

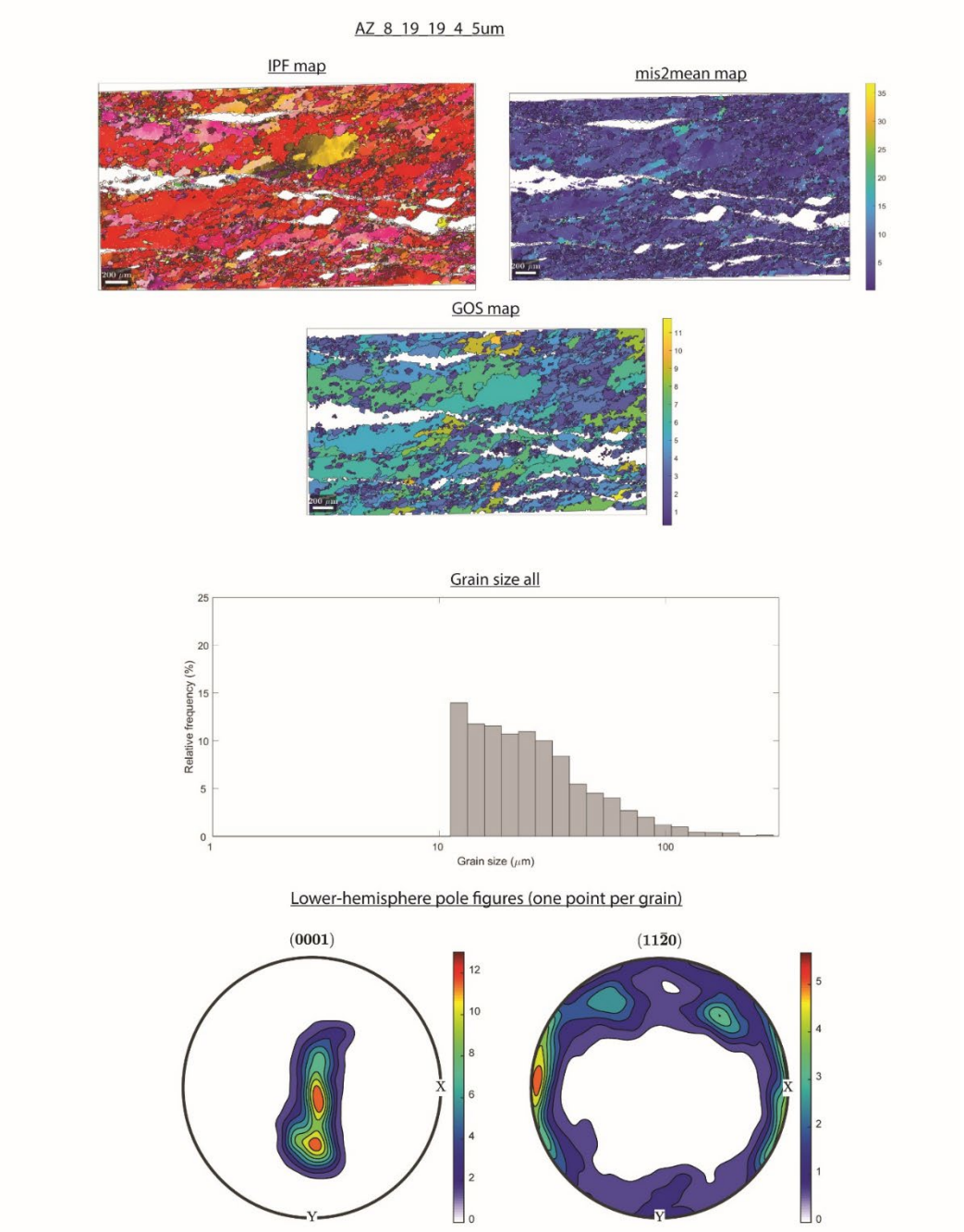

Figure 4.S3. (*continued*)

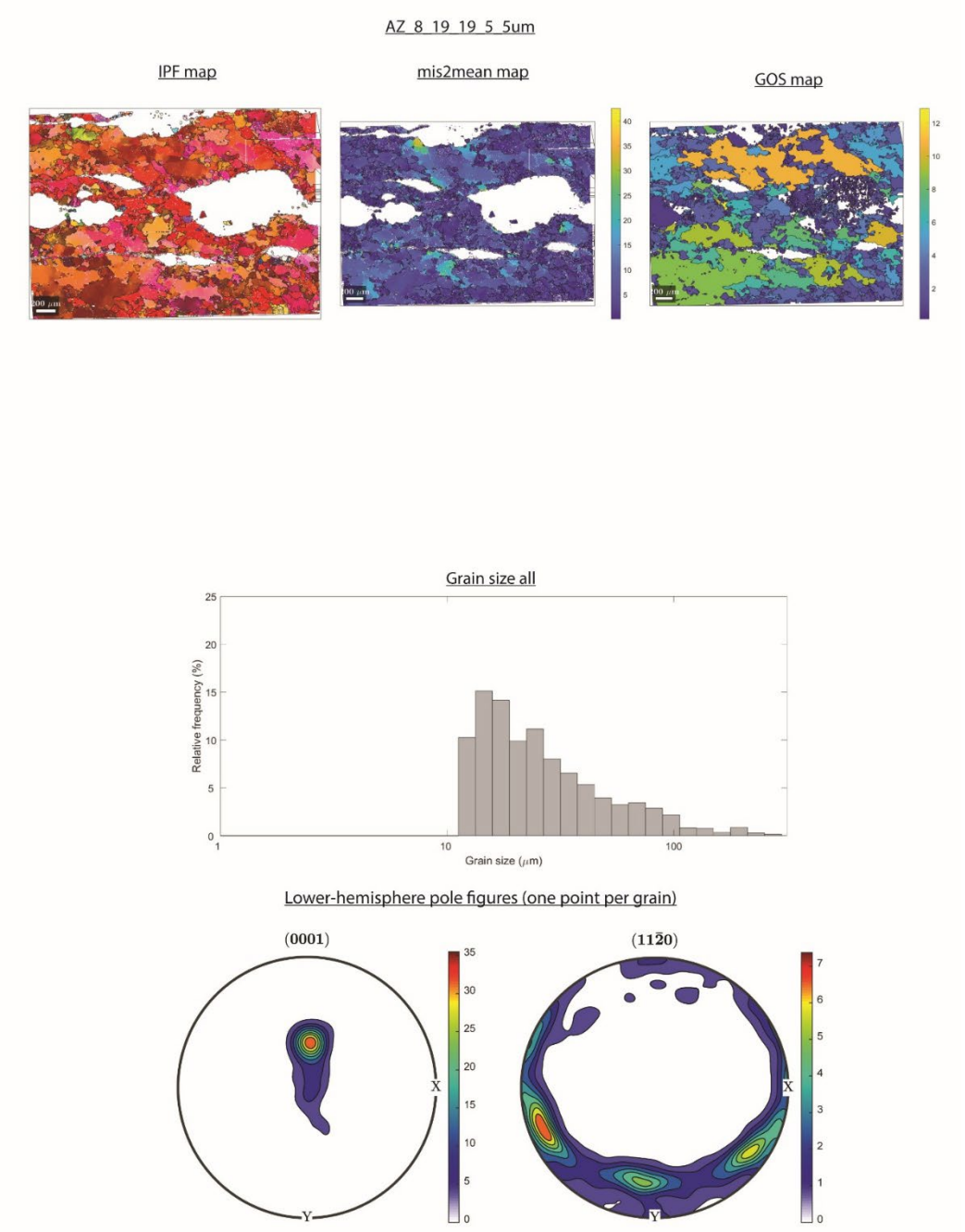

Figure 4.S3. (*continued*)

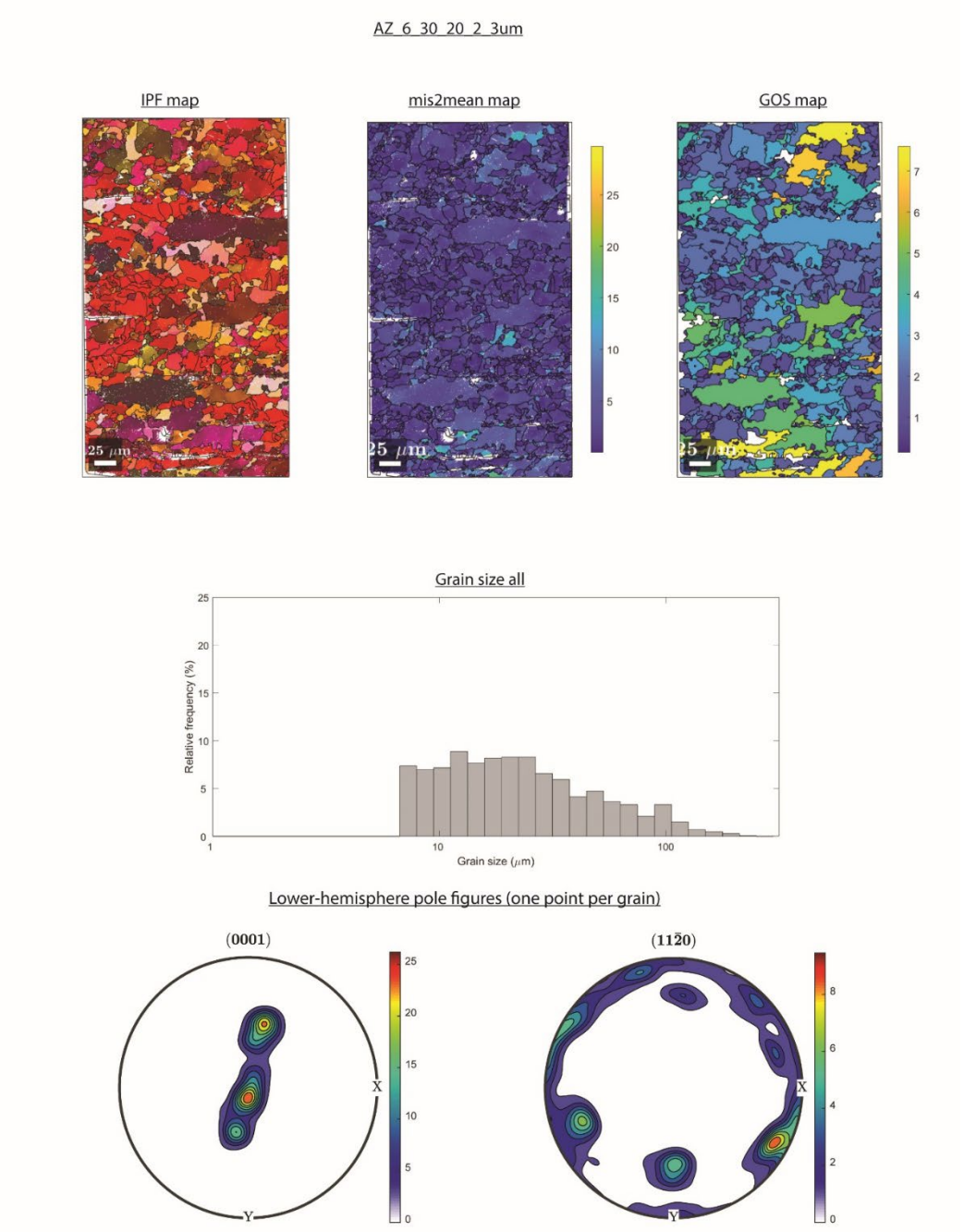

Figure 4.S3. (*continued*)

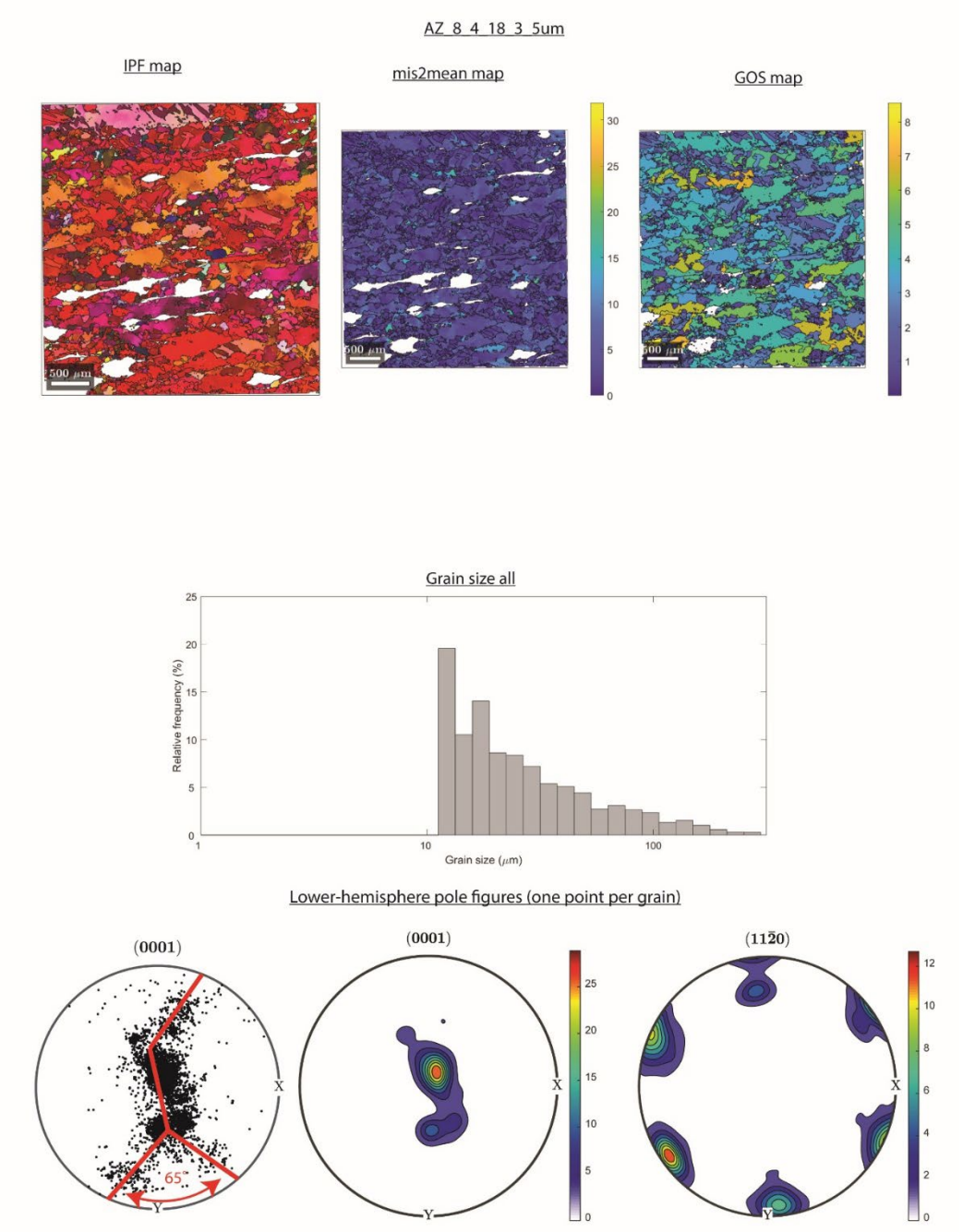

Figure 4.S3. (*continued*)

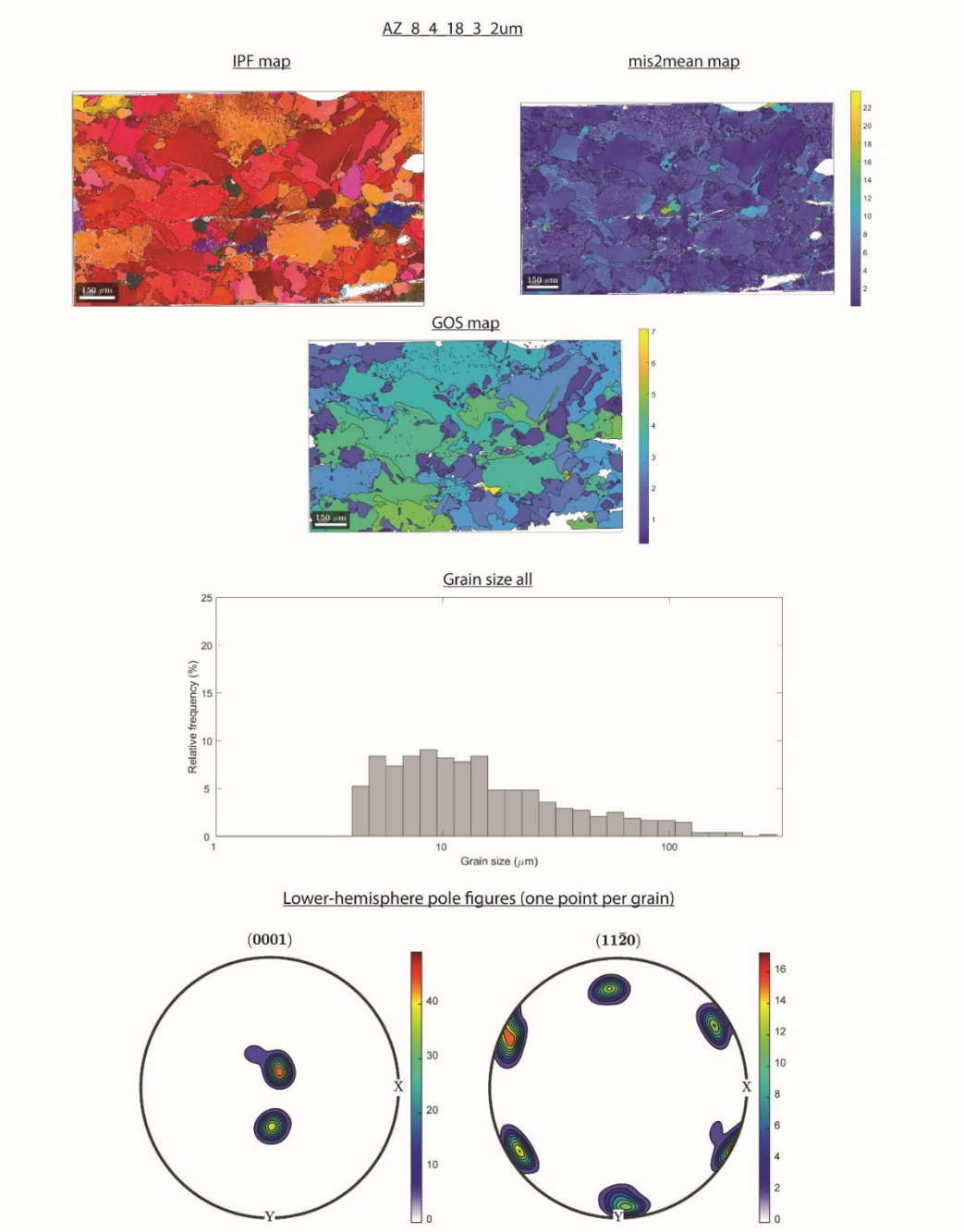

Figure 4.S3. (*continued*)

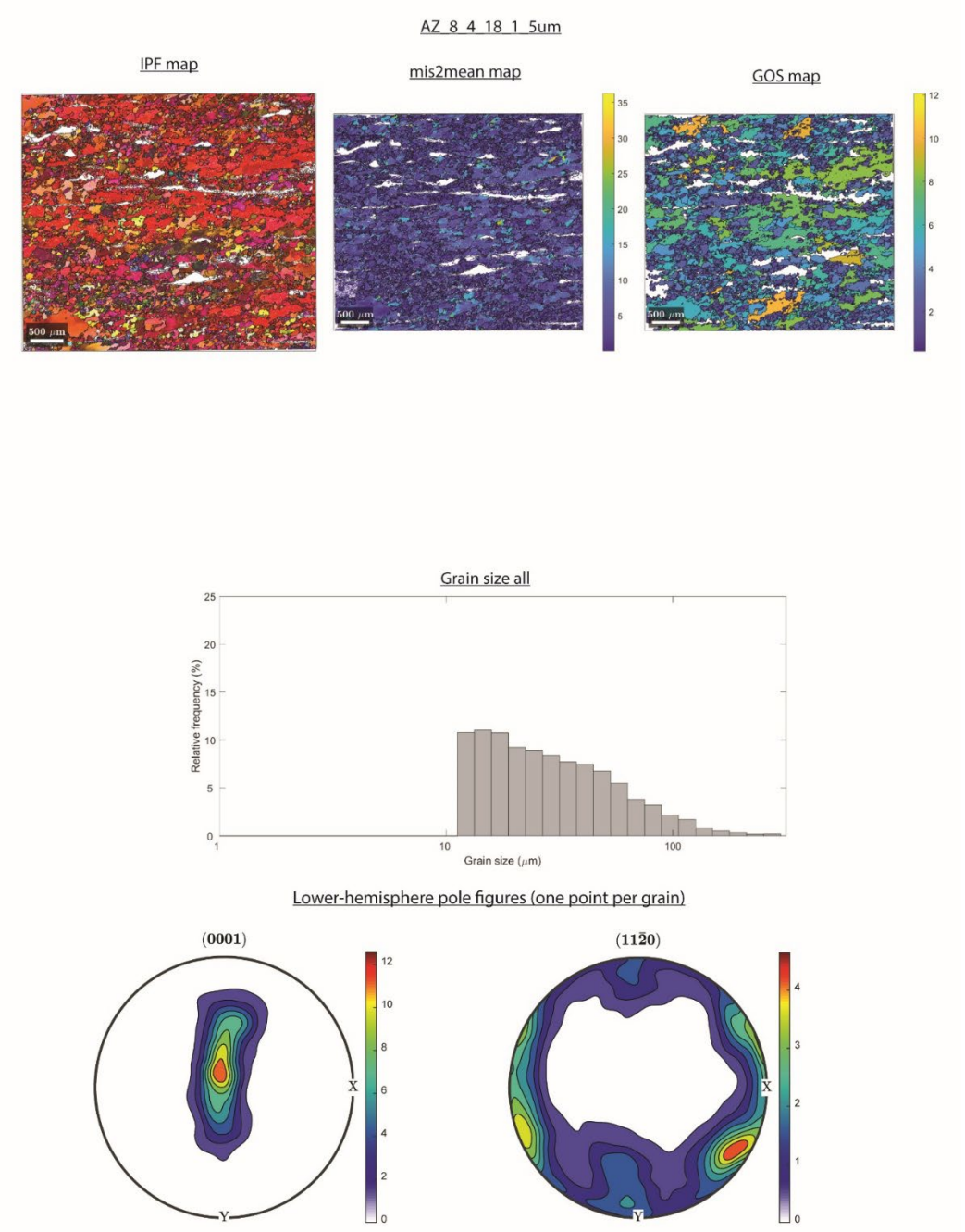

Figure 4.S3. (*continued*)

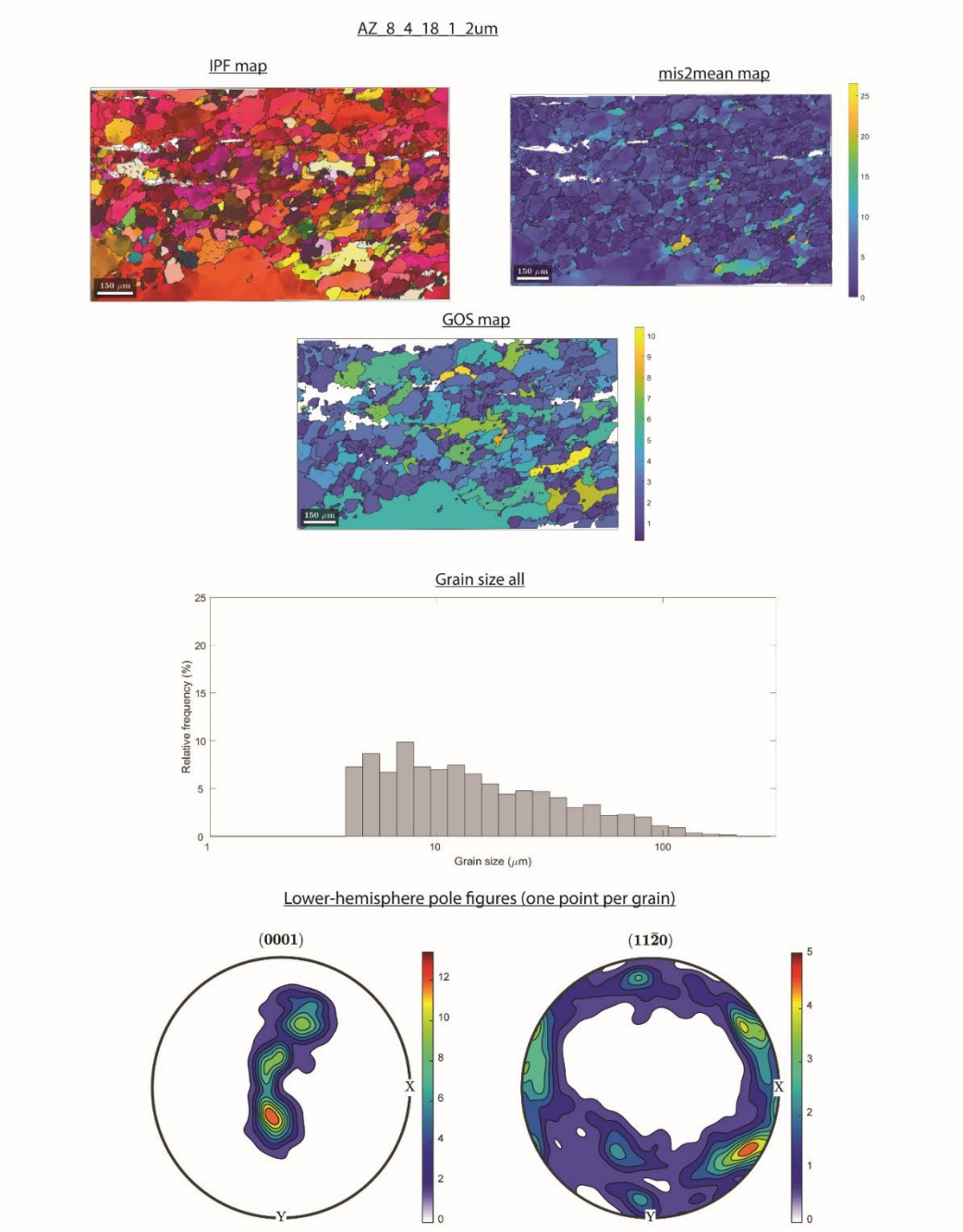

Figure 4.S3. (*continued*)

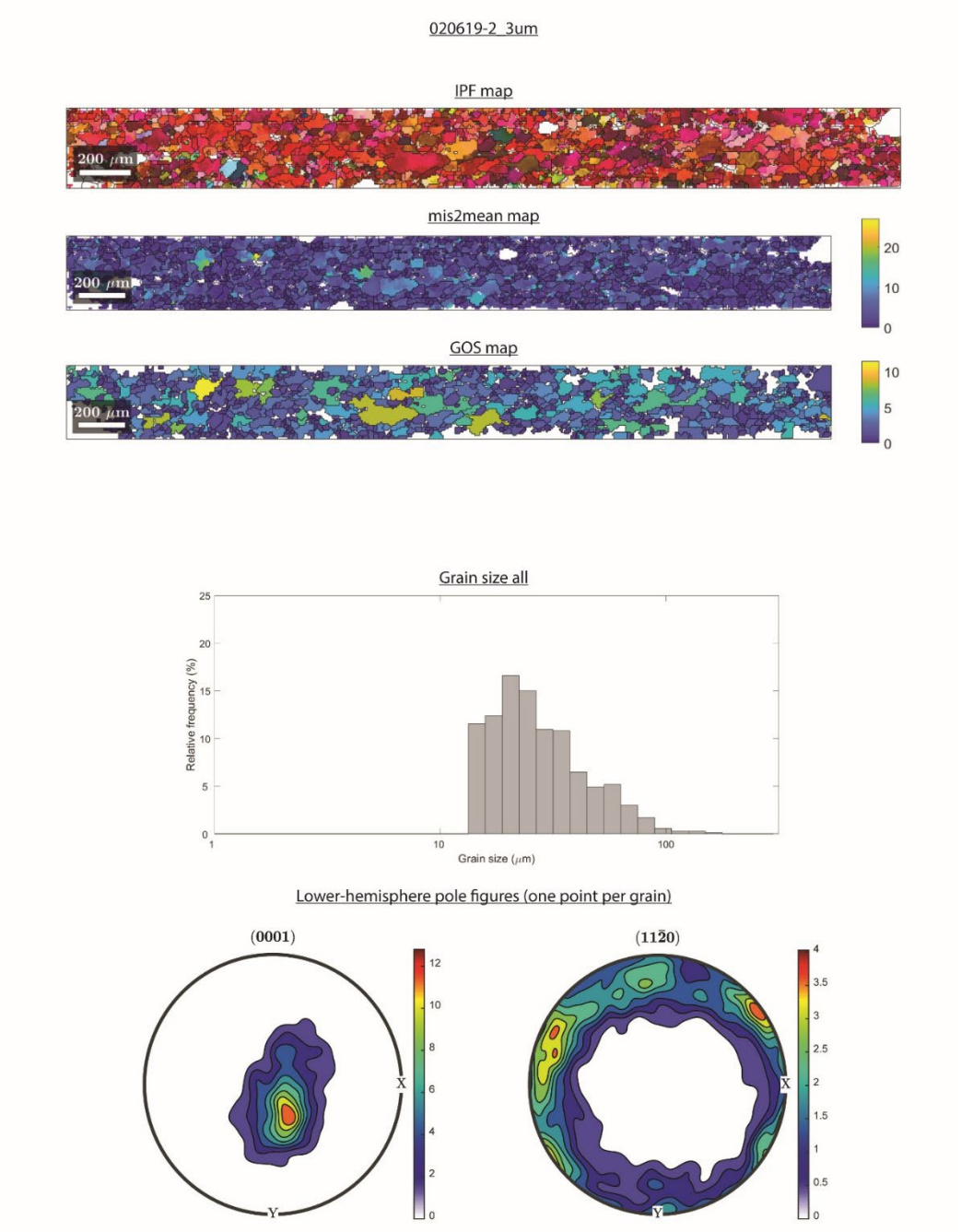

Figure 4.S3. (*continued*)

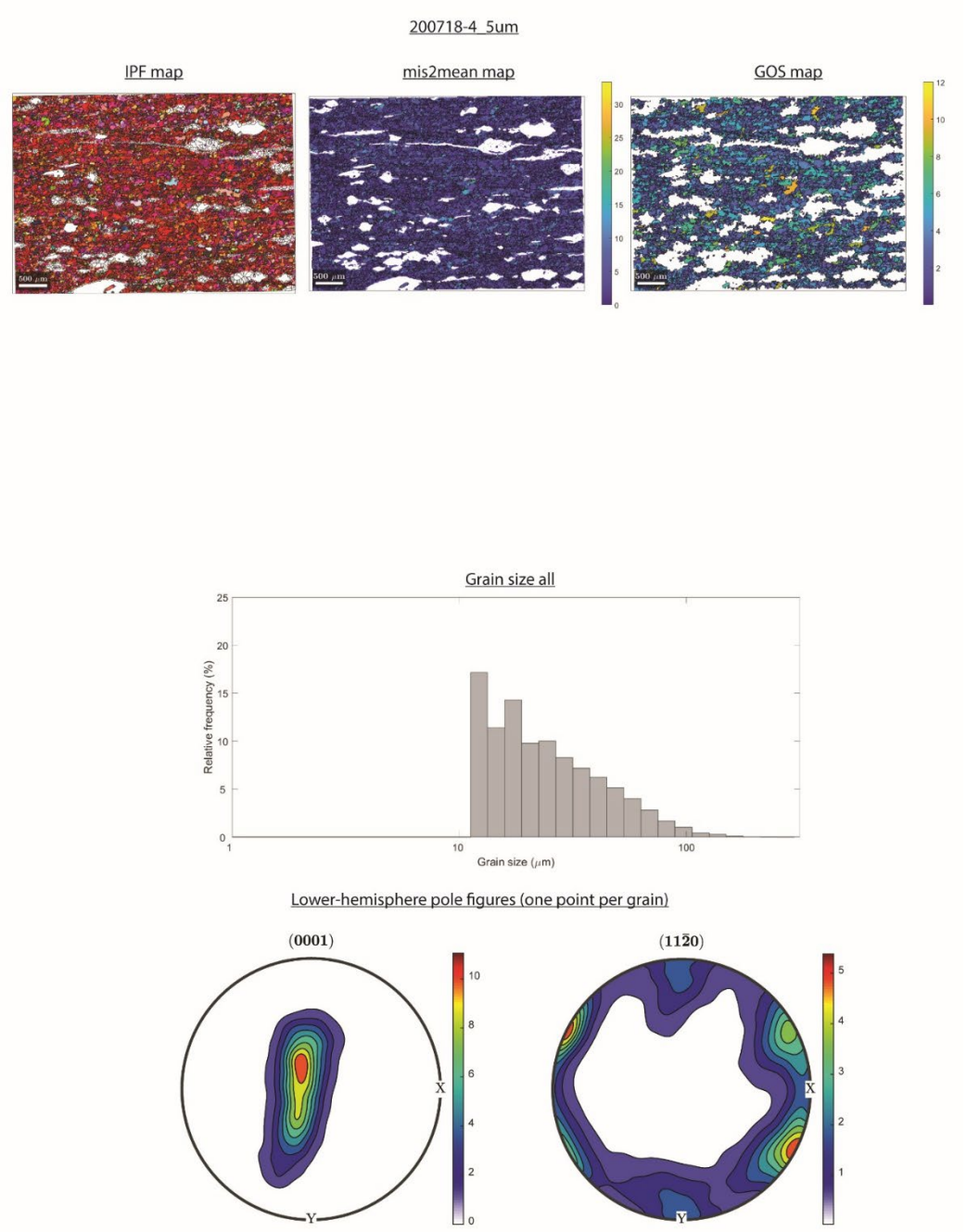

Figure 4.S3. (*continued*)

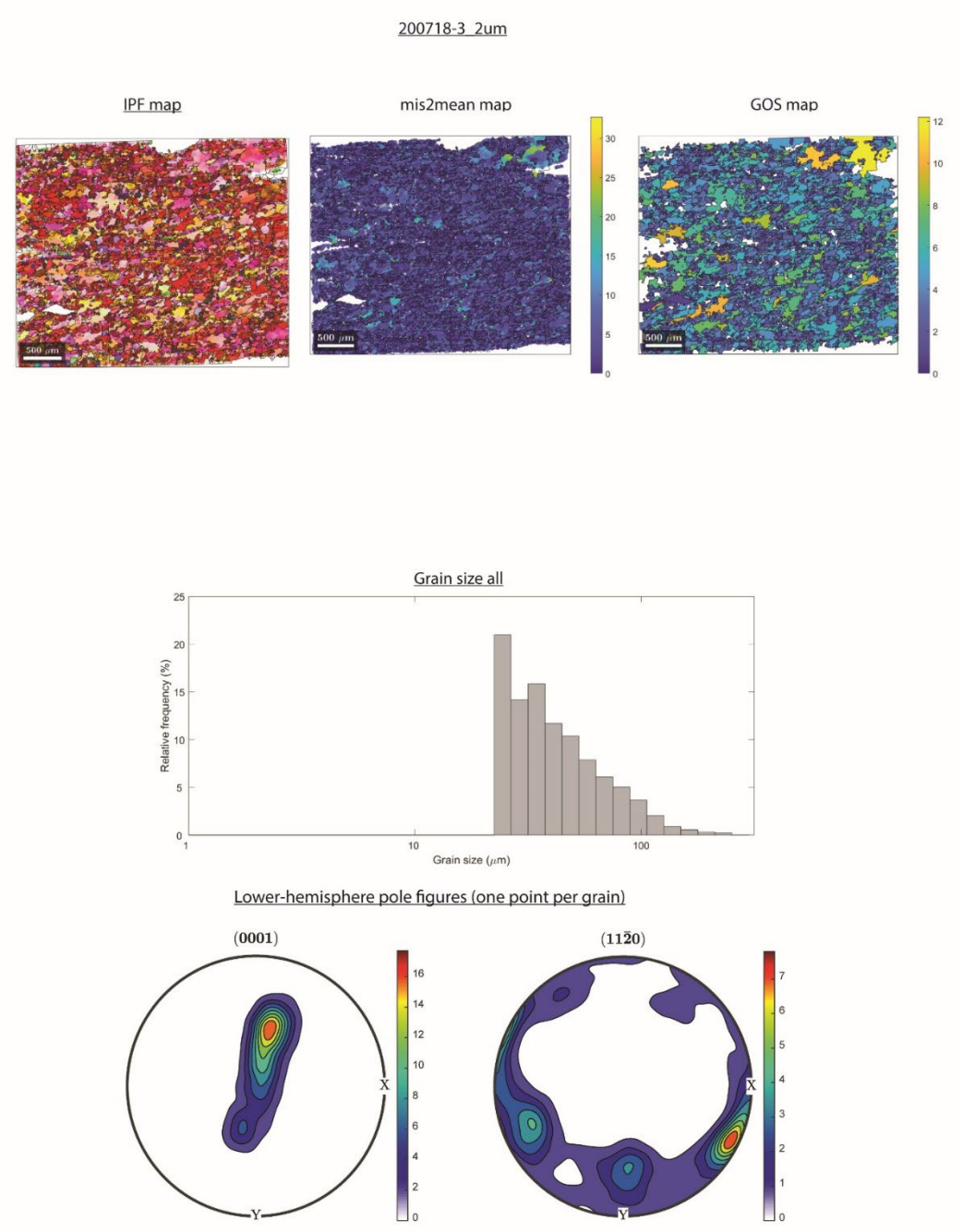

Figure 4.S3. (*continued*)

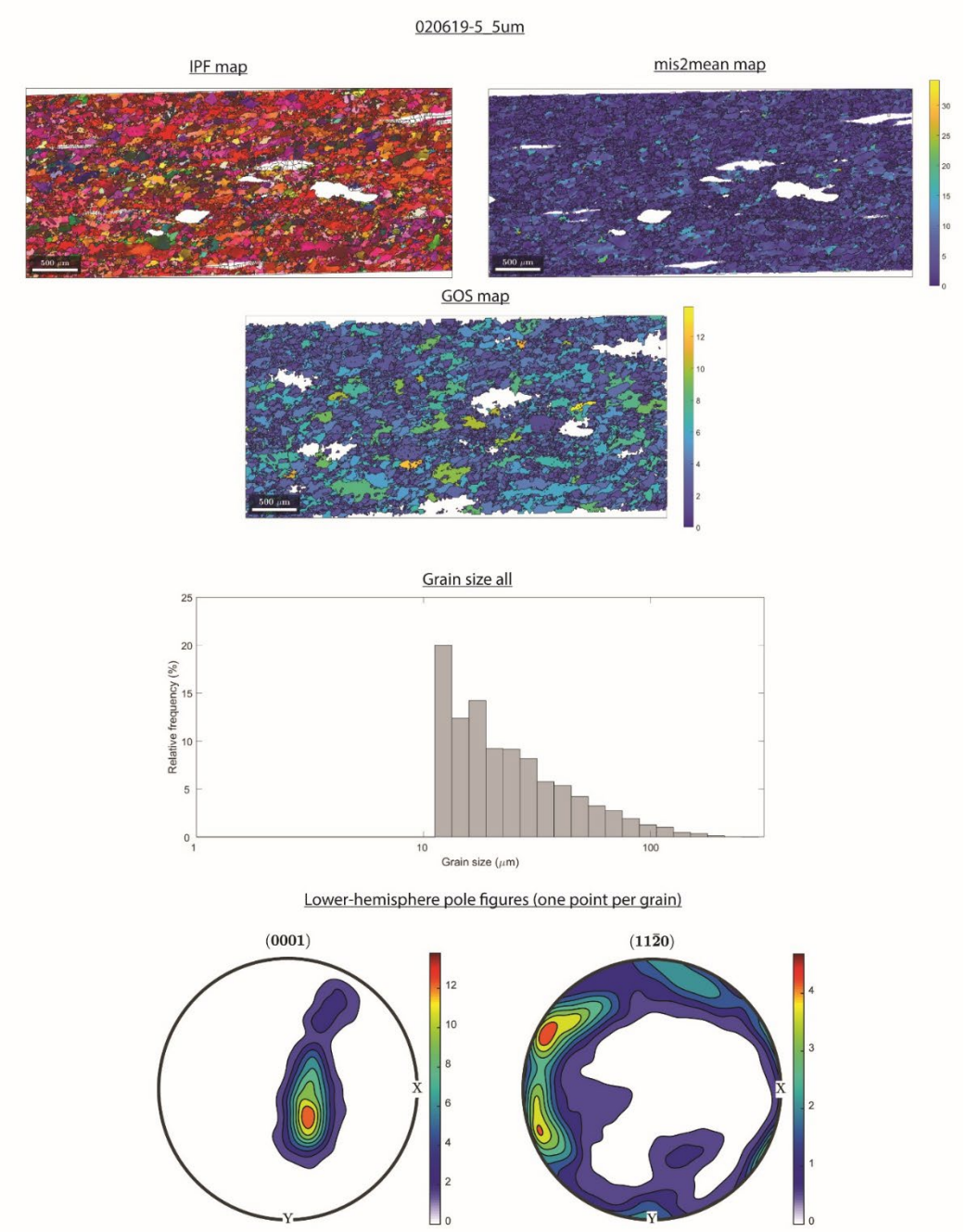

Figure 4.S3. (*continued*)

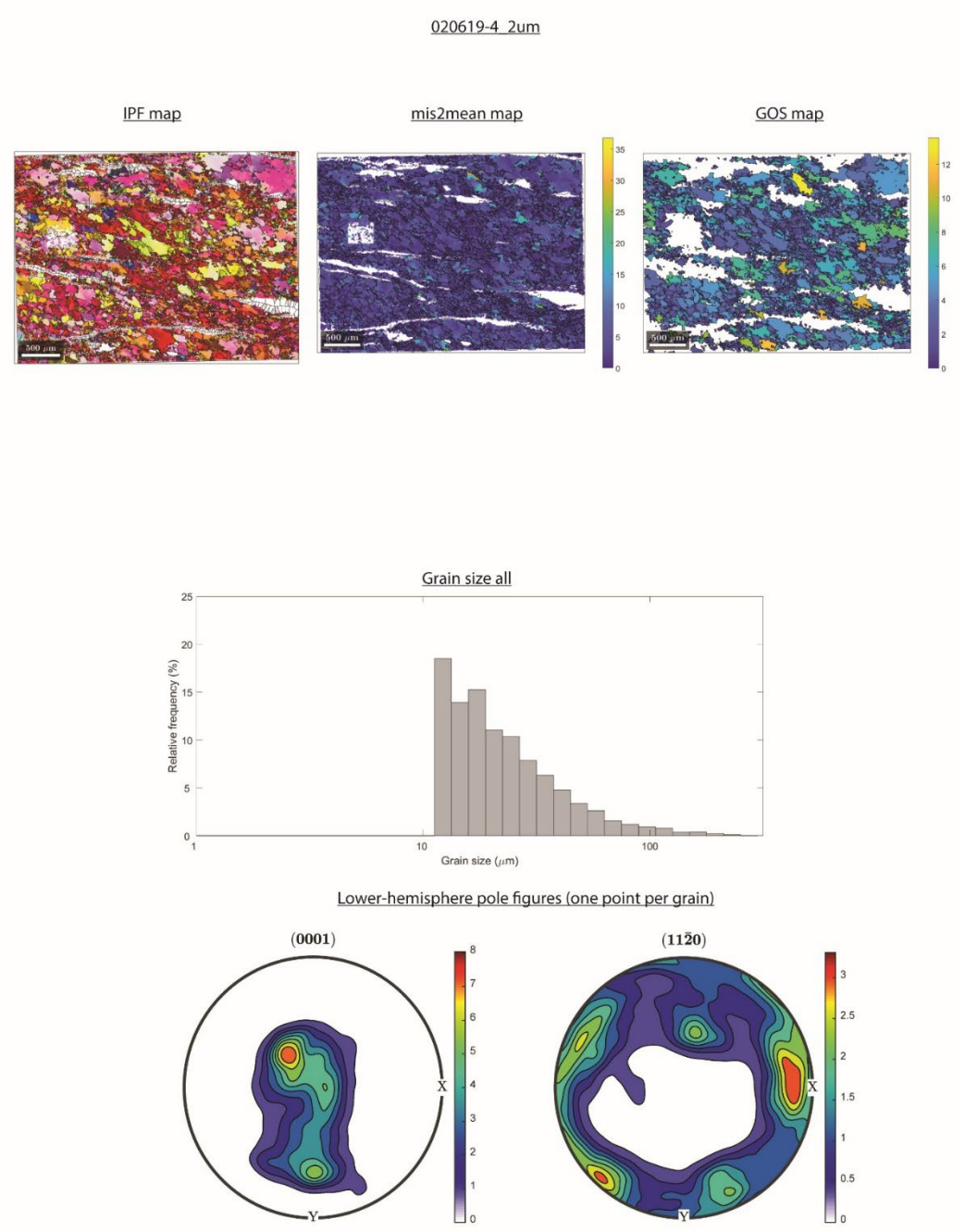

Figure 4.S3. (*continued*)

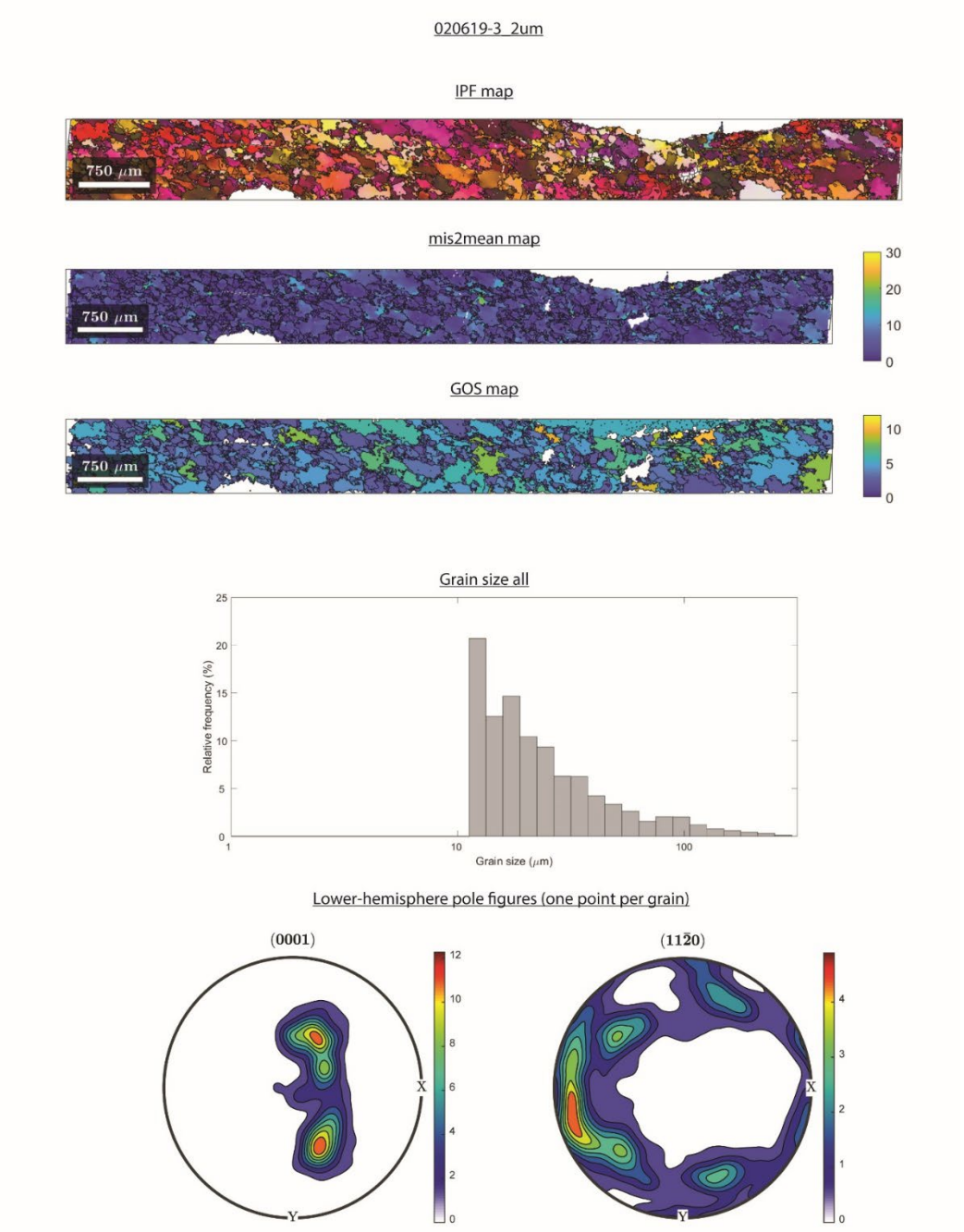

Figure 4.S3. (*continued*)

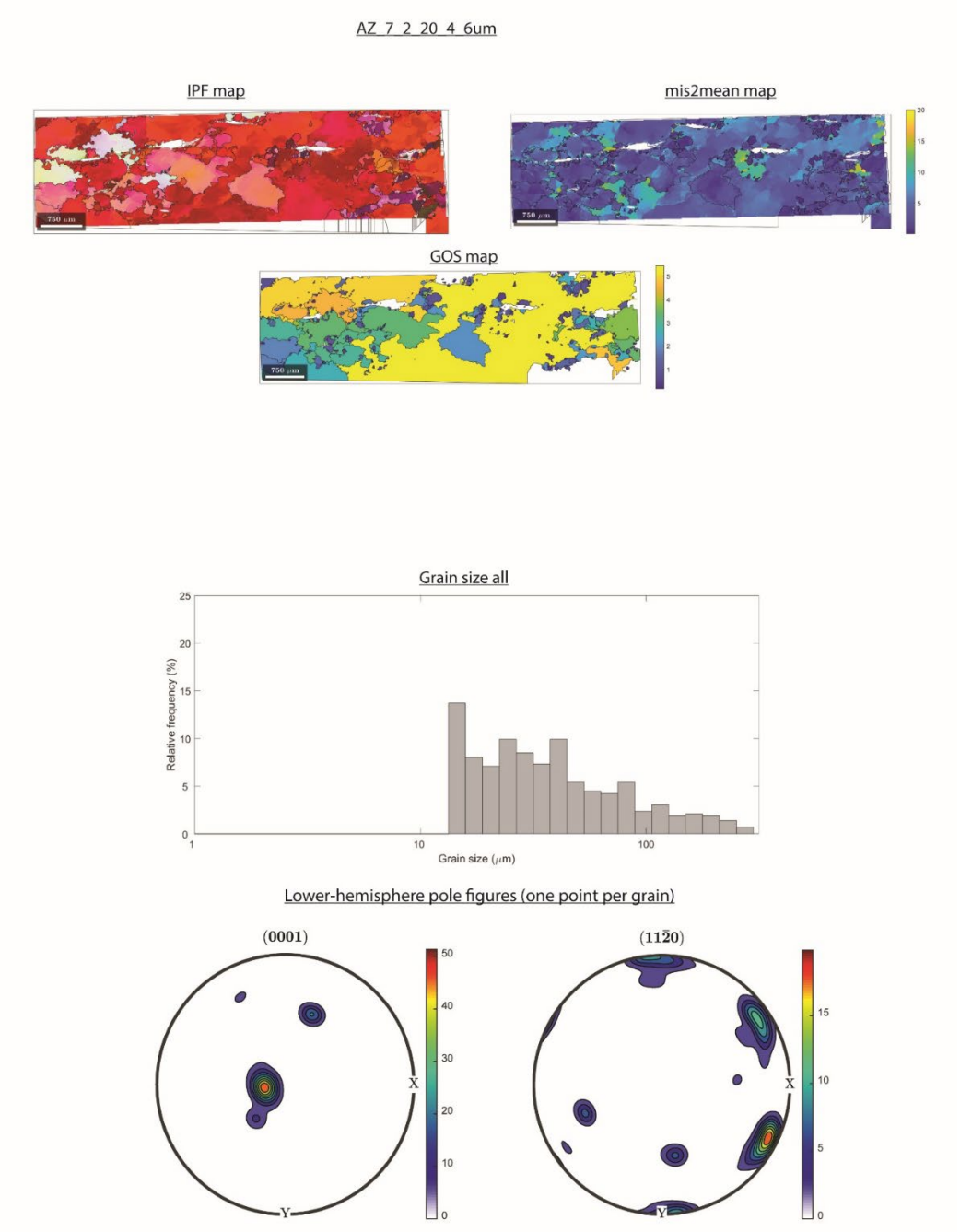

Figure 4.S3. (*continued*)

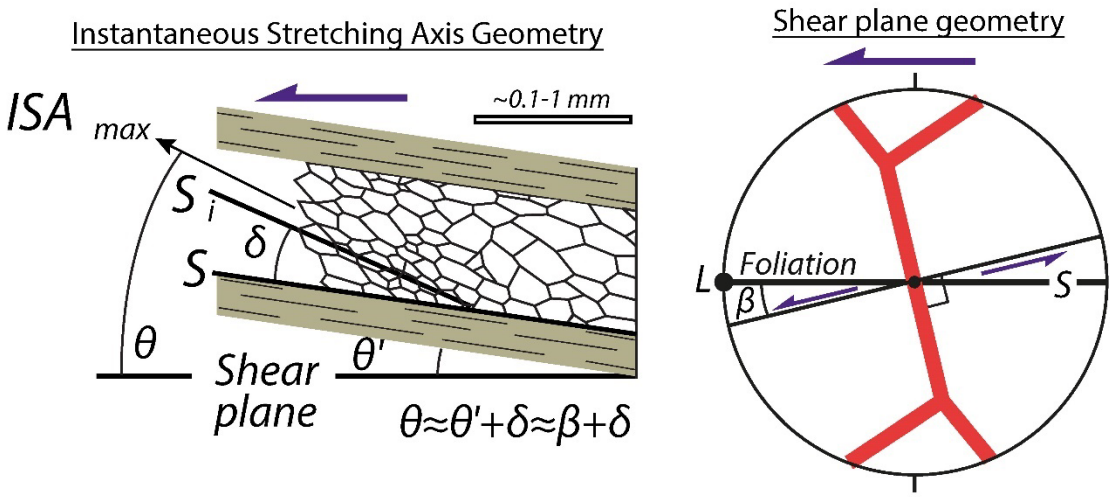

Figure 4.S4. Illustration of rock fabric and pole figure showing the geometric relationships between the instantaneous stretching axis (ISA), the foliation (S) and the shear plane.

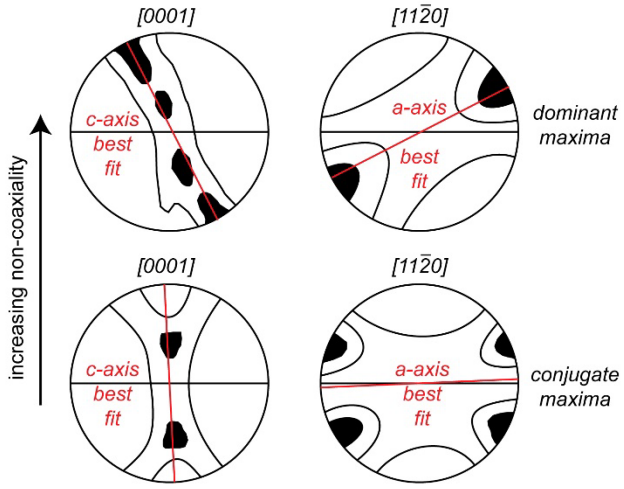

Figure 4.S5. Cartoon quartz pole figures displaying the relationships between c- and a-axes (modified from Law, 1990). The top pole figures show a case where a dominant a-axis maxima has developed perpendicular to the asymmetric c-axis single girdle. The bottom pole figures show a case where conjugate a-axis maxima are developed across the X plane and perpendicular to the c-axis girdle.

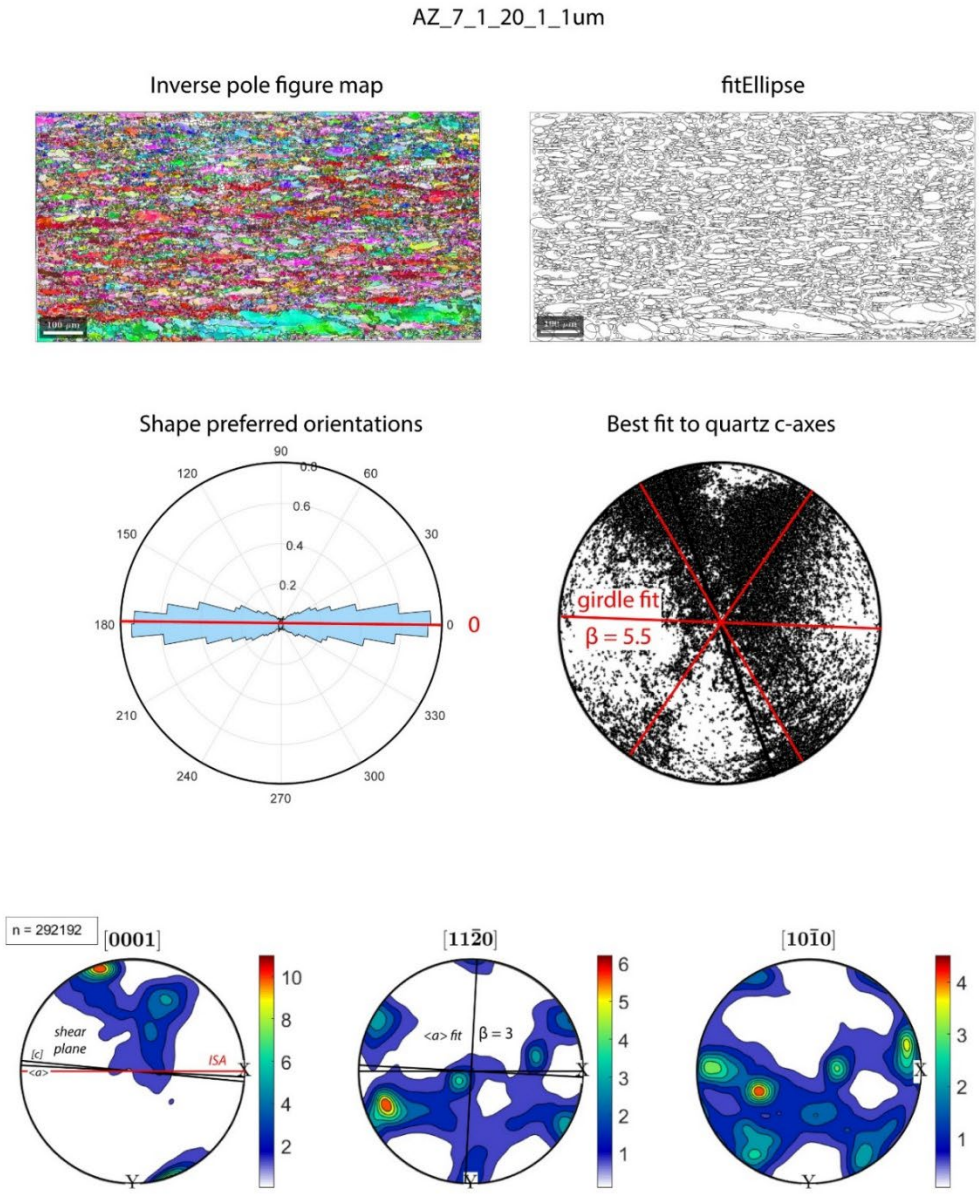

Figure 4.S6. Results of grain ellipse fitting and quartz c-axis fitting to calculate kinematic vorticity number. Inverse pole figure maps (IPF) and fitEllipse maps show the orientation of ellipses relative to the rock fabric. The shape preferred orientation plot shows the distribution of ellipse axes as a polar histogram. The best fit to quartz c-axes is shows as a black line plotted over all c-axis orientations. Pole figures plot all orientations and show the orientation of the ISA and shear plane derived from c- and a-axes fits. The pole figure color scales are multiples of uniform density (M.U.D.).

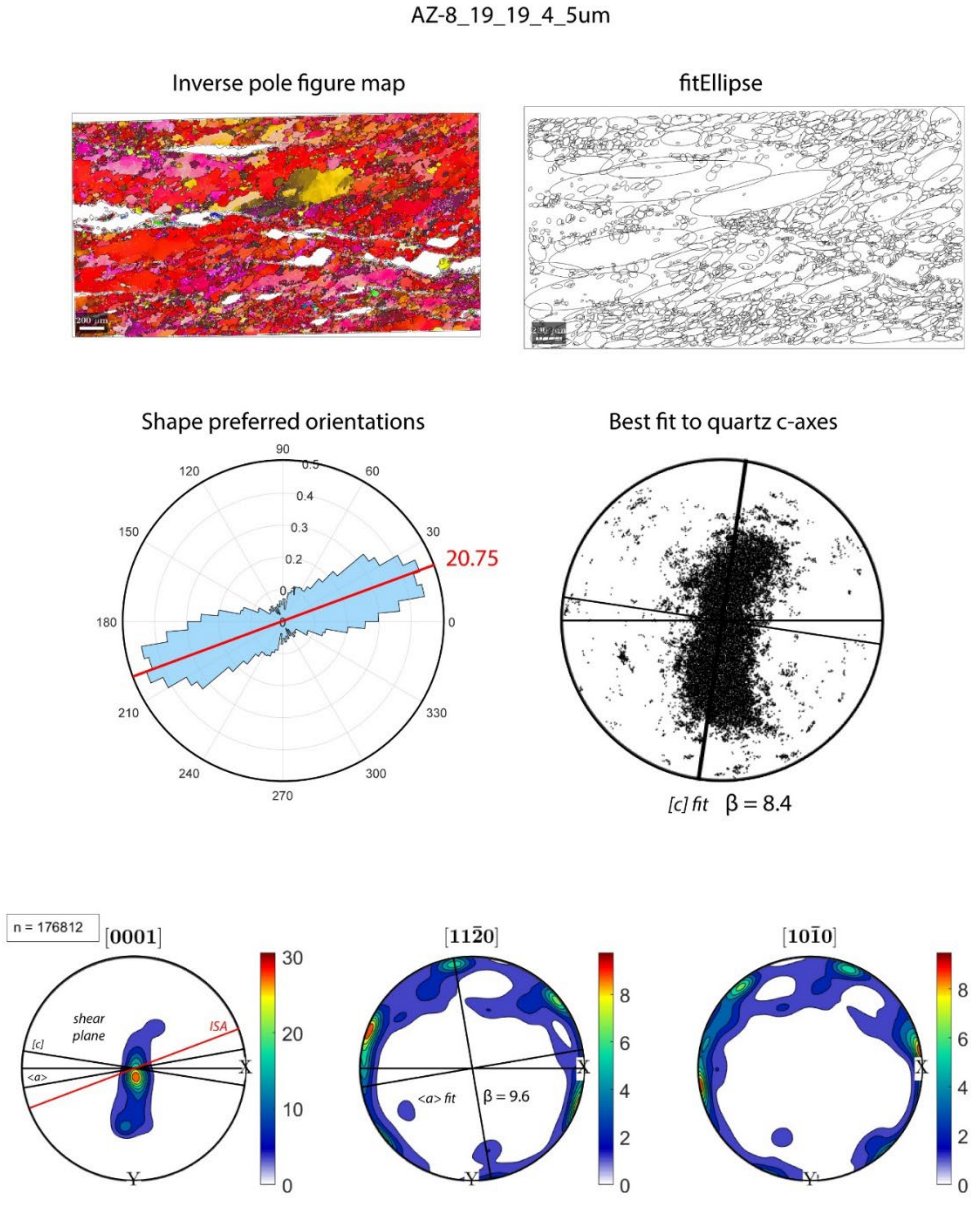

Figure 4.S6. (*continued*)

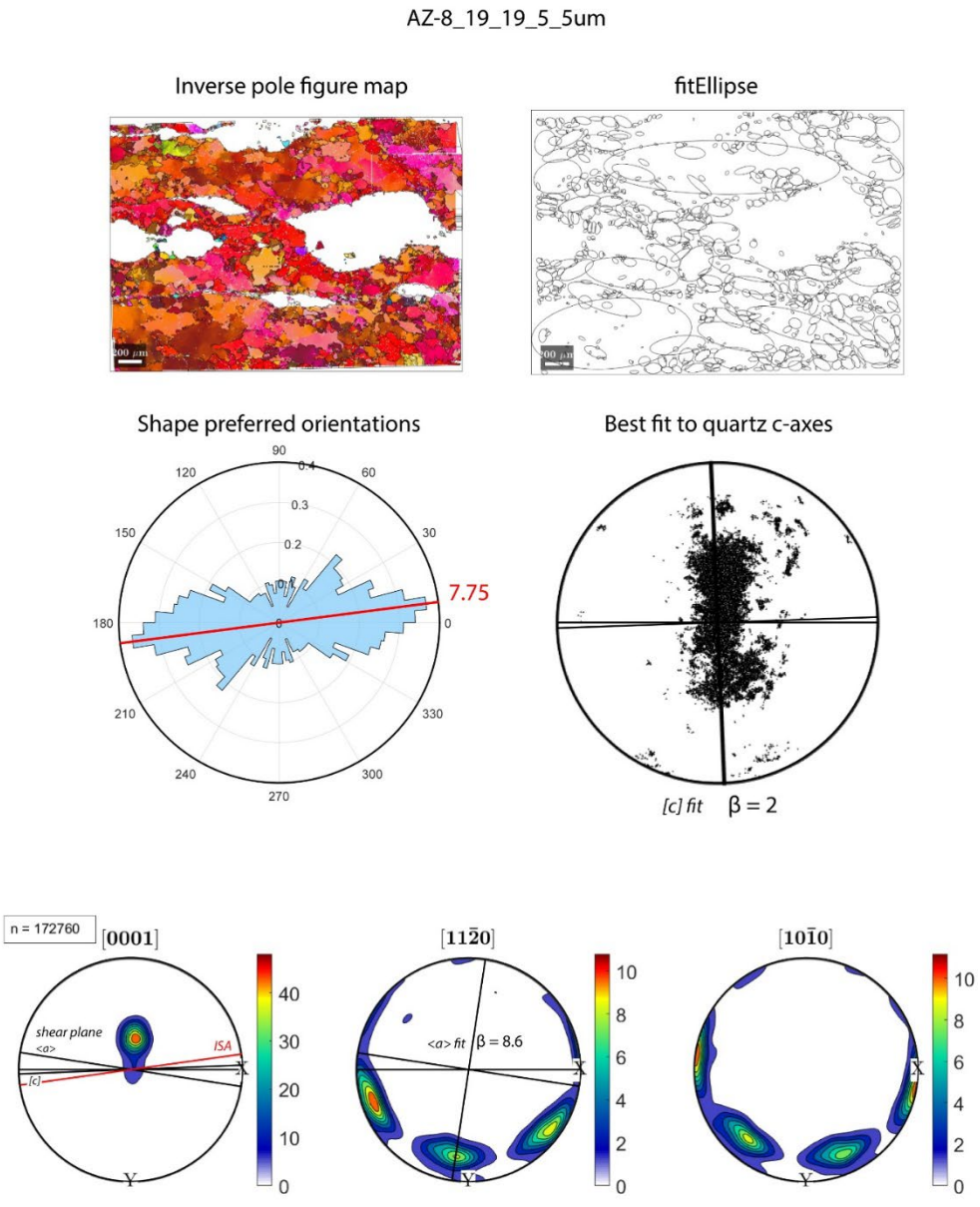

Figure 4.S6. (*continued*)

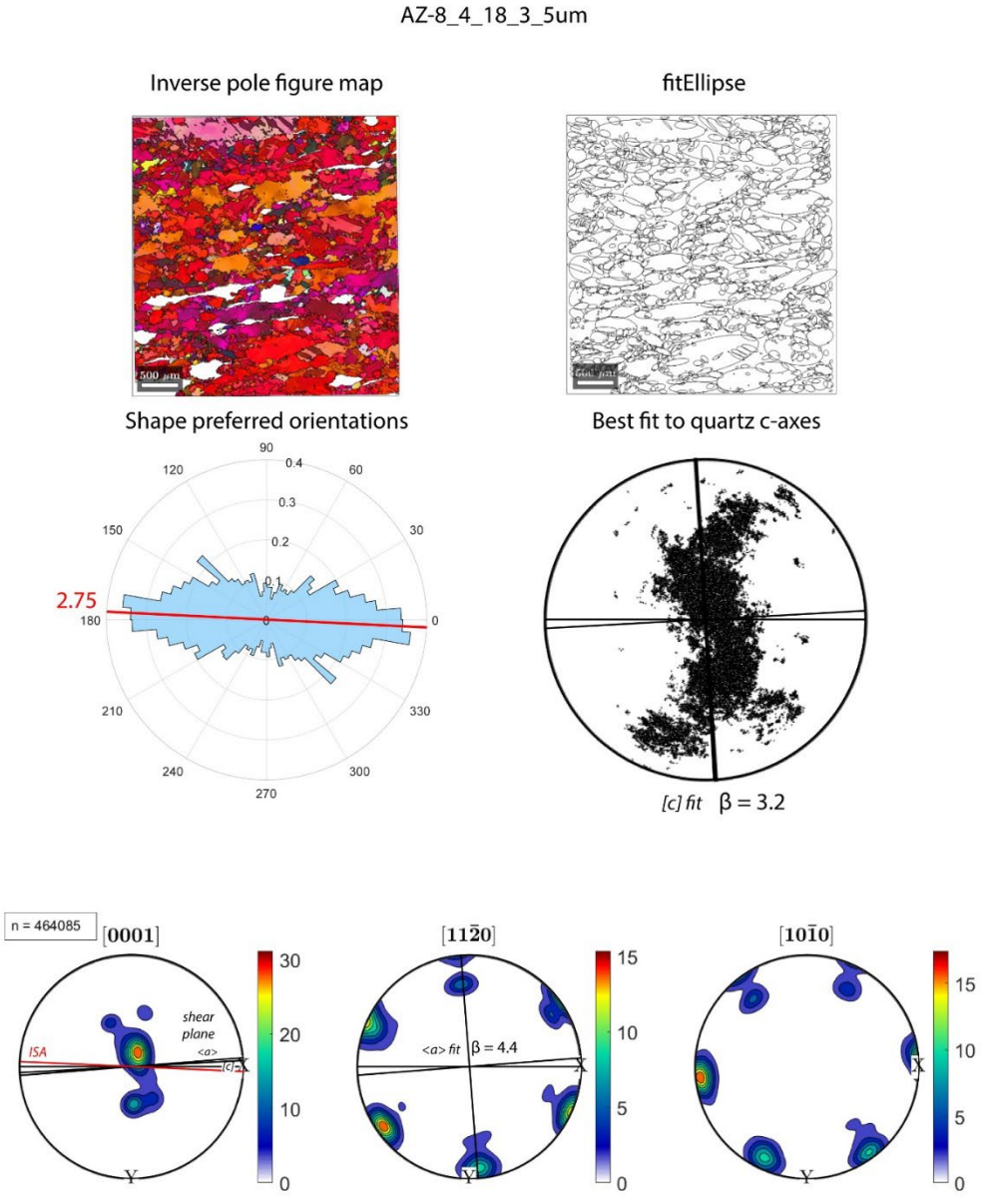

Figure 4.S6. (*continued*)

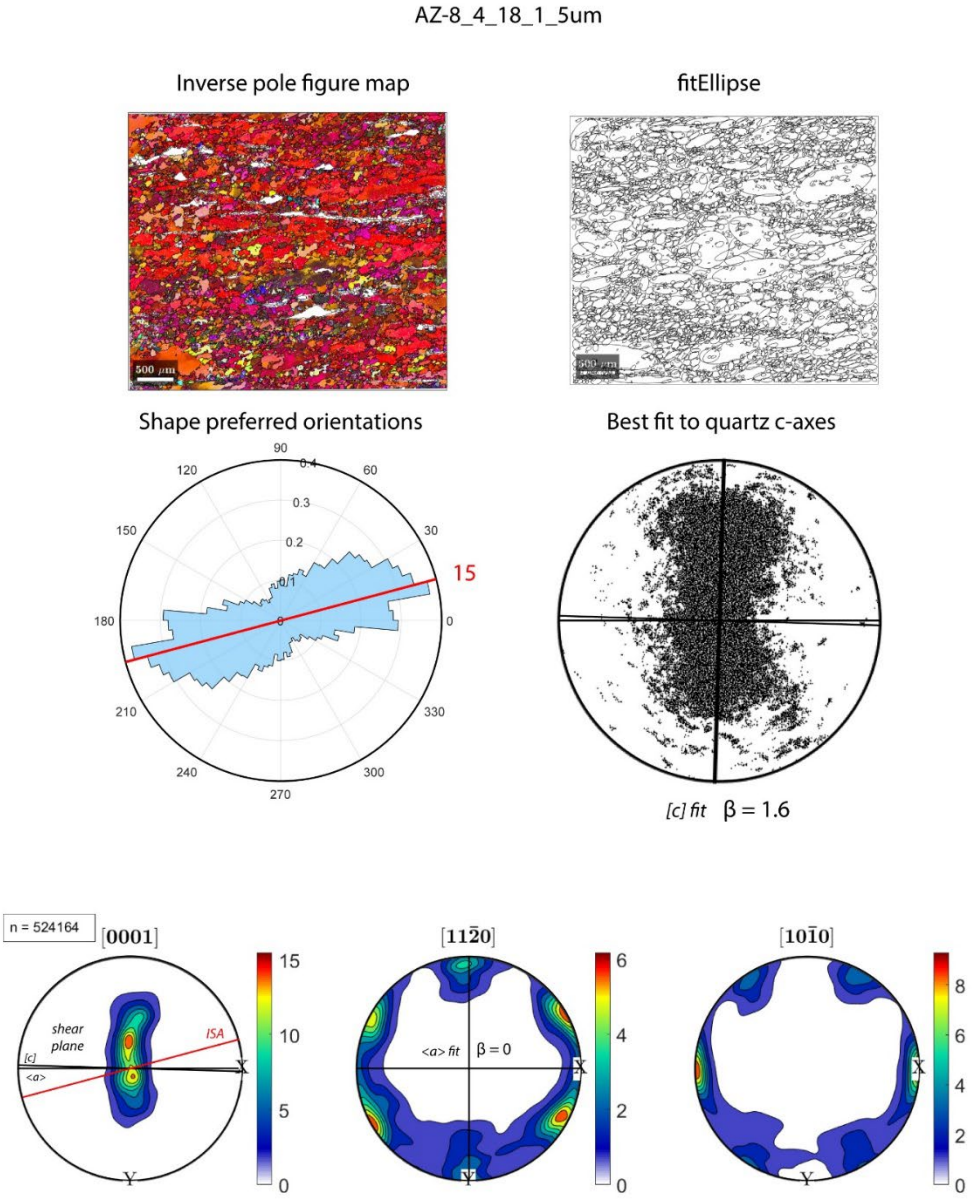

Figure 4.S6. (*continued*)

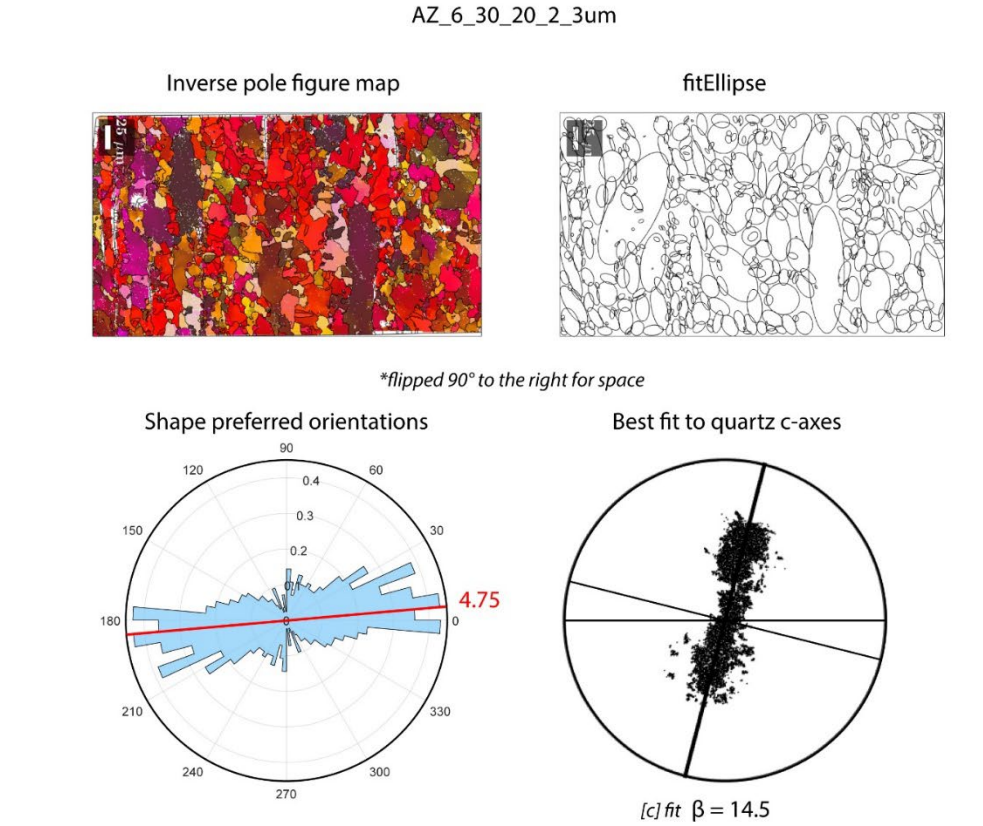

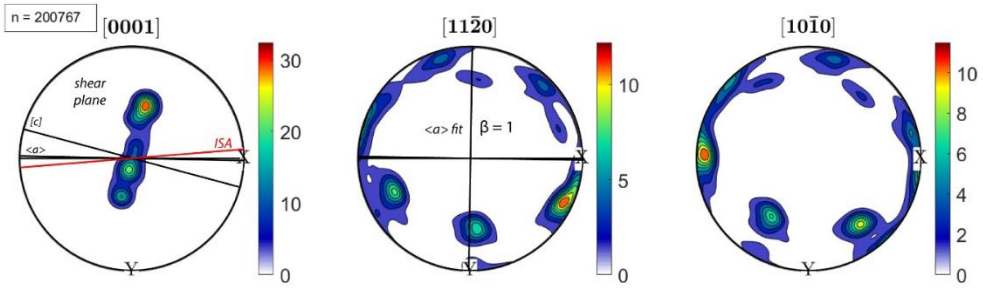

Figure 4.S6. (*continued*)

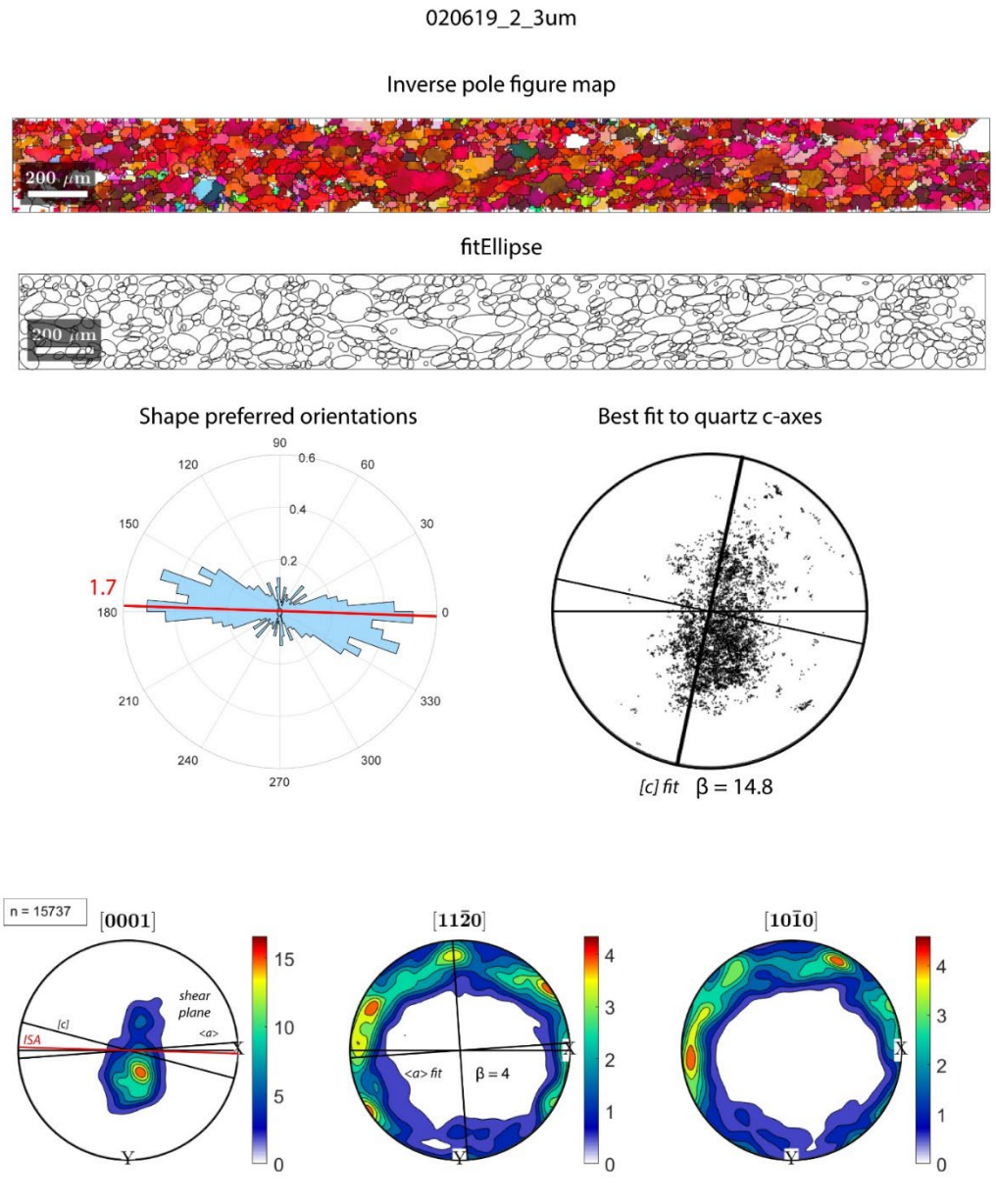

Figure 4.S6. (*continued*)

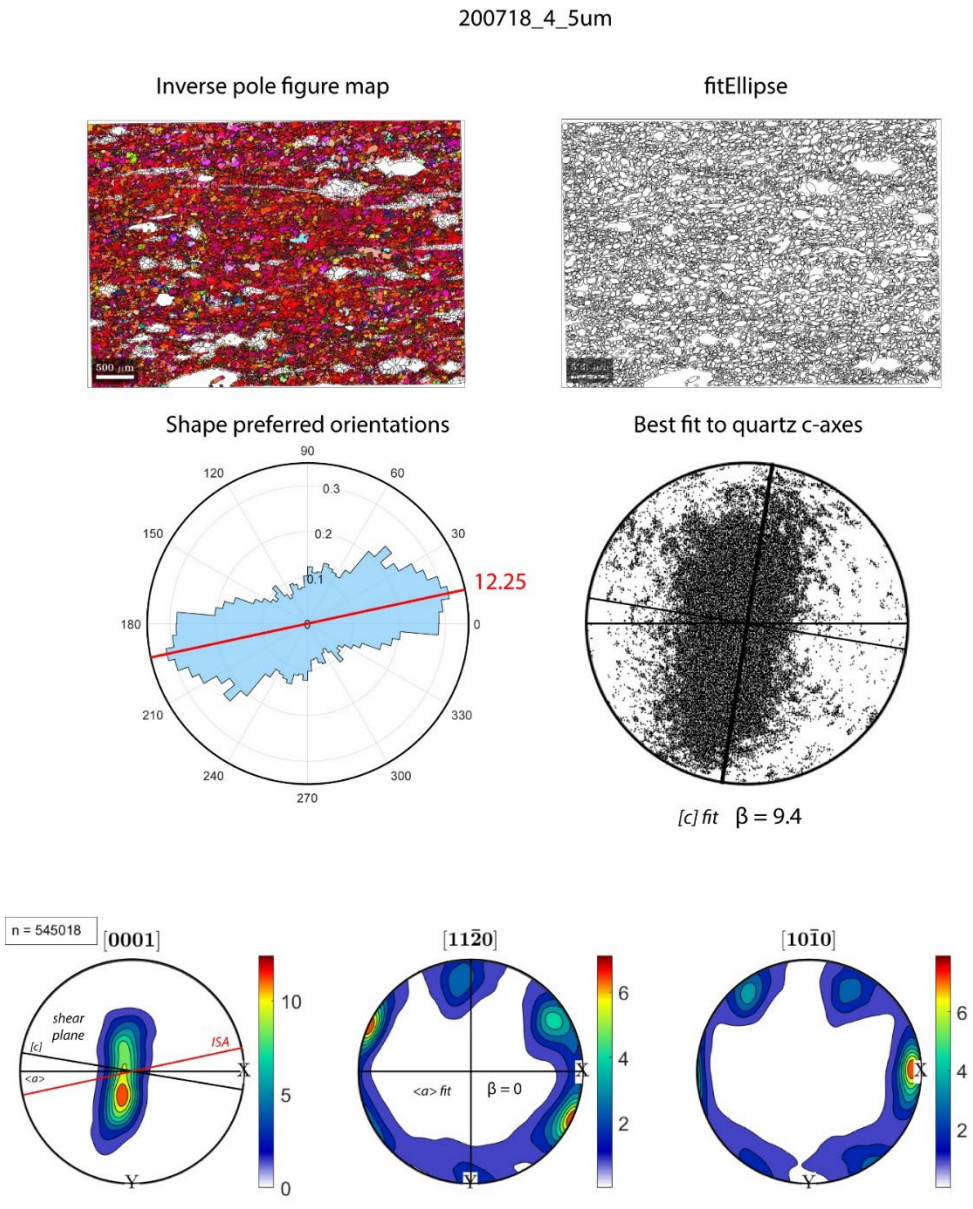

Figure 4.S6. (*continued*)

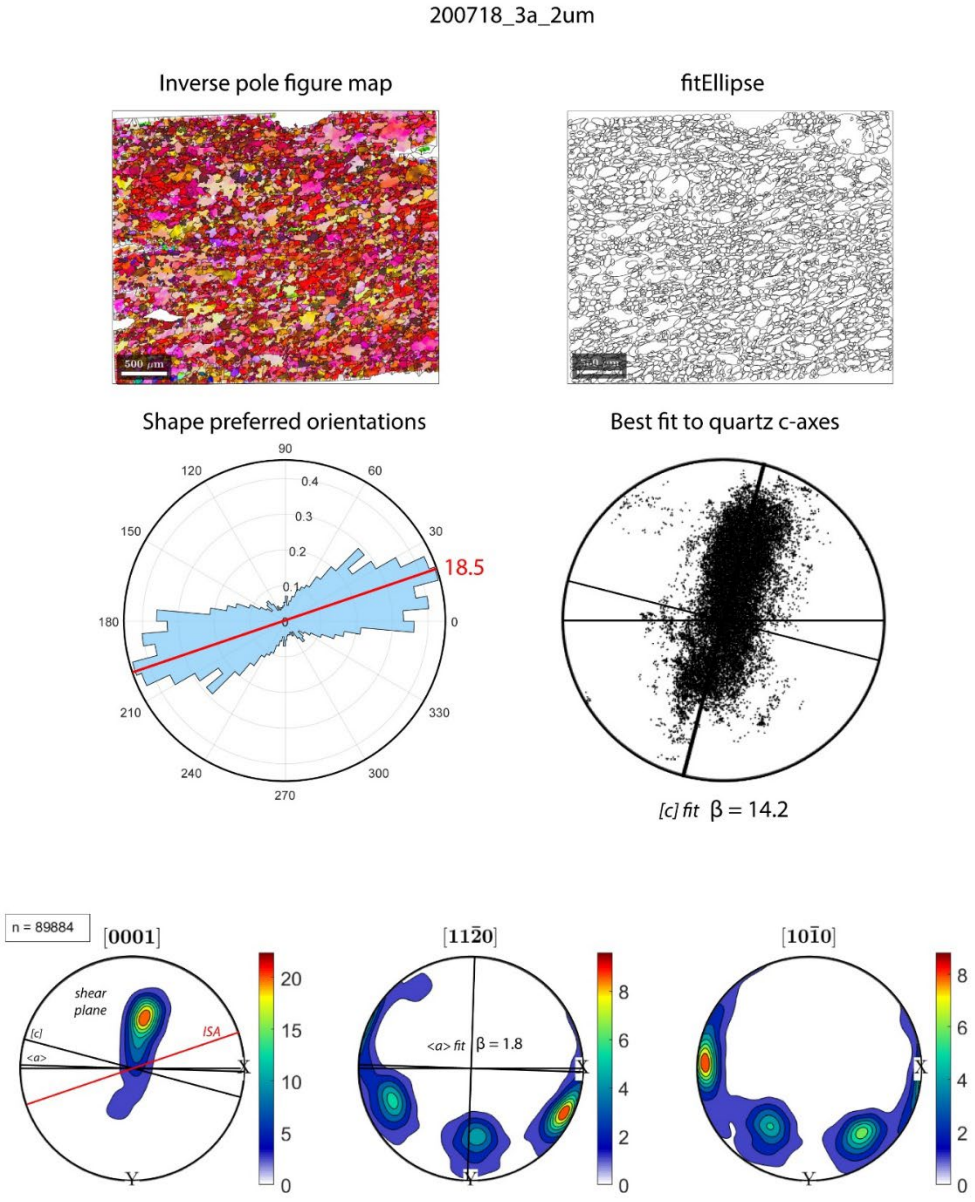

Figure 4.S6. (*continued*)

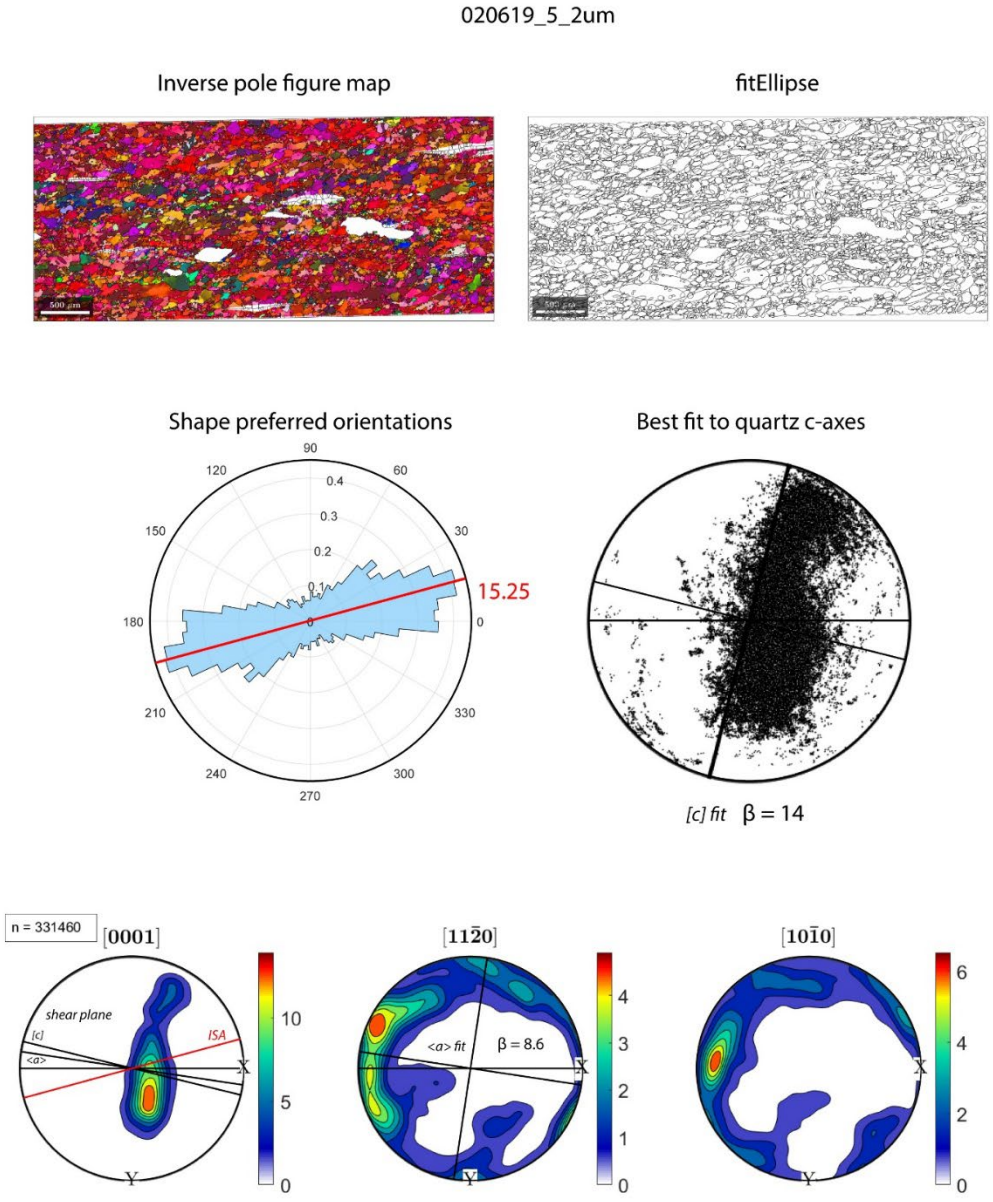

Figure 4.S6. (*continued*)

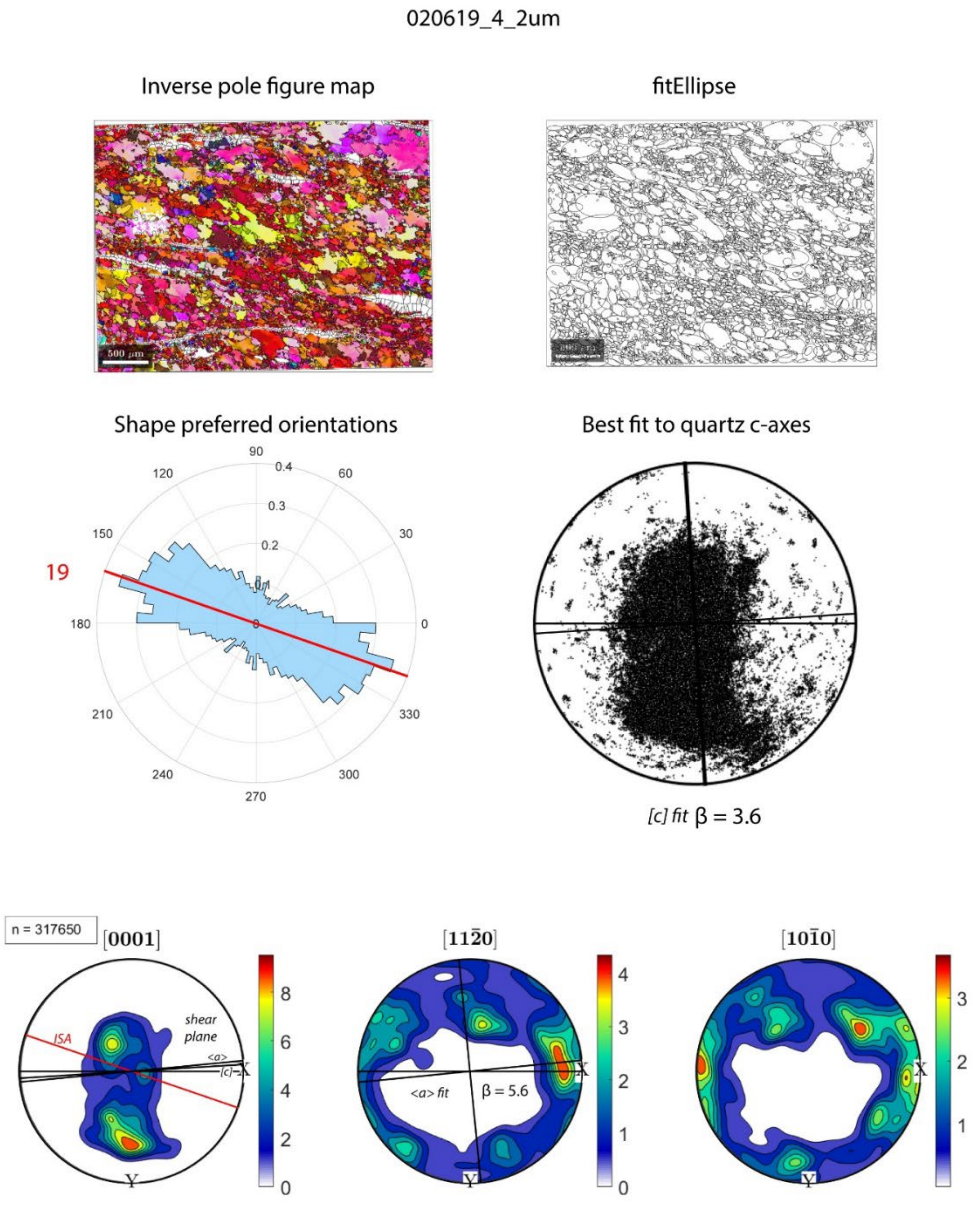

Figure 4.S6. (*continued*)

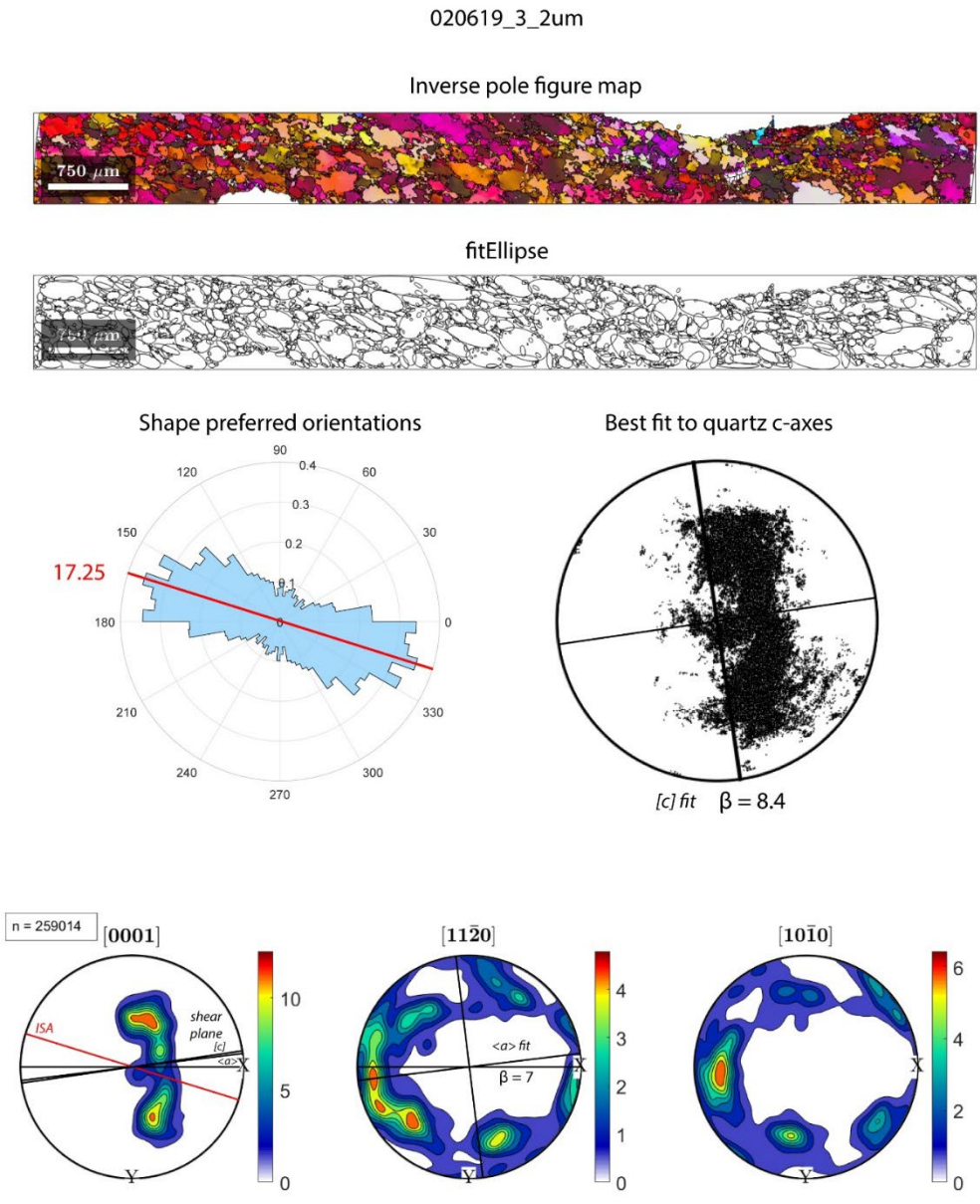

Figure 4.S6. (*continued*)

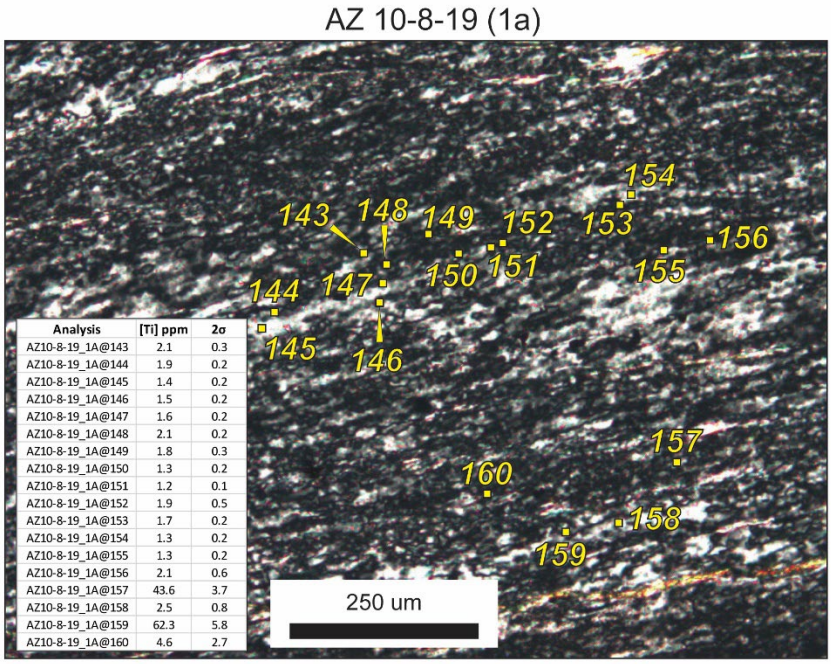

Analysis	[Ti] ppm	2σ
AZ10-8-19_1A@143	2.1	0.3
AZ10-8-19_1A@144	1.9	0.2
AZ10-8-19_1A@145	1.4	0.2
AZ10-8-19_1A@146	1.5	0.2
AZ10-8-19_1A@147	1.6	0.2
AZ10-8-19_1A@148	2.1	0.2
AZ10-8-19_1A@149	1.8	0.3
AZ10-8-19_1A@150	1.3	0.2
AZ10-8-19_1A@151	1.2	0.1
AZ10-8-19_1A@152	1.9	0.5
AZ10-8-19_1A@153	1.7	0.2
AZ10-8-19_1A@154	1.3	0.2
AZ10-8-19_1A@155	1.3	0.2
AZ10-8-19_1A@156	2.1	0.6
AZ10-8-19_1A@157	43.6	3.7
AZ10-8-19_1A@158	2.5	0.8
AZ10-8-19_1A@159	62.3	5.8
AZ10-8-19_1A@160	4.6	2.7

Figure 4.S7. Photomicrographs showing the locations and concentrations of SIMS Ti-in-quartz analyses.

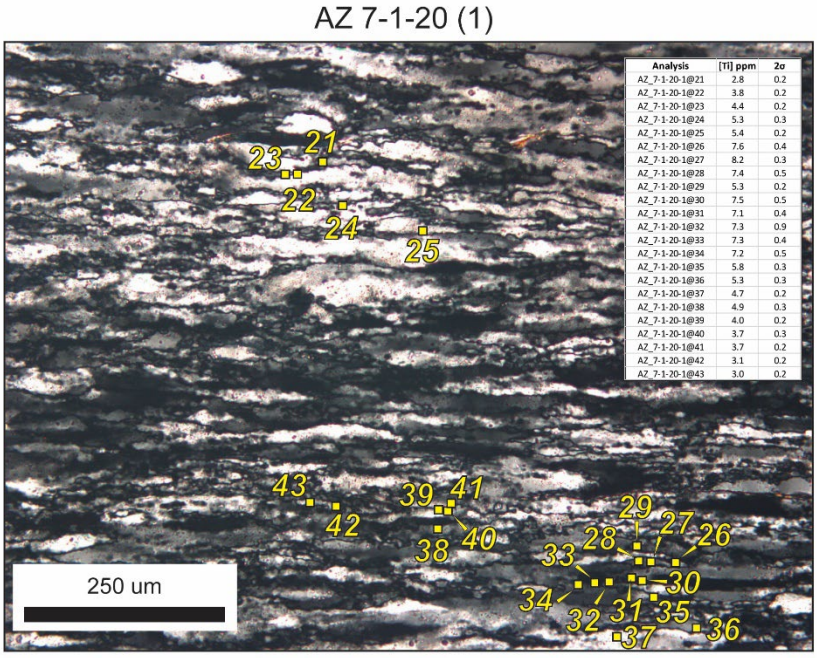

Analysis	[Ti] ppm	2σ
AZ_7-1-20-1@21	2.8	0.2
AZ_7-1-20-1@22	3.8	0.2
AZ_7-1-20-1@23	4.4	0.2
AZ_7-1-20-1@24	5.3	0.3
AZ_7-1-20-1@25	5.4	0.2
AZ_7-1-20-1@26	7.6	0.4
AZ_7-1-20-1@27	8.2	0.3
AZ_7-1-20-1@28	7.4	0.5
AZ_7-1-20-1@29	5.3	0.2
AZ_7-1-20-1@30	7.5	0.5
AZ_7-1-20-1@31	7.1	0.4
AZ_7-1-20-1@32	7.3	0.9
AZ_7-1-20-1@33	7.3	0.4
AZ_7-1-20-1@34	7.2	0.5
AZ_7-1-20-1@35	5.8	0.3
AZ_7-1-20-1@36	5.3	0.3
AZ_7-1-20-1@37	4.7	0.2
AZ_7-1-20-1@38	4.9	0.3
AZ_7-1-20-1@39	4.0	0.2
AZ_7-1-20-1@40	3.7	0.3
AZ_7-1-20-1@41	3.7	0.2
AZ_7-1-20-1@42	3.1	0.2
AZ_7-1-20-1@43	3.0	0.2

Figure 4.S7. (*continued*)

200718-6

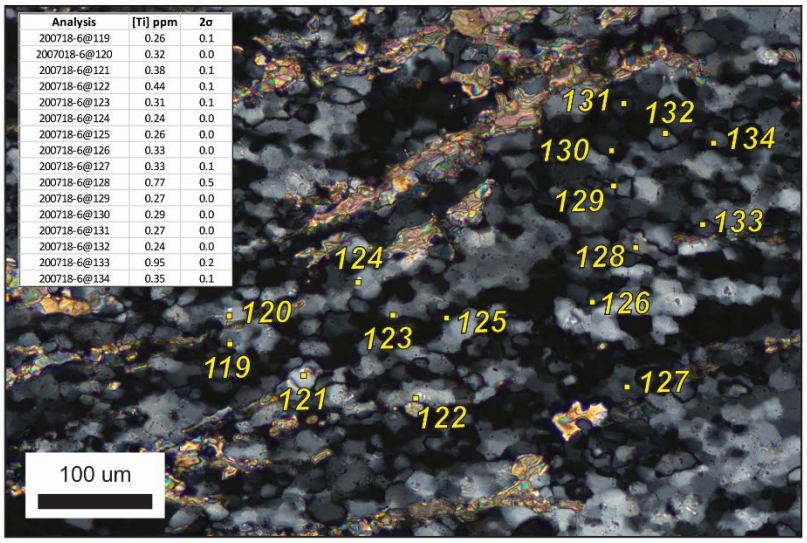

Analysis	[Ti] ppm	2σ
200718-6@119	0.26	0.1
2007018-6@120	0.32	0.0
200718-6@121	0.38	0.1
200718-6@122	0.44	0.1
200718-6@123	0.31	0.1
200718-6@124	0.24	0.0
200718-6@125	0.26	0.0
200718-6@126	0.33	0.0
200718-6@127	0.33	0.1
200718-6@128	0.77	0.5
200718-6@129	0.27	0.0
200718-6@130	0.29	0.0
200718-6@131	0.27	0.0
200718-6@132	0.24	0.0
200718-6@133	0.95	0.2
200718-6@134	0.35	0.1

Figure 4.S7. (*continued*)

AZ 8-4-18 (1)

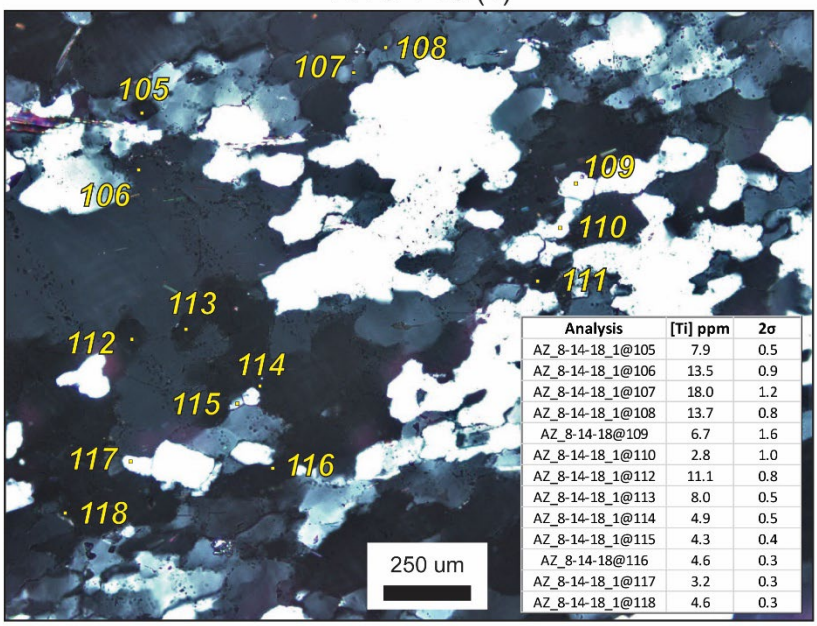

Analysis	[Ti] ppm	2σ
AZ_8-14-18_1@105	7.9	0.5
AZ_8-14-18_1@106	13.5	0.9
AZ_8-14-18_1@107	18.0	1.2
AZ_8-14-18_1@108	13.7	0.8
AZ_8-14-18@109	6.7	1.6
AZ_8-14-18_1@110	2.8	1.0
AZ_8-14-18_1@112	11.1	0.8
AZ_8-14-18_1@113	8.0	0.5
AZ_8-14-18_1@114	4.9	0.5
AZ_8-14-18_1@115	4.3	0.4
AZ_8-14-18@116	4.6	0.3
AZ_8-14-18_1@117	3.2	0.3
AZ_8-14-18_1@118	4.6	0.3

Figure 4.S7. (*continued*)

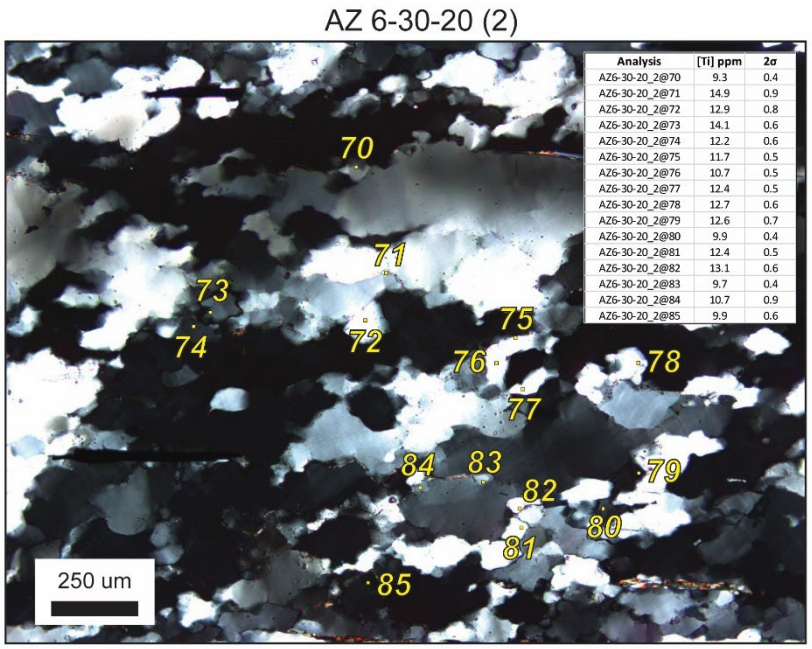

Figure 4.S7. (*continued*)

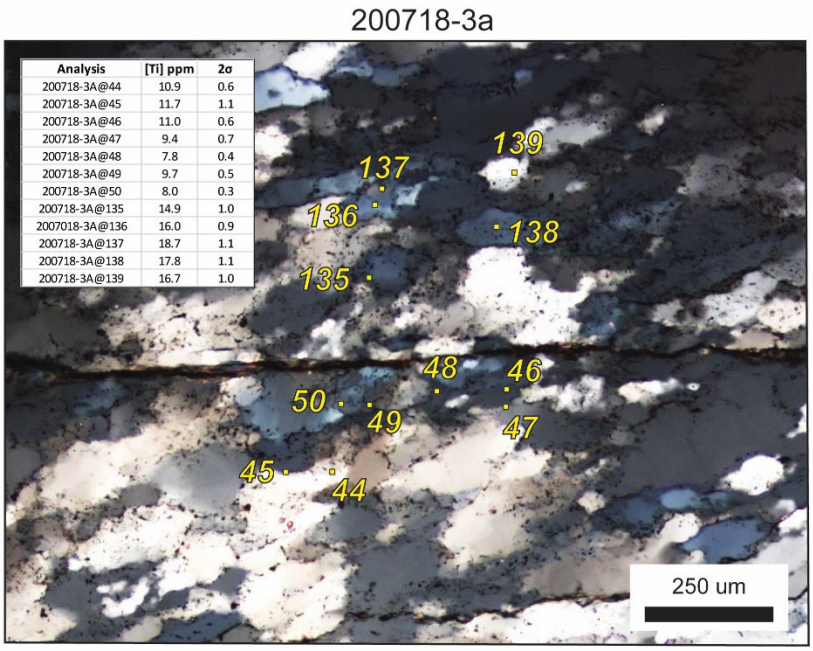

Figure 4.S7. (*continued*)

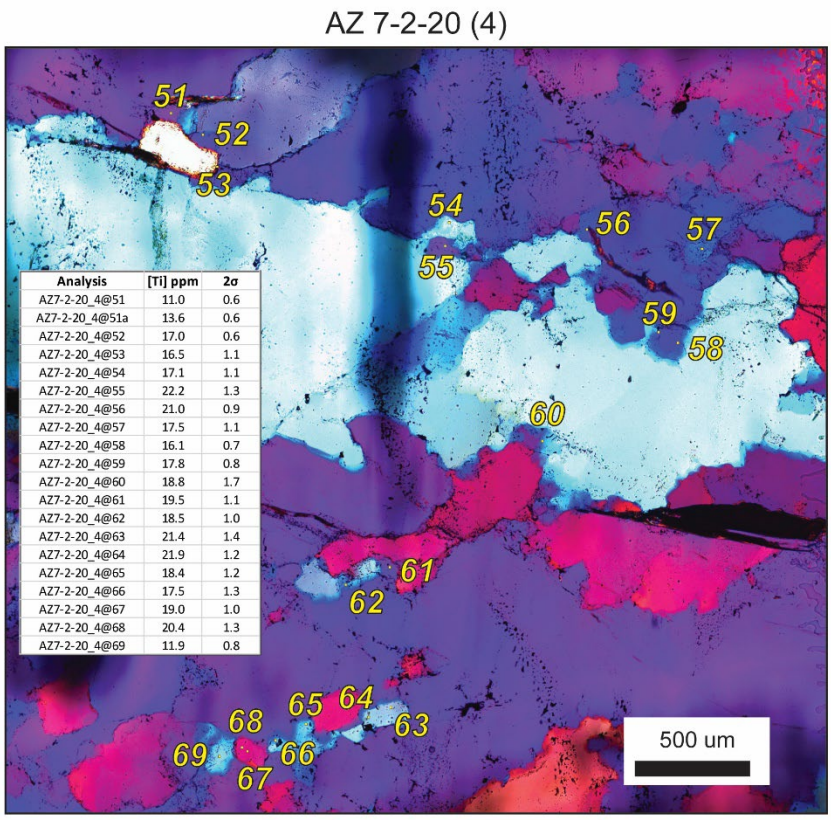

Analysis	[Ti] ppm	2σ
AZ7-2-20_4@51	11.0	0.6
AZ7-2-20_4@51a	13.6	0.6
AZ7-2-20_4@52	17.0	0.6
AZ7-2-20_4@53	16.5	1.1
AZ7-2-20_4@54	17.1	1.1
AZ7-2-20_4@55	22.2	1.3
AZ7-2-20_4@56	21.0	0.9
AZ7-2-20_4@57	17.5	1.1
AZ7-2-20_4@58	16.1	0.7
AZ7-2-20_4@59	17.8	0.8
AZ7-2-20_4@60	18.8	1.7
AZ7-2-20_4@61	19.5	1.1
AZ7-2-20_4@62	18.5	1.0
AZ7-2-20_4@63	21.4	1.4
AZ7-2-20_4@64	21.9	1.2
AZ7-2-20_4@65	18.4	1.2
AZ7-2-20_4@66	17.5	1.3
AZ7-2-20_4@67	19.0	1.0
AZ7-2-20_4@68	20.4	1.3
AZ7-2-20_4@69	11.9	0.8

Figure 4.S7. (*continued*)

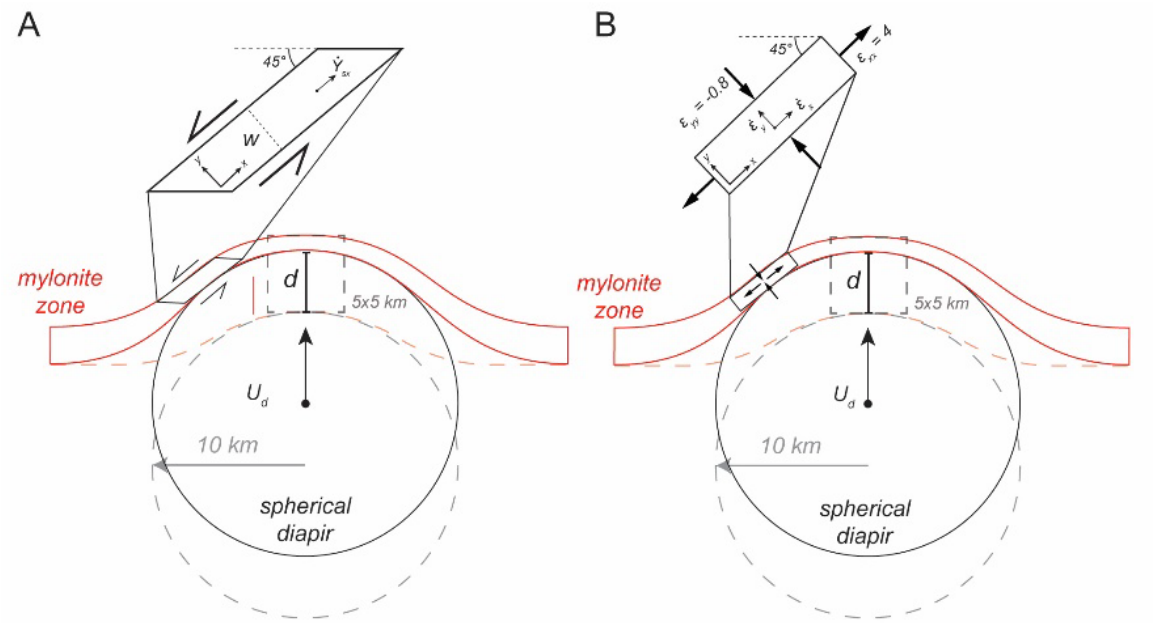

Figure 4.S8. Geometry of Stokes flow diapir ascent velocity and shear zone orientation for the simple shear (A) and pure shear (B) zones.

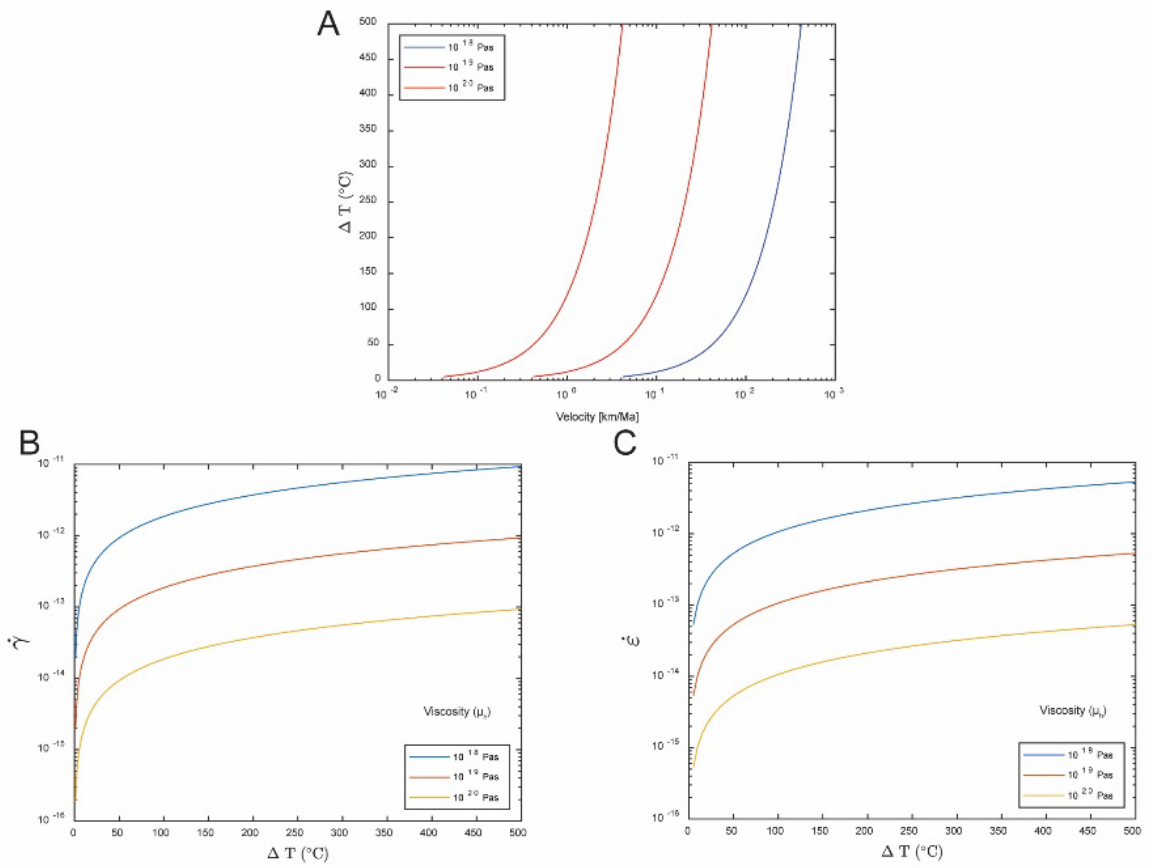

Figure 4.S9. Temperature-driven Stokes flow model results. A) Plot of velocity as a function of ΔT for three viscosity cases. B) Plot of simple shear strain rate as a function of ΔT for three viscosity cases. C) Plot of pure shear strain rate as a function of ΔT for three viscosity cases.

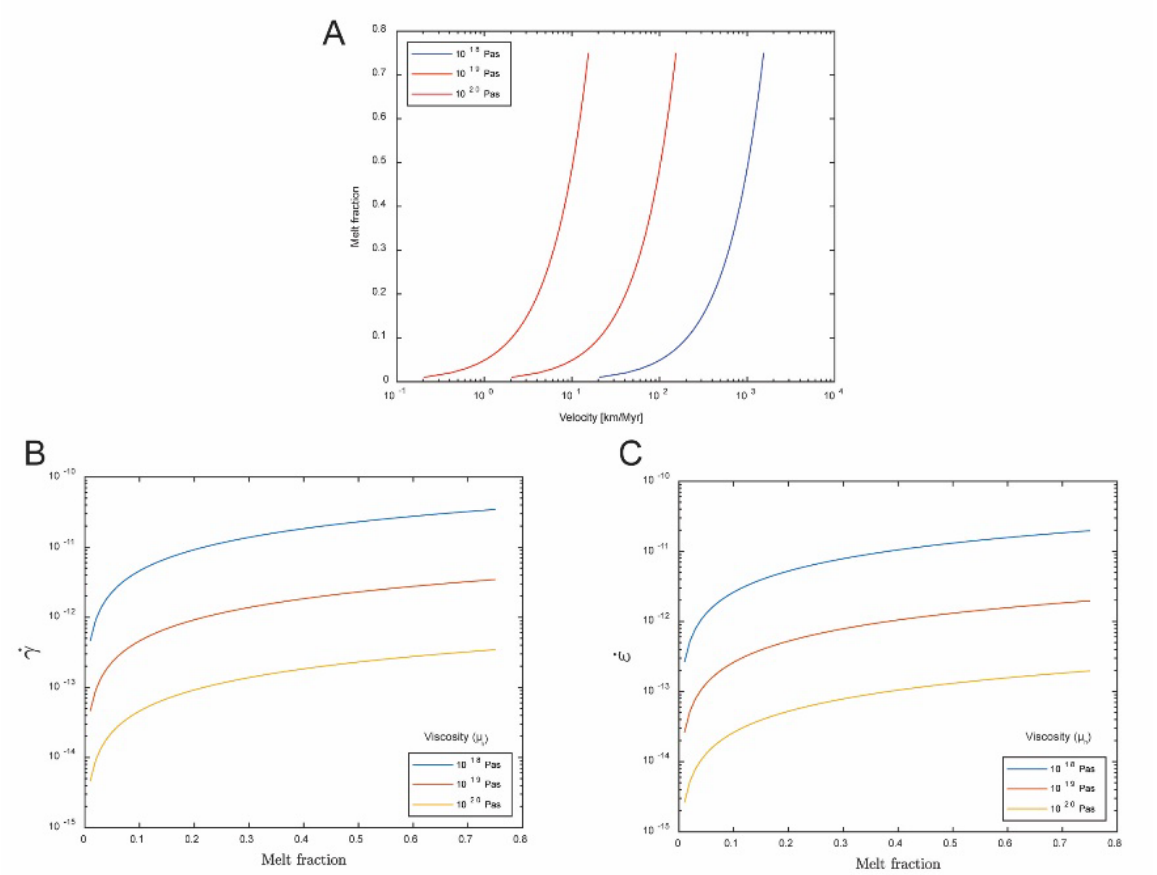

Figure 4.S10. Density-driven Stokes flow model results. A) Plot of velocity as a function of melt fraction for three viscosity cases. B) Plot of simple shear strain rate as a function of melt fraction for three viscosity cases. C) Plot of pure shear strain rate as a function of melt fraction for three viscosity cases.

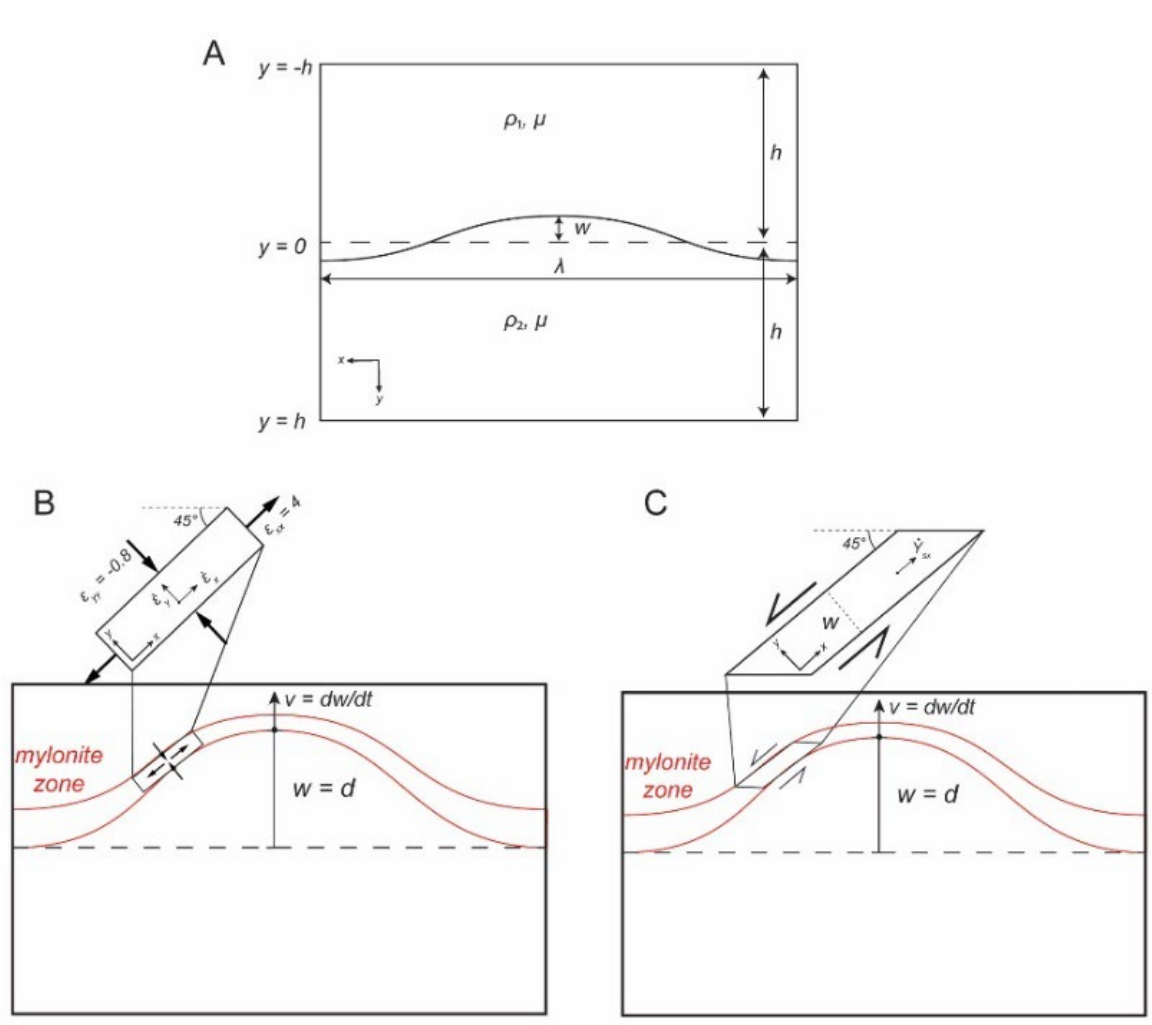

Figure 4.S11. Geometry of Rayleigh-Taylor diapir ascent velocity and shear zone orientation for the pure shear (B) and simple shear (C) zones.

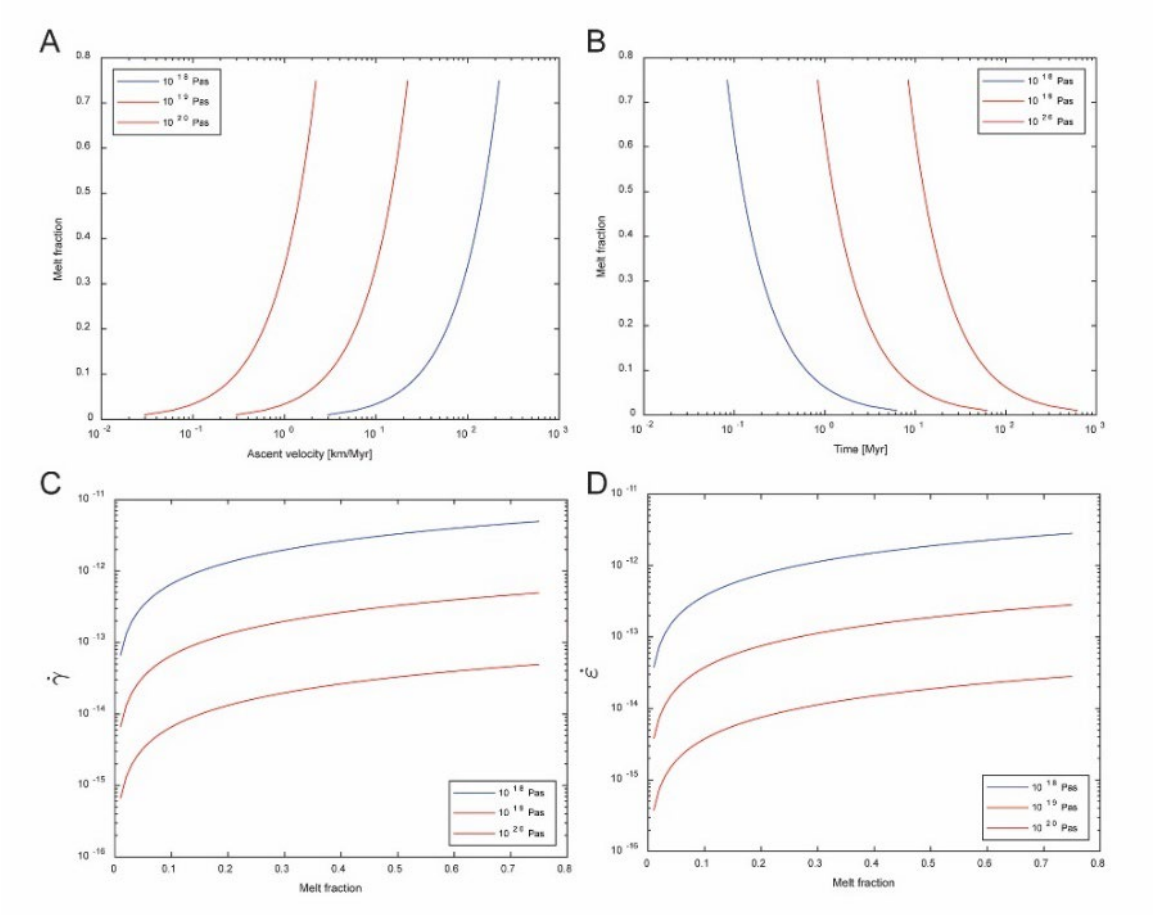

Figure 4.S12. Rayleigh-Taylor diapir model results. A) Plot of velocity as a function of melt fraction for three viscosity cases. B) Plot of diapir growth time as a function of melt fraction for three viscosity cases. C) Plot of simple shear strain rate as a function of melt fraction for three viscosity cases. D) Plot of pure shear strain rate as a function of melt fraction for three viscosity cases.

CHAPTER 5: Conclusion

CRUSTAL THICKENING AND POST-OROGENIC EXTENSION IN THE NORTH AMERICAN CORDILLERA

The U.S. section of the North American Cordillera preserves a series of thrust belts (i.e., Last Chance thrusts system, Luning-Fencemaker thrust belt, Central Nevada thrust belt, Elko thrust belt, Sevier fold-thrust belt) developed during Permian-Eocene subduction and accretionary orogenesis (e.g., DeCelles, 2004). These thrust belts accommodated east-propagating crustal shortening that culminated in the establishment of the Sevier fold-thrust belt during the Early Cretaceous-Eocene (e.g., Yonkee and Weil, 2015). Whereas the Sevier fold-thrust belt accommodated the majority of retroarc shortening (e.g., DeCelles and Coogan, 2006), it is apparent that the Sevier hinterland remained largely inactive following the Jurassic (e.g., Zuza et al., 2020). The Middle-Late Jurassic Elko thrust belt of northeast Nevada thus represents a key episode of crustal shortening and thrust burial in the development of the hinterland (e.g., Zuza et al., 2021). The presence of the Elko thrust belt was important in controlling the initial geometry of Cenozoic extension in the hinterland, however Eocene-Oligocene magmatism and metamorphic core complex development localized large-magnitude Middle Miocene extension. Such regional observations provide important insight into orogen scale interpretations of the timescales and mechanisms of orogenic growth and collapse.

Timescales and mechanisms of crustal thickening

The exposure of amphibolite facies metamorphic rocks within metamorphic core complexes of the Sevier hinterland is interpreted to suggest thrust burial of the passive margin sequence to depths >20 km (e.g., Hodges et al., 1992; Lewis et al., 1999; McGrew et al., 2000; Hoisch et al., 2002; Cooper et al., 2010; Hallett and Spear, 2014). Whereas the magnitude of shortening in the Sevier fold-thrust belt could accommodate this magnitude of burial (e.g., DeCelles and Coogan, 2006), the rocks exposed in the hinterland are structurally above the basal décollement of the Sevier belt inferred to underlie the hinterland (e.g., Oldow, 1984). Within the hinterland, field mapping, analysis of Mesozoic erosion patterns, and structural reconstructions have failed to identify contractional structures capable of burying the hinterland rocks greater than a few km below stratigraphic

depth (e.g., Armstrong, 1968; Gans et al., 1983; Miller and Hoisch, 1995; Long, 2012, 2019; Zuza et al., 2021; Chapter 4). The dichotomy between metamorphic conditions and regional field relationships calls into question the timing, magnitude and mechanism of hinterland crustal thickening.

To address this question, Chapter 4 presented a new structural reconstruction of extension in the Elko extensional domain, northeast Nevada, to evaluate the kinematics and magnitude of crustal shortening within the Sevier hinterland. The results illustrate Middle-Late Jurassic shortening was accommodated by a system of southeast directed thrust faults exhibiting imbricate- and fault-bend-fold geometries. The thrust system merged at depth into a regional décollement localized in the lower Cambrian section accommodating ~12 km (~ 20% strain) of shortening from Pequop Mountains to the Silver Island Mountains. An additional 25 km of shortening may have been accommodated by thrust faults beyond the study area indicating ~40 km of total shortening across northeast Nevada (e.g., Zuza et al., 2021). Structural burial during shortening was restricted to stratigraphic sections below footwall ramps and did not exceed 5 km across the study area.

These observations indicate minimal burial of the hinterland section during the Mesozoic, which requires alternative models to account for the metamorphic facies exposed in the core complexes, such as complete erosion or excision of addition thrust faults during subsequent extension (Camilleri and Chamberlain, 1997), or tectonic overpressure (Zuza et al., 2022; Hoiland, et al., 2022). Whereas new geological mapping, structural analysis and thermometry have provided strong evidence against the model of complete erosion or excision of hinterland thrust sheets (Zuza et al., 2020, 2021), the tectonic overpressure model is challenging to test given the extensive overprinting of Mesozoic metamorphic rocks during Cenozoic magmatism, metamorphism and extension. Furthermore, alternative models are required to explain the generation of Late Cretaceous leucogranites during orogen-scale crustal anatexis, such as relaxation of isotherms, heating or fluid flux from the mantle, or melting of underthrust metapelites below the basal décollement (Miller and Gans, 1989; Wells et al., 2012; Chapman et al., 2021; Gottlieb et al., 2022).

The paucity of evidence for upper crustal thickening of the Sevier hinterland requires any Mesozoic thickening to have occurred in the lower crust. Evaluating the magnitude of lower crustal thickening is challenging given basement rocks are not exposed in the hinterland. Geochemical proxies from crustal thickness have been used to infer 55-65 km thick crust from Sr/Y ratios in Jurassic-Cretaceous granitic rocks of the Sevier hinterland (Chapman et al., 2015). A simple solution allows lower crustal thickening to result from westward underthrusting of unrifted North American basement below the basal Sevier décollement (DeCelles and Coogan, 2006). Greater than 200 km of shortening within the Sevier fold-thrust belt must be kinematically balanced by westward transport of the lower crust. In addition to providing a mechanism for at least 10 km of thickening, this model can explain orogen scale patterns of deformation and magmatism modulated by episodic high-flux magmatic events fueled by melting of lower crustal rocks underthrust beneath the magmatic arc (e.g., DeCelles et al., 2009). A complimentary view of upper to lower crustal processes during Jurassic-Eocene orogenic growth provides a foundation for evaluating the history of post-orogenic extension in the North American Cordillera.

Timescales and mechanisms of post-orogenic extension

The development of the Basin and Range province marks the end of Mesozoic-Early Cenozoic orogeny in the Sevier orogenic belt. Two aspects of the Basin and Range suggest the crustal structure of the Sevier orogenic belt influenced the evolution of post-orogenic extension: the spatial extent of Cenozoic extension is largely confined within the boundaries of the magmatic arc to the west and the Sevier fold-thrust belt to the east (e.g., Wernicke, 1992), and the metamorphic core complexes are primarily within the Sevier hinterland aligned along the inferred axis of maximum crustal thickness (e.g., Crittenden et al., 1980). The metamorphic core complexes are generally considered expressions of initial large-magnitude crustal extension within the Sevier hinterland, which led to the model that they developed during gravitational collapse of an overthickened hinterland crustal section (Coney and Harms, 1984). Widespread crustal extension across the Sevier hinterland initiated later, during the Middle Miocene, likely due to growth of the Pacific-North American transform margin, as well as components of internal body forces, Farallon slab dynamics or volcanism (e.g., Sonder and Jones, 1999; Colgan and Henry, 2009). The

significance of metamorphic core complexes in this extensional evolution relies on the timing, mechanism, and magnitude of extension (e.g., Wernicke, 1981; Miller et al., 1983, 1999; Wells et al., 2000; Konstantinou et al., 2012), and an understanding of the pre-existing crustal structure within the Sevier hinterland (e.g., Coney and Harms, 1984; Long, 2019).

Chapter 4 and 5 of this dissertation investigated the significance of metamorphic core complexes within the Elko extensional domain. The results of these studies detailed the kinematics of initial hinterland extension, and found the presence of pre-existing structures influenced the style of extension. Within the Pilot-Toano ranges, initial extension was accommodated along the brittle Pilot Peak detachment fault, which reactivated the Middle-Late Jurassic Elko thrust belt. Extensional reactivation of the sub-horizontal thrust décollement limited footwall exhumation during this episode, which likely ceased as continued slip on a low-angle fault became mechanically unstable (e.g., Collettini, 2011). Range bounding high-angle normal faults accommodated final exhumation and unroofing of the Pilot Peak detachment footwall. Thermochronology and cross-cutting relationships constrain slip on the Pilot Peak detachment to the Oligocene(?)-middle Miocene, with final exhumation and unroofing completed by 12.9 Ma. The extensional evolution of the Pilot-Toano ranges reflects primarily brittle processes, with the deepest structural levels in the Pilot Range preserved mylonitic rocks indicating late Oligocene deep ductile flow decoupled from detachment faulting higher in the crust. The exposure of pervasive Oligocene mylonites in the Ruby Mountains-East Humboldt Range (REH) metamorphic core complex suggests drastically difference mechanisms of extension just ~70 km to the west.

The Cenozoic development of the REH metamorphic core complex is characterized by Eocene to Oligocene (40-29 Ma) magmatism, mid-crustal flow and the 29-23 Ma mylonitic shear zone (Wright and Snoke, 1993; MacCready et al., 1997). Field relationships indicate the mylonite zone accommodated >80% attenuation of the Neoproterozoic-Mississippian metasedimentary section. Microstructural analysis of quartzite samples from across the mylonite zone yields estimates of kinematic vorticity consistent with pure-shear dominated strain, or general shear. Integrating field, microstructural and thermometry results indicate

ductile shear took place at amphibolite facies conditions (>500 °C) and rapid strain rates (10^{-13} to 10^{-11} s^{-1}). The development of the mylonite zone ~10 Myr before extensional exhumation of the REH suggests decoupling between ductile deformation and brittle upper crustal extension. The kinematics and conditions of ductile shear in the REH metamorphic core complex are compatible with a model whereby buoyant doming due to thermal expansion or increased melt volume drove vertical ascent of a mid-crustal gneiss dome; dome ascent was accommodated by ductile attenuation within the mylonite zone. The development of the mylonitic shear zone localized later extensional exhumation, which took advantage of the pre-existing preferred orientation fabric and the presence of high-strain metapelites.

The new model for the development of the REH metamorphic core complex presented in Chapter 5 suggests the REH represents vertical crustal flow during magmatism similar to models for migmatite-cored gneiss domes (e.g., Whitney et al., 2004). Furthermore, this model does not attribute the mylonitic shear zone to ductile strain along the down-dip segment of a low-angle normal fault (e.g., Wernicke, 1981), which minimizes the amount of extension required to exhume the ductile metamorphic core (e.g., Miller et al., 1983). The timing of ductile shear and brittle extensional exhumation of the REH is incompatible with models of early extension within the metamorphic core complexes driven by gravitational collapse of overthickened hinterland crust (e.g., Coney and Harms, 1984). The above discussion of crustal thickening within the Sevier hinterland points to a largely uniform crustal thickness following Mesozoic shortening (e.g., Colgan and Henry, 2009; Long, 2019). The metamorphic core complexes within the Sevier hinterland may thus reflect areas of focused Eocene-Oligocene heating.

REFERENCES

Armstrong, R.L., 1968, Sevier Orogenic Belt in Nevada and Utah: Geological Society of America Bulletin, v. 79, p. 429, doi:10.1130/0016-7606(1968)79[429:SOBINA]2.0.CO;2.

Camilleri, P.A., and Chamberlain, K.R., 1997, Mesozoic tectonics and metamorphism in the Pequop Mountains and Wood Hills region, northeast Nevada: Implications for the architecture and evolution of the Sevier orogen: GSA Bulletin, v. 109, p. 74–94, doi:10.1130/0016-7606(1997)109<0074:MTAMIT>2.3.CO;2.

Chapman, J.B. et al., 2021, The North American Cordilleran Anatectic Belt: Earth-Science Reviews, v. 215, p. 103576, doi:10.1016/j.earscirev.2021.103576.

Chapman, J.B., Ducea, M.N., DeCelles, P.G., and Profeta, L., 2015, Tracking changes in crustal thickness during orogenic evolution with Sr/Y: An example from the North American Cordillera: Geology, v. 43, p. 919–922, doi:10.1130/G36996.1.

Colgan, J.P., and Henry, C.D., 2009, Rapid middle Miocene collapse of the Mesozoic orogenic plateau in north-central Nevada: International Geology Review, v. 51, p. 920–961, doi:10.1080/00206810903056731.

Collettini, C., 2011, The mechanical paradox of low-angle normal faults: Current understanding and open questions: Tectonophysics, v. 510, p. 253–268, doi:10.1016/j.tecto.2011.07.015.

Coney, P.J., and Harms, T.A., 1984, Cordilleran metamorphic core complexes: Cenozoic extensional relics of Mesozoic compression: Geology, v. 12, p. 550–554, doi:10.1130/0091-7613(1984)12<550:CMCCCE>2.0.CO;2.

Cooper, F.J., Platt, J.P., Anczkiewicz, R., and Whitehouse, M.J., 2010, Footwall dip of a core complex detachment fault: thermobarometric constraints from the northern Snake Range (Basin and Range, USA): Journal of Metamorphic Geology, v. 28, p. 997–1020, doi:10.1111/j.1525-1314.2010.00907.x.

Crittenden, M.D., Coney, P.J., and Davis, G.H. (Eds.), 1980, Cordilleran metamorphic core complexes: Boulder, Colo, Geological Society of America, Memoir - The Geological Society of America 153, 490 p.

DeCelles, P.G., 2004, Late Jurassic to Eocene evolution of the Cordilleran thrust belt and foreland basin system, western U.S.A.: American Journal of Science, v. 304, p. 105–168, doi:10.2475/ajs.304.2.105.

DeCelles, P.G., and Coogan, J.C., 2006, Regional structure and kinematic history of the Sevier fold-and-thrust belt, central Utah: Geological Society of America Bulletin, p. 24.

DeCelles, P.G., Ducea, M.N., Kapp, P., and Zandt, G., 2009, Cyclicity in Cordilleran orogenic systems: Nature Geoscience, v. 2, p. 251–257, doi:10.1038/ngeo469.

Gans, P.B., Miller, E.L. and Gurgel, K.D., 1983. Style of mid-Tertiary extension in east-central Nevada. Geological excursions in the overthrust belt and metamorphic core

complexes of the Intermountain region: Utah Geological and Mineral Survey Special Studies, v. 59, p.107-139.

Gottlieb, E.S., Miller, E.L., Valley, J.W., Fisher, C.M., Vervoort, J.D., and Kitajima, K., 2022, Zircon petrochronology of Cretaceous Cordilleran interior granites of the Snake Range and Kern Mountains, Nevada, USA, in Craddock, J.P., Malone, D.H., Foreman, B.Z., and Konstantinou, A. eds., Tectonic Evolution of the Sevier-Laramide Hinterland, Thrust Belt, and Foreland, and Postorogenic Slab Rollback (180–20 Ma), Geological Society of America, doi:10.1130/2022.2555(02).

Hallett, B.W., and Spear, F.S., 2014, The P–T History of Anatectic Pelites of the Northern East Humboldt Range, Nevada: Evidence for Tectonic Loading, Decompression, and Anatexis: Journal of Petrology, v. 55, p. 3–36, doi:10.1093/petrology/egt057.

Hodges, K.V., Snoke, A.W., and Hurlow, H.A., 1992, Thermal evolution of a portion of the Sevier Hinterland: The Northern Ruby Mountains-East Humboldt Range and Wood Hills, northeastern Nevada: Tectonics, v. 11, p. 154–164, doi:10.1029/91TC01879.

Hoiland, C., Hourigan, J., and Miller, E., 2022, Evidence for large departures from lithostatic pressure during Late Cretaceous metamorphism in the northern Snake Range metamorphic core complex, Nevada, in Craddock, J.P., Malone, D.H., Foreman, B.Z., and Konstantinou, A. eds., Tectonic Evolution of the Sevier-Laramide Hinterland, Thrust Belt, and Foreland, and Postorogenic Slab Rollback (180–20 Ma), Geological Society of America, doi:10.1130/2021.2555(07).

Hoisch, T.D., Wells, M.L., and Hanson, L.M., 2002, Pressure-temperature paths from garnet-zoning: Evidence for multiple episodes of thrust burial in the hinterland of the Sevier orogenic belt: American Mineralogist, v. 87, p. 115–131, doi:10.2138/am-2002-0113.

Konstantinou, A., Strickland, A., Miller, E.L., and Wooden, J.P., 2012, Multistage Cenozoic extension of the Albion–Raft River–Grouse Creek metamorphic core complex: Geochronologic and stratigraphic constraints: Geosphere, v. 8, p. 1429–1466, doi:10.1130/GES00778.1.

Lewis, C.J., 1999, Deep burial of the footwall of the northern Snake Range decollement, Nevada: Geological Society of America Bulletin, p. 13.

Long, S.P., 2019, Geometry and magnitude of extension in the Basin and Range Province (39°N), Utah, Nevada, and California, USA: Constraints from a province-scale cross section: GSA Bulletin, v. 131, p. 99–119, doi:10.1130/B31974.1.

Long, S.P., 2012, Magnitudes and spatial patterns of erosional exhumation in the Sevier hinterland, eastern Nevada and western Utah, USA: Insights from a Paleogene paleogeologic map: Geosphere, v. 8, p. 881–901, doi:10.1130/GES00783.1.

MacCready, T., Snoke, A.W., Wright, J.E., and Howard, K.A., 1997, Mid-crustal flow during Tertiary extension in the Ruby Mountains core complex, Nevada: Geological Society of America Bulletin, v. 109, p. 1576–1594, doi:10.1130/0016-7606(1997)109<1576:MCFDTE>2.3.CO;2.

McGrew, A.J., Peters, M.T., and Wright, J.E., 2000, Thermobarometric constraints on the tectonothermal evolution of the East Humboldt Range metamorphic core complex, Nevada: Geological Society of America Bulletin, v. 112, p. 45–60, doi:10.1130/0016-7606(2000)112<45:TCOTTE>2.0.CO;2.

Miller, E.L., Dumitru, T.A., Brown, R.W., and Gans, P.B., 1999, Rapid Miocene slip on the Snake Range–Deep Creek Range fault system, east-central Nevada: Geological Society of America Bulletin, v. 111, p. 886–905, doi:10.1130/0016-7606(1999)111<0886:RMSOTS>2.3.CO;2.

Miller, E.L., and Gans, P.B., 1989, Cretaceous crustal structure and metamorphism in the hinterland of the Sevier thrust belt, western U.S. Cordillera: Geology, v. 17, p. 59–62, doi:10.1130/0091-7613(1989)017<0059:CCSAMI>2.3.CO;2.

Miller, E.L., Gans, P.B., and Garing, J., 1983, The Snake Range Décollement: An exhumed Mid-Tertiary ductile-brittle transition: Tectonics, v. 2, p. 239–263, doi:10.1029/TC002i003p00239.

Miller, D.M., and Hoisch, T.D., 1995, Jurassic tectonics of northeastern Nevada and northwestern Utah from the perspective of barometric studies, in Geological Society of America Special Papers, Geological Society of America, v. 299, p. 267–294, doi:10.1130/SPE299-p267.

Oldow, J.S., 1984, Evolution of a Late Mesozoic back-arc fold and thrust belt, Northwestern Great Basin, U.S.A.: Tectonophysics, v. 102, p. 245–274, doi:10.1016/0040-1951(84)90016-7.

Sonder, L.J., and Jones, C.H., 1999, WESTERN UNITED STATES EXTENSION: How the West was Widened: Annual Review of Earth and Planetary Sciences, v. 27, p. 417–462, doi:10.1146/annurev.earth.27.1.417.

Wells, M.L., Hoisch, T.D., Cruz-Uribe, A.M., and Vervoort, J.D., 2012, Geodynamics of synconvergent extension and tectonic mode switching: Constraints from the Sevier-Laramide orogen: Tectonics, v. 31, doi:10.1029/2011TC002913.

Wells, M.L., Snee, L.W., and Blythe, A.E., 2000, Dating of major normal fault systems using thermochronology: An example from the Raft River detachment, Basin and Range, western United States: Journal of Geophysical Research: Solid Earth, v. 105, p. 16303–16327, doi:10.1029/2000JB900094.

Wernicke, B., 1981, Low-angle normal faults in the Basin and Range Province: nappe tectonics in an extending orogen: Nature, v. 291, p. 645–648, doi:10.1038/291645a0.

Whitney, D.L., Teyssier, C., and Vanderhaeghe, O., 2004, Gneiss domes and crustal flow, in Gneiss Domes in Orogeny, Geological Society of America, doi:10.1130/0-8137-2380-9.15.

Wright, J.E., and Snoke, A.W., 1993, Tertiary magmatism and mylonitization in the Ruby-East Humboldt metamorphic core complex, northeastern Nevada: U-Pb geochronology and Sr, Nd, and Pb isotope geochemistry: Geological Society of

America Bulletin, v. 105, p. 935–952, doi:10.1130/0016-7606(1993)105<0935:TMAMIT>2.3.CO;2.

Yonkee, W.A., and Weil, A.B., 2015, Tectonic evolution of the Sevier and Laramide belts within the North American Cordillera orogenic system: Earth-Science Reviews, v. 150, p. 531–593, doi:10.1016/j.earscirev.2015.08.001.

Zuza, A.V., Henry, C.D., Dee, S., Thorman, C.H., and Heizler, M.T., 2021, Jurassic–Cenozoic tectonics of the Pequop Mountains, NE Nevada, in the North American Cordillera hinterland: Geosphere, doi:10.1130/GES02307.1.

Zuza, A.V., Levy, D.A., and Mulligan, S.R., 2022, Geologic field evidence for non-lithostatic overpressure recorded in the North American Cordillera hinterland, northeast Nevada: Geoscience Frontiers, v. 13, p. 101099, doi:10.1016/j.gsf.2020.10.006.

Zuza, A.V., Thorman, C.H., Henry, C.D., Levy, D.A., Dee, S., Long, S.P., Sandberg, C.A., and Soignard, E., 2020, Pulsed Mesozoic Deformation in the Cordilleran Hinterland and Evolution of the Nevadaplano: Insights from the Pequop Mountains, NE Nevada: Lithosphere, v. 2020, p. 8850336, doi:10.2113/2020/8850336.